LONG-TERM MECHANICAL PROPERTIES OF RUBBER

SHAMSUL BIN KAMARUDDIN

Doctor of Philosophy
Faculty of Engineering and the Environment
Maritime Engineering & Ship Science
University of Southampton

LONG-TERM MECHANICAL PROPERTIES OF RUBBER

THESIS

presented for the degree of

DOCTOR OF PHILOSOPHY in the

UNIVERSITY OF SOUTHAMPTON

by

SHAMSUL BIN KAMARUDDIN

Faculty of Engineering and the Environment
Maritime Engineering & Ship Science
University of Southampton
University Road Highfield, Southampton, SO17 1BJ
and
Tun Abdul Razak Research Centre
Brickendonbury, Hertford, SG13 8NL

October 2013

Long-Term Mechanical Properties of Rubber

SHAMSUL BIN KAMARUDDIN

Abstract

Natural rubber has a good potential to be used as a material for the development of wave energy converters (WECs). Generally, rubber has the ability to withstand very large strains without permanent deformation or fracture and is not much affected by exposure to water. This makes it ideal for applications related to wave energy converter (WECs). However, there is a need to predict the efficiency of performance over the full lifetime of such an application given that WECs will represent large, expensive and novel products that must remain operational in an at-sea environment for 10-15 years. Pertaining to that criterion, fracture mechanics of rubber is an important aspect as well as strain-history and environmental effects.

The objective of this study is to gain a fundamental understanding of several factors that contribute to service lifetime: the effect of ozone and oxidation, stress-strain behaviour including hysteresis, set, and cyclic stress relaxation, mechanical fatigue and the possible role of poorly dispersed filler agglomerates in nucleating failure. The work includes studies of the effect of protective coating layers and of naturally aged rubber artefacts using a mathematical model for diffusion limited oxidation. A literature review has been performed to address rubber science and associated technology, including, the durability of rubber. Experiments encompassing the effect of ozone, cyclic stress-strain behaviour and crack growth & fatigue of rubber were performed to interpret the relevant properties for the consideration of the development of wave energy converters. New parameters for characterizing macro dispersion in rubber are introduced in an attempt to seek a correlation with the life span of rubbers.

All these observations and outcomes give an opportunity to enhance our understanding of the factors that determine long-term mechanical properties of rubber, to the general benefit of rubber science and technology.

Acknowledgements

Declaration

I hereby declare that the work carried out and presented in this thesis submitted for the degree of Doctor Philosophy is original and my own. Any literature or figure not emerged from this original piece of work are referenced as such.

SHAMSUL BIN KAMARUDDIN

Table of Contents

Nomenclature

A	Helmholtz free energy (J) - Chapter 2
A, b, B	Constant value (dimensionless) based in equation for crack growth characteristic
c	Crack length (mm)
c_1	Crack to grow from length 1 (mm)
c_2	Crack to grow from length 2 (mm)
c_i	Effective initial flaw size (μm)
c_0	Flaw size corresponding to $T=T_o$ (μm)
C	An arbitrary constant (dimensionless) - Chapter 2
C	Oxygen concentration (dimensionless) - Chapter 3 & 9
$C_{10}, C_{20}, C_{30}, C_{ij}$	Hyperelastic material constants (dimensionless)
dc	Increment in crack length (mm)
$\dfrac{dc}{dn}$	Cyclic crack growth rate (mm/cycle)
dU_e	Increment in total elastic energy (J)
D	Diffusion co-efficient (dimensionless)
D_0	Constant prefactor for Arrehenius expression for diffusion coefficient
ΔD_ε	Ratio of carriage throw to dumb-bell strain range (mm)
E	Crosslinking efficiency - ratio of sulfur and CBS (dimensionless)
E	Energy of activation for diffusion (kJ mol^{-1}) - Chapter 9
F	Nominal stress (N)
F	Force applied (N)
F_A, F_B	Forces applied to respective pairs of legs (N)
G	Shear modulus (MPa)
h	Height of test piece (mm)
h_o	Unstrained value of the height (mm)
H	Thickness (mm)
I	Light intensity (W/m^2)
I_m	Limiting value of I_1 (dimensionless)
I_1, I_2, I_3	Basic strain invariants (dimensionless) defined in Equation (2.14)
k	Boltzman constant (J^{o}K^{-1}) - Chapter 2
k	Function of strain (dimensionless) - Chapter 3
K	Coefficient of absorption (dimensionless)
L	Effective length of freely jointed links (mm)
L	Total thickness (mm) - Chapter 9
M	Amount reacted of oxygen per unit volume (kg.m^{-3})
N	Number of network chain per volume (MPaK^{-1}) - Chapter 2
N, n	Number of cycle (cycle)
N_c	Crosslink chain (dimensionless)
N_s	Entangled chain (dimensionless)
Q	Fractional concentration of ozone (pphm)

r	End-end length (m)
r	Rate of consumption of oxygen by chemical reaction (dimensionless)
r_A, r_B	Material constant (μm.cycle^{-1})
r_A	Linear region crack growth rate constant (μm.cycle^{-1})
r_t	Rate of tearing (μm.cycle^{-1})
r_z	Rate of ozone induced crack growth (μm.cycle^{-1})
s	Entropy of the individual chains (J^{o}K^{-1})
ΔS	Entropy change (J^{o}K^{-1})
S_o	Total entropy (J^{o}K^{-1})
S_c	Number of sulfur combinations in the monomer network
h	Rubber sheet thickness (mm)
T	Tearing energy (kJm^{-2})
T	Absolute temperature (^{o}K)
T$_g$	Glass transition temperature (^{o}C)
T_o	Threshold tearing energy (kJm^{-2})
t_c	Fraction of time in each cycle (s)
T_t	Transition Tearing energy (kJm^{-2}) at transition from linear to power law cyclic crack growth characteristics
T_c	Catastrophic tearing energy (kJm^{-2})
T_z	Ozone threshold tearing energy (kJm^{-2})
U	Internal energy (J)
U	Total strain energy (J)
W	Work of deformation for a unit volume (Jm^{-3}) - Chapter 2
W	Strain energy density (MJm^{-3}) - Chapter 3
W_A, W_B	Energy densities (MJm^{-3})
w	Test piece width (mm)
A	Extensibility (dimensionless)- Chapter 2 & 5, Appendix A
A	Dimensionless reaction rate - Chapter 9
α_s	Angle of opening (^{o}) for angled test piece - Chapter 2
α_p	Material constant (dimensionless)
B	Modifier to dimensionless rate - Chapter 9
γ	Surface energy (J/m^2) - Chapter 2
γ	Shear strain (%)
ε	Strain (dimensionless)
ζ	Volumetric thermal expansion co-efficient
η	Slippage (dimensionless) – Chapter 2 & 5
λ_A, λ_B	Extension ratios (dimensionless) for split testpiece
$\lambda_1, \lambda_2, \lambda_3$	Three principal extension ratios (dimensionless)
λ	Extension ratio (dimensionless)

μ_p	Material constant (dimensionless) in Ogden hyperelastic model
ρ_s	Dimensionless reaction rate at the surface
ρ_{ss}	Steady state dimensionless oxidation rate
ρ_z	Material constant (μm.s^{-1})
σ	True stress (MPa) - Chapter 2
σ_T	True stress (MPa) in tension
σ_C	True stress (MPa) in compression
ϕ	Diameter (mm) - Chapter 9
Φ	Volume fraction of black
τ	Shear stress (MPa)
ψ	Fraction of enthalpy of crystallization per unit volume - Chapter 5
Ω	Angle (^{o}) for split testpiece
$2M_{c,chem}$	Number of 'moles' of chemical crosslinks per g.rubber hydrocarbon

Abbreviations and Acronyms

BR	Polybutadiene rubber
CBS	N-cyclohexylbenzothiazole-2-sulphenamide
CCD	Charged Coupled Device
EDS	Engineering Data Sheet
EPDM	Ethylene-propylene rubber
EU	European Union
EV	Efficient Vulcanisation
FTIR	Fourier Transform Infrared Spectrometer
HAF	High Abrasion Furnace
HPC	High Performance Coating
HPPD	N-(1,3-dimethylbutyl)-N'-phenyl-p-phenylendiamine
LVDT	Linear Variable Differential Transformer
IMO	International Maritime Organisation
IR	Polyisoprene rubber
IIR	Butyl rubber
MT	Medium Thermal
MRPRA	Malaysian Rubber Producers' Research Association
NR	Natural Rubber
NBR	Acrylonitrile-butadiene rubber
PBN	Phenyl-β-naphthylamine
ppm	parts per million
pphm	parts per hundred million
pphr	parts per hundred of rubber
SBR	Styrene-butadiene rubber
SEM	Scanning Electron Microscope
SMR CV60	Standard Malaysian Rubber Constant Viscosity at 60 Mooney unit
TARRC	Tun Abdul Razak Research Centre
TGA	Thermo Gravimetric Analysis
TMQ	Polymerized 2,2,4-trimethyl-1,2-dihydroquinoline
UV	Ultraviolet
WECs	Wave Energy Converters

Chapter 1

Introduction

The focus of this thesis is to probe more deeply issues raised in a review of Natural Rubber (NR) in the Marine Environment (Muhr 2013) relating to the longevity of rubber components subjected to such arduous service conditions. The choice of environment and service conditions is motivated by the expanding interest in offshore energy harvesting, whether fossil fuel, wave, tidal stream or wind.

Understanding the factors that affect the mechanical properties of rubber is essential for the development of a rubber based wave energy converter (WEC). A qualitative understanding of these factors is required in order to develop durable rubber compounds which can be used for the wave energy converter. The ability of rubber to withstand very large strains without failure or permanent deformation is the primary consideration making it attractive for playing a key role in a wave energy converter (e.g. Archimedes wave swing, Aquabuoy, Anaconda, Duck, Clam).

In this thesis, several potential factors such as stress-strain behaviour, fatigue life of rubber and the ageing process have been addressed together with an extensive experimental programme to provide some insight regarding advantageous rubber compounds appropriate to the development of rubber based devices offshore.

1.1 Background – Wave Energy Conversion

Wave energy exploitation is not currently economically competitive with the more mature energy generation technologies, although studies within the European Union (CRES 2002) indicate both governmental and industry based interest are steadily increasing. Coupled to this, within the marine environment is the International Maritime Organisation (IMO) requirement to significantly reduce sulfur and other detrimental substances emission from all ships at sea. These requirements are becoming more stringent each year from 2012 (http://www.imo.org/blast/mainframe.asp?topic_id=233).

The idea of converting the energy of ocean surface waves into useful energy forms is not new. There are patents as early as 1799 (Girard & son 1799). A more recent implemented concept is that of Yoshio Masuda (1950's) in the context of Japanese navigation buoy lighting (http://e.wikipedia.org/wiki/Yoshio_Masuda). Wave energy extraction has recently become one of the priorities in the development of environmental friendly devices. According to Professors Rod Rainey and Francis Farley their proposed

Anaconda wave energy converter (WEC), is a cost effective wave energy device. The device seeks to exploit the concept of a distensible rubber tube. Filled with water, it is positioned just below the surface of the sea and tethered to the seabed. As each wave external incident travels over the pressurized tube, a pulse is created in the internal water. This pulse (bulge wave) is a means of energy transport down the tube, increasing the pressure as it goes, and ultimately powering a turbine in the 'tail' of the tube to generate electricity (Farley et al. 2006a, 2006b).

The concept of Anaconda has been proven at small laboratory scale and is seen as having low capital and operational costs (Valentin & Chaplin 2011, Chaplin et al. 2007a & 2007b).

It was estimated that about 200 tonne of rubber will be used to manufacture the actual scale of Anaconda where the wall thickness of rubber is about 28mm (Bucchi & Hearn 2013). It would probably to be the largest man-made rubber structure ever assembled. The rubber will be subjected to millions of waves per year and yet its functionality and integrity must remain.

Wave energy is generally considered to provide a clean source of renewable energy, with limited negative environmental impacts. In particular, wave power is seen as a large source of energy not involving large CO_2 emission. There will of course be some environmental damaging bi-products in the manufacturing of the rubber tube. However, this should be compensated by increasing the percentage of total energy required in any country by zero emission production procedures. Wave energy converters have the potential to reduce United Kingdom (UK) CO_2 emissions (perhaps by millions of tonnes) and hence contributing to the UK Government target of reducing emissions by 34% by 2020 (http://www.direct.gov.uk/en/Nl1/Newsroom/DG_179190). Typical farms of fifty 1MW devices could create enough electricity to fuel 50,000 homes with an average energy consumption rate of 0.5kW assuming that the average power output is 50% of the rated value of the device.

NR is expected to be the most appropriate choice of rubber, both because of its unsurpassed resistance to mechanical fatigue and because it is a sustainable material, not dependent on fossil organics or energy-consuming chemical synthesis.

1.2 Motivation

The present study was motivated by the challenge of developing large novel rubber-based devices for arduous service conditions in a marine environment. A new study of rubber properties is highly desirable, focusing on durability, with the aim of generating sufficient scientific insight to provide a predictive capability.

Generally, natural rubber can withstand very large strains without permanent deformation or fracture, and is relatively unaffected by the marine environment in terms of chemical or biological attack or pressurization due to depth (Muhr 2011), making it ideal for such applications. Economic viability will depend on output of energy, cost of manufacture and durability. To date there is insufficient relevant data in the open literature to enable the lifetime to be estimated with requisite confidence to establish the economic viability of several novel devices in the marine environment.

While many factors contribute to long-term durability, mechanical fatigue is the primary consideration, followed by the environmental effects. Hence there is a need to appreciate how the materials selected can influence both the efficiency of energy excitation and the service life given the device will represent a large, expensive and novel product. To be economically viable, even in the favourable regulatory climate being created by the EU for renewable energy, a first estimate of the necessary lifetime of a wave energy converter (WEC) might be considered to be 10 years. WECs are typically designed to operate at full rated power for about 30% of the time and undergo deformation cycles of mean period 10 seconds (a typical incident wave). Hence they experience of the order 10^7 cycles at full-power operation in about 10 years (Chaplin et al. 2007b). Therefore a major issue development must be the lifetime of the rubber subjected to any installed strain and dynamic induced variations of the strain due to wave excitation. The strain (and hence stress) experienced over a lifetime will be large and time varying. A reliable assessment of longevity is thus crucial. Progressive changes to the material properties caused by in-service ageing could lead to de-tuning, and hence inefficient performance, or to a reduced fatigue resistance.

Mathematical models are being developed to simulate the behaviour of rubber products, but such tools require a realistic and comprehensive description of material behaviour. It is known that computer simulation tools for predicting mechanical fatigue life are not presently available for routine design, despite the fact that fatigue testing can be the most expensive aspect of testing. Such tools have been developed for other materials, metal in particular. These are invariably ill-suited to rubber applications, due to highly

deformable and non-linear nature of rubber and its distinct mechanical failure characteristics.

Whilst earlier statements might imply environment is secondary to mechanical fatigue, partial and intermittent exposure of rubber to water and to the atmosphere could become an issue. Environmental cracking from atmospheric ozone can give rise to initiating flaws leading to fatigue. Oxygen attack may not only degrade the strength of the rubber, but also modify its elastic properties, possibly detuning it from the preferred design parameters.

1.3 Aims and Objectives

The principal aim of the reported research is to understand the long-term mechanical properties of rubber products. In particular, to identify an appropriate formulation of the rubber for the wave energy extraction device and to characterise its pertinent behaviour. Here rubber selection is also about constituents included or excluded, and the investigation should provide some insight regarding behaviour of different recipes (often designated 'formulation'). Several papers [e.g. Cadwell et al. (1940), Lake et al. (1966), Gent et al. (1964) and Mars et al. (2006b)] have reported the fatigue behaviour of typical rubbers subjected to selected stress regimes. However, there is less data quantifying effect of adjustments to the formulations or to the stress-strain conditions. Such insight is paramount to the optimization of the choice of material to provide design to maximize longevity. Thus new more extensive enquiry is necessary to quantify fatigue life and optimise material formulation for the particular stress-strain regime likely to be encountered. Additionally, such investigations provide the opportunity to enhance our understanding of the factors that determine fatigue life of rubber. Thus could be of a more general benefit to rubber science and technology.

The specific objectives of this research programme were:

(i) To quantify and build a good understanding of the range of stress-strain behaviour exhibited by different rubbers. In particular, the effect of strain rate, time and strain history on the stress-strain behaviour and the extent of hysteresis is addressed.

(ii) To provide further insight and experimental capability into fatigue of rubber. This includes the interpretation of fatigue data using crack growth

characteristics and energy release rate calculations and investigation of possible factors responsible for fatigue crack initiation. In particular, to investigate dispersion of fillers, surface cracks caused by ozone attack and the influence of hard surface layers and benefits (or otherwise) of coatings.

(iii) To evaluate the effects of oxygen, ozone and UV light upon the ageing of natural rubber in the marine environment. Prediction of the effects on stress-strain and strength properties of in-service conditions over at least 10 years of operation would be desirable.

(iv) To develop a mathematical model of diffusion-limited oxidation. Given oxidative ageing of rubber leads to changes in physical and mechanical properties, the developed model is intended to predict changes as a function of distance from the outer material surface. The depth of UV penetration into the rubbers will be considered in terms of contribution to inhomogeneous ageing.

1.4 Programme of New Work and Its Originality

The areas singled out for investigation are:

(i) *The effect of the proposed cyclic strain on the stress-strain properties of the rubber.*

The softening effect of a few large strain cycles on rubber is well known, However, there is little reporting of investigations based on a very large number of strain cycles with the unusual feature of incomplete relaxation. In this research, these are a large number of cycles at strains much greater than previously investigated.

(ii) *Fatigue life statistics under the proposed duty cycles.*

Apart from the data of Cadwell et al. (1940) and the Engineering Data Sheets (EDS) (Natural Rubber EDS 1979) there is no comprehensive data on fatigue properties of natural rubber under strain cycle levels relevant to arduous non-relaxing cycles. Only the data of Cadwell et al. (1940) extends to the full life time; in the EDS, fatigue tests were aborted at 2Mcycles. As well as being

limited to a single material, the data of Cadwell et al. (1940) gives no information on the range or standard deviation of the replicate tests, as would be required in any estimation of the number of expected failings over a preferred operational period of any rubber component. As in (i), scientific insight will be sought. A fracture mechanics interpretation of the fatigue results is used, together with consideration of the initiation of the cracks by mechanisms such as ozone cracking.

Such interpretations are not possible for the data of Cadwell et al. (1940), since they provided no information on stress-strain properties or ozone resistance of the rubber, nor any indication of the ambient ozone levels during the fatigue tests.

To facilitate investigation of the role of ozone, a novel ozone-free chamber has been built to enclose the multi-sample fatigue testing facility.

(iii)   *Sea environmental effects on rubber.*

There is little work in the open literature on the effect of ozone on submerged rubber, although a theory developed at TARRC (Lake & Thomas 1967a) predicts that water will have a strong mitigating effect. The interaction of UV light, oxygen and leaching of antioxidants by surrounding sea water is another area in which there is little published scientific work. These influences are considered here, and an indication given of future work to provide greater insight into outstanding issues.

1.5 Overview of Thesis

Whilst not explicitly dividing the dissertation into distinct parts, we may think of grouping the chapters to reflect different stages of the research.

The initial part consists of reviewing rubber science & technology and then rubber durability through Chapters 2 and 3 respectively. These reviews help identify pertinent challenges for artefacts to be exposed to the dynamics of the atmosphere - ocean interface. The relevant challenges for a device exploiting the benefit for natural rubber of non-relaxing conditions on fatigue life is addressed in Chapter 4 through Chapter 7. The dissertation relates to the identification of a durable rubber capable of meeting dynamic responsiveness to water wave excitation i.e. undergoing continuously cyclic loading. This section therefore investigates experimentally the influence of ozone exposure, filler impact

on stress-strain behaviour compared to unfilled rubbers, the influence of carbon black dispersion upon fatigue characteristics and concludes with an investigation of crack growth on both filled and unfilled rubbers.

The third section, through Chapters 8 and 9, addresses ageing of natural rubber. Two approaches of mitigation are also addressed: the use of antidegradants incorporated in the formulation, and the use of a surface coating. The impact of surface coatings on rubber fatigue recognises that uncoated test pieces were examined in the earlier experimental investigations. Thereafter additional testing seeks insight concerning possible changes in behaviour, due to materials becoming aged, through examination of the rubber characteristics of existing well-known aged artefacts at different depths from their outer surface. A mathematical model is used to provide further insight into diffusion limited oxidation and the effect of antidegradants on it.

The conclusions and closure, in Chapter 10, bring together the principal findings, observations and suggestions for future work.

Chapter 2

A Review: The Science and Technology of Rubber - Chemical and Physical Characteristics

Introduction

This chapter introduces natural rubber and addresses some of the more common synthetic rubbers prior to considering the process of rubber vulcanization and the resulting change in characteristic properties. When creating rubbers with difficult or preferential characteristics fillers are often introduced; they require quality checks for uniformity of dispersion throughout the rubber. How this is monitored is explained prior to looking at the ingredients in a rubber formulation. Since rubber is an extensible material stress-strain behaviour is addressed from different perspectives, theoretical, statistical and phenomenological prior to summarizing the principal factors presented.

2.1 Natural Rubber (NR)

Natural rubber is a versatile and adaptable material with 150 years of successful engineering applications. It is able to withstand large strains (up to 750%) and consequently stores more elastic energy per unit volume than steel. Furthermore, it is a hydrocarbon polymer with a small percentage of impurities, <0.5%, and a very high molecule weight. NR is made up of long chains of a repeating unit referred to as a monomer. The molecular chains are flexible at ambient temperatures and readily return to their original shape after deformation, especially when chemically cross linked. Latex, a fluid produced by many plants, is the untreated natural material used to form natural rubber, consisting of an emulsion of polymer droplets suspended in aqueous serum. Chemically, natural rubber is a polymer of the monomer isoprene (Figure 2.1), each long chain having around 10^4 monomer units. The chief source of crude rubber is the tree *Hevea brasiliensis* (of the Euphorbiaceace family). The plants gutta percha and balata (of the Sapotaceae family) also provide material related to rubber.

Before providing examples of different rubbers it is helpful to appreciate the implicit coding associated with different polymers. The notation used for organic molecules is built on numbering the carbon atoms in the molecular backbone from left to right. For example, the 2-methyl-1,3-butadiene structure of Figure 2.1 has the methyl group occurring at carbon atom 2 and the double bond occurring at carbon atoms 1 and 3. Butadiene is one of the most common constituents used in synthetic rubber.

methyl

C 2

C 1

C 3

C 4
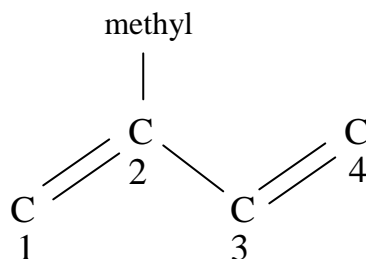
Figure 2.1: Chemical structure of isoprene (2-methyl-1,3-butadiene).

"1,3-butadiene" implies that the double bonds are located at C atoms 1 and 3,

(b) *cis* polyisoprene (natural rubber); CH_2 same side (*cis*)

(a) *trans* polyisoprene (gutta percha); CH_2 opposite side (*trans*)
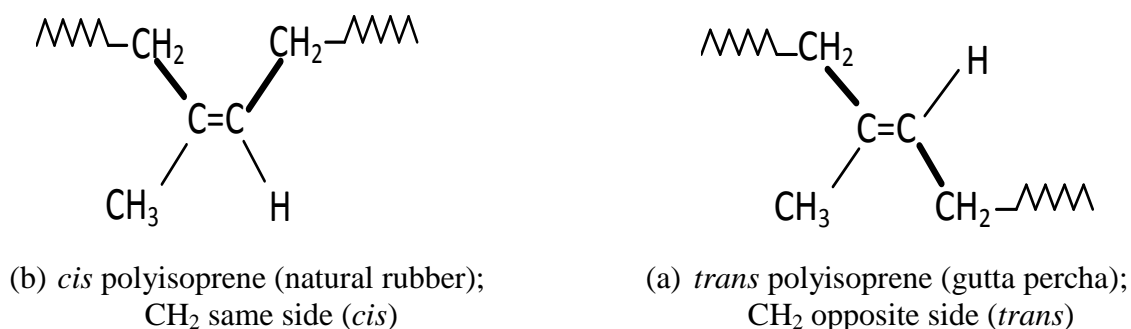
Figure 2.2: Chemical structure of polyisoprene.

The variation of the monomer associated with Hevea latex and gutta percha are illustrated in Figure 2.2. The Latin prefixes *cis* and *trans* specify the form of the C=C double bonds in the long chain backbone.

Figure 2.3 illustrates the chemical reaction of 1,3 butadiene monomers to form a polybutadiene polymer in particular 1,2-addition and cis- and trans- 1,4-addition of the monomer.
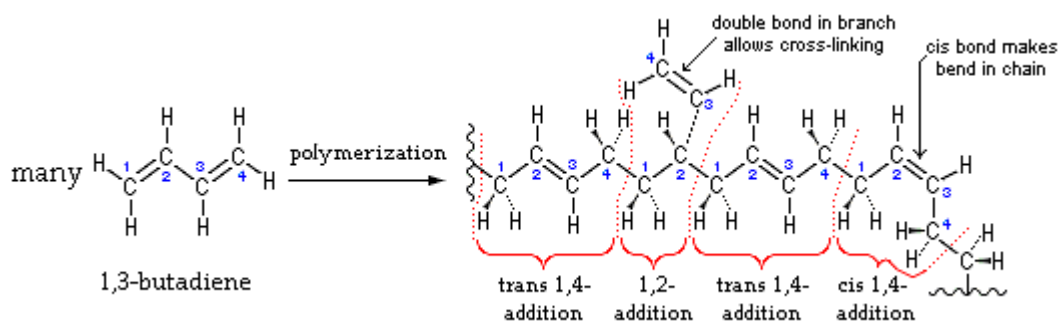
Figure 2.3: Chemical reaction diagram of 1,3 butadiene polymerization.
Again the prefix *cis* and *trans* indicaties relative position of common atom arrangements.

2.2 Synthetic Rubber

Synthetic rubber can be manufactured using polymerization. Some common synthetic rubbers are polymers of isoprene, chloroprene and isobutylene; for the latter using a small percentage of isoprene is used to enable crosslinking. Isoprene has the structure 2-methyl-1,3-butadiene as explained previously when discussing Figure 2.1. Chloroprene has the structure 2-chloro-1,3-butadiene, whereas isobutylene is 2-methylprop-1-ene. These monomers can be mixed in various desirable proportions to give copolymers with a wide range of physical, mechanical, and chemical properties. The monomers produced can be pure, whereas the addition of impurities or additives can be controlled by design to give optimal properties. Polymerization of pure monomers can be controlled to achieve a desired proportion of *cis* and *trans* double bonds.

Examples of synthetic rubbers used in rubber products are discussed next to indicate possible variations of their principle behavioural characteristics.

2.2.1 Styrene-Butadiene Rubber (SBR)

Styrene-butadiene rubber (SBR) is the most widely used general purpose rubber. SBR is a random copolymer of styrene and butadiene as illustrated in Figure 2.4.
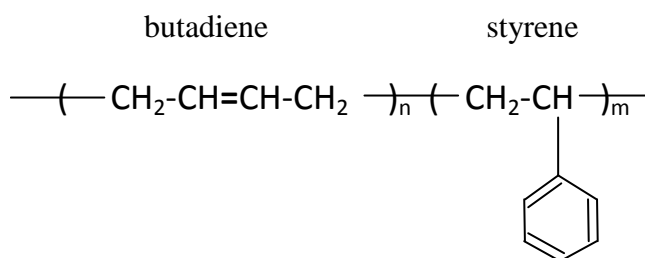
Figure 2.4 : Chemical structure of styrene-butadiene rubber (SBR). Left, butadiene unit, right, styrene unit. n and m vary randomly along the chain, but, as indicated, a degree of "blockiness" can occur.

It is synthesized via free radical emulsion polymerization or generated anionically in solution (by electrolysis). The most commonly used SBR consists of 23.5% styrene and 76.5% butadiene, and has a "glass transition" temperature, T_g, of approximately $-55^{o}C$ (Hamed 1992). SBR is an essentially non strain-crystallising rubber, because the molecules are not stereoregular. This feature results in significant differences between the mechanical properties of NR (a strain crystallising rubber) and SBR. Since SBR has both low tensile and low tear strength it is necessary to reinforce it with fillers such as carbon black to impart useful engineering properties. It is common practice to blend SBR with other rubbers to improve many of its basic properties.

2.2.2 Polyisoprene Rubber (IR)

Polyisoprene rubber (IR) is produced both anionically and by Ziegler-Natta or emulsion polymerization (Hamed 1992). IR is a synthetic rubber equivalent to NR with a similar chemical structure, except for a somewhat lower *cis*-content of between 94% to 98% of *cis*-1,4-polyisoprene and 6% to 2% of *trans*-1,4-polyisoprene (Blow and Hepburn 1982). Although both NR and IR are well known as strain-crystallising rubbers, the lower *cis* content of IR coupled with a lower concentration of effective nucleants for crystallization results in reduced capability to crystallize, so, the strength properties of IR tend to be inferior to those of NR. The lower content of impurities gives synthetic IR lower creep and stress relaxation than NR. Under large strains these rubbers exhibit extremely high strengths and fatigue resistance, with IR compounds having a lower modulus at high strain and higher elongation than similarly formulated NR compositions due to a reduction

in the strain-induced crystallization. This characteristic is particularly true at high rates of deformation.

2.2.3 Polybutadiene Rubber (BR)

BR is a homopolymer of 1,3-butadiene (C_4H_6); variation in the polymer structure are shown in Figure 2.3. BR can be made by either solution or emulsion polymerisation. It is a non-polar rubber like NR and SBR, with one of the lowest glass transition temperatures approaching -100°C (Hamed 1992). The 1,4-polybutadiene is an approximately equal mix of *cis* and *trans* repeating units. Figure 2.5 illustrates the structure of repeating units. Because of the regularity of its structure high *cis* 1-4 BR has a tendency to crystallise, although occurrence does depend upon the amount of *cis* and *trans* monomers present (Blow and Hepburn 1982).

$$—(— CH_2\text{-}CH=CH\text{-}CH_2 —)_n—$$
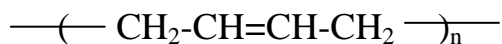
Figure 2.5 : Chemical structure of polybutadiene rubber (BR).

1,2 polybutadiene (vinyl BR) is also commercially available, but is less commonly used. BR is a very high resilience rubber commonly used in combination with NR and SBR in the production of long life rubber tyre treads.

Having introduced natural and synthetic rubbers, we next consider their production and vulcanization.

2.3 Impact of Vulcanization on Rubber Characteristics

Chemical crosslinks between macromolecules may occur in polymerization or in fabricating articles, resulting in polymers with network structures. The reaction during fabrication is known as "vulcanization" in the rubber industry, and "curing" or "hardening" in the plastics industry. The product is termed a "vulcanizate" in the rubber industry, and designated "thermoset" – as opposed to a thermoplastic – in the plastic industry. Crosslinks between unsaturated hyrocarbon long chain molecules are usually formed using sulfur as a "vulcanization agent" in the reaction. Charles Goodyear (1800-1860) discovered sulfur vulcanization of rubber in 1839. The process was refined and commercially exploited soon afterwards by Thomas Hancock (1786-1865) and others, and many new industrial applications for rubber were rapidly developed. Typical crosslinks formed in rubber

vulcanization consist of short chains of sulfur atoms linking the long chain molecules. The length of the short sulfur chains is greater when the concentration of accelerator (e.g. CBS) is low. The existence of crosslinks inhibit flow so that the resulting network retains the shape of mould. Since the crosslinks are thermally relatively stable, the formed and vulcanized rubber is regarded as a thermoset.

Figure 2.6 demostrates the various types of chemical groupings present in sulfur vulcanizates of natural rubber.
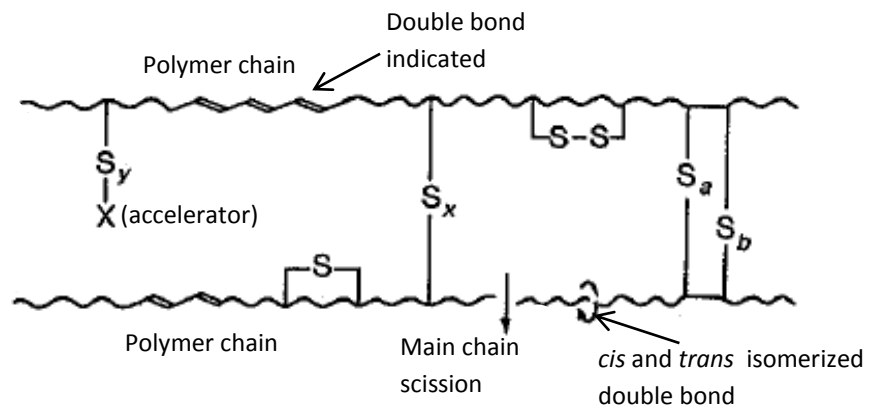
Figure 2.6: Networks structure of sulfur vulcanizate with different forms of crosslink. S_a, S_b, S_x and S_y indicate number of S molecules in linkage, with (a, b, x, y) ∈ (1, 2,…., 9) (Chapman and Porter 1988).

Not all the groupings illustrated are present in every case. The relative concentrations of each may vary widely, depending particularly on the molar ratio of accelerator to sulfur used, the concentration of activators (such as ZnO) and the time and temperature of Vulcanization. The number of vulcanizate structures produced in the production process is unlimited and hence so is the range of vulcanizing systems. Determination of the number of sulfur combinations in the network (S_c) and the number of physically-effective chemical crosslinks present ($[2M_{c,\text{chem}}]^{-1}$) yields an inverse measure E of the crosslinking efficiency of sulfur:

$$E = \frac{S_C}{[2M_{c,chem}]^{-1}} \tag{2.1}$$

where S_c is g.atoms of sulfur per g.rubber hydrocarbon in the network and $[2M_{c,chem}]^{-1}$ is the number of 'moles' of chemical crosslink per g.rubber hydrocarbon in the network. Thus the E is number of sulfur atoms combined in the network per chemical crosslink present. This gives an overall indication of the structural complexity of the network (Moore 1965). Values of E have been found to vary between 2 and 100 or more. High E

vulcanizing systems have very low accelerator:sulfur ratios (including unaccelerated sulfur systems) whereas low *E* vulcanizing systems have very high ratios of accelerator:sulfur. The latter case may also include systems in which sulfur donors replace elemental sulfur (Efficient Vulcanization (EV) systems). Most vulcanizing systems occupy positions between these extremes as the classifications within Table 2.1 illustrate.

Table 2.1: Classification of sufur vulcanizing systems.

Class	Sulfur concentration (p.p.h.r.)	Accelerator concentration (p.p.h.r)	Approximate range of crosslinking efficiency, E
EV	0.3 - 1.0	6.0 - 2.5	1.5 - 4.0
Semi-EV	1.0 - 2.0	2.5 - 1.0	4.0 - 8.0
Conventional	2.0 - 3.5	1.0 - 0.5	10.0 - 25.0
Very inefficient	3.5 - 10.0	0.5 - 0.0	25.0 - 100.0

In the initial stages of vulcanization all these systems are believed to give rather similar networks with relatively few crosslinks and the accelerator - terminated pendant groups are disulphidic or polysulphidic as shown in Figure 2.7.
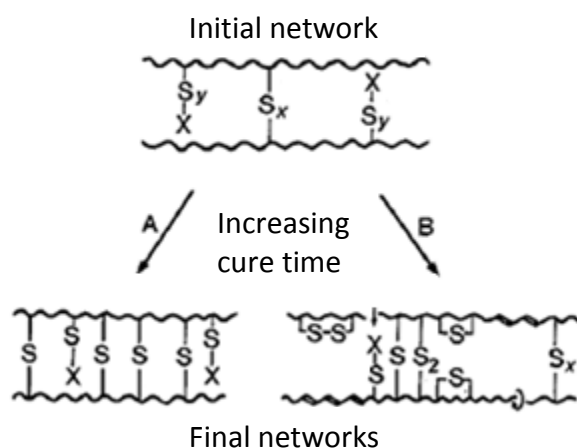
Figure 2.7: Dependence of network structure on vulcanizing system. (A) high accelerator: sulfur ratio (or sulfur donor/accelerator system) and high soluble zinc concentration; (B) low accelerator: sulfur ratio or low soluble zinc concentration. The symbols used are consistent with those in Figure 2.5 (Chapman and Porter 1988).

The disparity in the final networks in Figure 2.7 increases progressively as the cure time is increased. An EV system (A) eventually forms simple networks in which the crosslinks are exclusively monosulphidic with a high concentration of monosulphidic pendant groups. The networks from conventional more inefficient systems (B) become increasingly complex, containing mixtures of mono-, di-, and polysulphidic crosslinks. The rubber chains become more and more modified with olefinic and sulfur-containing groups. These

changes in structure are accompanied by corresponding changes in physical properties (Chapman and Porter 1988). Accelerated sulfur curing is more efficient when the activators zinc oxide and stearic acid are added. It is thought that these combine to create soluble zinc ions that activate the intermediate reactions involved in crosslink formation.

A common instrument used to determine the kinetics of crossslinking is the oscillating disk rheometer. An oscillating rotor surrounded by the test compound is enclosed in a heated chamber. The torque required to oscillate the rotor is monitored as a function of time. As the test piece of elastomer stiffens the torque rises. Chain scission may also occur. However, an increasing torque indicates that crosslinking is dominant. Figure 2.8 shows the types of cure curve found in practice.
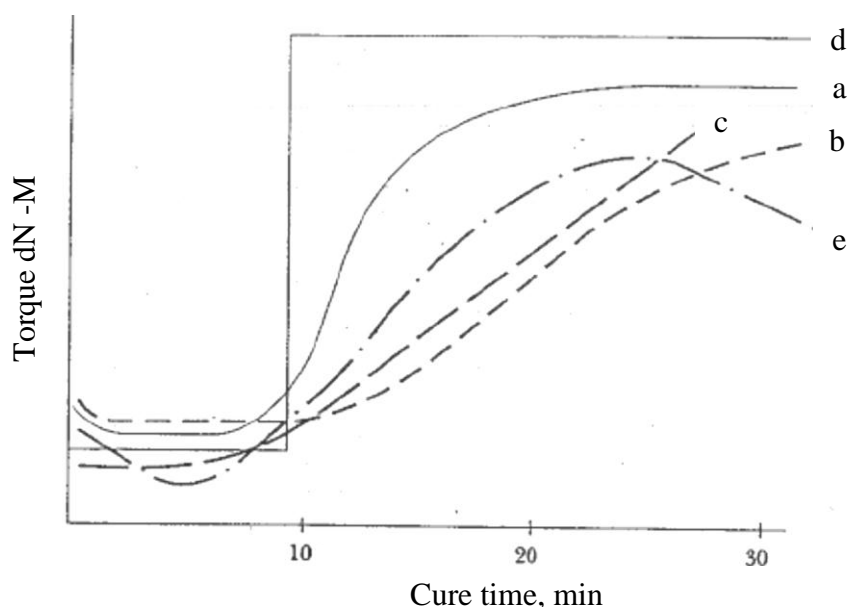
Figure 2.8: Types of cure curve (a) Short reaction time (high rate of cure to equilibrium torque) (b) Long reaction time (slow rate of cure to equilibrium torque) (c) Marching modulus (no maximum torque) (d) Ideal plot and (e) Cure to maximun torque with reversion (Kempermann 1988).

A plateau torque indicates completion of curing and good network stability. If chain scission becomes dominant during heating, torque decreases. This is termed reversion. Some natural rubber compounds, particularly at high curing temperatures, exhibit reversion. On the other hand, some compounds show a slowly increasing torque at long cure times, or creeping cure. This behaviour often occurs in compounds that initially form many polysulphidic linkages. With extended cure times, these linkages may break down and reform into linkages of lower sulfur rank, thereby increasing the total number of crosslinks (Hamed 1992).

To a large degree the crosslink density determines the physical properties of rubber (Treloar 1975). Higher crosslink density is associated with increased stiffness and reduced hysteresis. An optimum crosslink density results in the longest fatigue life. Hamed (1983) demonstrated that the peak in the fatigue life curve appears to be attributable to the competing effects of strengthening due to an increased number of crosslinks and the decreasing ability of the elastomer to dissipate energy through hysteresis. The type of crosslink formed during vulcanization has an effect on fatigue properties. Polysulfidic crosslinks appear to be superior to monosulfidic or direct carbon-carbon (peroxide cure) crosslinks. The superiority of polysulfidic crosslinks is attributed to the ability of the crosslink to break before the elastomer fails (Brown, Porter & Thomas 1985).

The effect of crosslink density on the physical properties of the vulcanizate, are summarized schematically in Figure 2.9. As the crosslink density increases, modulus, hardness, resilience, abrasion resistance and fatigue resistence all increase whereas elongation at break, heat build-up, solvent swelling, creep, set, and rate of low temperature crystallization all decrease. Tensile strength and tear strength first increase, then decrease with increased crosslinking. Tear strength, fatigue life and toughness are related to the stored energy into the rubber when failure occurs (Loganathan 2000).
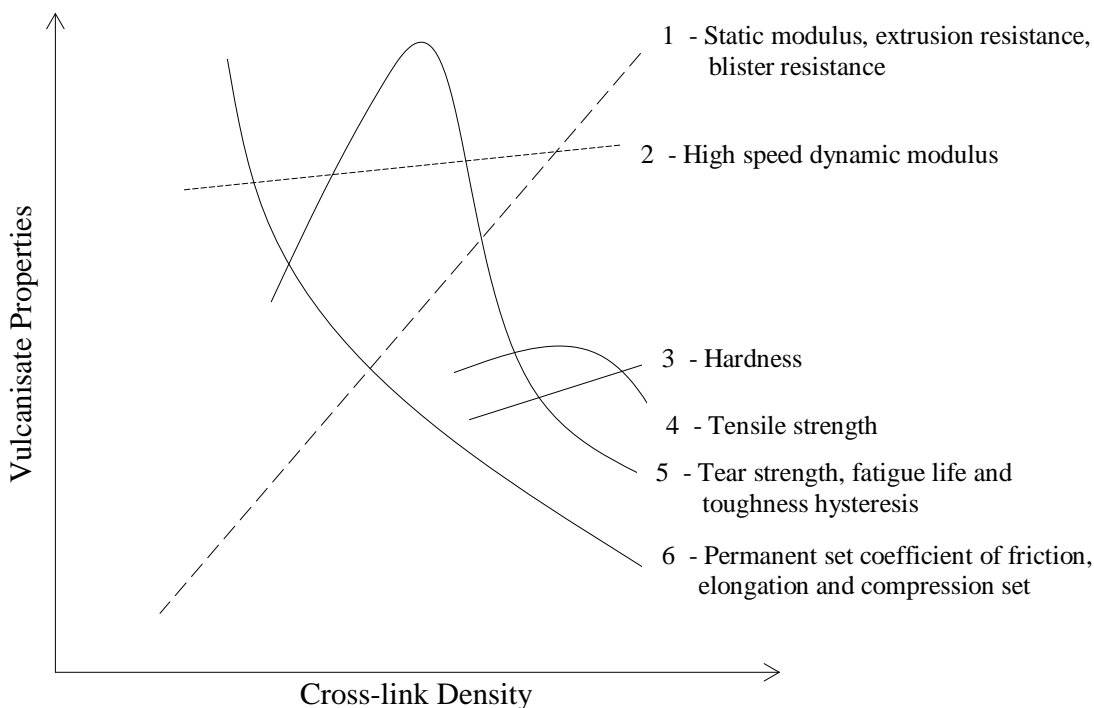
Figure 2.9: Property changes in vulcanization (Garvey 1965).

2.4 Material Properties of Vulcanized Rubber

Rubbers have the all-round ability to be used in extension, compression, shear, torsion or combinations of these deformations. Rubber may be considered as very deformable with almost complete recovery when loads are removed. Rubbers are resilient, that is, a high proportion of the energy of deformation is 'recovered' on unloading, giving rubber its bounce. Rubbers are characterized by high levels of elongation at failure. Owing to the small atomic masses of carbon, oxygen and hydrogen and inefficient packing due to random chain configurations and thermal motion, rubber densities are low compared with metals. Rubbers dissolve only slowly in appropriate solvents. The resultant solutions have high viscosities even at low concentrations. The penetration of small solvent molecules between tangled polymer chains is time and temperature dependent. The resistance to flow, offered by the coiling and tangling of chains, determine the viscosity of the polymer. Rubber has both viscous and elastic responses to deformation. The viscous stress is proportional to the rate of deformation, whilst the elastic stress is proportional to the extent of the deformation. The behaviour is designated viscoelastic. This viscoelastic characteristic is observed in the following forms:

(i) *creep*, i.e. increase in deformation over time after a fixed stress is applied;

(ii) *stress relaxation*, i.e. reduction in stress over time when a rubber vulcanizate is held at a constant strain;

(iii) *set* or *residual deformation* occurs after removal of a distorting load;

(iv) a *phase lag* between an applied oscillating stress and the resulting strain;

(v) when material vibrated, rubbers become stiffer with a *dynamic modulus* which is higher than the *static modulus*.

Rubber is a poor conductor of heat and has a high coefficient of thermal expansion. This means that vulcanization temperatures are reached slowly in the interior of a rubber product, and manufactured articles shrink when they cool to room temperature from the vulcanized temperature in a mould. This thermal contraction, sometimes referred to as "mould shrinkage", must be taken into account to fabricate rubber to close dimensional tolerances.

Rubbers are generally good insulators, i.e. poor conductors of electricity, since the bonding is covalent, and there are no charge carriers. Rubber is extensively applied in insulation applications when flexibility as well as high electrical resistance is needed.

Rubber, when dry, has a remarkably high coefficient of friction, but this is greatly reduced when wetted with water (Loganathan 2000).

Adjusting the conditions of vulcanization and adding fillers considerably changes rubber properties. During mixing, the finely divided particles of filler are well dispersed in the rubber, and this affects the physical properties of the vulcanized product; i.e. "reinforcing" fillers impart greater resistance to abrasion and tear, and higher modulus of elasticity, hardness and hysteresis in particular. For synthetic non-crystallizing elastomers reinforcing fillers are essential for imparting adequate strength when samples of unfilled and carbon-filled rubber vulcanizates are stretched for the first time and then allowed to retract, subsequent extensions to the same strain requires a lower force. Most of this softening occurs during the first deformation, while at higher strains than previously applied the stress-strain behaviour is not much affected. This phenomenon has been termed the "Mullins Effect" (Mullins 1947).

The dynamic properties of rubber are important in such diverse applications as tyres, conveyor belts, high-pressure hoses, antivibration mountings and bridge bearings.

Having observed the impact of fillers in rubber compounds we next consider the rubber formulation and the monitoring of filler distribution.

2.5 Rubber Formulation

A unique aspect of engineering with rubber is that a wide range of mechanical properties can be achieved by varying the formulation and manufacturing process. The main compounding factors that are known to influence fatigue behaviour are polymer type and type and quantity of fillers, antioxidants, antiozonants and curatives. Manufacturing processes also influence fatigue behaviour through factors such as ingredient dispersion and state of cure.

2.5.1 Polymer Type

Different types of polymer can influence fatigue behaviour. Polymer selection is a primary consideration irrespective of whether or not it exhibits strain crystallization. Strain crystallization can benefit fatigue performance at moderate or high strain levels and appears to be associated with reduced sensitivity to environmental effects (Gent & Hindi 1990). In a polymer where strain-crystallization is absent, continuous crack growth under a static load can be significant. Polymers that exhibit strain crystallization are natural rubber (NR), isoprene rubber (IR) and polychloroprene (CR). Polymers exhibiting a little

crystallization are polybutadiene (BR) and butyl rubber (IIR). Polymers that do not crystallize at all include such random copolymers as styrene-butadiene rubber (SBR), acrylonitrile-butadiene rubber (NBR) and ethylene-propylene rubber (EPDM). A review of rubber polymer types and their application is given by Hamed (1992).

2.5.2 Vulcanizing Agent

Sulfur serves as a vulcanizing agent for unsaturated rubbers such as natural, styrene-butadiene, butadiene, butyl and some other synthetic rubbers. For soft rubber (i.e. typical rubber) the dose is 0.5-4 phr and for SBR it is 1.5-2.2 phr. For hard rubber (i.e. ebonite) 35-50 phr of sulfur are added. Sulfur is insoluble in most solvents, but readily dissolves in carbon disulphide. Its solubility in rubber depends on the type of rubber and on the temperature.

Peroxides act as vulcanizing agents for diene elastomers. Peroxide curing occurs by free radical mechanism, and leads to carbon-carbon crosslinks, that are quite stable and result in vulcanizates with good ageing and compression set resistance.

Some elastomers, such as polychloroprene, can be cured with metal oxides, like ZnO and MgO. Generally, a mixture of ZnO and MgO are used for curing, since ZnO is too scorchy by itself, and MgO alone is insufficient (Hamed 1992). Zinc oxide was one of the first white reinforcing fillers. Even though its reinforcing effect is not high in comparison with more recent reinforcing fillers, it was used even in tyre treads until the time when the reinforcing effect at carbon black was recognized in 1912 (Franta 1989). Owing to its high volume price, it is used as a filler only where necessary. Otherwise, in amounts of 3-5phr, it is used as an activator in almost every sulfur cured formulation.

Stearic acid is added to most rubber compounds as an activator of vulcanization, but simultaneously fulfils the functions of processing aid and softener. In addition, stearic acid is adsorbed via its carboxy group on the surface of the filler particles, contributing to their wetting and improved dispersion.

2.5.3 Filler

Historically, fillers such as chalk, clay, and metal oxides were included in rubber formulations to reduce cost, being much cheaper than the use of a polymer. It was discovered that some fillers - notably high surface-area carbon blacks and silicas - "reinforce" rubber, increasing its modulus and abrasion resistance and enhancing, or at least not significantly degrading, strength characteristics.

The addition of carbon black to rubber compounds can have a pronounced strengthening effect, especially for non-strain crystallising rubbers (Medalia 1987), depending on both the filler type, and the volume fraction used (Dizon et al. 1974). Two main physical parameters are used to classify fillers – the surface area, inversely related to the size of the primary particles and the "structure" or degree of fusing of the primary particles into aggregates that do not break down during processing or straining the vulcanized rubber (Omar et al. 2011). Reinforcing effect is correlated with specific surface area, while higher structure blacks show lower hysteresis and lower stiffness reduction on straining, for a given specific area. The effect of filler on fatigue properties has been attributed to multiple mechanisms which include:

- pronounced changes in stiffness and hysteresis properties,
- crack tip blunting, deviation and branching induced by non-homogeneity of the rubber-filler composite at crack tip,
- agglomerates of filler particles, resulting in increased effective initial flaw sizes.

When comparison is based on equal energy release rate, an optimal filler loading is observed in SBR that minimizes crack growth rate and maximises fatigue life (Auer et al. 1958). Below the optimal volume fraction, improved reinforcement and dissipation result in improved fatigue life with increasing volume fraction. Above the optimal volume fraction, increases in effective initial flaw size apparently offsets other gains, resulting in overall reduced fatigue life. Based on the data of Auer et al., (1958), the optimal filler loading for HAF black in SBR is between 30 and 60 parts carbon black, per hundred parts of rubber by weight.

The widespread use of natural rubber followed the discovery of vulcanization 174 years ago, and it was not until well into this century that carbon black came into general use as a reinforcing filler. Originally fillers were used only to extend and cheapen rubber formulations. Other beneficial developments, such as the use of antidegradants, came much later (Davies 1988, Huntink 2003).

Lake and Lindley's (1964b) results for tearing energy as a function of cyclic crack growth rate (dc/dn) for eight polymer types with three different filler systems are shown in Figure 2.10. Carbon black reduces crack growth rates, relative to the gum rubber at the same tearing energy, by an amount that is strongly dependent on the type of carbon black.

Finer grades of carbon black (High abrasion furnace (HAF) type) are seen to be the most effective. Corresponding effects are observed on fatigue life, that is, the filled rubber is superior to the gum rubber, finer grades of carbon black are superior to coarser grades (Medium thermal, (MT) type).
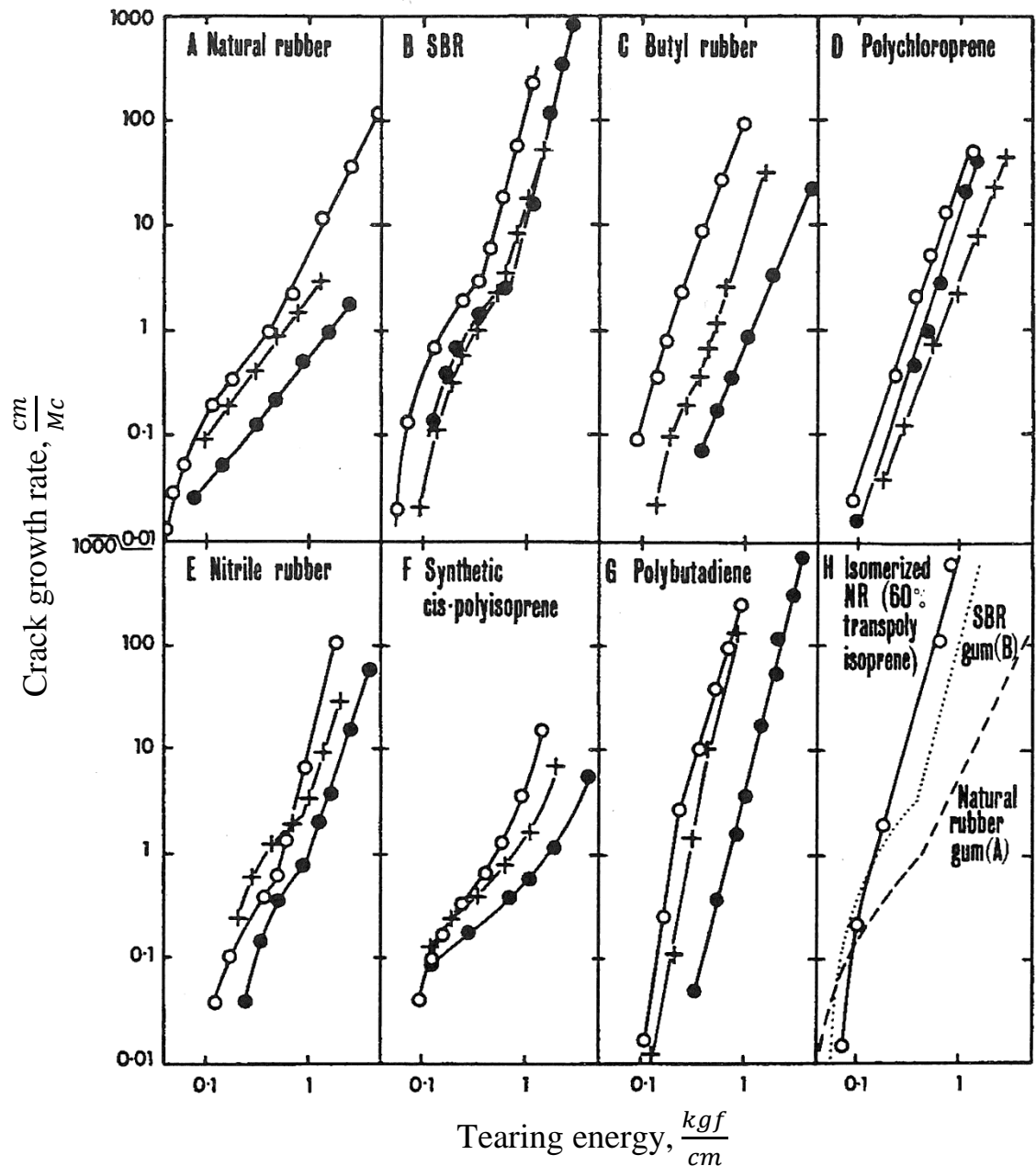
Figure 2.10: Mechanico-oxidative cut growth characteristics of vulcanizates of different polymers: (O) gum, with 50pphr MT black (+) and with 50pphr HAF black (•).

2.5.4 Antidegradants

Antidegradants can be added to rubber compounds to reduce the deleterious effects of ozone and oxygen. The various agents rely upon several mechanisms to prevent degradation by chemical reaction (Hamed 1992). Waxes in rubber compound migrate to the surface, providing a physical barrier between rubber and ozone in the environment. Other antidegradants function by chemically reacting directly with degradants, or with other entities required to complete degrading reactions. Several common types of antidegradant are provided in Table 2.2 together with their characteristics. A mechanism involving protective layer formation, as a result of reaction between a chemical antiozonant and ozone, appears to have been first suggested by Erickson et al. (1958).

Table 2.2: Common type of antidegradants in rubber formulation (based on information in The Natural Rubber Formulary and Property Index MRPRA 1984).

Type	Trademark	Antiozonant	Antioxidant	Anti-flex cracking	Non-staining
HPPD (also called 6PPD)	Santoflex B	✓	✓	✓	✕
IPPD	Santoflex IP	✓	✓	✓	✕
TMQ	FledolH	✕	✓	✕	✓
2246	Antioxidant 2246	✕	✓	✕	✓

2.5.5 Extenders

Oil is often present in the formulation, acting as a process aid, especially for stiff mixes with high filler loadings. It also decreases the modulus of the vulcanizate. Other extenders, such as recycled crumbs of rubber, and cross-linked vegetable and mineral oils, may be used to decrease the cost of the product per unit volume.

2.6 Quality Check for Uniformity of Filler Dispersion

The quality of rubber and plastic products containing reinforcing pigments or filler depends on the dispersion of these materials throughout the polymer matrix. Carbon black is the most important reinforcing filler for rubbers, although silica has become very widely used in tyre treads. The incorporation of carbon black into rubber vulcanizates generally results in increased strength, stiffness, hysteresis fatigue resistance and abrasion resistance. Rubber vulcanizate properties depend on the dispersion of additives in the rubber. Poor dispersion can lead to such detrimental effects of additives as poor product appearance, reduced product life, poor processing and manufacturing uniformity, waste of raw materials and excessive energy usage (Hess 1991). These inadequacies are generally the

result of the presence of rather large, undispersed agglomerates. Coran and Donnet (1995) reported that large agglomerates can give rise to poor mechanical strength properties. The large agglomerates can act as failure-initiating flaws. Agglomerates larger than the inherent flaw sizes for rubber could be responsible for decreases in mechanical properties such as tearing energy and fatigue resistance. Vegvari, Hess and Chirico (1978) demonstrated that processing characteristics, vulcanizate hysteresis, and physical failure properties can be significantly affected by the measured level of carbon black dispersion, the magnitude of the effects varying with the type of polymer system.

Methods of assessing carbon black dispersion in rubber compounds can be broadly classified into two categories:

(1) Direct visual or optical analysis,
(2) Measurements of indicative physical properties dependent on the degree of dispersion.

The first category includes the analysis of surfaces prepared by tearing, cutting, polishing, stretching or extruding as well as the examination of thin sections by optical microscopy, optical reflection from a cut surface and electron microscope. Indirect measurements of carbon black dispersion in rubber have been based on electrical conductivity, extrusion shrinkage, viscosity characteristics, vulcanizate strength and fatigue properties.

Since selected polymer and the additives included affect the behavioural characteristics of rubber we next consider how each can influence rubber fatigue.

2.7 Rubber Coating

An elastomeric coating is a new approach to rubber protection from the exposure to oxygen and ozone and enhances fluid resistance for a wide variety of elastomeric components. It is also used for cosmetic changes of the original colour of rubber components to more attractive colours. Several types of elastomeric coatings such as HPC-3B, HPC-5B and HPC-6 were developed by Lord (Lord Product leaflet 2010).

2.8 Elastic Stress-Strain Behaviour of Rubber

Once a rubber has been formulated and an engineering product made, engineers will need to know how it behaves when subjected to different loading conditions. This necessitates some appreciation of its stress-strain relationship. These dependencies are addressed here.

2.8.1 Theory Foundation

Natural rubber and synthetic elastomers form a distinctive class of engineering materials which may deform elastically to very large extensions under quite small stresses. This is known as hyperelasticity. Two distinct approaches to the study of rubber elasticity are the statistical theory and the phenomenological theory.

2.8.2 Statistical Theory

The statistical theory of rubber elasticity regards a rubber as a network of N flexible long chain molecules per unit volume attached to the network at each end by crosslinks, undergoing thermal motion so that the entropy of each chain is a function of its possible number of configurations. Statistical physics is used to predict the elastic behaviour of this structure. According to the statistical theory of rubber elasticity (Treloar 1949, 1975), the entropy of the individual chain is given by:

$$s = C - b^2 k r^2 \qquad , \qquad\qquad (2.2)$$

where C is an arbitrary constant, b^2 is the constant in the Gaussian distribution function which is equal to $\frac{3}{2}nl^2$, k is the Boltzman constant and r is the distribution of end-to-end chain lengths. The network contains N chains per unit volume each containing n identical, freely jointed links of length l. It is implicitly assumed that r has a Gaussian distribution and $r \ll nl$; that is the end-to-end length of the chains is much less than their fully extended length. The entropy of the network is the sum of the entropies of the individual chains. Figure 2.11 shows an individual chain having end-to-end distance represented by position vector r_0, with components (x_0, y_0, z_0), in the unstrained state of the network; (x, y, z) are the components of the vector length r of the same chain after deformation, or spatial variables for the volume integrals below.
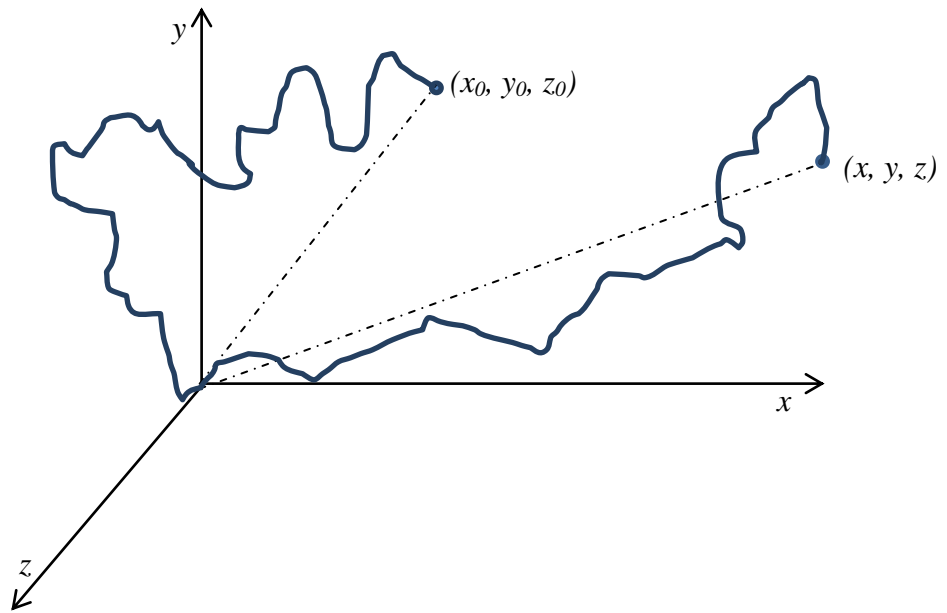
Figure 2.11: The 'affine' deformation of chains (Treloar 1975).

We shall consider a deformation such that a unit cube would be deformed into a cuboid of edge lengths λ_1, λ_2 and λ_3. λ_1, λ_2 and λ_3 are the three principal extension ratios (the ratios of stretched to unstretched length) along three mutually perpendicular axes. Then by the affine deformation assumption

$$x=\lambda_1 x_0, \quad y=\lambda_2 y_0, \quad z=\lambda_3 z_0, \tag{2.3}$$

the axes of coordinates being chosen to coincide with the principal axes of strain. The number of chains in the unstrained state having length components in the range dx, dy, dz is

$$dN = N\left(\frac{b^3}{\pi^{\frac{3}{2}}}\right)e^{-b^2(x^2+y^2+z^2)}dxdydz . \tag{2.3a}$$

The entropy of the chain in the original state, as given by Equation (2.2), will be

$$s_0 = C - kb^2 r_0^2 = C - kb^2(x_0^2 + y_0^2 + z_0^2). \tag{2.4}$$

The total entropy S_0 in the unstrained state is therefore

$$S_0 = \int s_0 dN = \frac{Nb^3}{\pi^{\frac{3}{2}}} \iiint_{-\infty}^{+\infty}[C - kb^2(x^2 + y^2 + z^2)]e^{-b^2(x^2+y^2+z^2)}dxdydz. \qquad (2.4a)$$

This integral can be shown to reduce to a very simple form:

$$S_0 = N(C - \frac{3k}{2}) \qquad . \qquad (2.4b)$$

The entropy of the same chain in the strained state is obtained by substituting the values of (x, y, z), thus

$$s = C - kb^2(\lambda_1^2 x_0^2 + \lambda_2^2 y_0^2 + \lambda_3^2 z_0^2), \qquad (2.5)$$

so that the total entropy in the strained state becomes

$$S = \int s \, dN = \frac{Nb^3}{\pi^{\frac{3}{2}}} \iiint_{-\infty}^{+\infty}[C - kb^2(\lambda_1^2 x^2 + \lambda_2^2 y^2 + \lambda_1^2 z^2)e^{-b^2(x^2+y^2+z^2)}dxdydz \qquad (2.5a)$$

leading to

$$S = N(C - \frac{1}{2}k(\lambda_1^2 + \lambda_2^2 + \lambda_3^2)). \qquad (2.5b)$$

Using Equations (2.4b) and (2.5b) to calculate the entropy change associated with deforming a chain and summing over all chains yields (Treloar 1975):-

$$\Delta S = S - S_o = -\frac{1}{2}Nk(\lambda_1^2 + \lambda_2^2 + \lambda_3^2 - 3) \qquad (2.6)$$

where ΔS is the change in entropy of the network per under the deformation λ_1, λ_2, λ_3.

For reversible deformation, the work of deformation is equal to the change in the Helmholtz free energy (Treloar 1975). The Helmholtz free energy, A, is defined as

$$A = U - TS, \qquad (2.7)$$

where U is the internal energy and T is the absolute temperature. Hence, for an isothermal deformation, the work of deformation, W, for a unit volume is given by

$$W = \Delta A = \Delta U - T\Delta S, \tag{2.8}$$

where T is the absolute temperature. Assuming no change in internal energy,

$$W = -T\Delta S \qquad . \tag{2.9}$$

Hence, from Equation (2.6):-

$$W = \frac{1}{2} NkT(\lambda_1^2 + \lambda_2^2 + \lambda_3^2 - 3) \tag{2.10}$$

The strain energy per unit unstrained volume (strain energy density), *W*, is also called the strain energy density function. Equation (2.10) may conveniently be written as:-

$$W = \frac{1}{2} G(\lambda_1^2 + \lambda_2^2 + \lambda_3^2 - 3) \tag{2.11}$$

with G defined as $\qquad G = NkT \qquad .$

Treloar (1975) shows that G is the shear modulus, and that (2.11) implies proportionality between shear stress and shear strain even for large strains. For the important case of simple extension (where $\lambda_1 = \lambda$ and $\lambda_2 = \lambda_3 = \lambda^{-1/2}$), the strain energy function in Equation (2.11) leads to the stress-strain relation (Treloar 1975)

$$f = \frac{\partial W}{\partial \lambda} = \frac{1}{2} \frac{\partial}{\partial \lambda} (\lambda^2 + \frac{2}{\lambda} - 3)$$

that is,

$$f = \frac{\partial W}{\partial \lambda} = G(\lambda - \lambda^{-2})$$

$$\tag{2.12}$$

where *f* is the nominal (engineering) stress defined as the force per unit unstrained cross-sectional area.

For an incompressible material the state of deformation is unaffected by the imposition of a hydrostatic stress. It follows that the true stresses defined as the force per unit area in the deformed state are indeterminate to the extent of an arbitrary hydrostatic pressure, *p*:-

$$\sigma_i = \frac{\lambda_i}{\lambda_1 \lambda_2 \lambda_3} \frac{\partial W}{\partial \lambda_i} + p \tag{2.13}$$

where σ_i is the true (or Cauchy) stress, (Treloar 1975) (*i* takes the values 1, 2 or 3 and no summation over *i* is implied). Since incompressibility implies $\lambda_1\lambda_2\lambda_3=1$, the denominator in expression (2.13) may be omitted.

The Statistical Theory occupies a central position in the understanding of the molecular basis of rubber elasticity and is the most simple and robust approximation to the behaviour of rubber. Nevertheless, many attempts have been made to refine the basic statistical theory.

More complex models are better expressed as function of the "strain invariants" I_1, I_2 and I_3 rather than directly as functions of λ_1, λ_2 and λ_3, where the invariants are:

$$I_1 = \lambda_1^2 + \lambda_2^2 + \lambda_3^2,$$
$$I_2 = \lambda_1^2\lambda_2^2 + \lambda_2^2\lambda_3^2 + \lambda_3^2\lambda_1^2 \text{ and}$$
$$I_3 = \lambda_1^2\lambda_2^2\lambda_3^2.$$

$$\tag{2.14}$$

Since for constant volume, $\lambda_1\lambda_2\lambda_3 = 1 = I_3$ then *W* is considered in the form

$$W = W(I_1, I_2), \tag{2.15}$$

where I_1 and I_2 are independent variables.

Edwards & Vilgis (1986) have extended the statistical theory to include effects of slip links due to topological entanglements, and the finite extensibility limit of the network chains. They desired an equation for *W* which can be written in term of the strain invariants as:

$$W = \frac{G_c}{2}\left\{\frac{(1-\alpha^2)I_1}{1-\alpha^2 I_1} - \ln(1-\alpha^2 I_1)\right\}$$

$$+ \frac{G_s}{2}\left\{\frac{(1+\eta)(1-\alpha^2)}{1-\alpha^2 I_1} \cdot \frac{I_1 + 2\eta I_2 + 3\eta^2}{1 + \eta I_1 + \eta^2 I_2 + \eta^3} + \ln(1 + \eta I_1 + \eta^2 I_2 + \eta^3)\right.$$

$$\left. - \ln(1-\alpha^2 I_1)\right\}$$

(2.16)

where $\frac{N_c}{2kT} = \frac{G_c}{2}$ and $\frac{N_s}{2kT} = \frac{G_s}{2}$. Here α and η are measures of the extensibility and slippage respectively and there are N_c crosslinked chains and N_s entangled chains. The determination of nominal stress for the Edwards & Vilgis model is shown in Appendix B.

Gent (1996) suggested an alternative strain energy function may be written as

$$W = -\frac{G}{2}(I_m - 3)\ln\left[1 - \frac{(I_1 - 3)}{(I_m - 3)}\right] \quad,$$

(2.17)

where I_m is the limiting value of I_1 corresponding to the deformation when the network is fully stretched. Gent arrived at his strain energy function as a mathematically simple approximation to the approximate molecular model of Arruda & Boyce (1993), which addresses the upturn in stress as the extension approaches the extensibility limit of the chains.

The parameters G and I_m in Equation (2.17) are not independent, but may both be related to the crosslink density of the polymer (Yeoh & Fleming 1997, Ahmadi & Muhr 2007), that is

$$G = NkT$$

(2.18)

and

$$I_m - 3 \approx n = \frac{N_{links}}{N} = \frac{kN_{links}}{G/T} \approx \frac{0.044}{G/T} \quad,$$

(2.19)

where N is the number of network chains per unit volume, $N_{links} = N_n$ is the total number of effective chain links in unit volume, n being the average number per chain, and the constant 0.044MPaK^{-1} having been calculated from the data of Yeoh and Fleming (1997).

Typically I_m has a value of about 100. This model is devised to reduce to the neo-Hookean model at small strains (Edwards & Vilgis 1986, British Standard 903 Part 5, 2004). It provides a straightforward way, with only one additional constant, I_m, of modelling rubber at high strains.

Yeoh & Fleming (1997) found that Equation (2.18), as for Equation (2.10), gives a relatively poor fit at small to moderate strains, and proposed an additional exponential term to meet this shortcoming:

$$W = \frac{A}{B}(1 - e^{-B(I_1 - 3)}) - C(I_m - 3)\ln\left(1 - \frac{(I_1 - 3)}{(I_m - 3)}\right),$$

$$(2.20)$$

where A and B are constants. This extra term was devised empirically, without basis in molecular theory, so is more correctly considered to be "phenomenological" in character – i.e. aiming only at a mathematical description of the behavior, as discussed in the next section. The constants, C and I_m, are related through the crosslink density by Equation (2.19), so there are only three independent constants in Equation (2.20).

2.8.3 Phenomenological Theory

The phenomenological theory treats the problem from the viewpoint of continuum mechanics. It provides a mathematical framework to describe rubbery behaviour, so that stress analysis and strain analysis problems may be solved without reference to molecular concepts.

Equation (2.11) may be written in the form (Treloar 1949, 1975)

$$W = C_{10}(I_1 - 3),$$

$$(2.21)$$

where C_{10} is a material constant equal to half the shear modulus, G. This model is recommended for general use in FEA in BS903 Part 5. Equation (2.21) is commonly known as the neo-Hookean material model because it is the simplest way to extend Hooke's Law of proportionality between stress and strain for elastic materials to hyperelastic materials (Rivlin 1948, Muhr 2005). Unfortunately, this model is approximate (Treloar 1975).

Mooney (1940) made the first significant attempt at developing a more general phenomenological theory. He developed Equation (2.22) to provide a more accurate representation of the behaviour of unfilled rubber in uniaxial tension, namely

$$W = C_{10}(I_1 - 3) + C_{01}(I_2 - 3),$$ (2.22)

where C_{10} and C_{01} are material constants to be determined from experiment, and I_1 and I_2 are given by Equation (2.14). This expression for *W*, known as the Mooney-Rivlin equation, describes an isotropic, incompressible hyperelastic material with a liner relationship between shear stress and shear strain. These attributes are shared with the neo-Hookean model. Although inclusion of the second term in Equation (2.22) enables a better fit than Equation (2.21) in tension, the model shows poorer representation of the behaviour in compression than the neo-Hookean model (Treloar 1975, Yeoh and Fleming 1997).

Rivlin (1956) expanded and generalized Mooney's approach and showed that the most general strain energy function for a homogenous, isotropic, incompressible, elastic material can be written as a Taylor expansion:

$$W = \sum_{i+j=1}^{n} C_{ij}(I_1 - 3)^i (I_2 - 3)^j .$$ (2.23)

where *W* is the strain energy density, C_{ij} are material constants, and I_1 and I_2 are given by Equation (2.14).

Another popular general phenomenological material model due to Ogden (1972), may be written as

$$W = \sum_{p=1}^{n} \frac{\mu_p}{\alpha_p} (\lambda_1^{\alpha_p} + \lambda_2^{\alpha_p} + \lambda_3^{\alpha_p} - 3)$$ (2.24)

where μ_p and α_p are material constants and λ_1, λ_2 and λ_3 the principal extension ratios. In the Ogden formulation, the indices α_p need not be integers. Both (2.23) and (2.24) are versatile, but can give very unrealistic predictions in some modes of deformation unless

fitting is carried out to a very comprehensive set of stress-strain data, covering a wide range of strains and modes of deformation (BS903:Part 5:2004). A more robust approach is to constrain W to be function of I_1 only, in which case a robust fit can be made on the basis of characterization in a single mode of deformation. Several experimental investigations (Gregory 1979, Gough et al. 1999, Yeoh 1998) have shown that such an approach makes little sacrifice in the precision of fit to comprehensive stress-strain data. Yeoh (1990) adopted this approach and proposed a cubic form of Equation (2.23), namely:-

$$W = C_{10}(I_1 - 3) + C_{20}(I_1 - 3)^2 + C_{30}(I_1 - 3)^3 . \tag{2.25}$$

This form is convenient for use with FEA computer programs. Again the parameters, C_{10}, C_{20} and C_{30} are material constants to be determined from experiment. This model is capable of modelling some of the non-linear features of rubber. Normally C_{10} and C_{30} are positive and C_{20} is negative. The exponential term in Equation (2.20) can be added to model the sharp downturn in stiffness with increasing strain at small strains.

2.8.4 General Expression for Stress-Strain Relationships in Tension Compression

The validity of a particular form of W may best be assessed by its ability to make an accurate prediction of the stress-strain behaviour in particular deformation from measurements. For such a check to be reasonably stringent, the chosen deformations should be as different as possible in terms of the combinations of I_1 and I_2. Rivlin (1948) showed that in terms of I_1 and I_2 Equation (2.13), the principal stresses for an incompressible material, may be determined according to:

$$\sigma_i = 2\left(\lambda_i^2 \frac{\partial W}{\partial I_1} - \frac{1}{\lambda_i^2}\frac{\partial W}{\partial I_2}\right) + p . \tag{2.26}$$

Consider the case of a sheet of rubber having its major surface normal to the z-axis and force-free. It follows from Equation (2.26) that:

$$\sigma_1 - \sigma_3 = \left[2\left(\lambda_1^2\frac{\partial W}{\partial I_1} - \frac{1}{\lambda_1^2}\frac{\partial W}{\partial I_2}\right) + p\right] - \left[2\left(\lambda_3^2\frac{\partial W}{\partial I_1} - \frac{1}{\lambda_3^2}\frac{\partial W}{\partial I_2}\right) + p\right] . \tag{2.27a}$$

So that $\sigma_3 = 0$, the condition of incompressibility implies $\lambda_3 = \frac{1}{\lambda_1 \lambda_2}$ and it follows that the stresses in the sheet are given by

$$\sigma_1 = 2\left(\lambda_1^2 - \frac{1}{\lambda_1^2 \lambda_2^2}\right)\left(\frac{\partial W}{\partial I_1} + \lambda_2^2 \frac{\partial W}{\partial I_2}\right).$$ (2.27b)

and

$$\sigma_2 = 2\left(\lambda_2^2 - \frac{1}{\lambda_1^2 \lambda_2^2}\right)\left(\frac{\partial W}{\partial I_1} + \lambda_1^2 \frac{\partial W}{\partial I_2}\right).$$ (2.27c)

Solving the pair of simultaneous Equation (2.27) yields:

$$\frac{\partial W}{\partial I_1} = \frac{\frac{\lambda_1^2 \sigma_1}{\lambda_1^2 - 1/\lambda_1^2 \lambda_2^2} - \frac{\lambda_2^2 \sigma_2}{\lambda_2^2 - 1/\lambda_1^2 \lambda_2^2}}{2(\lambda_1^2 - \lambda_2^2)}$$

and

$$\frac{\partial W}{\partial I_2} = \frac{\frac{\sigma_1}{\lambda_1^2 - 1/\lambda_1^2 \lambda_2^2} - \frac{\sigma_2}{\lambda_2^2 - 1/\lambda_1^2 \lambda_2^2}}{2(\lambda_1^2 - \lambda_2^2)}.$$ (2.28)

In theory Equations (2.28) enable $\partial W/\partial I_1$ and $\partial W/\partial I_2$ to be determined from biaxial test data. However, at small strain it is difficult to determine them separately with any accuracy, although their sum can be quantified (Gough 2000).

For uniaxial tension and compression, substituting $\lambda_2 = \lambda_3 = \frac{1}{\sqrt{\lambda_1}}$ and noting that in this case $\sigma_2 = \sigma_3 = 0$ then Equation (2.27a) gives:-

$$\sigma_T = 2(\lambda^2 - \lambda^{-1})\left(\frac{\partial W}{\partial I_1} + \frac{1}{\lambda}\frac{\partial W}{\partial I_2}\right)$$ (2.29)

where σ_T is the true stress in tension or compression. It is conventional to plot nominal, rather than true stresses; for tension and compression, the nominal stress being given by:-

$$f = \frac{\sigma_T}{\lambda}$$ (2.30)

and hence:-

$$f = 2(\lambda - \lambda^{-2})\left(\frac{\partial W}{\partial I_1} + \frac{1}{\lambda}\frac{\partial W}{\partial I_2}\right).$$ (2.31)

2.9 Inelastic Stress-Strain Behaviour of Rubber

The behaviour of rubber is not ideally elastic, as assumed in the hyperelastic model. For applications in which it is necessary to predict properties such as damping, or softening due to repeated straining and stress relaxation, a more sophisticated model would be necessary. A brief description of each mechanism follows.

2.9.1 Viscoelasticity

The vulcanized unfilled elastomer exhibits time-dependent stress-strain behaviour that in certain situations can be reasonably modelled as purely viscoelastic. Viscous behaviour is considered to arise from the time- and temperature- dependent mobility of molecular chains within the elastomer network. The amount of dissipation associated with viscous behaviour of the unfilled elastomer is usually negligible in comparison with the total inelastic behaviour of the filled elastomer (Gent and Scott 1992).

2.9.2 Mullins Effect

The Mullins effect refers to softening of rubber which happens predominantly on the first cycle. The first loading of the virgin material gives a much stiffer response than subsequent loadings. Subsequent loadings of lesser magnitude show much less relative softening. The Mullins effect is exhibited primarily by filled rubbers.

2.9.3 Strain-Crystallization

Certain elastomers exhibit another high-strain hysteresis mechanism, crystallization due to an applied strain (Rivlin & Thomas 1953, Lake & Lindley 1965, Choi & Roland 1996). At large strains, the polymer network chains become sufficiently aligned such that a highly ordered state exists (Treloar 1949).This causes a time-dependent phase change in the elastomer from an amorphous rubbery state to a crystalline state. When the strain is reduced sufficiently, the crystallized elastomer returns to the rubbery state.

2.9.4 Rate Independent Hysteresis

In typical filled rubbers, at low and moderate strains, an approximately rate-independent hysteresis loop is often observed. The rate-independent behaviour is not captured accurately by linear viscoelasticity. The loss mechanism is still active at high strains, its magnitude is small compared to losses associated with the Mullins effect and

strain crystallization. The hysteresis decreases with increasing temperature and increasing mean tensile strain (Luchini et al. 1994).

2.10 Summary and Conclusions

(1.) Proper selection of rubber type, filler type and antidegradants enables rubbers to be produced with a wide range of properties, so that a formulation needs to be developed and optimised for any specific application. Several constitutive rubber models have been discussed for describing the stress-strain behaviour of rubber.

(2.) The knowledge of how to protect rubber product from oxidation and degradation process is essential to produce a good rubber engineering product. Antidegradants can be incorporated in the rubber and coatings on the rubber surface can be beneficial to avoid degradation by ozone.

Chapter 3

A Review: The Durability of Rubber

3.1 Introduction

Some basic science and technology associated with natural and synthetic rubbers was reviewed in Chapter 2. Here, we consider rubber fatigue and fracture generally and through a fracture mechanics approach, together with the impact of environmental factors.

3.2 Consideration of Fatigue and Fracture for Rubber

The longevity of rubber is of particular relevance to engineers who are required to ensure material reliability and structural safety. The high resistance of natural rubber to crack growth under arduous mechanical loading is a major reason for its use in products where long fatigue life is essential. The term 'fatigue' may be taken to indicate a progressive deterioration in one or more material properties due to in-service use or long periods testing. More specifically, fatigue implies failure resulting from the growth of one or more cracks, particularly under repeated cyclic loading. In this case an artefact may ultimately fracture by breaking in two or more parts. The more extreme failure processes of tear and tensile failure also involve fracture and may be considered to correspond to a fatigue life of one cycle. To predict the potential life of an in-service component a primary requirement is an understanding of the basic failure mechanisms most likely to be involved. Extensive studies of the mechanics of crack propagation in rubber have shown that crack growth is driven by the release of energy stored in the rubber and in the system of forces experienced (Lake 1983, Gent, Lindley & Thomas 1964, Lake & Lindley 1965).

Failure modes of many rubber products generally involve fatigue. This may manifest itself as: groove cracking or tread and ply separation in tyres, failures in torsion springs, engine mounts and O-ring seals. In considering tyres or other rubber components subjected to rapid cycling, it is important to determine whether there is significant heat build-up, as temperature increases may directly affect material properties and result, over time, in a substantial alteration of the chemical structure. Hence the nature of failure may be very complex. Although, fatigue failure is generally accelerated by cyclic loading, it can occur under constant load or deformation in non-crystallizing rubbers. Pipe seals have failed under the latter conditions due to mechanical crack growth (Lake 1983). Chemical attack by ozone can cause cracking under both constant and cyclic loading. This is

especially true for thin artefacts subjected to tensile stresses. Sidewall cracking in tyres is often ozone induced. Many applications of rubber components involve 'non-relaxing' conditions, that is, the stresses do not return to zero during the load cycle. For example, if a relatively small dynamic deformation is imposed on a much larger static one. The fatigue life of crystallizing rubbers can be very greatly enhanced under these non-relaxing conditions (Cadwell et al. 1940, Lake 1972, Lindley 1973, 1974).

Mars (2004) emphasized the importance of understanding the factors that affect the fatigue life of rubber. He made three points:

- At least a qualitative understanding of these factors is required in order to develop durable rubber compounds, rubber components and systems that rely upon rubber components.

- The analysis and prediction of fatigue failure in rubber components depends on quantitative understanding of these factors.

- Many aspects of the fatigue process remain incompletely understood.

Future progress in understanding the fatigue behaviour of rubber requires identification of known factors and factors unknown. Mars also indicated that the factors influencing the fatigue life of rubber may be broadly classified as mechanical loading history, environmental conditions and aspects of the associated stress-strain behaviour.

Having generally discussed fatigue a more theoretical approach is presented next.

3.3 Theoretical Approaches for Predicting Fatigue Failure

Two different approaches to characterise rubber fatigue durability have been proposed. The first approach seeks to describe the fatigue life of the material simply in terms of the stresses and strains to which it is subjected. A major study of this kind is due to Cadwell et al. (1940). The outcomes of this approach are graphs of durability plotted against measures of loading severity (e.g. Wöhler 1867, Haigh 1915, Cadwell et al. 1940). The definition of durability is the number of cycles, *N,* performed before the occurrence of a predefined critical size crack. This leads to the general equation:

$$N = A.\ criterion\ ^{\alpha} \tag{3.1}$$

where *A* and *α* are two parameters dependent on the tested material and the load conditions, whereas *criterion* represents a measure of the applied mechanical load amplitude (Ostoja-Kuczynski et al. 2005).

This approach is often called crack initiation prediction and can assume that the test piece is initially uncracked. It is also sometimes called the crack nucleation approach and considers the fatigue life of rubber can be determined from the history of strain and stress at a point in the body. In Equation (3.1) the two most widely used criteria are "the maximum principal stretch" and "the strain energy density". However, both fail to give satisfactory predictions for multiaxial problems (Andriyana & Verron 2005). The "initiation approach" is reasonably applied to metals, but its application to rubber lacks any detailed micro-mechanistic foundation. Thus its practical utility in rubber assessment is questionable.

The second approach is based on prediction of crack propagation using the energetics or fracture mechanics approach introduced by Rivlin and Thomas (1953) and based on the work of Griffith (1920). Griffith introduced the idea of an energy balance between the mechanical energy of a cracked body (calculated using linear elasticity theory) and the energy associated with the crack surfaces. Griffith postulated that every body contains a distribution of cracks and failure is initiated from the larger cracks. An initial crack of length *c* in a metal plate of thickness *h*, and fixed displacement *L*, will grow if the plate's total elastic energy decrease dU_e for an increase in crack length *dc* is greater or equal to the surface free energy *γ* per unit area required to form the new crack surface. Thus, from energy considerations:

$$-\delta U_e \geq 2\gamma h \delta_c$$

$$\Rightarrow -\left(\frac{1}{h}\right)\left(\frac{\partial U_e}{\partial c}\right) \geq 2\gamma. \qquad (3.2)$$

The inclusion of the factor arises from the two fracture surfaces - two areas being involved one or each side of crack. The derivative is evaluated for fixed boundary (represented by fixed *L*) so that during the crack increment there is no energy change associated with the externally applied forces.

This approach was extended by Thomas (1958) and Greensmith, Gent, Lindley, Lake and colleagues during the 1950s and 1960s. The rate of release of energy by a growing crack is considered to be the parameter that drives the crack growth. It is widely used in rubber research. Rivlin and Thomas (1953) first suggested a connection with

tearing. In this case the energy release rate has become known as the tearing energy. For linear elastic materials tearing energy is directly related to the stress intensity factor, a widely used parameter in applications of fracture mechanics to metals. Both the energy release rate, (most commonly used in rubber fracture analyses), and the stress intensity factor relate the global structural loading to the local crack tip strain and stress field. However, the stress intensity factor is only applicable in linear elastic material, whereas the energy release rate is applicable for nonlinear elastic materials and finite strains.

Mars and Fatemi (2002) reviewed the currently available analyses for predicting the fatigue life of rubber. The review included both the "crack nucleation" as well as "crack growth" approaches. They explained that the distinction between 'crack nucleation' versus 'crack growth' approaches is based on the practical application of the two approaches. In a crack nucleation approach, the analysis is without regard to features such as initial crack or defect size, shape, orientation or distribution. In the crack growth approach, however, these cited crack or defect features are essential inputs to the analysis. Mars and Fatemi (2006a) presented evidence supporting the view held by Gent, Lindley & Thomas (1964), that fatigue crack "nucleation" in rubber results from the growth of flaws already present in the virgin material, so that it cannot be regarded as a distinct process from crack growth.

3.4 The Energetics Approach to Crack Growth in Rubber

In rubbers, the energy required to cause material fracture is not entirely due to surface energy effects. A much greater contribution results from energy dissipation effects associated with stress-strain hysteresis. For rubbers the total energy required to create the fractured surface is a material characteristic called the tearing energy, *T*. During fracture *T* is equal to the energy release rate, defined as the decrease in the total strain energy (*U*) produced by unit increase in the area (*A*) of one surface of the crack (Rivlin & Thomas 1953), that is

$$T = -\left(\frac{\partial U_e}{\partial A}\right)_L = -\frac{1}{h}\left(\frac{\partial U_c}{\partial c}\right)_L \qquad . \qquad (3.3)$$

The partial derivatives indicate that the clamped length *L* of a testpiece is kept constant. Since the external forces do no work *A*, *c* and *h* are respectively the area of one fracture surface, the crack length and testpiece thickness all measured in the unstrained state.

Clearly, the right hand side of Equation (3.3) is identical in form to the left hand side of Equation (3.2). However, Equation (3.3) generalizes (3.2) to cracks of other geometries than those through the thickness of plates, and to materials for which $T > 2\gamma$.

A validity check of this approach is possible since several test pieces of different shape were devised by Thomas and co-workers for which T could be expressed simply in terms of measured quantities. The most commonly used of these are: (a) the tensile strip, (b) pure shear and (c) the trouser test pieces illustrated in Figure 3.1 along with relevant references. The less common techniques include angle and split pieces of Figure 3.1 (d) & (e). Both are convenient for experimental investigation.
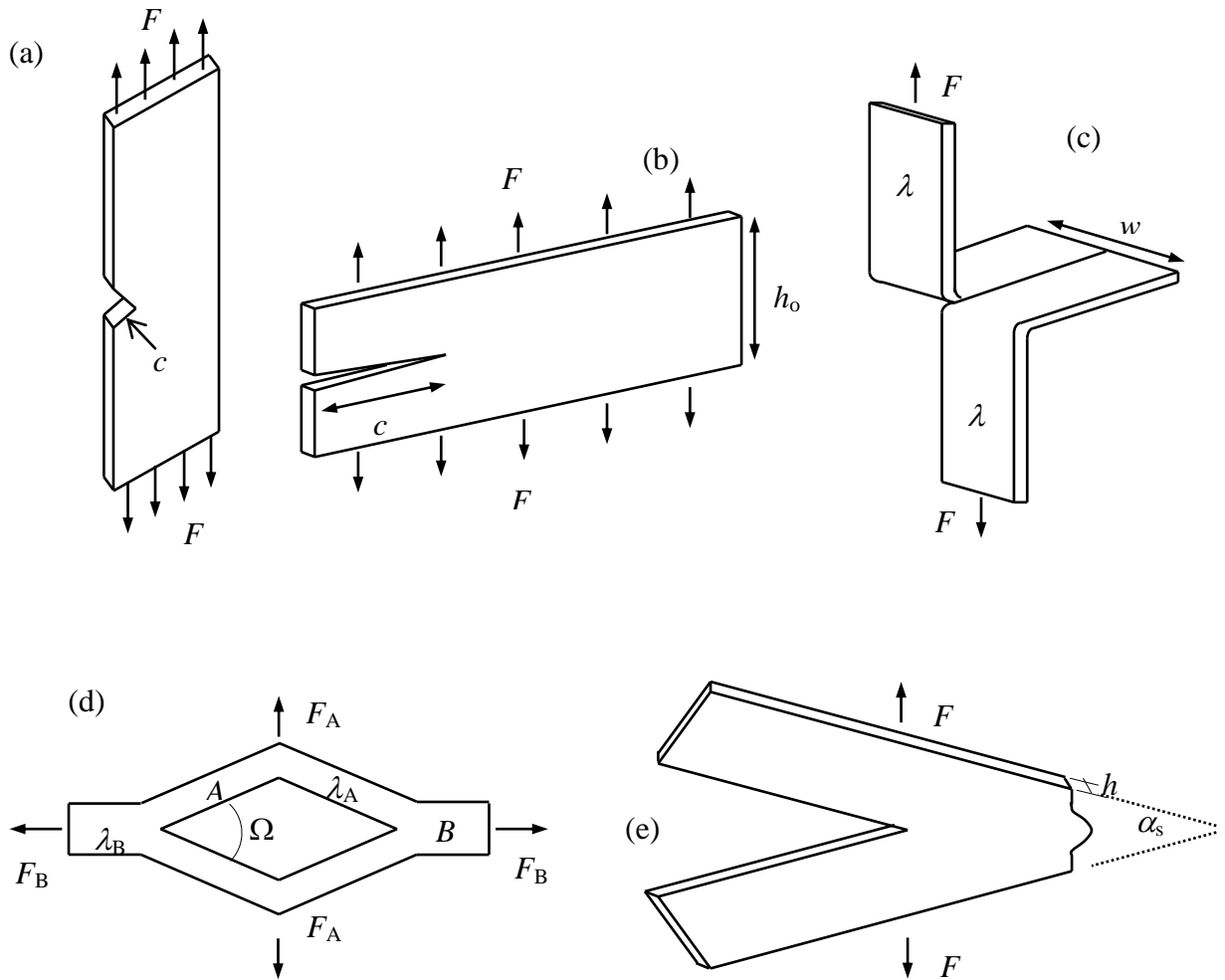
Figure 3.1: Some of test pieces used for tear and other fracture measurements on rubber: (a) tensile strip; (b) pure shear; (c) trouser; (d) angled (in which the angle α_s is held constant); (e) split tear; (Rivlin & Thomas 1953, Thomas 1960, Gent, Lindley & Thomas 1964, Lake & Thomas 1967a).

The formulae for tearing energy of each test piece of Figure 3.1 in terms of measured forces and dimensions are provided in Table 3.1.

Table 3.1: Tearing energy for each test piece shape.

Shape	Mathematical relationship	
(a) Tensile	$T = 2kWc$	(3.4)
(b) Pure shear	$T = Wh_o$	(3.5)
(c) Trouser	$T = \dfrac{2F\lambda}{h} - wW$	(3.6)
(d) Angle	$T = \dfrac{2F}{h}\sin\dfrac{\alpha}{2}$	(3.7)
(e) Split	$T = \left[F_A\lambda_A\sin\Phi + F_B(\lambda_A\cos\Phi - \lambda_B)\right]/h - w(W_A - W_B)$	(3.8)
Notation	Definition	
c	Crack length	
F, F_A, F_B	Force applied	
h	Thickness of rubber sheet	
h_o	Unstrained height	
k	Function of strain	
T	Tearing energy	
$\lambda, \lambda_A, \lambda_B$	Extension ratios	
W	Strain energy density	
w	Width	
Ω, α_s	Angles	

If crack growth data is to be useful the different techniques associated with the varied forms of test pieces should provide consistent results (Thomas 1960, Lake 1983). A non-crystallising styrene-butadiene rubber (SBR) vulcanizate gives values of T which depend on the rate of tearing r_t. This relation should be the same for all the test pieces, as illustrated in Figure 3.2. Similar agreement is also found for other rubbers, although the detailed nature of the tearing and the level of the tear strength may vary.
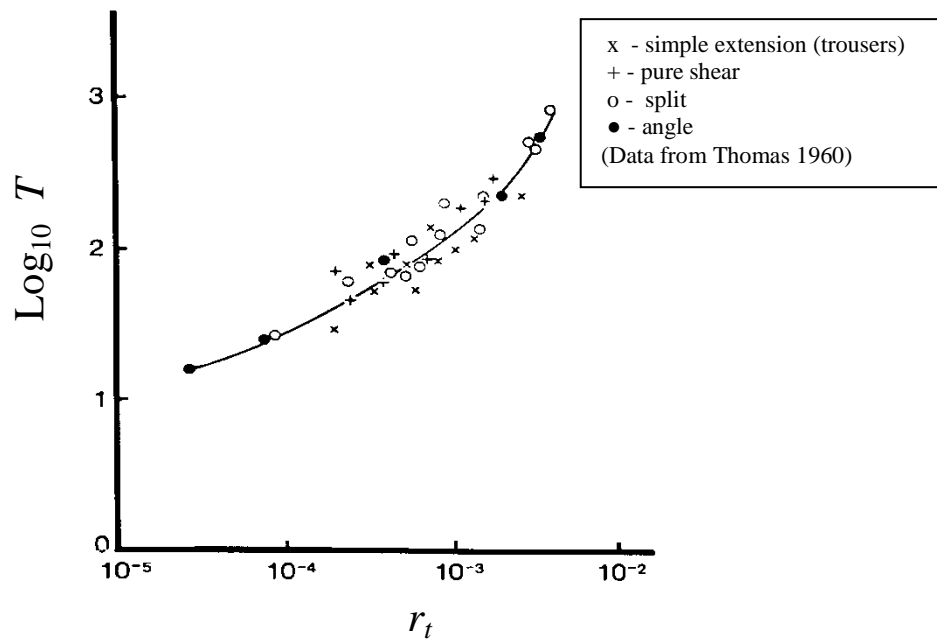
Figure 3.2: The tearing energy (T) in J/m^2 is a function of crack growth rate r_t in cm/s for an unfilled SBR using variety of test piece geometries of Figure 3.1.

The fracture mechanics approach is useful not only for time-dependent tearing, such as that illustrated in Figure 3.2 for SBR, but also for "stick-slip" tearing that generally occurs in strain-crystallizing elastomers. In the stick-slip process, the tear force and energy increase during the stick periods until a rapid failure point is reached at which the tear jumps forward. Depending on the way in which the force is applied this may completely sever the test piece. Values of T at the quasi-catastrophic failure point are substantially the same for different test pieces (Rivlin & Thomas 1953, Thomas 1994).

According to fracture mechanics, no solid is completely homogeneous. All solids contain inevitable flaws of various shapes and sizes which may be considered as effective cracks or stress-raisers associated with an energy release rate. The local stresses at the tips of these flaws are magnified and can be many times larger than the average applied stress. Generally, there will be a single flaw for which the energy release rate is greatest of all. Failure will initiate at this flaw, at much lower values of global stress than that at which a theoretical homogeneous material would fail.

3.5 Cut Growth and Mechanical Fatigue of Rubber

The term fatigue is most commonly used to refer to failure after a period of cyclic loading. Such failure can occur in all elastomers. For a non-crystallizing elastomer a similar failure process can occur under fixed load, because of time-dependent crack growth. Greensmith et al. (1955), Lake et al. (1983, 1992) and Thomas (1974, 1994) demonstrated that cyclic crack growth, similarly to time-dependent growth, could be characterised in terms of its dependence on the energy release rate. Whilst energy release rate varies during the course of the loading cycle it has been found that the amount of crack growth is determined primarily by the maximum tearing energy T_{max} attained. This phenomenon is illustrated in Figure 3.3, for different test pieces and captured in the equation:

$$\frac{dc}{dn} = f(T)|_{T=T_{max}}$$

(3.9)

where c is the crack length and, n the number of cycles and the form of *f(T)* is given below in equation 3.11 to 3.16 and depends in detail on the type of rubber.
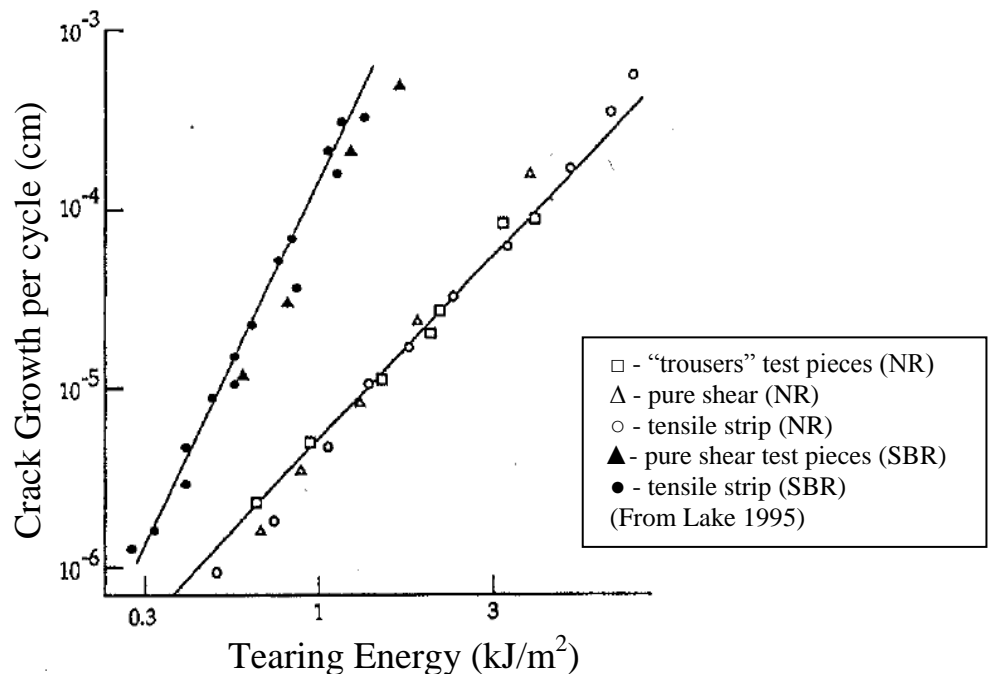
Figure 3.3: Results obtained for the cyclic crack growth rate, *dc/dn*, plotted against the maximum value of the strain energy release rate, or tearing energy, during the cycle.

Gent, Lindley and Thomas (1964) demonstrated that the required number of cycles for a certain amount of crack growth in an artifact can be estimated from the material crack growth characteristics, provided the relationship for *T* (in terms of the applied forces and dimensions) is known. Any type of test piece for which *T* can be evaluated, can be used.

The tensile test piece (Figure 3.1(a)) is easy to prepare and set up. The cut length can be readily measured and a very wide range of tearing energy can be covered. In particular, the test piece can be used at tearing energies similar to those met by many components under in-service conditions. From Table 3.1, the energy release rate in simple extension for a through-thickness edge crack as shown in Figure 3.4 is known (Rivlin & Thomas 1953).
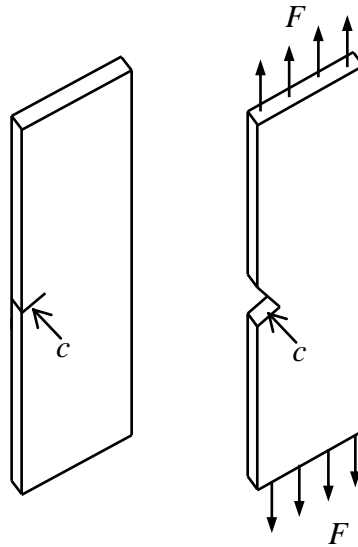
Figure 3.4: A tensile strip test piece containing an edge crack of length *c*.

Timbrell et al. (2003) reviewed earlier research showing that *k* of Table 3.1 is a slowly varying function of strain. A simple and useful approximate formula for *k* was derived by Lake (1970) from an estimate of the work required to close a crack in a rubber sheet. Based on an analytical argument and measurements of crack opening for test pieces containing central cracks, strained up to 200% or so, Lake found that

$$k \approx \pi / \sqrt{\lambda} \qquad . \tag{3.10}$$

The parameter λ is an extension ratio. Equation (3.10) is in reasonable accord with the FEA studies and review of Timbrell et al. (2003).

Cut growth occurs in inert atmospheres, but is more rapid in air or oxygen, and it is therefore usually termed mechanico-oxidative cracking (refer to Figure 2.10). It does not occur for a T value below a threshold value T_o. Ozone attack can also drive crack growth, even at very low tearing energy, provided T exceeds a threshold value designated T_z.

Lake and Lindley (1964a) identified four distinct regimes of fatigue crack growth behaviour, based on the maximum energy release rate per cycle, T, for fully relaxing (R=0) cycles* in rubber. Figure 3.5 illustrates the full range of behaviour, for unfilled natural rubber, NR and styrene butadiene rubber, SBR. Figure 3.5 indicates four distinct regimes of behaviour. Each is discussed next.
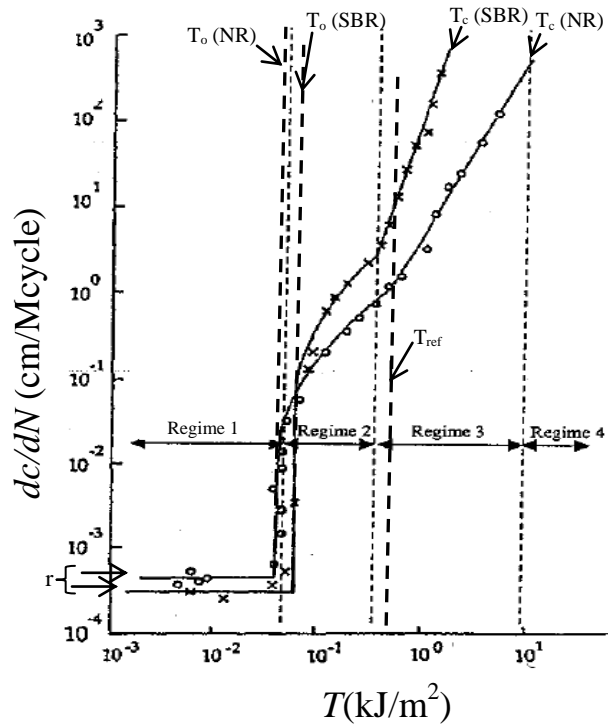
Figure 3.5: Regimes of fatigue crack growth behaviour in unfilled rubber under R = 0 loading (×, SBR; ○, NR) (From Lake & Lindley 1965).

In Regime 1, so long as the peak energy release rate T remains below the threshold tearing energy, T_o, but above T_z, cyclic crack growth proceeds at a constant rate r_z, due solely to ozone attack. Below T_o, the crack growth rate dc/dn, is independent of the mechanical loading, that is

$$\frac{dc}{dn} = r_z \qquad\qquad : T_z \leq T_{\max} \leq T_0, \qquad (3.11)$$

*Defining R= Minimum strain/Maximum strain, a fully relaxed cycle corresponds to R=0.

Here *r* is the rate of ozone-induced crack growth (µm/cycle) given by

$$r_z \equiv t_c \rho_z q \qquad , \tag{3.12}$$

where *q* is the fractional concentration of ozone (pphm), t_c is the fraction of time in each cycle for which the strain exceeds the threshold tearing, that is $T > T_z$, and ρ_z is the susceptibility of the rubber to ozone attack, i.e. the time-dependent rate of equation growth at *q*=1pphm for $T_z \leq T \leq T_o$.

Mechanico-oxidative cracking becomes the dominant crack growth mechanism above the threshold value, T_o. There are two mechanico-oxidative contributions to the crack growth - a time dependent contribution $\rho(T)$ that is zero for strain - crystallizing rubbers, and a cyclic contribution.

In Regime 2 the crack growth rate, $\frac{dc}{dn}$ is quite complex for $T_o \leq T_{max} \leq T_t$, where T_t is the transition tearing energy. In particular, the behaviour of $\frac{dc}{dn}$ is found to be:

$$\frac{dc}{dn} = \oint \rho(T)dt + r_A \cdot \left(\frac{T_{max} - T_o}{T_{ref}} \right) + r_z \qquad : T_o \leq T_{max} \leq T_t, \tag{3.13}$$

in which the mechanico-oxidative cracking term (the first two terms on the right hand side of 3.13) becomes the dominant crack growth mechanico above the threshold value of T_0. Here we have the time-dependent $\rho(T)$ contribution, together with a linear contribution dependent upon T-T_0 and the constant crack growth rate define in (3.12).

Regime 3 is a range between the transition tearing energy T_t and critical tearing energy, T_c over which the relationship between the fatigue crack growth rate and the cyclic crack growth contribution obeys a power-law:

$$\frac{dc}{dn} = \oint \rho(T)dt + r_B \cdot \left(\frac{T_{max}}{T_{ref}} \right)^{\beta} + r_z \qquad : T_t \leq T_{max} \leq T_c . \tag{3.14}$$

The associated material properties r_B and β are constant. For most vulcanizates β lies between 1 to 6, depending particularly on the elastomer used and to a lesser extent on other factors such as the degree of crosslinking. Gent et al. (1964) and Thomas (1958) reported that for natural rubber vulcanizates, β is often equal to 2. For elastomers, the value of β tends to be lower the higher the mechanical hysteresis at high strains of the material (Lake & Lindley 1965).

In Equations 3.13 and 3.14 a reference energy release rate T_{ref} has been introduced, so that the parameters r_A and r_B have simple dimensions of length increment per cycle. In this thesis T_{ref} is taken as 1kJm^{-2} for convenience, since this is in the middle of the crack growth characteristics and close to the transition value T_t for most rubbers, see Figure 3.5. This approach is thought more convenient than replacing T_{ref} by the catastrophic tearing energy T_c (Mars & Fatemi 2003), which is only evaluated in determinations of the complete crack growth characteristics and, being material-based, makes comparison of values of r_A and r_B for different materials more complicated to interpret.

Finally, Regime 4 lies beyond the critical tearing energy, T_c, and the crack growth rate is essentially infinite. That is, an extremely rapid 'catastrophic' rupture occurs (Rivlin and Thomas 1953) and is characterised by:

$$\frac{dc}{dn} \sim \infty \qquad\qquad T = T_c \qquad\qquad . \qquad\qquad (3.15)$$

When no initial cut is inserted, Gent et al. (1964) suggested that there are 'intrinsic' flaws which grow by the same process, and may be characterised by an initial effective length, say c_i.

Here it is sufficient to note the implied process, for an edge crack in a tensile test piece using Equation 3.4 for T,

$$N = \int_{c_i}^{\infty} \frac{dc}{dc/dn} = [\ \int_{c_i}^{c_0} + \int_{c_0}^{c_t} + \int_{c_t}^{\infty}\ ] \frac{dc}{dc/dn} \qquad\qquad (3.16)$$

subject to $\dfrac{dc}{dn} = r$ $\qquad\qquad\qquad\qquad : c_i \leq c \leq c_0$

$\qquad\qquad = r_A \left\{ \dfrac{2kWc - T_0}{T_{ref}} \right\} + r \qquad : c_0 \leq c \leq c_t$

$\qquad\qquad = r_B \left\{ \dfrac{2kW}{T_{ref}} \right\}^{\beta} + r \qquad\quad : c_t \leq c \leq \infty$

Using Equations (3.11), (3.14) and (3.15) subject to $\rho(T) \equiv 0$ and range of integrals covers regimes 1 to 3 respectively of Figure 3.5. Following integration of Appendix B it follows that

$$N = \int_{c_i}^{\infty} \frac{dc}{dc/dn}$$

$$= \frac{1}{r}(c_0 - c_i) + \frac{T_{ref}}{2kWr_A} \ln\left(\frac{(2kWc_t - T_0)r_A + T_{ref}r}{(2kWc_0 - T_0)r_A + T_{ref}r}\right) + \frac{1}{r_B(\beta-1)(2kW/T_{ref})^{\beta}c_t^{\beta-1}} \quad, \quad (3.17)$$

where N is the fatigue life and c_i the effective initial flaw size, and c_0 and c_t are effective flaw sizes corresponding to $T = T_0$ and T_t respectively. For $c_i > c_t$ only the 3rd integral of (3.16) applies and so Equation (3.17) becomes

$$N = \frac{1}{(\beta-1)r_B\left(\dfrac{2kW}{T_c}\right)^{\beta} c_i^{\beta-1}} \quad . \quad (3.18)$$

Gent, Lindley & Thomas (1964) found Equation (3.18) to work well for strain dependence of dumb-bell fatigue life of unfilled NR at moderate tensile strains. At low strain it is clearly not appropriate and should be replaced by Equation (3.17); at high strain it was found to overestimate the fatigue life. The effective flaw size required for quantitative agreement is similar to the scale of observable imperfections in rubber.

Equation (3.17) can be also extended to circumstances where the power law relations break down. This requires using an appropriate crack growth equation (Lake & Lindley 1966). Figure 3.6 shows fatigue results obtained for a natural rubber vulcanizate over a wide range of strains and compare them with a theoretical relation derived from crack growth characteristics. In particular the theoretical curves have been generated using Equation (3.17) subjected to: T_o=0.04kJm^{-2}, T_t=0.45kJm^{-2}, T_c=10kJm^{-2}, r_z=1.2x10^{-9}cms^{-1} (laboratory atmosphere), r_A= 2.5x10^{-6} cm cycle^{-1}/kJm^{-2}, r_B=5x10^{-6}cm cycle^{-1}/kJ^{2}m^{-4}, β=2 and c_0=2.5x10^{-3}cm. The strain energy density, W, would be obtained by numerical integration of the tensile stress-strain curve shown schematically in Figure 3.6 (b). The range of integration would be conducted over the interval $[0,\varepsilon_{max}]$. All the above quantities are measurable except c_0; a value of a few tens of microns, which applies for many vulcanizates, is consistent with the size of observable imperfections such as moulding and die-stamping flaws or particulate impurities. The sharp upturn in the predicted fatigue

curve of Figure 3.6(a) corresponds to the T_0 limit and constitutes a mechanical fatigue limit, below which failure is initiated solely by the presence of ozone (Lake & Lindley 1965).
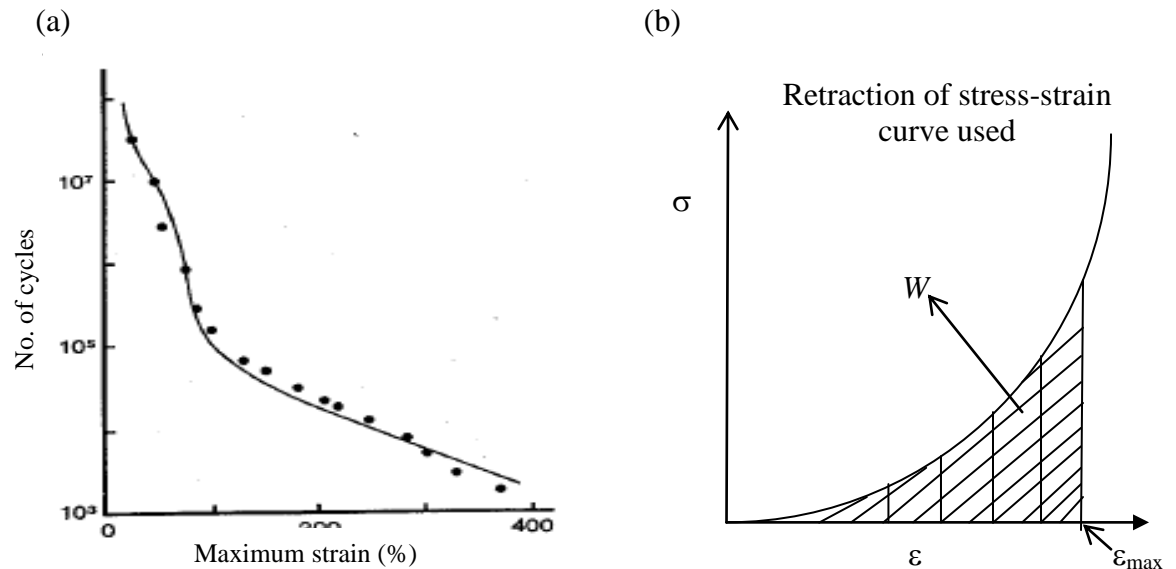
Figure 3.6: Tensile fatigue life plotted against maximum strain of the cycle (minimum strain zero throughout): averages of 4-8 experimental results (●); theoretical curve derived from the crack growth characteristics assuming a natural flaw size of 25μm (laboratory atmosphere). (From Lake 1983).

Thomas (1966) thought that the cut-growth at high tearing energy values, *T*, is strongly influenced by hysteresis. He proposed a theory of tensile strength of natural rubber based on the assumption that failure occurs through the growth of flaws during stressing, reaching an effective size c_c (such that $T=T_c$) and this resulting in catastrophic failure in a simple loading. He also refined the theory for fatigue failure. This theory covers tensile strength, which may be considered as being equivalent to a fatigue life of one cycle. The theory has been checked by model experiments with flaws of known size through fatigue measurements at high strains approaching critical strain (Thomas 1966).

To apply the fracture mechanics theory for fatigue, we need a well-defined geometry for the initial flaws – such as an edge crack. Attempts have been made to capture the essence of the theory from stress analysis in the absence of hypothetical flaws by using a "fatigue criterion" such as that those attributable to Mars (2001) and Andriyana & Verron (2005). These criteria can ideally be related to the fracture mechanics driving force for actual flaws.

3.6 Environmental Effects

Over long periods of exposure environmental effects play a crucial role in the fatigue process. Both the stress-strain and fatigue properties of rubber are highly dependent upon the temperature of the material and the presence and concentration of various chemical reactants in the vicinity of a rubber component.

3.6.1 Direct Effect of Temperature

Elevated temperature has a direct deleterious effect on the strength properties of rubber. At moderate temperatures, the effect is greatest in non-crystallizing rubbers. Figure 3.7 based on Lake and Lindley (1964b) indicates that for unfilled SBR in displacement-controlled tests, fatigue life drops by a factor of 10^4 over the temperature range 0°C to 100°C. For unfilled NR in displacement-controlled tests, Figure 3.7 shows that fatigue life drops by a factor of just 4 for the same temperature range. The incorporation of fillers may reduce the temperature dependence slightly (Lake & Thomas 1992).
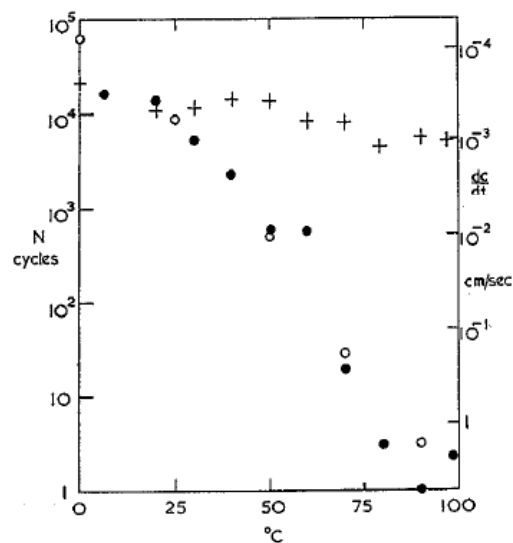
Figure 3.7: Direct effect of temperature on the dynamic fatigue life of dumbbell test pieces at 100 cycles/min: (●) SBR at 175% maximum strain; (+) natural rubber at 250% maximum strain (left-hand scale); (○) time-dependent cut growth rate at $T = 9.81$Ncm^{-1} obtained by Greensmith & Thomas (1955) on another SBR unfilled vulcanizate (right-hand scale).

3.6.2   Ageing

Temperature has a large effect on the rate of the chemical changes associated with ageing or continued vulcanization. This can result in additional degradation of fatigue life at elevated temperatures maintained for a long period of time.

Chemical ageing can be either anaerobic - typically a continuation of the chemical reactions associated with the vulcanizing system, or aerobic - in particular involving oxygen. When oxygen diffuses into the rubber, it may induce chemical changes over time to the bulk elastomer network structure. This process is commonly called oxidative ageing. Mars (2004) found that oxidative ageing causes embrittlement and reduced resistance to fatigue crack growth.

3.6.3   Ozone

Most chemically unsaturated rubbers are prone to attack by minute quantities of ozone present in the atmosphere. Such attacks not only detract from the surface appearance of rubber products but can also act as a source of flaws, initiating fatigue failure. Ozone attacks initiate cracks on strained rubber surfaces, and such cracks propagate to failure under dynamic conditions once they are large enough to provide a driving force in excess of T_o, the threshold value of tearing energy (energy available for unit area of crack growth) for the onset of mechanical crack growth.

It is believed that ozone (O_3) is a very potent oxidising agent which attacks the double bonds in the long chain molecules of unsaturated hydrocarbon rubber, like natural rubber, and butadiene rubber. Ozone reacts with the carbon-carbon double bond extremely rapidly and causes direct cleavage of the bond. Ozone attack is more damaging if the rubber is strained since it then causes cracking of the rubber surface.

Cracking occurs if the applied strain exceeds a threshold dependent on the pre-existing inhomogeneities or flaws in the rubber. The combined effect resulting in a driving force $T>T_z$, where T_z is a characteristic value for the rubber, independent of ozone concentration (above zero). Under static strain the threshold T_z can be raised by incorporating antiozonants. Antiozonants may substantially increase the threshold strain at which cracking occurs.

Ozone causes time-dependent crack growth even under constant loading. Crack growth can occur at very small tearing energy values in susceptible, unprotected rubber. Under cyclic loading, when mechanical crack growth is very slow or absent, ozone attack may be the dominant crack growth process until the cracks are large enough to permit

mechanical growth to take over when the "threshold" tearing energy is reached as shown in Figure 3.8 for 2 different ozone concentrations. For continuous cyclic loading (not undertaken at very low frequencies), the ozone contribution usually becomes negligible once the threshold tearing energy, T_o has been exceeded, as shown in Figure 3.8. The T_o value for this vulcanizate is about 40J/m^2.
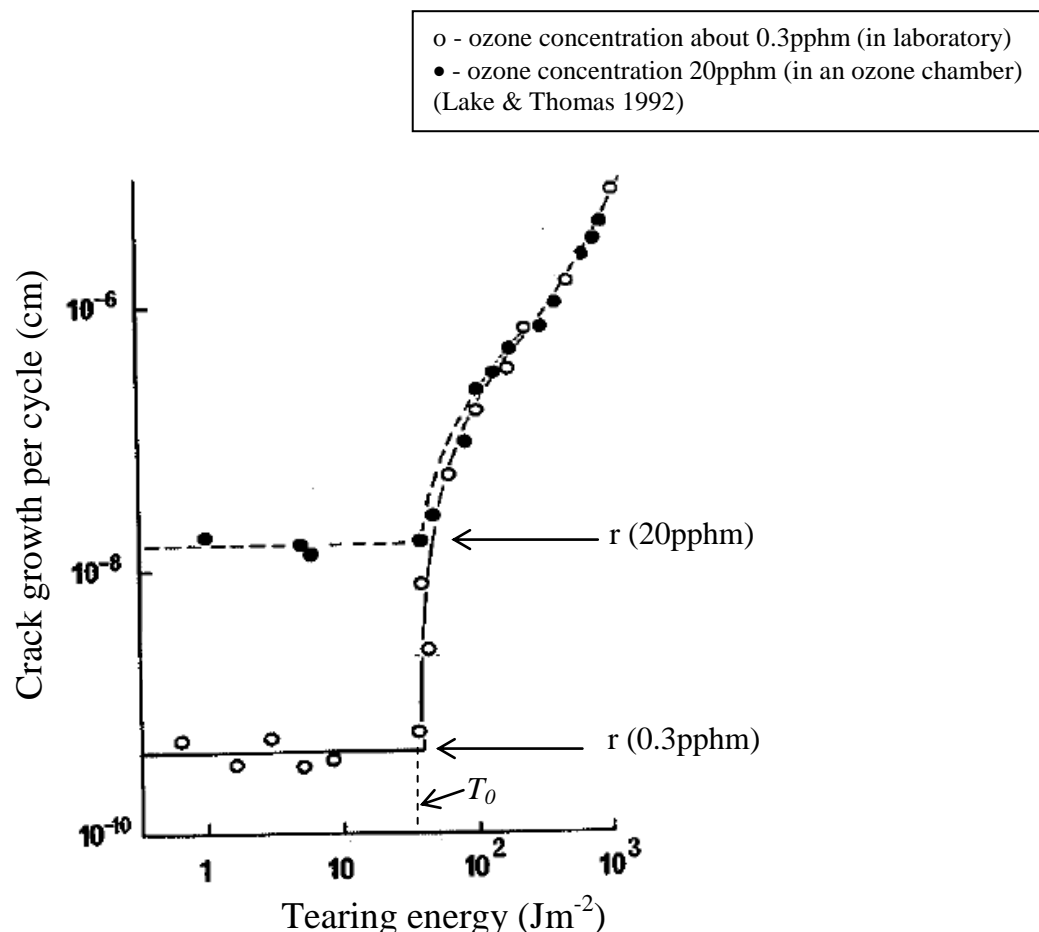
Figure 3.8: Effect of ozone on cyclic crack growth in a natural rubber vulcanizate.

Exposure to ozone during a long-term fatigue test significantly increases crack growth rate and shortens life (Braden & Gent 1960a, 1961). A few parts per hundred million of ozone concentration is sufficient to form ozone cracks. Cracking occurs more quickly as the ozone concentration increases. The reaction between ozone and the carbon-carbon double bond is one of the fastest-known chemical reactions. It is believed to cause direct cleavage of the polymer chains in NR and other unsaturated hydrocarbon rubbers. An increase in the concentration of these double bonds increases the rate of crack formation. Approximately 5% elongation is required to form cracks on a natural rubber

surface in the presence of ozone (Braden & Gent 1962, Lake & Thomas 1967b, Layer & Lattimer 1990).

Increasing the elongation of the rubber test piece increases the number of cracks which form. Braden and Gent (1960b) demonstrated that crack growth can occur when the rubber is stressed in cyclic fatigue at low strains and also under constant deformation. When a test piece contains no artificially introduced cracks the critical strain required for cracks to form must be above that for which $T>T_z$. They demonstrated that the rate of growth of a single crack is independent of strain above the critical value.

The work of Cheetham and Gurney (1961) demonstrated that increasing the velocity of the gas stream carrying ozone over a rubber sample increases the rate of crack growth. Lake and Thomas (1967b) proposed that this effect is due to the rapid consumption of ozone by growing cracks. For at low gas flow rates the supply is inadequate to drive crack growth at the rate corresponding to the inlet ozone concentration, especially for the cracks near to the outlet. In addition, the boundary layer through which the ozone must diffuse to reach the rubber becomes thicker towards the outlet, further reducing the rate of cracking there. For a flat sheet situated parallel to the direction of flow of a given fluid of the boundary layer thickness d depends on the stream velocity v and the distance x from the leading edge of the sheet, that is:

$$d = \eta \left(\frac{x}{v} \right)^{\frac{1}{2}}$$

(3.19)

where η is a constant. The existence of a relatively stationary boundary layer in the gas adjacent to the rubber surface constitutes a barrier through which ozone has to diffuse before it can react with the rubber. Lake and Thomas (1967b) attributed the decrease in rate of attack with increase in distance from the leading edge of a rubber sample in a gas flow to variation in the boundary layer thickness. Consider a gas stream containing ozone at a concentration q_0 and take the concentration at the rubber surface to be q. If a steady state situation exists, the rate of arrival of ozone M per unit area of the surface will be

$$M = \frac{D}{d}(q_o - q)$$

(3.20)

where D is the diffusion coefficient of ozone in the gas. The crack growth rate will be proportional to M, and hence, from substitution of Equation (3.19) into (3.20), inversely proportional the square root of the distance from the inlet. Ozone attack is of greatest significance in fatigue as a mechanism of initiation of surface cracks, which may subsequently grow primarily by mechanico-oxidative crack growth and result in failure. It

may also have a significant deleterious effect on fatigue life in non-relaxing conditions for strain crystallizing rubbers. In this case, the ozone cracking contribution will be increased, while the mechanico-oxidative contribution will be decreased.

3.6.4 Oxygen

Oxygen can play a major part in fatigue failure (e.g. Lake 1983). The detailed mechanism of the effect has remained obscure. However, it is clear that it is not simply a consequence of oxidative ageing, since even for a new rubber specimen with no prior exposure, the presence of oxygen increases the fatigue crack growth rate for a given energy release rate. The effect is conveniently described in terms of the energy release rate required to maintain a constant crack growth rate.

Lake and Thomas (1992) found that at low energy release rates, for a given crack growth rate in unfilled natural rubber, the requisite energy release rate in air is approximately half that in vacuum. The difference becomes less significant at higher energy release rates, and depends on the test frequency. For lower frequencies, the difference persists to higher energy release rates. The magnitude of the effect also depends on polymer type.

Figure 3.9 indicates how oxygen reduces T_0 and can increase the rate of crack growth for $T>T_0$ (Lake 1972). The effect of oxygen on crack growth rate tends to become negligible at high tearing energies, although it persists for longer at low frequencies of cycling. It is probable that the mechanism involves activation of the reaction of oxygen by mechanical stress at crack tip. The threshold energy is apparently reduced, suggesting that the primary bond strength is lowered by oxygen. The effect can be partially mitigated by incorporation of suitable antiflex-cracking antioxidants.
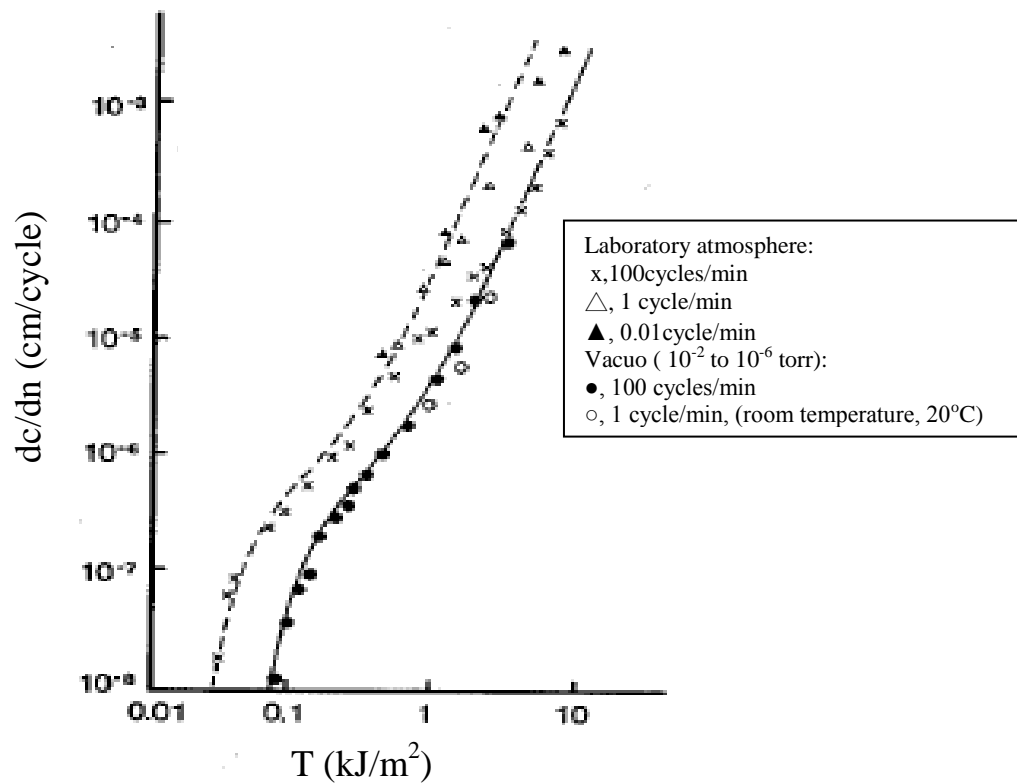
Figure 3.9: The effect of frequency on the crack growth behaviour of an unprotected NR vulcanizate (Lake 1983).

Gent and Hindi (1990) compared crack growth rates under both static and cyclic loading, in air and in vacuum, for natural rubber (NR), styrene butadiene rubber (SBR) and polybutadiene (BR). They only observed a factor-of-two change in the fatigue crack growth rate for NR, due to presence of oxygen. For SBR and BR, a factor of 8 between air and vacuum crack growth rates was observed. They demonstrated experimentally that when an oxygen atmosphere was applied and then removed alternatively that the oxygen effect on fatigue crack growth rate depended only on the current oxygen concentration and not on past levels. In the experiment, the rate of crack growth was observed first to increase, then decrease, then increase again to the first level, in correspondence with the presence or absence of oxygen.

3.6.5   Water

Lake and Pond (1989) compared fatigue of NR dumbbells under distilled water and in air. For an unfilled NR unprotected with 1pphr N-(1,3-dimethylbutyl)-N'-phenyl-p-

phenylendiamine (HPPD) and 1pphr antioxidant TMQ the longevity in air and water were similar up to at least 10Mcycles, corresponding to a maximum strain of about 40%. They suggested that this may, in part, reflect a cancellation of two opposing effects. Some reduction of fatigue life might have been expected in water because of leaching of the antioxidants. However, the absence of ozone and the increase in "set", which is the strain offset at zero stress as each loading-unloading cycle is undertaken, would be expected to result in an increased fatigue life. For a material without antioxidants the fatigue lives were lower than for the protected material. This observation was unaffected by whether the test was undertaken in air or water, except for the lowest strain amplitudes (maximum strain 50% or less), the fatigue lives were greatest under water. For a maximum strain of 40%, the material behaviour was similar to that of the protected material.

Latos and Spark (1969) reported that paraphenylenediamine (PPD) antioxidants are extracted from NR and SBR by water resulting in decreased ozone resistance, with losses increasing as the pH of the water is decreased. The ease of water leaching decreases with increasing molecular weight of the antioxidant and increasing acidity of the water. They suggested that to minimize the effect of leaching of the antioxidant, it is desirable to use antioxidants with a molecular weight at least 304gmol^{-1}.

3.7   Diffusion Limited Oxidation

Exposure of polymer to air during aging (radiation, thermal, UV) often results in heterogeneously oxidized samples, a complication that impedes our understanding of the oxidation process and our desire to extrapolate accelerated exposures to long-term conditions. Diffusion limited oxidation occurs when the rate of oxygen consumption in a material is greater than the rate at which oxygen is resupplied by diffusion from the surrounding air atmosphere. In order to extrapolate accelerated air ageing simulations to long-term prediction, the measurement of diffusion limited oxidation needs to be monitored quantitatively. Diffusion limited oxidation is also crucial for in-service performance of thick rubber products (e.g. Kamaruddin et al. 2011, Kamaruddin et al. 2013).

3.7.1   Theory of Oxygen Diffusion and Simultaneous Reaction

Consider the situation in which a thin film of polymer is exposed on both faces to a constant pressure of oxygen (Billingham & Walker 1975). If the *x* direction is defined as perpendicular to the faces of the film then for any point within the film we may write

$$\frac{\partial C}{\partial t} = D \frac{\partial^2 C}{\partial x^2} \qquad , \qquad (3.21)$$

where C is the oxygen concentration and D is the diffusion coefficient. This equation holds only if oxygen is not absorbed by the film and D is independent of concentration. However, oxygen consumption is a first-order reaction with the polymer. Hence Equation (3.21) must be modified to take this into account and the appropriate expression becomes

$$\frac{\partial C}{\partial t} = D \frac{\partial^2 C}{\partial x^2} - kC \qquad . \qquad (3.22)$$

Numerical solution of this equation is explained in Chapter 9

3.8   Conclusions

(1.) A fracture mechanics approach based on a tearing energy fracture criterion has been found to be reasonably successful in predicting rubber fatigue life in simple geometries either under continuous loads or repeated excitations. It is believed that mechanical fractures occur when a rubber component is subjected to a cyclic stress or strain. The initial crack usually propagates from an area of high tensile stress concentration and grows until complete fracture occurs. The growth rate increases with increasing temperature and increased stress or strain amplitudes. Fracture mechanics also appears to provide a rational basis for predicting the fatigue life of components made of rubber. It is necessary for the intrinsic crack growth behaviour of the rubber itself to be determined, at least approximately, using one or more of the appropriate test pieces. Prediction of fatigue failure can be made from the energy release rate versus the crack growth rate characteristics of the rubber, the shape and size of the initiating intrinsic cracks, i.e. the effective flaw size, and the calculation of the energy release rate imposed on such flaws results from the geometry and load conditions of the rubber component in which they lie.

(2.) Environmental factors can affect fatigue behaviour of rubber. Elevated temperatures and the presence of oxygen or ozone are detrimental. The rate of

crack growth may vary reversibly with these variables, in the short term. Exposure over long periods of time leads to irreversible changes in the rubber due to elevated temperature and oxidative ageing. These changes include evolution of both the elastic and strength properties.

Chapter 4

Experimental: Ozone Cracking on Rubber

4.0 Introduction

The previous chapter indicated that ozone could have a detrimental effect on the durability of rubber. For wave energy devices the ambient ozone levels can be high (Jones 1968). If their principal component is rubber, the issue of ozone cracking merits special attention in this research project. For an unprotected vulcanizate a strain of the order of a few per cent in simple extension is required to produce surface cracking (Braden & Gent 1960a). It has been observed that ozone cracking is retarded in water according to the earlier cited studies.

4.1 Ozone Cracking on Strained Rubber in Water and Air

Ozone attack is expected to be very substantially mitigated by immersion in water since:

- The rate of diffusion of ozone across the stagnant boundary layer adjacent to the rubber surface will be much lower in water than in air (Lake & Thomas 1967b).

- Ozone is more unstable in air than in water, so the ozone concentration away from the free surface water is likely to be very low (Roth & Sullivan 1981).

When chemical antioxidants/antiozonants are present in rubber, they form a surface layer as a direct consequence of the reaction between ozone and the antiozonant (Lake & Mente 1992). Antioxidants and antiozonants in rubber leach out in water, particularly if the water is turbulent. In order to investigate whether a rubber-like material is sufficiently sustainable and reliable for a device, a test providing a high concentration level of ozone exposure is required. Since high ozone concentration tests are yet to be commissioned at TARRC, a current short-term ozone testing procedure at a lower concentration was conducted to check consistency with the theory of Lake & Thomas (1967b). There is also a need to provide additional evidence as to whether this procedure provides results consistent with the more extensive experimental testing programme of Zuev & Malofeevskaya (1961).

In the present study, an examination of the effect of ozone attack on strained rubber immersed in distilled water is addressed. In addition, the minimum time for cracks to first appear on the strained sample housed in an ozone cabinet is determined. An investigation of crack length formed with different strains has been conducted. The observation of the effect of ozone attack on unstrained rubber was also undertaken. Crack formation initiated by ozone is a common observation for rubber subjected to uniaxial tension. The investigation of the crack formation in biaxial strain is less reported and it is therefore interesting to see how the strain directions affect the formation of cracks. This work was initiated after observing the crack formation on the Bramfield-solid cartwheel tyre reported in Chapter 9.

4.2 Material, Test Procedures and Results

For the investigation of ozone cracking an unfilled rubber sheets were prepared based on the Engineering Data Sheet formulation EDS19 without antiozonant & antioxidant additives, which will be referred to as R1 (EDS19A) in this thesis. For a filled rubber sheet, EDS14 without antiozonant & antioxidant additives were prepared which will be referred as R2 (EDS14A). The proportions of ingredients of each compound by weight are as follows:

	R1	R2
Ingredient	parts per hundred rubber (pphr)	
Natural rubber SMR CV60	100	100
Carbon black, HAF N-990	0	15
Process oil, 410 oil	0	1.5
Zinc Oxide	5	5
Stearic acid	2	2
CBS*	0.6	0.6
Sulfur	2.5	2.5
Cure Temperature (^{o}C)	140	140
Cure Time (min)	45	38

*CBS- N-cyclohexyl-2-benzothiazolesulphenamide

Both formulations were press-cured in the form of a 229mm square sheet with a thickness of 2mm. Five distinct ozone tests were conducted to investigate crack formation in the rubber surface.

4.2.1 20% Strain Ozone Test in Water and Air: Procedure

In the first test, four test-pieces measuring 160mm × 10.5mm were cut from the R1 cured 229mm square rubber sheet and placed in tension clamps. A reference length was marked out on each test piece to facilitate subsequent measurement of the strain. All four samples were elongated to 20% strain as shown in Figure 4.1. The cut edges of each sample were coated with paraffin wax to protect them from ozone attack and hence prevent the growth of cracks from the flaws introduced by the cutting process. Paraffin wax was also applied to the rubber surface near to the clamping jig to protect this area of stress concentration in each test piece. In order to investigate the attack of ozone under water, two strained samples were immersed in distilled water in aluminium trays. The water depth was 35mm, whereas the water depth from the top surface of the specimen to the surface of the water was 15mm. In the ozone chamber, the ozone concentration was 50pphm and the internal temperature was maintained at 40°C (BS ISO 1431-1:2004). The overall test duration was 72 hours. The other two samples were placed in an aluminium tray without water, for comparison. Figure 4.2 shows the four test pieces in the ozone cabinet. The surface of each test piece was inspected using the 'Peak scale loupe 7x'(handy) microscope every 24 hours. To record the extent of the crack, light micrographs of the top and bottom surfaces were undertaken using an Olympus S2X7 Stereo light microscope. Throughout these measurements each sample remained in the same 20% strain state.
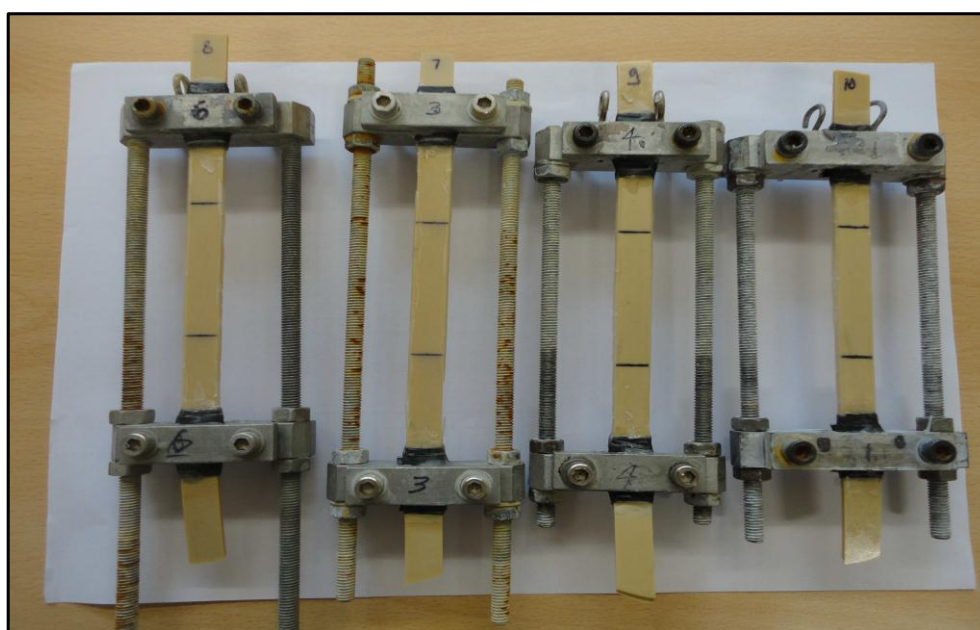
Figure 4.1: Test pieces placed in tension jigs at 20% strain.

Aluminium tray filled with distilled water. (Tray size: L315xW268xT55mm)

Aluminium tray. (Tray size: L310xW242xT55mm)

Figure 4.2: Ozone chamber and ozone cabinet THE-P3C6R manufactured.
by Satra Technology.

4.2.1a 20% Strain Ozone in Water and Air: Results
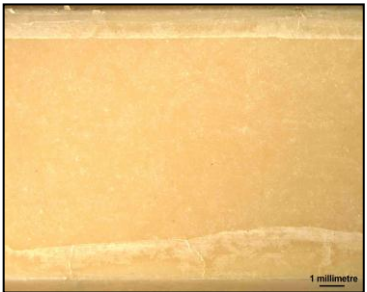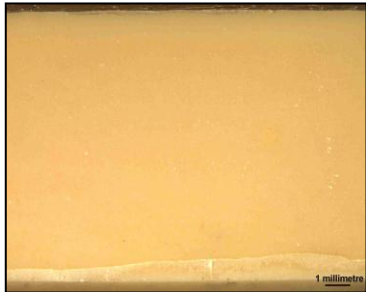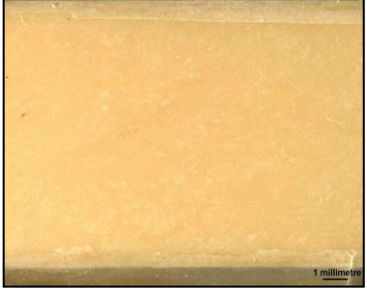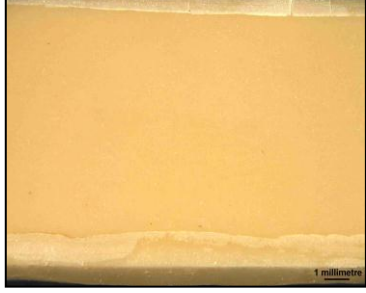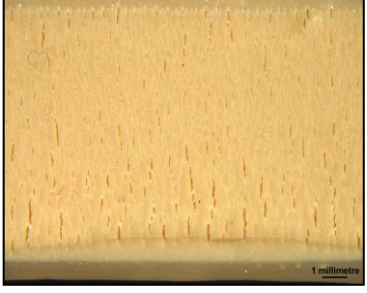
Small cracks were found in the non-immersed samples after 24 hours. In the case of strained samples immersed in distilled water, no cracking was found on the top and bottom surfaces after 72 hours. Table 4.1 provides the recorded observations for each test piece every 24 hours. Every 24 hours the depth of water diminished from 35mm to 32mm due to evaporation in the ozone chamber. To maintain the initial prescribed level of water, more water was added to restore the level to 35mm prior to starting next testing period. Evaporation of water, and the consequent need to replenish it, had not been appreciated in the first attempt at an immersion test, and crack generation occurred as the samples became exposed to the ozone injected air.

Observations during all the tests, given in Table 4.1, confirm that cracks were formed only on the samples not immersed in distilled water in the ozone cabinet. All micrographs were taken at the same magnification using illumination. Table 4.2 shows the micrographs of all samples after the completed ozone chamber tests.

Table 4.1: Observation of test pieces at every 24 hours.

Sample No.	Location/Condition	Observations
007, (H$_2$O)	Ozone Cabinet 50pphm, 40°C, 24 hours	No cracks, no bloom
	Ozone Cabinet 50pphm, 40°C, 48 hours	No cracks, no bloom
	Ozone Cabinet 50pphm, 40°C, 72 hours	No cracks, no bloom
008, (H$_2$O)	Ozone Cabinet 50pphm, 40°C, 24 hours	No cracks, no bloom
	Ozone Cabinet 50pphm, 40°C, 48 hours	No cracks, no bloom
	Ozone Cabinet 50pphm, 40°C, 72 hours	No cracks, no bloom
009	Ozone Cabinet 50pphm, 40°C, 24 hours	Several large cracks at ends both sides, Several small, several medium cracks at both sides along edges.
	Ozone Cabinet 50pphm, 40°C, 48 hours	Several large split cracks at end of test piece. Several medium, many small cracks mainly at edges.
	Ozone Cabinet 50pphm, 40°C, 72 hours	Many medium, many small cracks at all surface. Several large cracks mainly at edges. Several large splits at end of test piece – both sides.
010	Ozone Cabinet 50pphm, 40°C, 24 hours	Several medium and several large cracks at end of test piece.
	Ozone Cabinet 50pphm, 40°C, 48 hours	Several large splits and large cracks at both side end of test piece.
	Ozone Cabinet 50pphm, 40°C, 72 hours	Several large splits and large cracks at end of test piece – both sides. Several large cracks at edges, many small cracks at whole surface and several medium cracks at edges – both sides.

Table 4.2: Micrographs of samples in chamber 50pphm ozone concentration after 72 hour.

Test Piece No.	Top Surface	Bottom Surface
007 (H_2O)		
008 (H_2O)		
009		
010 Direction of tension ⟷		

Ozone tests (up to 72hours at 50pphm ozone, $40^{o}C$) using two test pieces stretched to, and maintained at, 20% strain whilst immersed in distilled water had no cracks on their top and bottom surfaces. In contrast, many medium cracks formed on the two test pieces at 20% strain not immersed in the distilled water. Maintaining a 15mm water depth over the strained rubber surface prevented such crack formation. It is concluded that ozone cracking in natural rubber vulacanizate is much slower in water than in air and that any hydrogen peroxide formed by the interaction of the ozone with water does not cause cracks to

appear. Presumably a water layer 15mm thick serves as a barrier to transport of ozone to the rubber surface, in accord with the theory of Lake & Thomas (1967b), and experimental observation of Zuev & Malofeevskaya (1961).

4.2.2 20% Strain Ozone Tests to Measure Cracking Initiation Time: Procedure

A second separate ozone test was carried out to make a quantitative check of the theory of Lake and Thomas (1967b). This requires measurement of the time required to observe ozone cracking for immersed rubber. The time required for ozone induced cracking of a specimen immersed in water is predicted to be about 10^4 times greater than for test pieces exposed to the atmosphere in the ozone cabinet. Ideally, the minimum time of exposure needed for cracks to first appear both for exposed and immersed test pieces needs to be determined. Therefore, six test-pieces R1 were prepared in a similar way to those illustrated in Figure 4.1 and placed in tension jigs at 20% strain. Paraffin wax was again applied to the rubber edges and the surfaces near to the clamping jig to protect this area of stress concentration in each test piece. The specimens were placed in the ozone cabinet at an ozone concentration of 50pphm with internal temperature maintained at 40^oC. All the jigs with test pieces were hung from a steel rod located in the ozone cabinet.

Each test piece was removed from the ozone cabinet after one hour and the top and bottom rubber surfaces were inspected using the 'Peak scale loupe 7x'(handy) microscope. The Scanning Electron Microscopic (SEM) was also used because the cracks in the test pieces were too small for good images to be obtained by the loupe. In order to use the SEM, it was necessary to transfer a test piece to a shorter jig fitted to the largest SEM stub (a circular metal plate 15cm in diameter). Since the rubber test pieces were non-conducting material, a conductive coating was applied to prevent them 'charging up' in the electron beam. In this case the test pieces were coated under vacuum with gold/palladium vapour from a 6cm length of gold/palladium wire. The top surface of both test pieces designated 19 and 20 were coated at the same time. After the top surfaces had been micrographed, the test pieces in their jigs were inverted and the bottom surfaces were coated with gold/palladium in the same way.

4.2.2a Cracking Initiation Time: Results
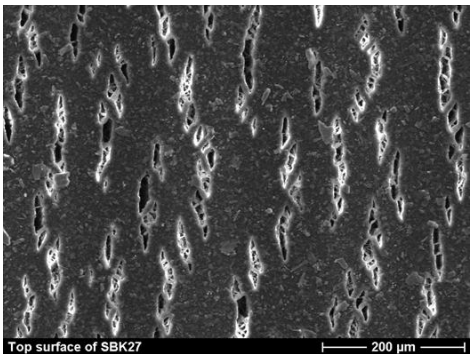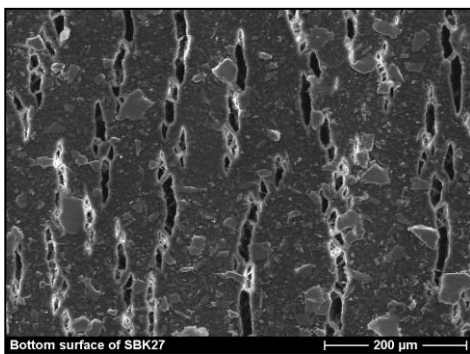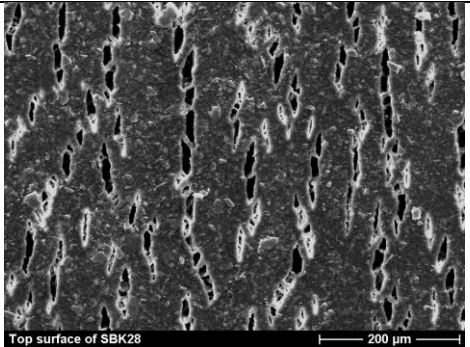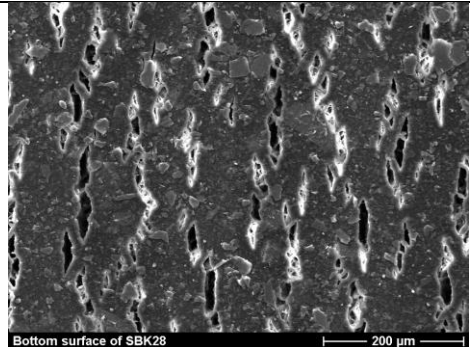
Table 4.3 presents the results of hourly observation over six hours test pieces. Crazing formation was observed on the rubber surface after three hours and small cracks were found on the rubber test-pieces after the next one-hour interval to observation.

Table 4.3: Observation of test pieces at every one hour.

Sample No.	Location/Condition	Observations
017	Ozone Cabinet 50pphm, 40°C, 1 hour	No cracks, no bloom
018	Ozone Cabinet 50pphm, 40°C, 2 hour	No cracks, no bloom
019	Ozone Cabinet 50pphm, 40°C, 3 hour	Starting craze in strain area
020	Ozone Cabinet 50pphm, 40°C, 4 hour	Several very small cracks running in the waxed edge
021	Ozone Cabinet 50pphm, 40°C, 5 hour	Many very small cracks running in the waxed edge
022	Ozone Cabinet 50pphm, 40°C, 6 hour	Many very small cracks running in the waxed edge

Table 4.4 provides the images taken using SEM after three and four hours. In all the SEM micrographs the direction of stretching is left to right.

Table 4.4: SEM images of samples in chamber 50pphm ozone concentration after 3 and 4 hour.

Test Piece No.	Top Surface	Bottom Surface
019 - after 3 hour Direction of tension ←→		
020 - after 4 hour Direction of tension ←→		

Cracks were seen in both surfaces of both samples except near the edges where the samples had been covered with paraffin wax. Many flat particles were present on both surfaces of both test pieces and these can be seen in all the micrographs (though attempts were made to avoid them). These particles were more numerous on the bottom surfaces

than the top surfaces. They might be small pieces of wax. The length of the initial crack was less than 200µm. More small cracks can be observed on the top and bottom rubber surfaces after a four-hour period compared to the sample after 3 hour in the ozone cabinet. Cracks appear after ~3 hours, suggesting that might appear after 3×10^4 hour $\cong$ 1,278 days or three and a half years immersion according to the theory of Lake & Thomas (1967b). Unfortunately neither the ozone cabinet nor a high ozone concentration apparatus was available for further tests to check the theory.

4.2.3 20% Versus 40% Strain Investigation: Procedure

A third test involved using four test pieces R1 of dimensions $150 \times 10 \times 2$mm with two stretched to 20% strain and two stretched to 40% strain using tension jigs. Paraffin wax was again used as described earlier. All the test pieces were placed in the ozone chamber for 72 hours. The ozone concentration was 50pphm and the temperature maintained at 40°C. The objective of this test is to investigate crack formation at two different strain conditions and also to have quantitative data on different crack lengths on strained rubber surface.

4.2.3a 20% Versus 40% Strain Tests: Results

Ozone crack lengths of both samples stretched to 20% strain and 40% strain after ozone exposure tests were measured using a travelling microscope with magnification of 7.5. Two lines were made in the centre of the testpiece. The distance between two lines was 10mm. Twenty locations were chosen on each testpiece. These locations were chosen in sequence following the pattern shown in Figure 4.3. The travelling microscope was moved 2mm in either the horizontal or the vertical plane. The longest crack in the 9.5mm diameter microscope view was measured. These lengths are recorded in Figure 4.4.
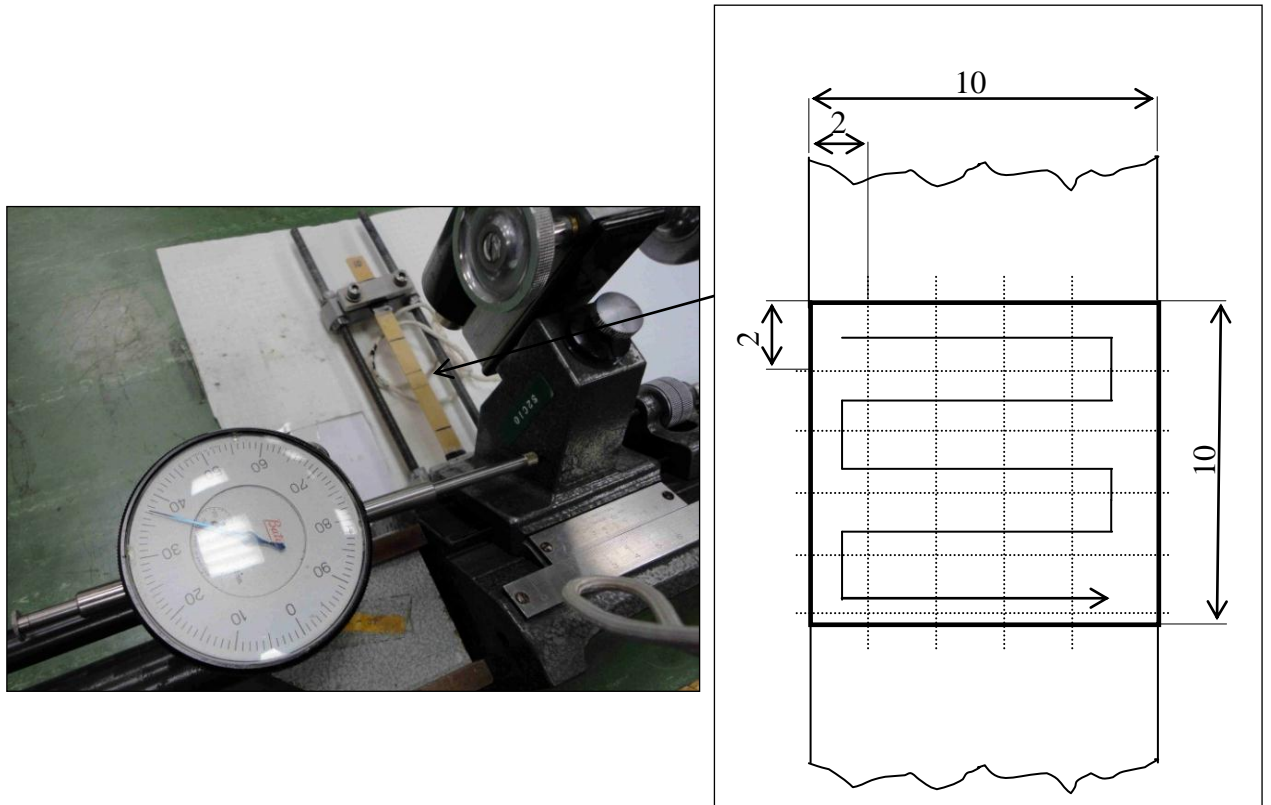
Figure 4.3: A travelling microscope with the pattern location of measurement area.

Figure 4.4 confirms that crack lengths of samples stretched to 20% strain is longer than the samples stretched to 40% strain. The range of crack length on the samples stretched to 40% strain was 0.15 ~ 0.56mm. In contrast, the range of crack length of the samples stretched to 20% strain was 0.45 ~ 0.96mm. It is confirmed that the number of cracks is greater at 40% strain than at 20% strain.
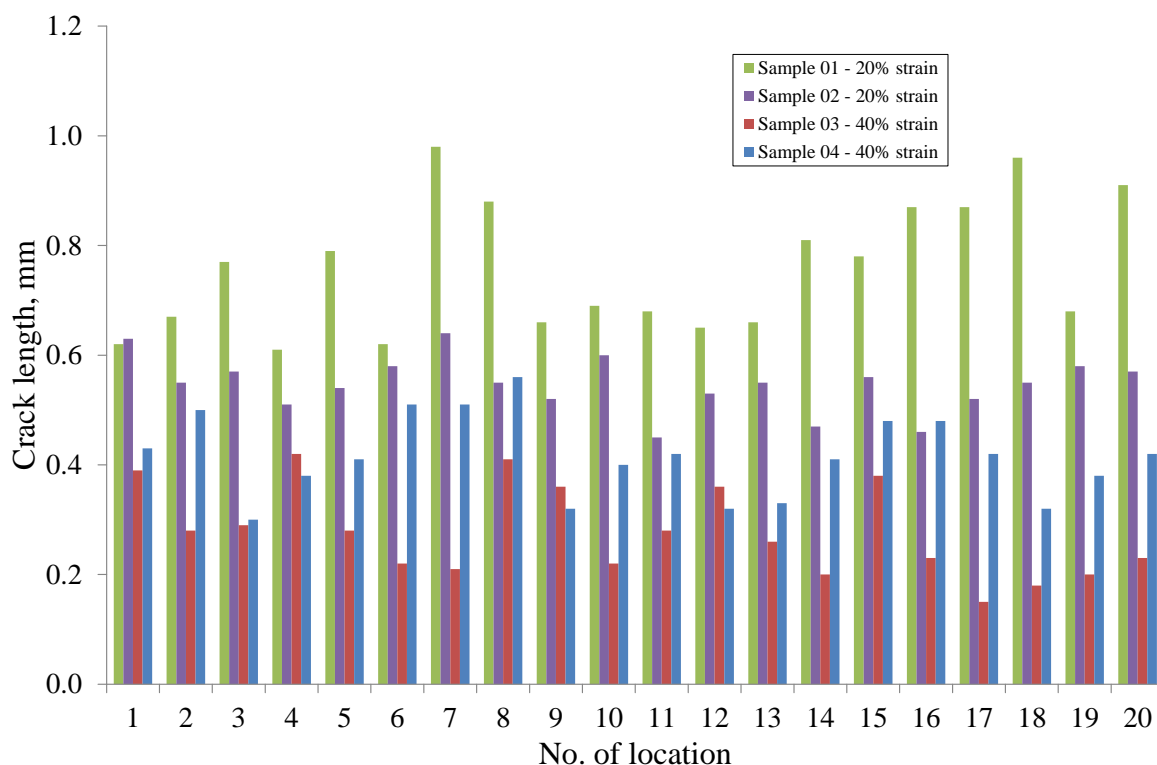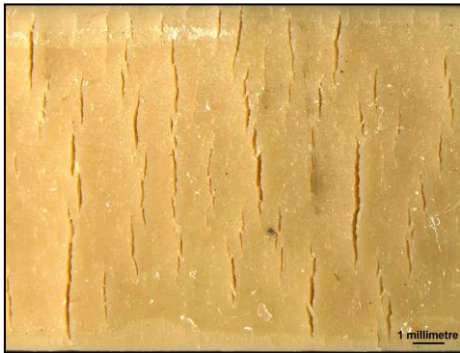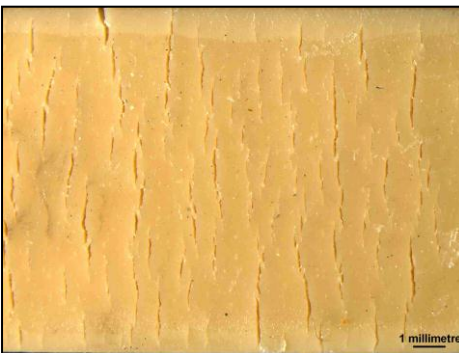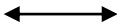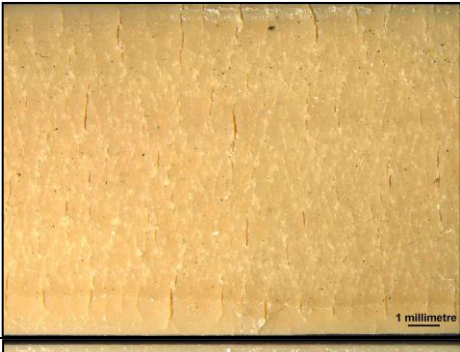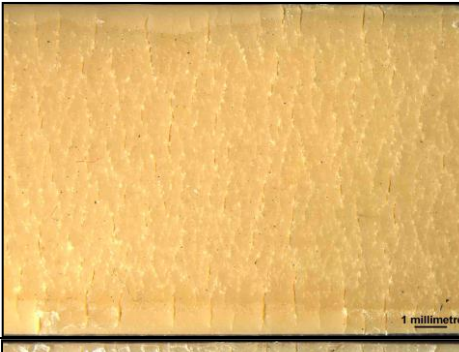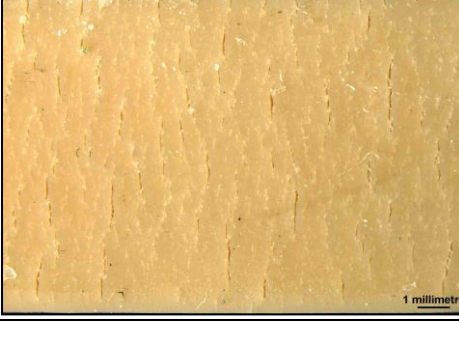
Figure 4.4: Crack lengths as a function of predetermined location.

Table 4.5 shows the micrographs of samples after 72 hour exposure in the ozone chamber tests. In order to observe clearer crack formations, light micrographs of the top and bottom surfaces were required. The test piece surfaces were observed using the Olympus S2X7 Stereo light microscope. Stretching the cracked test piece caused the cracks to open up and become more visible, so it was decided to stretch all of the samples by 10% in a stretching jig and micrograph them in that stretched state. All of micrographs were taken at the same magnification using incident illumination. Since all of the samples had pieces of wax on their surfaces, most of these were removed with tweezers before the micrographs were taken.

Table 4.5: Micrographs at 10% strain of samples in chamber 50pphm ozone concentration after 72 hour.

Sample No.	Top Surface	Bottom Surface
01 after 72 hour Direction of tension ←——→ 20% strain		
02 After 72 hour Direction of tension ←——→ 20% strain		
03 after 72 hour Direction of tension ←——→ 40% strain		
04 after 72 hour Direction of tension ←——→ 40% strain		

It is observed that crack lengths are larger when the rubber testpiece stretched to 20% strain compared to 40% strain. The number of cracks is larger on the rubber surface stretched to 40% strain compared to 20% strain.

4.2.4 Biaxial Testing at 100pphm Ozone Concentration: Procedure

A special jig was fabricated to carry out ozone tests in biaxial strain. A cross test piece (R1) with legs of 25mm width and a thickness of 1.97mm was cut from a sheet. The unstretched width of "cross" was 95mm in each direction. Then it was stretched to 20% strain on both sides to create a central biaxial condition where the orthogonal uniaxial strain fields in the legs merge. The sample was placed in an ozone cabinet with 100pphm ozone concentration at $40^{o}C$ (as stipulated by BS ISO 1431-1:2004). The ozone test was carried out for 144 hours and several micrographs were taken using a compound light microscope to investigate the evolution of cracks in the rubber sheet. Figure 4.5 shows the sample in the special jig in place in the ozone cabinet.

a.) Front view of the sample

b.) Back view of the sample
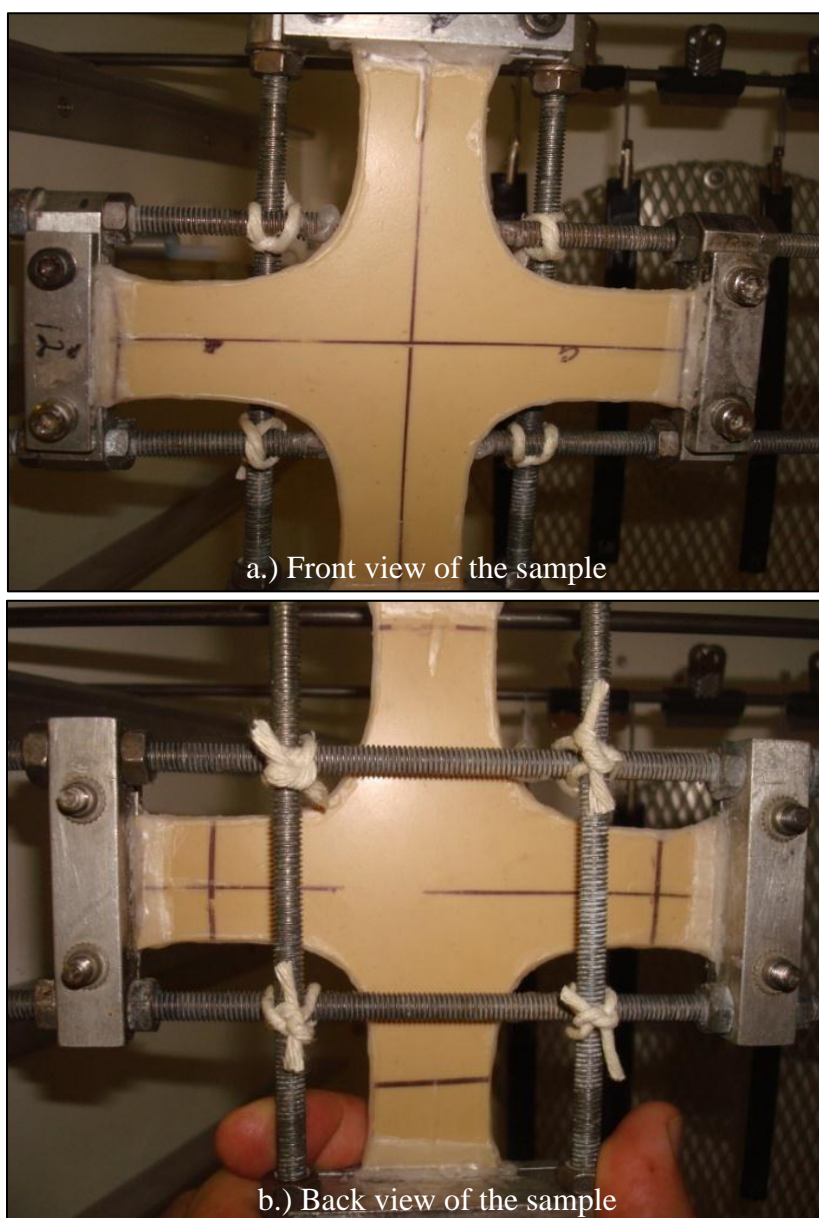
Figure 4.5: The observation of rubber sample at the beginning stage.

4.2.4a Biaxial Test: Results

Table 4.6 shows the observation of the cross test piece in biaxial condition with different time durations.

Table 4.6: The observation of rubber in biaxial condition.

Time	Observations
After 72 hours	Many medium cracks all over test piece. Central region has many small 'crazing' cracks resembling shrinkage cracks. Many ozone cracks parallel to bisector at junction of legs. Many very large splits on all 4 legs, back towards grips. 2 small holes, one extremely large hole adjacent to one grip. 2 medium holes adjacent to grip. The strain reduced to 19.5% and 18.9% strain owing to holes formation.
After 144 hours	Many large and extremely large cracks all over test piece. Central region has many large 'crazing' cracks resembling shrinkage cracks. Many ozone cracks parallel to bisector at junction of legs. Many extremely large splits on all 4 legs, back towards grips. Many very large and extremely large holes adjacent to grips.

Figures 4.6, 4.7 and 4.8 illustrate the cracks formed following exposure to ozone. The depth of the cracks was deeper after 144 hours (Figures 4.7 and 4.8). The longer the period of ozone exposure, the greater the ozone penetration into rubber and damage to the rubber surface. The orientation of cracks was normal to the principal tensile strain directions, except where they were equal and then the pattern resembled shrinkage cracks. Figure 4.6 shows the variation of crack orientation, after 72 hours, over the test piece. After 144 hours the cracks could be observed more clearly and their depth was greater as shown in Figures 4.7 and 4.8.

Arrows indicate portion of test piece magnified to show cracks.
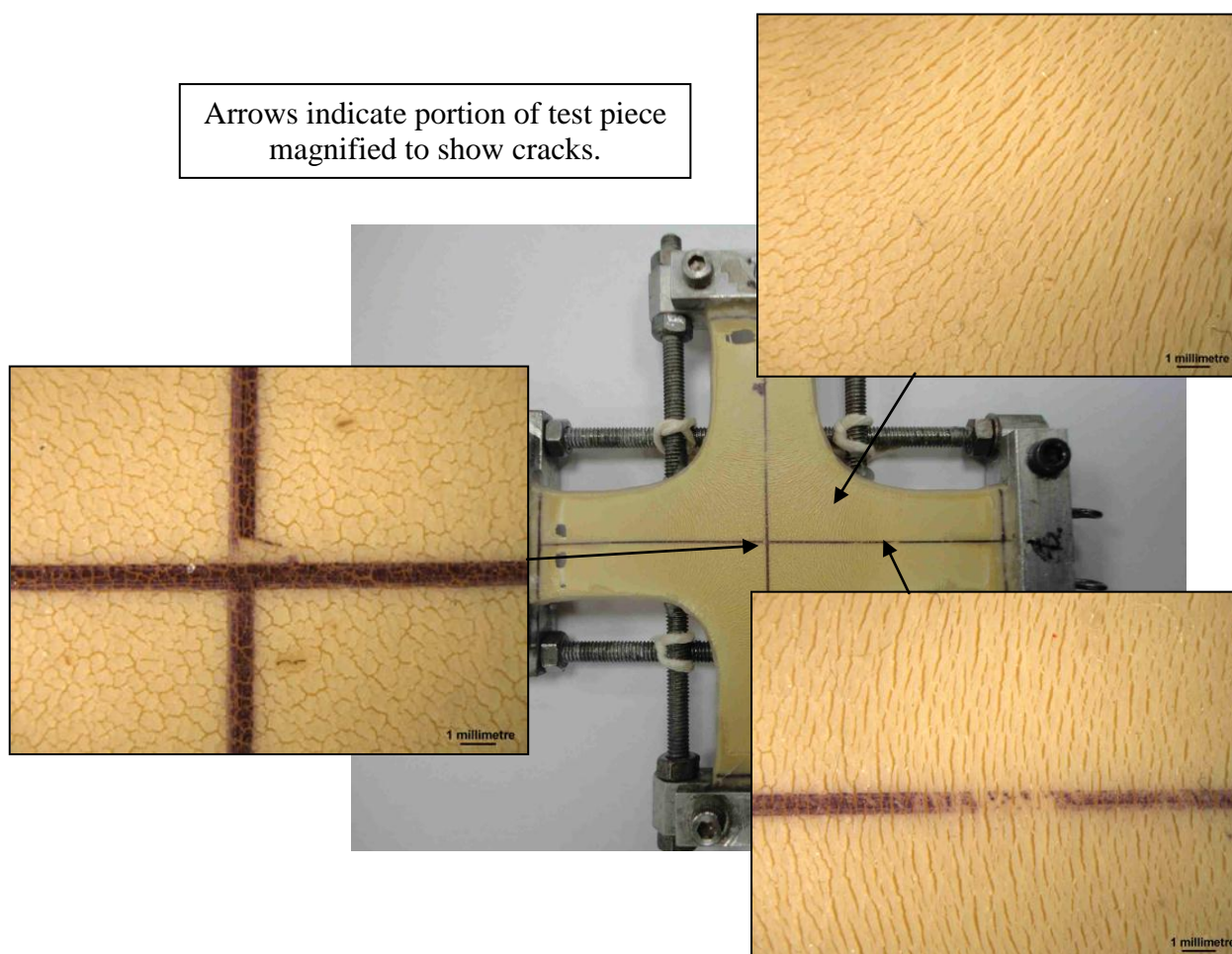
Figure 4.6: Crack formation on the rubber surface after stretched in biaxial direction for 72 hours in the ozone cabinet with ozone concentration of 100pphm.
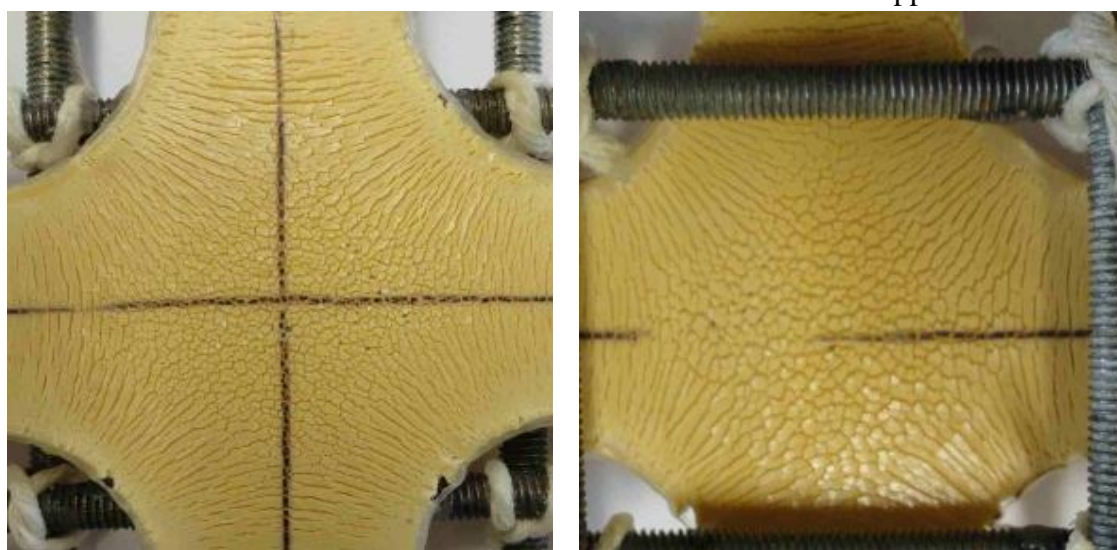
a.) Front view of the sample   b.) Back view of the sample

Figure 4.7: The observation of cracks on the rubber surface after 144 hours.

Arrows indicate portion of test piece magnified to illustrate multiplicity of cracks form.
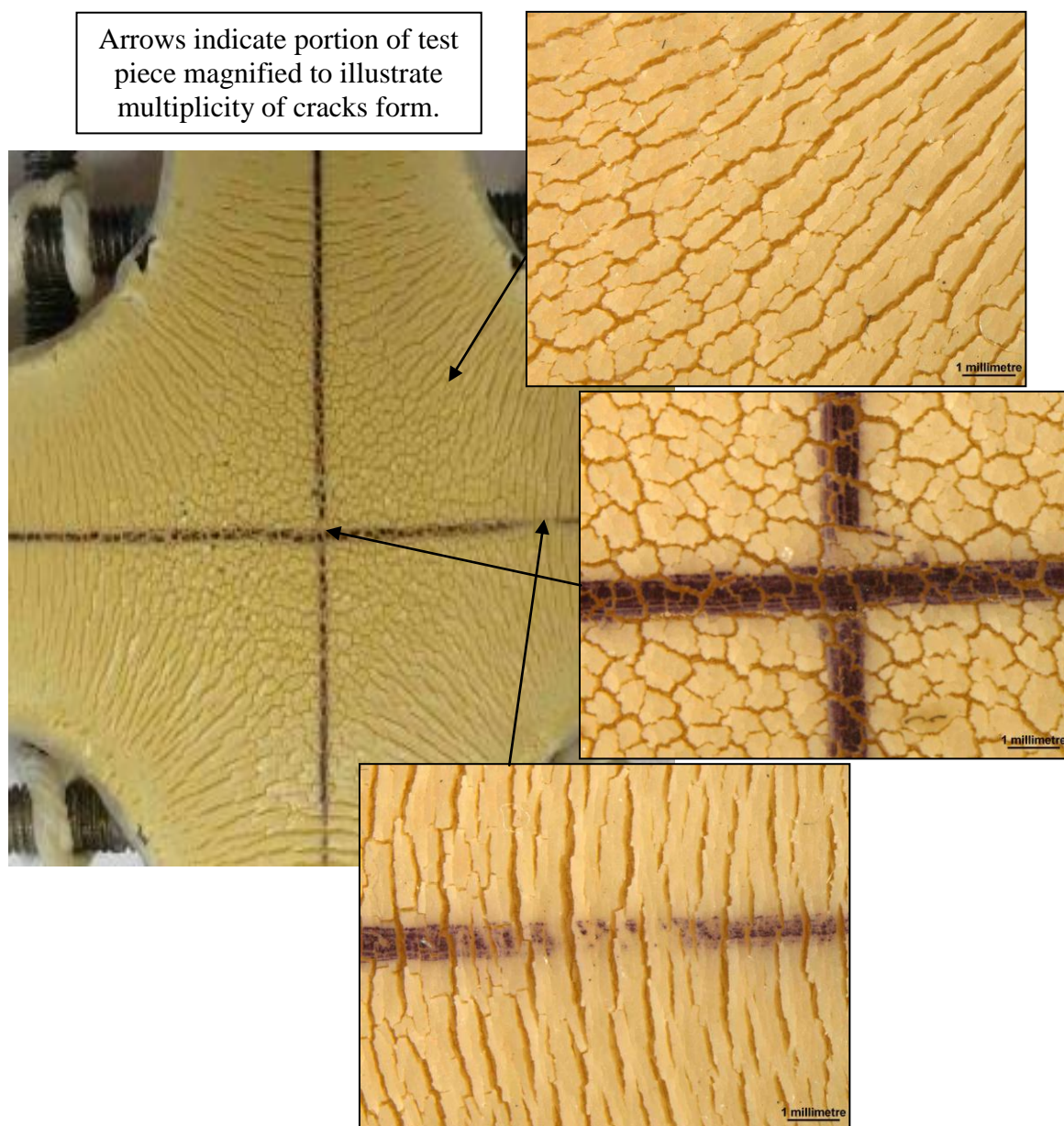
Figure 4.8: Crack formation on the strained rubber surface after exposure in biaxial strain for 144 hours in the ozone cabinet with ozone concentration of 100pphm.

4.2.5 Unstrained Different Rubber Compounds: Procedure

Unstrained rubber samples were also tested in the ozone chamber at the ozone concentration of 50pphm and the internal temperature was maintained at 40°C. The overall test duration was 96 hours. Six samples were prepared with three samples using R1 and the other three samples using R2.

All the test pieces were hung using crocodile clips and paper clips from a steel rod located in the ozone cabinet as shown in Figure 4.9. They were removed from the ozone cabinet every 24 hours to enable inspection of the surfaces using the 'Peak scale loupe 7x'(handy) microscope. The hardness and the thickness of each test piece was measured after 96 hours. The objective was to investigate the properties of any layer of ozonised rubber that might form at the surface.

Figure 4.9: Unstrained test pieces hung in the ozone cabinet.

4.2.5a Effect of Ozone Exposure on Unstrained Rubber: Results

Tables 4.7 and 4.8 provide observations made after every 24 hour period for R1 and R2 exposed in the ozone chamber tests.

Table 4.7: Observation of R1 surfaces at 50pphm ozone concentration and 40°C.

R1 (EDS19A)

Sample No.	Time	Observation
1	24 hours	No cracks, no bloom. Shiny appearance. Slightly tacky.
2		No cracks, no bloom. Shiny appearance. Slightly tacky.
3		No cracks, no bloom. Shiny appearance. Slightly tacky.
1	48 hours	No cracks, no bloom. Shiny appearance and tacky.
2		No cracks, no bloom. Shiny appearance and tacky.
3		No cracks, no bloom. Shiny appearance and tacky.
1	72 hours	No cracks, no bloom. Shiny appearance and tacky.
2		No cracks, no bloom. Shiny appearance and tacky.
3		No cracks, no bloom. Shiny appearance and tacky.
1	96 hours	No cracks, no bloom. Shiny appearance and tacky.
2		No cracks, no bloom. Shiny appearance and tacky.
3		No cracks, no bloom. Shiny appearance and tacky.

Table 4.8: Observation of R2 surfaces at 50pphm ozone concentration and 40°C.

R2 (EDS14A)

Sample No.	Time	Observation
4	24 hours	No cracks, dull and shiny mottled bloom.
5		No cracks, dull and shiny mottled bloom.
6		No cracks, dull and shiny mottled bloom.
4	48 hours	No cracks, less dull patching more shiny bloom.
5		No cracks, less dull patching more shiny bloom.
6		No cracks, less dull patching more shiny bloom.
4	72 hours	No cracks, shinier bloom with a few dull areas.
5		No cracks, shinier bloom with a few dull areas.
6		No cracks, shinier bloom with a few dull areas.
4	96 hours	No cracks, shiny bloom with a few dull areas remaining.
5		No cracks, shiny bloom with a few dull areas remaining.
6		No cracks, shiny bloom with a few dull areas remaining.

All the testpieces formed shiny layers without any cracks after exposure to ozone. It is believed there is a reaction of some ingredients with the ozone reaction.

Micrographs of all the samples were taken using a stereo light microscope with illumination. The control samples were cleaned using ethanol and fibre-free lens tissue to remove the talcum powder on the surfaces before being micrographed. The talcum powder was applied after the mixing process to avoid tackiness. Figure 4.10 shows the different surfaces of R1. It was difficult to distinguish between both surfaces by naked eyes since the materials were pale. A probe was used to remove some of the shiny layer and the micrograph shown in Figure 4.11, reveals that the shiny material has formed a thin layer on the surface.

(a) Control sample   (b) After test (96 hours exposed to ozone)
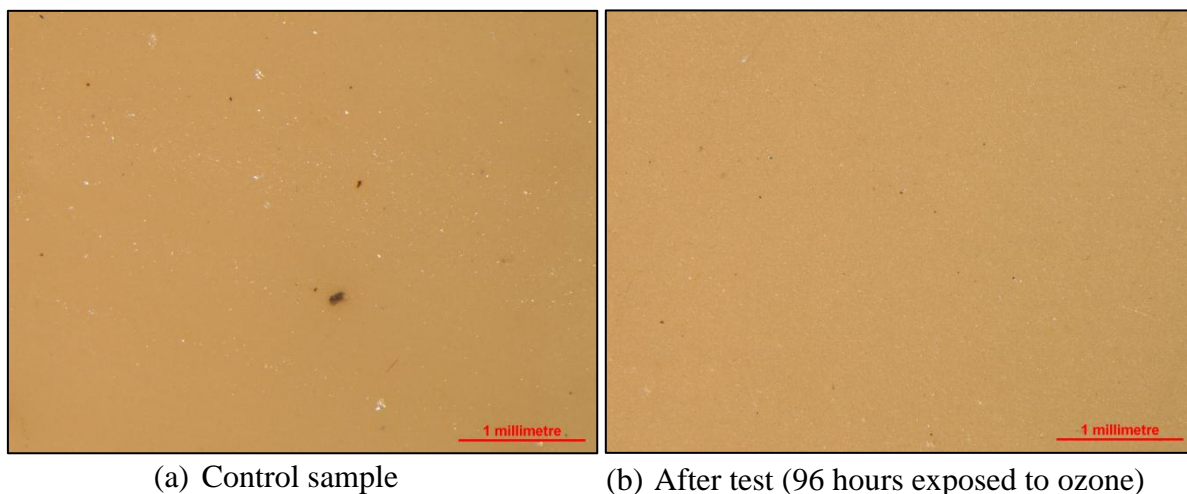
Figure 4.10: Different surfaces of sample R1 (EDS19A).

Figure 4.11: Surface for R1 (EDS19A) after scraping the shiny layer using a probe.

Figure 4.12 illustrates the different appearance of R2 (EDS14A) between control sample and the tested sample. The surfaces are markedly different. A shiny layer had formed homogeneously on the surface exposed to ozone. This layer has been removed from a portion of the exposed sample, as shown in Figure 4.13.

(a) Control sample   (b) After test (96 hours exposed to ozone)
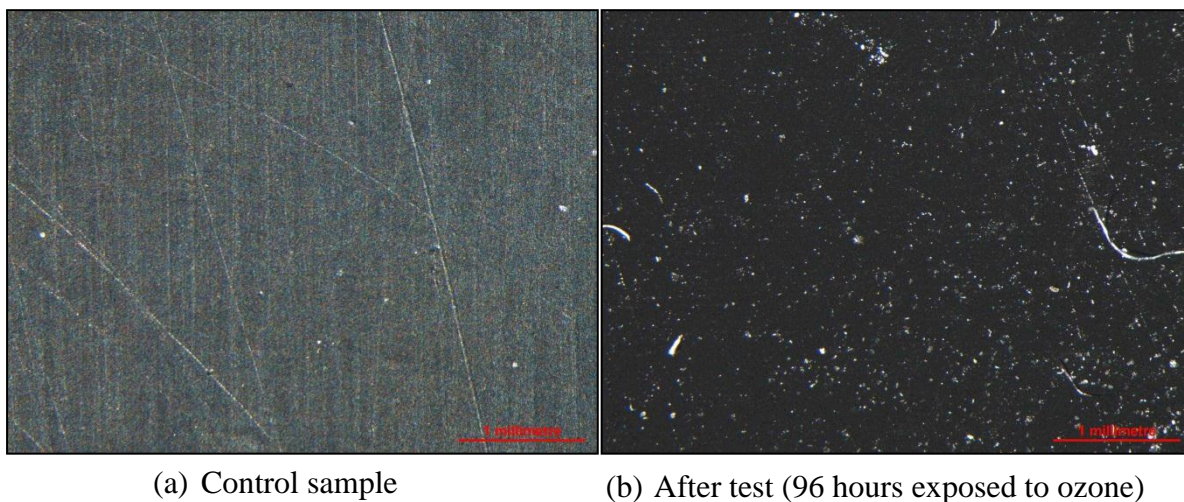
Figure 4.12: Different surfaces of sample R2 (EDS14A).
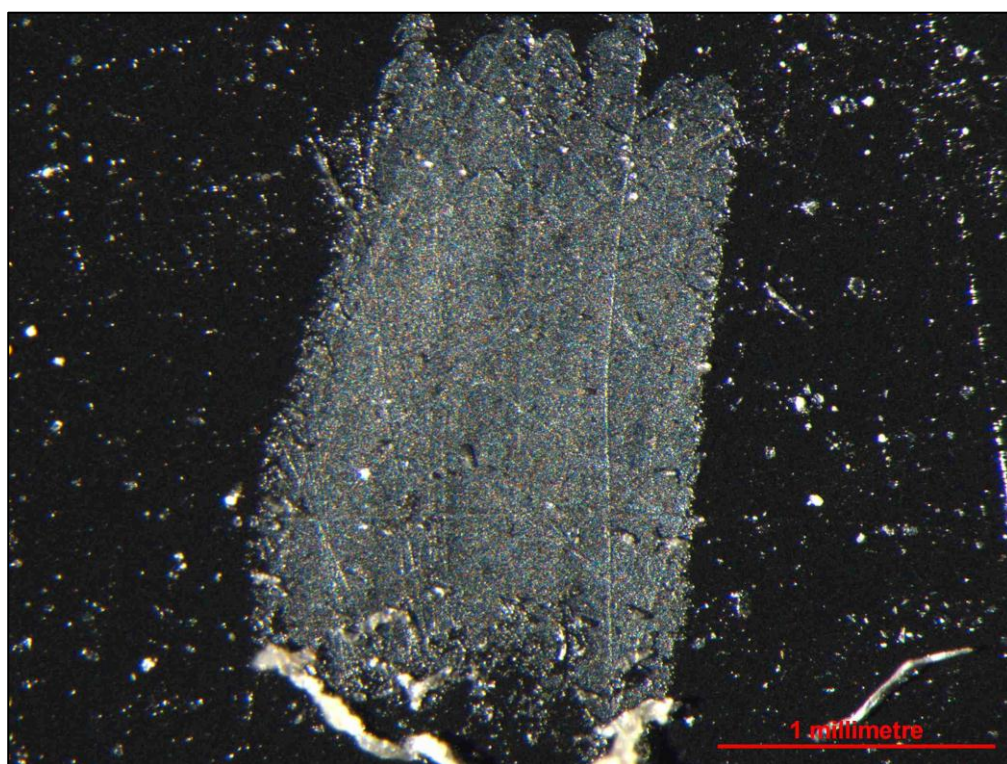
Figure 4.13: Surface for R2 (EDS14A) after scraping the shiny layer using a probe.

In unstrained rubber, ozonolysis occurs uniformly on the rubber surface. Ozonolysis is the cleavage of an alkene or alkyne with ozone to form organic compounds in which the multiple carbon–carbon bond has been replaced by a double bond to oxygen. A micrograph of the shiny layer was taken. Cross section shown in Figure 4.14 for R2. It appeared to be somewhat less than 10μm thick.
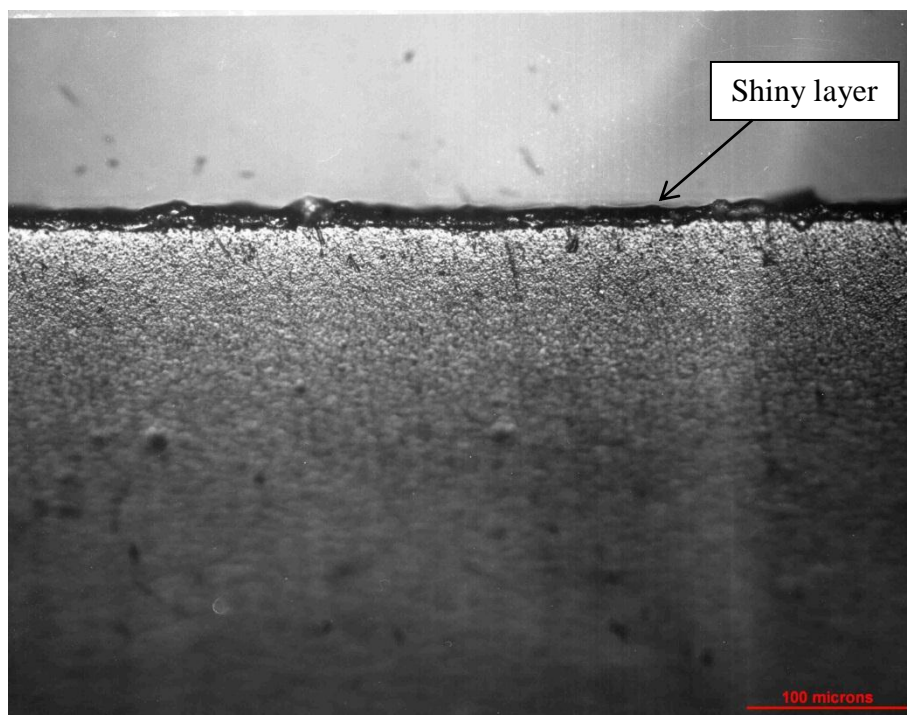
Figure 4.14: Shiny layer on the rubber surface R2 – Side view of the test piece.

The hardness of each sample was measured using a micro hardness device in accordance with BS ISO 48:2007. No difference of hardness of either sample before and after ozone testing was observed. The hardnesses of R1 (EDS19A) and R2 (EDS14A) are respectively 44 IRHD and 52 IRHD. Measurement of the thickness of each sample showed no significant difference could be observed.

Both samples (R1 and R2) were sent to the Material Characterization Unit (MCU) at TARRC for examining the external surface, particularly the substance of the shiny appearance. All the samples were examined by Fourier transform infrared spectroscopy-Attenuated total reflectance (FTIR-ATR). It was found some talcum powder (magnesium silicate) at various parts of both samples surface which have been deposited from another external source. There were also some peaks related to an ester component [C-O] which for absorption of medium intensity occur near 1300-1000cm^{-1} (1236, 1162 and 1095cm^{-1}).

Esters are chemical compounds consisting of a carbonyl adjacent to an ether linkage. A possible source is the ethanol used for sample preparation. The external surface of R2 sample showed a higher level of ester than the external surface of R1. The ester component seen in these rubbers is difficult to reconcile with anything stated in the formulation, unless it is related to non-rubbers from the natural rubber. In sample R1 only a very small amount of ester is observed in the interior but a high concentration existed on the surface. In sample R2, it occurred at a high concentration in the interior but also accumulated on the surface.

4.3 General Discussion

Attack on unstretched rubber results in to a very shiny thin surface layer. There seems to be no practical consequence, although in the tests the rubber became tacky suggesting a material of low molecular weight is formed. It seems likely this low molecular weight material is a reaction product of NR and ozone. The thickness of this layer, determined from a micrograph of a section as <10µm after 96 hours at 50pphm, suggests it would not be a significant mechanism of attrition of the rubber.

If the rubber test pieces were strained, the tearing energy will increase and may exceed the threshold value T_z. When $T > T_z$ micro cracks or small cracks are expected to form (see Section 3.4). If ozone continues to reach to crack tips, they will continue to propagate into the rubber.

When the rubber is stretched beyond the threshold value, the values of T associated with flaws may increase above T_z. So, cracks form on the surface. The fact that more cracks form at 40% strain than at 20% is consistent with a statistical distribution of values of flaw size c_i, so that at a given strain there is a distribution of tearing energies $T \sim 2kWc_i$, and the number exceeding T_z will increase as W is increased. However their rate of growth is usually reduced, since the local ozone concentration is reduced if there are a large number of active cracks consuming it.

Ozone exposure of a rubber test piece stretched to 20% equibiaxial strain led to development of cracks normal to the local maximum principal tensile strain direction. If the local strain state is equibiaxial, the cracks had a more random orientation and resembled shrinkage cracks. The fact that the pattern of cracks accurately reveals the strain field shows that there are sufficient flaws to initiate cracks in any orienation or location where the local strain field provides a driving force above T_z.

According to Beatty (1964), ozone attack may lead to stress relaxation of points of stress concentration at the surface, either by chain scission or by opening up a multitude of small cracks which can serve to relieve major strain around defects at the surface. It is not therefore surprising that in equibiaxial strain ozone crack formation resembles shrinkage cracks stress relief by a myriad of ozone cracks may also play a role in retarding crack growth under non-relaxing conditions, judging from photographs of crack tips under such conditions (Lindley & Thomas 1962a, Muhr 2006).

The preliminary results for attack of ozone on samples of immersed strained rubber could not be pursued further, due to the remaining need to recommission the high ozone apparatus. Nevertheless, they corroborate the theory of Lake & Thomas (1967b) and the previous experimental work (Zuev & Malofeevskaya 1961). It would be expected from the time to initiate cracks in 50pphm ozone found here, that in sea water in an area having a typical ozone concentration of 5pphm (Jones 1968) that it would take (~5pphm/50pphm $\times$ 3hour $\times$ 10^4) ~ 8.2 years for NR to suffer from ozone cracks.

4.4 Conclusions

(1) In hourly checks, micro cracks were first observed on the top and bottom surfaces of the strained rubber after three hours exposure in the ozone cabinet at 50pphm.

(2) Preliminary results for ozone attack on immersed rubber show a substantial reduction in rate, in qualitative accord with the theory of Lake & Thomas. This theory may therefore be used to predict the time to ozone cracking of immersed natural rubber products with some confidence.

(3) Results for number of cracks per unit area corroborate the literature. Many large cracks formed on the rubber surface at 20% strain. In contrast, many medium cracks formed on the rubber surface strained at 40%. Only large flaws initiate cracks when the test piece was stretched to 20% strain. At higher extensions, smaller flaws can also initiate cracks so the number of cracks is larger. At low strains, very few cracks form and any crack can grow in length, and hence in depth, without interference or competition with neighbours for ozone. However, at high strains many cracks are formed and no given crack can grow far in length before

mutual interference or competition with its neighbours for ozone reduces its rate of growth.

(4) Shiny, tacky, layers were found on unstrained samples exposed to ozone. The formation of the shiny layer is probably due to ozonolysis of rubber but ozone reaction with some rubber ingredients that have a low molecular weight and migrate to the external rubber surface might also contribute.

(5) Ozone attack of a rubber surface subjected to a non-uniform strain field reveals the nature of the field through the pattern of cracks formed where the principal strains are unequal, the crack orientation is normal to the maximum principal tensile strain. Shrinkage cracks like cracks in drying mud were observed clearly in the middle of the test piece where the strain is equibiaxial.

(6) The analogy with shrinkage cracks can be taken further: in accord with the observation of Beatty (1964), ozone cracking can be a mechanism of relieving stress concentrations, e.g. at crack tips in rubber undergoing non-relaxing strain cycles.

Chapter 5

Experimental: Stress and Strain Behaviour of Rubber

5.0 Introduction

All rubbers, filled or unfilled, exhibit some hysteresis in their stress versus strain behaviour. Hysteresis corresponds to dissipation of strain energy and is given by the area between the loading and unloading curves on a force-deformation plot. Harwood, Mullins Schallamach and Payne (1965, 1966, 1967, 1967a & 1967b) found that hysteresis was approximately proportional to the energy input for filled and unfilled natural rubber for simple cycles. Hysteresis, as a proportion of the energy input, is greater in filled than in unfilled rubber. Recovery is generally incomplete after unloading, as rubber requires greater stress to produce a given elongation in its first extension than during subsequent extension. Also, its stress-strain behaviour is simpler. For this reason unfilled rubber is discussed first.

5.1 Experimental Observation of Stress and Strain Behaviour of Unfilled Natural Rubber at High Strain

The purpose of the planned experimental work is to observe and evaluate the stress-strain behaviour of unfilled natural rubber. Thereafter using rubber models one might seek some fundamental understanding of rubber behaviour. There is also a need to verify the applicability and reliability of the different mathematical rubber models discussed in Chapter 2. In particular how well they can fit experimental data at low and high strain. First of all, stress-strain tests were carried out using unfilled rubber and in a separate section (Chapter 7) on filled rubber. The relationships of stress and strain energy density with strain are also explained. The fitting of observed data to molecular and hyperelasticity models presented in Chapter 2 is discussed. Stress-strain tests are also reported in Chapter 7 and used to calculate the energy release rate required in theoretical fracture mechanics and to interpret crack growth characteristics.

5.1.1 Material and Test Procedures

The constituents of R1 (EDS19A) and R2 (EDS14A) have already been noted in Chapter 4. Additional one may consider such formulas with and without additives such as antiozonant/antioxidant N-(1,3-dimethylbutyl)-N'-phenyl-p-phenylendiamine (HPPD). Nominal 2mm thick sheet of selected rubber compound was moulded using a cure time of 45 minutes at $140^{o}C$. The ingredients of the compounds are as follows:

Ingredient	parts per hundred rubber (pphr) by weight	
	R0 (EDS19)	R1 (EDS19A)
Natural rubber, SMR CV60	100	100
Zinc Oxide	5	5
Stearic acid	2	2
Antioxidant/antiozonant HPPD	3	-
Antiozonant wax-Negazone 3467	2	-
CBS	0.6	0.6
Sulfur	2.5	2.5

Two simple-extension strip test pieces were cut and tested on the Instron 4301 machine. The width and length dimensions of the test piece were 6mm × 150mm (between clamps) with a thickness of 1.90mm.

The first test piece R0 was stretched and then fully relaxed, to 500% of original length, for 10 cycles subject to a crosshead velocity of 150mm/min. This stretching rate gives a strain rate of $0.016s^{-1}$. A personal computer with a Picologger was used to record all the force and displacement data.

The second test piece (R1) (25mm × 150mm (between clamp) × 1.95mm) was stretched to 50% of original length at a crosshead speed of 120mm/min for 3 cycles, that is, a strain rate of $0.0133s^{-1}$. Thereafter a sequence of 3-cycle tests with increments of 25% to the maximum strain was made until 500% strain was achieved. The maximum initial length was selected to meet the maximum strain of 500% within the maximum feasible separation of the Instron testing machine of 950mm.

Figure 5.1 shows a simple strip test piece that was strained to 500%. The recoverable strain energy density (W) was calculated numerically from the unloading 3rd stress-strain curve using the trapezium method.
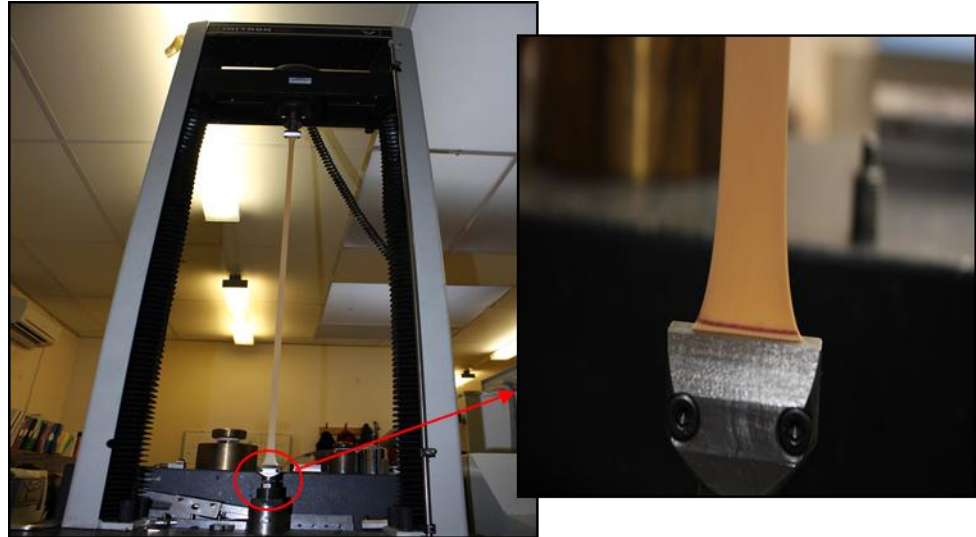
Figure 5.1: Overview of the simple-extension strip test piece (25mm × 150mm (between clamp) × 1.90mm) on the Instron 4301 machine at strain to 500%. Marking lines were created at the clamping areas to check any slippage.

Next three test pieces of R0 were used to investigate the effect of different strains rate in tests to high strain. The dimensions of the test piece were 6mm × 100mm (between clamp) with thickness between 1.90 ~ 2.01mm. Each test piece was stretched to 500% of original length and then fully relaxed, for 3 cycles using crosshead velocities of 150mm/min, 24mm/min and 5mm/min. These stretching rates correspond to strain rates of $0.025s^{-1}$, $0.004s^{-1}$ and $0.00083s^{-1}$. A personal computer with a Picologger was used to record all the force and displacement data.

For curiosity a test piece (R0) which had been stretched to 500% strain for 10 cycles previously, was retested after seven months in the relaxed state. The test was carried out at a strain rate of $0.025s^{-1}$. The test was conducted only for one loading cycle due to the sample snapped out at the clamping area during unloading cycle.

One rubber hardness button (R0) with a diameter of 25mm and thickness of 7.65mm was used to carry out a compression test. The hardness button was placed between two chrome coated metal plates lightly coated with a film of detergent mixed with water, intended to reduce the coefficient friction to as close to zero as possible. A small spike was fabricated in the middle of the plates to avoid the test piece moving laterally or popping out. The compression test was conducted on the Instron 4301 machine with a 5kN load-cell and two Linear Variable Differential Transformers (LVDT) placed as shown in Figure 5.2 to obtain more accurate displacement data. The hardness button was compressed to 6mm and back for three cycles. The compression rate was 3mm/min and the data were recorded

using a Fylde modular data logger. The first cycle in tension and compression tests was used to compare with other rubber models.
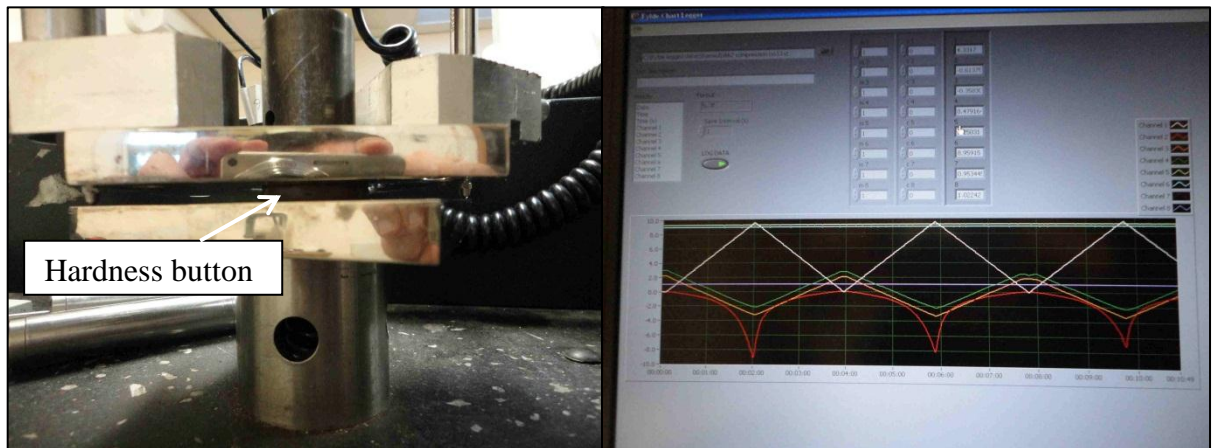
Figure 5.2: Overview of the hardness button on the Instron 4301 during compression test. Fylde modular data logger on the right-side shows the real time graph relevant to the compression tests.

One test piece R0 was used to carry out stress-strain tests in a non-relaxing condition. The objective is to see the effect of very large pre-strains on dynamic stiffness and stress relaxation. The dimensions of the test piece were 6mm × 150mm (between clamp) × 2mm. It was first tested to 500% strain for 5 cycles at a crosshead velocity of 500mm/min where the results were recorded and then immediately a stress-strain test in non-relaxing was performed at a crosshead velocity of 150mm/min which gives a strain rate of $0.025s^{-1}$. The test piece was then held for 13 hours, with the full in load logged, at a strain of 3.2 after completing the non-relaxing cyclic stress-strain test. The non-relaxing testing procedure is shown in Figure 5.3.
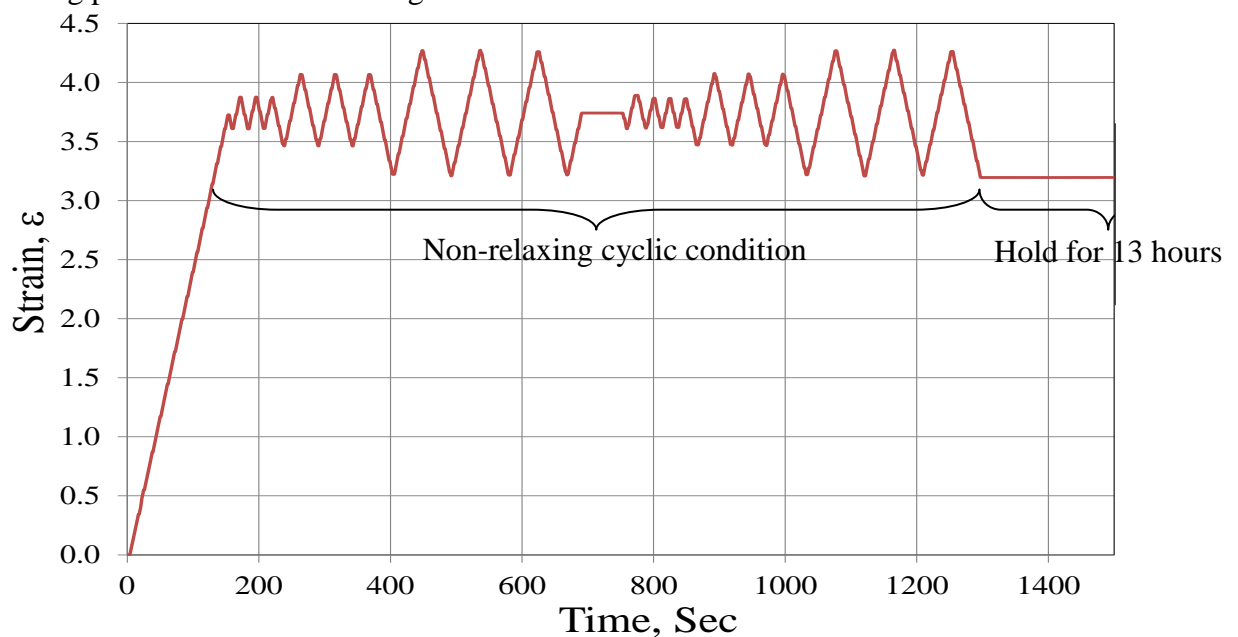
Figure 5.3: Stress-strain test in non-relaxing procedure.

5.1.2 Experimental Evaluation of the Rubber Models

Fits of hyperelastic rubber models such as neo-Hookean, Yeoh, Yeoh & Fleming, Ogden, Gent and Edwards & Vilgis (specified Section 2.8), to the experimental data collected from the first cycle of the test piece (R0) stretched to 500% strain, at a strain of $0.025s^{-1}$, were compared. The fits were achieved using analytical calculations in Microsoft Excel 2007 software, with the exception that ABAQUS CAE ver 6.10-1 software was used to choose values for the parameters in the Ogden model. In this analysis, the corrected experimental extension data was used to operate the automatic curve fitting procedure in CAE software. This fitting process was performed to obtain the best fit parameter of the model. Before executing the fitting process, the rubber model - Ogden - in stress-strain response plot was selected. Then, the fitting evaluation process was proceeded and all coefficients of the model were obtained.

5.1.3 Results and Discussion

During elongation considerable rearrangements of the molecular chains will necessarily occur (Muller 1957). A consequence of these rearrangements is large stress softening. Figure 5.4 demonstrates this phenomenon. The R0 rubber sample was stretched to 500% strain for 10 cycles. The initial maximum stress of 5.72MPa reduced to 3.10MPa after 10 cycles. Figure 5.4 demonstrates there is substantial hysteresis above 200% strain, greatest in the first cycle and of similar magnitude for all subsequent cycles. The period of 7 months shows that the rubber has partially recovered to a state between the curves of 1st cycle and 2nd cycle.
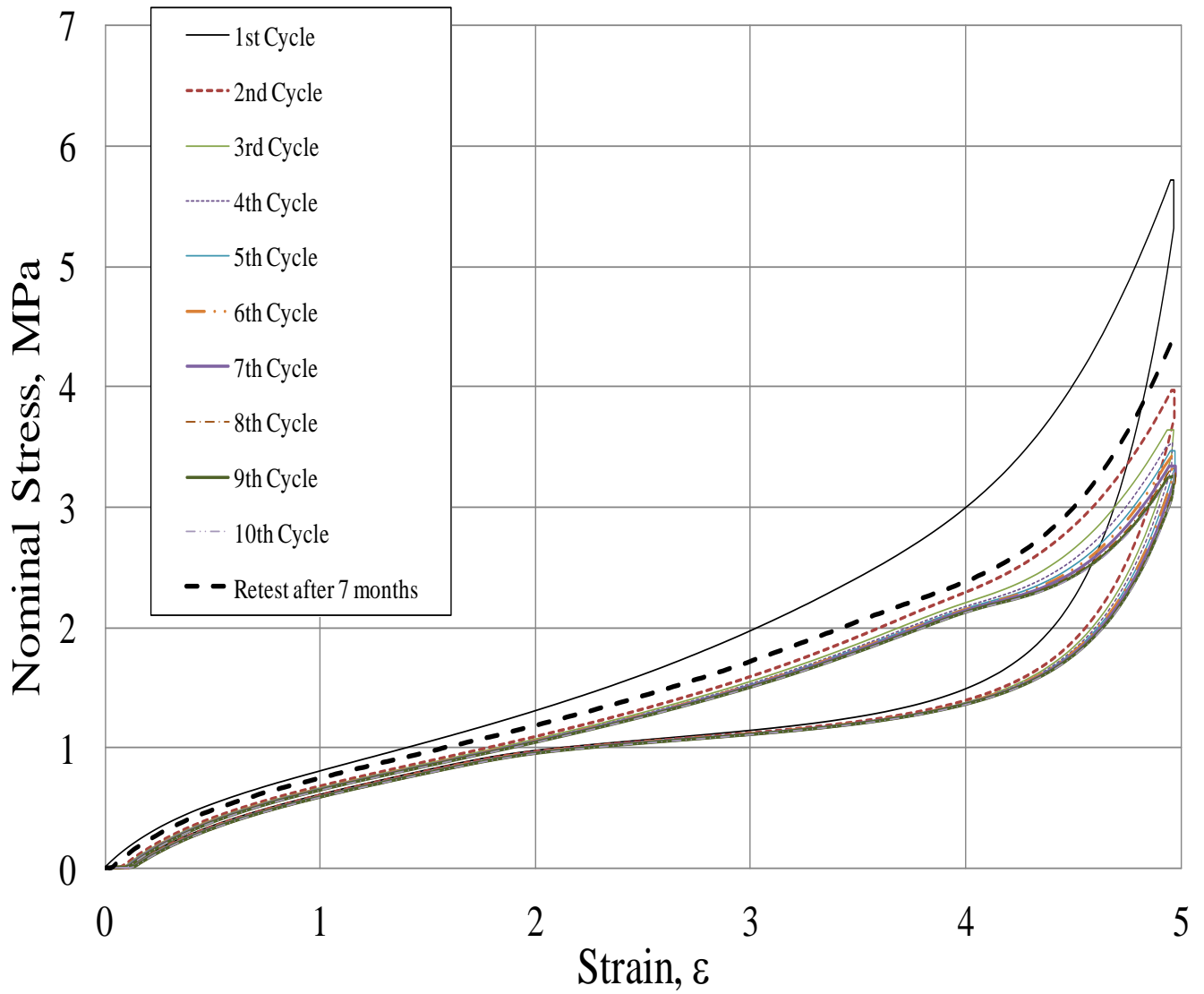
Figure 5.4: Effect of stress-strain cycles on an unfilled natural rubber (R0). A strip test piece was strained to 500% for ten cycles at strain rate of 0.025^{-1}.

Figure 5.5 shows the 3rd cycle curves for the second test piece. As before the hysteresis is low for strains less than 200%, but increases significantly at high strains. This high hysteresis at high strains is thought to be a consequence of strain-crystallisation (see Section 2.9.3).
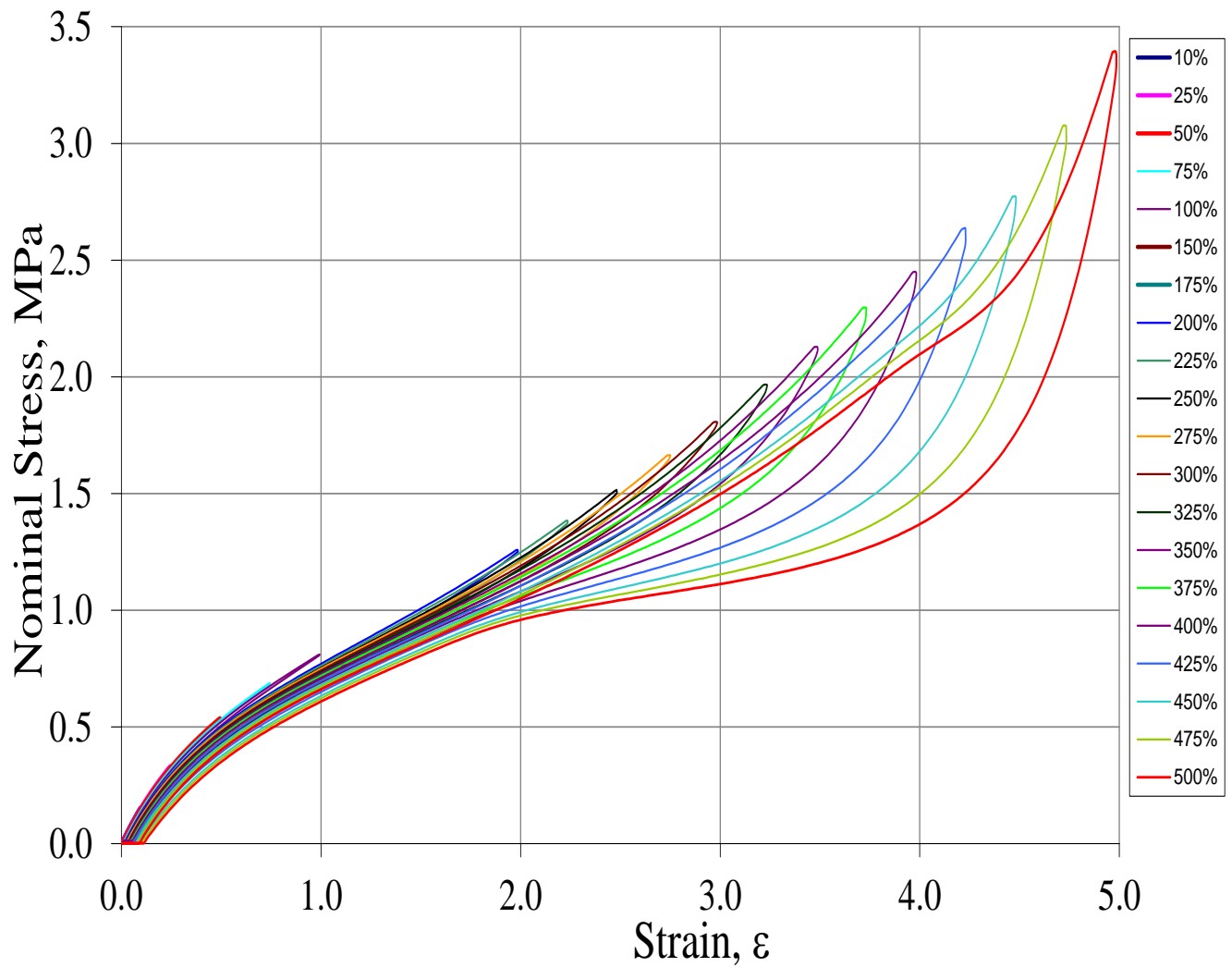
Figure 5.5: Stress-strain curves for 3rd cycle unfilled natural rubber for different maximum strain levels (R1).

The hysteresis energy density for a selected strain was calculated by subtracting the area under the stress-strain retraction curve from that under the extension curve. The fractional hysteresis was obtained by dividing the hysteresis energy density by the extension energy, i.e. the area under the extension curve. Figure 5.6 provides a plot of fractional hysteresis versus maximum strain of the cycle. The upturn in the curve about 300% is ascribed to crystallization.
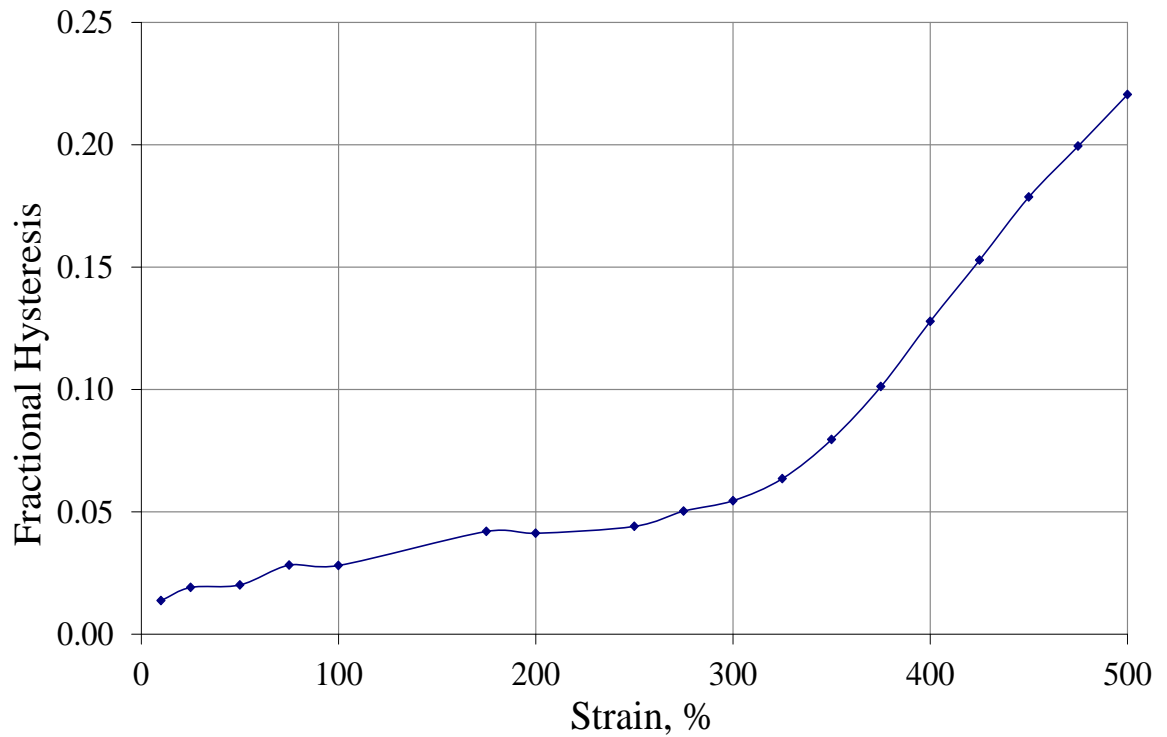
Figure 5.6: Fractional hysteresis as a function of strain using strip test piece (R1).

The enthalpy of crystallization *(ΔH)* of unfilled natural rubber is 64.0 (J/g) according to Roberts and Mandelkern (1955). The hysteresis was also expressed as a fraction ψ of enthalpy of crystallization per unit volume, calculated by the following equation:

$$\psi = \frac{Hysteresis \text{ Energy Density}}{\rho \Delta H} \tag{5.1}$$

where ρ is the rubber density (0.96 g/m^3) (Natural Rubber Engineering Data Sheet 1979). Figure 5.7 shows ψ as a function of strain. It is interesting to note that the dependence of ψ on strain in form resembles that of the fractional crystallinity shown in Figure 5.11 (Toki et. al 2002) but is about 1/10th of the magnitude.
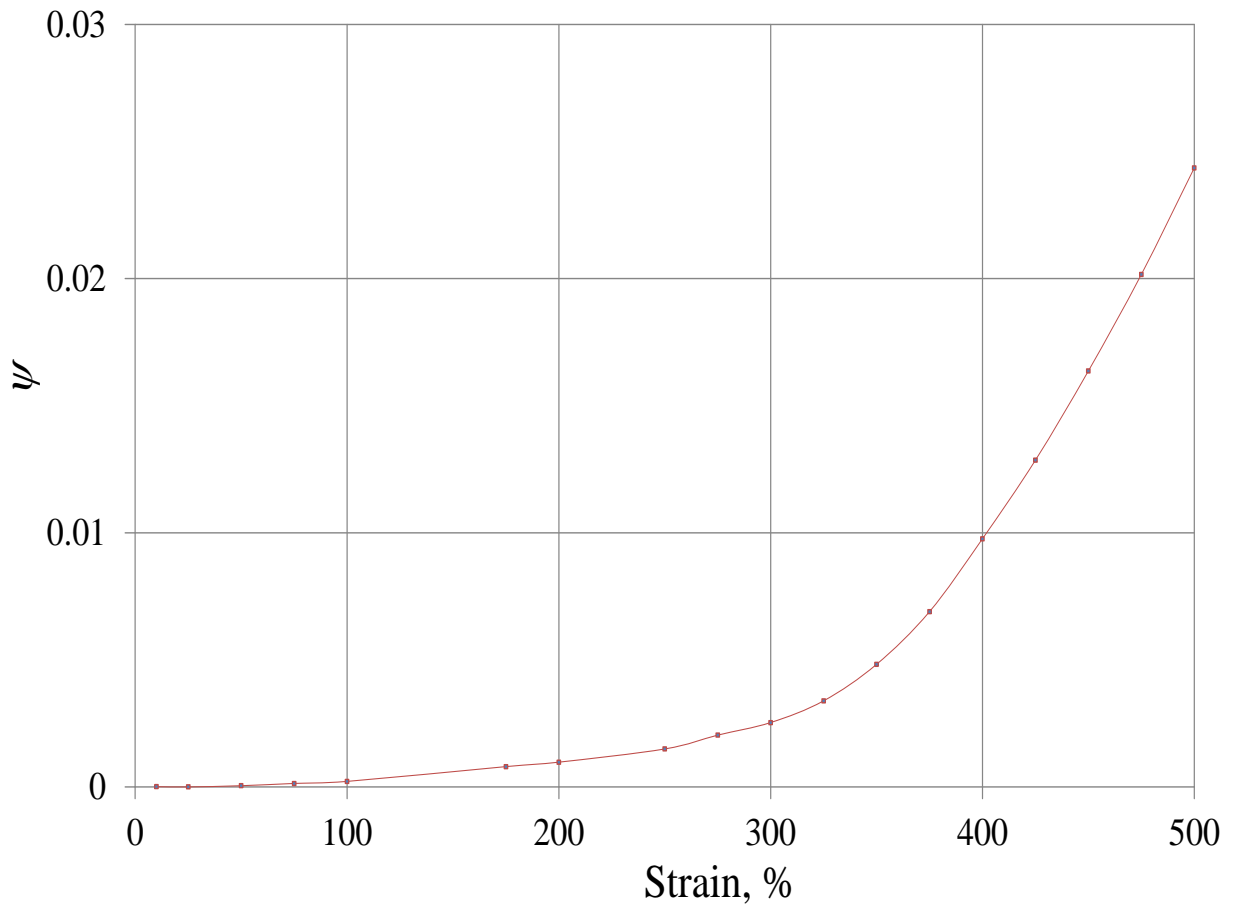
Figure 5.7: Plot of ψ = hysteresis/$\rho\Delta$H as a function of strain using strip test piece (R1).

The crystallization behaviours of rubber have been discussed in the literature (Mitchell and Meier 1968, Field 1941). Figure 5.8 shows the excess temperature rise occurring in a stretched rubber sample (Mitchell and Meier 1968).   If other enthalpy changes accompanying the stretching of polymer network are small relative to the heat liberated by crystallisation, the excess temperature rise would be proportional to the extent of crystallisation in the sample. The extent of crystallisation first becomes significant around 300% elongation and further increases with elongation similar to that shown in Figures 5.7 and Figure 5.8.
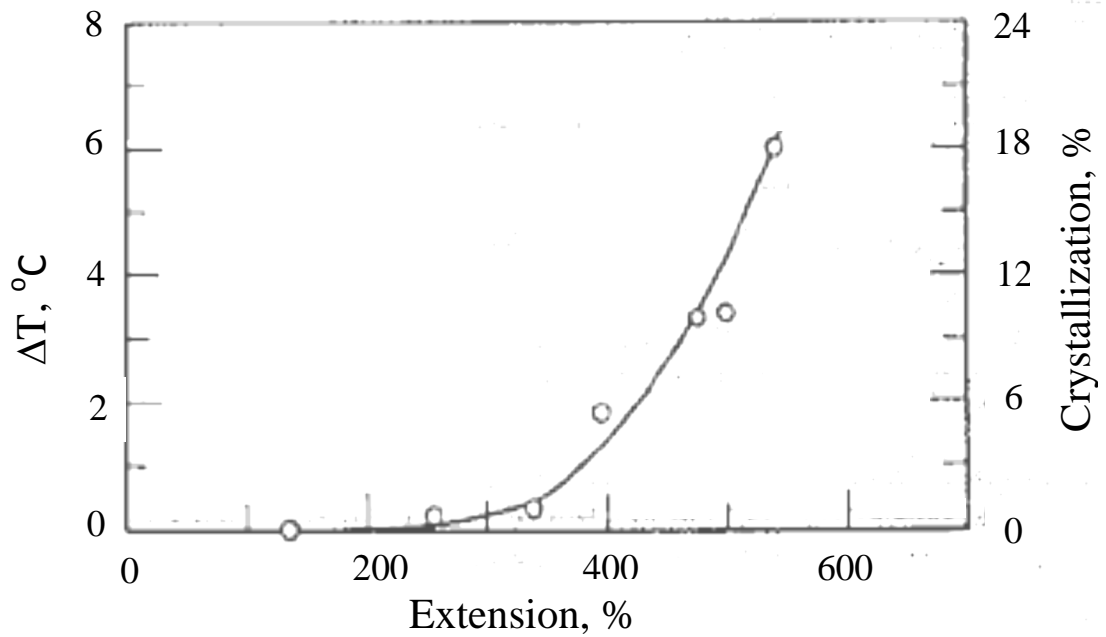
Figure 5.8: Excess temperature rise at 0.4 sec versus extension attained at maximum rate (Mitchell and Meier 1968).

Goppel (1946) has determined the proportion of crystalline matter present in both stretched and unstretched rubber using a measurement of the intensity of the X-ray diffraction pattern. Figure 5.9 shows his results in term of the percentage of crystalline material as a function of percentage elongation.
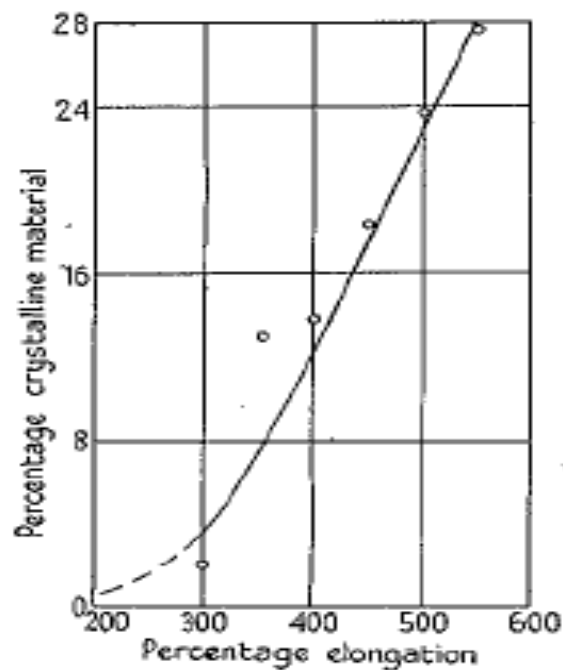
Figure 5.9: Percentage crystallinity as function of elongation in vulcanized rubber (Goppel 1946, referred from Treloar 1949).

These results show that the initial crystallisation occurred at the region 200 to 400 percent extension and can be correlated with the crystallisation region in Figure 5.7. Goppel used the same principle as Field (1941), but he claims to have eliminated possible errors, for example from variations in intensity of the incident beam, variations in development of the photographs, and the effect of scattered radiation.

Toki et al. (2002) explained only a small fraction of chains are oriented and crystallised (20%) as shown in Figure 5.10, this suggests that the strain-induced crystalline form an additional physical cross-linking network, carrying most of the applied load.
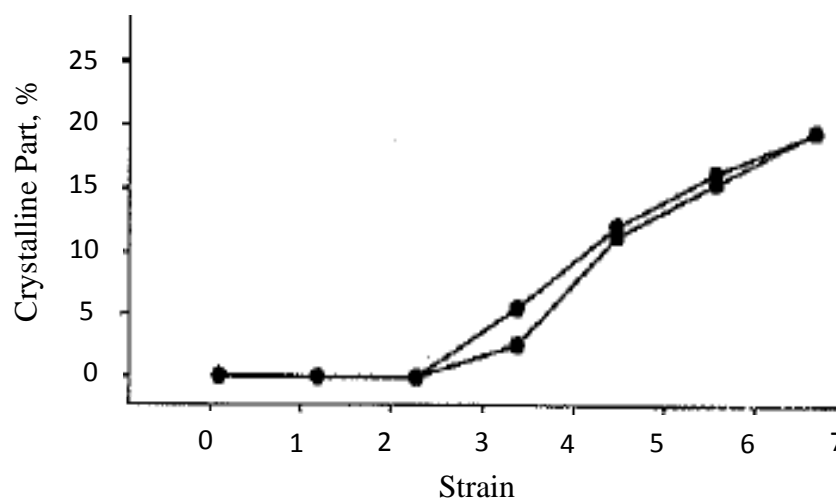
Figure 5.10: Fractions of crystalline phase at each strain during stretching and relaxation (Toki et al. 2002).

It is assumed that the degree of crystallisation is determined approximately by the amount of elongation. The effects are more complex if crystallisation takes place concurrently with stretching.

Figure 5.11 presents the recoverable strain energy density, W, as a function of the strain. The retraction strain energy density was calculated from previously obtained stress-strain curves using the trapezium method. The statistical theory (refer to Equation 2.11- neo-Hookean model) was compared with experimental data. It is found that the strain energy density is similar below 400% strain, but that for the statistical theory increases are more rapid above 400% strain. Since the statistical theory assumes "perfect elasticity", there is no distinction between the loading and unloading processes.
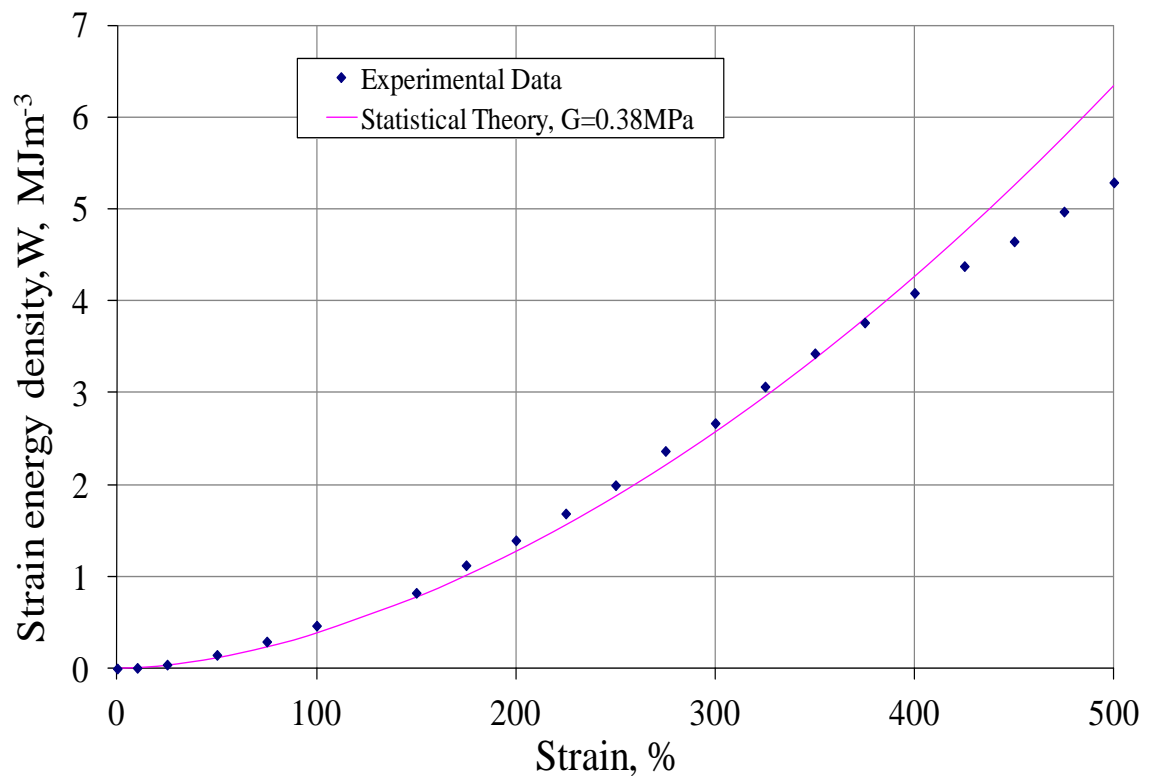
Figure 5.11: Results of the 3rd cycle retraction strain energy density from 0% to 500% (R1).

Figure 5.12 shows the stress-strain curves are relatively insensitive to different extension rates. Again, the curve exhibits a Mullins effect that is partially recovered after 7 months (loading only) was plotted for comparison with the curves with different rate.
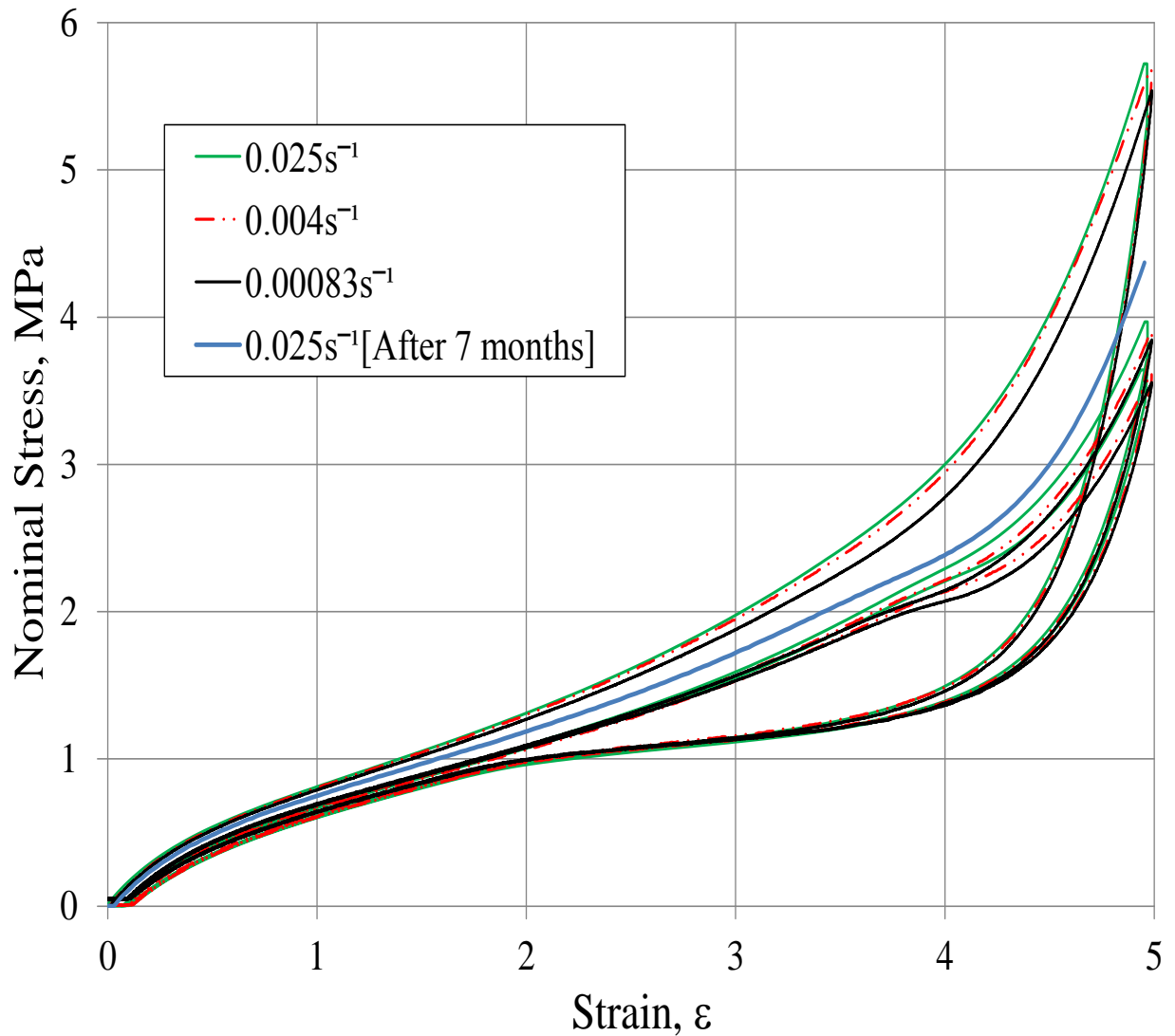
Figure 5.12: Stress-strain curves at different strain rates. A virgin strip test piece was used for each rate and strained to 500% for three cycles (R1).

Figure 5.13 shows the stress response to the imposed strain history. Stress relaxation occurred while the test piece was held for 60 seconds as shown in the middle of the graph.
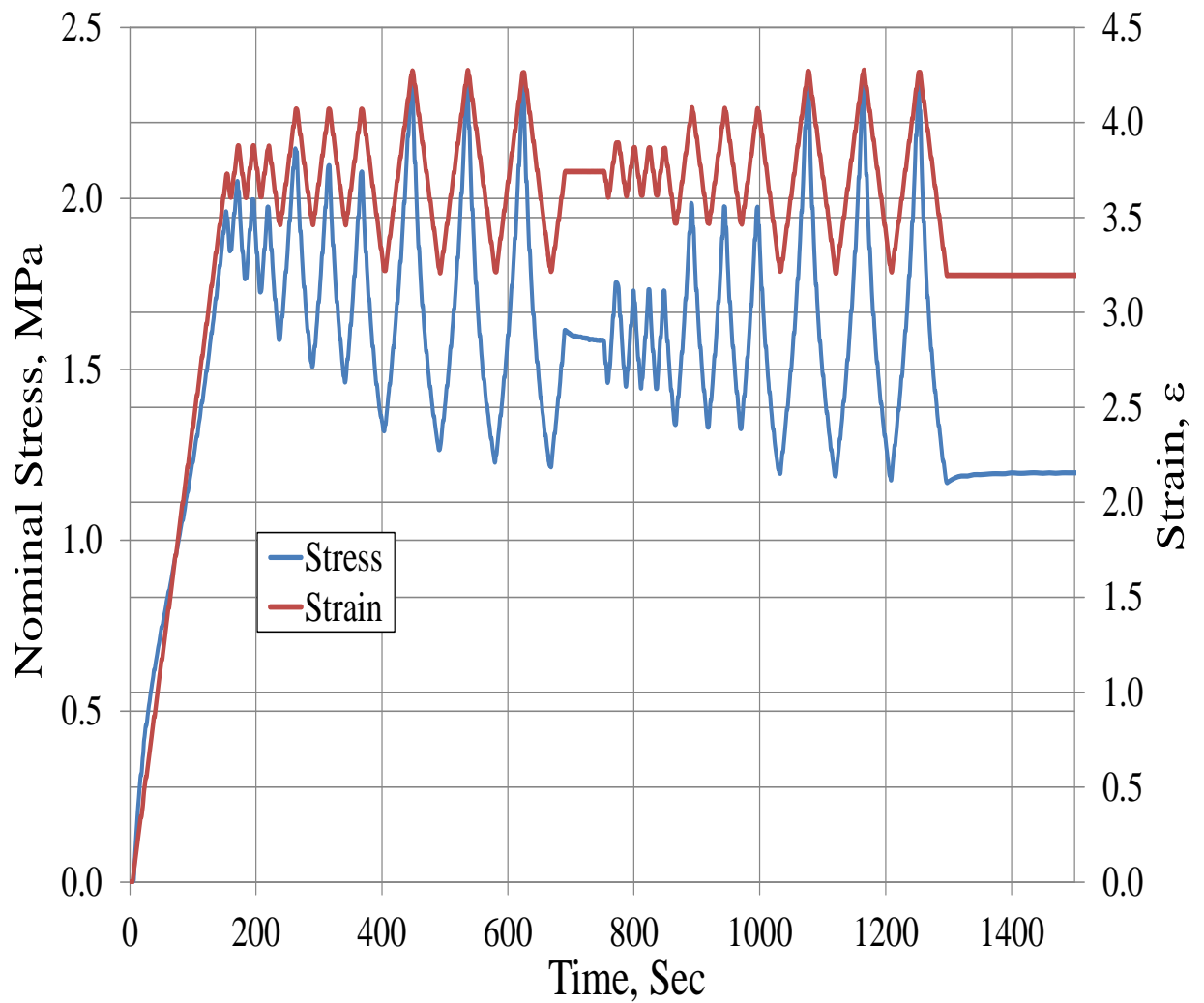
Figure 5.13: Stress-strain curves in non-relaxing condition as a function of time.

The hysteresis curves of stress-strain exhibited a slight increase of cyclic stiffness associated with small amplitude cycles when a large static strain (ε=4.25) is imposed. However, the most striking effect is the stress relaxation throughout the cyclic test as shown in Figure 5.14 with magnified view in Figure 5.15.
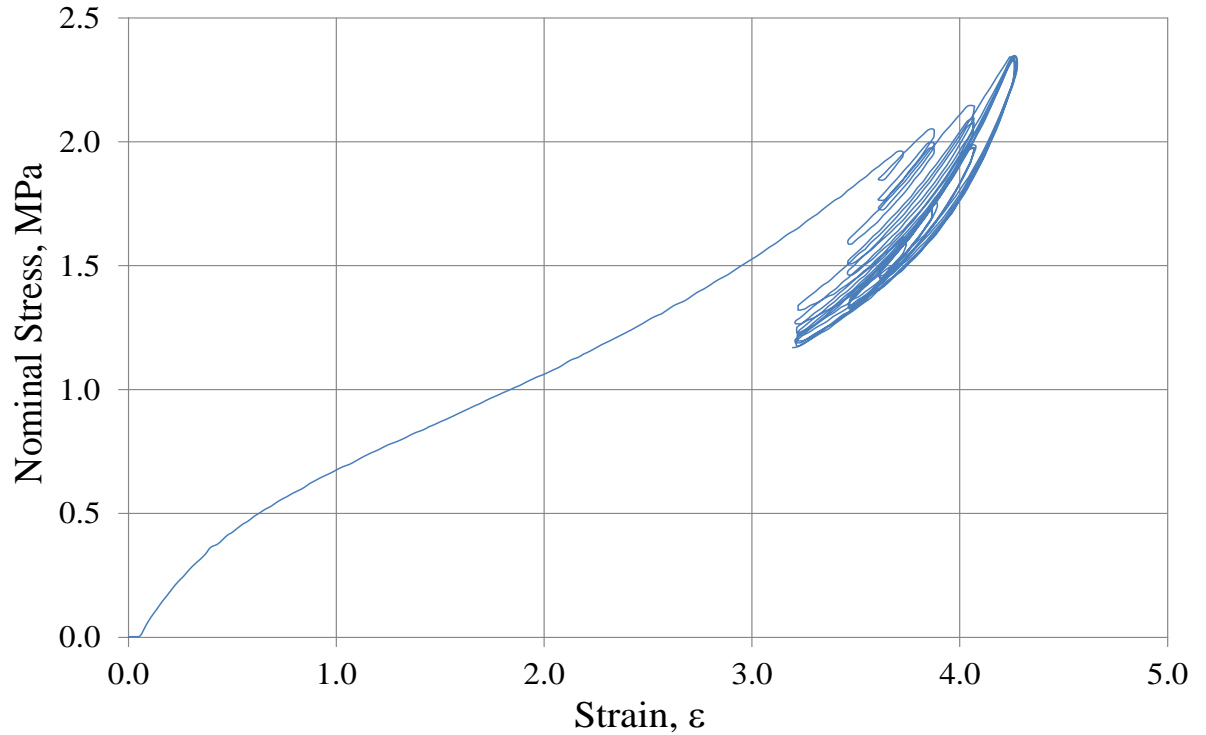
Figure 5.14: The hysteresis curve of stress-strain in non-relaxing condition.
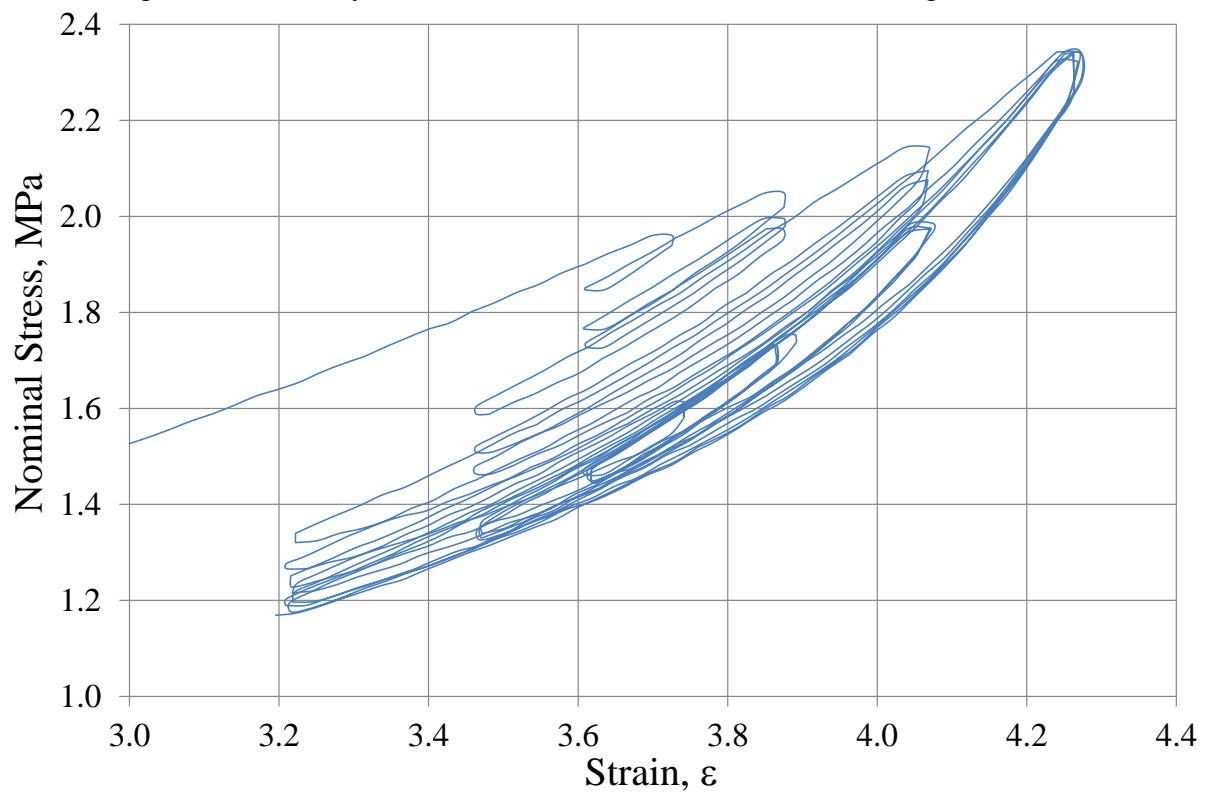
Figure 5.15: The increment of stiffness in the hysteresis curves in non-relaxing condition.

Flory's theory (1947, 1953) relates elongation, stress and fractional crystallinity, if crystallisation occurs only at constant high elongation after straining, and predicts a lower stress when the crystallinity is higher, such as when at lower temperatures. If crystallisation and elongation occur concomitantly, the oriented crystallites will "reinforce" the amorphous rubber matrix, resulting in high incremental stiffness. The strain-dependence is opposite to the effect of particulate fillers: reinforcement increases as the strain is applied, rather than breaking down. This implies also a different origin of the hysteresis: viscoelastic loss as the polymer molecules reconfigure in much more severe microscale strain cycles than those imposed macroscopically.

Figure 5.16 shows the stress relaxation at the end of the cycles when the strain of 3.2 is held fixed. The plot appears to show three phases of behaviour (i) on initial rise in stress, as the rubber recovers from being driven to a smaller extension and (ii) two relaxation processes are perhaps due to viscoelastic effects and changes in the state of crystallinity. Alternatively the second slope could correspond to the lower room temperatures after night fall. Two trendlines were introduced to predict the stress relaxation processes as shown in Figure 5.16. It is confirmed that the stress relaxation rate is about 5% at the low temperature compared to the daylight period which is about 1% in the room temperature.

The figure shows a plot of Stress, MPa (y-axis, from 1.10 to 1.20) against Time, s (x-axis, logarithmic from 1 to 100000). Legend: "plotted against elapsed time" and "plotted against time". Trendline equations: $y = -0.01175\log_{10}(x) + 1.23$ and $y = -0.0647\log_{10}(x) + 1.46$.
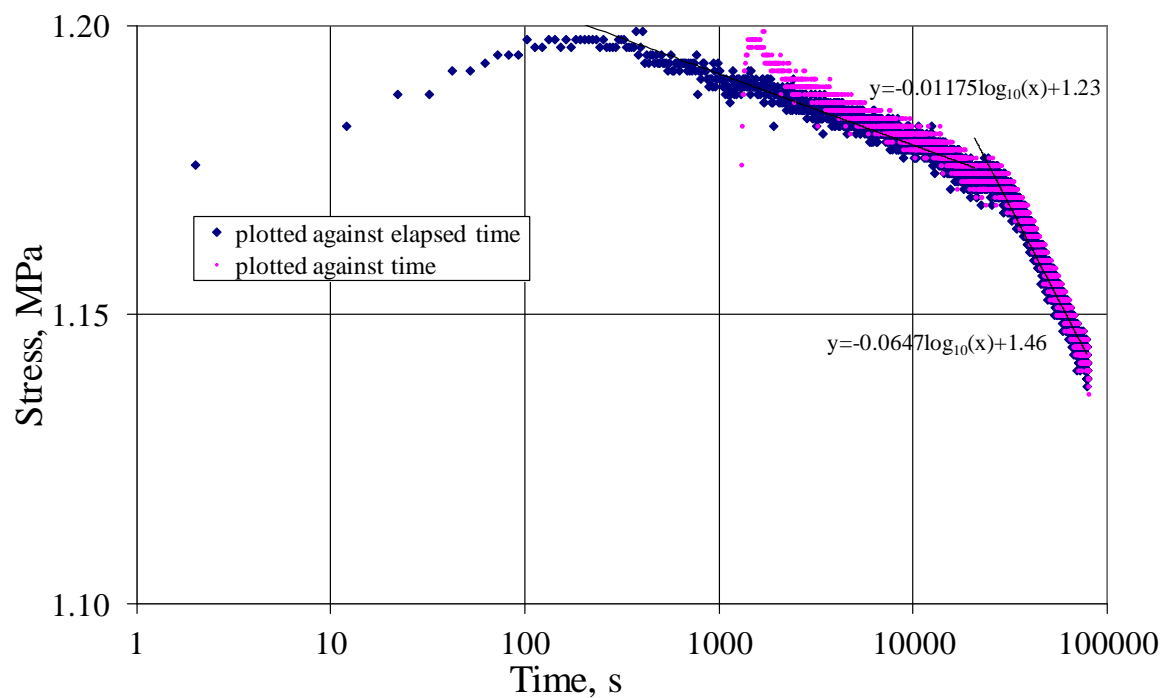
Figure 5.16: The reduction of stress as a function of time since the start of loading from zero strain (as in Figure 5.14), or elapsed since cessation of load cycles (1307s).

We will now look at hyperelastic models to assess their ability to fit measured data and expected behaviour. Figure 5.17 provides a comparison of the experimental results with analytical calculation using neo-Hookean and Gent models. Most of the curves fitted experimental data until the strain of 1 but variation can be seen when the strain exceed 1. A shear modulus of G=0.475MPa is required for the neo-Hookean model to fit the stress-strain data moderately well up to ε=3, although the stress is somewhat under predicted in the range up to ε=0.7, and overpredicted for $0.7 < ε < 2.7$. The Gent model (Equation (2.17)) with the Yeoh & Fleming co-efficient, Y=0.044 (I_m=30.14 for G=0.475) shows much too early an upturn compared to experimental data. There is an improvement to the fit with experimental data with Y = 0.120 (I_m=77.02), but the upturn curvature is too weak. Further increase in Y to 0.500 (I_m=311.42), gives very similar behaviour to the neo-Hookean fit up to 500% strain. For a better fit in the strain range 0 to 1, a value for G of ~0.5 would be needed, but the Gent (or neo-Hookean model) then exceeds the experimental data for strain above 1 and before the experimental upturn. When G=0.325 (Y=0.055), the upturn at a high strain fitted the experimental data but the fit to the experimental results at low and moderate strain was poor.
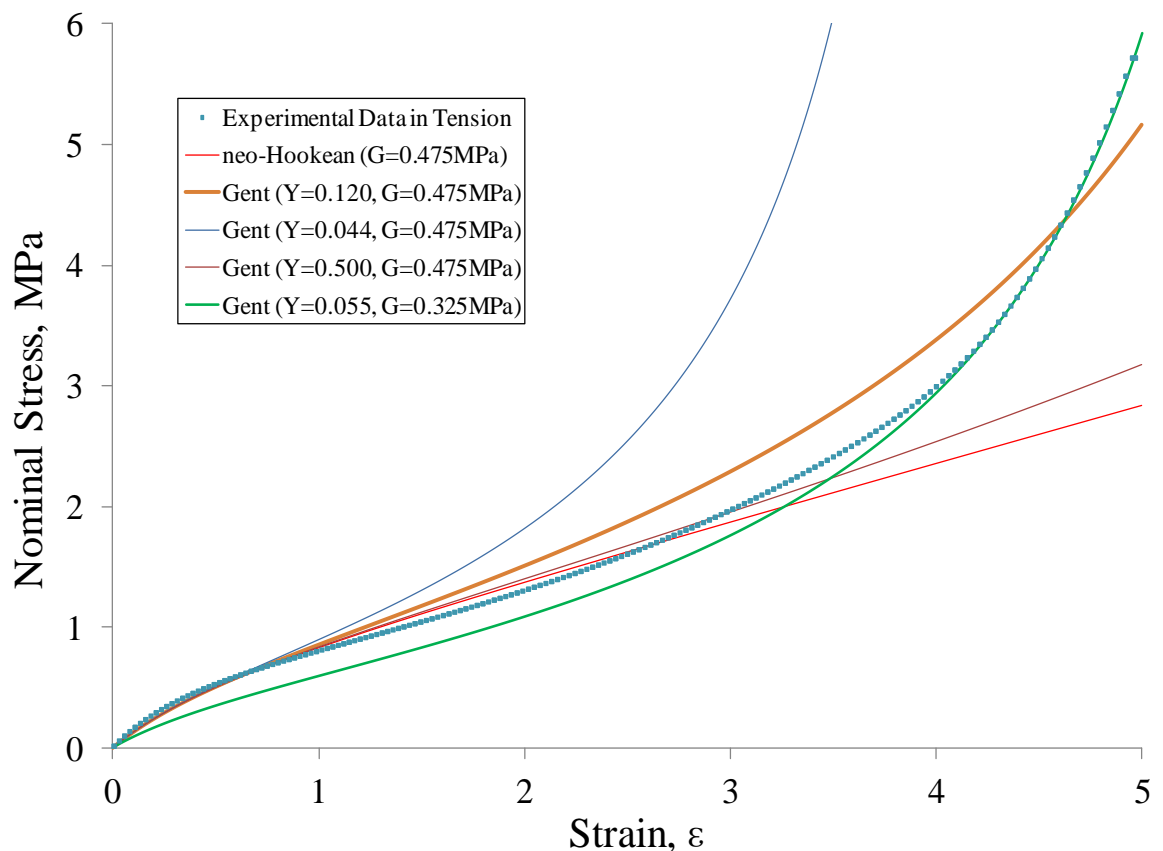
Figure 5.17: First cycle stress-strain loading curve compared to rubber models (neo-Hookean and Gent model) with I_m=3+YT/G fit to experimental data in tension (R0).

Figure 5.18 and 5.19 illustrate the effect of the adjustment in the Edward & Vilgis model of Equation 2.16 of the two parameters η (slippage) and α (inverse measure of extensibility) respectively, with $G_c=\frac{1}{2}N_ckT=0.5$. The curve for $G_c=0.5$ as the only non-zero parameter is equivalent to the neo-Hookean fit $G=0.5$ and appears in both figures. With this exception, $G_s=0.5$ for all curves in Figure 5.18, which shows the effect of adding slip links to be permanent ones. Figure 5.19 shows the effect of the finite extensibility parameter α in the case that there are no slip links ($G_s=0$).
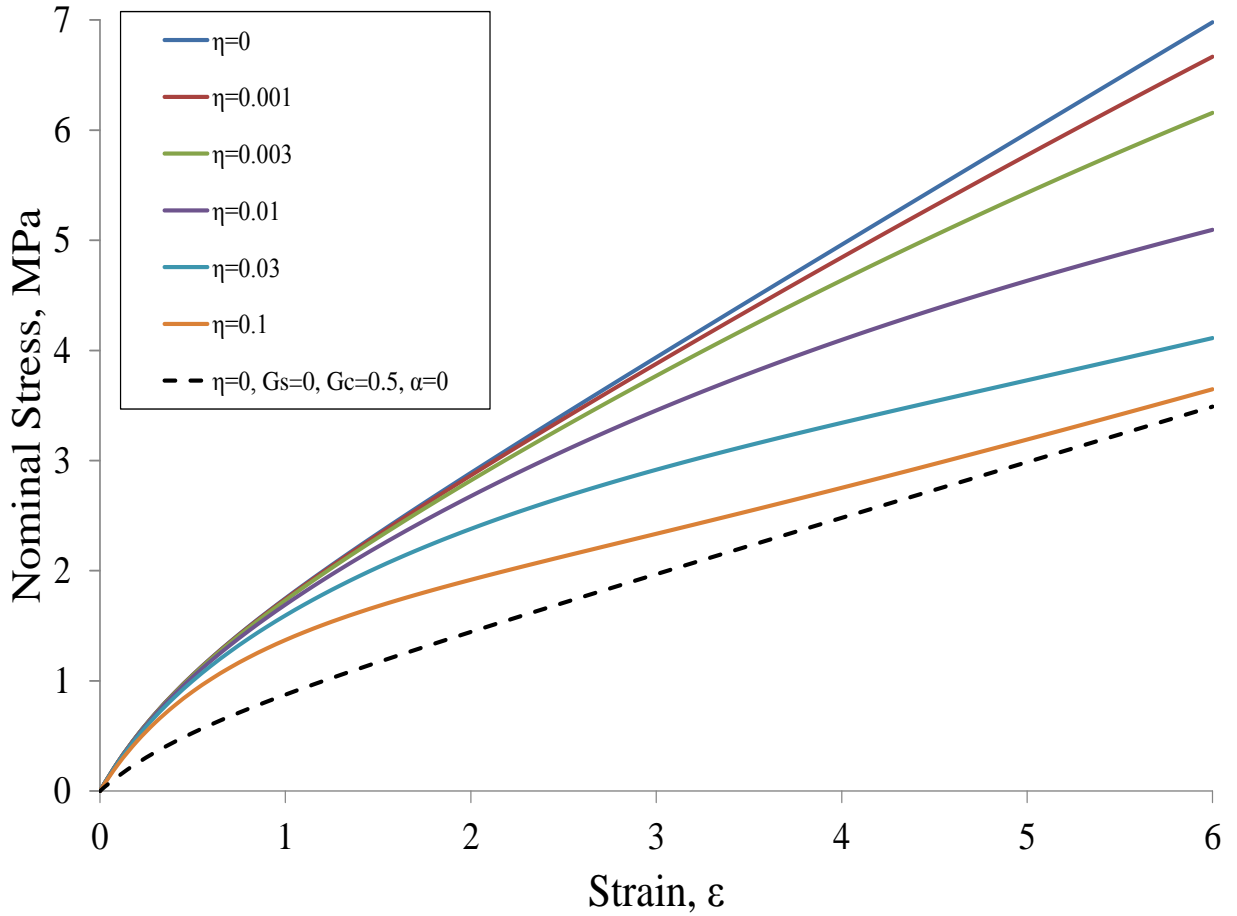
Figure 5.18: Stress-strain curves using different values of η; $G_s=G_c=0.5$, $\alpha=0$.

From Equation (2.16), the neo-Hookean model of (2.11) corresponding to $G=G_s+G_c$ results when $\eta=0$ (no slip) and $\alpha=0$ (no upturn). Increasing η corresponds to softening due to slippage of entanglements. For $\alpha=0$, Figure 5.19 demonstrates that the higher the value of η, the lower the strain at which the curve falls below the neo-Hookean curve with $G=G_s+G_c$ towards that for $G=G_c$. For total slip ($\eta\sim\infty$) we might expect $G=G_c$.

The effect of variation of α to model limited chain extensibility is shown in Figure 5.19. The higher the value of α for η=0, the lower the strain at which upturn occurs.
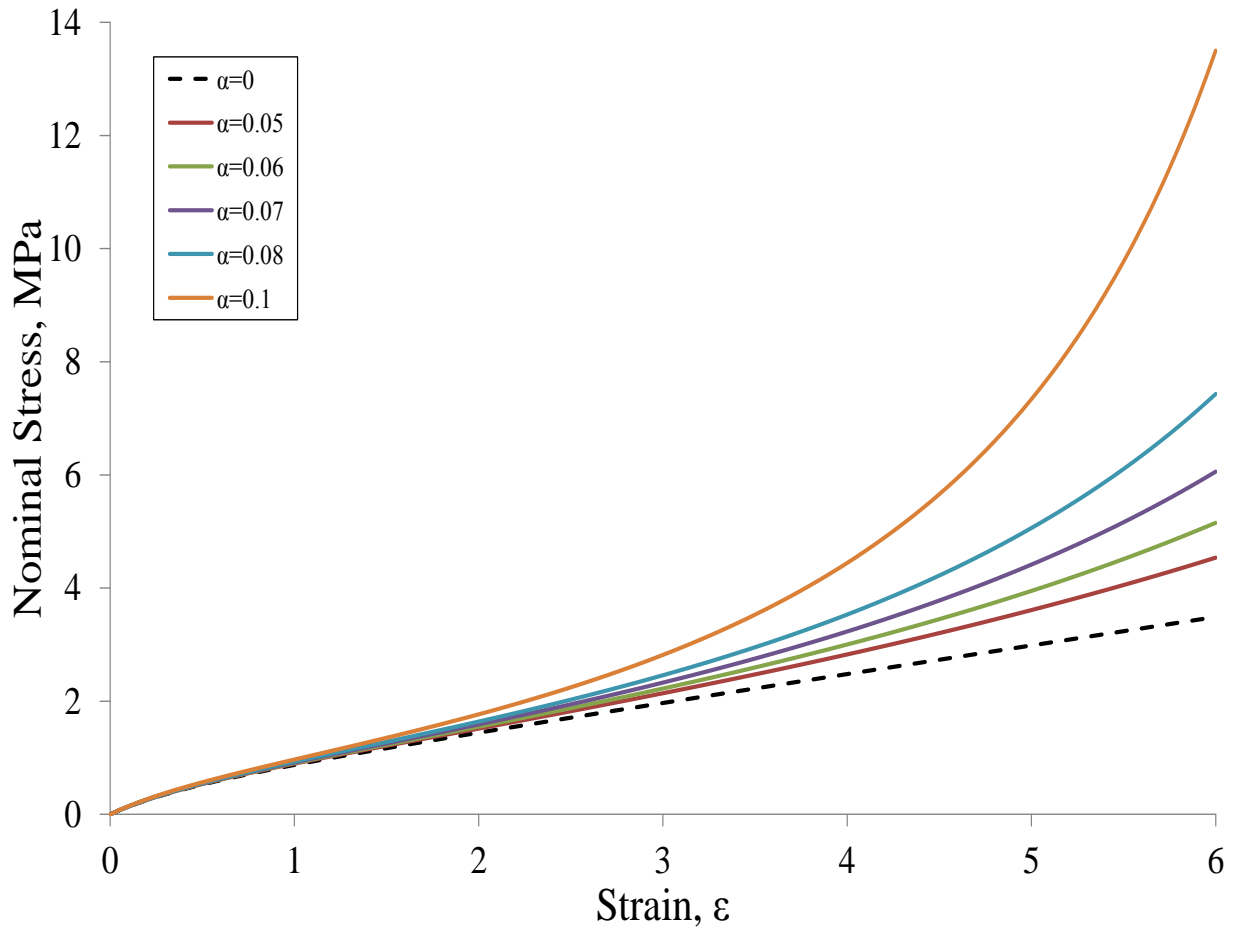
Figure 5.19: Stress-strain curves using different value of α using Edwards and Vilgis model; η=0, G_s=0, G_c=0.5.

Figures 5.18 and 5.19 indicate the influence of η for α=0, and α for η=0 whereas Figure 5.20 provides an α and η combination that fits the experimental data.

Figure 5.20 provides comparisons of the experimental results with fits using the Edwards & Vilgis and the Ogden model. The Ogden model enables a more accurate fit to the experimental results. The Edwards and Vilgis model behaves slightly different at the high strain values.
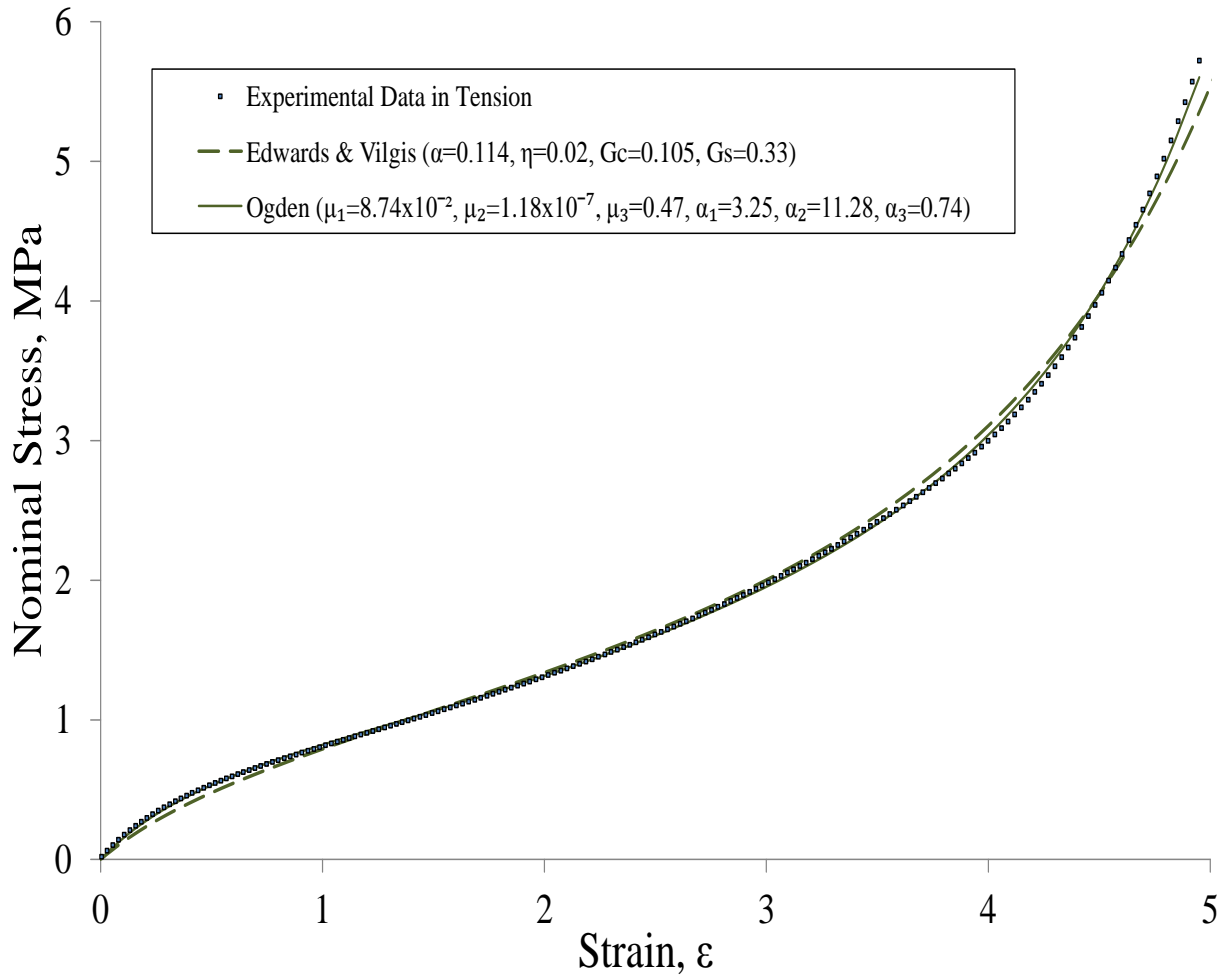
Figure 5.20: Typical stress-strain curves of rubber models (Edwards & Vilgis and Ogden models) fit to experimental data.

Figure 5.21 indicates how the Yeoh model captures the behaviour of the experimental data. The extension behaviour of strip test piece can be fitted quite well using this rubber model. However, the neo-Hookean model only fits the experimental data up to the strain of 2.8.
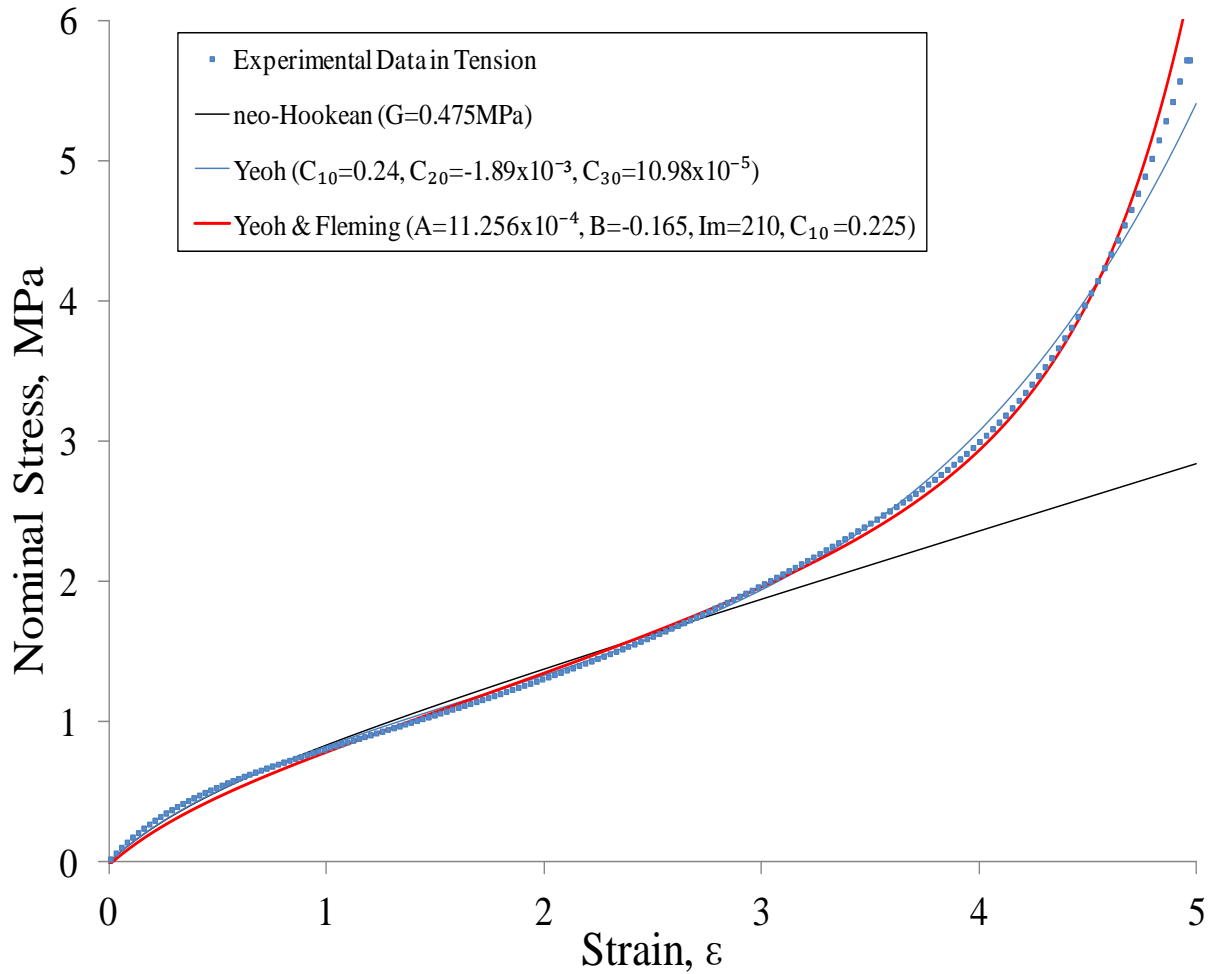
Figure 5.21: Typical stress-strain curves of rubber models (neo-Hookean, Yeoh and Yeoh & Fleming models) fit to experimental data.

It has been found experimentally that $\partial W/\partial I_1 << \partial W/\partial I_2$ and the strain energy function, W can then greatly be simplified by making the assumption $\partial W/\partial I_2 = 0$ (Gregory 1979, Gough 2000). If this assumption is made at the outset, Equation (2.29), for tension, may be rearranged to give an expression for an apparent $\partial W/\partial I_1$ term, which incorporates a component for $\partial W/\partial I_2$ if the latter is non-zero, that is

$$2\left(\frac{\partial W}{\partial I_1}\right)_{app} = \frac{\sigma_T}{(\lambda^2 - \lambda^{-1})} \quad , \tag{5.2}$$

where σ_T is the true stress in the straining direction.

The nominal stress in tension may be expressed from Equation (2.30) as:

$$f = \sigma_T . \lambda_2 \lambda_3 = \frac{\sigma_T}{\lambda} = 2(\lambda - \lambda^{-2})\left(\frac{\partial W}{\partial I_1}\right)_{app} \quad , \tag{5.3}$$

where $2\partial W / \partial I_1$ is evaluated at the I_1-3 value appropriate to tension.

Figure 5.22 compares to apparent value of $2\left(\frac{\partial W}{\partial I_1}\right)_{app}$ calculated from the experimental tensile stress results, and fits using different theoretical models. It is concluded that none of the fits are very good. This type of plot, known as a Gregory plot (after Gregory 1979), is a more demanding test of a models capability than simply comparing experiment and fit of the model in the stress-strain domain as per Figures 5.17, 5.20 and 5.21.
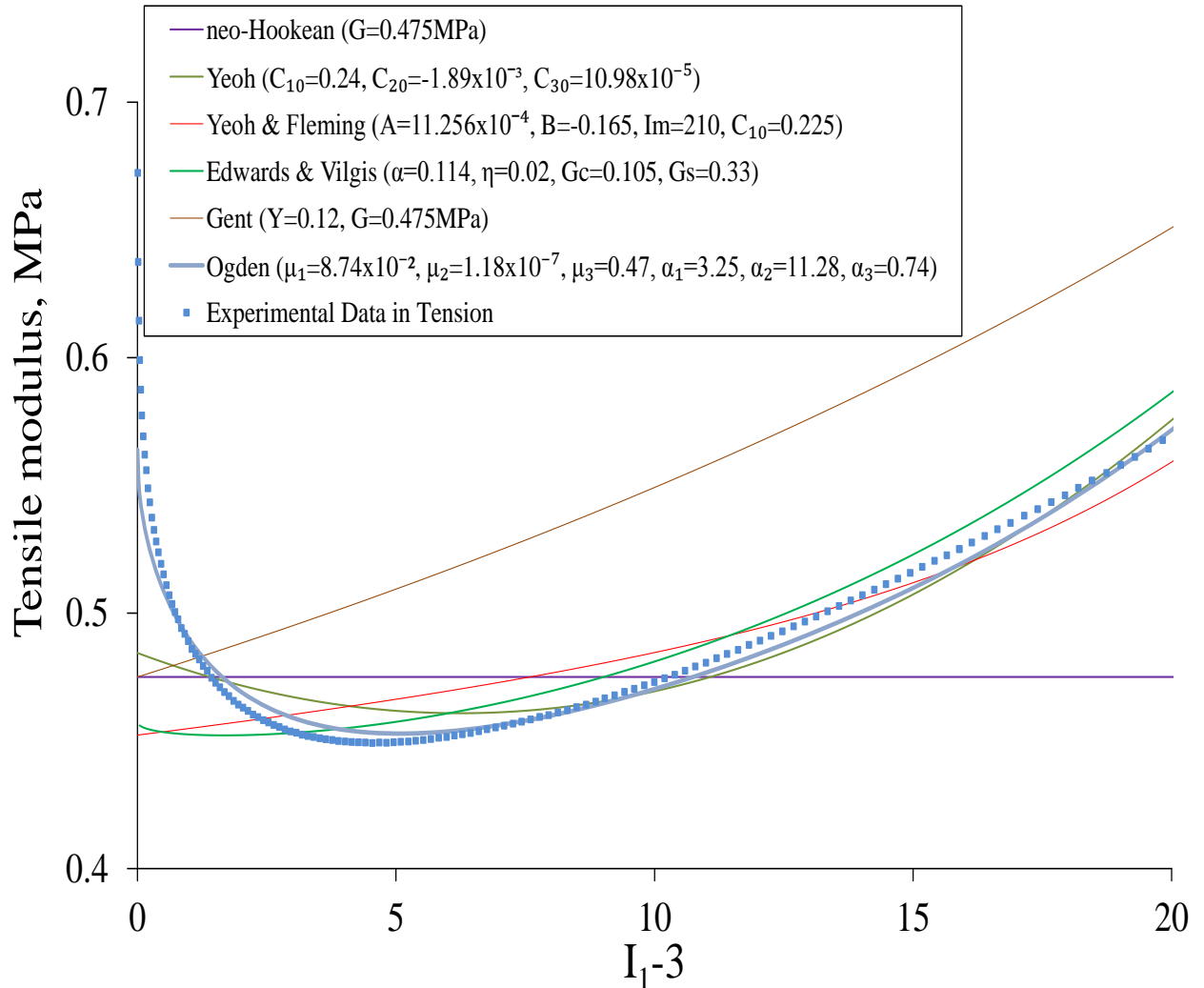
Figure 5.22: Plots of modulus, defined as $2\partial W / \partial I_1$ for W=W(I$_1$) as a function of I$_1$-3.

Although for unfilled rubber there does appear to be a small dependence on I_2 (Rivlin & Saunders 1951, Gough 2000), several reports (Yeoh 1990, Gregory et at. 1997, Gough 2000) have suggested that the dependence of W, and hence stress on I_2 may be neglected for practical purposes in comparison with that on I_1. If this were strictly true, the tensile data can be used to directly predict the behaviour in compression (Marlow 2003), as shown in Figure 5.23. This figure includes the data measured directly in compression as well as the extrapolations of models from their fits to the data in tension.
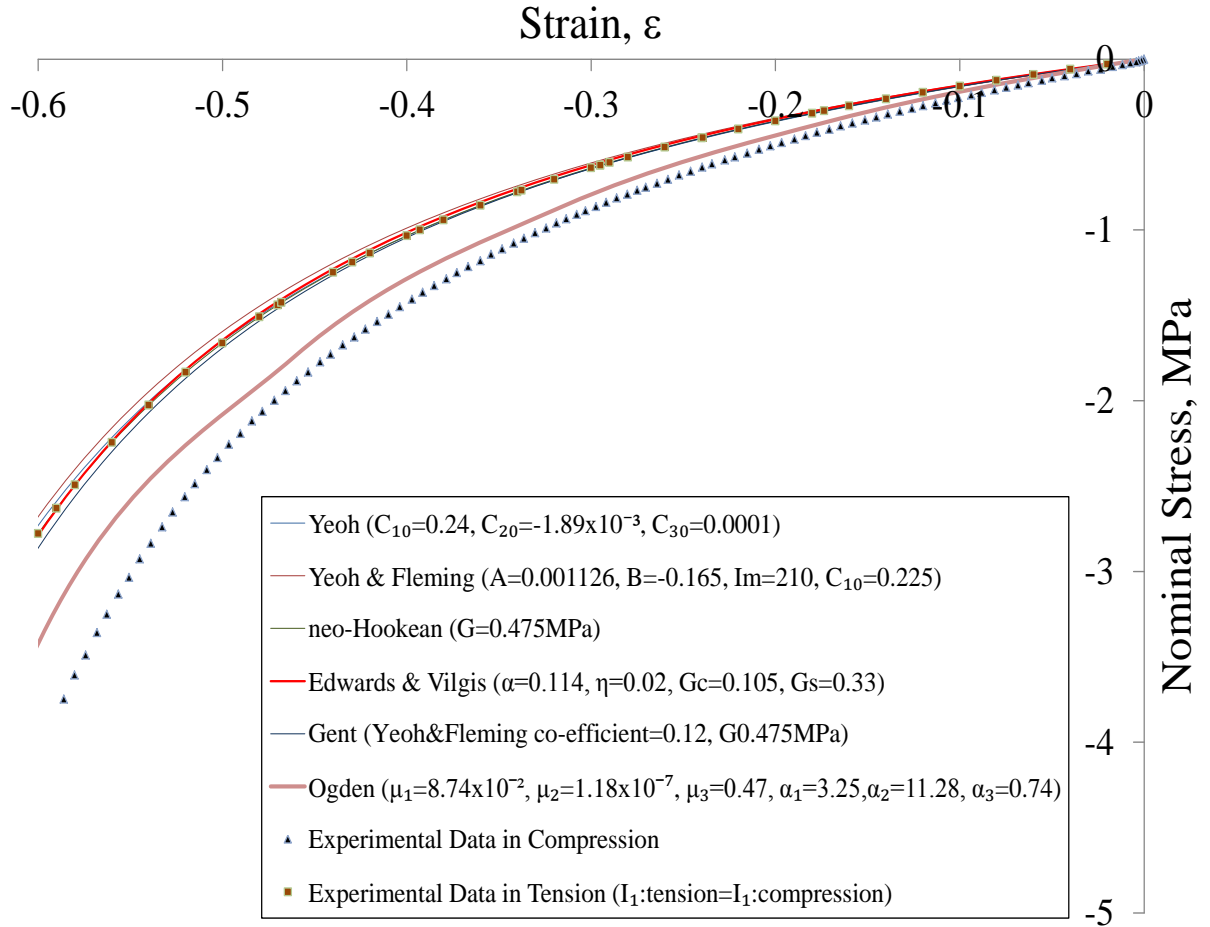
Figure 5.23: Typical stress-strain curves of rubber models compared with experimental data in compression.

The numerical compression $\lambda_c \in (0,1)$ corresponding to the same value of I_1 as a uniaxial tensile stretch $\lambda_T \in (1, \infty)$ was found by using Microsoft Excel 2010 to solve $\lambda_c^2 + \frac{2}{\lambda_c} = \lambda_T^2 + \frac{2}{\lambda_T}$. The uniaxial tension data can then be re-plotted as compression on the assumption that $\frac{\partial W}{\partial I_2} = 0$ (see Equation (2.27b)), and the equation given in Appendix A, leading to the prediction that :

$$\sigma_c = 2 \left(\lambda_c^2 - \frac{1}{\lambda_c} \right) \frac{\partial W}{\partial I_1}$$

$$= \frac{\lambda_c^2 - \frac{1}{\lambda_c}}{\lambda_T^2 - \frac{1}{\lambda_T}} \sigma_T \qquad (5.4)$$

where σ_c, σ_T are true stress in compression and tension respectively. In term of nominal stress, this equation becomes

$$f_c = \frac{\sigma_c}{\lambda_c} = \frac{\lambda_c - \frac{1}{\lambda_c^2}}{\lambda_T - \frac{1}{\lambda_T^2}} f_T \quad . \qquad (5.5)$$

The discrepancy between the experimental data and the models is greater in compression than in tension. The experimental data in compression has higher stress values than the predictions of the models. It should be pointed out that the discrepancy between the directly measured compression data and the replot of the tension using the assumption that $\frac{\partial W}{\partial I_2} = 0$ may will be an experimental artefact. Not only are the testpieces moulded separately with a different shape, but, more significantly, higher stresses when directly measured in compression could be caused by a failure of the soapy water lubricant to reduce the friction between loaded rubber and platen to zero. It is therefore suggested that the discrepancies in Figure 5.23 between the two sets of experimental data, and between the Ogden and other models, demonstrate the problem of stress-strain characterisation of rubber rather than provide a clear conclusion.

Table 5.1 presents the coefficient values for a selected number of models based on use of Excel and ABAQUS fitting software available within its FEA capability.

Table 5.1: The fitting parameters used for the hyperelastic models.

Hyperelastic model	Parameter
neo-Hookean[a]	G=0.475MPa, 0.38MPa
Yeoh[a]	$C_{10}=0.24$, $C_{20}=-1.89 \times 10^{-3}$, $C_{30}=10.98 \times 10^{-5}$
Yeoh & Fleming[a]	$I_m=210$ $A=11.256 \times 10^{-4}$ $B=-0.165$ $C_{10}=0.225$
Ogden[b]	$\mu_1=8.74 \times 10^{-2}$ $\mu_2=1.18 \times 10^{-7}$ $\mu_3=0.47$ $\alpha_1=3.25$ $\alpha_2=11.28$ $\alpha_3=0.74$
Gent[a]	Y=0.12, G=0.475MPa
Edwards & Vilgis[a]	$\alpha=0.114$, $\eta=0.02$, $G_c=0.105, G_s=0.33$

a - Fit to experimental data using Microsoft Excel 2010.
b - Fitted by ABAQUS ver 6.10-1.

5.1.4 Conclusions

(1.) Large softening of the rubber occurred in the first deformation and after a few cycles of deformation the rubber approached a steady state with a constant stress-strain curve. Based on the extension and compression results, adjustment of the coefficient of Yeoh & Fleming (1997) affected the position of the stress-strain upturn, but setting it at the original value Y=0.044 (I_m=30.14) given by Yeoh & Fleming does not give a good fit if G is adjusted to fit the experimental data at small strain (G=0.475MPa). A comparison of rubber models fitted to the experimental data was made. In extension behaviour, Yeoh, Ogden and Edwards & Vilgis models closely fit the experimental tensile data. In contrast, neo-Hookean, Yeoh Fleming and Gent models give a less close fit to the experimental data. Ogden model is not anticipated to be appropriate for predicting stress-strain behaviour in compression from experimental data. It is confirmed that tensile experimental data can be used to predict approximately rubber behaviour in compression.

(2.) From the literature the volume fraction of the strain-induced crystallites at high strain for a typical NR is about 10% to 20%. These results explained the role of orientation and strain induced crystallization in the mechanical properties of natural rubber, because most rubber has been considered to contain oriented chains.

(3.) It is confirmed that the stress declines linearly with log(t) at longer times. An approximately linear relation could be fitted to the experimental data points over a limited time range. The associated slope provides a convenient measurement of the rate of relaxation over short periods of time. In the unfilled rubber vulcanizate, the stress decay rate increased at ~50,000s; this is possible due to continued crystallization at constant strain.

5.2 Cyclic Stress-Strain Screening Tests

5.2.1 Introduction

It is well-known that addition of reinforcing filler greatly complicates the stress-strain behaviour of rubber, increasing stiffness and hysteresis (Ahmadi & Muhr 1997). For many applications increased modulus brings an economic benefit – less rubber is needed to achieve the design stiffness. However, a balance must be sought in which this benefit is not at the expense of excessive hysteresis, cyclic stress relaxation or unacceptable shortening of the fatigue life.

For this project the stress-strain properties a range of filled candidate rubbers for a particular application have been compared to establish whether or not behaviour superior to the unfilled natural rubber of the previous section (i.e. R0 (EDS19)) could be identified in terms of stress strain behaviour. In all, 24 other distinct compounds were investigated as summarised in Tables 5.2, 5.3 and 5.4. Some of these were proprietary materials, the formulation details of which are not known to the author or should not be disclosed even if known. The extent of the testing required examining

- stress softening under cyclic uniaxial tension.
- relaxing and non-relaxing strains.

The purpose of this experimental work is to characterise the stress-strain behaviour in a manner appropriate to the application. In the present experimental work, the investigation of stress softening of a filled rubber under cyclic uniaxial tension was carried out. A comparison in relaxing and non-relaxing condition was performed and the interpretation of the results was made. Uniaxial tension was chosen as being very simple, yet not so dissimilar to the actual mode of deformation in the application. The modulus and loss angle were calculated from the experimental measurements. Stress-strain cycles with amplitudes about a mean strain were examined, this being representative of the service conditions in the application.

5.2.2 Materials and Test Procedure

The sheets of investigated compounds of Tables 5.2 and 5.3 had a nominal thickness of 2mm and were moulded according to the cure conditions specified in each table. Each table also provides the proportions by weight of the non-proprietary rubber compounds. Most of the proprietary compounds (designated R10, R11, R12, R13, R19, R20, R21, R22, R23, R24, R25 and R26) were cured at TARRC as nominal 2mm thick sheets, some were supplied ready moulded as sheet. The cure characteristics of the mixed compounds were determined by an oscillatory disc rheometer (Mosanto Rheometer MDR2000). The test pieces were cut from the appropriate sheet and the dimensions of each test piece (following sample ID) are provided in Table 5.4.

Table 5.2: Formulations of the rubber compounds mixed at TARRC.

Ingredients	R1	R4	R5	R6	R7	R8	R9
	pphr						
Natural rubber, SMRCV60	100	100	100	100	100	100	100
Carbon black, HAF (ASTM N-330)	-	15	30	45	-	-	-
Carbon black, HAF (ASTM N-990)	-	-	-	-	30	37.5	45
process oil (410 Oil)	-	1.5	3.0	4.5	3	3.8	4.5
Zinc oxide	5	5	5	5	5.5	5.5	5.5
Stearic acid	2	2	2	2	1.5	1.5	1.5
Antioxidant 2246	-	3	3	3	-	-	-
Antioxidant HPPD	-	-	-	-	3	3	3
Antiozonant wax (Negazone)	-	2	2	2	-	-	-
Accelerator,CBS	0.6	0.6	0.6	0.6	0.8	0.8	0.8
Sulfur	2.5	2.5	2.5	2.5	2.9	2.9	2.9
Cure Condition (Time, Temperature)	45min, 140°C	38min 140°C	40min, 140°C	40min, 140°C	30min 140°C	30min 140°C	30min 140°C

Note: The compound formulations referred to Engineering Data Sheet (EDS) which were developed in TARRC.

Table 5.3: Rubber formulations mixed at TARRC with different curing systems.

Ingredients	R14	R15	R16	R17	R18
	pphr				
Natural rubber, SMRCV60	100	100	100	100	100
Carbon black, HAF (ASTM N-330)	15	15	15	15	15
Petrofina 2059	1.5	1.5	1.5	1.5	1.5
Zinc oxide	5	5	5	5	5.5
Stearic acid	2	2	2	2	2
Antioxidant HPPD	3	3	3	3	3
Antiozonant wax (Negazone)	2	2	2	2	2
Accelerator,CBS	0.48	0.6	0.72	0.84	0.96
Sulfur	2	2.5	3	3.5	4
Cure Condition (Time, Temperature)	40min, 140°C	37min, 140°C	36min, 140°C	36min, 140°C	31min 140°C

Three hardness buttons of each compound were cured and used for hardness tests in accordance with the standard BS ISO 48:2007; results are provided in Table 5.4. The hardness of the R13 sample was measured using a micro-hardness method, since the material supplied had a limited dimension.

Table 5.4: Dimension of each tensile strip and the hardness test results.

Sample ID	Dimension (mm)	Hardness, Median, IRHD
R1	1.92 x 5.92 x 160	41
R4	2.01 x 5.92 x 160	49
R5	1.92 x 5.95 x 160	57
R6	1.95 x 5.91 x 160	66
R7	1.90 x 5.85 x 160	53
R8	2.06 x 5.86 x 160	36
R9	1.93 x 5.82 x 160	57
R10	1.93 x 5.88 x 160	48
R11	1.94 x 5.78 x 160	69
R12	2.08 x 5.79 x 160	73
R13	3.29 x 6.35 x 110	33
R14	2.05 x 5.68 x 160	45
R15	2.13 x 5.72 x 160	48
R16	2.08 x 5.66 x 160	52
R17	2.19 x 7.04 x 160	54
R18	2.07 x 5.74 x 160	54.5
R19	1.51 x 6.24 x 160	53.5
R20	1.44 x 6.22 x 160	49.5
R21	1.92 x 5.62 x 160	60.5
R22	1.45 x 6.22 x 160	54.5
R23	1.65 x 6.22 x 160	48.5
R24	1.44 x 6.22 x 160	51.5
R25	1.95 x 6.22 x 160	56.5
R26	1.43 x 6.29 x 160	67

Three tensile dumb-bells (Type 2, BS ISO 37:2005) were cut from cured sheet from each compound. Tensile strength tests were conducted using an Instron 5567 machine equipped with an extensometer. The crosshead speed was 500mm/min, a load cell of 500N was used and all the data recorded using an Instron BlueHill software program. A gauge length on the narrow part of the dumbbell test piece was marked using a ϕ6mm white sticker. The gauge length of the test piece was approximately 20mm in the extensometer viewfinder, which has a range of 500mm in height and 50mm in width. The initial distance between the two grips was 50mm. All the tests were carried out according to BS ISO 37:2011.

The room temperature stress-strain cyclic tests were conducted, on parallel sided tensile strips (as specified in Table 5.6) using an Instron 4701 universal test machine. The length of each sample between clamps was 150mm. The one exception was the R13 sample with 100mm between clamps.

Each testpiece was stretched to 50%, 100%, 150%, 200%, 250% and 300% of original length consecutively for 3 cycles at each strain and at a strain rate of $0.0167s^{-1}$, returning to the original clamp separation between each stretch. Again the exception was the R13 sample tested at a strain rate of $0.025s^{-1}$.

Next each sample was tested one half cycle to 160% followed by three cycles, starting from 160%, with a sequence of strain amplitudes of 15%, 25%, 35%, 45%, 55%, 95% and 105%. These strain cycles were chosen to represent possible excitation during the impingement of waves on the application device, in addition to its design static strain of 160%. The cycle 160±105% represents the maximum excitation.

A personal computer with Picologger was used to record all the force and displacement data. The data acquisition sampling rate was 1.5Hz, so that a load-deflection data point was captured for every 3s approximately. The load-cell used in the tests typically had a range of ±1kN. The load-cell was changed to 100N when uniaxial tension tests were conducted on rubber compounds with a hardness below 50IRHD, to obtain more accurate results.

Stress and strain data were calculated based on the dimensions of each test piece using Microsoft Excel 2010.

5.2.3 Results and Discussion

Table 5.5 shows the overall results of rubber compounds for modulus, tensile strength and elongation at break. Different fillers give different properties of modulus, tensile strength and elongation at break. The higher the content of filler, the greater the modulus and decrease the elongation at break. In contrast, the elongation at break decreases as the filler content is increased. The tensile strength is not significantly affected by filler content.

Table 5.5: Overall results of modulus, tensile strength and
at elongation at break for all compounds.

Sample ID	Median Modulus (100%), (MPa)	Median Tensile Strength (MPa)	Median Elongation at Break (%)
R1	0.79	26.67	693
R4	1.09	29.54	725
R5	1.83	31.47	621
R6	2.49	28.47	557
R7	1.44	25.80	587
R8	1.55	25.91	647
R9	1.67	24.09	590
R10	1.13	23.42	611
R11	2.96	21.29	465
R12	2.73	24.68	472
R13	0.64	9.99	658
R14	0.93	25.66	664
R15	1.13	30.45	673
R16	1.32	29.51	644
R17	1.51	28.59	618
R18	1.59	27.39	566
R19	1.36	34.20	682
R20	1.21	34.05	688
R21	2.04	33.04	603
R22	1.50	35.55	642
R23	1.04	29.16	724
R24	1.40	31.42	649
R25	1.67	30.42	664
R26	2.51	28.09	607

When the content of carbon black is increased so the modulus, hysteresis and stress-softening also increase. Most softening occurs during the first deformation, and after a few stress cycles a steady state is approached. This phenomenon has been termed the Mullins effect and discussed in Section 2.9.2. Figure 5.24 illustrates the displacement–time plot of one of the tensile stress-strain cyclic tests. Figure 5.25 shows the plot of all data point of displacement and force in non-relaxing for one of the tensile stress-strain cyclic tests.
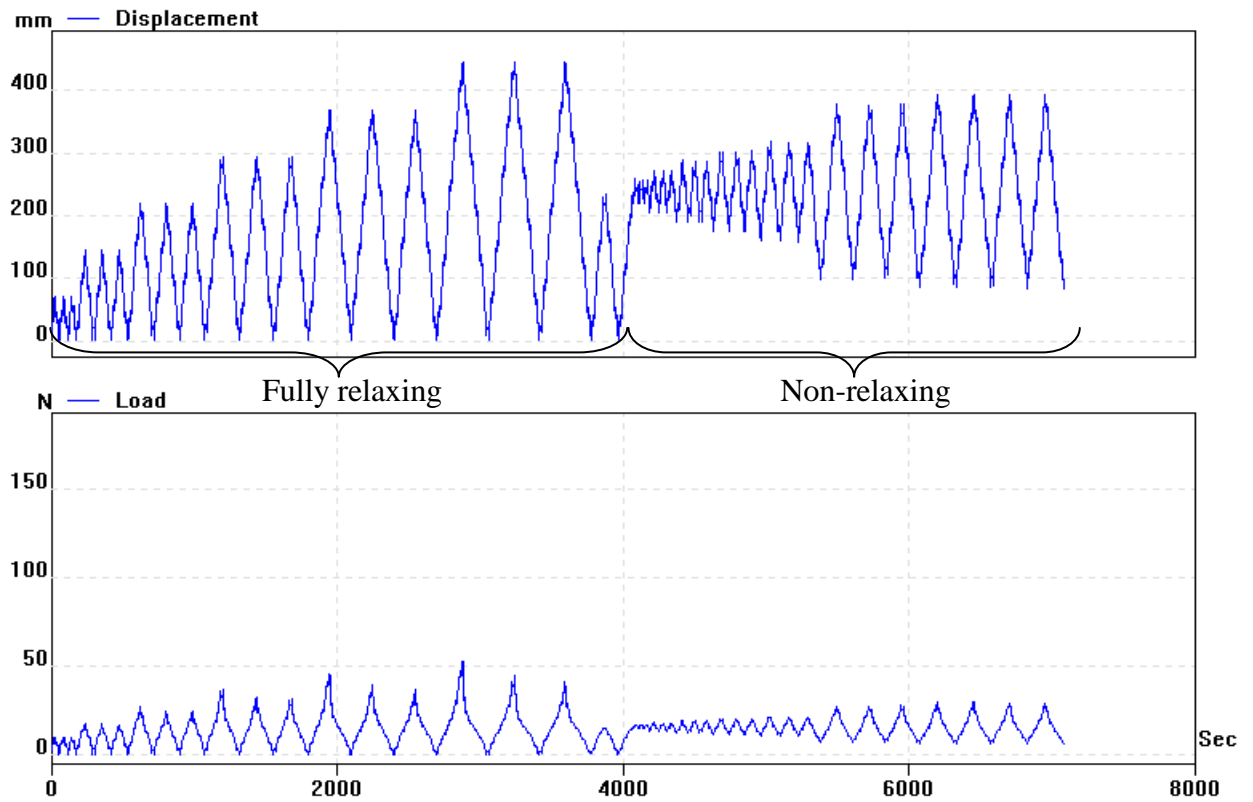
Figure 5.24: Example of displacement-time plot of cyclic test for R8 compound.
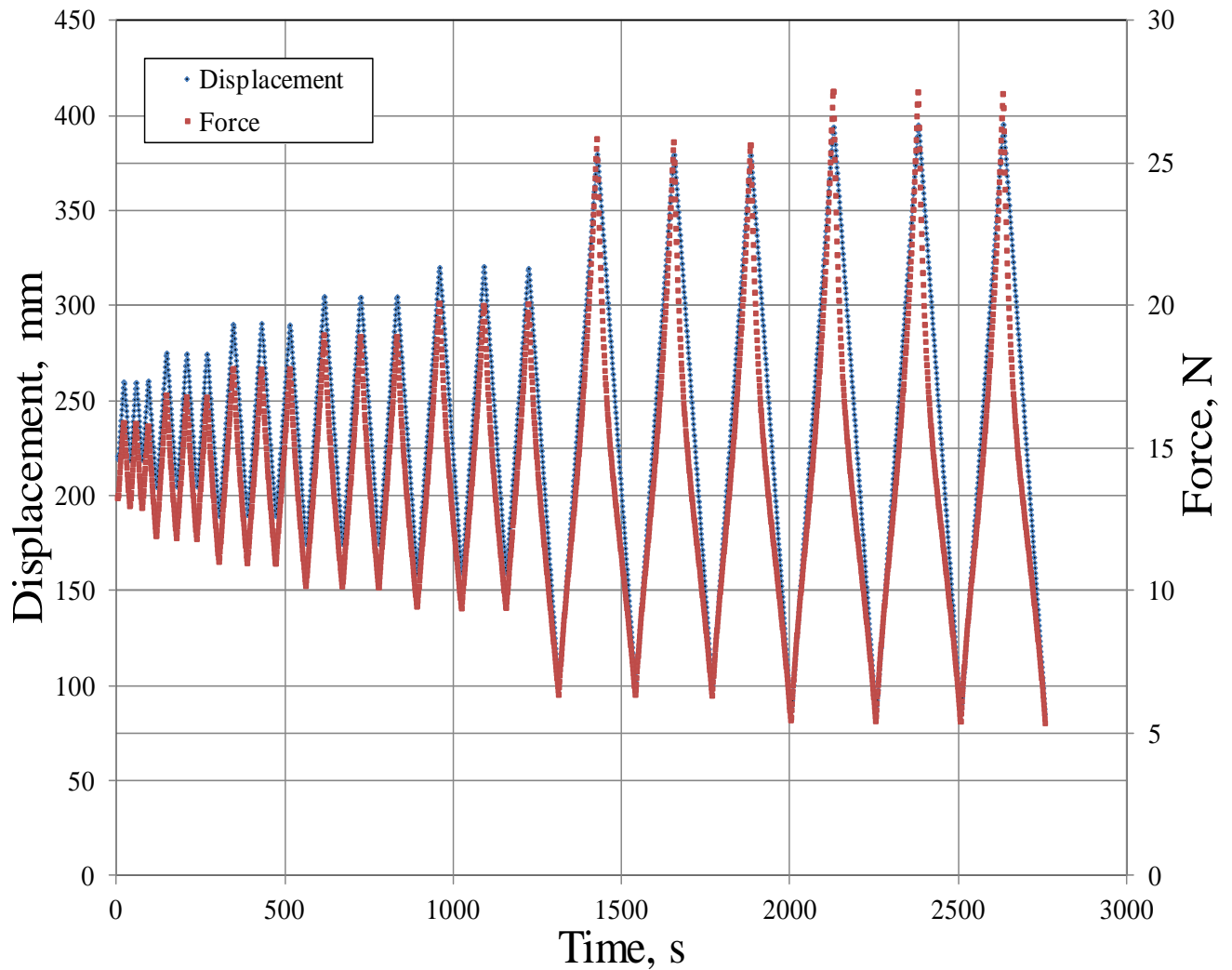
Figure 5.25: Example of the data point plot of force and displacement in non-relaxing for R8 compound.

Figures 5.26 - 5.33 provide relaxed and non-relaxed stress strain curves for materials of Table 5.2. Appendix C – Figures C1 - C38 illustrate the stress-strain response of the other rubbers submitted to a strain-control cyclic uniaxial tension and the non-relaxing stress-strain curves for the earlier indicated range of strain amplitudes.

R1 is unfilled, and hence Figures 5.26 and 5.27 reveal the desirable characteristics of very low set, hysteresis and stress-softening, but the material is rather soft. Other materials reported in Figure 5.28 to 5.33 are reinforced and exhibit more hysteresis and stress-softening. This might be worth tolerating in return for the higher stiffness.

The presence of filler reduces the fatigue for the given conditions, in the coarse non-reinforcing types like N990 used in the R7 ~ 9 materials -having a particularly adverse effect, despite being mixed in TARRC in a similar way to the EDS series using N330 black. It is confirmed that the rubbers with reinforcing filler have shown a higher set, hysteresis and stress for a given strain where these characteristics are evident in the results shown for the proprietary materials in Appendix C. It can be deduced that those rubber compounds also have significantly loadings of reinforcing filler (notably R11, R12, R15, R24, R25 and R26). Those proprietary materials (R10 & R13) showing similar characteristics to R1 can equally well deduced to have negligible filler content. Thus key aspects of material formulations can be predicted by comparing their stress-strain behaviour including the modulus, tensile strength, elongation at break and hardness.
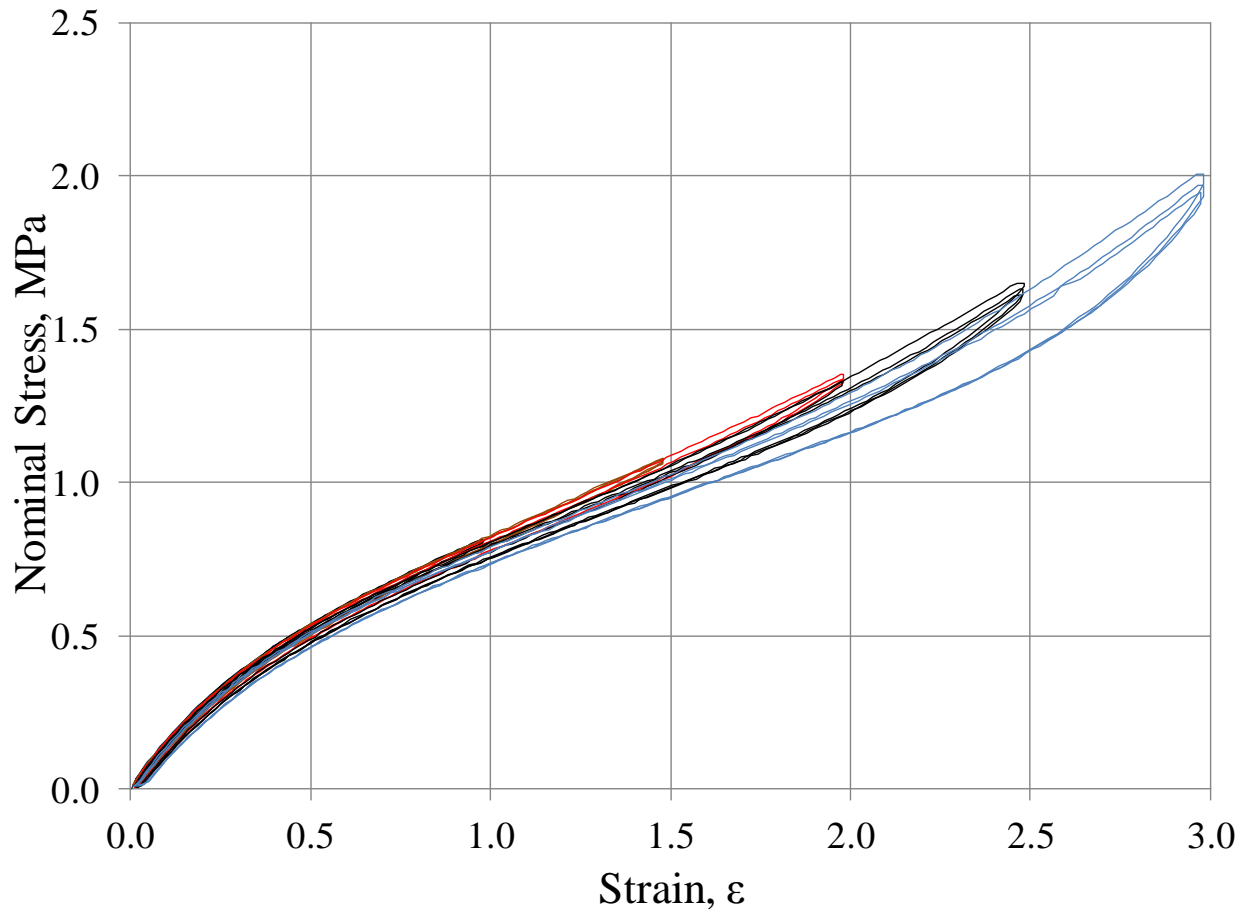
Figure 5.26: Stress-strain in simple extension for R1 from zero strain.
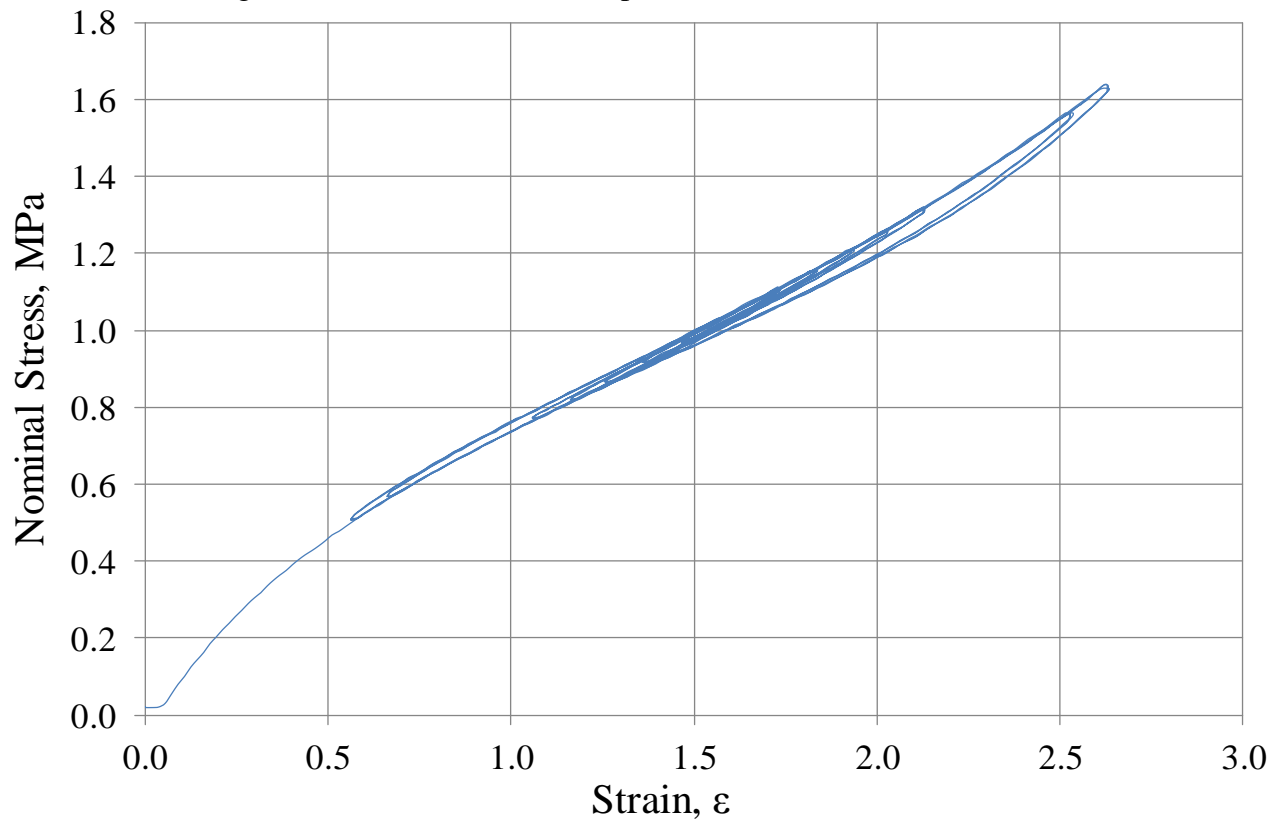
Figure 5.27: Typical non-relaxing stress-strain curves of R1 at strain amplitude of 15%, 25%, 35%, 45%, 55%, 95% and 105%.
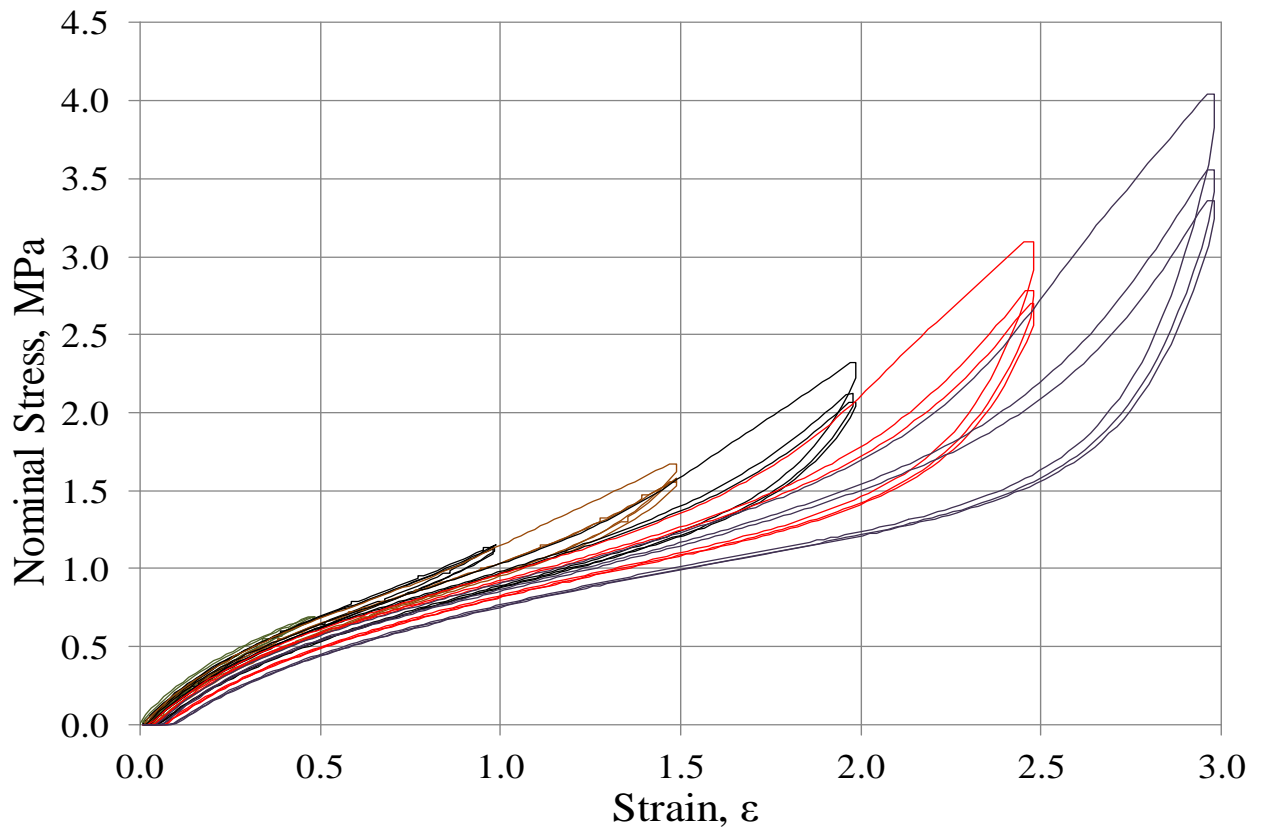
Figure 5.28: Stress-strain in simple extension for R4 from zero strain.
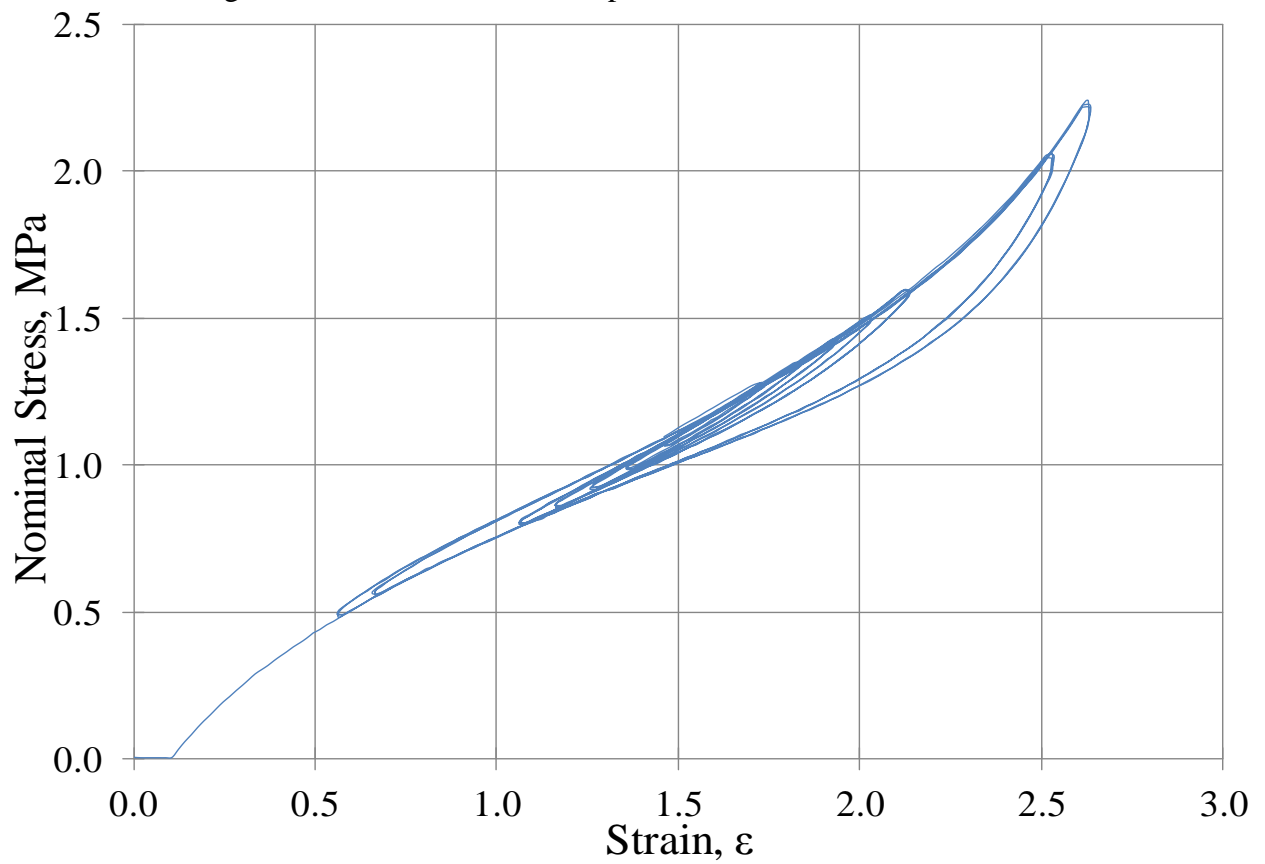
Figure 5.29: Typical non-relaxing stress-strain curves of R4 at strain amplitude of 15%, 25%, 35%, 45%, 55%, 95% and 105%.
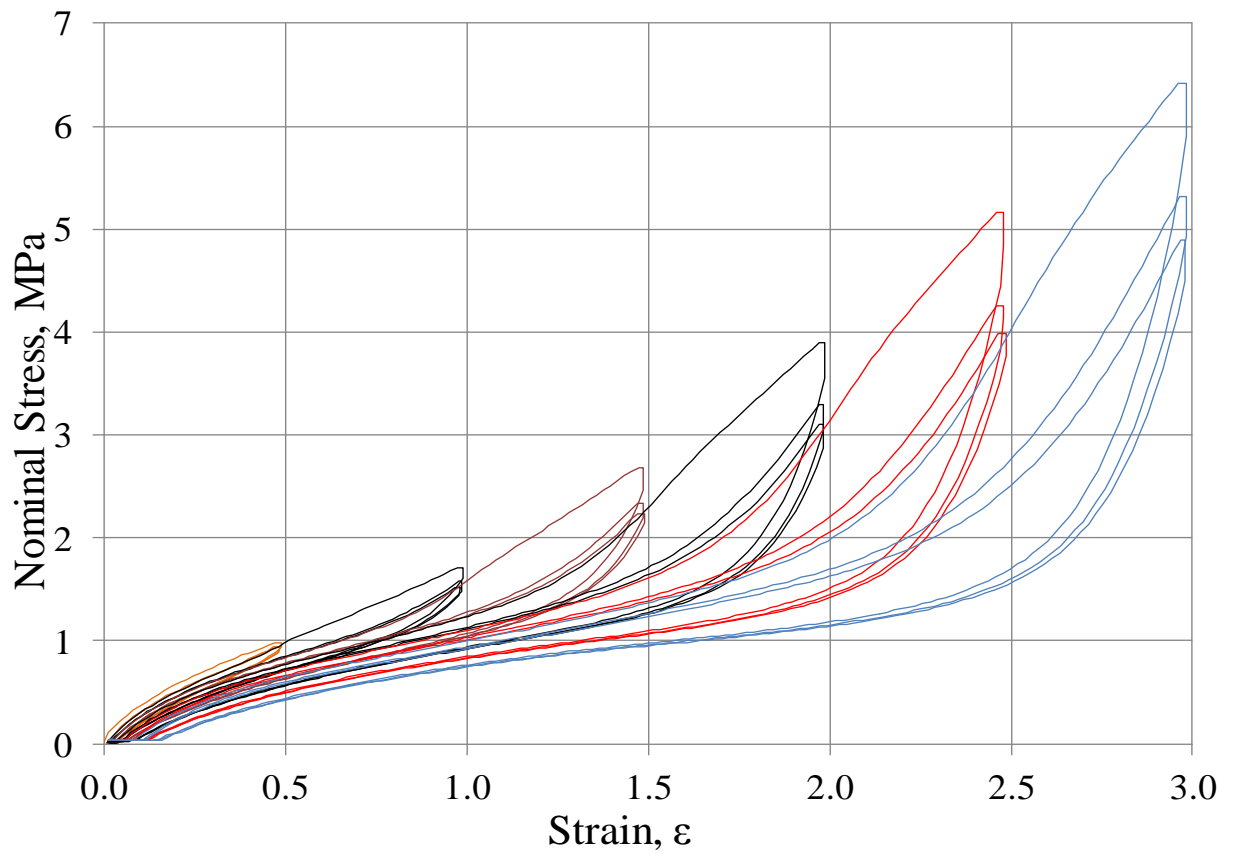
Figure 5.30: Stress-strain in simple extension for R5 from zero strain.
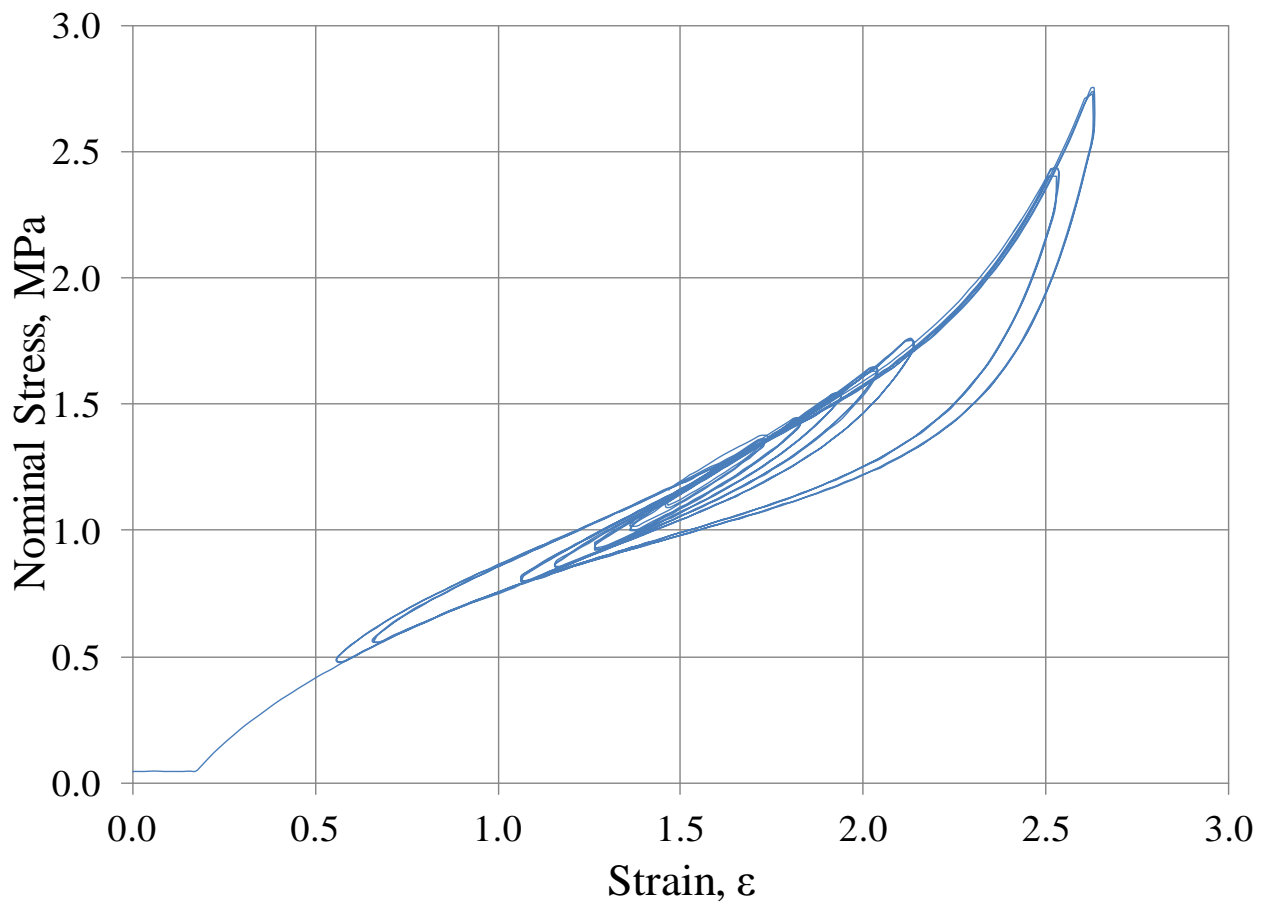
Figure 5.31: Typical non-relaxing stress-strain curves of R5 at strain amplitude of 15%, 25%, 35%, 45%, 55%, 95% and 105%.
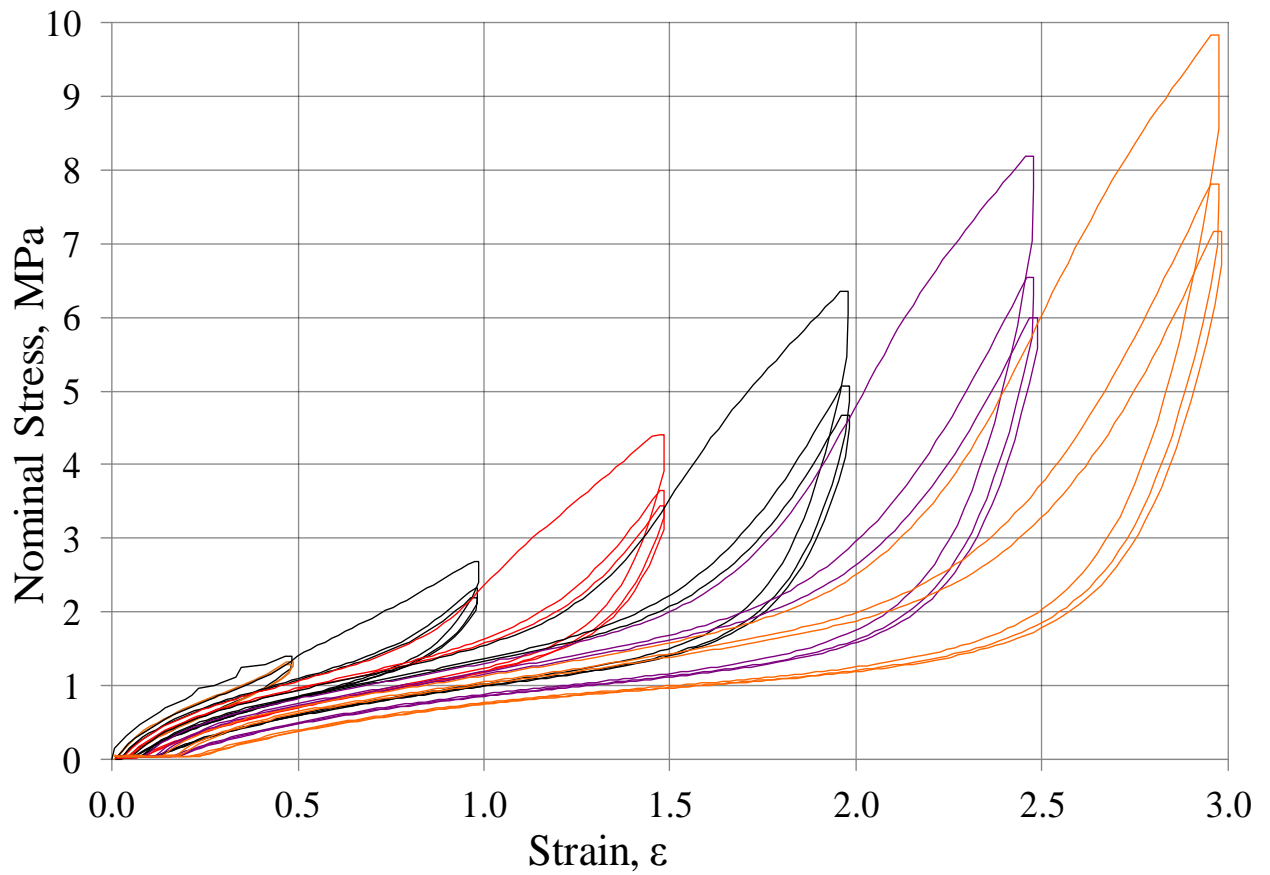
Figure 5.32: Stress-strain in simple extension for R6 from zero strain.
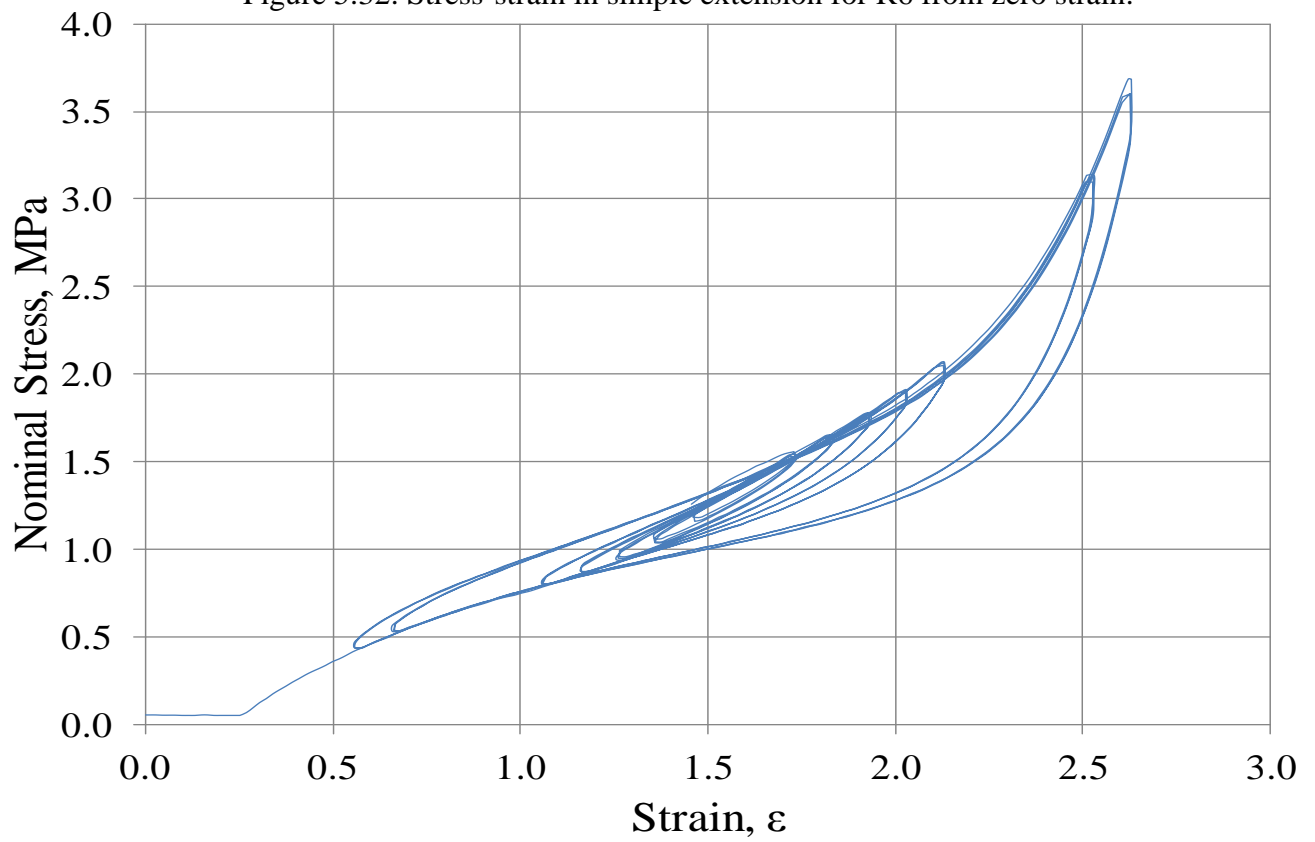
Figure 5.33: Typical non-relaxing stress-strain curves of R6 at strain amplitude of 15%, 25%, 35%, 45%, 55%, 95% and 105%.

All the rubber compounds showed stress softening at large strain, but the magnitude of the effect increased strongly with increase in filler content.

Based on the stress-strain curves in relaxing and non-relaxing condition provided in Appendix C, it can be surmised that R12 and R11 are probably highly filled, whereas R10 and R13 appear to be only lightly filled. The stress-strain curves were nearly stabilized after 3 cycles although the stress slightly diminishes with further cycles.

It is found that for unfilled natural rubber at low strain, there is little hysteresis, but it is very much greater at high strain. It is believed that the large hysteresis for unfilled natural rubber at high strains is due to crystallization.

The large initial hysteresis for the filled compound is believed to be associated with rearrangement of loading paths or bonds in the elastomer filler material system (Bueche 1962). After cyclic uniaxial tension tests, rubbers show a permanent set in the direction of stretching.

All the non-relaxing stress-strain cycles were carried out immediately after completing the fully relaxing stress-strain tests. There was little further stress-softening in the non-relaxing tests. The rubber compounds of R10, R13, R17, R18 as well as R1 showed less effect of stress softening in non-relaxing cyclic excitation.

Comparison of results for rubbers with different curing systems shows different nominal stresses. The main effect on stress-strain behaviour in relaxing and non-relaxing state conditions is determined by the number of crosslink (see Section 2.3). This is demonstrated in additional plots provided in Appendix C (Figures C15 - C24). The formulations of R4, R15, R20 and R23 were identical and their stress-strain behaviours were in accord with each other.

It is found that the stress-strain behaviour of R5 and R25 was similar. This phenomenon also occurred for R6 and R26.

Generally, the difference between the various tested materials was less striking for the non-relaxing cycles. It is possible partly because they are in the "scragged" (see Kingston & Muhr 2011) or "post-Mullins" state. Low hysteresis in non-relaxing stress-strain cycles is often desirable, for example for a rubber device designed to store energy.

5.2.4 Calculation of Dynamic Modulus, E* and Loss Angle, δ

Design for the application requires knowledge of the elastic modulus of the rubber. For a typical application, it may be sufficient to know the equivalent linear dynamic properties, stiffness and loss angle, for dynamic strain cycles applied to the component in its static state of strain. In case of rubber in a strain state approximating to tension, these dynamic properties may readily found using the secant method (Ahmadi & Muhr 1997), adapted to a cyclic tensile strain superimposed on a static tensile strain. The basic equation are given in Equations (5.4) and (5.5), with the symbols defined in the hysteresis loop shown in Figure 5.34. The loss angle provides a measure of the damping or hysteresis energy losses within rubber subjected to cyclic deformation. The modulus and loss angle were determined by applying the secant method illustrated in Figure 5.34:
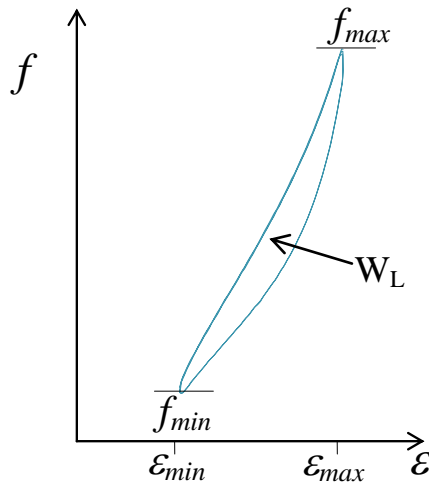
$$\delta = \frac{4W_L}{(\varepsilon_{max} - \varepsilon_{min})(f_{max} - f_{min})} \qquad (5.4)$$

$$|E^*| = \frac{f_{max} - f_{min}}{(\varepsilon_{max} - \varepsilon_{min})} \qquad (5.5)$$

Figure 5.34: Hysteresis loop showing non-linear behaviour typical of filled rubber at high strain (Ahmadi & Muhr 1997).

Note that this equivalent linearisation does not distinguish between kinematic and material origin of nonlinear stress-strain behaviour. In Equation (5.5) the strain is calculated with respect to the reference length of the test piece. If instead the dynamic strain amplitude were calculated with respect to the prestrained state, the dynamic strain would be reduced according to

$$e = \frac{\Delta x}{(1+\varepsilon_0).x_0} = \frac{1}{1+\varepsilon_0}.\frac{\Delta x}{x_0} = \frac{1}{1+\varepsilon_0}.\varepsilon \qquad (5.6)$$

where ε_0 is the static prestrain, equal to 1.6 here.

A visual basic program, given in Appendix C, was created to calculate the modulus and loss angle using Equations (5.4) to (5.6). All the experimental data sets were partitioned into a number of distinct cycles using Excel. The program then enabled the calculation of

the modulus and loss angle by specifying the columns of time, displacement and force, as well as the number of the cycle. Tables 5.6 to 5.12 show the resulting values of modulus and loss angle for each rubber compound.

Modulus and loss angle were calculated from the average of the results obtained for each of the three consecutive full non-relaxing cycles starting from the given minimum strain.

Figure 5.35 shows stress-strain curves of each strain amplitude for R6 where the centre position of each hysteresis loop is at a strain of 1.5.
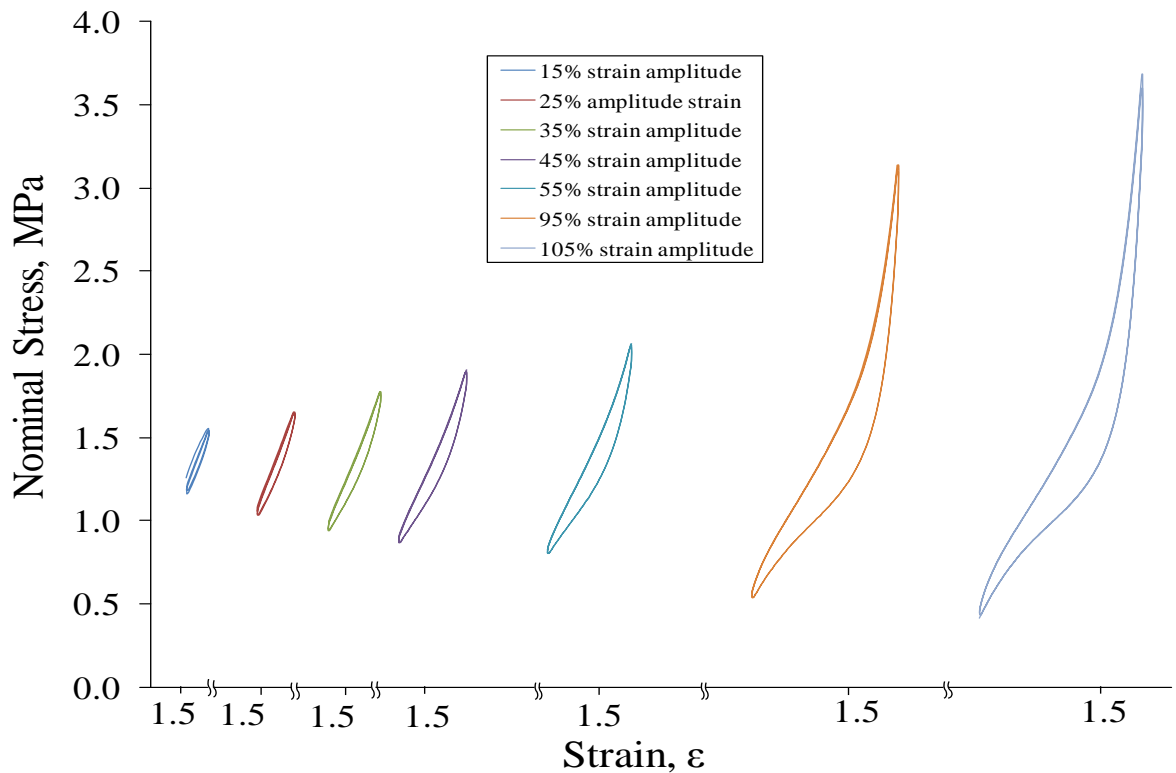
Figure 5.35: Separation of stress-strain curves for each strain amplitude (R6).

Table 5.6: Results of dynamic modulus and loss angle for R1, R4~6 rubber compounds.

Amplitude, %	R1		R4		R5		R6	
	Loss angle (degrees)	Modulus (secant) (MPa)	Loss angle (degrees)	Modulus (secant) (MPa)	Loss angle (degrees)	Modulus (secant) (MPa)	Loss angle (degrees)	Modulus (secant) (MPa)
15	6.88	0.50	8.55	0.78	12.33	0.98	15.29	1.34
25	3.92	0.49	5.91	0.75	9.06	0.93	11.36	1.24
35	3.18	0.50	5.23	0.75	8.30	0.91	10.77	1.22
45	2.72	0.51	5.08	0.74	8.27	0.88	10.82	1.18
55	2.57	0.51	5.37	0.74	8.78	0.87	9.81	1.13
95	2.14	0.52	4.74	0.77	7.42	0.94	9.34	1.38
105	2.40	0.55	5.26	0.83	7.85	1.06	8.58	1.55

Note: Average of 3 loops reported

Table 5.7: Results of dynamic modulus and loss angle for R7, R8 and R9.

Amplitude, %	R7		R8		R9	
	Loss angle (degrees)	Modulus (secant) (MPa)	Loss angle (degrees)	Modulus (secant) (MPa)	Loss angle (degrees)	Modulus (secant) (MPa)
15	7.70	0.86	8.39	0.94	8.98	0.93
25	5.00	0.86	5.36	0.92	5.81	0.94
35	4.43	0.82	4.67	0.90	5.13	0.90
45	4.06	0.81	4.36	0.91	4.96	0.90
55	3.61	0.82	3.86	0.88	4.45	0.87
95	4.73	0.86	4.95	0.94	5.88	0.93
105	4.87	0.88	5.03	0.96	5.96	0.95

Note: Average of 3 loops reported

Table 5.8: Results of dynamic modulus and loss angle for R10, R11, R12 and R13.

Amplitude, %	R10		R11		R12		R13	
	Loss angle (degrees)	Modulus (secant) (MPa)	Loss angle (degrees)	Modulus (secant) (MPa)	Loss angle (degrees)	Modulus (secant) (MPa)	Loss angle (degrees)	Modulus (secant) (MPa)
15	7.36	0.65	14.82	1.47	16.61	1.49	11.27	0.30
25	4.45	0.64	10.50	1.40	11.99	1.39	5.89	0.28
35	3.54	0.63	9.74	1.33	11.30	1.34	4.70	0.28
45	3.04	0.62	9.62	1.32	11.15	1.30	4.03	0.28
55	2.84	0.63	8.90	1.25	10.15	1.24	3.75	0.28
95	2.76	0.66	8.97	1.49	9.36	1.52	3.86	0.29
105	2.80	0.68	8.24	1.66	8.64	1.71	3.87	0.30

Note: Average of 3 loops reported

Table 5.9: Results of dynamic modulus and loss angle for R14, R15, R16 and R17.

Amplitude, %	R14		R15		R16		R17	
	Loss angle (degrees)	Modulus (secant) (MPa)	Loss angle (degrees)	Modulus (secant) (MPa)	Loss angle (degrees)	Modulus (secant) (MPa)	Loss angle (degrees)	Modulus (secant) (MPa)
15	9.56	0.56	9.05	0.75	8.41	0.92	7.81	1.02
25	6.37	0.56	6.18	0.72	5.48	0.91	5.15	1.03
35	5.72	0.56	5.61	0.72	4.95	0.89	4.52	1.00
45	5.76	0.56	5.36	0.72	4.69	0.89	4.31	1.00
55	5.22	0.55	4.80	0.70	4.12	0.87	3.77	0.99
95	6.28	0.59	5.57	0.78	4.65	0.97	4.25	1.11
105	6.21	0.63	5.43	0.82	4.67	1.03	4.26	1.18

Note: Average of 3 loops reported

Table 5.10: Results of dynamic modulus and loss angle for R18, R19, R20 and R21.

Amplitude, %	R18		R19		R20		R21	
	Loss angle (degrees)	Modulus (secant) (MPa)	Loss angle (degrees)	Modulus (secant) (MPa)	Loss angle (degrees)	Modulus (secant) (MPa)	Loss angle (degrees)	Modulus (secant) (MPa)
15	7.85	1.18	9.56	0.93	8.70	0.83	13.02	1.28
25	5.12	1.15	6.69	0.90	5.58	0.83	9.48	1.24
35	4.35	1.14	6.22	0.90	5.05	0.81	9.07	1.19
45	4.05	1.15	6.35	0.89	4.99	0.80	9.28	1.17
55	3.46	1.14	6.08	0.87	4.64	0.79	8.79	1.12
95	3.81	1.29	7.39	0.97	5.99	0.86	9.04	1.36
105	3.86	1.36	7.22	1.06	6.02	0.90	8.43	1.52

Note: Average of 3 loops reported

Table 5.11: Results of dynamic modulus and loss angle for R22, R23, R24 and R25.

Amplitude, %	R22		R23		R24		R25	
	Loss angle (degrees)	Modulus (secant) (MPa)	Loss angle (degrees)	Modulus (secant) (MPa)	Loss angle (degrees)	Modulus (secant) (MPa)	Loss angle (degrees)	Modulus (secant) (MPa)
15	9.10	0.93	9.80	0.76	10.99	0.81	12.16	1.07
25	6.11	0.93	6.52	0.73	7.22	0.81	8.79	1.01
35	5.74	0.89	5.92	0.71	6.71	0.76	8.12	1.01
45	5.84	0.88	5.79	0.71	6.69	0.76	8.21	0.98
55	5.59	0.87	5.29	0.70	6.15	0.74	7.57	0.95
95	6.76	0.99	6.18	0.77	7.20	0.81	8.09	1.10
105	6.59	1.08	6.15	0.80	6.97	0.88	7.71	1.20

Note: Average of 3 loops reported

Table 5.12: Results of dynamic modulus and loss angle for R26.

Amplitude, %	R26	
	Loss angle (degrees)	Modulus (secant) (MPa)
15	15.63	1.19
25	11.51	1.11
35	11.08	1.08
45	11.18	1.05
55	10.31	1.00
95	10.43	1.18
105	9.66	1.30

Note: Average of 3 loops reported

5.2.5 Discussion

The rubbers with low levels of filler showed low hysteresis for strain <300% e.g. R1, R13 and R10. Crystallization has been put forward as a possible cause of the increase in hysteresis at high strain (Harwood & Schallmach 1967, Toki et al. 2002).

The hysteresis under non-relaxing conditions is smaller compared to that under relaxing conditions, presumably due to less change in the fraction of crystallinity during the stress-strain cycle. The values of loss angle and modulus for strain cycles about a static prestrain of 160% depend on the amount of carbon black in the rubber compound and also the range of strain amplitude (15% to 105%).

It would be expected that the loss angle of unfilled NR is similar at any strain amplitude (Natural Rubber Engineering Data Sheet 1979). It is surprising for unfilled rubber R1 at small strain amplitude, the value of the loss angle is slightly higher compared to other strain amplitude. This phenomenon is interesting to investigate since the determination of loss angle from tension method would expect to give different results from double shear test method.

Reinforcing filler increases the hysteresis in rubber to a much greater extent than might be expected from the rather small increase it brings about to the stress relaxation rate (Ahmadi et al. 2008)

The addition of filler caused a large increase in magnitude of the modulus and hysteresis. The modulus of filled rubber is approximately constant except for a small increase at the highest amplitudes whereas the modulus of unfilled rubber is little affected by strain amplitude.

Filled vulcanizates give higher loss angles, with the value depending upon the type and amount of filler. The higher angles are associated with breakdown of the interactions responsible for the high stiffness at low strains (Lindley et al. 1994).

5.2.6 Conclusions

(1) The primary loading cycle of unfilled NR to high strain results in significant softening that shows only partial recovery after 7 months. The magnitude of the softening depends on the maximum strain applied. The larger the maximum strain applied, the greater the softening. This is known as the Mullins effect. The higher the carbon black loading, the greater the stress-softening and hysteresis.

(2) Hysteresis of the unfilled rubbers does become large at very high amplitudes, probably indicating strain-crystallisation.

(3) Modulus and loss angle of each rubber were determined in tension for samples prestrained to 160% for a range of dynamic amplitudes (15% to 105%). It was found that the loss angle decreased when the dynamic amplitude increased, and was surprisingly large (6.4^o for unfilled NR) at the smallest amplitude (15%). For filled NR, the Payne effect - i.e. fall in dynamic modulus as the strain amplitude is increase - was surprisingly weak. At the highest two strain amplitudes (95% and 105%) the modulus of the filled rubber increases, presumably because the maximum strain is very high (255% and 265% respectively) so that affects of strain crystallization and/or finite extensibility result in an upturn in the stress-strain curves.

Chapter 6

Experimental: Investigation of Carbon Black Dispersion in Rubber

6.1 Introduction

Carbon black dispersion in rubber is very important since it is expected to affect mechanical rubber properties such as tensile strength, modulus, hardness, abrasion resistance, tear strength and fatigue life. Carbon black is also said to prevent the penetration of UV light into rubber, and hence photolytic oxidation of the rubber, but no literature quantifying the amount and type of black necessary to achieve this has been found during this project.

An important objective of this study is to establish a useful measure of the size of inclusions in rubber mixes that may correlate with the effective flaw size concept in fatigue failure. Another objective is to develop a theory for the effect of filler volume fraction and dispersion on the absorption of UV light.

In this chapter, parameters relating to the dispersion of fillers in rubber have been investigated for several aged rubber artefacts and for the freshly mixed materials used in the experimental work elsewhere in the thesis. The significance of these parameters to other phenomenona such as fatigue life and penentration of UV light is discussed in later chapters.

6.2 Sample Preparation and Method of Measurement

Small yellow circles showing the cut location of aged NR artefacts are presented in Figure 6.1.
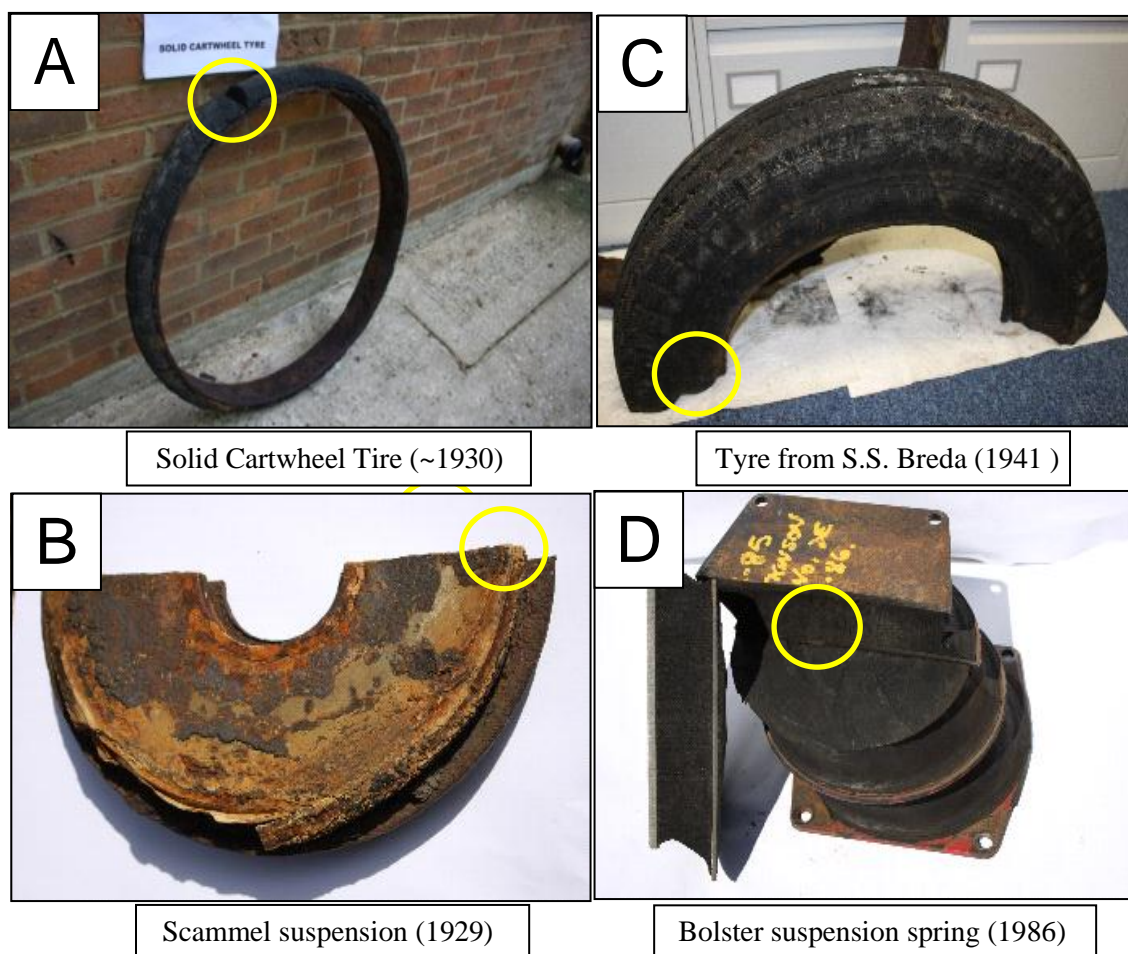
Figure 6.1: Rubber artefacts for the analysis of dispersion.

The ingredients of each artefact were analysed by the TARRC Material Characterization Unit (MCU). The deduced rubber formulation and hardness of each artefact is presented in Table 6.1.

Table 6.1: Rubber formulation of each artefact from the MCU and hardness results.

Ingredients	Rubber source			
	A	B	C	D
	pphr			
Natural rubber	100	100	100	100
Carbon black	54	0	40	42
Ash (includes ZnO, CaO etc.)	15	46	-	4[*]
Extract	1	23	-	4
$CaCO_3$ (detected from CO_2 evolved)	*c.d.*	69	-	-
Sulphur	4.84	3.03	2.5	2.01
ZnO	-	18	5.5	4″
Mercaptobenzothiazole (MBT)	-	-	0.75	-
Stearic acid	2	-	2.0	-
Hardness, (Median IRHD)	63	42	68	61

Note: Rubber sources A, B, C & D illustrated in Figure 6.1,
   * -includes ZnO, ″-estimated by calculation.

Hardness was tested in accordance to BS ISO 48:2007. The microhardness was also measured for each artefact by cutting a small portion with a thickness of 2mm.

A curing process was carried out to obtain rubber hardness buttons of each compound (as shown in Chapter 5 – Table 5.2 to 5.5) and used for hardness measurement and the dispersion analysis. The samples were prepared to compare with artefact samples. Each sample was cut as a slice 5-10mm wide using a new razor blade to ensure sharpness. The hardness values (as shown in Chapter 5 – Table 5.4) are a few degrees lower than those published in the Natural Rubber Engineering Data Sheet (1979); this may be a consequence of different cure conditions and /or (for the filled rubbers) a different degree of dispersion. The hardness of the material affected the cutting path during dispersion analysis. In particular, the harder the rubber, the more marks were left on the surface due to passage of the blade.

The macro dispersion of each surface was analyzed using the disperGRADER DG1000NT of Figure 6.2. The instrument was left to warm-up for 20 minutes to stablize. The sample was placed on the anvil of the disperGRADER unit, which offers the slice of rubber into the testpiece holder with the newly cut surface against the aperture. The image (100×) of a 2.1 × 1.6mm (3.36×10^6 µm^2) portion of surface used for the assessment can be obtained as a micrograph generated by the dispergrader software. This procedure was conducted 3 times for each material using a fresh cut surface to check the uniformity of the dispersion. The software analysis yields: the percentage of dispersion, a histogram of the number of particles in different size categories and the white area of the sample (corresponding to the total area of inclusions detected; see Figure 6.4). The percentage of dispersion was evaluated based on the comparison of the white area of the selected image stored in the software's library of disperGRADER. The microdispersion was defined as below:

$$\% \ of \ black \ microdispersion \cong \frac{Total \ black \ volume \ fraction - Area \ fraction \ in \ microdispersion}{Total \ black \ volume \ fraction}$$

(6.1)

where the area fraction in microdispersion is equal to $\frac{white \ area}{total \ area}$.
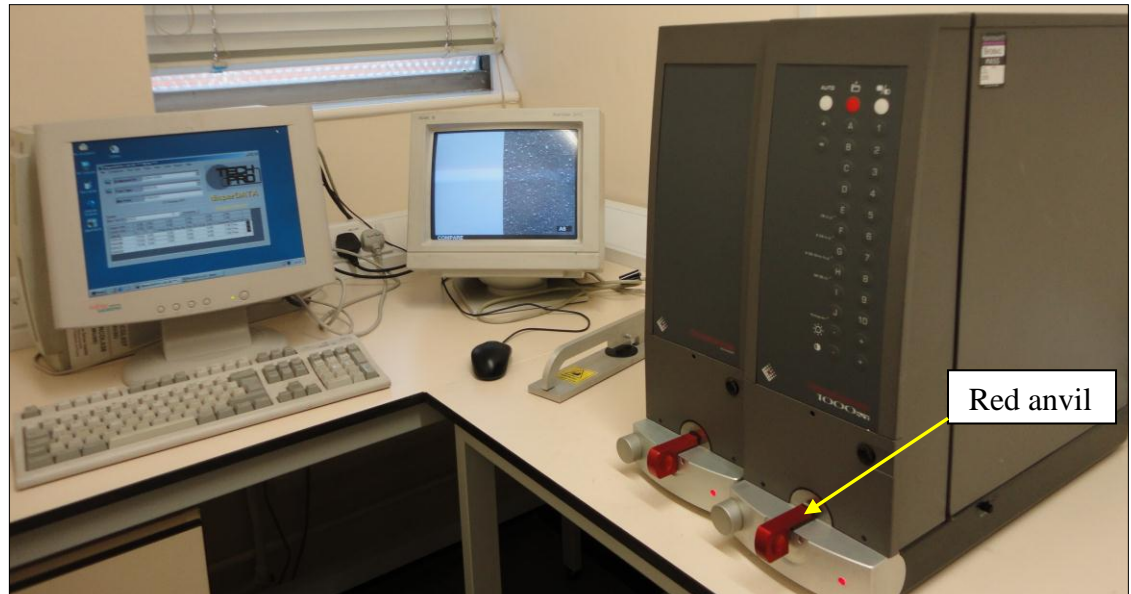
Figure 6.2: Overview of disperGRADER DG1000NT analyzer.

According to the method described in BS ISO 11345:2006 the disperGRADER works with a light source at an angle of 30° with respect to the test surface [Figure 6.3] and uses a magnification of x100. A Charged Coupled Device (CCD) camera is used together with a monitor to provide a composite side-by-side picture of the test piece as illustrated in Figure 6.4. The light dots of the grey scale image of Figure 6.4 are associated with filler and agglomerates (macrodispersion), whereas the dark background is associated with rubber matrix incorporating very finely dispersed filler (microdispersion). This image is transformed by numerical treatment into the inversed image shown on the right in Figure 6.4.

It is believed that hard inclusions in the rubber are displaced from the freshly cut surface as the cutting edge meets them. However, they return to an equilibrium position as the elastic forces relax after the blade has passed on. This results in a roughness to the cut surface that scatters light. It is from this scattering that data on the distribution of inclusions can be obtained.

Being an optical technique, particle sizes can be resolved down to about 1µm, and the disperGRADER is capable of quantifying the distribution of particle sizes above this scale. It might be expected that such a scale would be appropriate for the effect of dispersion on fatigue, since the effective flaw sizes are thought to be at least a few microns

Key

1 lamp
2 CCD camera
3 electronics
4 microcomputer
5 test piece

6 reference
7 digital memory (reference images)
8 light beam
9 test piece holder
10 keyboard
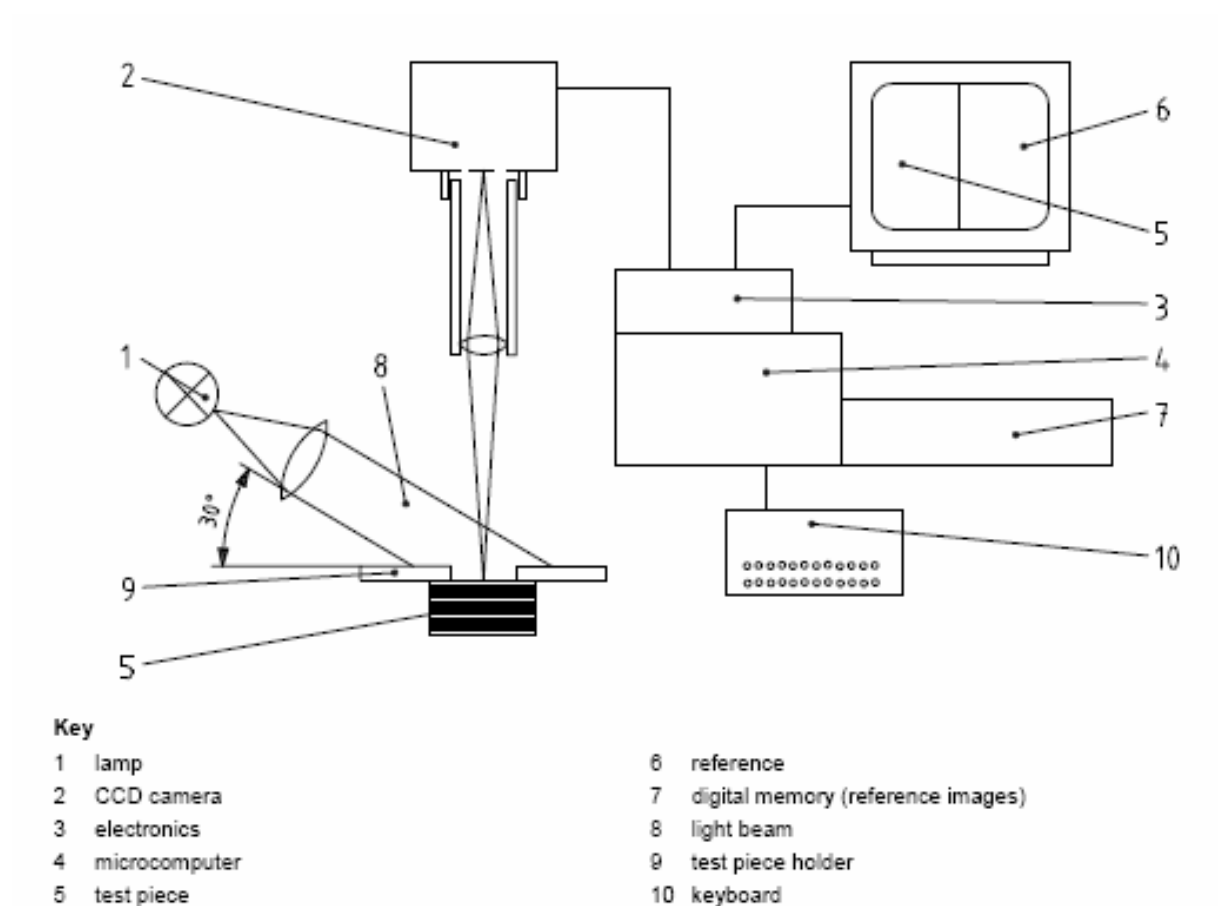
Figure 6.3: disperGRADER principle (Prufen & Messen 2005).
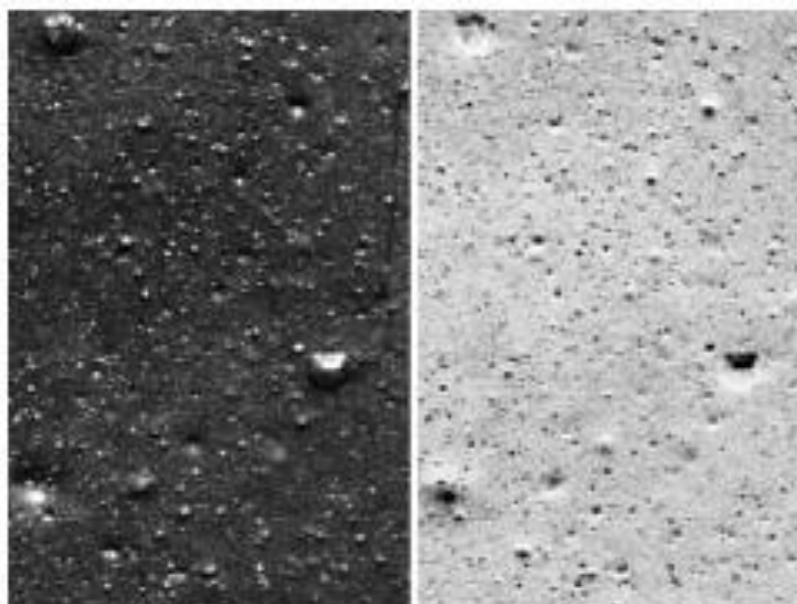
Figure 6.4: disperGRADER image (left) and inversed disperGRADER image (right) (Prufen & Messen 2005).

The x-value of dispersion quality is determined by comparing the image with electronically stored standard reference images under oblique illumination at 30°, to generate a numerical rating from 10 (excellent) to 1(very poor). An appropriate set of reference dispersions, depending on grade of filler, can be selected. The numerical comparison is automatically done by the dispergrader software. The comparisons are performed using reference micrographs appropriate to different classes of labelled material: carbon black CB(x,y); reinforcing carbon black RCB(x,y); semi-reinforcing carbon black SRCB(x); and Ethylene-Propylene-Diene-Monomer EPDM(x) classes. In these clause, x and y denote different options of rating system, x explained as above and y below. The most used test method is the carbon black, CB(x,y) class but not using the x-rating for rubber in general. The visual dispersion ratings normally indicate the following levels of compound quality indicated in Table 6.2 (BS ISO 11345:2006).

Table 6.2: Level of dispersion quality.

Visual dispersion rating	Dispersion classification
9 to 10	Excellent
8	Good
7	Acceptable
5 to 6	Doubtful
3 to 4	Poor
1 to 2	Very Poor

For the y-value a histogram of size distribution is calculated and a value from 1 to 10 is attributed to the image as a function of quantity of agglomerates larger than 23µm. The y-value only takes into account the bigger agglomerates. Since all agglomerates can have an impact on rubber properties, the y-value may not be very useful and values are not reported here.

For the purpose of research it would be expected that greater insight could be obtained from more sophisticated analyses of the data shown in the histograms of size distribution than using the x and y ratings, although these might suffice for quality control.

6.3 Results and Discussion

Figures 6.5(a)-(d) provide the generated histograms of the distribution of the average number of particle count for 3 scanning process and white area for each sample of artefact. The sample area is 2.1mm × 1.6mm=$3.36 \times 10^6 \mu m^2$. The quality of dispersion for the solid cartwheel tyre (artefact A) is the best among other artefacts.
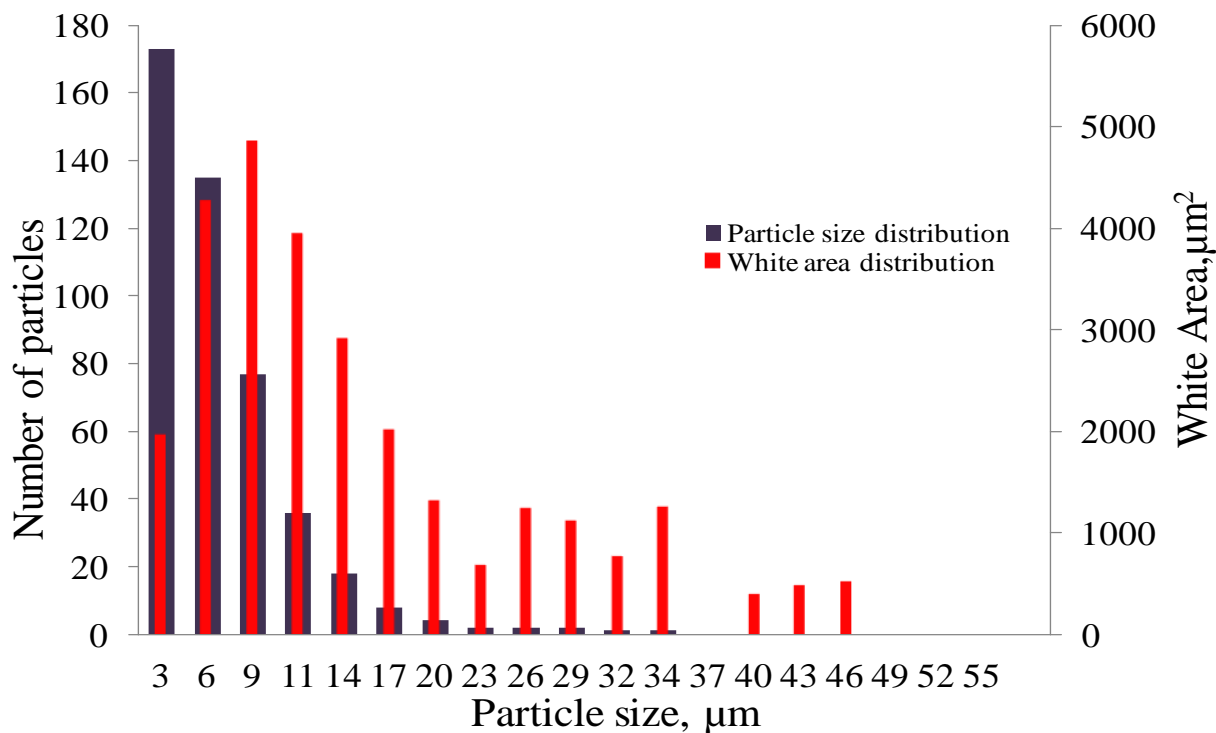
(a) Solid cartwheel tyre (A).
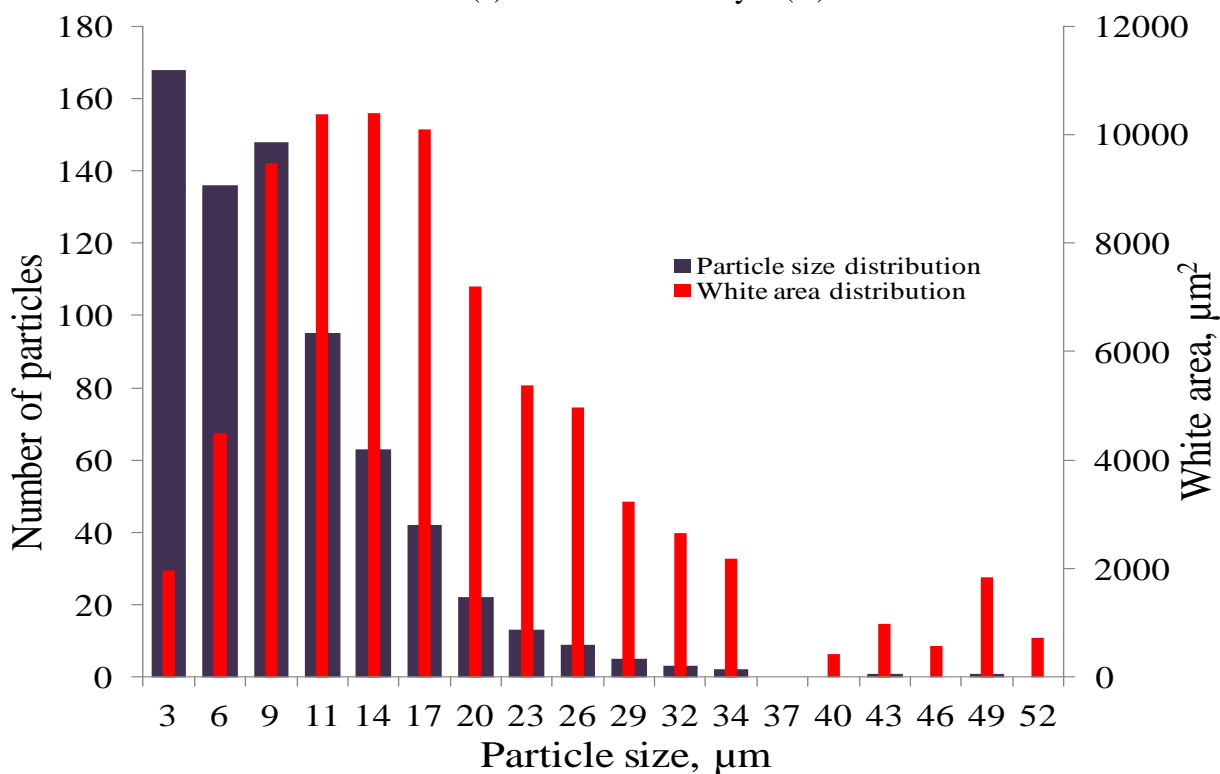
(b) Scammel suspension (B).
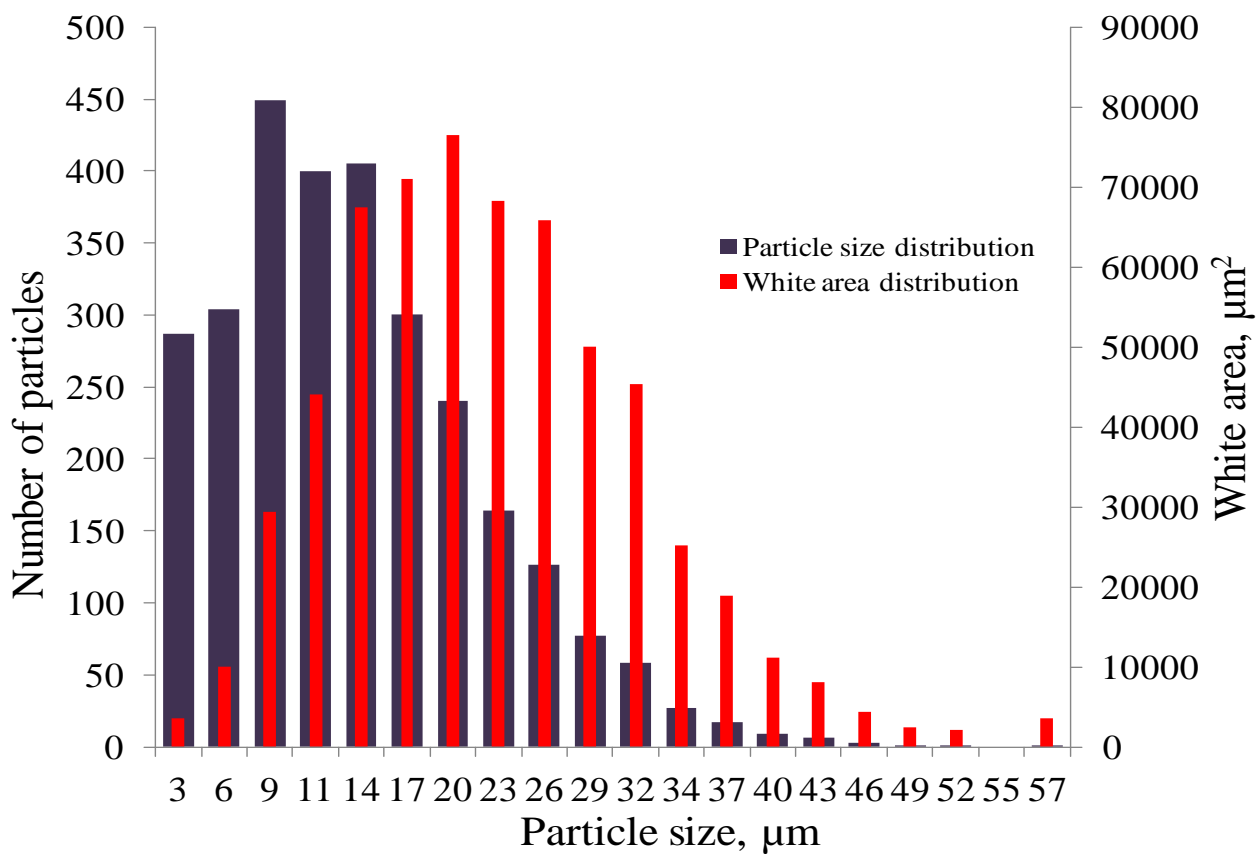
(c) Tyre from S.S. Breda (C).
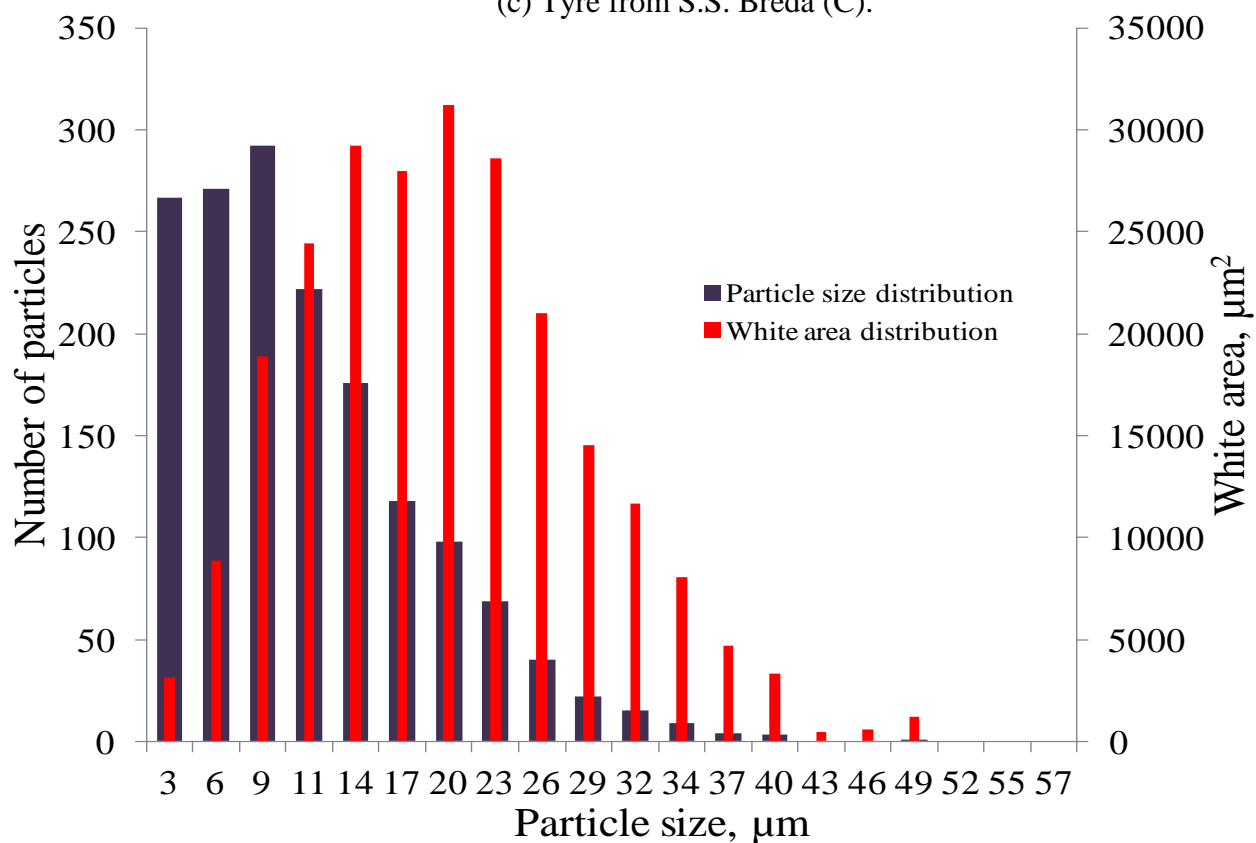
(d) Bolster suspension (D).

Figure 6.5: Distribution of agglomerates as a function of diameter of particle size in micron for rubber artefact. Area analysed $3.36 \times 10^{6} \mu m^{2}$.

Most agglomerate particles were less than 30μm. This technique works well for white fillers as well as evaluate dispersion level (e.g. Scammel suspension). Figure 6.6 shows images of fresh surfaces cut from each artefact.
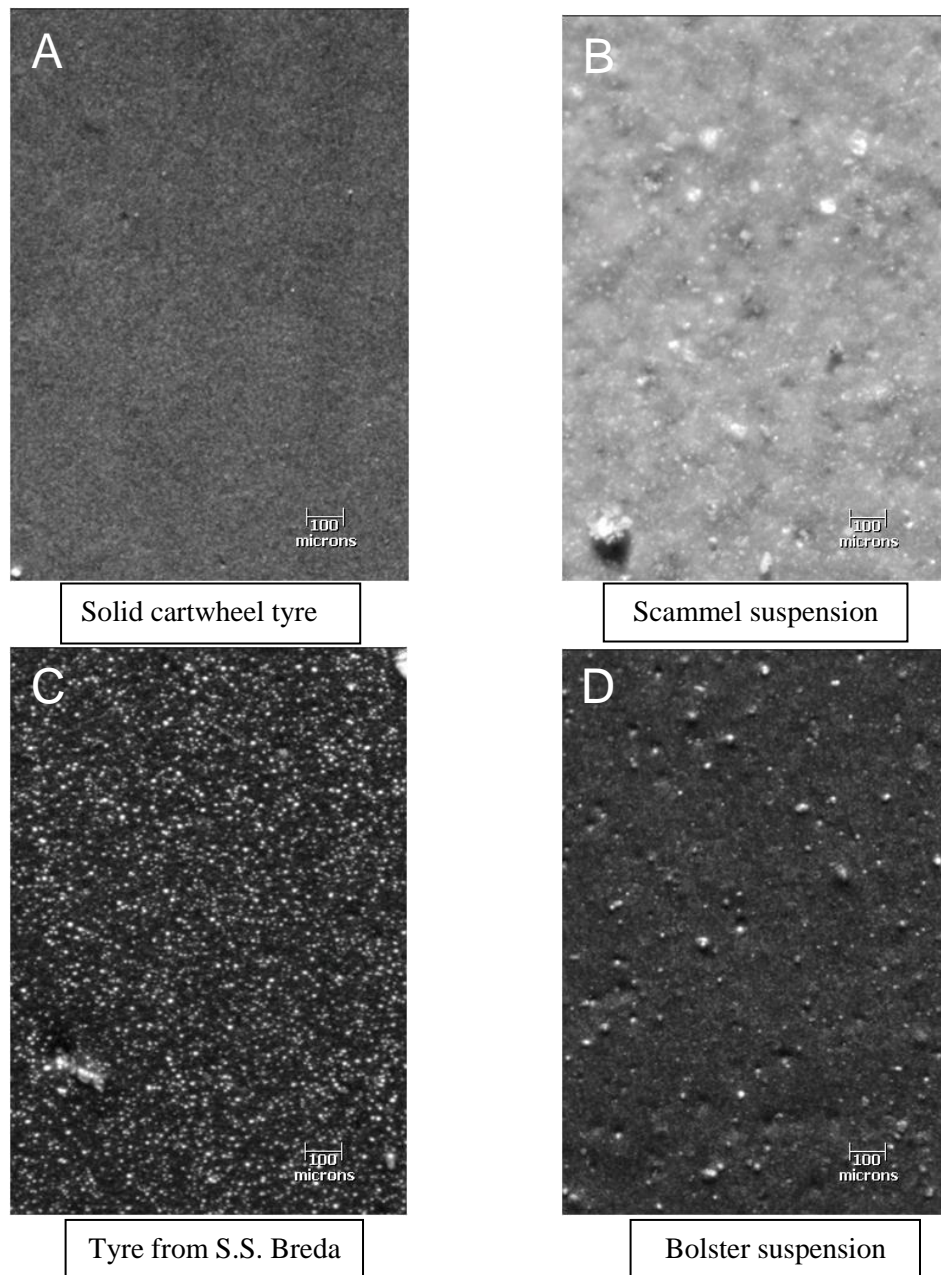
Figure 6.6: The observation of cut-surface from different artefacts.

Figures 6.7 (a)-(c) show the histograms of the average agglomerate count for 3 scanning process for each sample of rubber compound R4, R5, and R6. No agglomerates can be observed in the unfilled rubber (R1) in either the micrograph or the histogram. Appendix D provide the histograms of the average agglomerate count for 3 scanning process for each sample of rubber compound (R7, R8, R9, R10, R11, R12, R14, R15, R16, R17, R18, R19, R20, R21, R22, R23, R24, R25 and R26).

(a) R4.

(b) R5.

(c) R6.
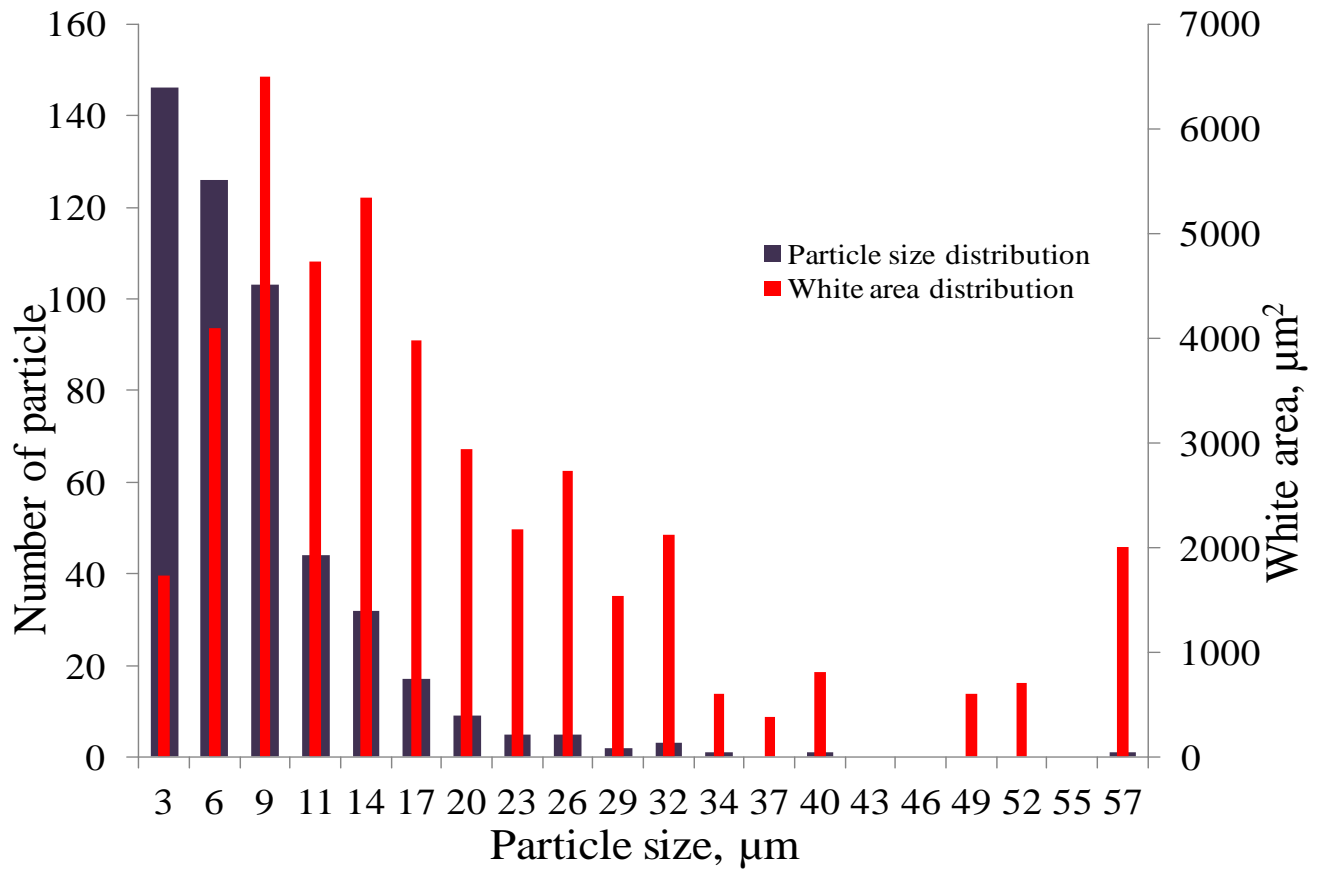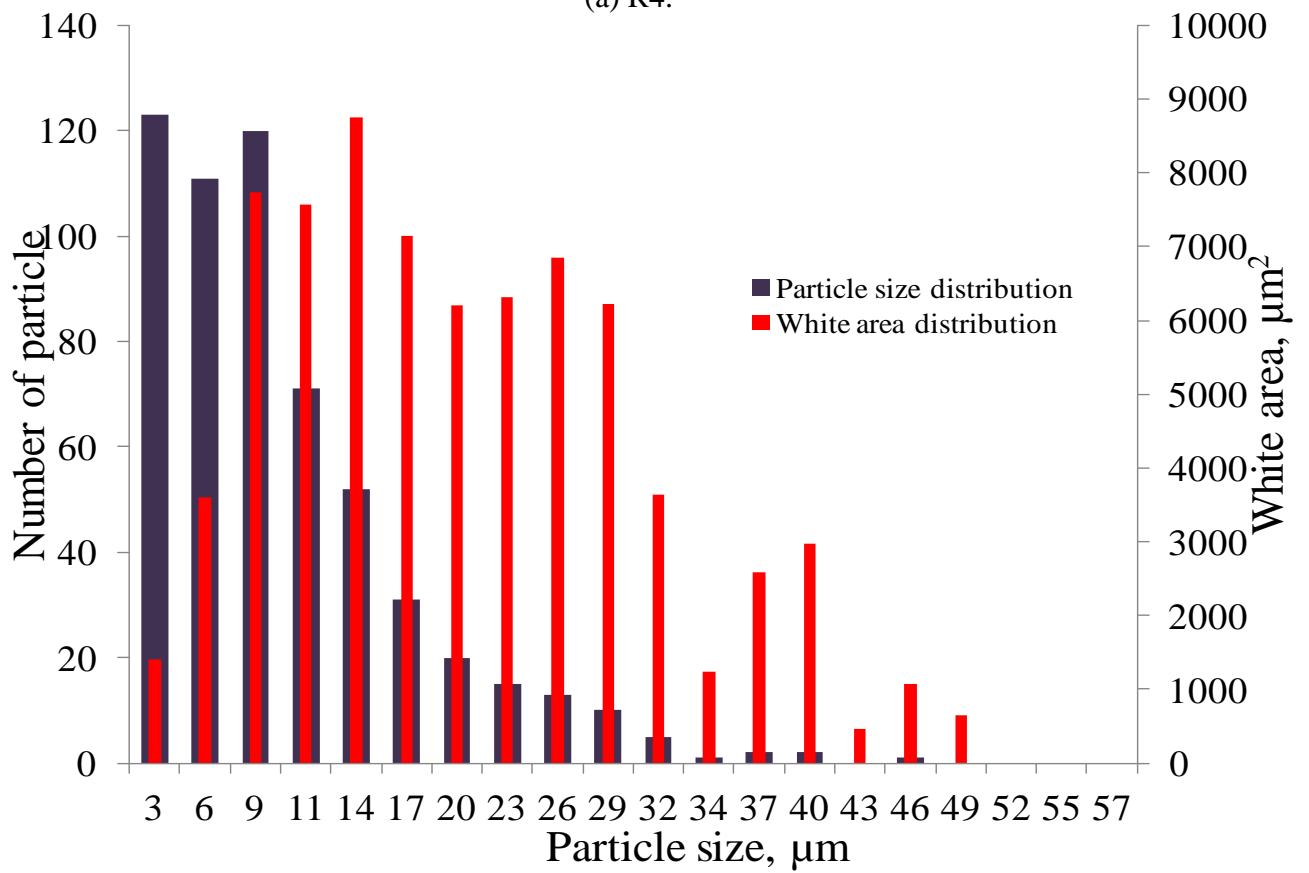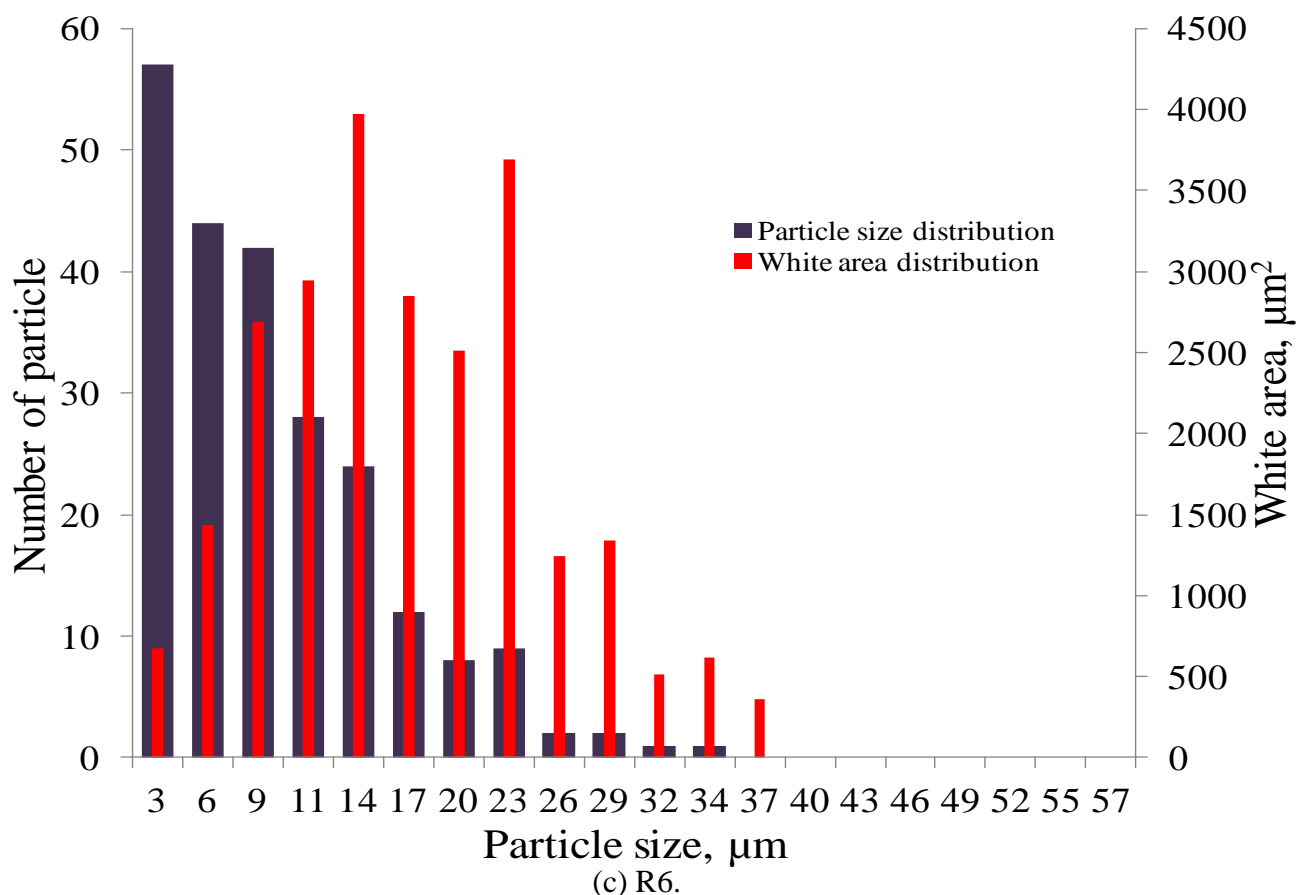
Figure 6.7: Distribution of agglomerates as a function of diameter of particle size in micron for EDS compounds. Area analysed $3.36 \times 10^6 \mu m^2$.

Figure 6.8 to 6.12 show the images of freshly cut surfaces of each rubber compound. A lower percentage of white areas corresponds to good dispersion. Based on Table 6.3, the quality of dispersion of R6 is good compared to R4 and R5. However , the image analysis of R1 is too light and hence not comparable with the filled rubbers (Figure 6.8). The rubber compounds differ in the surface features (e.g. cut marks) that they show and while some particles of filler can be observed. These were relatively few, unlike the images for B, C & D shown in Figure 6.6. Cutting marks on the cut surface were most evident for the harder rubbers; they did not affect the dispersion analysis.
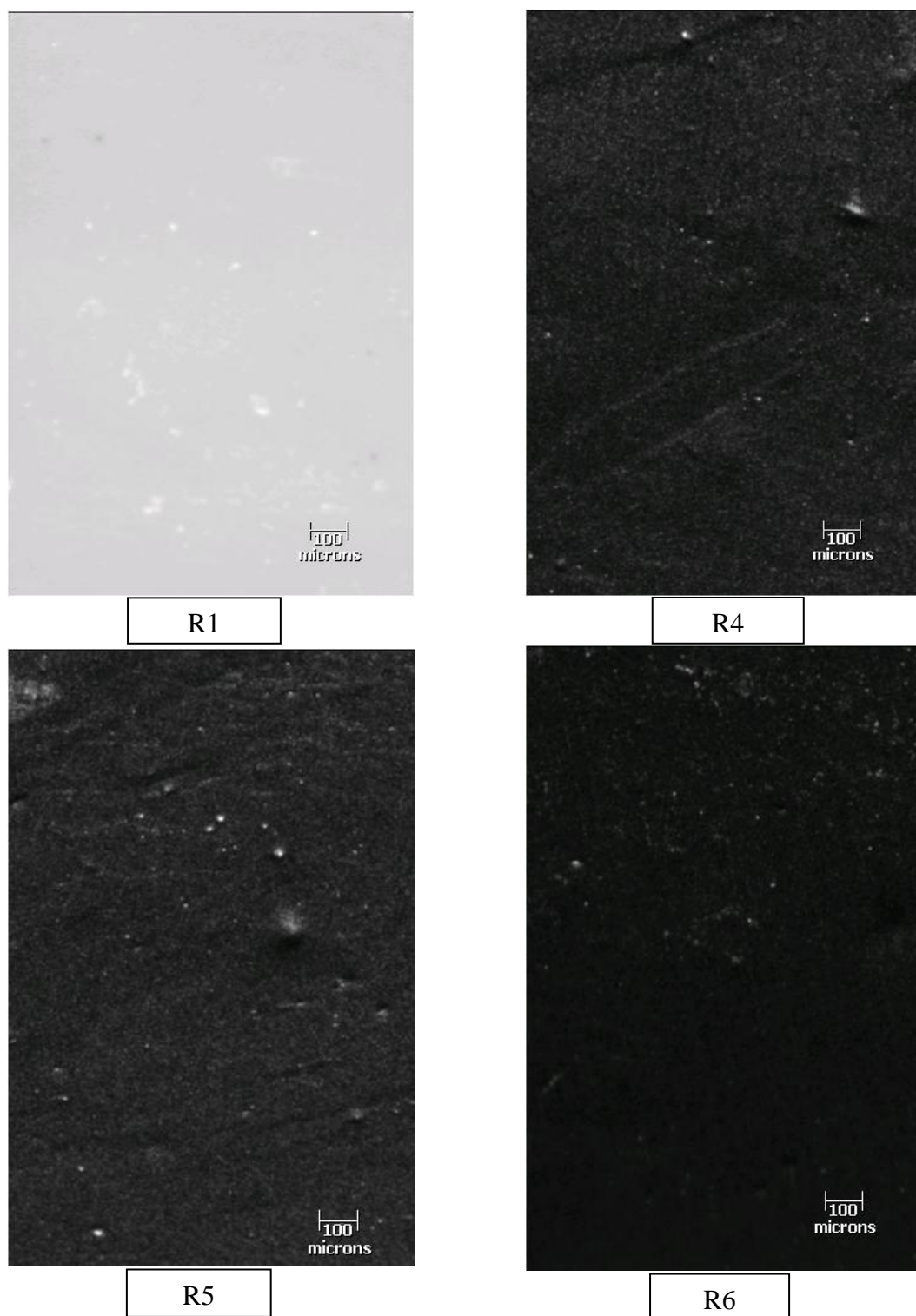
Figure 6.8: The cut-surface of each EDS compound.
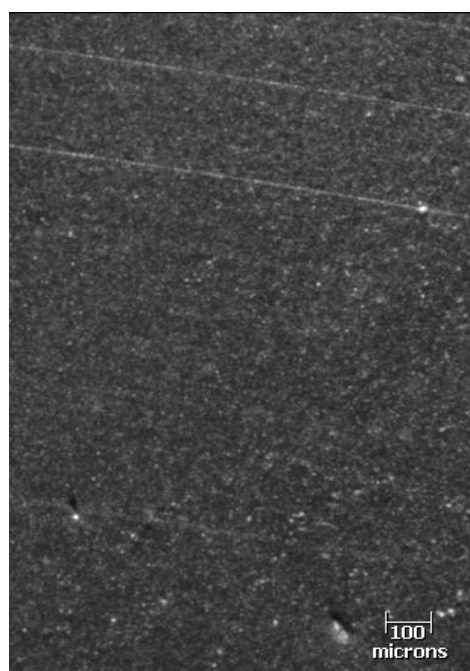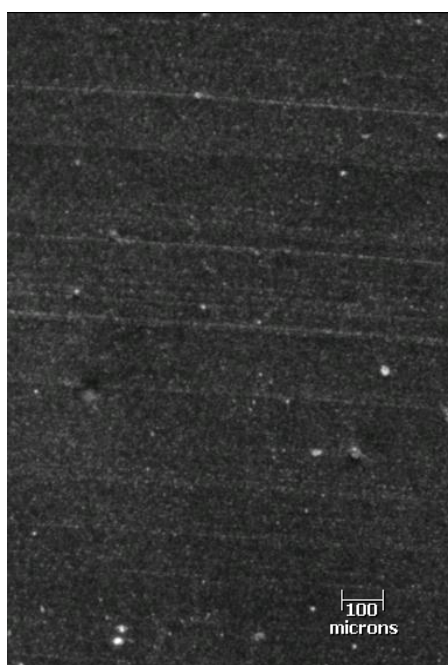
Figure 6.9: The cut-surface of each proprietary compound.
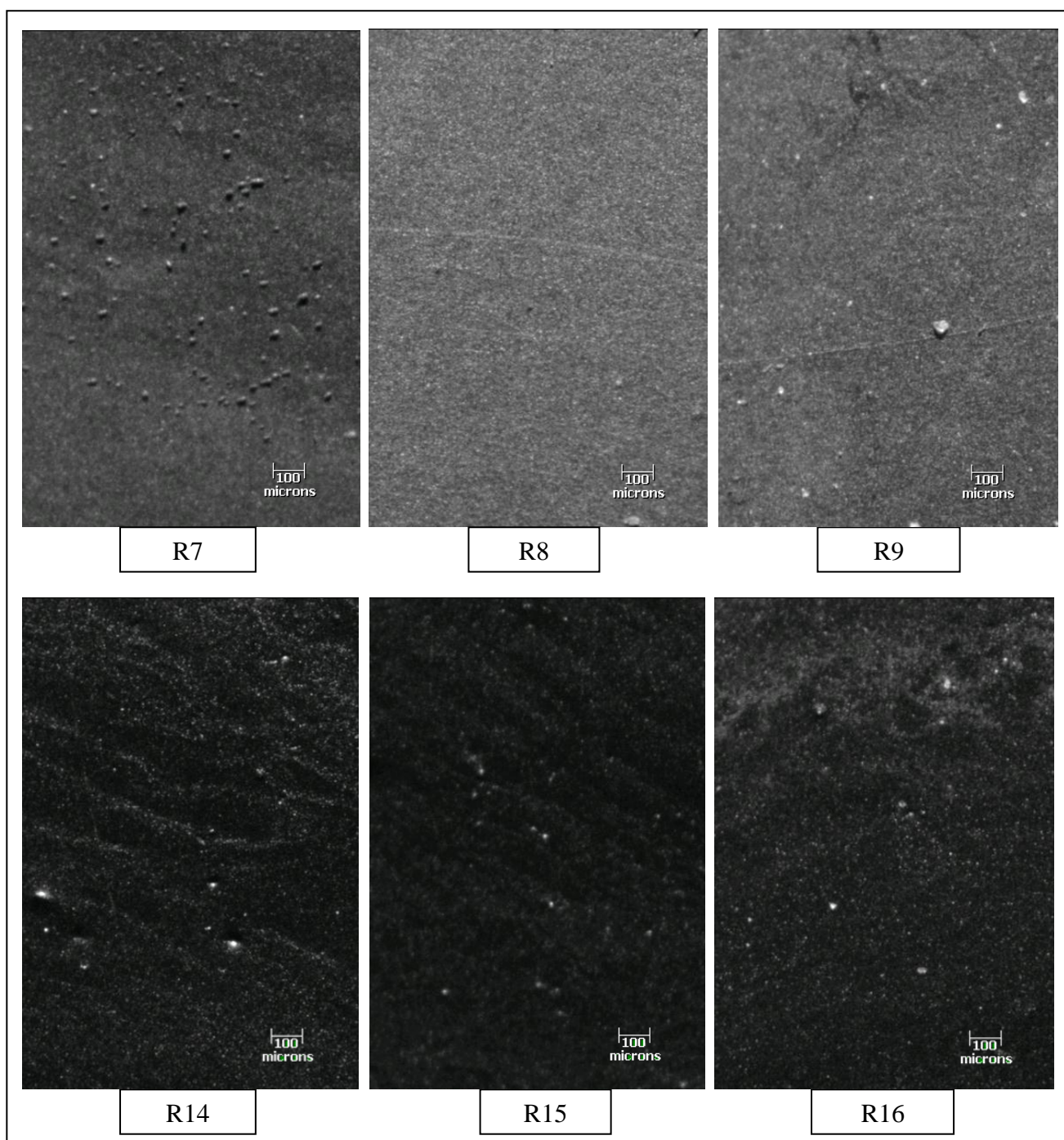
Figure 6.10: The cut-surfaces of R7 ~ R9 and R14 ~ R16 compounds.
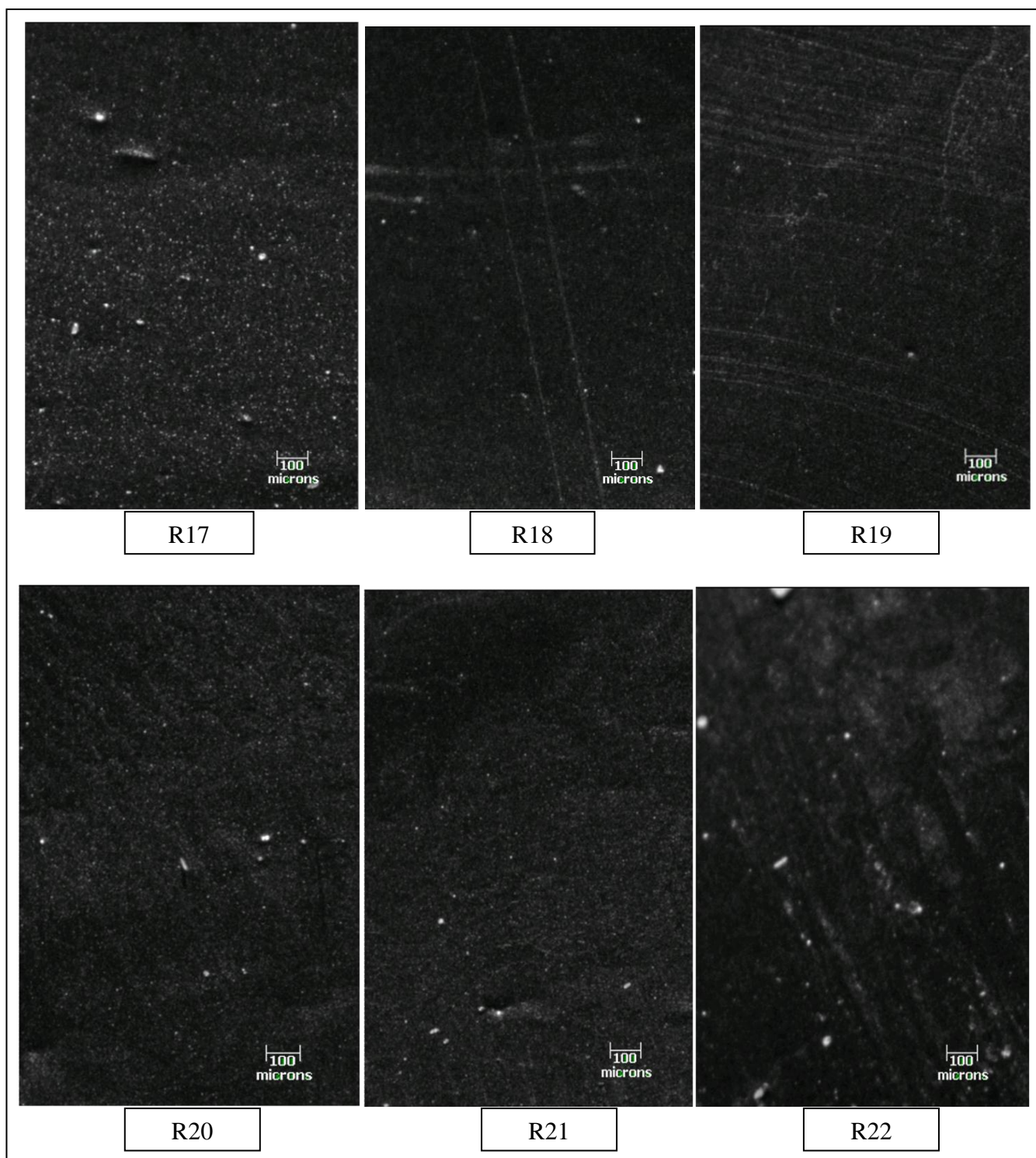
Figure 6.11: The cut-surfaces of R17 ~ R22 compounds.
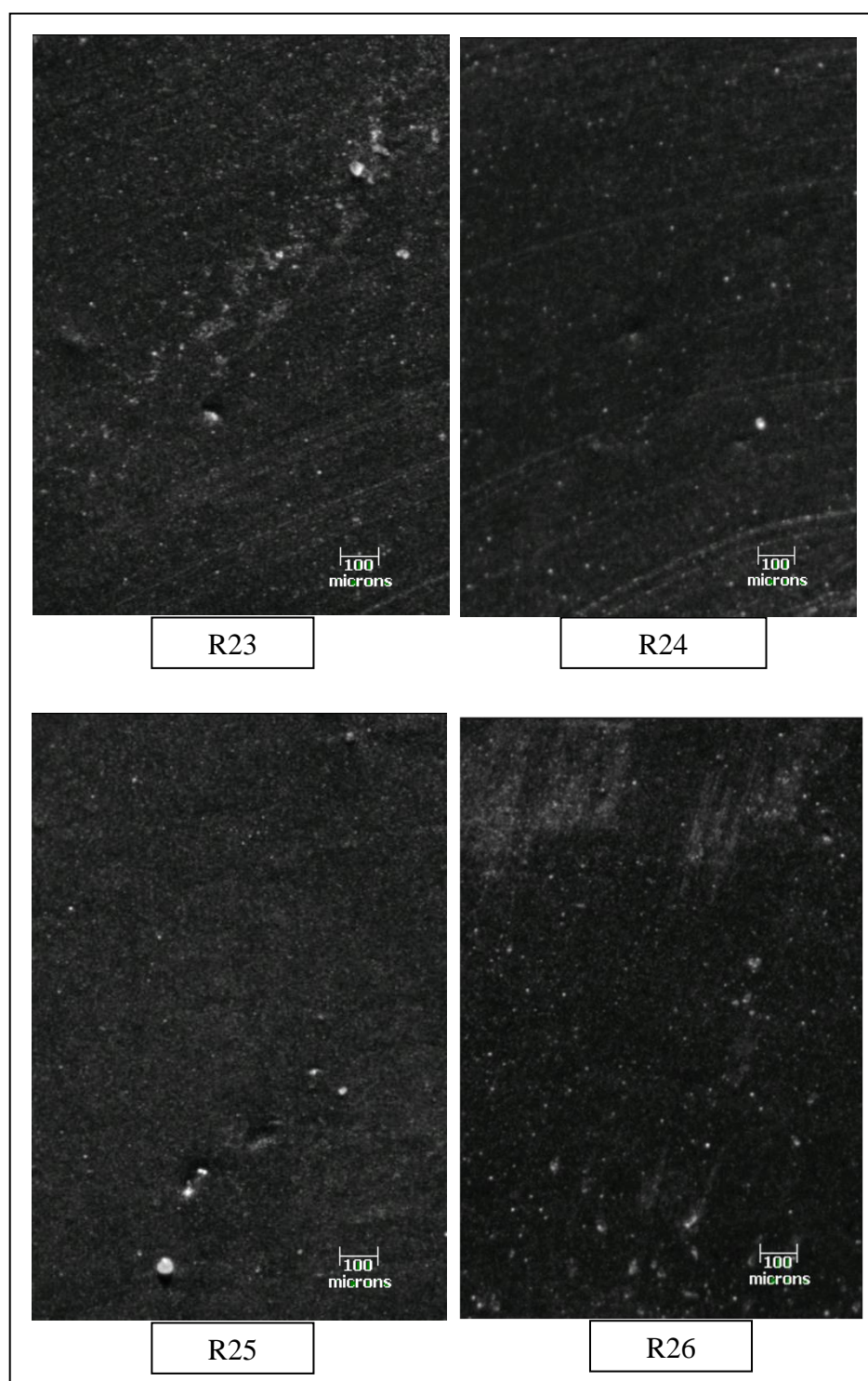
Figure 6.12: The cut-surfaces of R23 ~ R26 compounds.

Table 6.3 to 6.7 show the x-values for each artefact and the various rubber compounds. White area is defined as the area from which light is reflected by all agglomerates larger than 1.5μm. Expressed as a percentage of total area, it provides another measure of dispersion. It is apparent from the histograms that the modal particle size band is usually near the smallest (3μm). Hence it is not a very informative indicator of size significant for differentiating between materials. Instead, the number – weighted average particle size may be more informative. Another posibility, suggested here, is to take the particle size band making the largest contribution to the total white area as an indicator of a significant particle size. The particle size band making the maximum contribution to white area was taken from the histogram together with the number of particles in that band to generate a new combined contribution to white area (termed modal contribution to white area). The average values of number-weighted average particle size and white-weighted average area particle size are calculated based on the equations as below.

$$\text{Number average particle size} = \frac{\sum \text{Size} \times \text{Number (size)}}{\sum \text{Number (size)}} \qquad (6.2)$$

$$\text{White area weighted average particle size} = \frac{\sum \text{Size} \times \text{White area (size)}}{\sum \text{White area (size)}} \qquad (6.3)$$

Table 6.3: The level of dispersion quality for rubbers from naturally aged artefacts.

Type of compound	Solid Cartwheel Tyre	Scammel suspension	Tire from S.S. Breda	Bolster suspension spring
Modal contribution to white area, μm^2	4846	10398	76496	31218
Number of particles in model white area band	77	63	240	98
Particle size, μm in model white area band	9	14	9	20
Surface density of portion in modal white area band, mm^{-2}*	22.9	18.8	71.4	29.2
Carbon black dispersion rating x	8.26	6.61	2.98	4.7
% White area	0.98	2.69	20.99	8.22
Standard deviation of agglomerate size, μm	5	6.55	8.1	7.27
% Dispersion	99.47	97.81	81.84	90.44
Number average particle size, μm	7	9	14	11
White area weighted average particle size, μm	15	19	23	20

*- surface density = number of particles in band $/3.36\mu m^2$

Table 6.4: The level of dispersion quality for EDS compounds.

Type of compound	R1	R4	R5	R6
Modal contribution to white area, μm^2	0	6496	8748	3976
Number of particles in modal white area band	0	103	52	24
Particle size, μm in modal white area band	0	9	14	14
Surface density of particles in modal white area bond, mm^{-2*}	0	30.7	15.5	7.1
Carbon black dispersion x	0	7.1	5.87	7.43
% White area	0	1.49	2.57	0.86
Standard deviation of agglomerate size, μm	0	6.15	7.32	6.42
% Dispersion	0	99.15	96.74	99.63
Number average particle size, μm	0	8	10	10
White area weighted average particle size, μm	0	19	20	17

*- surface density = number of particles in band $/3.36\mu m^2$

Table 6.5: The level of dispersion quality for R7 ~ R12 compounds.

Type of compound	R7	R8	R9	R10	R11	R12
Modal contribution to white area, μm^2	9890	12494	11664	18055	10895	8333
Number of particles in model white area band	158	202	187	168	173	76
Particle size, μm in model white area band	9	9	9	11	9	11
Surface density of portion in modal white area band, mm^{-2}*	47.0	60.1	55.7	50.0	51.5	22.6
Carbon black dispersion x	8.02	8.39	8.23	7.33	7.5	7.3
% White area	1.52	1.66	1.72	3.51	2.07	1.67
Standard deviation of agglomerate size, μm	4.7	4.12	4.31	5.07	5.07	5.35
% Dispersion	99.63	99.7	99.61	99.31	99.21	99.45
Number average particle size, μm	7	7	7	8	8	8
White area weighted average particle size, μm	13	12	12	14	14	15

*- surface density = number of particles in band /$3.36\mu m^2$

Table 6.6: The level of dispersion quality for R14 ~ R20 compounds.

Type of compound	R14	R15	R16	R17	R18	R19	R20
Modal contribution to white area, μm^2	34183	12399	19429	22567	12600	12106	11787
Number of particles in model white area band	318	198	306	209	201	191	186
Particle size, μm in model white area band	11	9	9	11	9	9	9
Surface density of particles in modal white area bond, mm^{-2*}	94.6	58.9	91.1	62.2	59.8	56.8	55.4
Carbon black dispersion x	6.77	7.41	6.88	5.84	7.49	7.88	7.48
% White area	6.24	2.32	3.57	5.09	2.46	2.1	2.02
Standard deviation of agglomerate size, μm	5.24	5.47	5.49	6.5	5.55	4.94	5.35
% Dispersion	97.98	98.74	97.99	94.84	98.62	99.88	99.28
Number average particle size, μm	9	8	8	10	8	8	8
White area weighted average particle size, μm	15	16	17	20	16	14	16

*- surface density = number of particles in band /$3.36\mu m^2$

Table 6.7: The level of dispersion quality for R21 ~ R26 compounds.

Type of compound	R21	R22	R23	R24	R25	R26
Modal contribution to white area, μm^2	8868	8695	14569	18223	9720	17240
Number of particles in model white area band	83	52	90	111	155	78
Particle size, μm in model white area band	11	14	14	14	9	14
Surface density of particles in modal white area bond, mm^{-2*}	24.70	15.48	26.79	33.04	46.13	23.21
Carbon black dispersion x	6.36	7.09	6.69	6.79	7.9	7.21
% White area	2.94	2.23	2.86	3.81	1.73	2.51
Standard deviation of agglomerate size, μm	7.77	6.51	5.99	6.01	5.1	5.5
% Dispersion	97.36	99.13	99.11	99.01	99.7	99.37
Number average particle size, μm	9	10	9	10	8	9
White area average particle size, μm	24	18	17	17	15	15

*- surface density = number of particles in band $/3.36\mu m^2$

Most of the rubber compounds have a dispersion percentage of more than 95% except the S.S. Breda tire which is about 87%. All the aged rubbers show good dispersion characteristics, even though the rubber compounds were mixed by unknown processes. The dispersions achieved for all the rubbers mixed are better than for the rubbers from three of the four historical artefacts investigated.

6.4 Conclusions

(1.) By image analysis of a freshly cut rubber surface and software for classifying agglomerates in number and sizes, it is possible to quantify the homogeneity of rubber compound in the scale 3 - 100μm. A correlation between coarseness of the macro dispersion and shortness of fatigue life would be expected.

(2.) The best dispersion among the materials were seen for R19 – the laboratory mix with most black (25pphr N330) and material A – the 80-year old cartwheel tyre, incorporating 54pphr of black.

(3.) Since the modal particle size is typically the smallest size band resolvable by the optical, it seems unsuited to characterise the typical agglomerate size in a material. Instead, two parameters, the number-weighted average particle size and the white area-weighted average particle size, are suggested to characterise agglomerate size in a rubber compound. It might be expected that they would correlate inversely with the fatigue life.

Chapter 7

Investigation of Crack Growth and Fatigue Life of Rubber

Different rubbers have been evaluated through a range of uniaxial strain tests to provide strain energy density, crack growth characteristic and fatigue performance.

In this initial study of fatigue life of rubber, strip test pieces were used to perform stress-strain tests. Based on the data, the strain energy density was calculated, the energy being stored in unit volume of rubber at certain strain. Then, the basic crack-growth characteristics were determined using a simple-extension strip with a small edge crack. Fatigue life was also determined in simple tension and the effective flaw size of the rubber from it and the crack growth characteristics. The purpose of this work is to evaluate rubber (e.g. with/without antioxidant) from crack growth and fatigue tests as well as to check the theory of flaws characterisation. Filled rubber was evaluated from crack growth for comparison with unfilled rubber.

7.1 Specification of Samples Tested

Based on single representative samples, one without (designated R1 – see Section 5.1.1) and one with (designated R3) both antiozonant-Negazone (2pphr) and antioxidant-Type-2246 (3pphr), stress–strain behaviour was investigated to permit derivation of the associated stress energy function of uniform width samples made from unfilled natural rubber EDS19 in each case. In fact the differences were found to be insignificant. The dimensions of the uniform width samples were 110mm by 25mm with a thickness of 2mm.

Stress-strain behaviour has also been investigated for a filled rubber with additives, R15 (see Table 5.3). In this case the uniform dimensions were 160mm by 6mm with a thickness of 2mm.

Two distinct series of crack growth tests are addressed concerning unfilled EDS19 (R1 & R3). In one series of crack growth tests relaxed conditions were facilitated with 10 test pieces. In the second series of such tests no relaxation is permitted and the 2 test pieces used from R1 compound. The dimensions of the uniform width samples of unfilled EDS19 [without (R1) & with antiozonant/antioxidant (R3)] are 150mm by 25mm with a thickness of 2mm.

Crack growth tests with the filled rubber R15, as specified in Table 5.3, were undertaken using 5 samples of uniform width of 150mm by 25mm with a thickness of 2mm.

In the fatigue tests, the 70 samples are of the usual dumb-bell Type 2 (BS ISO 37:2005). A concern about this choice of test piece was that may have a more severe local stress concentration than other dumb-bells; Appendix J gives an initial FEA investigation on this point, but in any case the failure loci did not usually coincide until the stress concentration locus, so this concern was thought not to be very significant. In this case all samples are based on the unfilled rubber EDS19, with only half the samples containing 3pphr of the antioxidant (Type 2246) and 2 pphr of antioxidant (Negazone) (designated R3).

Table 7.1 shows the summary of the samples used.

Table 7.1: Specification of materials and tests.

Type of rubber compound	No. of test piece	Dimension (mm)/ Type	Type of test
R1	1	$110 \times 25 \times 2$	Stress-strain
R3	1		
R15	1	$160 \times 4 \times 2$	
R1	7	$150 \times 25 \times 2$	Crack growth
R3	5		
R15	5		
R1	35	Type 2 (BS ISO 37:2005)	Fatigue
R3	35		

7.2 Test Procedures Adopted

Having specified material and dimensions of different samples used we may next consider the test procedures and the observations made for the 4 distinct types of testing.

7.2.1 Stress Strain Measurement

One test piece of each rubber (R1 & R15) was stretched for 3 cycles in an Instron 4301 machine to each of the strain levels of 5%, 10%, 25%, 50%, 75% and 100% in sequence using a cross-head speed of 60mm/min for R1 and 150mm/min for R15. Equivalent strain rate can be defined as cross-head speed divided by sample length. Hence here we have equivalent strain rates of $0.01s^{-1}$ and $0.016s^{-1}$ respectively. A personal computer with a Picologger was used to record all the data of force and displacement at a sampling rate of 1.5Hz. The strain energy density (W) was interpolated from the 3rd cycle stress-strain retraction curves using the trapezoidal method of integration. The retraction energy is

thought to be more appropriate for the crack growth characteristic tests used here, and use of the third cycle which is a compromise between speed of test and proximity to the stabilised behaviour after many cycles.

7.2.2 Crack Growth Rate Measurement

The TARRC fatigue machine was used since it has an eccentric drive to deliver a fixed stroke to the clamp at one end of test piece, while the other clamp was mounted on a load cell. Figure 7.1 provides an overview of the crack growth test setup with the simple strip test piece superimposed.

Figure 7.1: Overview of crack growth test using a simple-extension strip test piece with an edge crack at 50% strain. The test piece was installed with the testing machine in relaxed condition.

A cut (nominally 0.5mm) was then made with a razor blade at the centre of one edge of the test piece, care being taken to ensure that the cut was perpendicular to the edge and that the tip was normal to the major surface (Gent et al. 1964). The test piece was then cyclically deformed at a rate of 5Hz.

In the relaxed mode of testing, crack growth tests were undertaken for maximum strains of 5%, 10%, 25%, 50% and 75%. For each selected upper strain level W was calculated as described in 7.2.1. In the non-relaxed crack growth experiments the strain ranges were restricted to one of the ranges of 10% to 30% and 10% to 50%. Additionally in this non-relaxed condition ozone-free testing was used too. Ozone-free conditions were reviewed in section 3.6.3.

The presence of ozone contributed to the rate of crack propagation: in its absence there is no crack growth at all if $T<T_o$. It was expected that the contribution of ozone to crack growth of NR in non-relaxing cycles would be a significant complication, so a method was devised to carry out tests in an atmosphere substantially free of ozone. In order to create an ozone free condition, an artificial ozone-free chamber was developed. Figure 7.2 shows the overall test set-up with the ozone measurement device. Manganese dioxide was used to catalyse decomposition of ozone in the chamber (Chang et al. 1997). The ozone-free condition was maintained by injecting a low flow of air from a compressed air cylinder into the chamber at approximately 0.02Pa. Since the air would have been in the air cylinder for several weeks, and the half-life of ozone in dry air is 3 days, it is believed that the air supply would be free of ozone. The air pressure level was monitored using a digital pressure gauge and by observing a plastic bag. Bulging of the bag indicates a small positive pressure hence that the air flow connected to the cabinet through a sealed tube is sufficient. This bag is visible at the right-bottom side of the testing machine in Figure 7.2. Ozone concentration in the test chamber was measured using the UV Photometric Ozone Analyser-Model 1008 illustrated in Figure 7.3. Ozone concentration was recorded every time the motor was stopped for a crack growth measurement and always read 0.000ppm; establishing that intended atmosphere had been created and maintained.

Figure 7.2: The overview of the crack growth test
in an ozone free chamber. B - plastic bag.

Figure 7.3: The UV Photometric Ozone Analyser used indicated
a zero ozone concentration in the chamber.

The amount by which the crack grows during a single extension of the test piece is so small as to make observation difficult. The length of crack *c* was therefore measured at intervals using a travelling microscope with an eyepiece scale. A slight strain of the test piece was used to facilitate observation of the crack tip. The crack length was recorded against the number of cycles (*n)* the sample had experienced at the time of measurement. The load-deflection behaviour of the test pieces was not monitored during the crack growth tests.

7.2.3 Fatigue Life Test and Flaws Size Determination

Fatigue tests were performed at a range of strains in fully relaxing cycles in an attempt to identify the fatigue limit. To avoid failure occurring at the clamps, dumb-bell test pieces Type 2 (BS ISO 37:2005) were used as depicted in Figures 7.4 and 7.5. The dumb-bell test pieces were cut from the same 229 × 229 × 2mm sheet as mentioned in Chapter 5. Seventy dumb-bell test pieces were used to conduct fatigue tests on two servo-hydraulic fatigue test machines, an Instron 1271 and a Servotest machine. The Instron 1271 servo-hydraulic machine was used to conduct fatigue tests using 5 replicates for 50% and 75% maximum strain. Since the maximum displacement amplitude of the Instron 1271 was only ±25mm, the Servotest machine was used to carry out the remaining fatigue tests for 100%, 125%, 150% and 200% maximum strain. The Servotest machine has displacement capability of ±50mm which is able to perform fatigue tests at large strain. The test pieces were clamped on a battery fatigue rig that has 15 stations (Figures 7.4 and 7.5). This allowed a number of different strains to be investigated simultaneously by the adjustment of the static clamp-to-clamp separation of each test piece. The fatigue tests were performed at 1 Hz. An adjustable connector was used to ensure that the two halves of the jig were parallel. An Epson 3100z digital camera was used to monitor the test, taking pictures (using the flash) at pre-determined intervals. The cycle count was monitored using two separate systems for backup, one using a Hall effect sensor and a magnet attached to the battery rig and the

other connected to the displacement output of the Instrons 1271. The counter connected to the Hall effect sensor was in the camera's field of view. Figures 7.4 and 7.5 show the overview of the fatigue test set-up.
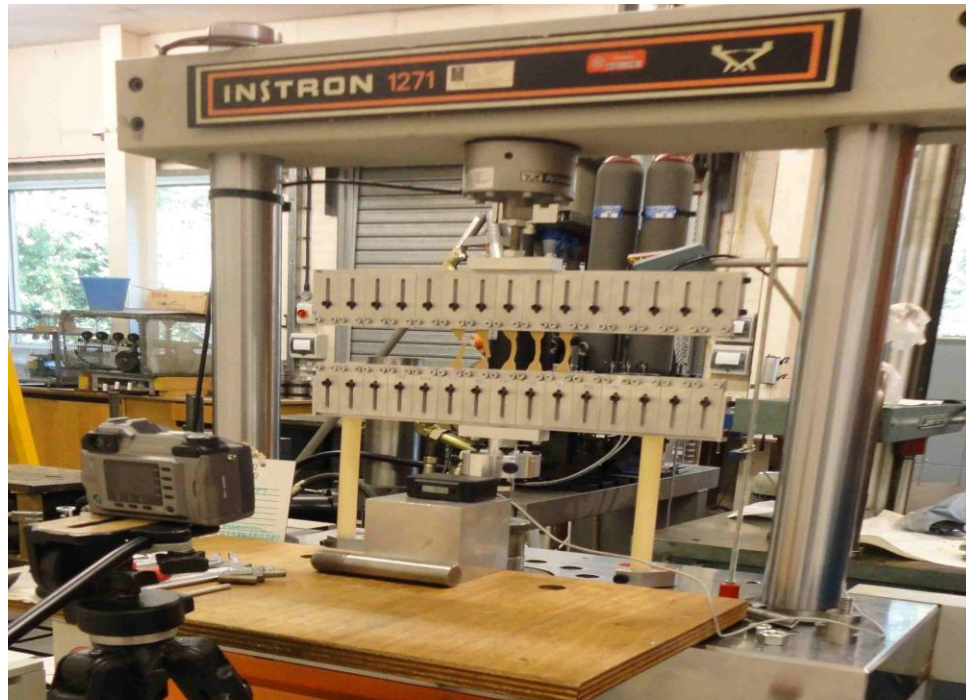
Figure 7.4: Overview of fatigue test set-up using Instron 1271 machine at 1 Hz, with an amplitude of ±14.25mm equivalent to 75% strain.

Figure 7.5: Overview of fatigue test set-up using Servotest machine at 1 Hz, with an amplitude of ±28.5mm equivalent to 150% strain.

It is possible to obtain the effective sizes of the failure initiating flaws (c_i) from the theory presented as Equation (3.17) and (3.18), the crack growth characteristics, and the results of fatigue tests.

7.2.4 New Test Facility for Non-Relaxing Fatigue Tests

For the present studies, a versatile tensile fatigue test machine was assembled and commissioned to increase TARRC's capacity and the quality of data. It should enable a better understanding of fatigue, including non-relaxing fatigue to be developed for rubber or any other materials. The layout of the fatigue machine is described in Appendix H - samples tested are referred to in terms of their location in the test facility. Thus sample or smp 1-n and sample or smp 2-m are located in top and bottom rows respectively in position n and m with position 1 designated as far left position.

In these tests, the non-proprietary rubber formulations are those specified in Chapter 5 – (Tables 5.2 and 5.3) and the proprietary rubbers were also used. Twelve tensile dumbbells Type 2 (BS ISO 37:2005) were cut from 26 different cured sheets. Two gauge lines were introduced with a separation of 22mm in the middle of each test piece. The 12-station fatigue test machine is presented in Figure 7.6. The desired frequency of the fatigue tests is not attained instantaneously. Typically the first 150 cycles may be considered transient in recording behaviour from test initialization to attainment of require oscillation frequency. There are 12 dedicated load cells monitoring the loading of the 12 samples. A Labview-based system records all the data for each load cell. It also logs the LVDT transducer giving the carriage position as a function of time [see Appendix H]. We can define a stable user interrogation frequency once the first 150 cycles have been completed. In these experiments the interrogation frequency for generating output record is 1000 cycles at a frequency of 4.49Hz until sample failure occurs in all 12 test pieces. All materials were subjected to non-relaxing strain cycles with a minimum strain of 55% (34.1mm displacement) and maximum strain of 265% (80.3mm displacement). Figure 7.7 shows the upper six samples set at the maximum strain and the lower six samples experiencing the minimum strain. As the upper samples attain maximum strain so the lower samples undergo the minimum strain and increasing to maximum strain.

The separation of the indicated gauge lines were measured accurately using a vernier calliper. The fatigue lives of all rubbers in the non-relaxing tests were compared. Ozone concentration in the test chamber was measured using UV Photometric Ozone Analyzer-Model 1008. The average ozone concentration in the test chamber was 0.003ppm. The

temperature and humidity in the test chamber were also measured using a digital combination of thermometer, hygrometer and clock (TEMPTEC Indoor and Outdoor Temp: Thermo-Hygrometer-Clock). The average temperature and humidity were 20°C and 752%, respectively.

| Figure 7.6: Overview of new fatigue test machine. | Figure 7.7: Non-relaxing fatigue test setup – Top at 265% strain and bottom at 55% strain. |

The temperature on the rubber surface was measured in a separate test experiment using a thermocouple while the fatigue machine was running. It was found that temperature reached 29.4°C on the surface of test piece and remained about this value until failure.

7.3 Results and Discussion

7.3.1 Stress-Strain Behaviour in Rubber

Stress-nominal strain plots were obtained from the experimental data of force and displacement. Strain energy density was obtained by calculating areas under the curves of stress and strain using the trapezium method in on Excel worksheet. The 3rd cycle, retraction curves were taken as being reasonably representative of the release energy for the cyclic tests. Figures 7.8 and 7.9 show all graphs of 3rd cycle at strain of 5%, 10%, 25%,

50%, 75% and 100%, together with a neo-Hookean fit with a shear modulus of 0.49MPa and 0.67MPa respectively.
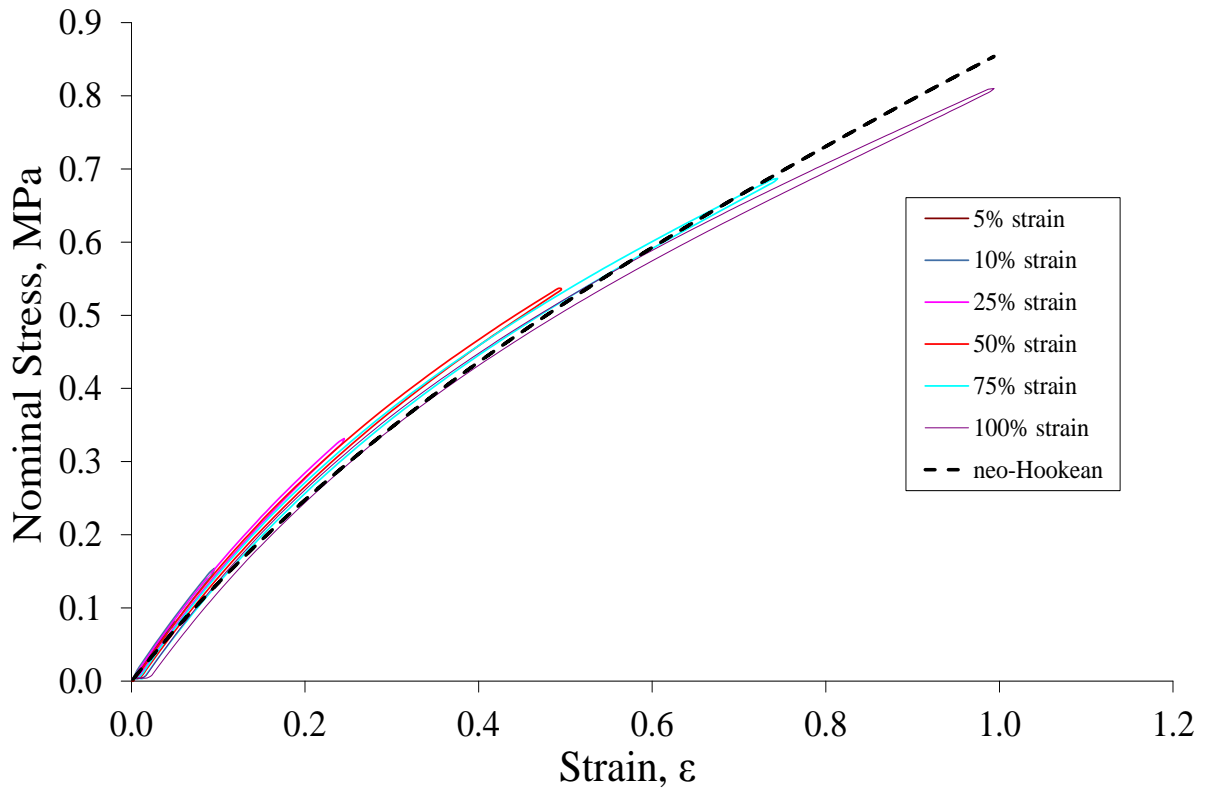
Figure 7.8: Typical curves of stress versus strain to 5%, 10%, 25%, 50%, 75% and 100% using R1 at 3rd cycle retraction compared with neo-Hookean model (G=0.49).
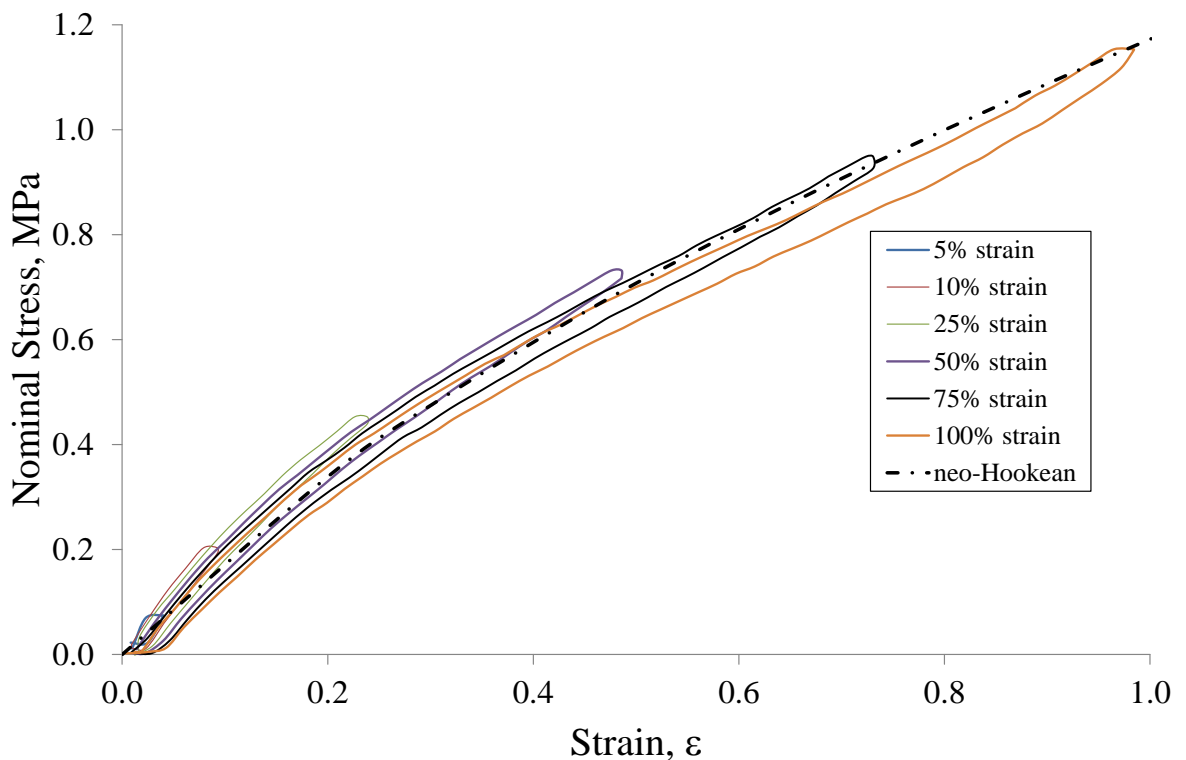
Figure 7.9: Typical curves of stress versus strain to 5%, 10%, 25%, 50%, 75% and 100% using R15 at 3rd cycle retraction compared with neo-Hookean model (G=0.67MPa).

7.3.2 Crack Growth Behaviour in Rubber

Figures 7.10 and 7.11 show the crack growth in a simple strip test piece as a function of the number of cycles for EDS19 without (R1) and with antioxidant (R3), respectively. Between total cycles induced, n_1 and n_2, the corresponding measured crack lengths of c_1 and c_2, permit the crack growth rate $dc/dn = (c_2-c_1)/(n_2-n_1)$ to be estimated at the associated average crack length of $(c_1+c_2)/2$.

The crack growth results are given in Figure 7.10 as log-log plots of the crack growth per cycle versus the maximum strain energy release rate achieved in the cycle, calculated from Equation (3.3).
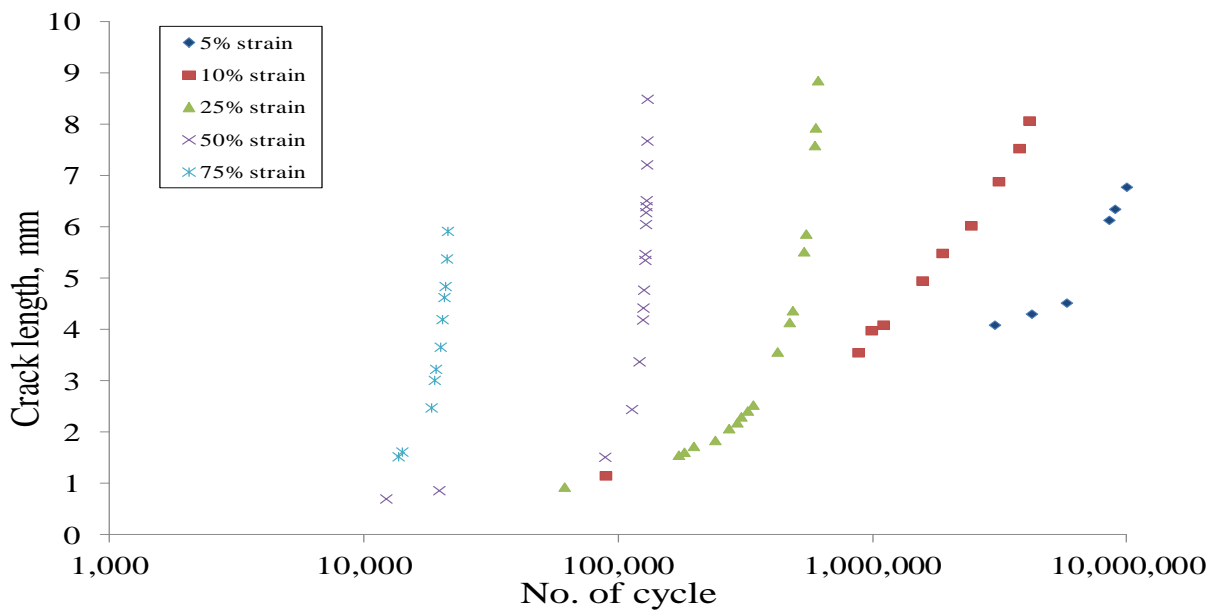
Figure 7.10: Crack length in an unfilled natural rubber simple strip test pieces as a function of the number of cycles (R3).
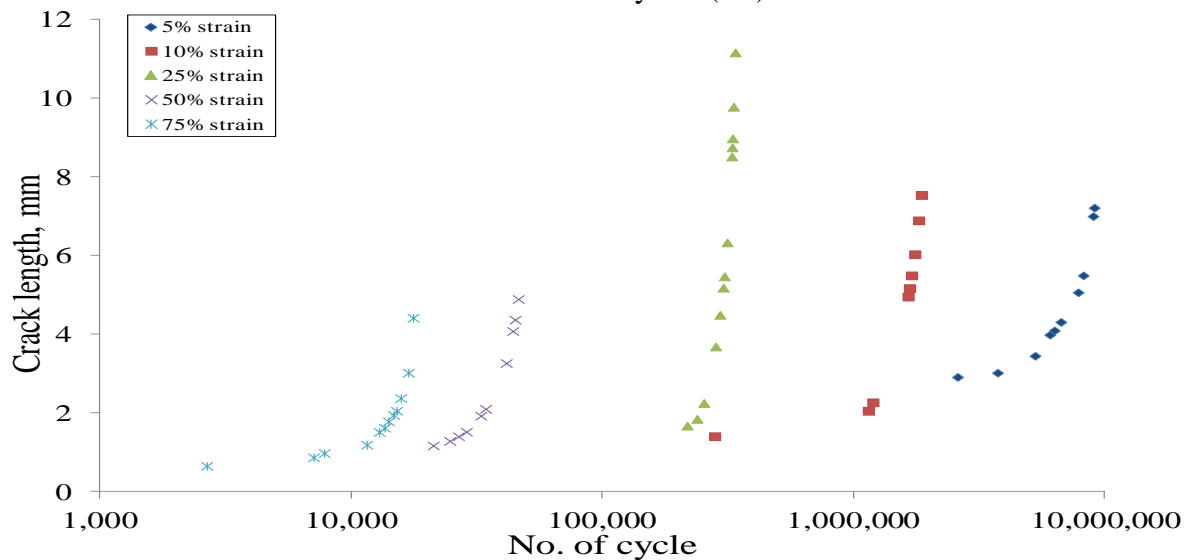
Figure 7.11: Crack length in an unfilled natural rubber simple strip test pieces as a function of the number of cycles (R1).

Power law fits (shown by the straight lines on the log-log plot) for the dependence of crack growth rate on tearing energy described the data reasonably well for the energies examined. The crack growth rate at low strains was found to depend approximately linearly on T, as shown in Figure 7.13 and as expected (Lake & Lindley 1964a). This linear regime was extrapolated and used to find the threshold mechanical fatigue limit, T_o, as shown in Figure 7.13. The comparison of R1 and R3 was made and found that the threshold tearing energy, T_o of R3 was higher than R1. The parameters (obtained from the trend line equations of Figure 7.12 for r_B and β and Figure 7.13 for T_o) of the power law crack growth are given in Table 7.2. The derived factors were compared with those given by Lake and Thomas (1967a). The discrepancy of r_B, defined in Equation 3.15, value between EDS19 with antioxidant 2246 in place of HPPD and Lake and Thomas's results for their compound, a similar formulation with Phenyl-β-naphthylamine (PBN) was small. In contrast, there was a significant difference of r_B values if no antioxidant was used.

Table 7.2: The cyclic crack growth properties of the compounds ($T_{ref}=1$).

Rubber Compound	$r_B(\mu mcycle^{-1})$	$T_o(kJm^{-2})$	β
R1	$7.20x10^{-5}$	0.032	1.60
R3 (antioxidant 2246)	$4.60x10^{-5}$	0.056	2.02
Lake and Thomas (1967a)*	$5.00x10^{-5}$	0.050	2.00

*antioxidant- Phenyl-β-naphthylamine (PBN)
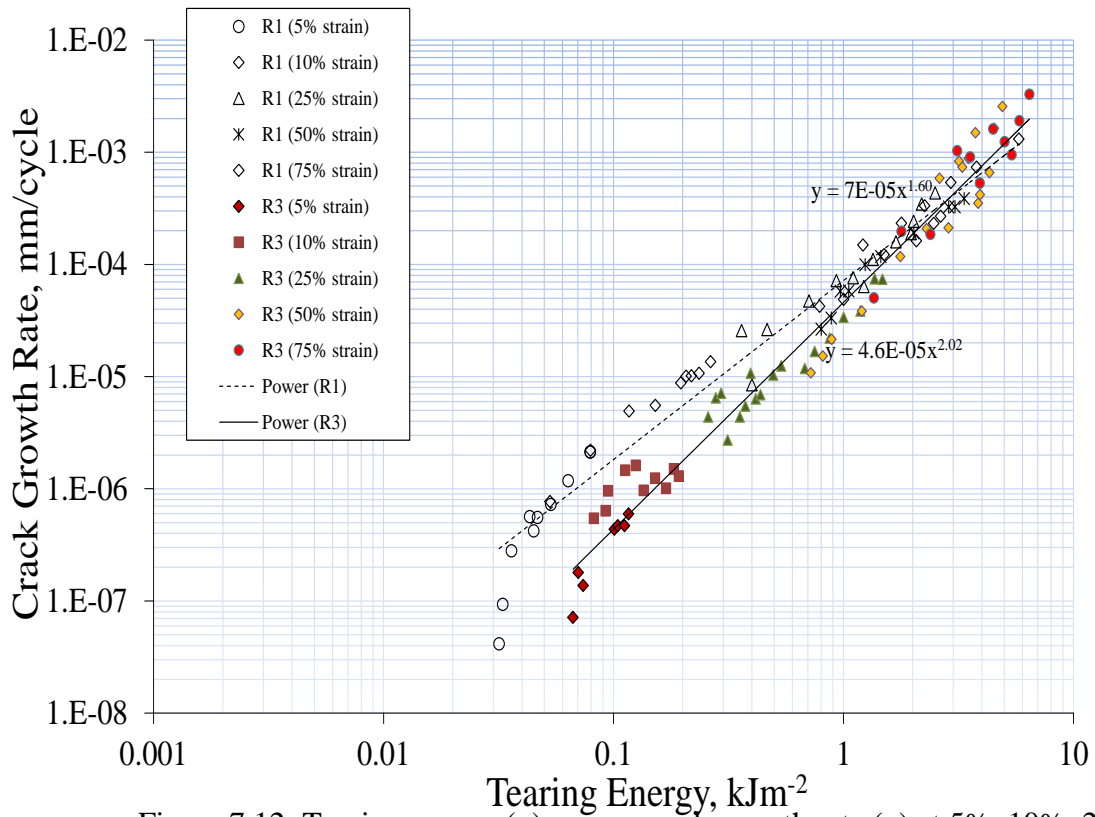
Figure 7.12: Tearing energy (x) versus crack growth rate (y) at 5%, 10%, 25%, 50% and 75% strain. (Trend line equation treated as $y = r_B.x^\beta$)
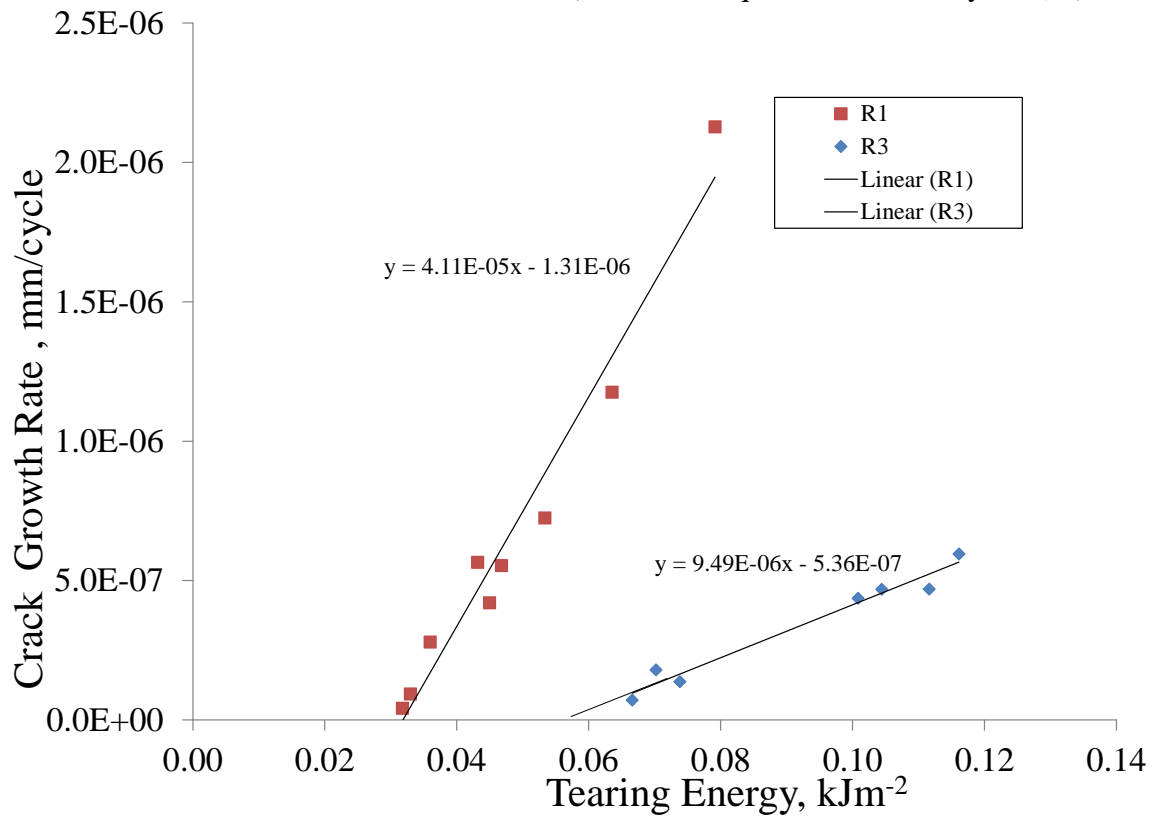
Figure 7.13: Crack growth rate (y) versus tearing energy (x) for 5% strain. The linear regime was extrapolated and indicated $T_0 \simeq 0.032$ kJm^{-2} (R1) & $T_0 \simeq 0.056$ kJm^{-2} (R3).

Figure 7.14 shows the crack growth in a simple strip test piece as a function of the number of cycles for R15. Based on the results, the strain amplitude applied for each crack growth test required a large number of cycles to propagate an initial crack. The cracks were easily propagated after the first three crack lengths were obtained.
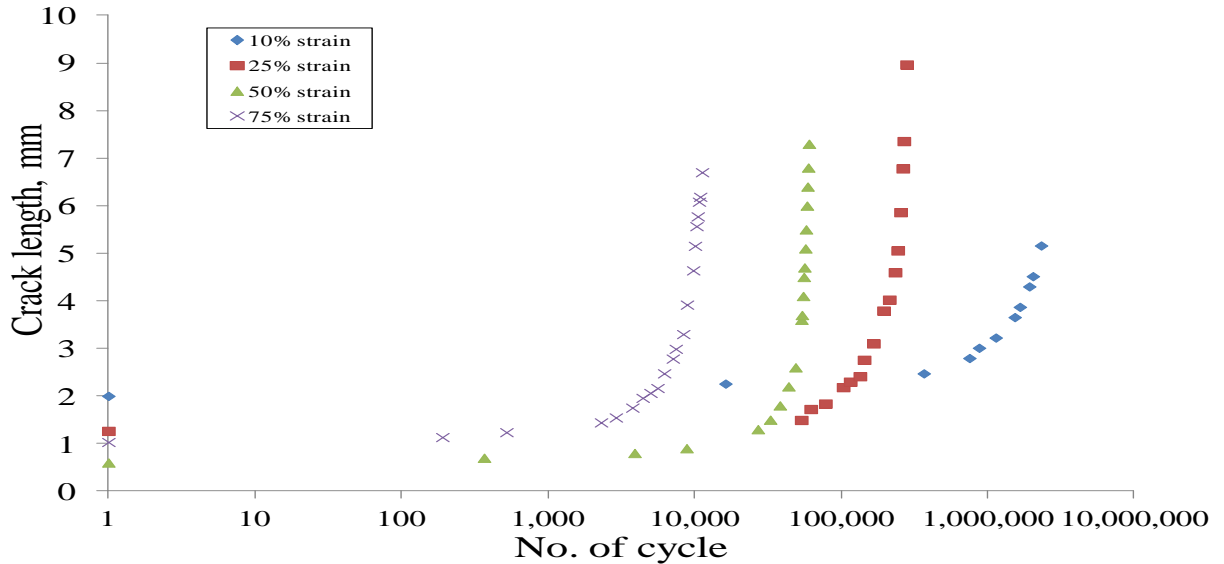
Figure 7.14: Crack length in an unfilled natural rubber simple strip test pieces as a function of the number of cycles (R15).

Figure 7.15 shows log plots of the crack growth rate measured in mm per strain cycle, versus the strain energy release rate, measured in kJm^{-2}; of R15. It is expected that the tearing behaviour of R15 is higher compared to R1. Parameters for the crack growth characteristic of R15 are given in Table 7.1.
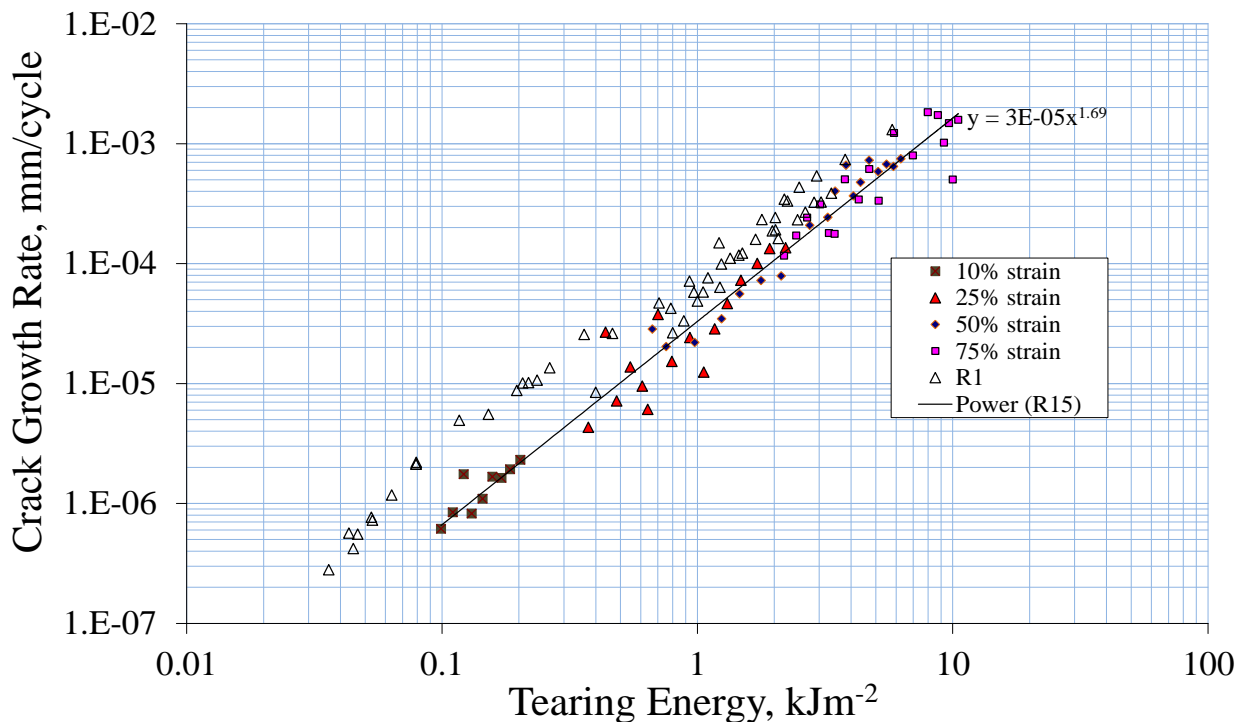
Figure 7.15: Tearing energy versus crack growth rate at 10%, 25%, 50% and 75% strain for R15, with R1 data included for comparison.

Non-relaxing state condition of crack growth tests were conducted and a comparison with a relaxing condition for R1 undertaken. Figure 7.16 shows the comparison results of crack growth tests of R1.
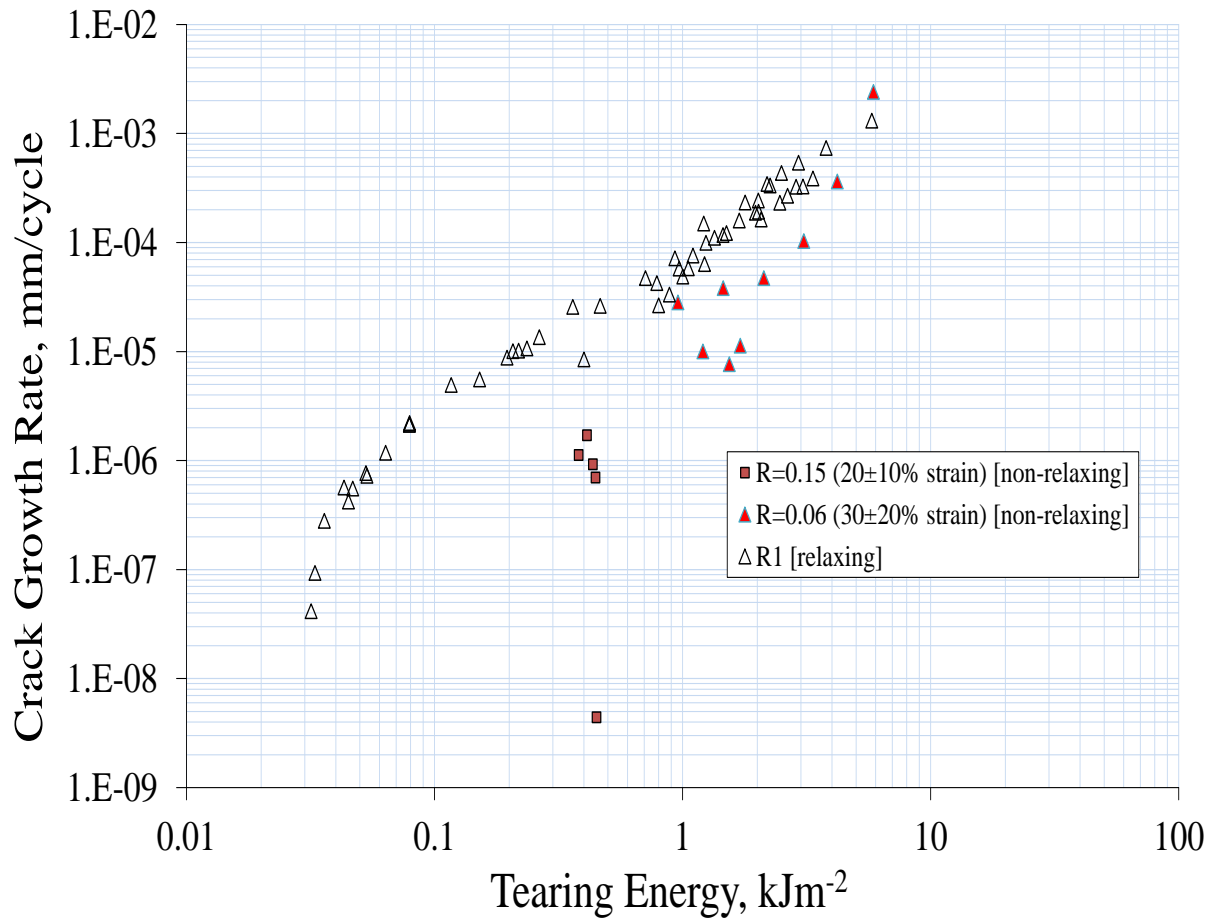
Figure 7.16: R1 results of crack growth rate as a function of minimum tearing energy. R=0.15 and R=0.06 were conducted in ozone free chamber and compared with data fully relaxing cycles of R1 in laboratory's atmosphere.

In the crack growth test at R=0.15, the crack initially grew, but soon stopped and showed no further propagation up to 2,919,808 cycles whereas at R=0.06, the crack was propagated at a variable rate.

7.3.3 Fatigue Life Tests

Figure 7.17 shows the result of fatigue tests for die-stamped dumb-bell test pieces relaxed completely during each cycle. It is confirmed that the antioxidant/antiozonant improved the fatigue life of rubber, consistent with the reduction in crack growth rate.
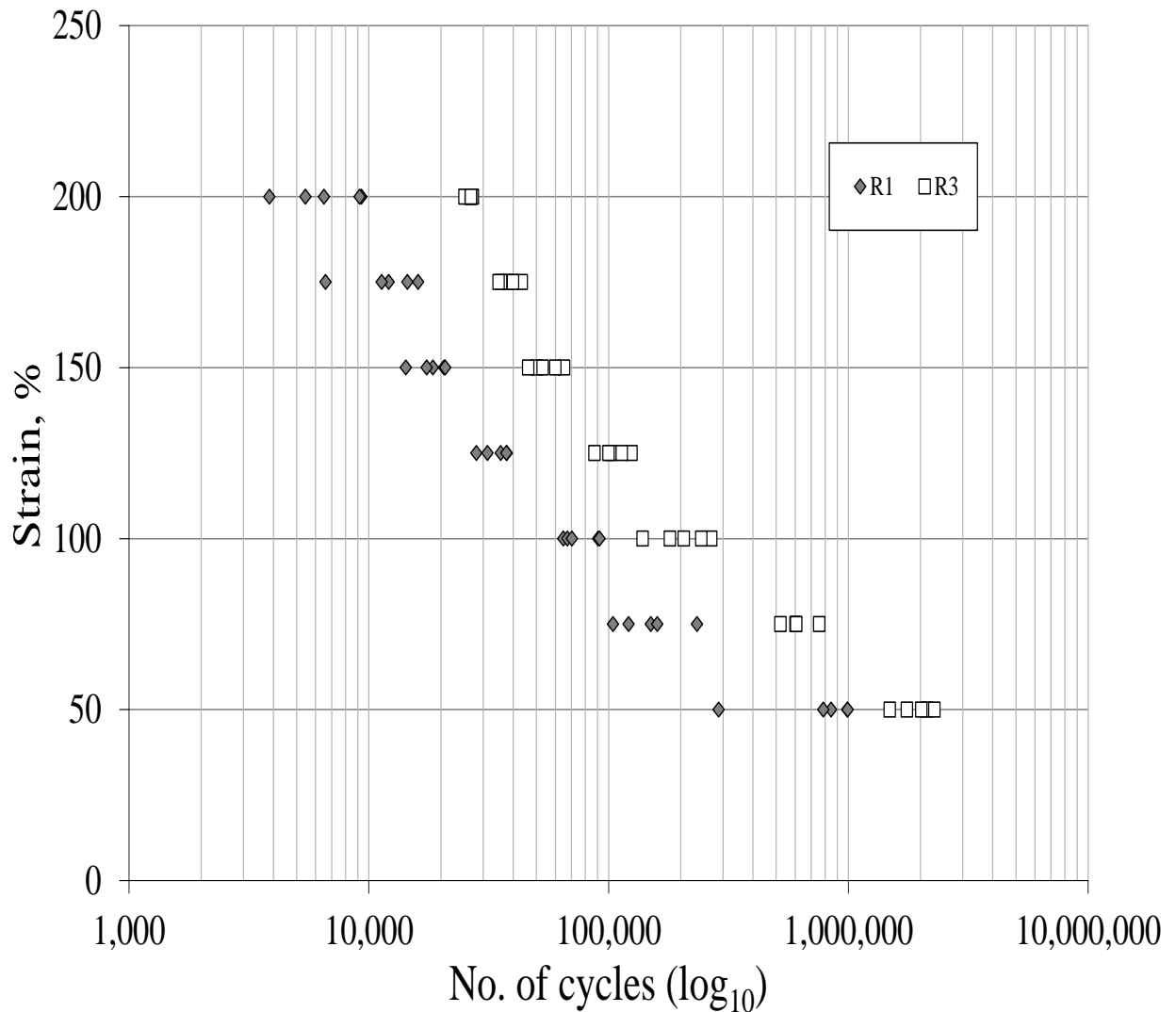
Figure 7.17: The maximum strain plotted against the number of cycles to failure *N*.

7.3.4 Estimation of Effective Flaw Sizes From Fatigue Results

According to theory (Gent et al. 1964; also Equation 3.17) the fatigue life of tensile dumbbells can be estimated from an effective initiating flaw size c_i. The estimation of effective initiating flaw size in the rubber literature often uses only the last term in Equation (3.17), which only considers the power law regime (Gent et al. 1964, Choi & Roland 1996). At flaw sizes lower than c_i, the fatigue life of the rubber would become infinite without ozone attack. Figures 7.18 and 7.19 show the full fatigue life prediction

based on Equation (3.17) for the modified EDS19 (solid lines), and that assuming the power law dependence (last term of Equation (3.17) only; dotted line).

Placement of data points representing the measured fatigue lives are superimposed on the theoretical lives in Figures 7.15 and 7.16 lead to fits for effective flaw sizes given in Tables 7.3 and 7.4. Unfortunately, the resulting values are significantly dependent on the fatigue strain, especially for the material without antioxidant. Such results conflict with expectation from the theory, and this mismatch has been observed and discussed previously by Kingston & Muhr (2013). Table 7.3 and 7.4 give the effective flaw size values deduced from different strains for R1 and R3. In the present work, the effective flaw sizes were calculated using parameters from Table 7.2. In Equation (3.12), t_c is the time during each cycle that rubber is strained such that $T>T_z$, q is the ozone concentration and ρ_z is the susceptibility of the rubber to ozone attack $T>T_z$. For $T_{max} <T_z$ there is no crack growth. Estimated values are: $q \sim$ 0.003ppm by volume (the test laboratory varied between 0.002 and 0.003ppm); $\rho_z \sim$ 6.8nm.s^{-1}ppm^{-1} (Braden & Gent 1960), and $t_c \sim$ 0.17s (for the test frequency of 4.44Hz and typical time fraction of full relaxation). The r value was taken to be 3μm/Mcycle to make the predictions in Figures 7.18 and 7.19, which is similar in magnitude to that found to be appropriate to the conditions and materials of Lake and Lindley (1965). The r value is $\cong \rho_z.q.t_c \cong$ 0.003 × 6.8 × 0.17 nm.cycle^{-1} $\cong$ 0.004 nmcycle^{-1} or 4 × 10^{-6} μm cycle^{-1}. The apparent effective flaw size was calculated using Equation (3.18).

Table 7.3: The effective flaw sizes associated with the imitation of fatigue failure of the dumb-bell testpieces (R1).

Strain, %	N (kilo cycles)	Method Power law C_i, μm	Full analysis C_i, μm
200	3.9	297.9	297.3
	5.4	167.2	167.0
	6.5	124.2	124.3
	9.2	70.2	79.5
	9.3	68.2	78.3
Average	**6.9**	**145.5**	**149.3**
175	6.6	192.1	192.2
	11.3	78.3	91.0
	12.1	70.0	84.6
	14.5	51.9	68.1
	16.1	43.6	58.9
Average	**12.1**	**87.2**	**99.0**
150	14.3	107.2	121.8
	17.4	76.7	97.7
	18.5	69.6	90.6
	20.6	58.1	78.4
	20.8	57.2	77.5
Average	**18.3**	**73.8**	**93.2**
125	28.1	75.6	102.7
	31.3	63.3	87.5
	35.5	51.3	71.6
	37.5	46.8	65.0
	37.6	46.6	64.6
Average	**34.0**	**56.7**	**78.3**
100	64.8	29.2	38.0
	67.3	27.4	35.5
	70.3	25.5	32.9
	90.5	16.7	22.3
	91.7	16.4	21.8
Average	**76.9**	**23.0**	**30.1**
75	104.5	37.9	48.9
	121.3	29.5	38.0
	150.0	20.7	29.5
	159.6	18.7	28.0
	234.0	9.9	24.4
Average	**153.9**	**23.3**	**33.8**
50	287.8	35.3	52.2
	786.4	6.6	20.6
	847.6	5.8	18.7
	990.6	4.5	14.4
	993.6	4.5	14.3
Average	**781.2**	**11.3**	**24.0**

Table 7.4: The effective flaw sizes associated with the imitation of fatigue failure of dumb-bell testpieces (R3).

Strain, %	N (kilo cycles)	Method	
		Power law C_i, µm	Full analysis C_i, µm
200	25.1	44.6	35.1
	26.6	42.2	31.8
	26.7	42.1	31.6
	26.7	42.1	31.5
	27.2	41.2	30.5
Average	**26.5**	**42.4**	**32.1**
175	34.8	48.3	34.4
	35.6	47.1	33.0
	38.2	44.0	29.5
	40.0	42.1	27.3
	43.4	38.8	24.3
Average	**38.4**	**44.1**	**29.7**
150	46.2	54.6	36.6
	50.4	50.0	31.9
	53.1	47.5	29.8
	60.0	42.2	25.3
	65.3	38.8	23.3
Average	**55.0**	**46.6**	**29.4**
125	87.4	64.6	38.0
	100.0	56.6	33.2
	102.5	55.3	33.1
	113.5	50.0	30.8
	124.6	45.7	29.6
Average	**105.6**	**54.4**	**32.9**
100	138.7	55.5	35.7
	180.2	42.9	33.6
	206.0	37.6	32.4
	243.6	31.9	33.1
	268.3	29.1	33.1
Average	**207.4**	**39.4**	**33.6**
75	520.7	34.3	49.5
	602.9	29.7	49.4
	604.0	29.7	49.1
	606.4	29.6	49.3
	755.7	23.8	48.9
Average	**617.9**	**29.4**	**49.2**
50	1488.2	41.6	92.4
	1755.4	35.4	92.3
	2014.9	30.9	91.8
	2132.8	29.3	92.0
	2286.2	27.3	91.9
Average	**1935.5**	**32.9**	**92.1**

For R1, values for average size of flaws at 200% strain were much larger compared to those for other strains and the average size result of 25µm reported by Lindley and Thomas (1962). The effective sizes of flaws at 50% were much more scattered, this strain probably corresponds to $T_z< T_{max}<T_o$ for flaws and the scatter could relate to variations in ozone concentrations.

For R3, the effective size of flaws using the full analysis are in the range of 29.4 - 92.1µm in fair agreement with Lindley and Thomas's results. The effective flaw sizes are not significantly different for the two materials, given the great uncertainty in the magnitudes calculated.

Figures 7.18 and 7.19 show four different fatigue strains with the prediction of fatigue life from the size of flaws of R1 and R3.
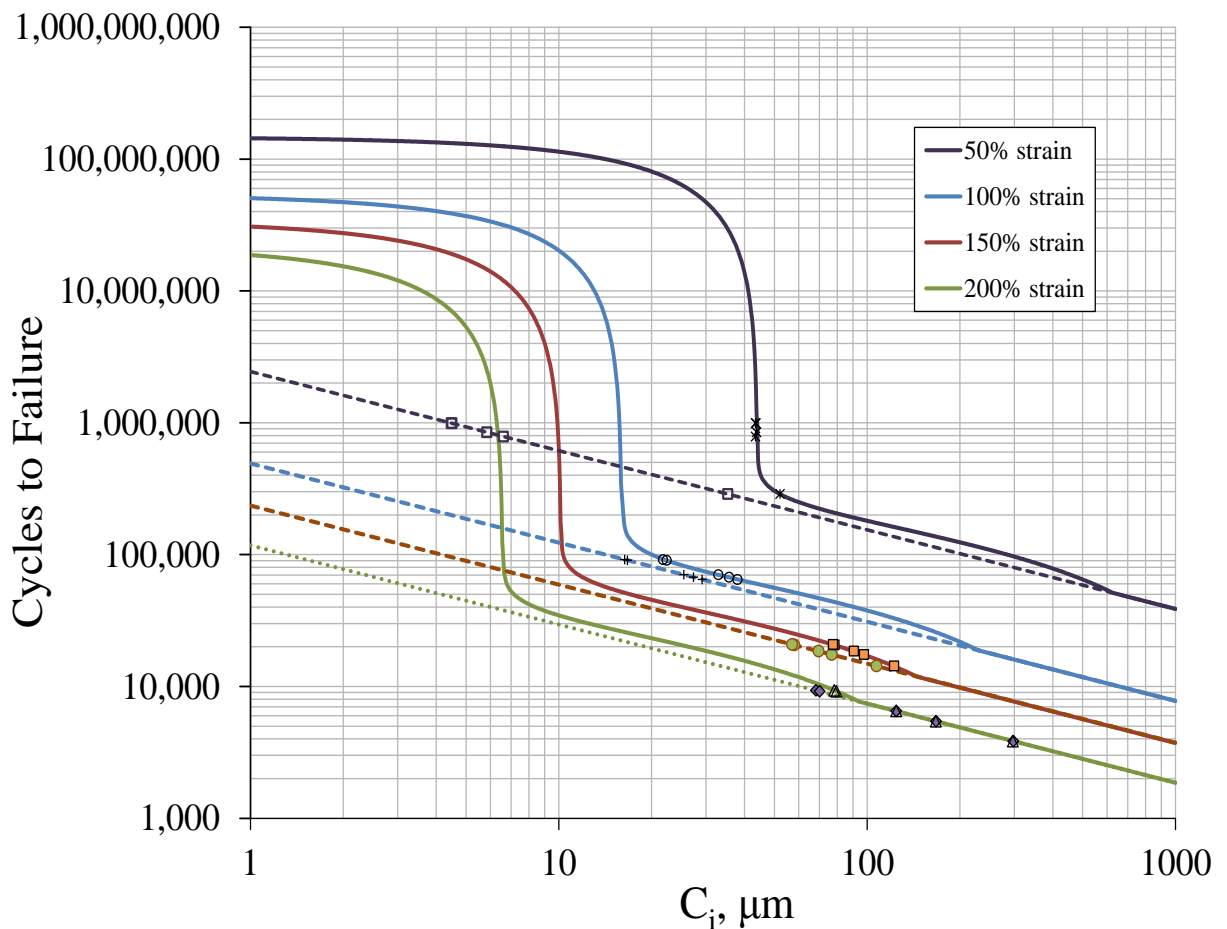
Figure 7.18: Predicted fatigue lives for R1 '---' extrapolated power law; points fatigue tests and deduced effective flaw sizes.
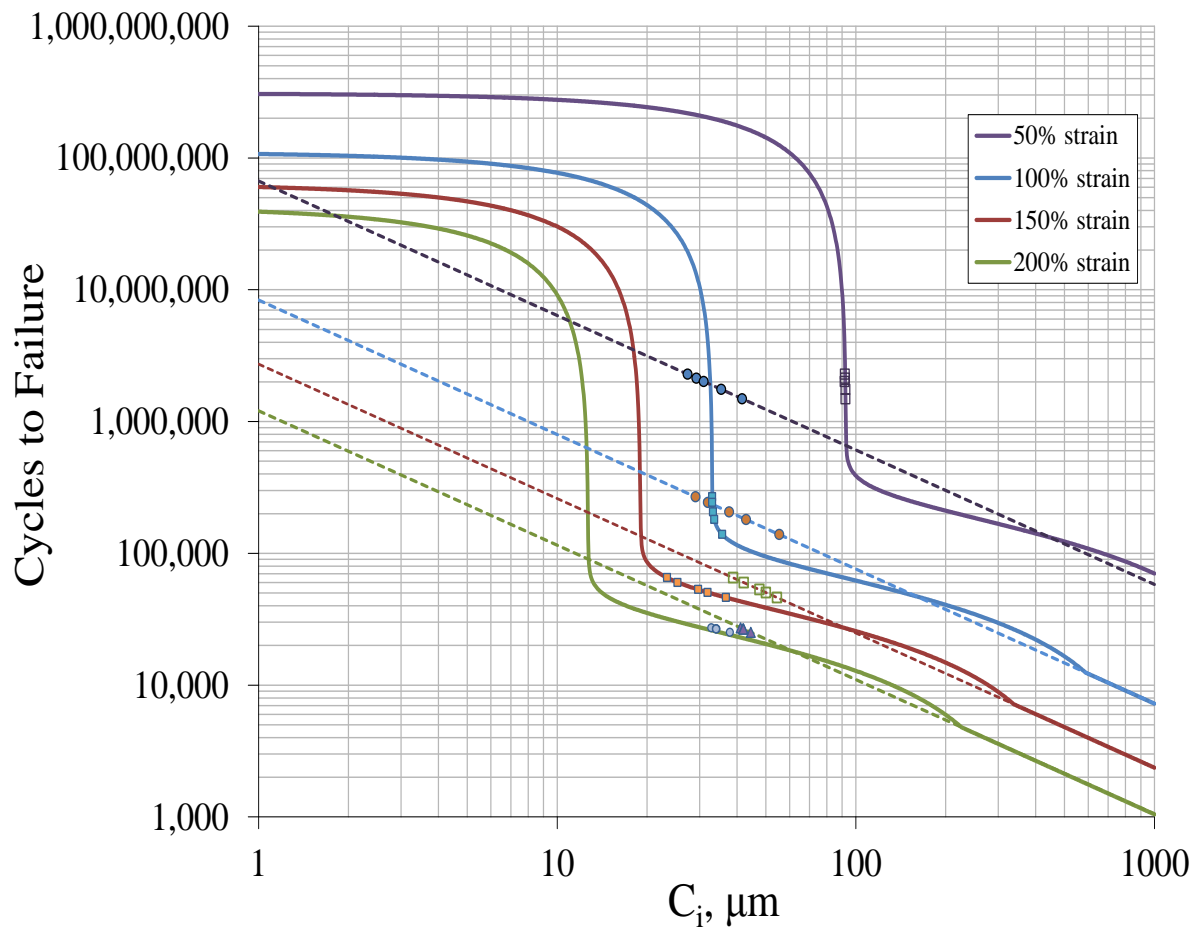
Figure 7.19: Predicted fatigue lives for R3 '---' extrapolated power law; points fatigue tests and deduced effective flaw sizes.

The apparent values for c_i calculated from fatigue and crack growth data depended on the strain level used for the fatigue tests for R1, but was much less so if antioxidant 2246 is used. This is the case whether the power-law relationship (Equation 3.16) or the full prediction method (Equation 3.17) is used. This situation seems to arise from the different power laws used to fit the crack growth data. Had β been taken as 2 in both cases (as in the literature of Lake and Thomas 1967a) c_i would have been much less dependent on fatigue strain.

7.3.5 Non-Relaxing Fatigue Analysis

Tables 7.5 to 7.8 show the results of fatigue tests in a non-relaxing state condition for all rubbers. The average number of cycles to failure for R3 was 100 times higher than R1. This is very surprising, since unlike paraphenylene diamine (HPPD), antioxidant 2246 is not considered to be an anti-flex cracking antioxidant (MRPRA 1984). The comparison with other rubbers was made based on the average of the number of cycles to failure. The

numbers of cycles to failure of the author modified EDS19 recipe, R1 and R3 were much better than others. It is confirmed that carbon blacks contained in author modified rubber R4 has minimised the fatigue life under these conditions of fixed strain.

Table 7.5: Fatigue results in screening tests (160±105% strain) for R1, R3, R0 and R4.

Sample	No. of cycle			
	R1	R3	R0	R4
1-1	39,480	570,050	2,087,760	46,160
1-2	46,120	546,160	1,581,310	48,050
1-3	108,140	456,410	1,617,940	49,890
1-4	71,420	592,490	1,807,520	39,360
1-5	49,210	572,540	1,823,390	35,110
1-6	90,820	578,350	1,710,220	40,060
2-1	173,570	618,280	2,094,240	35,700
2-2	108,590	552,200	1,766,150	40,020
2-3	99,300	548,120	1,279,350	44,630
2-4	40,640	406,080	1,324,710	37,800
2-5	62,050	478,790	1,504,590	35,010
2-6	115,860	476,200	1,479,220	35,540
Average	**83,767**	**532,973**	**1,673,033**	**40,611**
Standard Deviation	**40,060**	**63,757**	**261,788**	**5,308**
Median	**81,120**	**550,160**	**1,664,080**	**39,690**

Table 7.6 also shows that rubber containing a high level of carbon black reduces the fatigue life. This characteristic can be observed clearly by comparing R1 with R2 in Table 7.5 and R5 with R6 in Table 7.6, which clearly have different amounts of carbon black in parts per hundred of rubber (pphr) on reverting to Table 5.2.

Table 7.6: Fatigue results in screening tests (160±105% strain) for R5, R6, R7, R8, R9, R10, R11, R12 and R13.

Sample	No. of cycle								
	R5	R6	R7	R8	R9	R10	R11	R12	R13
1-1	4,240	7,110	54,130	34,720	26,670	73,160	3,190	2,470	159,249
1-2	11,520	6,220	75,600	16,550	17,110	59,350	3,250	5,440	152,632
1-3	7,490	2,000	64,210	50,910	45,760	65,960	3,450	5,450	183,324
1-4	7,120	5,140	59,170	36,160	45,020	45,050	3,100	2,870	163,472
1-5	10,220	4,620	67,970	16,270	20,300	69,020	3,150	3,970	157,071
1-6	9,560	4,960	66,230	68,400	41,210	63,050	2,370	3,600	220,406
2-1	13,080	4,720	80,290	43,340	44,570	24,250	2,020	2,610	143,310
2-2	15,010	1,920	25,950	5,040	25,030	14,340	1,890	4,650	143,336
2-3	9,440	5,460	82,710	51,700	7,820	23,850	2,130	4,140	151,206
2-4	14,330	4,850	22,900	7,400	34,900	24,100	2,300	3,940	132,819
2-5	12,580	4,030	92,910	5,550	11,420	40,540	2,610	3,600	116,746
2-6	13,600	4,890	83,790	71,500	20,450	44,170	2,810	4,600	134,959
Average	**10,683**	**4,660**	**64,655**	**33,962**	**28,355**	**45,570**	**2,689**	**3,945**	**154,878**
Standard Deviation	**3,275**	**1,492**	**21,848**	**23,848**	**13,578**	**20,477**	**539**	**992**	**26,669**
Median	**10,870**	**4,870**	**67,100**	**35,440**	**25,850**	**44,610**	**2,710**	**3,955**	**151,919**

Different particle sizes of carbon black also give different fatigue lives. This relates to rubber compounds of R7, R8 and R9 specified in Table 5.2. It presumed that a large particle size of carbon black (N-990) mixed with rubber with fewer rubber molecular bondings adversely affects the fatigue life of rubber. Other rubber materials of unknown formulation, designated R10, R11 and R12, have short fatigue lives compared with R0 and R3.

The variants of EDS14 designated R14, R15, R16, R17 and R18 show significantly different numbers of cycles to failure as shown in Table 7.7 and reflect different curing system specified in Table 5.3. The increase of sulfur specified in Table 5.3 affects the fatigue life of rubber in the non-relaxing test conditions.

Table 7.7: Fatigue results in screening tests (160±105% strain) for R14, R15, R16, R17, R18 and R19.

Sample	No. of cycle					
	R14	R15	R16	R17	R18	R19
1-1	73,230	16,910	173,680	22,350	13,190	165,310
1-2	207,760	342,900	130,430	17,610	6,290	69,070
1-3	236,580	332,560	130,420	5,750	3,340	164,210
1-4	217,980	401,520	136,840	12,380	9,400	89,950
1-5	202,210	362,540	195,650	34,810	7,760	176,420
1-6	216,370	364,540	118,560	39,970	10,010	140,550
2-1	317,890	366,040	128,600	27,200	8,150	136,660
2-2	280,910	306,400	146,990	49,540	7,630	136,410
2-3	276,630	434,180	160,210	10,310	4,940	166,050
2-4	281,190	441,840	30,250	13,050	4,470	139,820
2-5	299,690	243,690	123,620	59,720	7,010	132,890
2-6	311,880	416,440	172,350	16,140	5,910	132,990
Average	**243,530**	**335,800**	**137,300**	**25,730**	**7,340**	**137,530**
Standard Deviation	**67,890**	**114,930**	**41,280**	**16,940**	**2,690**	**31,360**
Median	**256,600**	**363,540**	**133,640**	**19,980**	**7,320**	**138,240**

Table 7.8: Fatigue results in screening tests (160±105% strain) for R20, R21, R22, R23, R24, R25 and R26.

Sample	No. of cycle						
	R20	R21	R22	R23	R24	R25	R26
1-1	203,410	19,620	75,520	53,360	30,840	12,280	6,520
1-2	186,640	17,870	85,860	47,280	50,370	12,310	8,400
1-3	161,430	19,110	161,800	60,220	32,530	10,070	3,800
1-4	156,500	8,890	51,770	56,700	47,130	8,060	8,400
1-5	187,940	15,550	58,330	23,030	35,780	9,580	10,720
1-6	158,700	18,370	139,240	18,180	38,660	5,080	4,080
2-1	225,220	21,870	85,290	79,530	33,040	14,970	8,160
2-2	108,810	18,120	84,190	89,440	30,780	13,800	9,770
2-3	183,950	14,890	90,610	43,980	28,130	19,480	5,630
2-4	125,550	15,050	122,850	47,980	29,110	20,380	8,090
2-5	49,550	12,080	69,260	29,180	12,010	5,610	4,590
2-6	98,230	25,000	124,760	83,840	23,800	16,630	5,940
Average	**153,830**	**17,200**	**95,790**	**57,730**	**32,680**	**12,350**	**7,010**
Standard Deviation	**50,080**	**4,290**	**33,900**	**23,090**	**10,060**	**4,970**	**2,250**
Median	**160,060**	**18,000**	**85,580**	**50,670**	**31,690**	**12,300**	**7,300**

It is surprising that similar formulations stated in Table 5.3, which have a slightly different curing time, give different fatigue results. The fatigue results of Table 7.8 for R20 and R15 (Table 7.7) confirmed that different sources of mixing process show inconsistency of fatigue results in non-relaxing condition. It is known that filler dispersion affects mechanical properties of the rubber (Payne 1965). However, the fatigue test results show that the finer grade of black in the R22 mix (see Table 5.4) does not result in a longer fatigue life compared to the R19 mix. The fatigue results of R23, R24, R25 and R26 show that increase of carbon black significantly reduces the fatigue life in non-relaxing fixed displacement cycles.

Figure 7.20 shows the overall results of fatigue test for all rubber compounds by ranking based on the number of cycles to failure. The hardness value of each compound was measured and a weak inverse correlation with fatigue test results is evident in Figure 7.20.
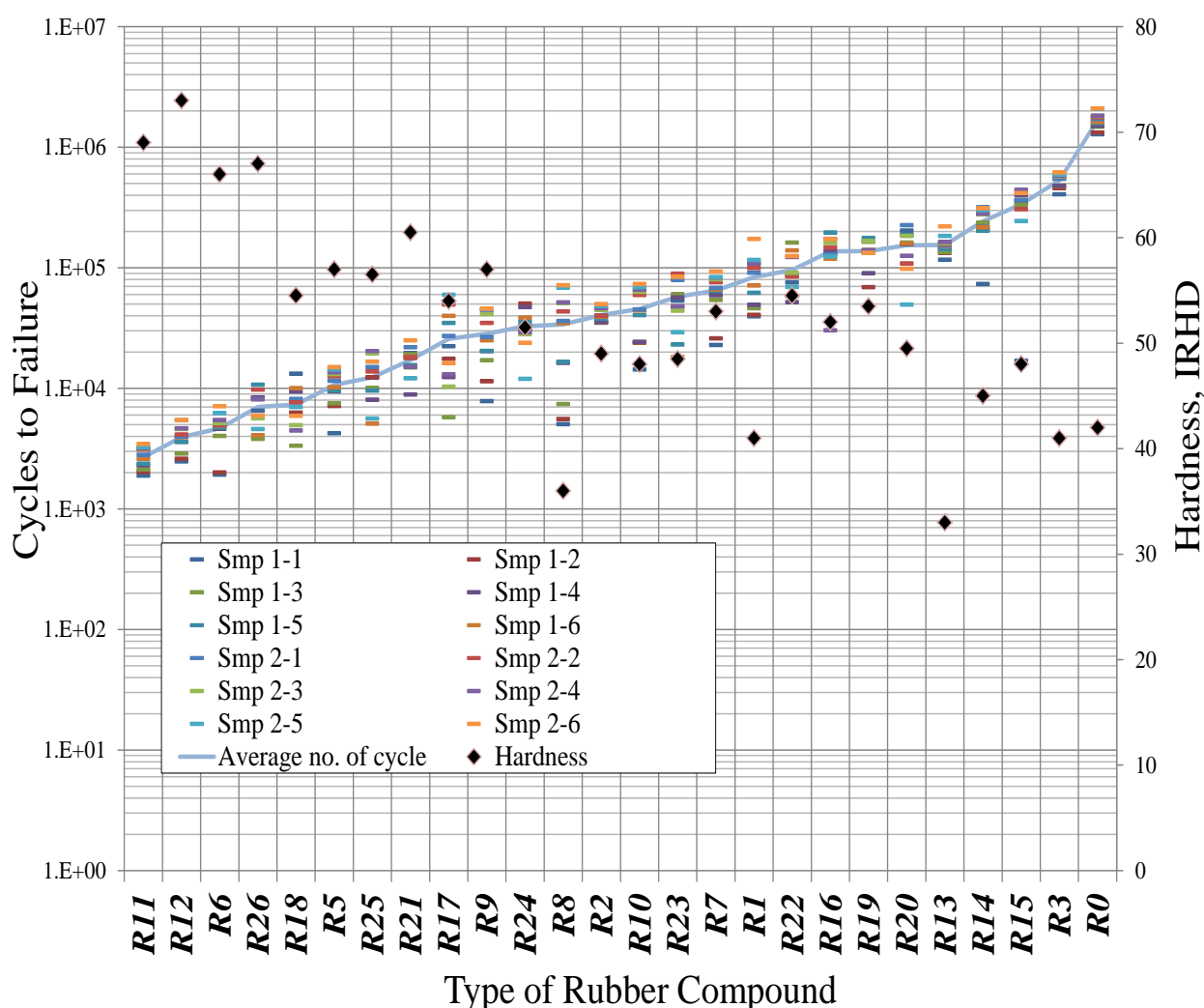
Figure 7.20: Overall fatigue test results of all rubber compounds at 160±105% strain. The relationship of fatigue test results and hardness was plotted for comparison.

Figure 7.21 presents fatigue test data with tensile strength data for each compound. It is apparent that the tensile strength is not correlated with fatigue life.
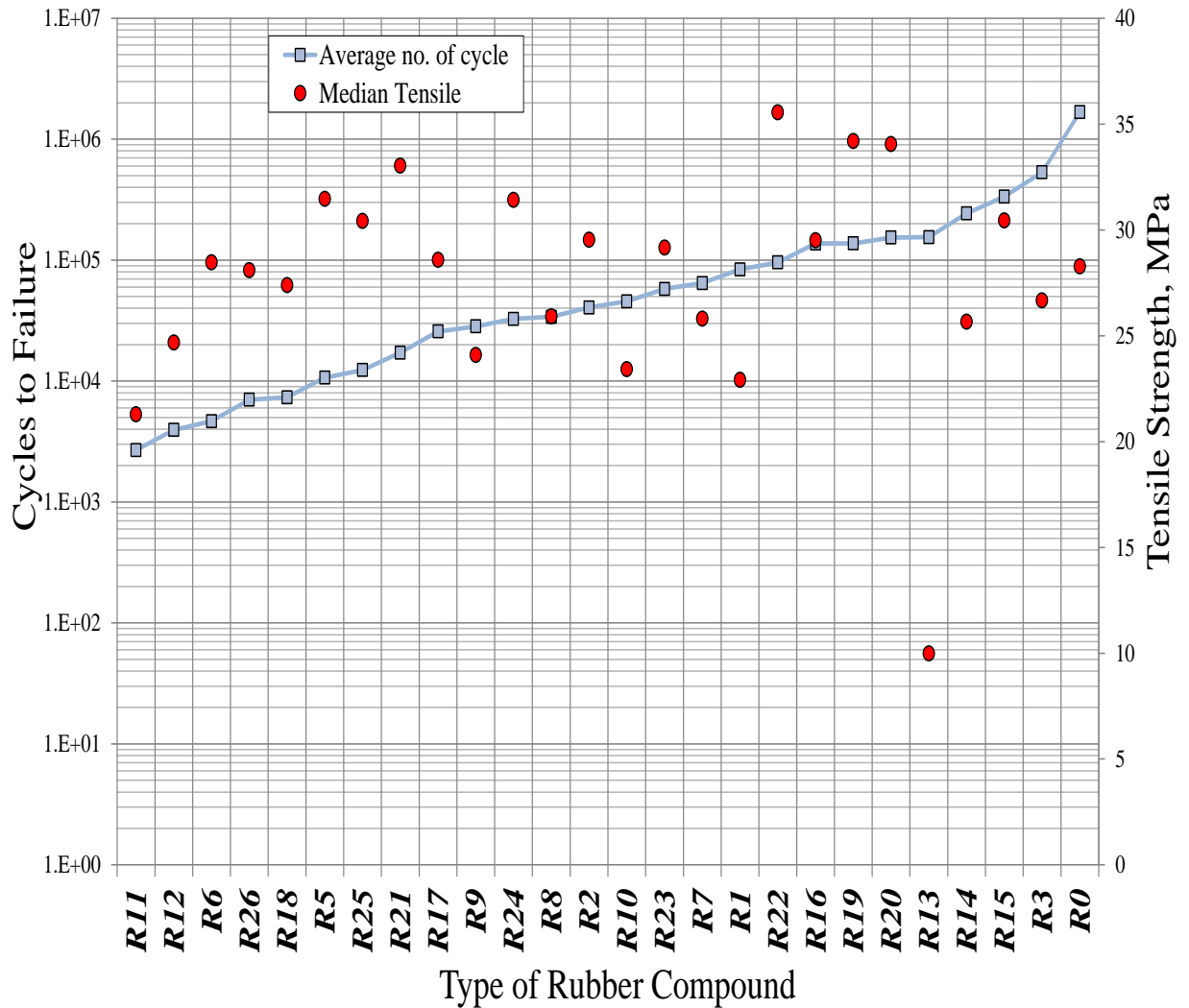
Figure 7.21: Overall fatigue test results of all rubber compounds at 160±105% strain. The relationship of fatigue test results and tensile strength was plotted for comparison.

Figure 7.22 addresses elongation at break and fatigue test data for rubber compounds examined. It is apparent that high elongation at break correlates fairly well with fatigue life.
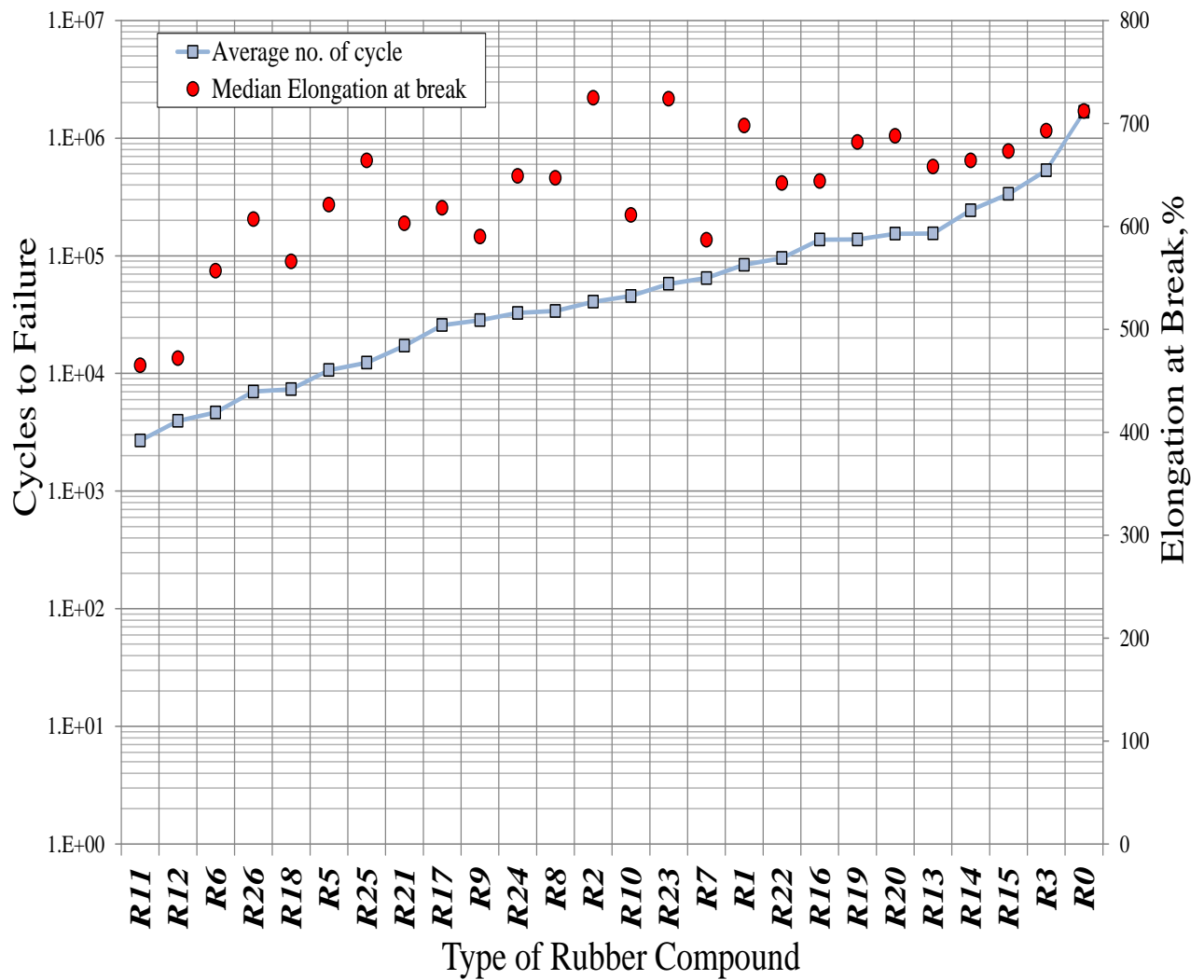
Figure 7.22: Overall fatigue test results of all rubber compounds at 160±105% strain. The relationship of fatigue test results and elongation at break was plotted for comparison.

Figure 7.23 shows that the mean fatigue life of the rubber compounds correlates inversely with that modulus (100%). This is expected from Equation (3.17), assuming the underlying crack growth characteristics (r_B, β etc.) are the same for all the materials as seems likely since they are all NR. If the power law dominates then $N \propto W^{\beta}.c_i^{1-\beta}$; furthermore, if β~2, we might expect $N \propto E^{-2}.c_i^{-1}$. Such a correlation is explored in Figure 7.26.
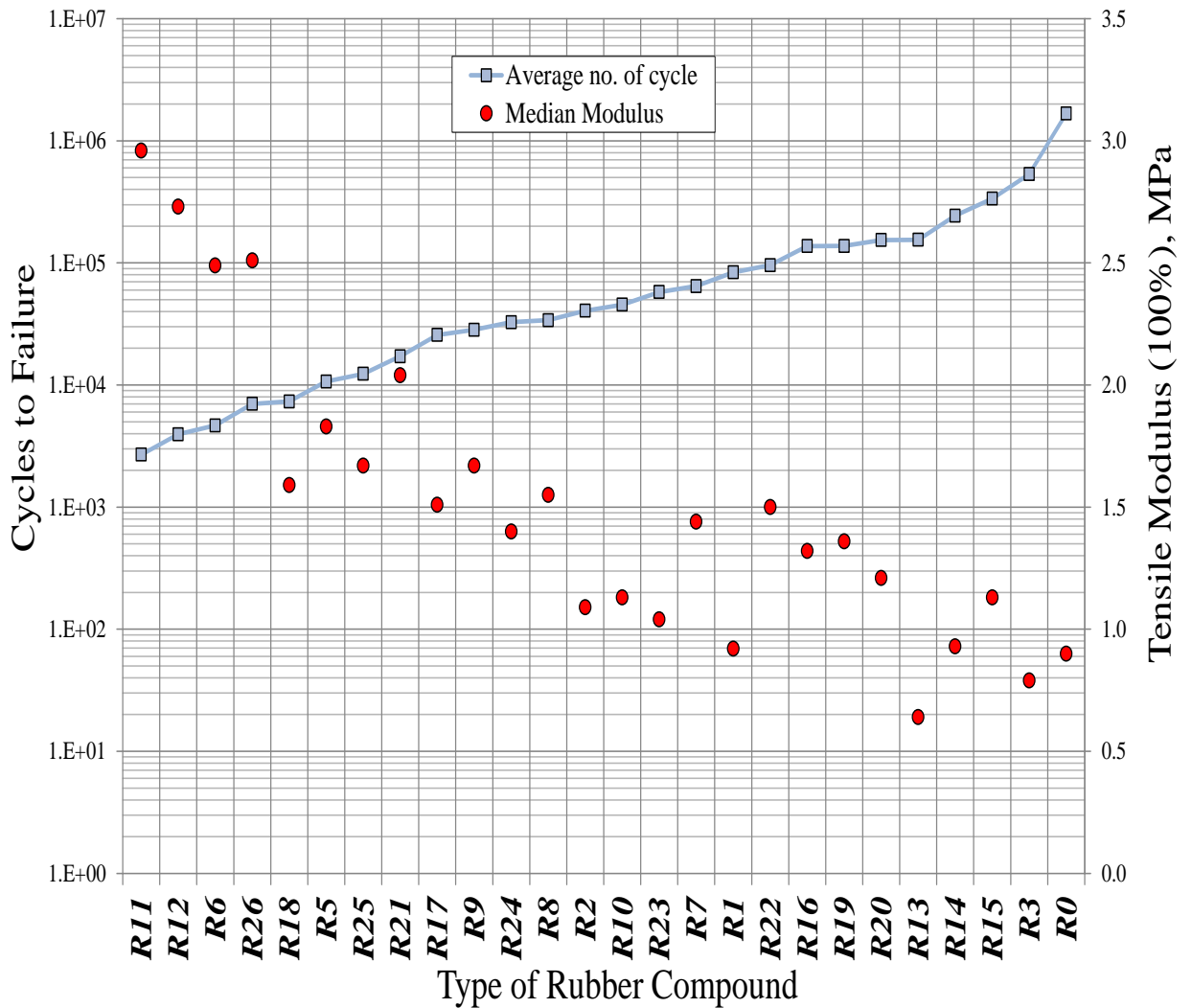
Figure 7.23: Overall fatigue test results of all rubber compounds at 160±105% strain. The relationship of fatigue test results and modulus at 100% was plotted for comparison.

Number-weighted average particle size value of all the rubber compounds were plotted with the fatigue life results, as shown in Figure 7.24. The number average particle size was obtained using the Equation 6.1. The number-weighted average particle size and the fatigue life show little correlation. However, small average particles size does not show a longer fatigue life when referring to R7, R8 and R9.
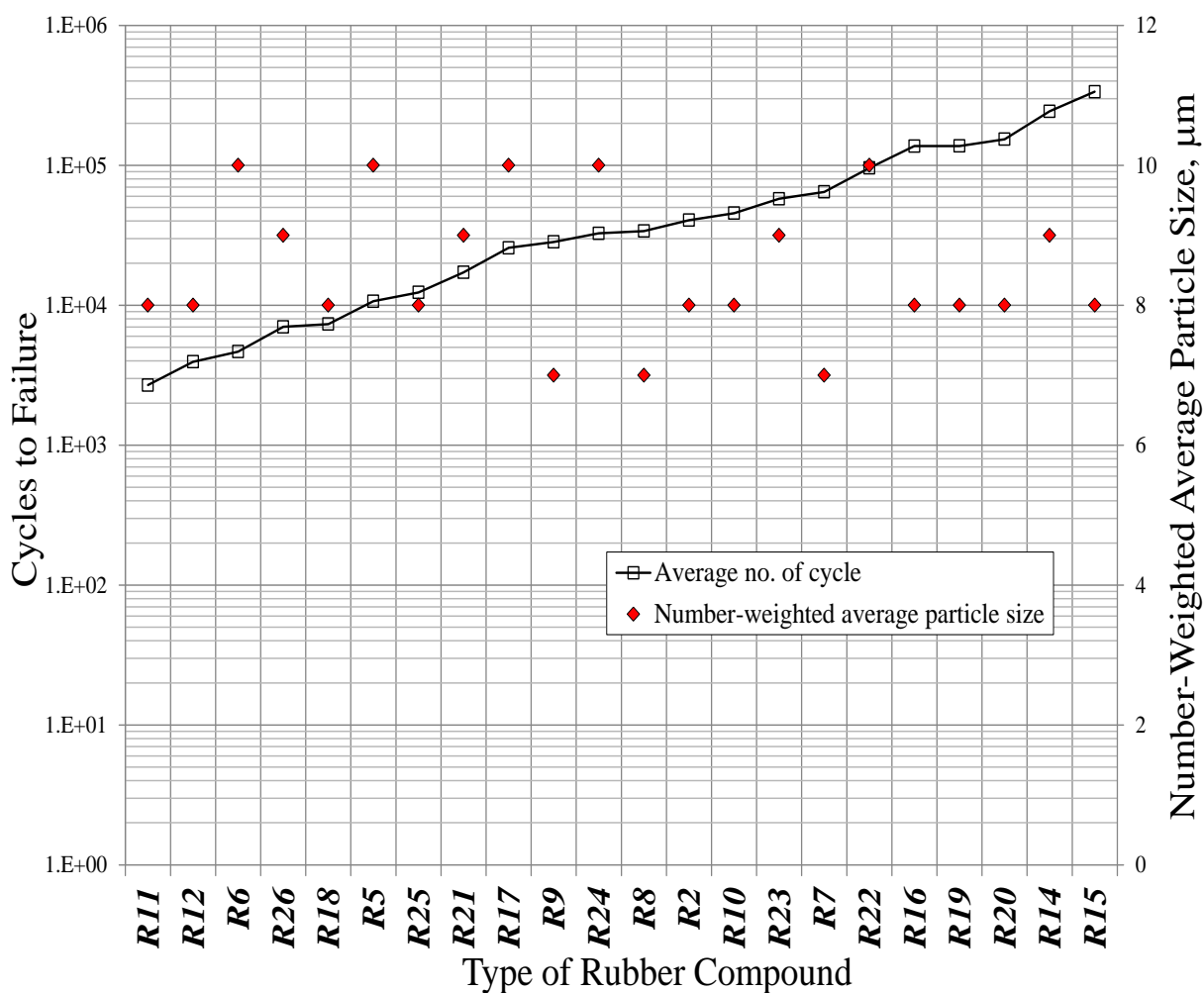
Figure 7.24: The relationship of the fatigue life and the number weighted averaged particle size of the filled rubber compounds. Fatigue tests at 160±105% strain.

Figure 7.25 shows the relationship between white area-weighted average particle size, (weighted by white area fraction using Equation 6.2), and the fatigue life results. This white area weighted average particle size is larger than the previous addressed number-weighted average particle size of the rubber compounds. Again, there is little correlation with fatigue life.
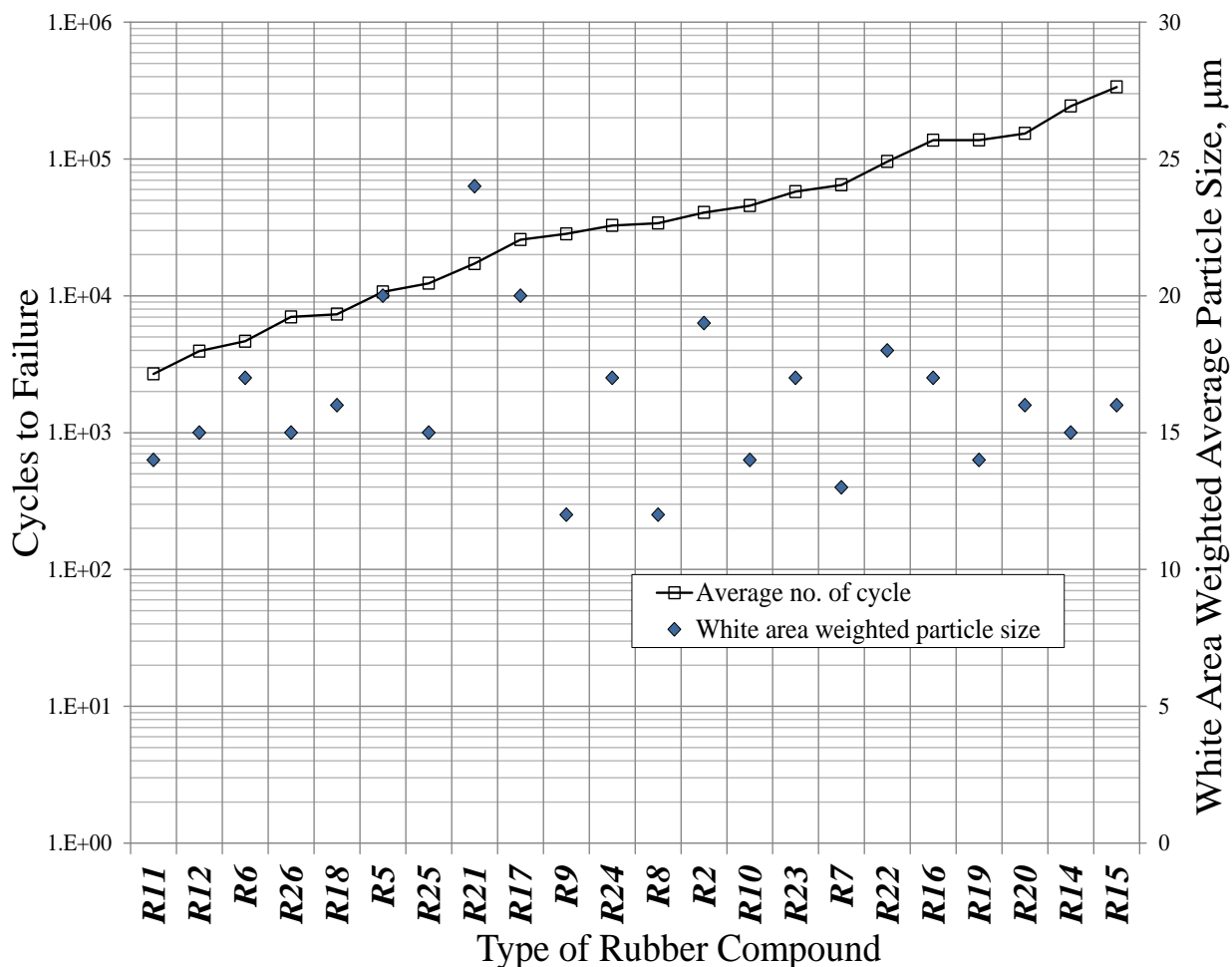
Figure 7.25: The relationship of the white area weighted average particle size and the fatigue life of the filled rubber compounds. Fatigue tests at 160±105% strain.

Figure 7.26 shows the correlation between the fatigue life and the correlation of $(modulus)^{-2}$, $(modulus)^{-2} \times$ (number weighted average particle size)$^{-1}$ and $(modulus)^{-2} \times$ (white area weighted average particle size)$^{-1}$. A power line of each correlation was introduced to investigate any relationship that can be deduced. According to the R value of each correlation as shown in Figure 7.26, it is apparent that inclusion of a particle size offers no improvement one on its own.
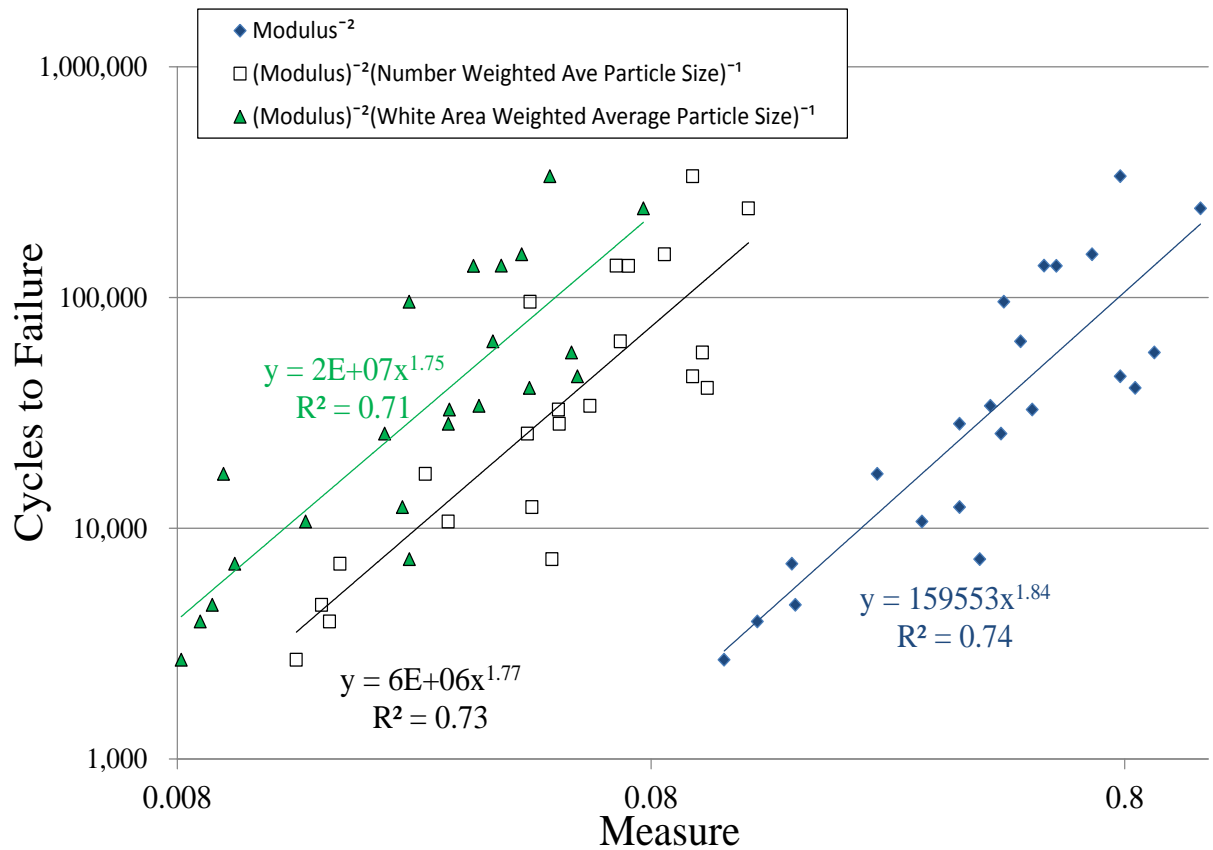
Figure 7.26: Scatter plots for three measures that might correlate with the fatigue life of the filled rubber compounds. Fatigue tests at 160±105% strain. The data covers the set of rubbers R0 to R26, except R1, R3, R4 and R13.

Figure 7.27 provides the hysteresis of load-displacement of R0 after 1,000 cycles from fatigue test at 160±105% strain for the 12 replicates. It is evident that the reproducibility of stress-strain behaviour is reasonably good, without sample 2-3 is an outline. Every single hysteresis curve of the sample has the average load between the range of 7.95N to 8.89N.
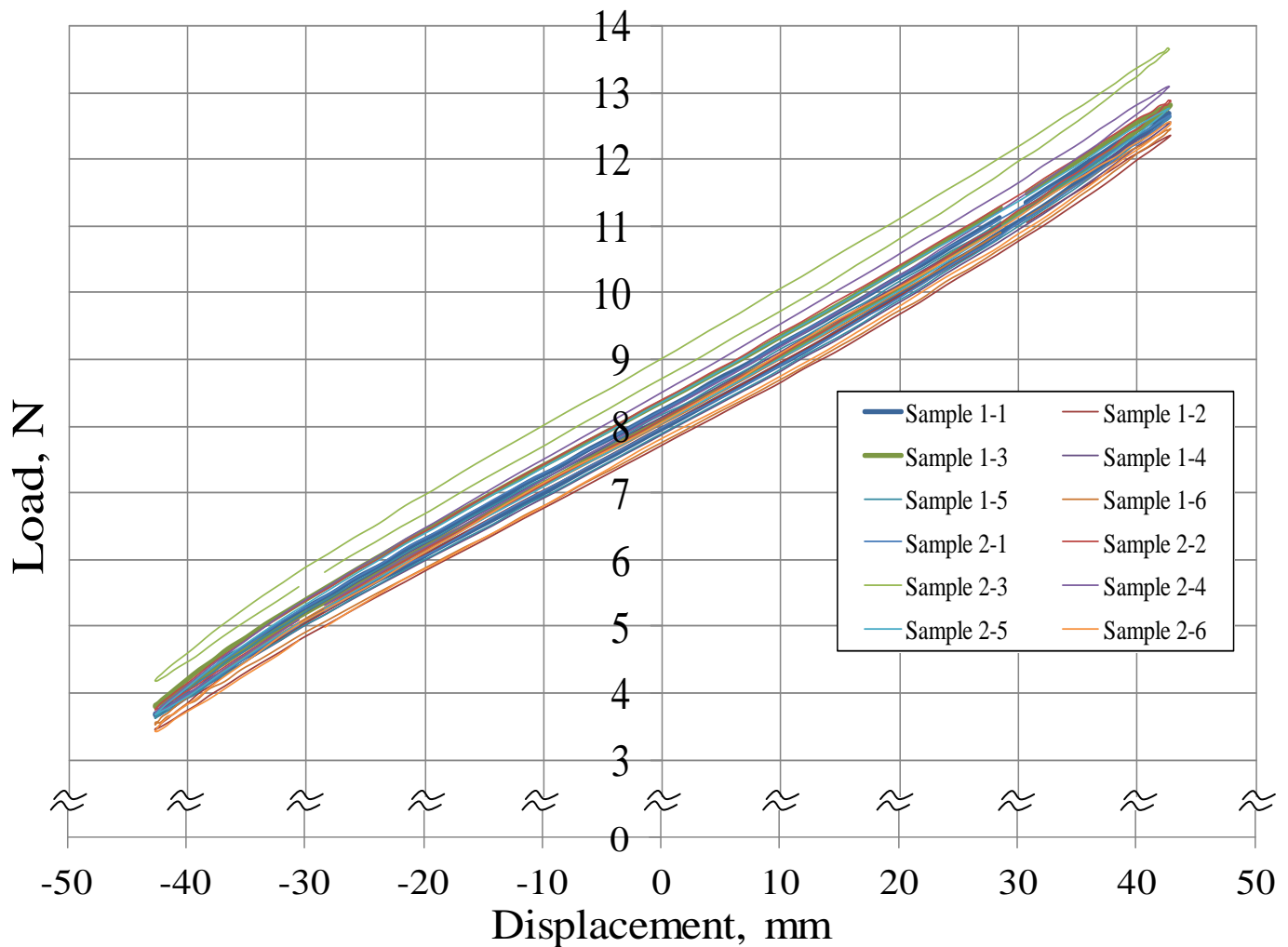
Figure 7.27: Hysteresis load displacement of R0 at 1,000 cycles.

Figure 7.28 shows the example of the load displacement hysteresis curves of R0 for Sample 2-1 at 1k, 100k, 1M and 1.5M cycles. The mean load slightly decreases with increase in the number of cycles and there seems also to be a slight drop in dynamic stiffness.
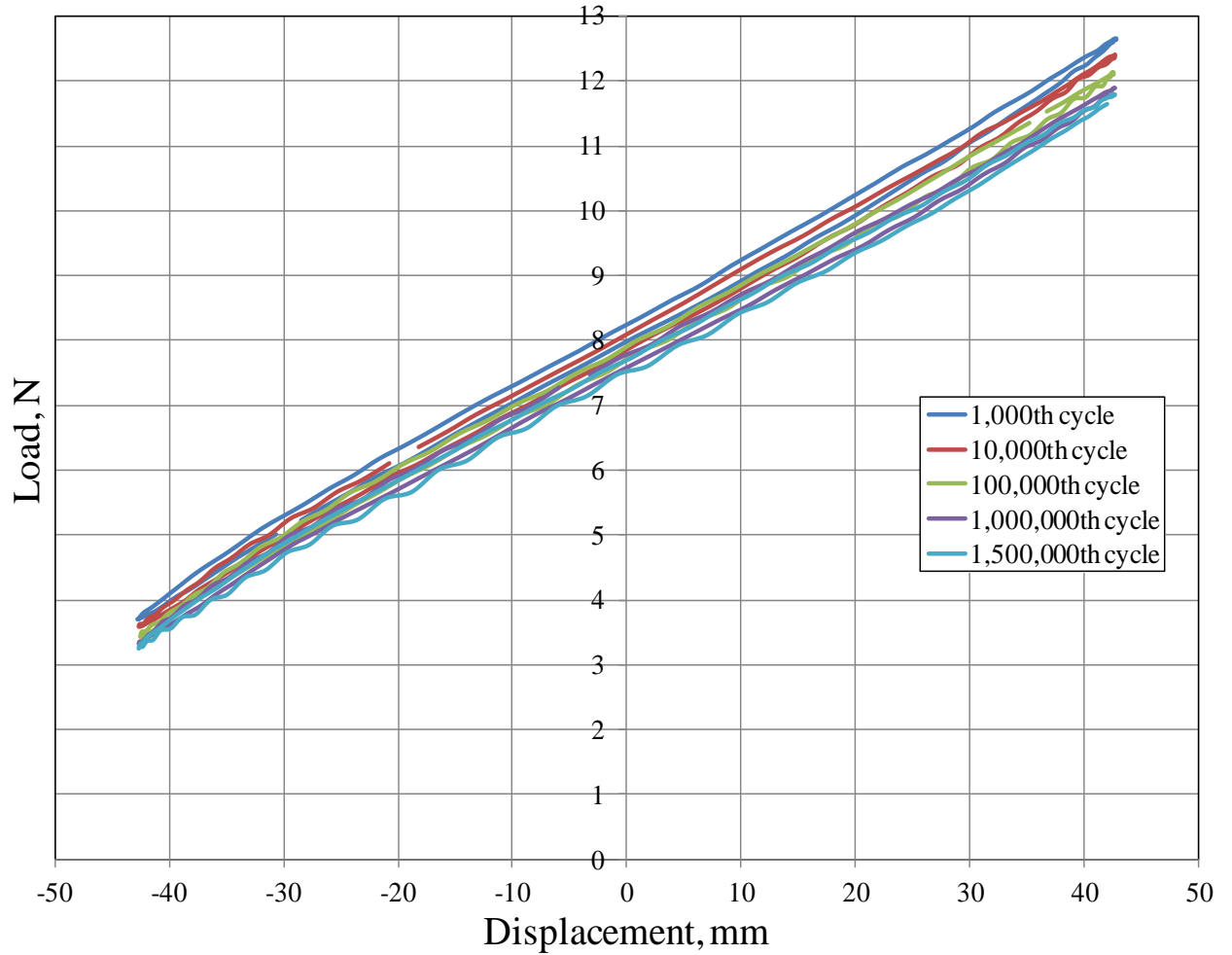
Figure 7.28: Load displacement loops of R0 (Sample 2-1) at 1k, 100k, 1M and 1.5M cycles.

Stress and strain can be estimated from the load and displacement data by considering the narrow part of the dumb-bell using the equations as below:

$$Stress = \frac{Force}{4mm \times thickness} \tag{7.1}$$

$$Strain = \frac{1}{\Delta D_\varepsilon}|[\ LVDT\ (Current) - LVDT\ (\text{Max})]| + 55\% \tag{7.2}$$

where

$$\Delta D_\varepsilon = \frac{LVDT\ (Max) - LVDT\ (Min)}{210\%} \quad .$$

Figure 7.29 shows the effect of number of cycles for R0 and R6 samples chosen as close to the average behaviour. It is confirmed that the stress was reduced as the number of cycle increased.
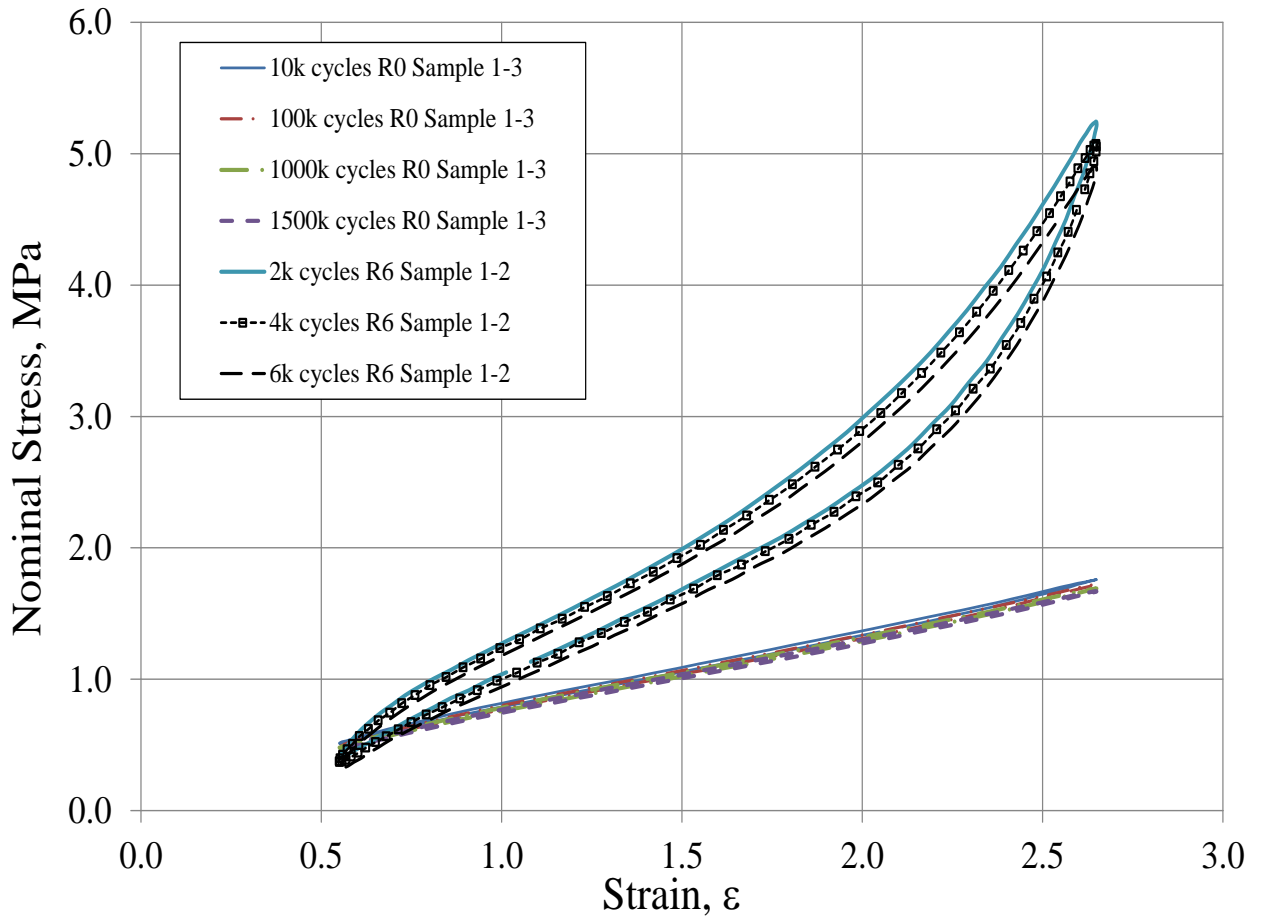
Figure 7.29: Stress strain curves of R0 and R6 obtained from the load-displacement data.

Figures 7.30 and 7.31 show the load as a function of number of cycles for R0 and R6 respectively. It is apparent that the loads for each test piece at the maximum and minimum positions are scattered within a band of ±10%.
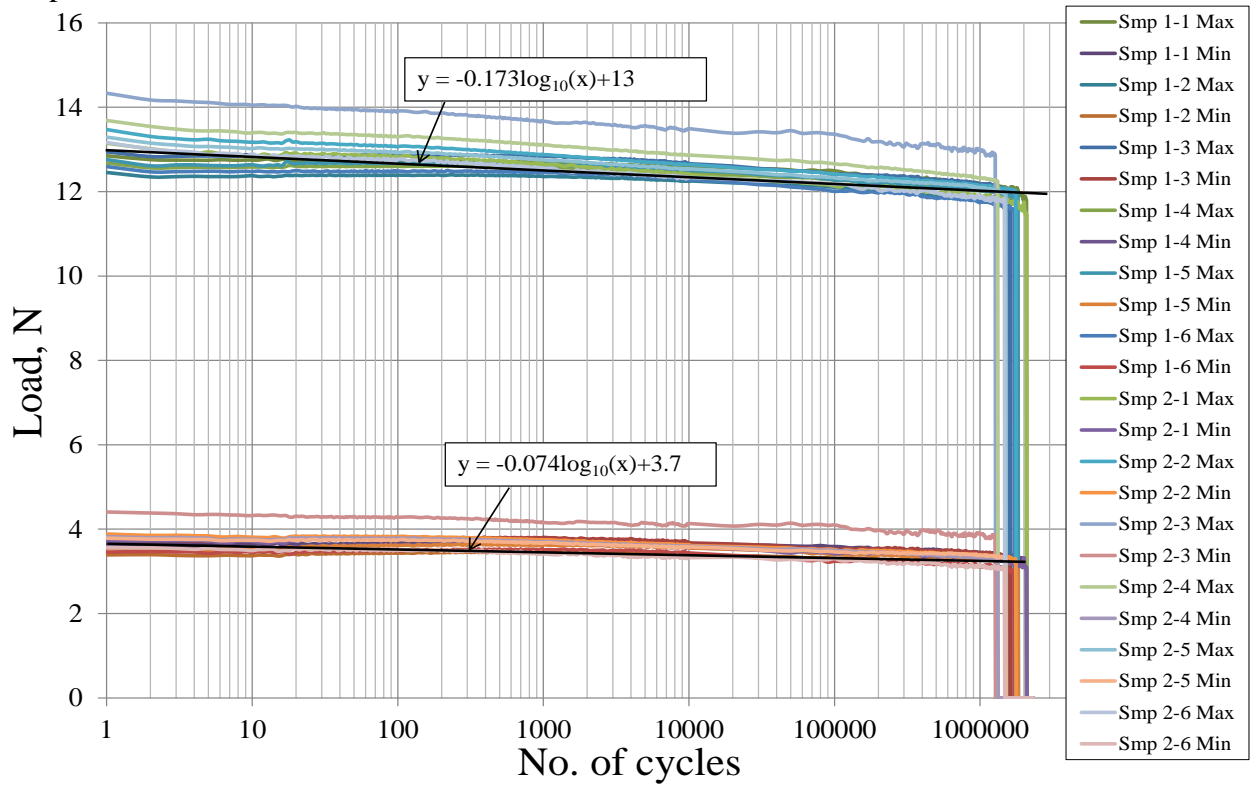
Figure 7.30: Curves of load as a function of number of cycle for R0, (160±105% strain).
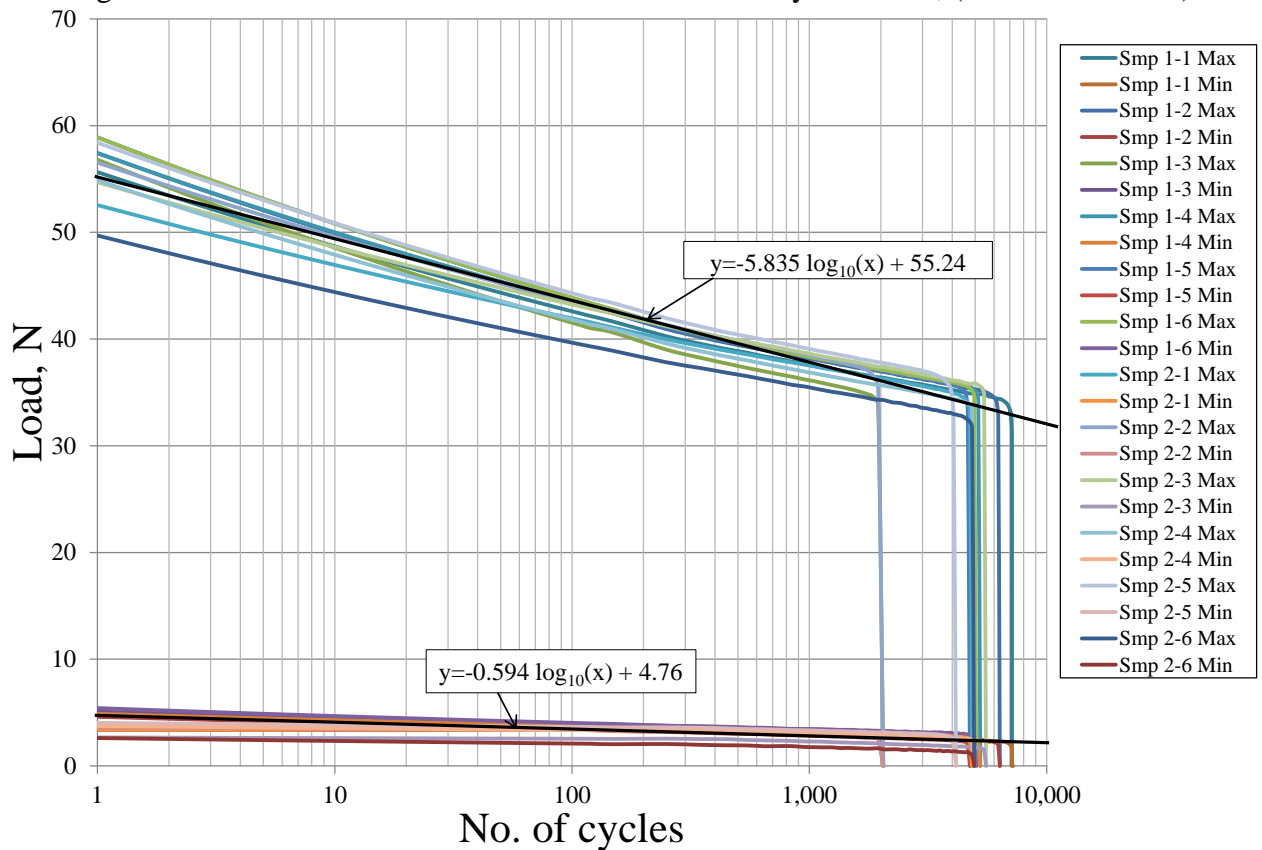
Figure 7.31: Curves of load as a function of number of cycle for R6, (160±105% strain).

The relaxation rate was investigated by introducing trendlines of each compound (R0 & R6) at maximum and minimum position (see Figures 7.30 and 7.31). The trendlines were made based on the observation by naked eyes and then their equations were determined using Microsoft Excel 2010. The cyclic stress relaxation rate is given by

$$S = \frac{f_{Ni} - f_{N1}}{f_{N1} \times log_{10}\left(\frac{N_i}{N_1}\right)} \tag{7.3}$$

where f_{Ni} is the peak nominal stress after Ni cycles, and the reference value was taken after $N_1=1$ cycle. Experimental as % per tenfold increase in number of cycles, the cyclic relaxation rates for maximum and minimum stresses from these trendlines are (1.3%, 2.0%) and (10.6%, 12.5%) per tenfold increase in number of cycles for R0 and R6 respectively.

It can be seen that the minimum strain of the cycle affects the stress relaxation rate, provided it is 55% or more. It is deduced that cyclic loading has little effect on the stress relaxation at 265% peak strain. The cyclic stress relaxation rate of R6 is quite similar compared with the results from Kingston & Muhr (2007) which their stress relaxation is 14.1% and 11.9% with cyclic creep from Pond (1989). It would be expected that the strain amplitudes affected the cyclic relaxation rate of the rubber compound.

7.4 Conclusions

(1) Tensile test pieces with an edge crack provide a simple method to determine how the crack growth rate depends on the energy release rate. The most common method used to estimate effective flaw size in rubber is by using it as a parameter to fit the fatigue lifetime Equation (3.17) simplified to incorporate only the measured power law crack growth term to the measured fatigue life. The power law under-predicts the crack growth rate in the linear region. The power law seems to give less strain-dependent values for effective flaw size for natural rubber than does the full theory. While this effective flaw size may not correspond to the size of a real feature in the material, it is considered sufficiently representative to be useful for predicting the fatigue life of the material. Values for effective flaw size determined in conflict with Kingston & Muhr (2013) for unfilled natural rubber with antioxidant (R3) lie within the range 29 to 92μm depending on the strain in the determination, whereas for unprotected NR (R1) the strain-dependence of the values was larger, and within a range 11 to 149μm.

(2) If the flaw size is below c_0, the fatigue life depends on the rate of ozone attack, which may not be well quantified. Furthermore, for c_i slightly greater than c_0, there is a lot of scatter in the fatigue life (see Figures 7.18 and 7.19). It is believed that some flaws will grow very slowly under ozone attack, others will grow much faster due to mechanical crack growth. In order to maximise the fatigue life of a rubber material, it is best if $c_i < c_o$ so that the flaws in the material do not grow mechanically.

(3) A 12-station fatigue test machine integrated with a Labview data logging was successfully developed. This machine can be used to apply a wide range of strain amplitudes in either relaxing or non-relaxing conditions. For the fixed strain conditions (160±105%) used to screen candidate rubbers, EDS19 performed the best compared both to the same unfilled rubber with antioxidant 2246 or no antioxidant in place of HPPD, and a wide range of filled rubbers.

(4) Dynamic stress-strain loops and cyclic stress relaxation rates can be estimated from the data logged during fatigue tests on dumb-bells.

(5) There is an issue with the theory expressed in Equation 3.17 that the effective flaw size determined depended in this work on the strain magnitude.

(6) In these tests being constant strain, the modulus of the test rubber correlates inversely with fatigue life.

Chapter 8

Experimental: Investigation of the Properties of Natural Rubber with Thin Coatings

Earlier chapters have dealt with the investigation of untreated samples subjected to different tests. Here protection by surface coatings is examined.

8.1 Introduction

Surface coatings of rubber are available to provide proctection from bio-fouling or chemical agents. A protective layer formation to address the reaction between a chemical antiozonant and ozone was first suggested by Erickson et al. (1958). It should also be mentioned that certain waxes and antiozonant/antioxidant paraphenylene diamines offer good protection for rubber engineering products and enhance the fatigue life of natural rubber by forming protective layers of surface "bloom". A range of antidegradants is available for natural rubber with each enhancing one or more aspects of resistance to environmental degradations such as flex cracking resistance, ozone resistance and oxidation resistance (Lewis 1972). Such antidegradants are mixed into the rubber, but are slowly used up in service due to chemical reactions, evaporation and leaching. To avoid the problem of loss of antidegradants from NR through leaching an alternative strategy might be to cover natural rubber with a coating that can accomodate large strains and exhibit a much higher resistance to ozone attack and UV-initiation of photo-oxidation than NR. However, it needs to be confirmed that such coatings are effective for the intended levels of in service strain.

In the investigation now reported, coatings were applied to natural rubber dumb-bells to compare their behaviour with an antioxidant filler free natural rubber.

8.2 Material and Test Procedures

The coated and non-coated rubbers are EDS14 (TARRC 1979) without any antidegradant component as specified in Chapter 4 - 4.2 (designated R2). The first coating investigated was supplied by Lord Corporation. Lord High Performance Coating (HPC)-5B is a room temperature curing coat which is said to feature "robust adhesion and exceptional mechanical properties" (Lord Technical leaflet, 2010). Lord Corporation claimed that their coating improved the fatigue life of rubber and provided ozone protection. According to the material safety data sheets, the composition of HPC-5B includes 3-aminopropyltriethoxysilane (<5%), di-isobutyl ketone (<5%), isobutyl ketone (60-100%)

and trimethoxyvinylsilane (<5%). The rubber to be coated in first treated with the primer Chemlok 7701. The composition of Chemlok 7701 includes Ethyl acetate (60-100%) and Trichloroisocyanuric acid (<5%).

8.2.1 Ozone Exposure Test for Lord High Performance Coating

Eight strips of nominal dimensions $150 \times 5 \times 2$mm were cut from the cured nominal 229mm square 2mm thick rubber sheet. Chemlok 7701 and elastomeric coating Lord HPC-5B were applied to coat six (Oz-3 to Oz-8) of the eight test pieces as specified in the upper portion of Table 8.1.

All eight test pieces were stretched to 20% strain using tension clamps. A reference length was marked out on each test piece to facilitate subsequent measurement of the strain. The cut edges of each sample were coated with wax to protect them from ozone attack and hence prevent the growth of cracks from the flaws introduced by the cutting process. Wax was also applied to the rubber surface near to the clamping jig to protect this area of stress concentration in each test piece.

In the ozone chamber, the ozone concentration was 50pphm and the temperature was maintained at 40 $^{\circ}$C. The overall test duration was 72 hours. The surface of each test piece was inspected using the 'Peak scale lupe 7x'(handy) microscope every 24 hours. To record the extent of surface cracks, light micrographs of the top and bottom surfaces were taken using an Olympus S2X7 Stereo light microscope. Throughout these measurements each sample remained in the same 20% strain state. Results for the ozone-exposed test pieces are reported in Section 8.3.

8.2.2 Tensile Strength Test

These tests will be undertaken for two distinct coatings of R2 rubber (mix specified in Chapter 4 - 4.2).

Twelve tensile dumbbells (Type 2, BS ISO 37:2005) were cut from a second cured 2mm sheet. Lord Chemlok 7701 [Primer] and HPC-5B [High Performance Coating 5B] were applied to coat nine (Ts-4 to Ts-12) of the twelve tensile dumb-bells detailed in lower section of Table 8.1. Each coating is approximately 40 to 60μm thick. All sample preparations were conducted in a TARRC fume cupboard.

Table 8.1 identifies samples with/without coating and the coating procedure for different coating thicknesses.

Table 8.1: Procedure of used to coat the R2 samples for ozone and tensile strength tests.

No. of tespiece and ID.	Cleaned all rubber surfaces with ethanol	Pre-treatment with Chemlok 7701 by dipping. Dried for 30minutes.	Dipped in the HPC-5B and dried for 30 minutes.	Second dip in the HPC-5B and dried for 30minutes.	Third dip in the HPC-5B and dried for 30minutes.	Average Thickness, mm
Oz-1.	√					2.05
Oz-2.	√					
Oz-3.	√	√	√			2.11
Oz-4.	√	√	√			
Oz-5.	√	√	√	√		2.15
Oz-6.	√	√	√	√		
Oz-7.	√	√	√	√	√	2.17
Oz-8.	√	√	√	√	√	
Ts-1.	√					1.99
Ts-2.	√					
Ts-3.	√					
Ts-4.	√	√	√			2.03
Ts-5.	√	√	√			
Ts-6.	√	√	√			
Ts-7.	√	√	√	√		2.11
Ts-8.	√	√	√	√		
Ts-9.	√	√	√	√		
Ts-10.	√	√	√	√	√	2.13
Ts-11.	√	√	√	√	√	
Ts-12.	√	√	√	√	√	

Note: Oz - Ozone test
Ts - Tensile test

The second coating investigated is a cyanacrylate adhesive (Wickes – Instant Super Glue) which had to be applied using a metal rod. Such a coating is stiff and the investigation was intended to demonstrate the negative impact on the extensibility of natural rubber.

Three (Type 2, BS ISO 37:2005) tensile dumb-bells (Ts-13 to Ts-15) were cut from the same initial mix R2 (as specified in Chapter 4 - 4.2). Before coating the thicknesses were 2.01, 2.02 and 2.01mm respectively and with single coating of cyanacrylate adhesive thicknesses became 2.20, 2.18 and 2.21mm respectively. As for the HPC coating, the cyanoacrylate coating was dried for 30 minutes in TARRC fume cupboard.

To provide a second uncoated reference material three tensile dumb-bells (Type 2, BS ISO 37:2005; Ts-16 to Ts-18) were cut from a cured sheet of EDS14 with antioxidant (HPPD) and antiozonant added as per R15 of Table 5.3. Hence effect of additive is again examined. This compound was only subjected to tensile strength tests for comparison.

Tensile strength tests were conducted on each of Ts-1 to Ts-18 in turn using an Instron 5567 machine equipped with an extensometer. The crosshead speed was 500mm/min, a load cell of 500N was used and all the data recorded using an Instron BlueHill software program. A gauge length on the narrow part of the dumb-bell test piece was marked using a 6mm diameter white sticker. The gauge length of the test piece was 20mm in the extensometer viewfinder, which has a range of 500mm in height and 50mm in width. The initial distance between the two grips was 50mm. All the tests were carried out according to BS ISO 37:2011.

8.2.3 Fatigue Test

Fifty four tensile dumb-bells (Type 2, BS ISO 37:2005) were cut from the remaining (same mix) cured sheets of R2 (as specified in Chapter 4 - 4.2) and two lines marked in the middle section of each test piece 22mm apart. All dumbbell test pieces were cleaned using ethanol and thirty six were treated using Chemlok 7701 and HPC-5B. Eighteen of the 36 had one layer and eighteen had two layers of said coating. The coating procedure of the treatment was as in Table 8.1. All the coating preparations were conducted in a fume cabinet.

The 12-station fatigue test machine described in 7.2.4 and Figure 7.6, with an eccentric rotary drive (4.49Hz), was used to give a common displacement cycle to one end of 6 dumb-bell samples placed in the upper row of the test facility. A Labview-based system was set-up to record the data as specified in 7.2.4. Fatigue tests for 6 samples were conducted using fully relaxing cycles. For the 18 samples of each condition defined in Table 8.3, the maximum strains were 50%, 75% and 100% respectively for the first 6, second 6 and third 6 samples investigated. The stretch length of each test piece was measured accurately using vernier callipers. The temperature and humidity in the test chamber were measured using a thermo-hygrometer-clock. The average temperature and humidity were $20^{o}C$ and 52% respectively. Table 8.2 shows the average thickness of dumb-bell testpieces with and without HPC-5B coatings.

Table 8.2: The average thickness of dumb-bell testpiece.

Total of dumb-bell	Average of thickness, mm
18 testpieces without HPC-5B	2.00
18 testpieces with HPC-5B (1 layer)	2.07
18 testpieces with HPC-5B (2 layer)	2.13

8.3 Results and Discussion

Figure 8.3 shows some tested samples after 24 hour exposure to ozone. Table 8.3 records observations during the ozone test for each test piece every 24 hours. The samples without HPC-5B coating exhibited medium cracks on the rubber surface after 48 hours. In the case of strained samples coated with HPC-5B, no cracking was found on the top and bottom surfaces after 72 hours. No ozone should reach the rubber because the HPC-5B impedes transport of ozone.

Large splits

Sample No. Oz-1   Sample No. Oz- 4   Sample No.Oz- 6   Sample No. Oz-8
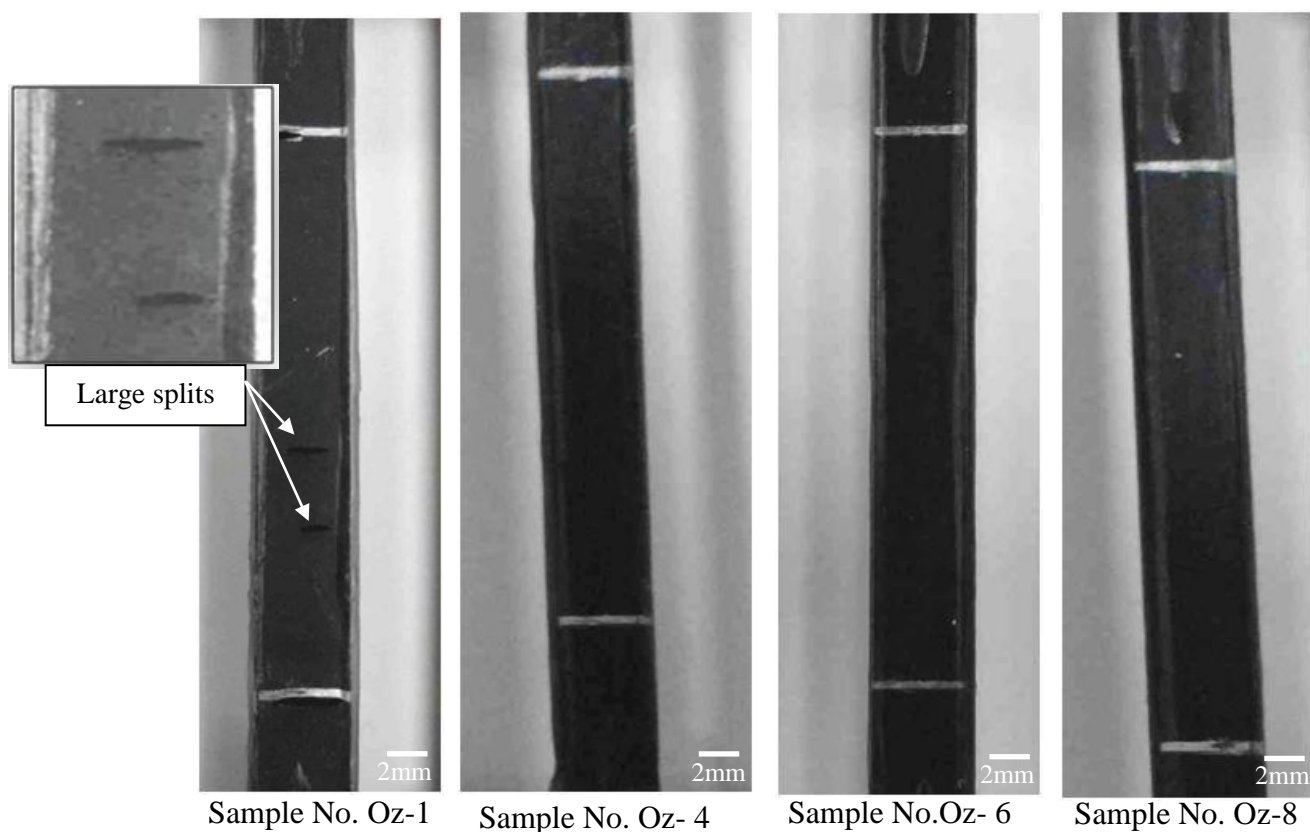
Figure 8.1: Samples stretched to 20% strain after 24 hour exposed to ozone.
– see Table 8.1 for identication of each sample (R2).

Table 8.3: Observation of test pieces after every 24 hour period.

Sample Identification	Time, hour	Test piece No.	Observations
R2 (Without HPC-5B)	24	Oz-1	Both exhibit very many small cracks, a few small splits and several extremely large splits. No bloom.
		Oz-2	
	48	Oz-1	Both exhibit very many small cracks, several small splits and several medium splits. Several extremely large, deep splits. No bloom.
		Oz-2	
	72	Oz-1	Both exhibit large hole developed in three of the extremely large splits. Very many small cracks, several medium splits and several large splits. Several extremely large splits. No bloom.
		Oz-2	
R2 with HPC-5B-1 (Single layer)	24	Oz-3	No cracks, no bloom.
		Oz-4	
	48	Oz-3	No cracks, no bloom.
		Oz-4	
	72	Oz-3	No cracks, no bloom.
		Oz-4	
R2 with HPC-5B-2 (Double layer)	24	Oz-5	No cracks, no bloom.
		Oz-6	
	48	Oz-5	No cracks, no bloom.
		Oz-6	
	72	Oz-5	No cracks, no bloom.
		Oz-6	
R2 with HPC-5B-3 (Triple layer)	24	Oz-7	No cracks, no bloom.
		Oz-8	
	48	Oz-7	No cracks, no bloom.
		Oz-8	
	72	Oz-7	No cracks, no bloom.
		Oz-8	

Figure 8.2 (a), (b) and (c) presents the tensile stress results as a function of axial strain for samples Ts-1 to Ts-18. The tensile strength and elongation at break reduced when the HPC elastomeric coating layer was applied on the rubber surface (see (a) and (b)). All the coatings started to peel at 300% strain during the tensile stress-strain tests as illustrated in Figure 8.3.
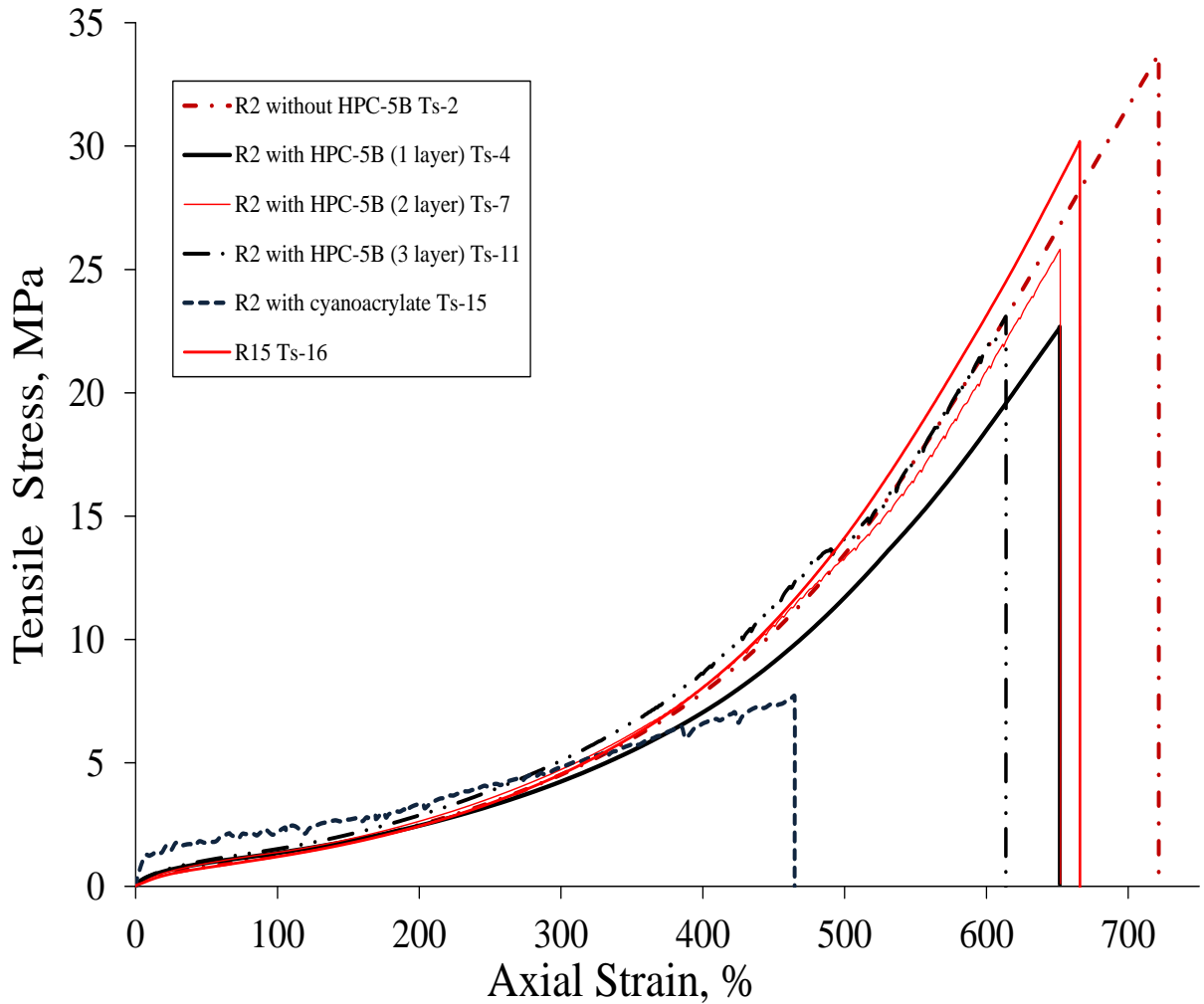
Figure 8.2: Tensile stress-strain for the dumb-bell test pieces of R2 and R15 reach median values of tensile strength.

The stress-strain curves are less smooth for test pieces with 3 coating layers. This characteristic may be attributed to extensometer lost marks due to surface peeling. Table 8.4 indicates the overall tensile properties for each dumbbell testpiece. The median values (bold font) were taken between the maximum and minimum values of each property. Rubber samples coated with cyanoacrylate show lower tensile strength and elongation at break compared to other rubber samples.

The coated dumb-bell test pieces show less tensile strength and less elongation at break compared to the uncoated dumb-bell test pieces. In addition, the coated test pieces with 3

layer of HPC-5B show a reduction of the tensile strength and the elongation at break. This is due to the test pieces became more stiff and tend to decrease their properties. In contrast, the modulus of the 3 layer coated dumb-bells test pieces was slightly inreased.

Table 8.4: Tensile properties of each dumb-bell test piece.

Surface treatment	Sample ID	Strain					Tensile strength, MPa	Elongation at break, %
		100%	200%	300%	400%	500%		
		Modulus, Mpa						
(R2) No layer	Ts-1	**1.21**	**2.38**	**4.35**	**7.59**	**13.12**	32.78	713
	Ts-2	1.24	2.48	4.52	7.84	13.46	**33.73**	**722**
	Ts-3	1.21	2.36	4.32	7.54	13.09	33.91	724
(R2) 1 layer (HPC-5B)	Ts-4	1.35	2.45	4.24	7.05	11.70	**22.66**	653
	Ts-5	1.38	2.71	4.85	8.28	14.05	22.47	608
	Ts-6	**1.35**	**2.51**	**4.43**	**7.50**	**12.62**	22.93	**635**
(R2) 2 layer (HPC-5B)	Ts-7	1.37	**2.63**	**4.73**	**8.08**	**13.28**	**25.80**	654
	Ts-8	**1.40**	2.69	4.85	8.28	13.98	26.04	**653**
	Ts-9	1.41	2.63	4.61	7.64	12.58	22.66	645
(R2) 3 layer (HPC-5B)	Ts-10	**1.55**	**2.94**	**5.17**	**8.69**	13.39	22.36	589
	Ts-11	1.51	2.87	5.09	8.61	**14.07**	**23.08**	**614**
	Ts-12	1.60	3.13	5.53	9.64	14.50	25.39	626
(R2) 1 layer (cyanoacrylate)	Ts-13	**1.95**	3.11	4.71	-	-	5.09	319
	Ts-14	1.94	**3.25**	**5.34**	8.58	13.41	17.71	572
	Ts-15	2.19	3.32	5.25	7.63	-	**9.41**	**468**
(R15) No layer	Ts-16	1.20	2.44	4.54	8.05	14.13	**30.18**	666
	Ts-17	**1.18**	**2.40**	**4.39**	**7.52**	**12.84**	30.25	691
	Ts-18	1.16	2.30	4.13	6.98	11.72	29.20	705

-**Bold** font is the median value

Figure 8.3 illustrates test piece surfaces after testing samples with various layer of coating of HPC-5B. The coatings failed when the test pieces were stretched beyond 300% strain in the tensile strength tests.

<center>(a.)   (b.)   (c.)</center>
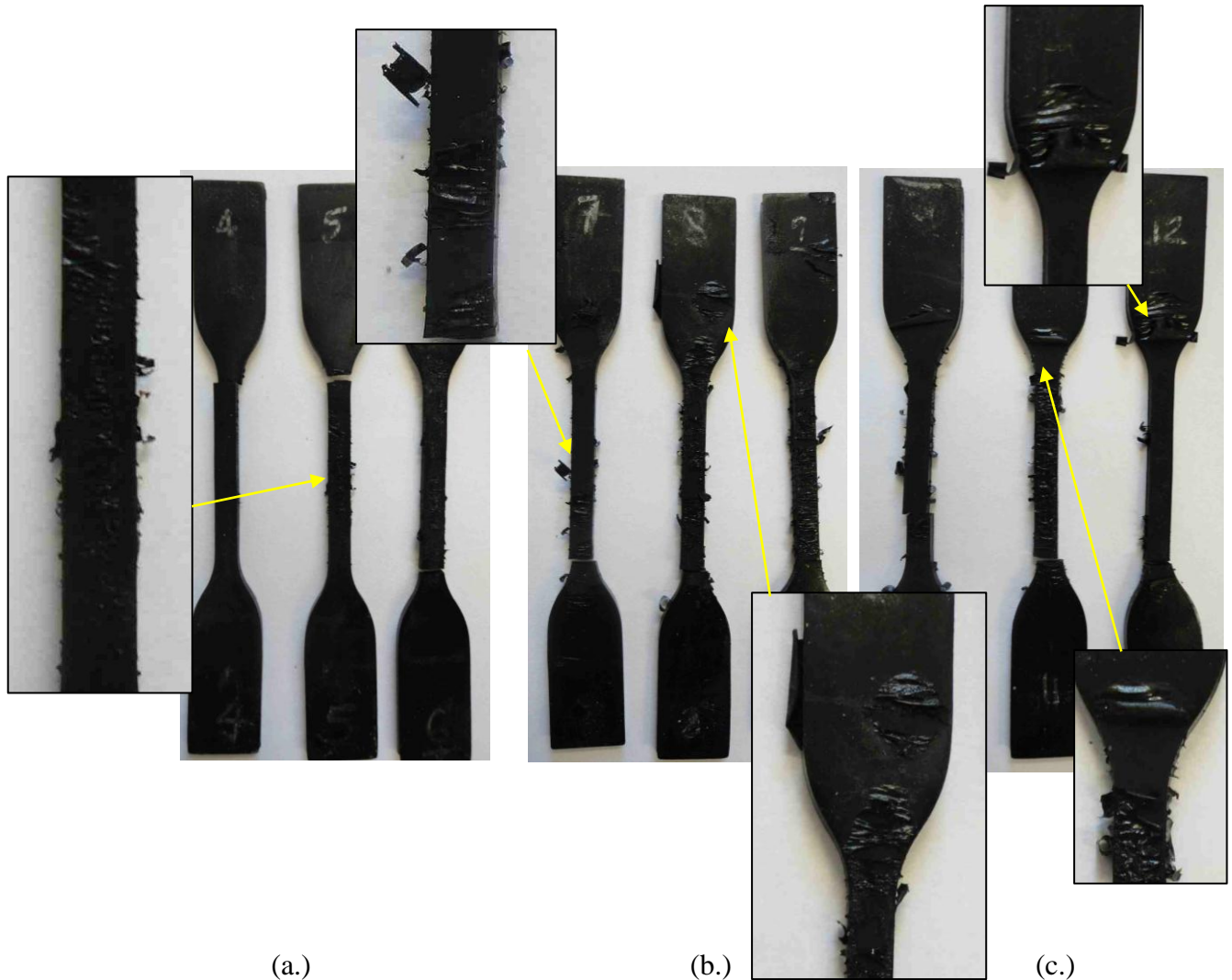
Figure 8.3: Photographs taken after the tensile tests showing that the coating layer has peeled from the rubber surface.
(a.) One layer of HPC-5B. (b.) Two layer of HPC-5B. (c.) Three layers of HPC-5B.

The peeling surfaces are more obvious for the dumb-bells coated with 2 and 3 layers of HPC compared to the dumb-bells coated with a single layer of HPC. Flaking layers of HPC were markedly observed at the narrow part of the dumb-bell test pieces.

Figure 8.4 provides photographs of the central part of dumb-bell coated with cyanoacrylate after conducting a tensile strength test. The rubber surface became stiff due to the cyanoacrylate coating. Since the bond is good, cracks forming in the high-modulus cyanoacrylate coating result in high local stresses in the rubber, so that cracks propagate into the rubber (as shown in Figure 8.4) and hence reduce the tensile strength and

elongation at break. A similar though less extreme mechanism could operate when the HPC-5B coatings fail.
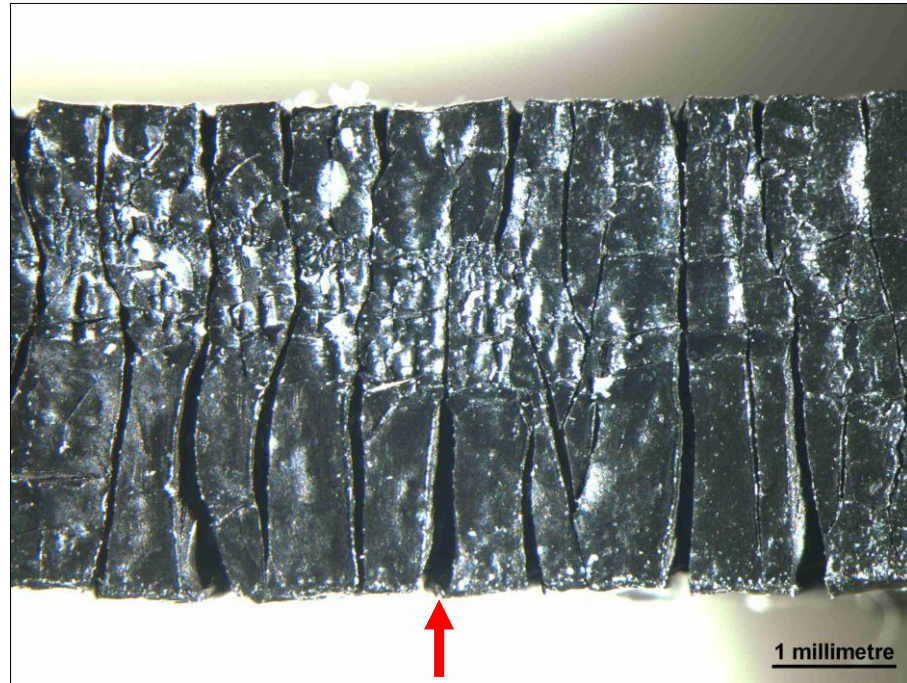
(a.) Dumb-bell Ts-13 at 20% strain condition (Top view).
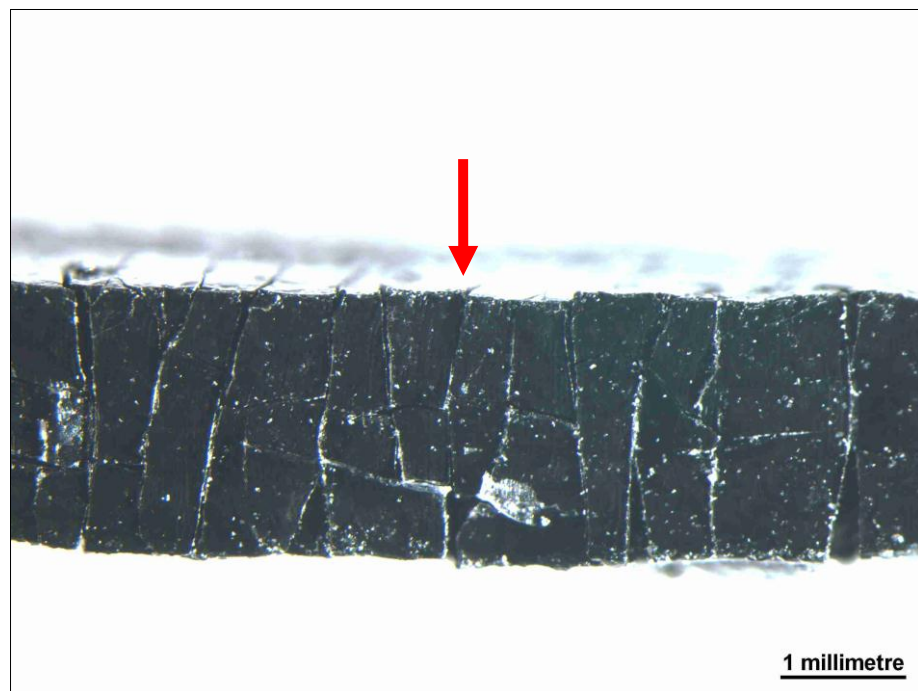
(b.) Dumb-bell Ts-13 in unstrained condition (Side view).

Figure 8.4: Example of the centre part of dumb-bell (R2) coated with cyanoacrylate after tensile strength test. Red arrow indicate same corresponding transverse section of sample.

Table 8.5 and Figure 8.5 indicate number of cycles prior to sample failure in the fatigue tests using dumb-bell test pieces with and without HPC-5B. The fatigue life became shorter for the test pieces coated with HPC-5B and tested at 75% and 100% strain. However, fatigue life was longer on the test pieces coated with 2 layers of HPC-5B and tested at the lower 50% strain. Hence coatings appear beneficial for strains up to 50% strain.

Table 8.5: Fatigue test results of R2 dumb-bells coated with and without HPC-5B.

Sample condition	Max. strain, %	No. of kilo cycles							
		Test piece 1	Test piece 2	Test piece 3	Test piece 4	Test piece 5	Test piece 6	Standard Deviation	Mean
Without HPC-5B	50	607.9	399.1	318.9	399.9	355.9	135.3	152.5	369.5
	75	131.4	121.2	61.8	76.9	79.9	124.8	29.8	99.4
	100	38.9	34.8	49.8	44.0	47.4	54.4	7.2	44.9
1 layer of HPC-5B	50	431.4	487.8	609.0	642.9	342.1	314.7	135.3	471.3
	75	63.4	74.4	28.1	92.0	84.2	84.3	23.2	71.1
	100	475	40.4	40.0	47.5	50.0	31.2	6.9	42.8
2 layers of HPC-5B	50	580.7	517.4	336.9	806.6	995.2	475.8	240.3	618.8
	75	50.7	59.3	54.2	37.1	52.2	64.5	9.3	52.9
	100	47.4	40.3	40.0	47.5	49.9	31.1	7.0	42.7
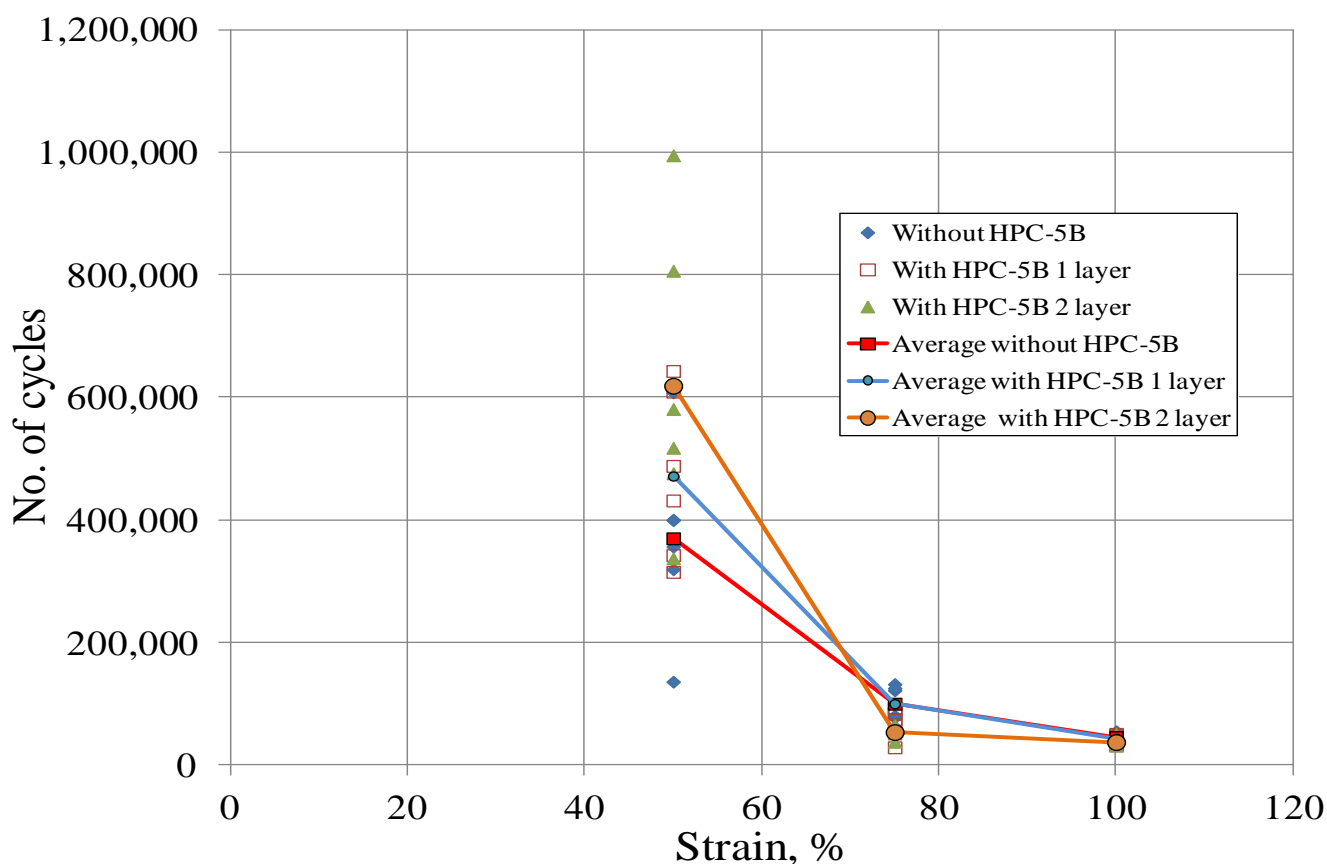
Figure 8.5: Results of fatigue test in relaxing condition at 50%, 75% and 100% strain.

8.4 Conclusions

(1.) The experimental investigation clearly indicates that the HPC-5B coating impedes crack formation on test pieces strained to 20% when subjected to ozone exposure. The tensile strength of dumb-bells of R2 coated with two layers of HPC-5B were slightly higher compared to those coated with one or three layers; none were as high as uncoated ones.

(2.) Rubber samples (R2) coated with cyanoacrylate show a high apparent modulus at low strain and very low strength because of the high modulus and low elongation at break of the cyanoacrylate and its good adhesion to the rubbers. This results in cracks being driven into the rubber when the coating fails. It is suggested that this mechanism also explains the negative impact of HPC-5B on tensile strength and elongation at break.

(3.) It is concluded that cracks form in the HPC coating at moderate strain and act as stress raising initiators, driving cracks deep into the rubber and reducing the tensile strength. In the tensile strength tests the coatings fractured and there was a loss of adhesion to the rubber surface after achieving a strain of 300%.

(4.) The fatigue life is slightly increased by the addition of HPC-5B coatings for a maximum strain amplitude of 50% but reduced for higher maximum cyclic strain amplitudes. The coating layer might be appropriate for rubber components subjected to a low strain range, when fatigue life is dominated by ozone attack.

Chapter 9

Experimental and Modelling: Naturally Aged Natural Rubbers

Having tested fresh samples with and without coatings, we now look at existing aged artefacts for evidence of degradation. Some of the work has been undertaken in collaboration with researchers with other institution as indicated later in the chapter. Care is taken to quantify inhomogeneity of rubber properties caused by ageing.

9.1 Introduction

Economic viability of a rubber based wave energy extractor device will require successful operation and survival in seawater for a long period of time. Knowing rubber is susceptible to UV light, oxidation and ozone attack, helpful insight might be gained by examining the effect of ageing on the rubber properties of historical rubber artefacts.

High temperature ageing of thick vulcanized natural rubber indicates that the outer layers initially soften followed by hardening (Knight & Lim 1975, Lindley & Teo 1977). Lindley and Teo (1977) concluded that above a temperature of about 80°C, the reaction of oxygen and elastomer is so rapid in relation to the diffusion rate that oxygen can penetrate only a small depth before being absorbed, resulting in non-uniform degradation, and in the exterior, a highly oxidised surface "crust" eventually forms. Lindley & Teo (1977) suggested no crust would be formed at ambient temperature for times less than ~ 144 years, in conflict with the observations on naturally aged natural rubber by Kamarudin & Stevenson (1992). Investigations on naturally aged rubber components by Fuller & Roberts (1999) and Fujita et al. (1995) emphasise that far from the surface material properties are fairly stable over a very long period of time.

To cast further light on such issues, a small portion of the Bramfield tyre (see Chapter 6), aged over 80 years, and the Pelham Bridge bearing, aged over 50 years were investigated in detail to produce a more unified analysis.

Fresh results for the near surface properties gradient of some samples investigated previously by Fuller & Roberts (1999) and additional work on original samples of Bramfield tyre and the Pelham Bridge bearing should provide the sought insight. Furthermore a numerical model for the ageing process was developed. This quite distinct study should help in the assessment of the longevity of rubber, the primary material for the development of different wave energy devices.

9.2 Aged Rubbers

The source of each rubber artefact and the results are described next; prior to providing test procedures, results and development of numerical tools.

9.2.1 Bramfield Tyre

A pair of steel cartwheel rims of diameter 775mm and width 95mm, with approximately 40mm thick solid rubber tyres attached was discovered in Bramfield Wood (grid reference TL284169) about 11km north west of Hertford in April 2004. Figure 9.1 indicates the location of Bramfield Wood. Figure 9.2 provides a long shot of the surrounding environment at Bramfield Wood whereas Figure 9.3 shows the solid rubber tyre discovered and later brought to TARRC to investigate the state of rubber.

It is believed that the rims would have originally been fitted to wooden spoked (artillery-type) wheels. The only other readily identifiable items at the site were two steel hubs incorporating brake drums, of a design to accommodate wooden spokes, probably manufactured not later than the 1920s (see Figure 9.4). It is possible that the complete vehicle had not been abandoned at the site, but only a few elements of it, perhaps just those with significant steel content. However, it seems more likely that the steel and rubber parts had simply outlasted the wooden parts, since they comprised a full two-wheel set with no other unrelated artefacts and some ash members in a very poor state of presentation were also found as shown in Figure 9.5.
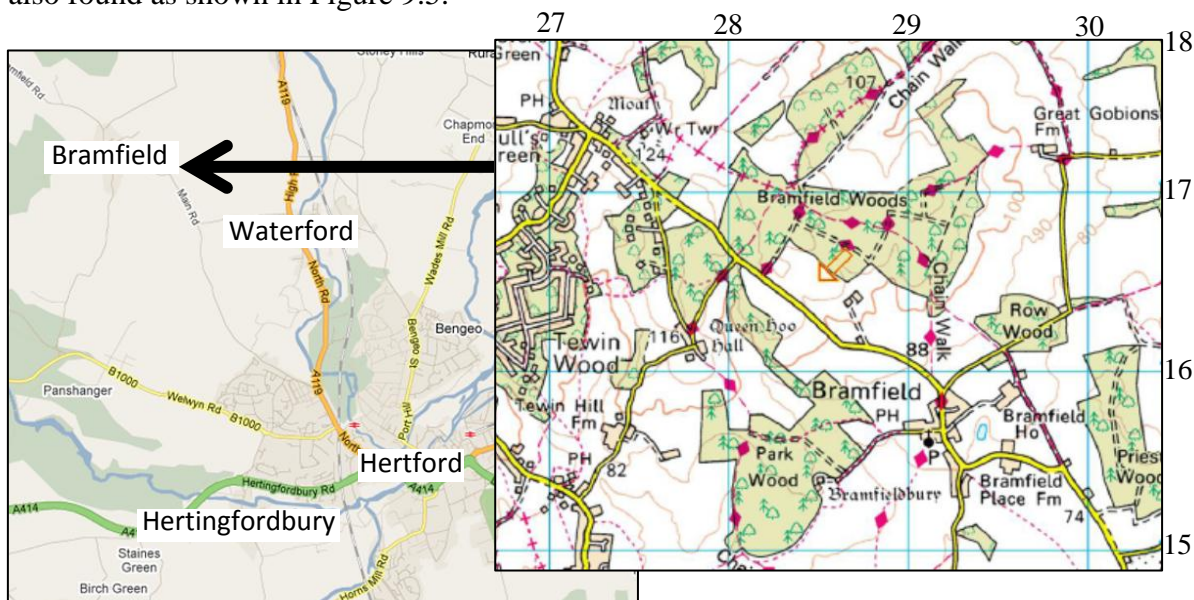
Figure 9.1: A map of the location of Bramfield Wood.The grid on the detailed map shows 1km squares from area TL of the UK Ordinance Survey (approximately Lat 51° 41^oN, Long 0° 27'W at 000 000). Grid reference for tyre location is TL284169.

Figure 9.2: A long shot of the surrounding environment at Bramfield Wood where the tyres were found.

Figure 9.3: Solid rubber tyre from Bramfield Wood (left and centre) and a small portion of the tyre was taken for investigation (right).

Figure 9.4: Close-up view of wood.

Figure 9.5: Close-up view of steel hub and axle.

9.2.2 Pelham Bridge Bearing

The first bridge in the United Kingdom to be supported by laminated rubber steel bearings is the Pelham Bridge in Lincoln, England. The original bearings (Figure 9.6) were manufactured by the Andre Rubber Company in 1957 (Fuller & Roberts 1999). Samples cut from one of the bearings removed in 1994 (Fuller & Roberts 1999, Kato et al. 1996) have since been stored indoors at TARRC.
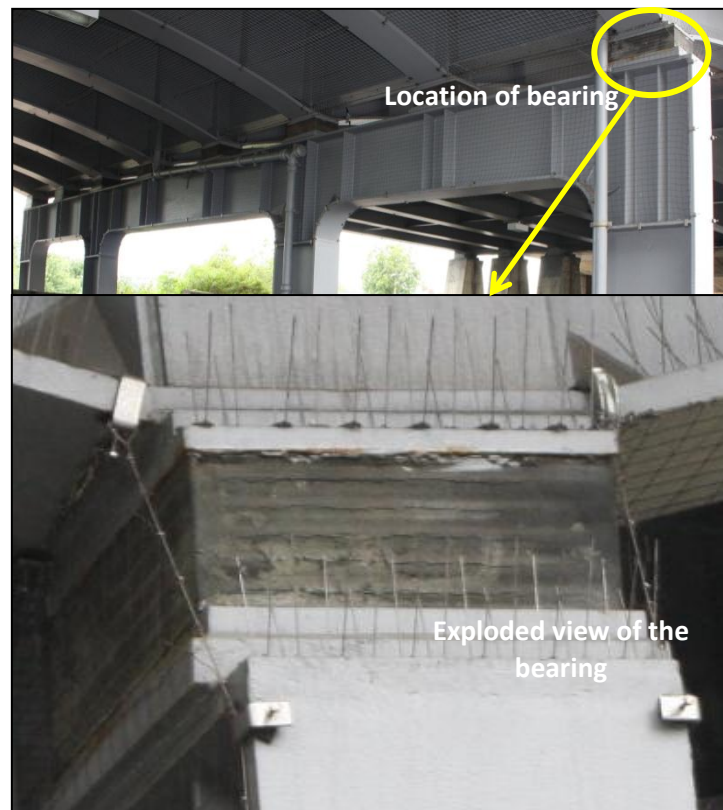
Figure 9.6: Rubber bearings in place under Pelham Bridge, Lincoln, England.

Figure 9.7 provides details of the construction of the Pelham Bridge bearings which consist of rubber steel-laminations bonded together during vulcanization as a single moulding. A rubber cover layer encapsulated the steel, protecting it from corrosion and hence achieving a maintenance - free thermal expansion bearing.
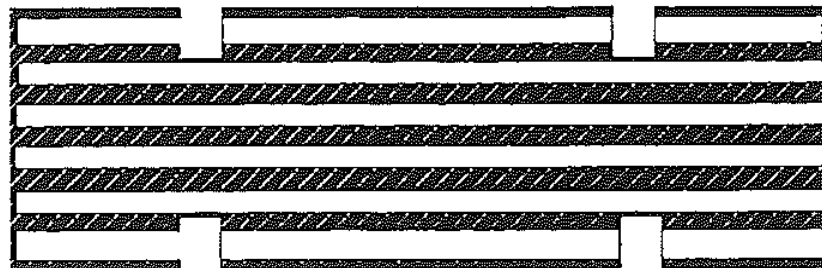
Figure 9.7: Section side view of Pelham bearing; dimensions 596 x 394 x 182 (high) mm; internal rubber layers 18 mm thick, though the middle one is closer to the nominal 20mm; steel plates 11.4mm thick except end ones which are 15.8mm.

9.3 Rubber Formulations, Test Procedures and Results

Through contact with Dr Alan Muhr, interest in examining naturally aged rubber was expressed by Dr Yann Marco and Dr Vincent Le Saux of the University of Brest (ENSTA) and Dr Paul Davies and Pierre-Yves Le Gac (PhD candidate) of IFREMER. Samples of the Bramfield tyre and Pelham Bridge bearing were supplied to each institution. Except where these institutions are indicated, the analyses were carried out by the Material Characterization Group at TARRC.

Samples of each artefact were examined for constituents, hardness, density and glass transition temperature, tensile strength and modulus. Details of analysis for each artefact are reported next.

9.3.1 Bramfield Tyre

Analysis of Constituents

Portions of a sample were cut at various depths in the profile and submitted for analyses to the Material Characterization Unit (MCU) at TARRC. Analyses were performed using Thermogravimetric Analysis (TGA), Fourier Transform Infrared (FTIR) Spectrometry, and Scanning Electron Microscope (SEM) X-ray.

TGA measures the weight of material as a function of temperature in a controlled atmosphere (air or nitrogen). The results are used primarily to determine composition.

FTIR was coupled to the TGA to examine chemical groups in the evolved gases. A sample of the acid-insoluble material from the dry ash at the end of TGA was mounted on carbon tape on a carbon SEM stub. It was coated with a thin layer of evaporated carbon to prevent it charging up in the electron beam, and then analysed by SEM X-ray to identify the major elements present.

The basic formulation of the rubber is summarized in Table 9.1 (Full details are contained in the MCU Report Ref: SBK32(MC1671)).

Table 9.1: Basic formulation from TGA.

	Rubber (wt%)	Carbon Black (wt%)	Ash (wt%)	T_{max} (^{o}C)
Surface	47.2	47.7	5.0	445
1-3mm	55.0	38.3	5.4	446
4-7mm	59.5	31.5	8.6	418
Bulk	59.2	31.9	9.0	413

The total sulfur content was determined for the bulk rubber as being 3% by weight leading to the basic formulation in Table 9.2.

Table 9.2: Rubber formulation based on the analysis results and density of individual ingredients.

Ingredients	pphr by weight	Density,[b] gcm^{-3}
Natural rubber	100	0.92
Carbon black(N550)	54	1.80
Sulfur	4.84	2.07
Ash	15	5.60*
Stearic acid	2	0.94
MBT	0.6	1.28
Extractables	1	-

*- value for ZnO
b- values taken from Gehman (1967)

The ash is likely to include zinc oxide and perhaps some clay. SEM X-ray confirmed the presence of S, Zn, Mg, Al, Si and possibly a trace of Ba. The carbon black had a mean particle size of 45.5nm, equivalent to a 'group 5 black' such as N550 (FEF). FTIR spectra for different depths from the outer surface of the sample are shown in Figure 9.8.
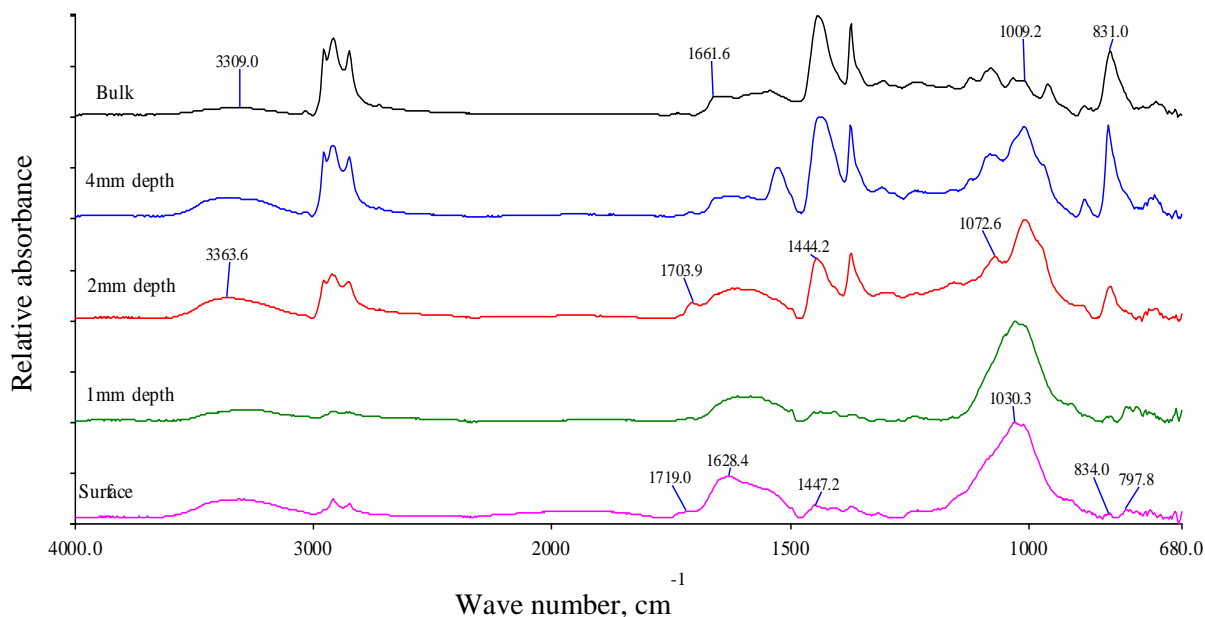
Figure 9.8: FTIR spectra (relative absorbance vs wave number) at different depths (labelled in mm) into the rubber.

The spectra reveal a rise in –OH and C=O groups with a decline in C=CH groups through the transition zone towards the surface. This behaviour is consistent with oxidative attack of the unsaturated backbone of NR (see Figure 2.2). The nature of this change is shown in Figures 9.9 and 9.10.
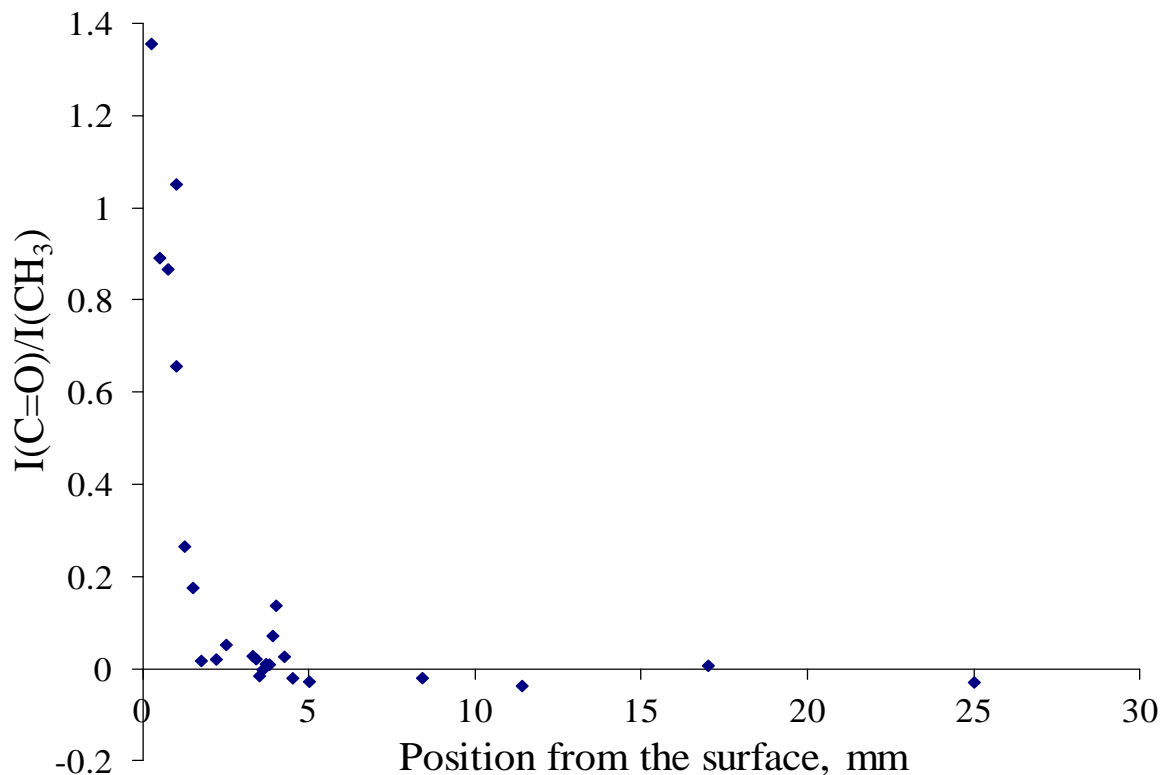
Figure 9.9: C=O intensity, at different distance from the surface (left) to bulk (right) (Le Gac, IFREMER).
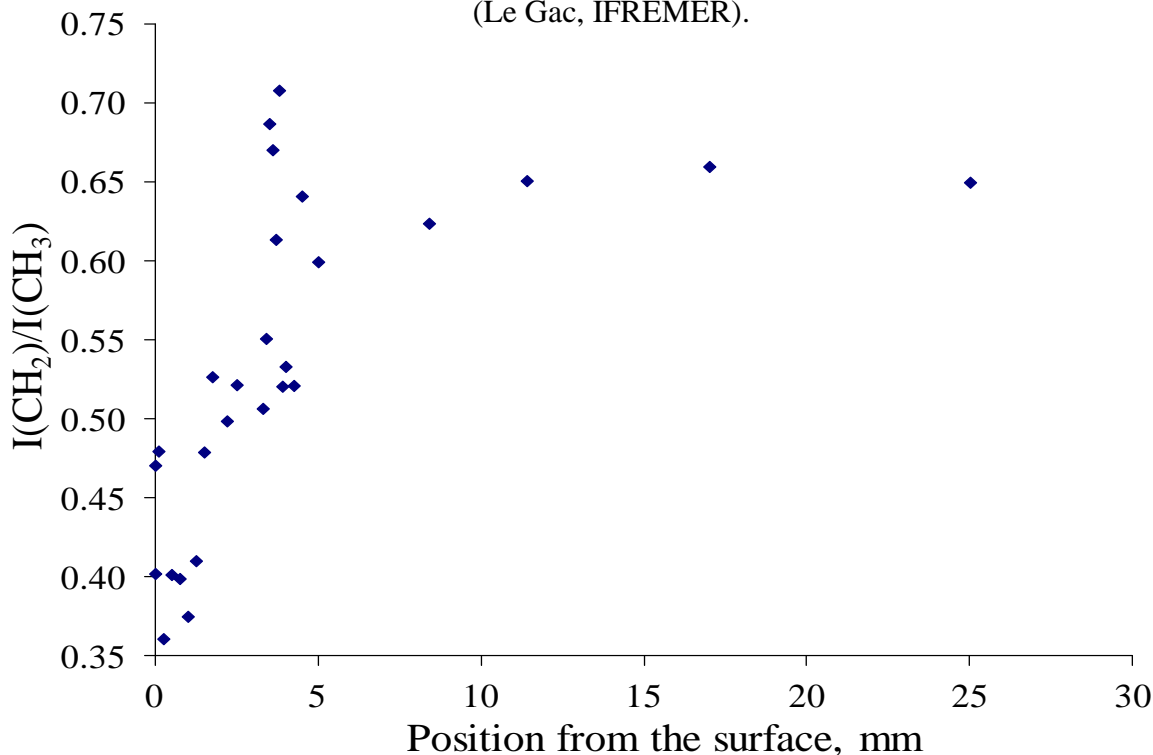
Figure 9.10: CH$_2$ intensity, at different distance from the surface (left) to bulk (right) (Le Gac, IFREMER).

Measurement of Hardness, Density and Glass Transition Temperature (T_g)

The hardness of the rubber tyre was measured by the author using a Durometer Shore A- pocket hardness gauge applied both on the exposed outer surface and on a freshly cut surface exposing the bulk rubber. Since many cracks had formed on the outer surface, great care was exercised to ensure the indenter was not offered into a crack.

The density was measured according to BS ISO 2781:2008-Method A. The test pieces used for determination of density were conditioned by leaving them open to the atmosphere prevalent in the test laboratory for at least 16 hours at 23^oC.

Portion of the tyre was cut and submitted for analyses using Differential Scanning Calorimetry (DSC) by the Material Characterization Unit at TARRC. Prior to testing the DSC had been calibrated according to an accredited procedure with accredited and certified reference material. Sample was heated at 10^oC/min. The exposed surface of the rubber was very hard and cracked as shown in Figure 9.11. However, further into the interior, the material exposed by the cut section was still soft and rubbery.
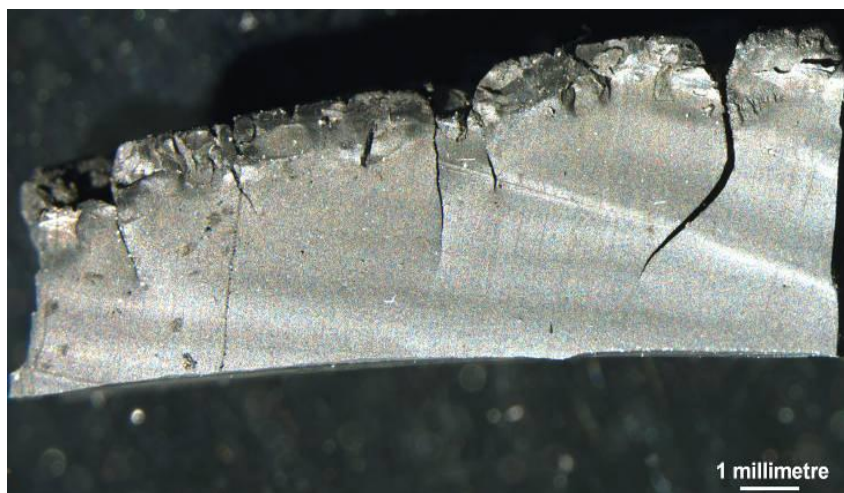
Figure 9.11: Section cut through rubber showing the hard layer
(~0.5mm thick) and cracks into the transition layer (~4mm deep).

Table 9.3 shows that very different values of hardness, density and glass transition temperature, T_g were determined for the surface crust and for the interior material.

Table 9.3: Results of hardness, density and glass transition temperature, T_g.

Pocket hardness gauge, Shore A		Density, Mg/m^3		T_g, ^{o}C	
Surface	Bulk	Surface	Bulk	Surface	Bulk
91	62				
93	63	1.381	1.259	76.3	-51.4
92	61				
Average (92)	Average (62)				

Measurements of the Tensile Modulus, Micro-Indentation and FTIR in Brest, France

The tensile modulus of aged rubber was measured using Dynamic Mechanical Analyzer DMA 2980 photographed in Figure 9.12 from TA Instrument by Pierre-Yves Le Gac (IFREMER, France). Films of rubber sample 100μm thick were cut using a Leica microtome (Figure 9.15) after cooling by liquid nitrogen.

Figure 9.12: The overview of Dynamic Mechanical Analyzer DMA 2980 (IFREMER).

The physical properties of the rubber were determined as a function of distance from the surface. Figure 9.13 illustrates tensile modulus from micro-tensile test strips. The tensile modulus is higher on the surface compared to the bulk rubber.
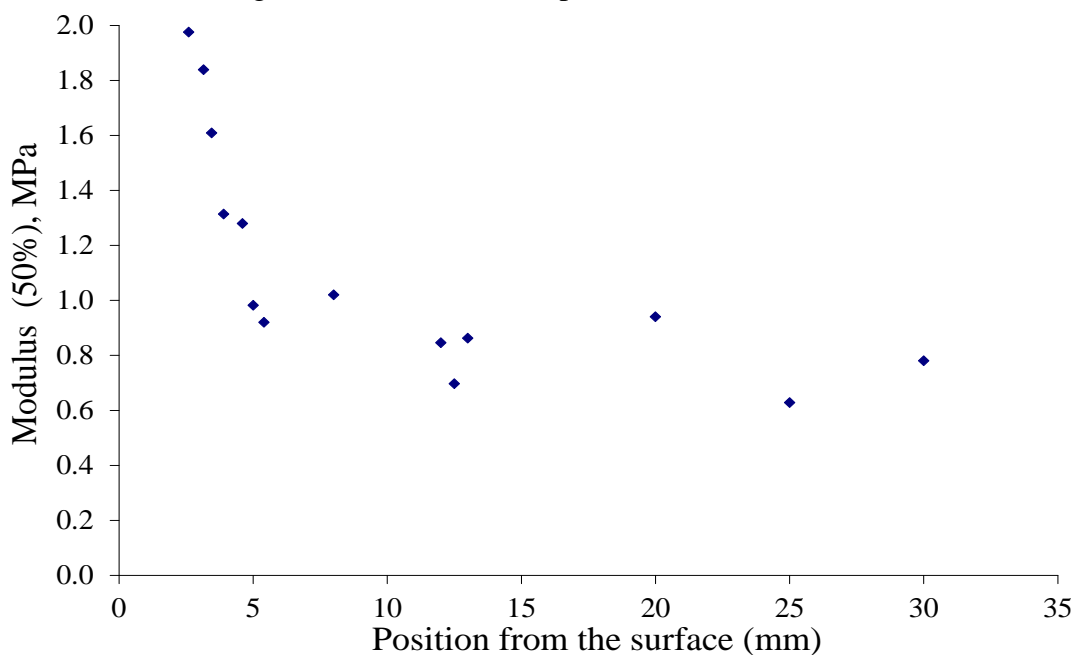
Figure 9.13: Tensile modulus (ratio of nominal stress to strain) at 50% extension at different distances from the surface (Le Gac, IFREMER).

Measurement of Reduced Modulus

Microhardness measurements were carried out at by Dr Marco at ENSTA Bretagne, using an instrument manufactured by CSM Instruments SA. Samples were 8mm long (in direction normal to the tyre surface) and 4mm wide, encapsulated in epoxy resin to improve sample handling and to ensure repeatability. Surface measurements deliberately avoided cracks. A 10mN preload was used to detect contact, followed by loading to 100mN at 200mN/min, holding for 30s and unloading. The retraction stiffness of a Vickers tip (angle: 136°) indenter was used to calculate the "reduced modulus" according to the procedure developed by Oliver and Pharr (1992) (see Appendix E for definitions).

Figure 9.14 show how the reduced modulus changes with distance from the surface. Every point in Figure 9.14 represents the mean value of up to 8 separate readings. The reduced modulus is 2 to 3GPa for the surface, more typical of glassy or highly crystalline polymers and ~10MPa for the bulk rubber. This high value for the bulk rubber suggests that the Oliver & Pharr analysis may not be appropriate for a nearly elastic material like rubber.
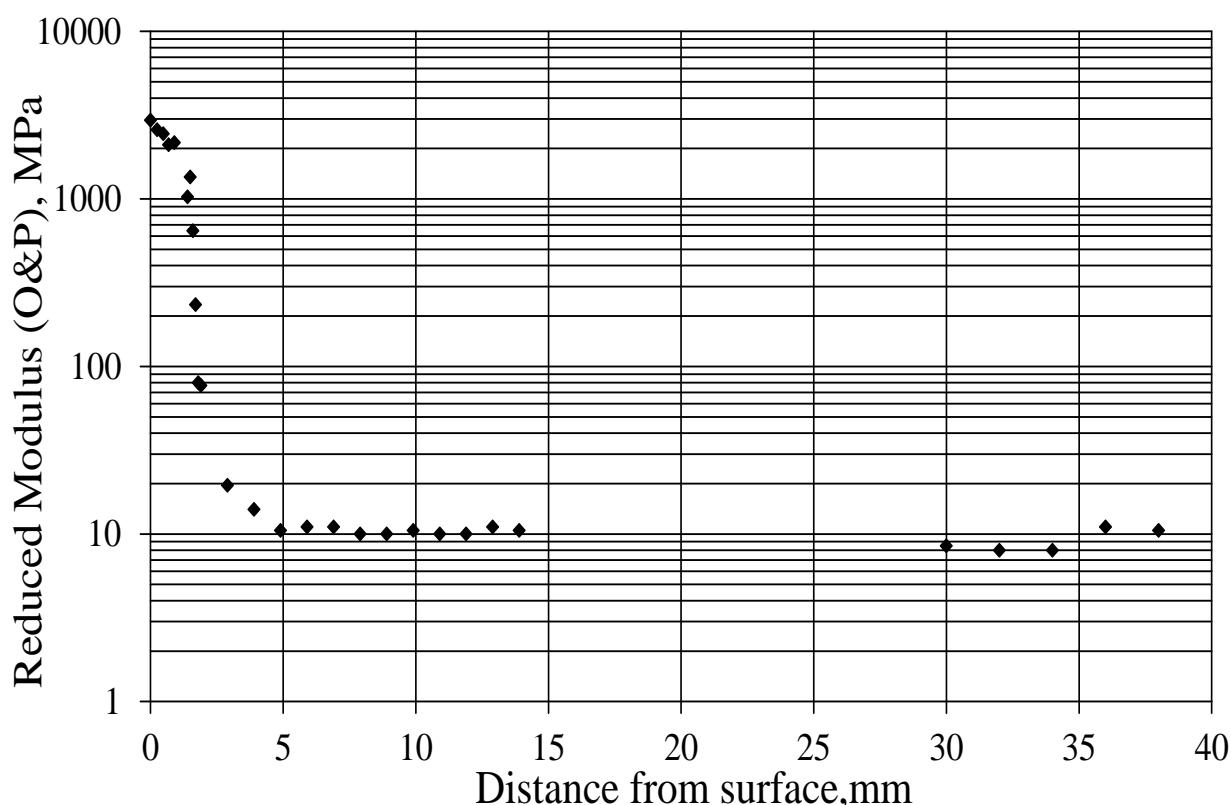
Figure 9.14: Result of reduced modulus from micro-indenter (Marco, ENSTA) according to the analysis of Oliver & Pharr (1992) at different distances from the surface.

9.3.2 Measurement and Interpretation of Light Transmission

Sections (~5x10mm) of the ~80-year old Bramfield Wood solid tyre were cut at IFREMER on a microtome. A microtome Leica RM2245 was used to cut thin layers in the range 90-500µm as shown in Figure 9.15. Liquid nitrogen was used to cool the sample to the glassy state. In the cutting process, an adjustment of the cutting blade was undertaken to obtain several microns in thickness. All the samples were sandwiched between a pair of microscope slides taped (Sellotape) together to keep the sample flat.

Figure 9.15: Cutting rubber sample using Leica microtome.

In order to measure the transmission factor, rubber test pieces of selected thicknesses (in microns) were placed between two glass microscope slides of a thickness 1.2mm each (see Figure 9.16). Light transmission was measured from a small laser module (dimension: ϕ10.5mm x 28mm (L) ±0.5mm, beam aperture: ϕ2.8mm) capable of delivering up to a 0.99mW visible red (670nm wavelength) beam from a low voltage supply as shown in Figure 9.16. Several types of neutral density filters were used to calibrate the solid state laser beam. The transmitted intensity was measured by a photometer.
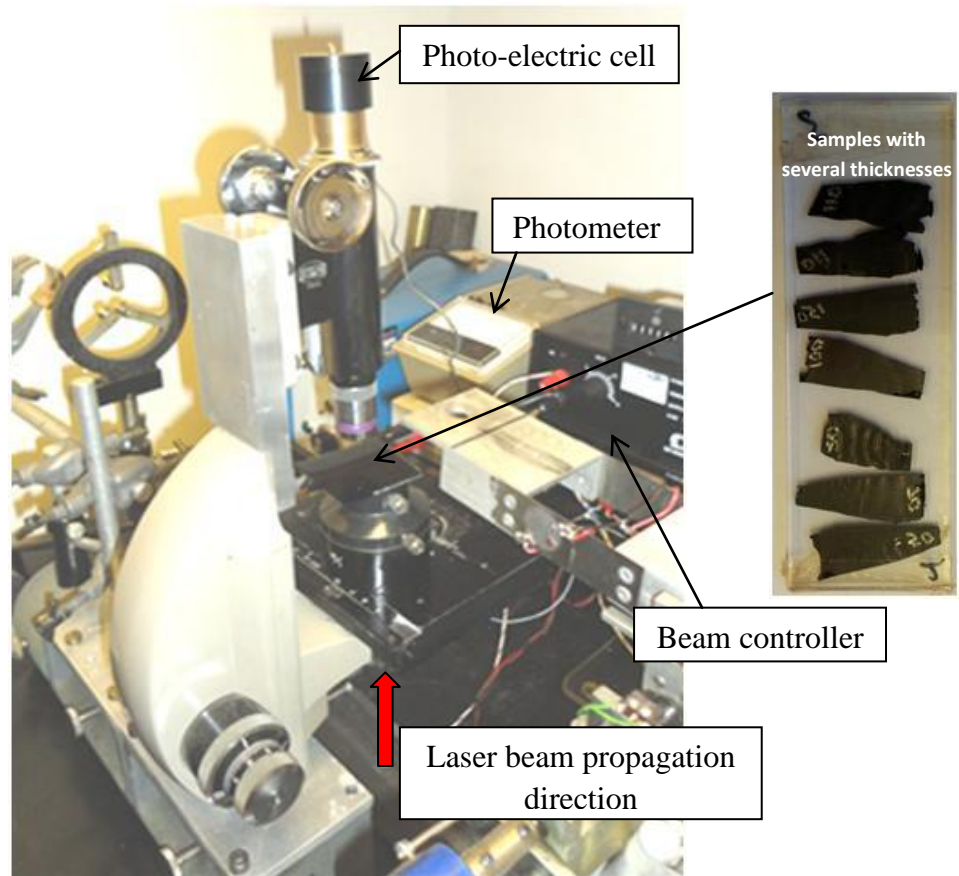
Figure 9.16: Measurement of transmission factor using a red laser with beam aperture of 2.5mm diameter.

Analysis of Measurement

Oxidation can be initiated by UV light, which will penetrate to a depth that depends upon scattering and absorption by pigments (Kubelka 1948). Making the assumption that all light incident on black particles is absorbed, the Kubelka-Munk equations are simplified (in accordance with the details of Appendix F) to a single differential equation for light intensity *I* of the form:

$$\frac{dI}{dx} = -KI \ . \tag{9.1}$$

Denoting I_o as the intensity at the front face of the sample it follows that

$$I = I_o e^{-Kx} \tag{9.2}$$

That is,

$$\ln(I) = \ln(I_o) - Kx \tag{9.3}$$

where $K = \frac{\varphi}{L}$ is the co-efficient of absorption, φ is the volume fraction of black. *L* is a characteristic length associated with the black particles (Appendix F). Thus the extent to

which UV light might be expected to catalyse oxidative degradation will decline exponentially from the surface, with a decay length $1/K$ of the order of L/φ.

Figure 9.17 shows the transmission factor Ln(I) versus different aged rubber thicknesses. The results are consistent with an exponential decline in light intensity with depth into the rubber. Based on the graph obtained in Figure 9.17, the value for K was $0.0353\mu m^{-1}$ i.e. the decay length $1/K$ is $28.3\mu m$. The volume fraction of black, φ, may be calculated by assuming the volume contribution made by each ingredient is not affected by mixing and hence satisfies Equation (9.4).

$$\varphi = \frac{\frac{w_b}{\rho_b}}{\sum \frac{w_i}{\rho_i}} \quad , \tag{9.4}$$

where w_b, and ρ_b is total weight and density of black particles and w_i and ρ_i is weight and density of ith ingredient of rubber mix. Using the density of each ingredient from Table 9.2 and Equation (9.4), the volume fraction of black, φ, is found to be 0.2. This gives an apparent value for L: $L = \frac{\varphi}{K} = \frac{0.2}{0.00353} \approx 5.7\mu m$.
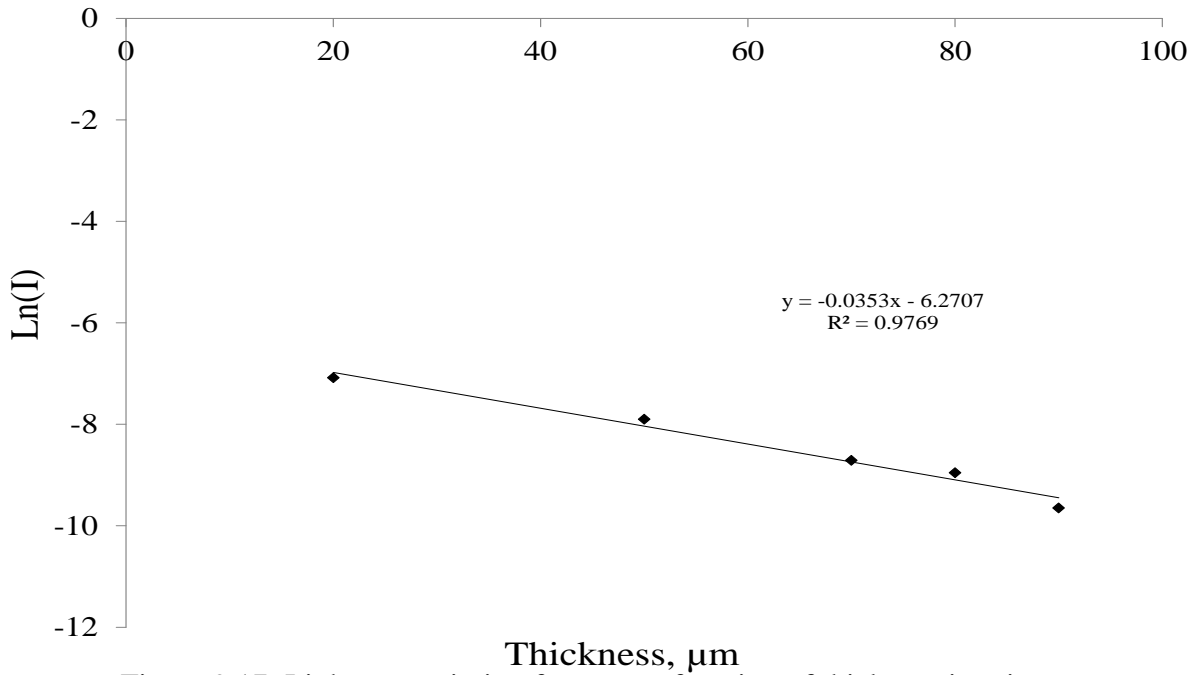
Figure 9.17: Light transmission factor as a function of thickness in micron.

So, the depth of penetration of UV light, and hence of photolytic degradation, for this rubber is of the order of only a few tens of microns. The different K value to the results presented in the paper by Kamaruddin et al., (2011) is thought to be attributable to poor sample quality resulting from the TARRC cutting process; the samples were much less uniform than the samples generated at IFREMER and in some cases had through-holes.

9.3.3 Pelham Bridge Bearing

Analysis of Constituents

The rubber was analysed at TARRC (Fuller & Roberts 1999) and the results are shown in Table 9.4; as expected, the apparent formulation is similar to the published advice (Lindley 1962). The main antiozonant is evidently di-octyl paraphenylene diamine (DOPD), the diffusion co-efficient of which is given as an Arrhenius plot in Figure 9.18, based on measurements by Lake & Mente (1992).

Table 9.4: Comparison of formulation from analysis with those recommended; parts per hundred of rubber (pphr) by weight.

Ingredients	Recommended formulations[a]			Pelham bearing[b]
NR	100	100	100	100
Lampblack	15	35	60	50
ZnO	6	10	30	24
Oil	2	2	2	
DOPD	4	4	4	>3
Sulfur	2.5	2.5	2.3	2.8[c]
CBS	0.7	0.7	0.7	-
Stearic Acid	1	1	1	-
PBN	1	1	1	~0.2
BS Hardness	51	60.5	70.5	70

a – Lindley (1962)

b – BS hardness from Gent (1959); analysis provided by Fuller & Roberts (1999) –Medium Thermal (MT) type black; traces of antioxidants included PBN but also BLE25

c – Total sulfur includes any sulfur in the accelerator [e.g. CBS molecules]

DOPD is considered (MRPRA 1984) to be an excellent antiozonant and does not need to be supplemented with wax to provide good protection under static strains. On the other hand, it is said to be a less effective antioxidant than alkyl-phenyl paraphenylene diamines, and was probably for this reason supplemented with phenyl β-naphylamine (PBN) and acetone/diphenylamine condensate (BLE25) both of which were identified and are believed to be effective as anti-flexcracking antioxidants (MRPRA 1984). It is surprising that the quantities were found to be so small, suggesting they had largely decomposed during ageing and/or vulcanization. The diffusion coefficient of PBN in BR at 20°C is approximately $2 \times 10^{-12} \text{m}^2 \text{s}^{-1}$ (van Amerongen 1964), suggesting a value in NR around five times that of DOPD.
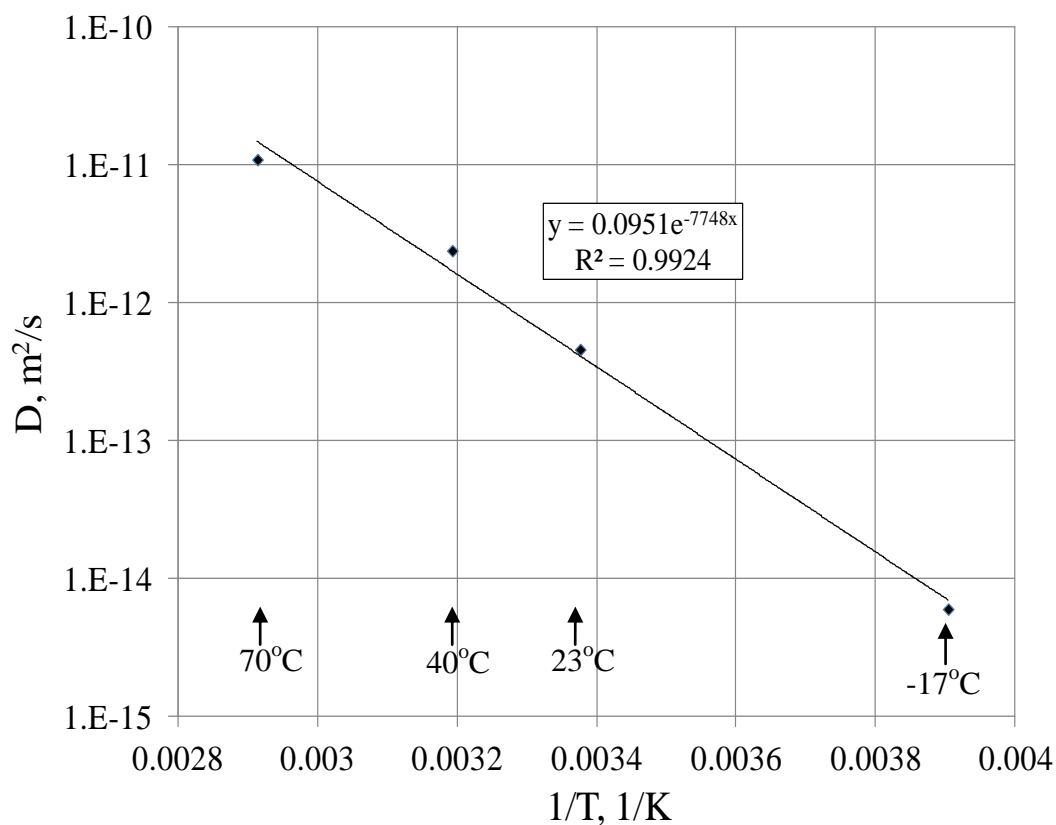
Figure 9.18: Arrhenius plot for diffusion coefficient *D* of DOPD into NR based on data of
Lake & Mente (1992).

Chemical Concentration Profile

Tables 9.5 and 9.6 provide TARRC generated results reported by Fuller & Roberts
(1999).

Table 9.5: Quantity of unconsumed anti-degradant in
Pelham Bridge Bearing rubber.

Depth below surface, mm	0~1	20	50, bulk
DOPD, wt%	0.26	0.74	1.3

DOPD decreased markedly from the bulk value between a depth of 50 mm and the surface.
Near the surface the fall may represent consumption in oxidative reactions. Further from
the surface, it is possibly due to diffusion towards the near surface region where it is being
consumed by chemical reaction.

Table 9.6: Oxygen content of the rubber.

Depth below surface, mm	2	4	6	8	20	bulk
Oxygen, wt%	3.0	2.7	2.3	2.3	2.2	2.0

The results in Table 9.6 indicate a level of oxygen in the bulk that is comparable to that expected from natural rubber non-hydrocarbon material. Most of the rise, as the surface is approached, occurs at depths less than 6mm. It assumed that a moderate level of oxidation took place in view of the extra 1wt% increase oxygen close to the surface.

Mechanical Properties Profile

As described by Fuller & Roberts (1999) one of the Pelham bearings was cut into 9 blocks (Figure 9.19) and these were stored indoors at TARRC. For the current work, slabs of rubber approximately 5mm thick were cut parallel from the top face through the top internal rubber layer of block D. From these slabs, samples of nominal dimensions $135 \times 25 \times 5$mm were provided to ENSTA and IFREMER, each with the internal and external ends (135mm apart) clearly marked.

exterior

G	D	A
H	E	B
I	F	C
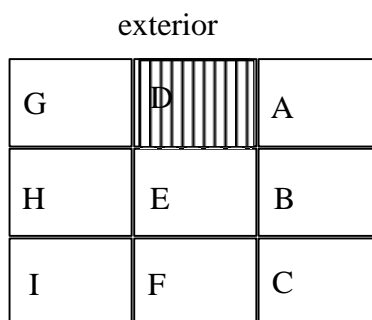
Figure 9.19: Top view of bearing 1 identifying location of cut sections (shaded area). Block D was stored on a shelf indoors from 1994 until further sectioned and investigated as reported here.

i.) Tensile Modulus (IFREMER)

Figure 9.20 shows extension modulus from micro-tensile test strips cut in 2013 from 100μm sections cut with a Leica microtome from sample cooled with liquid nitrogen. The modulus shows no significant variation with distance from the surface, up to 5mm in.
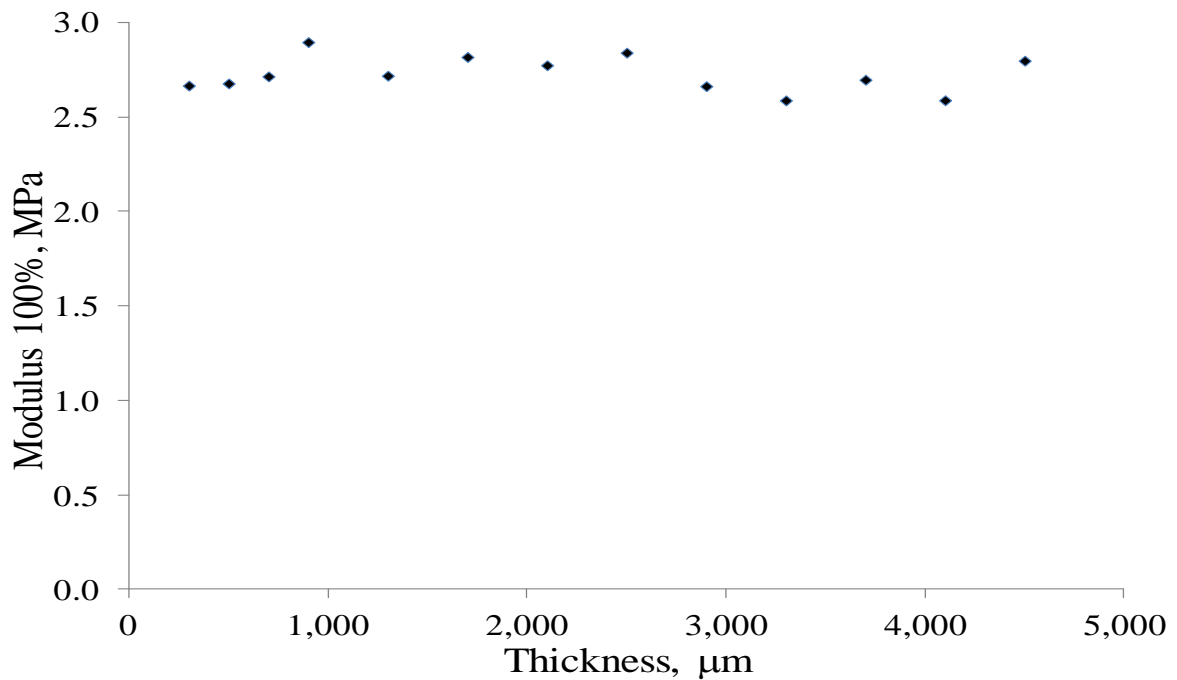
Figure 9.20: Tensile modulus at 100% extension at different distance from the surface (Le Gac, IFREMER).

ii.) Nanohardness (ENSTA)

The Pelham bridge bearing sample ($135 \times 25 \times 5$) mm, was divided into 4 parts of equal length and embedded in a resin to improve its manipulation. The surfaces of the samples were then polished with grinding media of decreasing granulometry until reaching a surface free of evident "peaks" and "valleys" by optical microscope. After at least 2 hour, to let the sample cool down to the ambient temperature (23°C) after grinding, measurements were performed on a CSM nano-hardness tester equipped with a Berkovitch indenter. The resolution of the device is ±5µN and ±3nm for a full range of 300mN and 100µm. All the tests were load controlled. The Oliver & Pharr (1992) methodology was applied to the loading protocol and interpretation. In this study, the instrumented hardness and the instrumented elastic modulus only were addressed.

Each point of the experimental results shown in Figures 9.21 and 9.22 corresponds to the mean of 5 measurements, indicating that about 200 measurements were performed to improve resolution of profile illustrated. A clear gradient exists between the skin and the bulk over an affected length of about 40mm. Beyond this value, there is no significant variation.
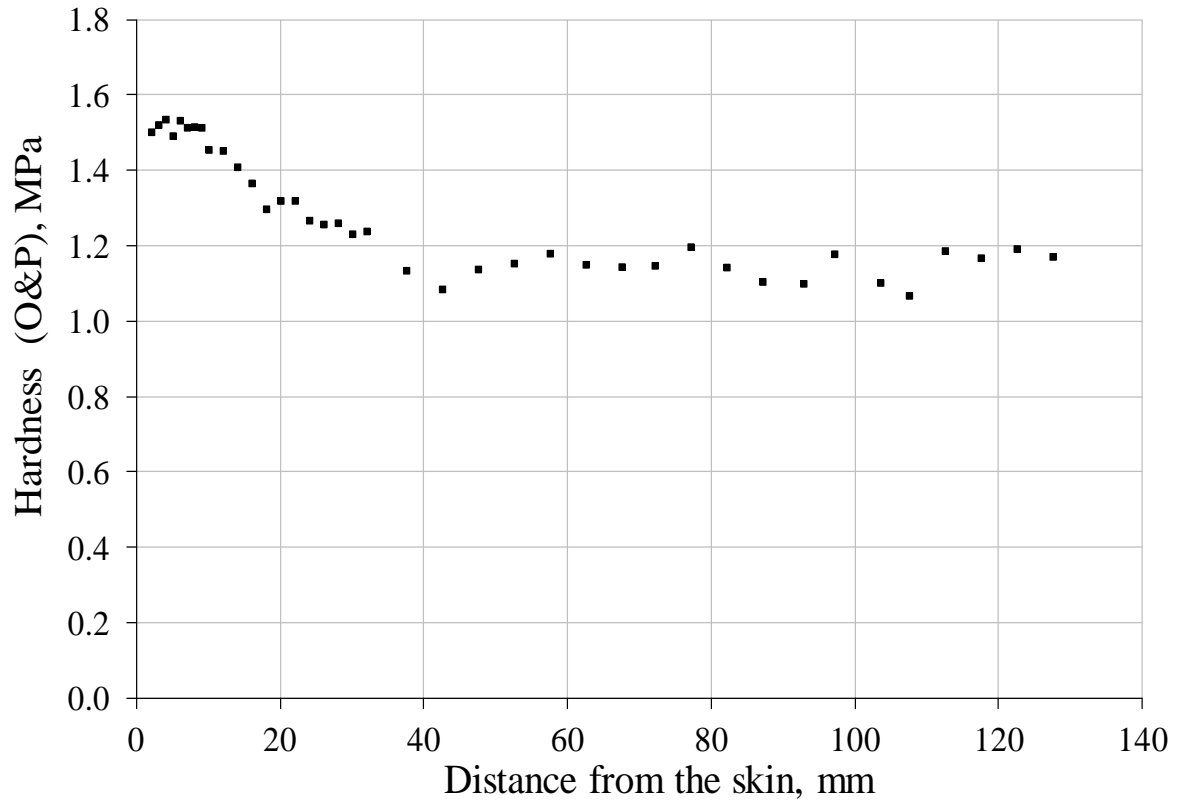
Figure 9.21: Hardness values (Oliver & Pharr interpretation) as a function of distance from the surface (Le Saux, ENSTA).
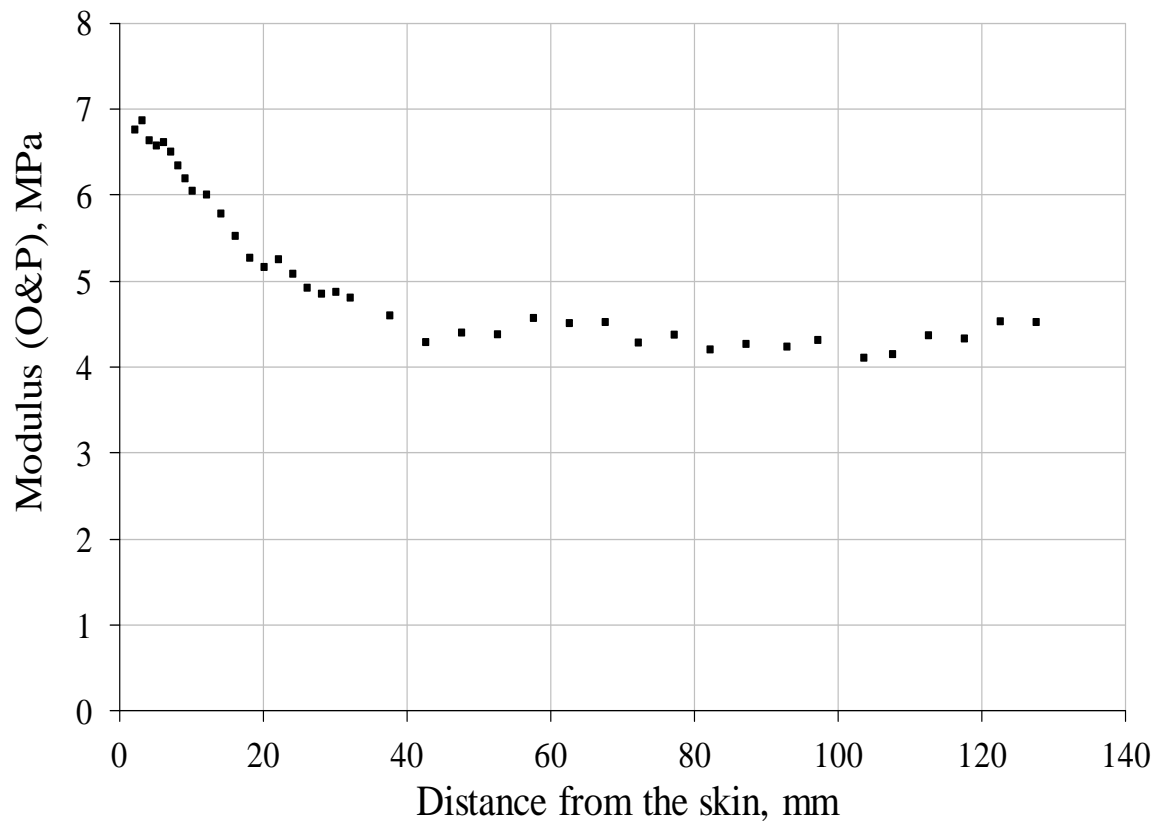
Figure 9.22: Young's modulus values (Oliver & Pharr interpretation) as a function of distance from the surface (Le Saux, ENSTA).

9.4 Model for Diffusion Limited Reaction

9.4.1 Diffusion Without Reaction

The kinetics and distribution of ageing in bulky rubber mouldings to be controlled by the relative rates of diffusion and chemical reaction of key substances. The Arrhenius expression for diffusion assumes the form:

$$D = D_0 \exp\left(\frac{-E}{RT}\right) \, , \qquad\qquad (9.5)$$

where D_o is a constant prefactor, E is the energy of activation for diffusion, R is the universal gas constant ($8.314 \mathrm{Jmol^{-1}K^{-1}}$) and T is the absolute temperature. This equation was used to calculate diffusion coefficients D from the values of D_0 and E given in Table 9.7.

Table 9.7: Values of parameters in Equation (9.4).

Substance	D_o $m^2 s^{-1}$	E $kJmol^{-1}$	Reference
Oxygen	0.000194	34.7	van Amerongen (1964)
DOPD	0.0951	64.4	Regression fit, Figure 10.17

The representative ageing temperature for Pelham Bridge is 10°C (Fuller & Roberts 1999). Figure 9.22 gives predicted normalized concentrations, calculated assuming no chemical reaction in the rubber. The boundary and initial conditions are respectively 0; 1 for DOPD and 1; 0 for oxygen, it being assumed that all the DOPD that reaches the surface reacts or is lost by leaching or evaporation, and that all the oxygen initially dissolved in the rubber is consumed in reactions during vulcanisation. The concentration in the rubber can be found by multiplying the normalized concentration by the pphr of DOPD or the solubility of oxygen in natural rubber from air [$\sim$33.6μg.cm^{-3}; van Amerongen 1964] respectively. Plane diffusion was assumed with a total thickness L of 394mm. Taking $D = 1.25 \times 10^{-7}$ mm^{2}s^{-1} for DOPD and 7.7×10^{-5} mm^{2}s^{-1} for oxygen gives $L^2/D = 39,000$ years and 64 years for DOPD and oxygen respectively.

The diffusion equation

$$\frac{\partial c}{\partial t} = D \frac{\partial^2 c}{\partial x^2} \quad ,$$

(9.6)

was integrated numerically using a Crank-Nicolson method (William 1969) programmed in MATLAB. This programme was developed together with Dr Alan Muhr at TARRC (Appendix I). This is a special single case of $k_1=0$ in the model discussed later, and serves as a benchmark for the latter. Figure 9.23 shows that after 60 years we would expect a uniform distribution of DOPD in rubber deeper than 60mm from the free surface.
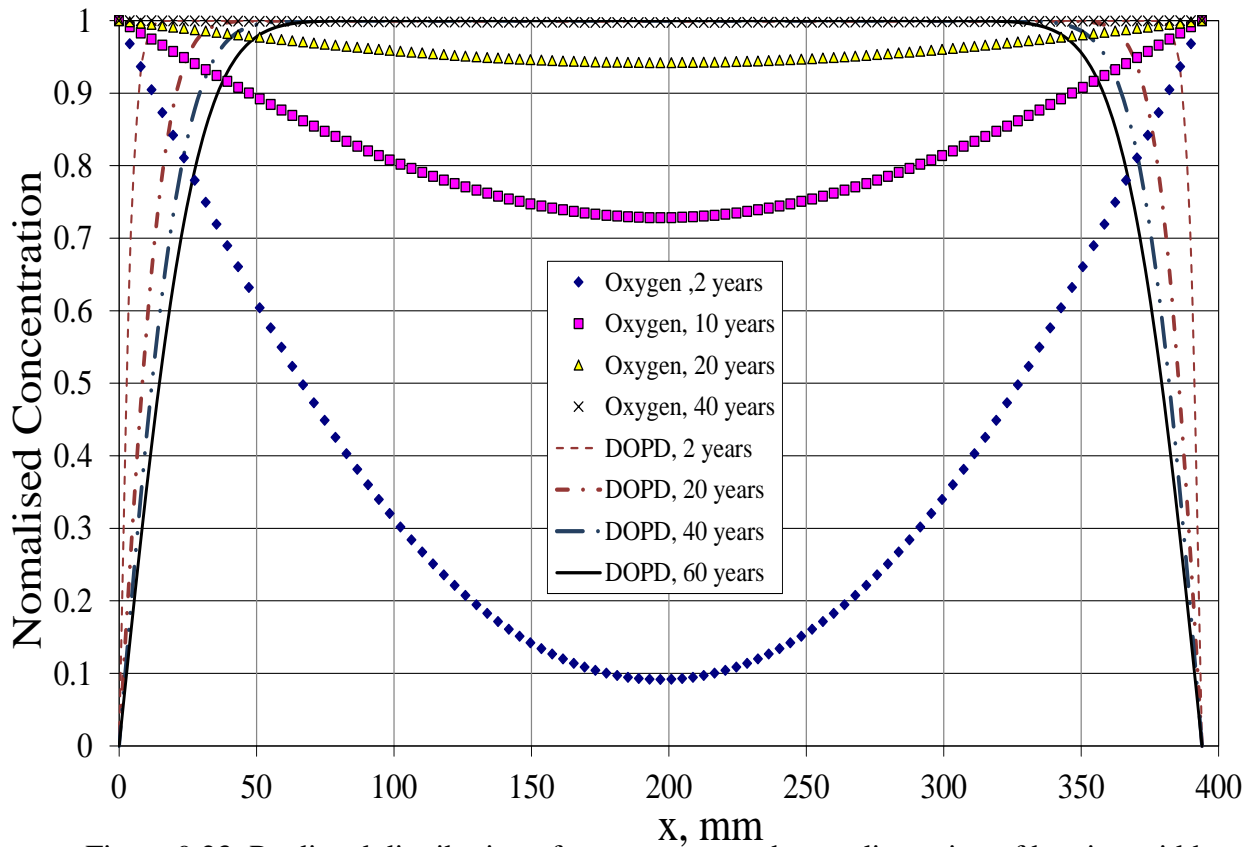
Figure 9.23: Predicted distribution of oxygen across shorter dimension of bearing width assuming only plane diffusion with a constant concentration at the surface and no source or sink in the interior.

On the other hand, the figure shows that diffusion would result in uniform oxygen concentration throughout in less than 40 years, again assuming there is no reaction. These figures have been checked against equivalent results published by Crank (1975), serving as a first benchmark check of the MATLAB program.

For the Bramfield tyre**,** plane diffusion of oxygen only was assumed, with a total thickness *L* of 80mm and *D*= 7.7x10^{-5} mm^{2}s^{-1} the same diffusion coefficient as for the Pelham Bridge bearing at 10°C. The maximum time of oxygen (L^2/D) is 2.6 years. Figure 9.24 illustrates a non-uniform oxygen concentration throughout in less than 2 years.
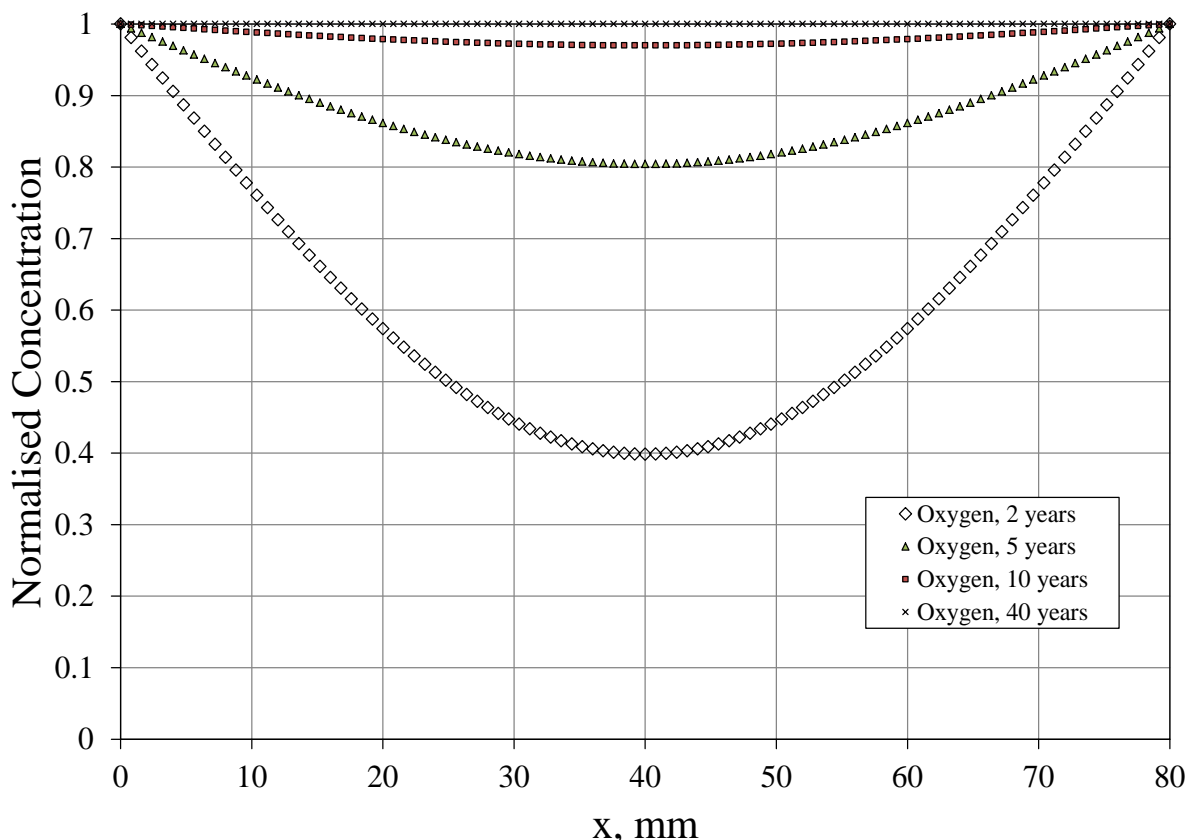
Figure 9.24: Predicted distribution of oxygen across shorter dimension of width for Bramfield tyre assuming only plane diffusion with a constant concentration at the surface and no source or sink in the interior. No antioxidant was present for this tyre.

9.4.2 Diffusion-Limited Oxidation Model

In the case of the Bramfield tyre, it is thought that only oxidation could penetrate as deep as ~1mm to form the crust; with ozone attack, photo-oxidation and loss of scission products by leaching and evaporation contributing at the surface (see Figures 9.9 & 9.11). In order to understand the phenomenon of oxidation, a diffusion-limited oxidation model has been programmed using MATLAB software.

The general model for uniaxial diffusion limited oxidation is:

$$\frac{\partial c}{\partial t} = \frac{\partial}{\partial x} D(M(t,x),c)\frac{\partial c}{\partial x} - r(M(t,x),c) \qquad (9.7)$$

where c is the oxygen concentration, D the diffusion coefficient of oxygen, $M(t,x)$ the amount of oxygen dissolved in the rubber at position, x and time, t. r is the rate of consumption of oxygen by chemical reaction. t is the time elapsed since diffusion started and x is the distance from the surface.

In general, r and D both depend on M, the amount of reacted oxygen per unit volume:

$$M(t,x) = \int_0^t r.\,dt \qquad . \qquad (9.8)$$

Assuming that D is constant, Cunliffe & Davies (1982) justified the following dependence of r on c on the basis of critical steps in the multiple chain reactions in the Basic Autoxidation Scheme:

$$r = \frac{k_1 c}{1+k_2 c} \qquad . \qquad (9.9)$$

Here, k_1 is first order reaction constant and k_2 is an attempt to capture the effect of actual sequence of several chemical reactions. Equation (9.7), with constant D and Equation (9.9) for r can be cast into the non-dimensional form (Cunliffe & Davies 1982):

$$\frac{\partial \emptyset}{\partial T} = \frac{\partial^2 \emptyset}{\partial X^2} - \frac{\alpha \emptyset}{1+\beta \emptyset} \qquad (9.10)$$

where $\phi = c/c_s$, $T = Dt/L^2$, $X = x/L$, $\alpha = (k_1 L^2)/D$ and $\beta = k_2 c_s$ where subscript s denotes the surface of the rubber. Here α is dimensionless and β is dimensionless modifier to make r nonlinear in c. In the case that $\beta = 0$ there is an analytical steady-state solution to (9.10):

$$\emptyset_{ss} = \frac{cosh\left(\sqrt{\alpha}\left(X-\frac{1}{2}\right)\right)}{cosh\left(\frac{\sqrt{\alpha}}{2}\right)} \qquad (9.11)$$

where ss refers to steady state, and boundary conditions are $d\phi/dX=0$ at $X=\frac{1}{2}$ and $\phi=1$ at $X=0,1$. (Refer to Appendix G).

According to Clough & Gillen (1992), β for hydrocarbon polymers typically satisfies $1<\beta<10$. For $\beta\neq0$ they and others (e.g. Cunliffe & Davis 1982, Wise et al. 1997) obtained steady state solutions numerically, with some success in comparison with laboratory aged samples. They also calculated the steady state dimensionless oxidation rate ρ_{ss} by substitution of numerical solution for ϕ_{ss} into (9.10) to yield:

$$\rho_{ss} = \frac{\alpha\emptyset_{ss}}{1+\beta\emptyset_{ss}} \Rightarrow \frac{\rho_{ss}}{\rho_s} = \frac{1+\beta\emptyset_s}{1+\beta\emptyset_{ss}}\cdot\frac{\emptyset_{ss}}{\emptyset_s} = \frac{1+\beta}{1+\beta\emptyset_{ss}}\cdot\emptyset_{ss} \qquad (9.12)$$

since by definition $\emptyset_s = 1$; ρ_s is the dimensionless reaction rate at the surface. As long as the steady state solution prevails, the additional (dimensionless) amount of oxygen reacted in a period of time Δt is $\rho_{ss}\Delta t$. If t is so large that the contribution to *M(t)* during the transient phase is small, so that the error in equation transient and steady state rates during the transient period is negligible. Equation (9.12) could serve as a basis for estimating the total amount of oxygen absorbed at any point in the material, and hence the variation in physical properties with distance from the surface.

9.4.3 Numerical Implementation

In the preliminary work, the scheme expressed by Equations (9.7) to (9.10) was restricted to the case that *D*, k_1 and k_2 are independent of *M*. Solutions were obtained numerically using a modified Crank-Nicolson method implemented in MATLAB and included transient behaviour as well as steady-state.

In the case of the Pelham Bridge bearing, by keeping $L^2/D = 64$ years, appropriate for oxygen in natural rubber at $\sim10^{o}$C, k_1 and k_2 were set to values corresponding to the set of 4 combinations of α and β given in Table 9.8. In each case the program was run to calculate profiles of oxygen concentration and amount of oxygen reacted.

Table 9.8: Predicted amount of reacted oxygen (M/c$_s$)
(scaled to the surface concentration $\sim34\mu$g.cm^{-3}) for Pelham bearing.

Model parameter			40 years			60 years		
α	β	x=	0	0.1	0.5	0	0.1	0.5
10	0		6.3	4.7	2.2	9.4	7.2	3.4
10	10		0.57	0.56	0.52	0.85	0.84	0.80
100	0		63	23	0.81	94	34	1.2
100	10		5.7	5.4	3.3	8.5	8.1	5.2

Figures 9.25 to 9.28 show the oxygen concentration and the amount of oxygen reacted for different values of α and β for L^2/D appropriate to Pelham Bridge bearing.

Figure 9.25: Oxygen concentration (dotted) and amount absorbed normalised with respect to values at the surface; $\alpha=10$, $\beta=0$, (Pelham bearing).

Figure 9.26: Oxygen concentration (dotted) and amount absorbed normalised with respect to values at the surface; $\alpha=10$, $\beta=10$, (Pelham bearing).

Figure 9.27: Oxygen concentration (dotted) and amount absorbed normalised with respect to values at the surface; α=100, β=0, (Pelham bearing).

Figure 9.28: Oxygen concentration (dotted) and amount absorbed normalised with respect to values at the surface; α=100, β=10, (Pelham bearing).

In the case of the Bramfield tyre, by keeping L^2/D=2.6 years, appropriate for oxygen in natural rubber at ~10^oC, k_1 and k_2 were set to values corresponding to the set of 4 combinations set out in Table 9.9. Again, in each case the program was run to calculate profiles of oxygen concentration and amount of oxygen reacted.

Table 9.9: Predicted amount of reacted oxygen (M/c$_s$)
(scaled to the surface concentration ~34µg.cm^{-3}) for Bramfield tyre.

Model parameter			40 year			60 years		
α	β	x=	0	0.1	0.5	0	0.1	0.5
10	0		15.14	11.29	5.70	22.70	17.01	8.69
10	10		1.38	1.37	1.32	2.07	2.05	1.99
100	0		151.4	55.60	2.02	227	83.50	3.00
100	10		13.77	13.14	8.50	20.65	19.72	12.89

Figures 9.29 to 9.32, show the oxygen concentration and the amount of oxygen reacted with different values of α and β for L^2/D appropriate to the Bramfield tyre.
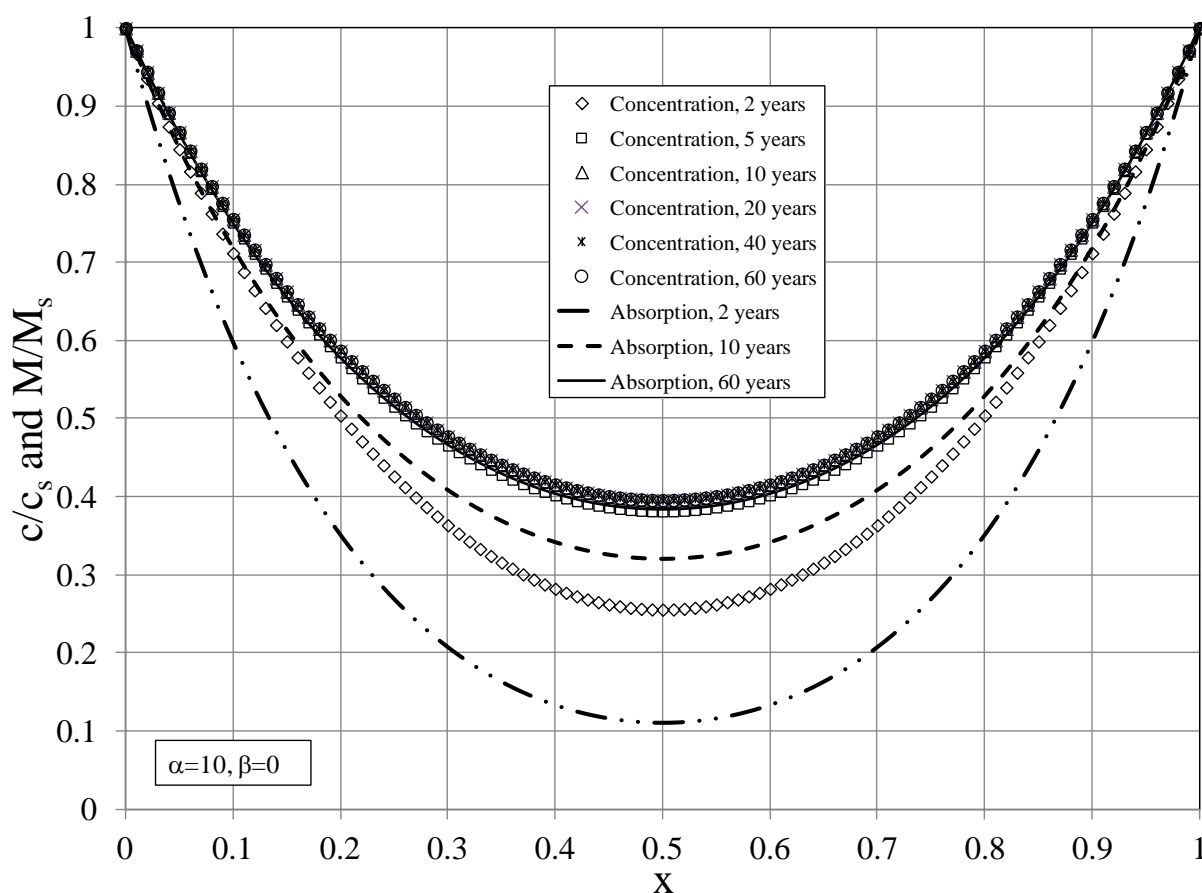
Figure 9.29: Oxygen concentration (dotted) and amount absorbed normalised with respect to values at the surface; α=10, β=0, (Bramfield tyre).
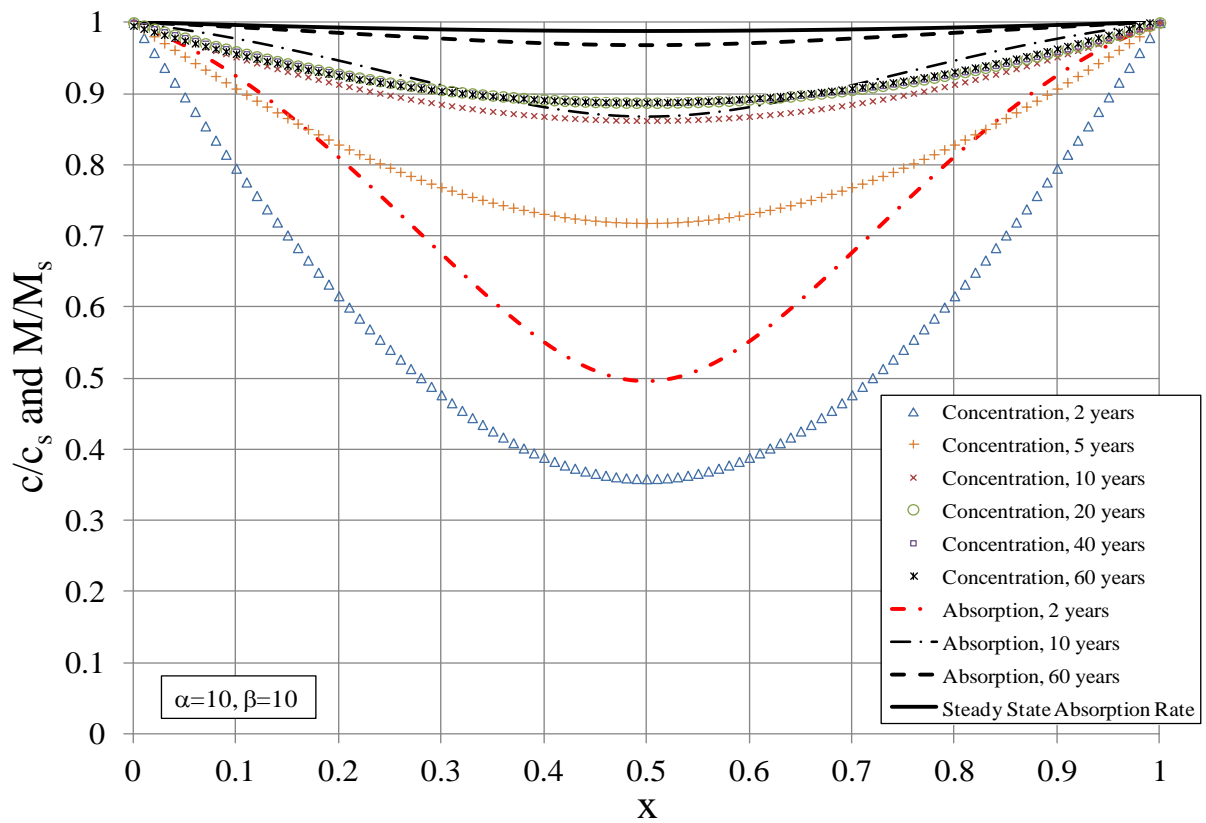
Figure 9.30: Oxygen concentration (dotted) and amount absorbed normalised with respect to values at the surface; α=10, β=10, (Bramfield tyre).
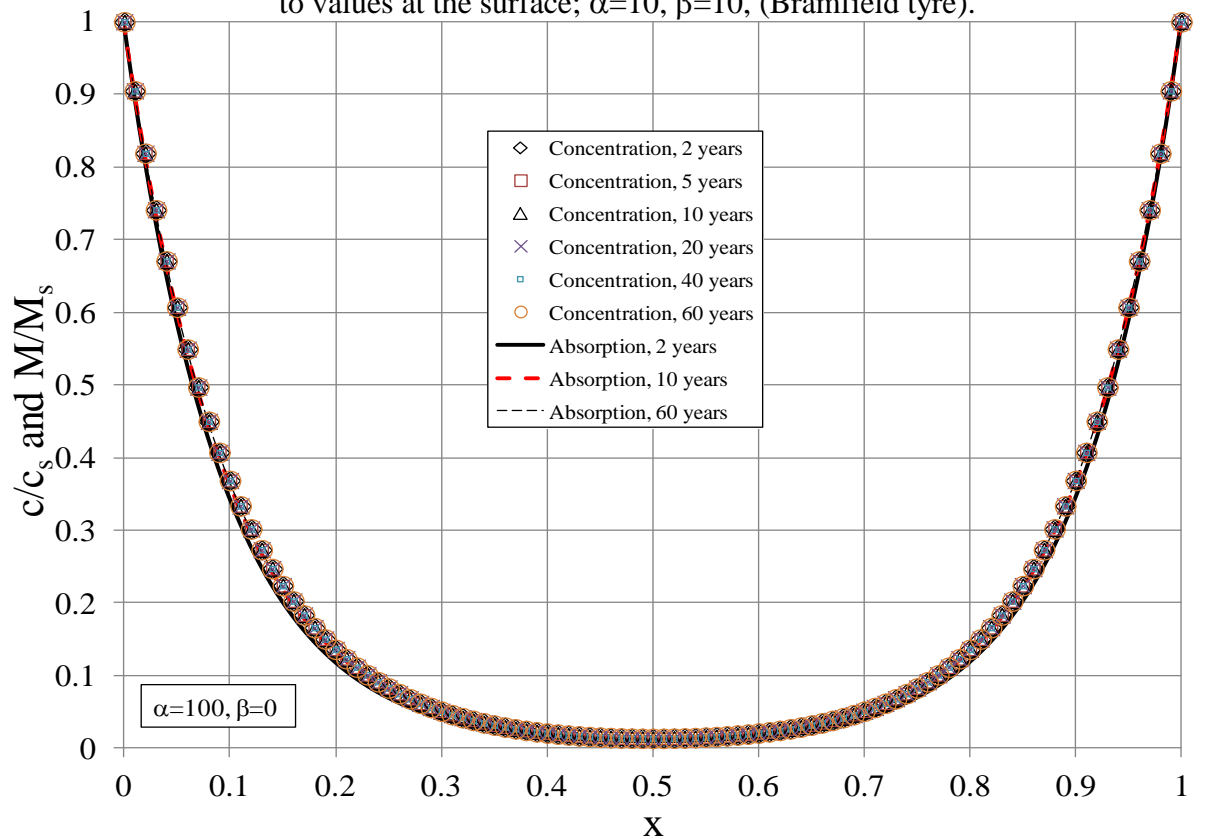
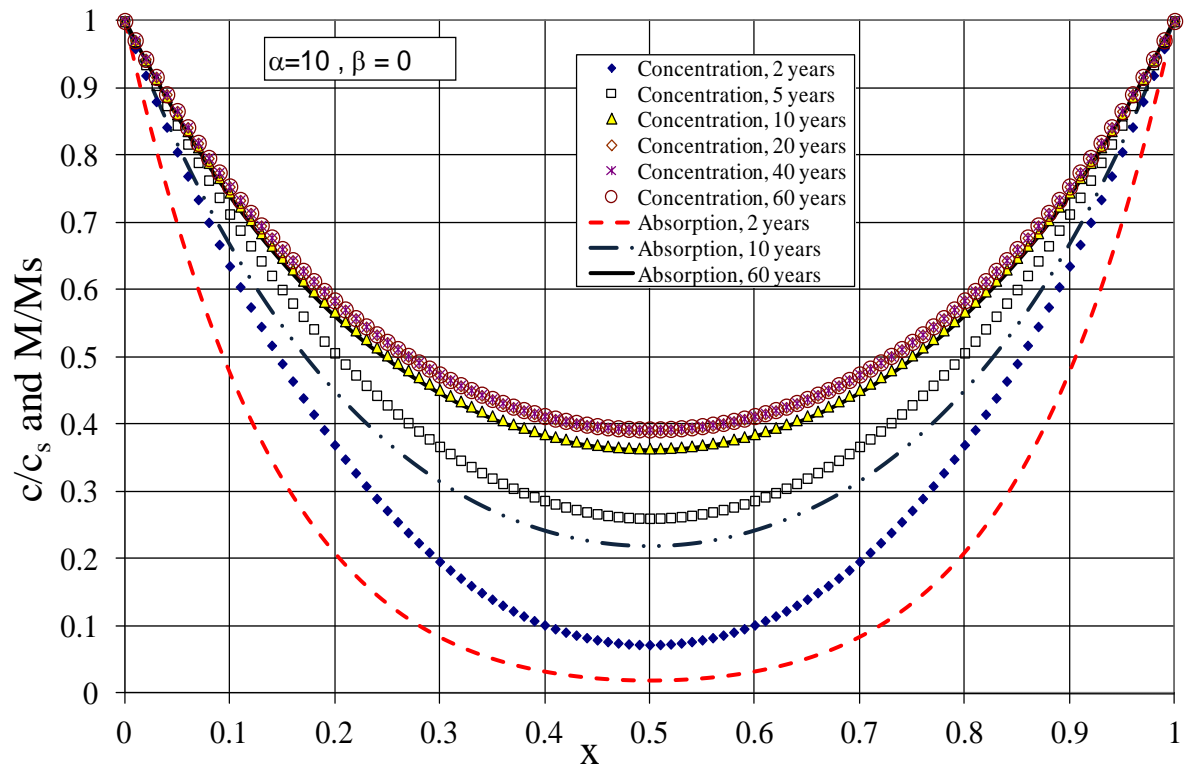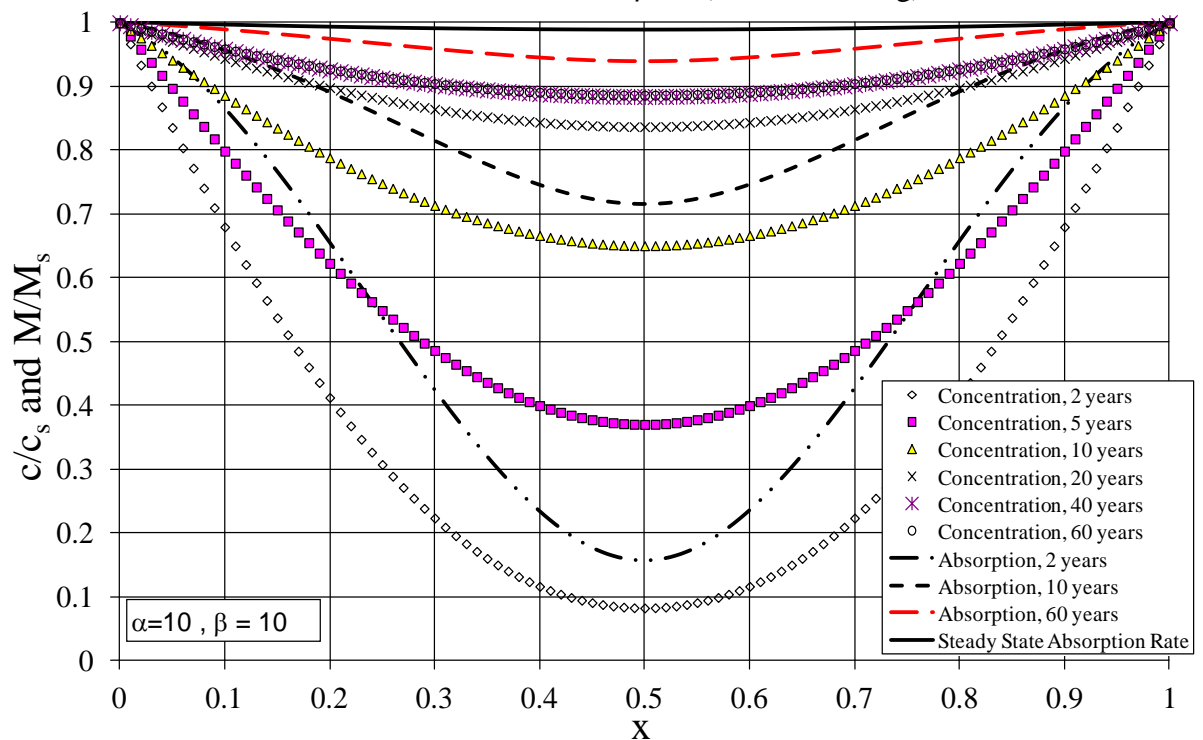Figure 9.31: Oxygen concentration (dotted) and amount absorbed normalised with respect to values at the surface; α=100, β=0, (Bramfield tyre).
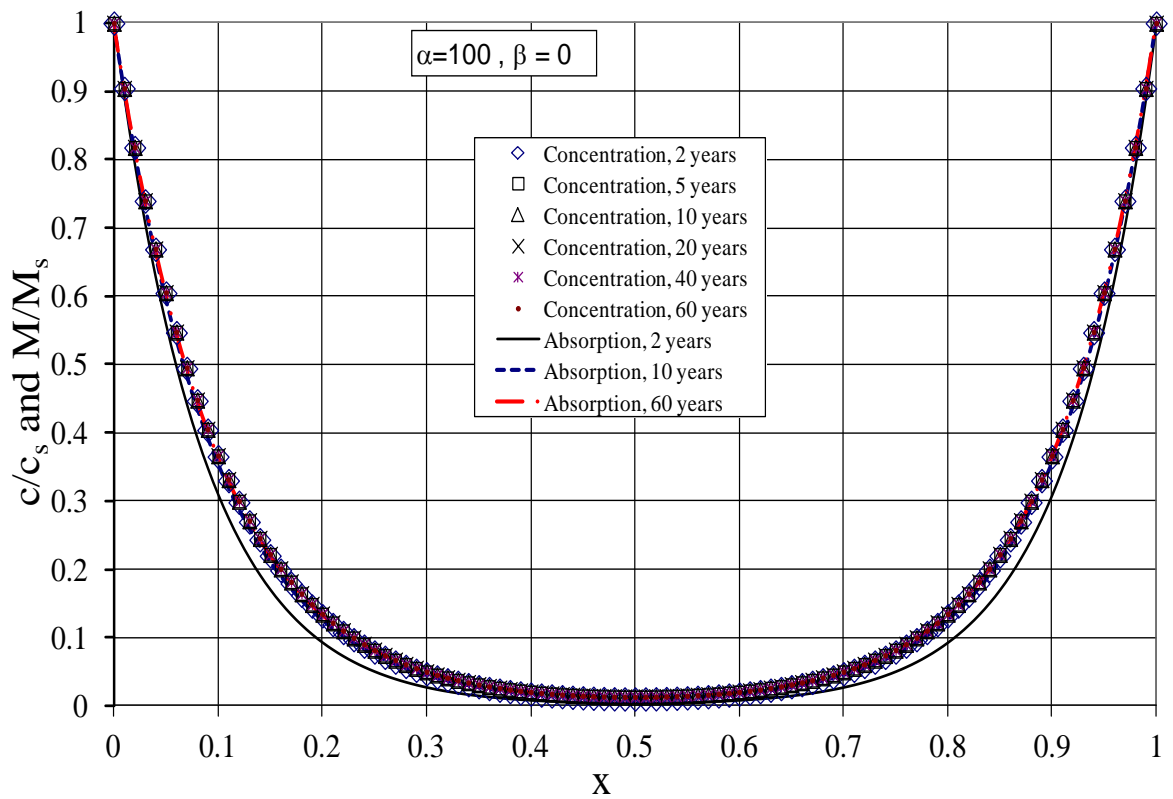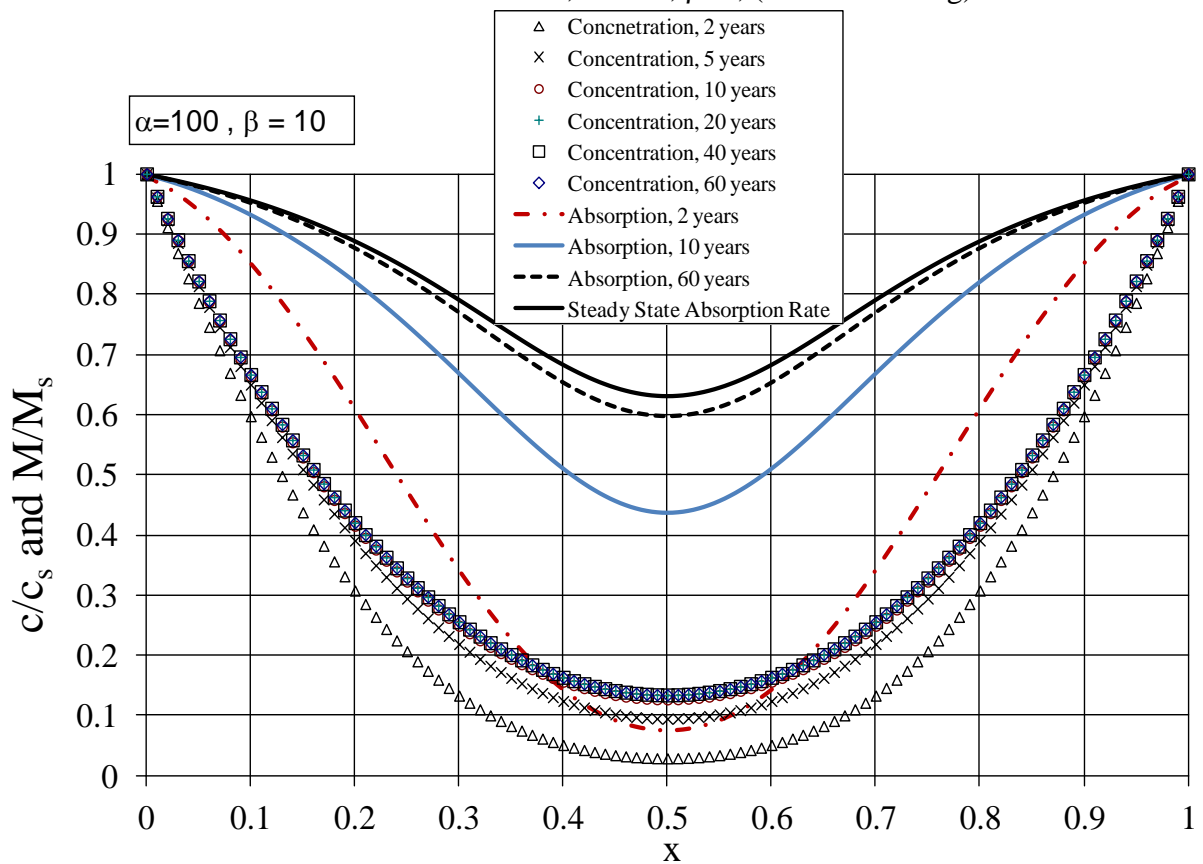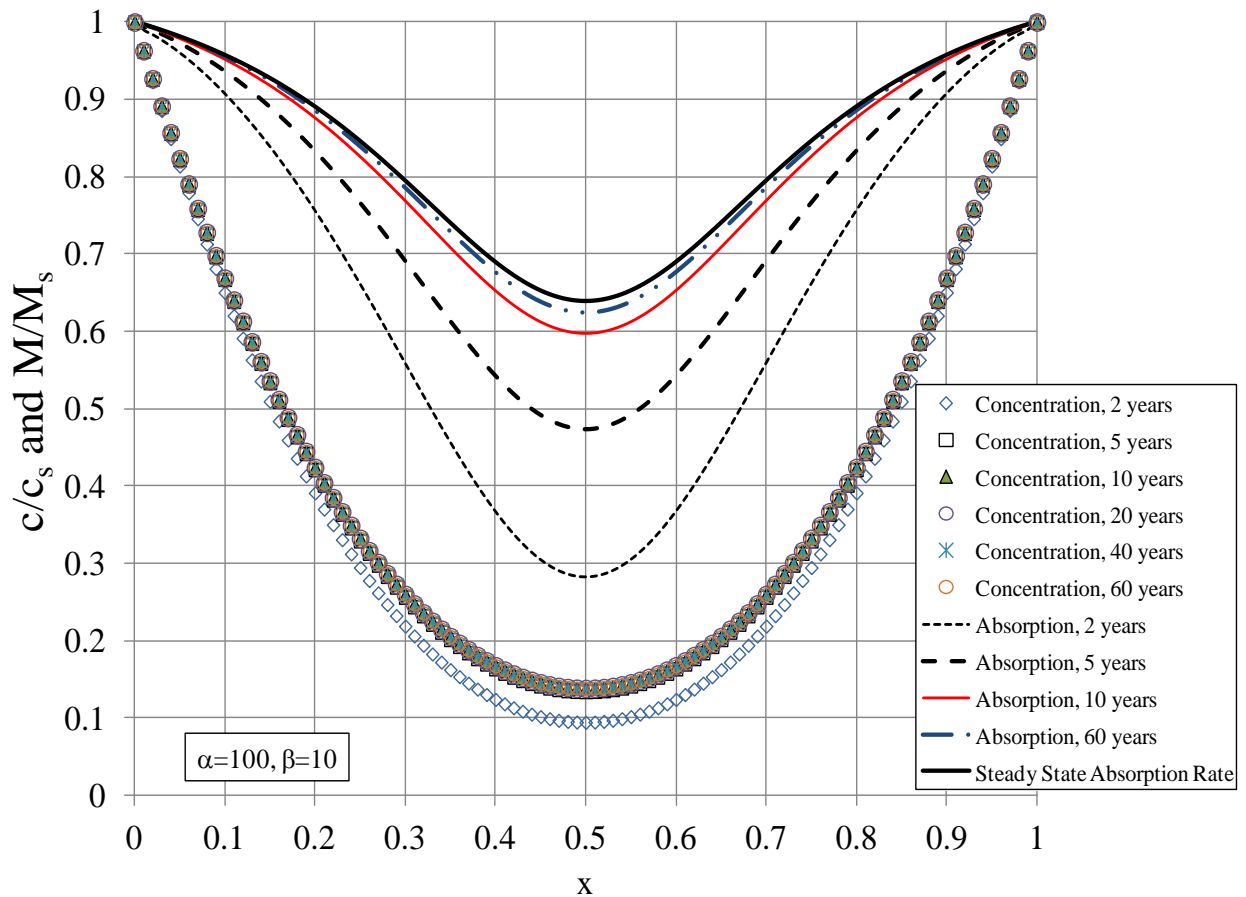
Figure 9.32: Oxygen concentration (dotted) and amount absorbed normalised with respect to values at the surface; α=100, β=10, (Bramfield tyre).

Figures 9.25 to 9.32 show the potential importance of transient behaviour, since for lower rates of reaction much or all of the lifetime of large rubber mouldings can be spent before steady state profiles of concentration and amount of oxidation are reached. Except in the case of Figures 9.27 and 9.31 corresponding to the highest rate of reaction, the steady state analysis of Cunliffe & Davis (1982) would be misleading for the systems shown here.

On the other hand, the experimental observation that the properties and chemical content are reasonably uniform in the interior, defined as deeper than ~50mm from the free surface of the Pelham bridge bearing, and deeper than ~5mm from the free surface of Bramfield tyre. This suggests that an even higher value of α would be needed to achieve a fit as shown in Figure 9.27 and 9.31.

Figure 9.33 shows the variation of the reaction constant, α when the dimensionless modifier, β is zero. The prediction of the plot when α is 1000 and β is zero was the nearest to the observation of the Pelham bearing.
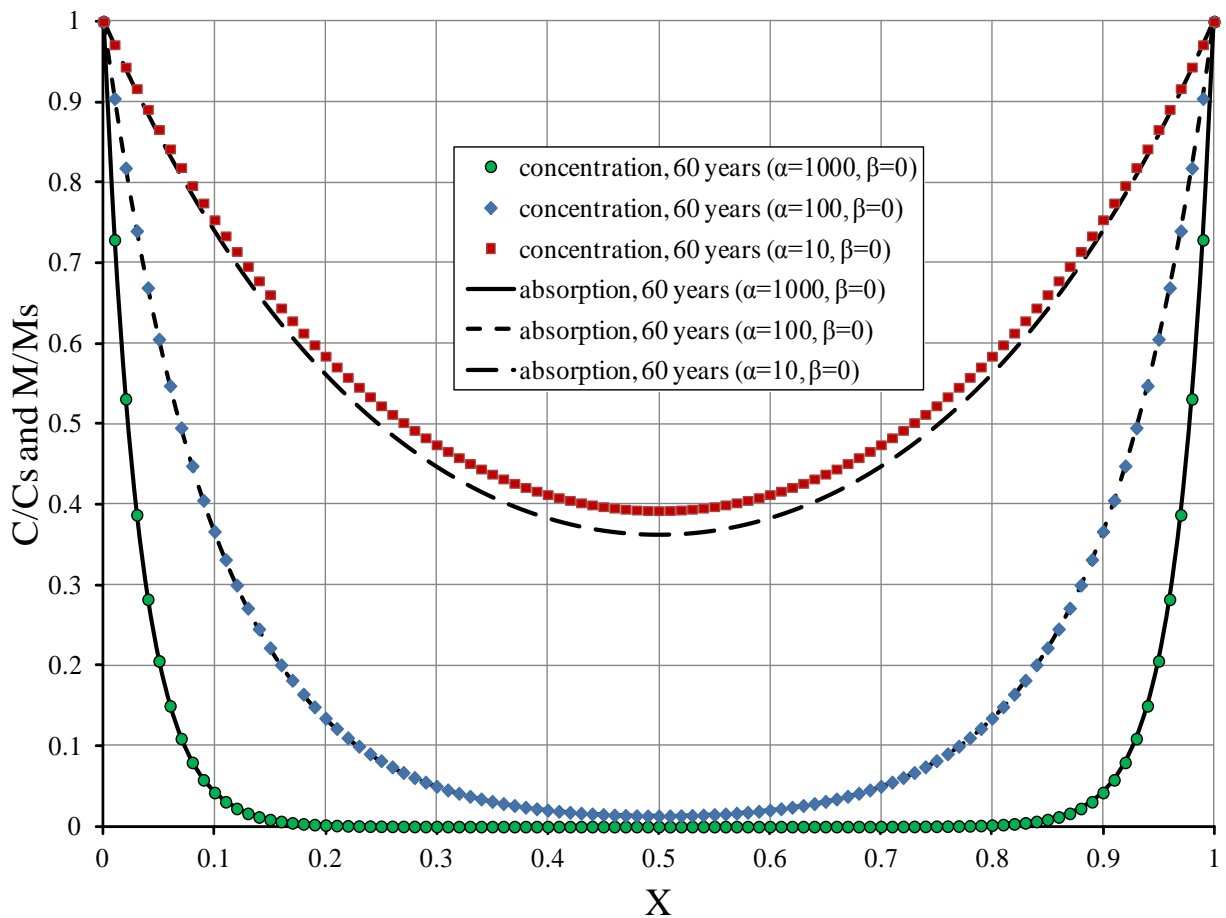
Figure 9.33: Oxygen concentration (data points) and amount absorbed (lines) normalised with respect to values at the surface; α=1000, 100, 10 when β=0, (Pelham bearing).

9.5 Discussion

The observations on the Pelham Bridge bearing rubber contrast with those on the Bramfield tyre, naturally aged in woodland for about 80 years (Kamaruddin et al. 2011) and with those on the Melbourne viaduct rubber pads, aged for about 96 years (Kamarudin & Stevenson 1992).

For the Bramfield tyre, also natural rubber, a very hard crust had formed to a depth of ~1mm and the rubber properties were reasonably uniform at depths greater than 5mm.

For the Melbourne viaduct rubber pads, the surface of the rubber was hard and shows evidence of oxidation (Kamarudin & Stevenson 1992). They found the rubber to be free from such degradation below a depth of 1.5mm and still to have a hardness of only 63 IRHD compared to a hardness of 80 IRHD on the surface. There was no evidence of

significant deterioration of the rubber below the depth of 1.5mm and in the centre of the pad. This provides convincing evidence that the weathering of natural rubber in normal conditions is limited to the exposed surface.

There are some key differences between the three cases:

(1) The total thickness of the solid tyre was ~40mm and only the tread surface was exposed, compared to 394 mm thick and symmetrical exposure of the edges of the Pelham bearings and 25mm thick exposure of the edges of the Melbourne viaduct rubber pads.

(2) As explained before, there were probably no antioxidants in the Bramfield tyre rubber and the Melbourne viaduct rubber pads.

(3) The Bramfield tyre was exposed to the weather, whereas the Pelham bearings and the Melbourne viaduct rubber pads are substantially shaded by the bridge deck from rain and direct sunlight.

(4) The period of exposure of the Bramfield tyre was about double that of the original 1995 study of the Pelham bearings (38 years). The period of exposure of the Melbourne viaduct rubber pads was 96 years at the time it was investigated.

It is logical to believe that the aged rubber tyre from Bramfield Wood was formulated without antidegradants since the first deliberate addition of antioxidants in rubber formulations was in the 1920s (for US military gas masks), and antiozonants were first used after the Second World War (Huntink 2003). Moreover, there was no evidence of antioxidant and antiozonant in the constituent analysis results. The cracks formed in the exterior surface of the aged rubber are apparently due to shrinkage associated with extensive ageing; highly oxidised natural rubber being more dense than unoxidised rubber (Table 9.3). Possibly a state of biaxial tension caused by moulding directly onto the steel rim contributed to the penetration of cracks beyond the more grossly oxidised rubber. Taking the coefficient of volumetric thermal expansion of the rubber to be $\zeta \approx 5.3\text{x}10^{-4}\text{K}^{-1}$, and the vulcanization temperature to be ~100°C above ambient implies, a linear shrinkage strain of $1.8\text{x}10^{-2}$ in all three orthogonal direction, if the tyre were unconstrained. However, because of the constraint of the steel tyre, no shrinkage is possible in either the hoop or transverse directions at the area of interface between steel and rubber. This will impose tractions on the tyre at the interface, causing tensile stresses in the rubber in planes normal to the interface, which may contribute to the cracking. These stresses will be increased in

magnitude by loss of any mobile ingredients in the rubber, such as processing oil, by evaporation or leaching by rain. It is noted that the extractable content is only 1pphr, less than might be expected to have been used originally.

The depth of the hard material seems to be greater than can be explained by photo-oxidation. It was noted in Chapter 4 - Section 4.2.5a that ozone attack also only affects a thin layer; moreover, it reduces the molecular weight so cannot explain the formation of a hard crust. This leaves oxidation as the primary cause. The depth scale would appear to be determined by diffusion-limited oxidation (Nasdala 2001, Nasdala 2003, Steinke et al. 2011). An additional contribution, consistent with the presence of shrinkage cracks and a higher volume fraction of black in the crust, is loss of low molecular weight material, including low molecular weight products of ozonolysis and oxidation of the rubber molecules by evaporation and leaching. However, loss of such material cannot explain the very substantial rise in T_g (see Table 9.3).

It appears that the presence of antidegradant is the primary cause of the different behaviour, suppressing crust formation at the expense of allowing a deeper penetration of oxidation, but with a more mild effect on the physical properties of rubber, in the Pelham, Bridge bearing.

Because of the low diffusion rate of DOPD, it will remain available as an antioxidant for a very long time. The boundary condition used to generate the DOPD profile in Figure 9.23 will not be appropriate if DOPD diffusion and reaction are coupled to diffusion limited oxidation, since the consumption of DOPD will move inwards from the surface, and be smeared out over the sample thickness. However, the absence of evidence of an effect of oxidation on physical properties in the bulk rubber and the uniform DOPD concentration suggests that oxidation cannot explain the apparent shortage of antioxidants there. Instead, their consumption during vulcanization and/or difficulty in quantitative analysis because of adsorption on the filler are possibilities to consider. It is interesting to consult existing literature and to compare the role of diffusion of DOPD and the mechanism for the antiozonant action of DOPD. Braden (1962) showed that the hypothesis that DOPD works by scavenging ozone at the rubber surface was inconsistent with the rate of diffusion of DOPD to the surface. Instead, it is believed that a layer of ozonised DOPD forms on the rubber surface, which acts as a passive barrier to ozone transfer from air to the reactive rubber molecules (Lake & Mente 1992). Such a mechanism would be ineffective for oxidation, since the concentration of oxygen in the air is so high that no thin organic deformable layer would be very effective as a permeation barrier.

9.6 Conclusions

(1) A theory has been presented for the effectiveness of carbon black filler for the reduction of penetration by light into rubber. Initial experimental results are consistent with it.

(2) A crust has formed on a naturally aged unprotected natural rubber, seemingly in conflict with the prediction of Lindley & Teo (1977). Ozone attack and photo-oxidation would be expected to lead to degraded layers only a few microns thick, whereas the observation is of a crust several hundredfold thicker.

(3) Although a complicated interplay of several processes is likely to have contributed to the crust formation, including leaching by rain, it seems most likely that the primary mechanism determining the crust thickness is diffusion-limited oxidation.

(4) The T_g of the crust is 76°C. This points to a substantial chemical change to the polymer molecules, reducing their flexibility. It could not be explained by leaching alone.

(5) It should be emphasised that in all cases studied, the interior of bulky NR mouldings remains fit for purpose for very long periods, whether (as in the case of the Bramfield tyre) or not (as for the Pelham bearings) a surface crust forms. The presence of an antioxidant appears, from this work, to suppress the formation of a hard, highly oxidised crust, though the minimal exposure of the bearings to directly incident sunlight and rain may also be significant factors.

(6) It is believed that the transient period can be long, so steady state solutions (e.g. Cunliffe & Davis 1982) may be inadequate.

(7) It appears possible to reach agreement with observation by using a high and reaction rate constant α of around 1000.

Chapter 10

Conclusions and Recommendations for Future Work

This final chapter consists of two sections. The first delineates the most significant conclusions arising from the work described and discussed in this thesis. Conclusions presented relate to Chapters 3 to 9 in this order. The second section provides suggestions regarding potential further research based on the findings of the present work that would lead to broader, more definitive or more reliable quantitative conclusions regarding the choice and performance of rubbers for arduous fatigue cycles in a marine environment. It also suggests several developed techniques of experimental works that are useful tools for future research and worthy for further exploration and refinement. A feature of the thesis that is both a limitation and a distinction is that nearly all the characterisation has been done in simple extension. This creates new challenges with respect to phenomena noticed for the more simple and familiar characterisation in simple shear.

10.1 Principal Observation and Conclusions from Completed Research

(1) Fracture mechanics applied in Chapter 3 enables a rational basis for predicting mechanical fatigue of rubber articles. Even though natural rubber is susceptible to oxidative degradation and ozone attack, it is able to sustain high strain and has excellent fatigue resistance relative to other rubbers, especially under non-relaxing conditions with high maximum strains.

Placement of data points representing the measured fatigue lives superimposed on the theoretical lives lead to fits for effective flaw sizes. Nevertheless, the resulting values are significantly dependent on the fatigue strain, especially for the material without antioxidant. The obtained results conflict with expectation from the theory, and this mismatch has been observed and discussed previously by Kingston & Muhr (to be published).

(2) No crack was observed on natural rubber strained to 20% for test piece totally immersed in distilled water in an atmosphere with 50pphm ozone concentration at 40°C for 3 days, in accord with the theory of Lake & Thomas (1967b). Ozone attack of a rubber surface subjected to a non-uniform strain field reveals the nature of the field through the pattern of cracks formed due to the equibiaxial strain field where the principal strains are unequal, the crack orientation is normal to the maximum principal tensile strain.

(3) Softening to cycling between fixed strain limits continues at an approximately constant rate per tenfold increase in number of cycles. The amount of carbon black content affects the softening behaviour of rubber. Lower amounts of carbon black result in less hysteresis and a longer fatigue life for fixed strain cycles. It is surprising that the use of antioxidant 2245 in unfilled rubber reveals that it has an anti-flex cracking characteristic in conflict with expectation (MRPRA 1984) although it is less effective than antioxidant HPPD.

(4) Stress-strain hyperelastic models have been used to describe the extension behaviour of rubber. Tensile experimental data can be used to approximately predict rubber behaviour in compression. Several rubber hyperelastic models have been compared and the prediction of the stress-strain behaviour has been successfully evaluated using the Edwards & Vilgis model which includes effects of slippage and a limit to extensibility. It would be interesting to fit the time-domain viscoplastic model developed by Ahmadi et al. (2008) to the experimental data of uniaxial tension of filled rubber.

(5) Methods have been described to estimate dynamic properties (loss angle and dynamic modulus) from quasistatic tensile load-deflection plots even if done on dumb-bells and with a static prestrain. A surprisingly high loss angle was found in the latter case for low strain amplitude, even for unfilled natural rubber. For filled natural rubber in tension about a static pre-strain of 160%, the Payne effect was surprisingly weak.

(6) Two macrodispersion parameters, the number average particle size and the white area weighted average particle size, were introduced to characterise the macrodispersion of a filled rubber. Neither shows much correlation with the fatigue life of rubber, suggesting that macrodispersion does not strongly affect fatigue life, contrary to expectation.

(7) The most common method used to estimate effective flaw size in rubber is based on using the lifetime results of fatigue tests and the measured power law crack growth characteristics. Apparent original flaw size is that which enables a fit between fatigue lifetime predicted from the crack growth characteristic and that observed. While this effective flaw size may not correspond to the size of a real feature in the material, it is expected to be a useful metric for predicting the fatigue life of the material. It has been observed that the power law under-predicts the crack growth rate at low tearing energies. These studies have confirmed the disturbing conclusion of Kingston & Muhr (2013) that

the best-fit flaw size depends on the strain amplitude of the fatigue test, suggesting a fault in the basic theory. The power law seems to give less strain-dependence of the apparent values for effective flaw size for natural rubber than does the full theory, but this is presumed to be fortuitous.

(8) An ozone free test cabinet has been successfully built. Time did not permit this important facility to be used for more than preliminary experiment.

(9) A recently designed fatigue test machine with twelve stations was successfully assembled and commissioned and integrated with a Labview program for automated recording of observations. This machine can be used to apply a wide range of strain amplitudes subject to relaxing or non-relaxing conditions. For the fixed strain conditions (160±105%) used to screen a wide variation of different rubbers, it was found that load deflection loop decreased with an increase in the number of cycles.

(10) Chapter 7 addressed many different rubber mixes within the context of fatigue testing. For marine applications of rubber exposed to waves, fatigue cycles exceed 3Mcycles per annum. Certain rubber mixes had significantly better performances in terms of fatigue than others and further researches of EDS materials group and other ingredients (yet to be identified) is considered worthy of further exploration. However, unfilled natural rubber is the most appropriate material that should be used since it has a long fatigue life for large strain amplitudes and non-relaxing conditions with low modulus. It is not a good idea to use a lot of filler in natural rubber because it will make the fatigue life of rubber shorter.

(11) Coatings have been suggested to protect rubbers from ozone attack. However, experimental investigation showed the coatings to be vulnerable to cracking at higher strain. Cracks in such a coating can act as stress raising initiators, propagating into the rubber and reducing the tensile strength. It is confirmed that a particular commercially available coating layer fractured and lost adhesion to the rubber surface during tensile strength tests. The fatigue life was significantly enhanced by the coating for 50% strain amplitude but reduced when the strain exceeds 50% strain range, so this coating layer would only be appropriate for rubber components subjected to a low strain range.

(12) Natural rubber compounded with antioxidant seems not to develop a hard surface crust when naturally aged, unlike early rubber artefacts compounded without antioxidants. Also antioxidants can have a strong influence on fatigue life.

(13) A study was made of the depth of penetration of light into black-filled rubber. A theory has been developed relating filler nature and loading to the decay length of light intensity and preliminary results look promising.

(14) Ozone attack makes rubber softer and photo-oxidation would be expected to lead to degrade layers only a few microns thick, whereas hard crusts developed over long periods at ambient temperature are several hundredfold thicker. Although a complicated interplay of several processes is likely to have contributed to such crust formation, including leaching by rain and the minimal exposure to directly incident sunlight, it seems most likely that the primary mechanism determining the crust thickness is diffusion-limited autocatalytic oxidation, possibly initiated by UV light incident on the surface.

(15) A numerical model of diffusion limited oxidation was developed for predicting both transient and steady state profiles of both oxygen concentration and amount of oxygen absorbed.

10.2 Recommendation for Future Work

The present studies have provided insight into some factors that may influence the service-life of rubber. However, there is tremendous scope for further investigation. For instance the following ideas may prove very useful:

- Techniques that look promising could be exploited and developed further:-
    - Ozone free chamber
    - Use of light absorption decay length as a measure of
        - (i)   Effectiveness of different fillers to control photo-oxidation.
        - (ii)   Dispersion of such fillers
    - Use of fatigue machine for cyclic stress relaxation and extension to dynamic properties (i.e. phase angle) as a function of number of cycles.
    - Introduce force-feedback or fatigue machine to enable fatigue tests under constant force and measurements of cyclic creep.

- Investigate the fatigue mechanism using X-ray tomography. This non-destructive technique is a new method to analyze the evolution of the defects population under fatigue loading.

- Evaluate critical tearing energy, T_c, at high rates of tearing and investigate how time-dependent crack growth is related to high strain fatigue when $T \leq T_c$.

- Carry out diffusion and ageing tests using microtome-based cutting to form thin sections through which material profiles can be measured. Currently reliance was placed on collaborators from ENSTA and IFREMER for such techniques, limiting the scope of this aspect of the project.

- Investigate how much antioxidant might be used up during vulcanization.

- Investigate alternative antioxidants with respect to their balance between resistance to leaching and effectiveness as anti-flex cracking.

- Investigate the properties of rubbers coated with Gummiwax and Gummipaint. Both coating materials have been commercialized, but no results have been published regarding their effect on rubber longevity under long-term mechanical fatigue and tensile strength tests.

- Investigate transient effects under fatigue loading and understand crack growth characteristics using pure shear test piece.

- Investigate the rubber fracture surfaces after fatigue test using micrographic technique. Determine the starting crack initiation and identify nature of initiating flaws.

- Investigate the effect of ageing rubber on its crack growth characteristics and fatigue behaviour.

List of References

Ab Malek, K. and Stevenson, A., (1992), "A 100-year case study of the life prediction of natural rubber for an engineering application", Journal of Natural Rubber Research, Vol. 7(2), pp 126-141

Ahmadi, H.R., Kingston, J.G.R. and Muhr, A.H., (2008), "Dynamic properties of filled rubber I-Simple model, experimental data and simulated results", Journal of Rubber Chemistry and Technology, Vol.8, pp 1-18

Ahmadi, H.R. and Muhr, A.H., (2007), "Dynamic properties of filled rubber II-Physical basis of contributions to the model", presented at the Fall 172nd Technical Meeting of the Rubber Division of the American Chemical Society, Inc. Cleveland OH, no. 39, pp. 1-22

Ahmadi, H.R. and Muhr, A.H., (1997), "Modelling dynamic properties of filled rubber", Plastics, Rubber and Composites Processing and Applications, Vol.26, No.10, pp 451-461

Andriyana A. and Verron E., (2005), "Effect of hysteretic response of elastomers on the fatigue life", Constitutive Models for Rubber IV, Austrell & Kari, Eds, pp 31-36

Auer, E.E., Doak, K.W. and Schaffener, I.J., (1958), "Factors affecting laboratory cut-growth resistance of cold SBR tread stocks", Journal of Rubber Chemistry and Technology, Vol. 31, pp 185-201

Arruda, E. M. and Boyce, M.C., (1993), "A three-dimensional constitutive model for the large stretch behaviour of rubber elastic materials", Journal of Mechanics and Physics of Solids, Vol.41, No.2, pp 389-412

Beatty, J.R., (1964), "Fatigue of rubber", Journal of Rubber Chemistry and Technology, 37, pp 1341-1364

Billingham, N.C. and Walker, T.J., (1975), "Autoxidation of poly-4-methylpentene-1.I. The role of diffusion in autoxidation kinetics", Journal of Polymer Science: Polymer Chemistry Edition, 13 (5), pp 1209-1222

Blow, C.M. and Hepburn, C., (1982), Rubber Technology and Manufacture, Published for the Plastics and Rubber Institute by Butterworths, 2nd Edition, pp 1-608

Braden, M. and Gent, A.N., (1960a), "The attack of ozone on stretched rubber vulcanizates. I. The rate of cut growth, Journal of Applied Polymer Science, Vol. III, Issue No. 7, pp 90-99

Braden, M. and Gent A.N., (1960b), "The attack of ozone on stretched rubber vulcanizates. II Conditions for cut growth", Journal of Applied Polymer Science, Vol. III, Issue No.7, pp 100-106

Braden, M. and Gent, A.N., (1961), "Ozone cracking", Proceeding of International Research Institute, pp 88-97

Braden, M., (1962) "Role of diffusion in antiozonant action", Journal Applied Polymer Science, 6, S6-S8

Braden, M. and Gent, A.N., (1962), "The attack of ozone on stretched rubber vulcanizates. III Action of antiozonants", Journal of Applied Polymer Science, Vol. VI, Issue No.22, pp 449-455

Brown, P.S., Porter, M and Thomas, A.G., (1985), "Influence of crosslink structure on properties in crystallising and non-crystallising polyisoprenes", International Rubber Conference, Kuala Lumpur pp 1-26

BS ISO 2781:2008 Rubber, vulcanized or thermoplastic- Determination of density, pp 1-8

BS ISO 48:2007 Rubber, vulcanized or thermoplastic- Determination of hardness (Hardness between 10 IRHD and 100 IRHD), pp 1-19

BS ISO 6943:2007 Rubber, vulcanised- Determination of tension fatigue, pp 1-16

BS ISO 11345:2006 Rubber- Assessment of carbon black and carbon/silica dispersion- Rapid comparative methods, pp 1-26

BS ISO 37:2005 Rubber, vulcanized or thermoplastic- Determination of tensile stress-strain properties, pp 1-25

BS 903-5:2004 Physical testing of rubber- Part 5: Guide to the application of rubber testing to finite element analysis, pp 1-38

BS ISO 1431-1:2004 Rubber, vulcanized or thermoplastic- Resistance to ozne cracking – Part 1: Static and dynamic strain testing, pp 1-13

Bucchi, A. and Hearn, G.E., (2013), "Delay or removal of aneurysm formation in the Anaconda wave energy extraction device", Journal of Renewable Energy, 55, pp 104-119

Bueche, F., (1962), "Mullins effect and rubber-filler interaction", Journal of Rubber Chemistry and Technology, 35, pp 259-273

Cadwell, S.M., Merril, R.A., Sloman, C.M. and Yost, F.L., (1940), "Dynamic fatigue life of rubber", Industrial and Engineering Chemistry, Analytical Edition, Vol 12, No.1, pp 19-23

Chang, C.Y., Tsai, W.T., Cheng, L., Chiu, C.Y., Huang, W.H., Yu, Y.H., Liou, H.T., Ku, Y., Chen, J.N., (1997), "Catalytic decomposition of ozone in air", Journal of Environmental Science and Health Part A – Environmental Science and Engineering & Toxic and Hazardous Substance Control", Vol.32, Issue. 6, pp 1837-1874

Chaplin, J.R., Farley, F.J., Prentice, M.E., Rainey, R.C.T., Rimmer, S.J. and Roach, A.T., (2007a), "Development of the Anaconda all-rubber WEC", The Proceeding of the 7th European Wave and Tidal Energy Conference, Lisbon, pp 1-13

Chaplin, J.R., Farley, F.J, Prentice, M.E. and Rainey, R.C.T., (2007b), "Power conversion in the Anaconda WEC", 22nd International Workshop on Water Waves and Floating Bodies, pp 1-4

Chapman, A.V. and Porter, M., (1988), "Sulphur vulcanisation chemistry," in Roberts, A.D., (ed.), Natural Rubber and Technology, Oxford University Press, Chapter 12, pp 513-620

Cheetham, I.C. and Gurney, W.A., (1961), "Ozone-air velocity factor in ozone-cracking", Transaction of the Institution of the Rubber Industry, Vol.37, No.2, pp 35-42

Choi, I.S. and Roland, C.M., (1996), "Intrinsic defects and the failure properties of cis-1,4-polyisoprenes", Journal of Rubber Chemistry and Technology, Vol. 69, pp 591-599

Clough, R.L. and Gillen, K.T., (1992), "Oxygen diffusion effects in thermally aged elastomers", Polymer Deradation and Stability 38, pp 47-56

Coran, A.Y. and Donnet, J.B., (1995), "The dispersion of carbon black in rubber Part I. Rapid method for assessing quality of dispersion", Journal of Rubber Chemistry and Technology", Vol.65, pp 973-997

Crank, J., (1975), "The mathematics of diffusion", Published OUP, 2nd Edition

CRES - Centre for Renewable Energy Sources, (2002), Wave energy utilization in Europe-Current status and perspectives, pp 1-27

Cunliffe, A.V. and Davis, A., (1982), "Photo-oxidation of thick polymer samples – Part II: The influence of oxygen diffusion on the natural and artificial weathering of polyolefins", Polymer Degradation and Stability, 4, pp 17-37

Davies, B., (1988), "The longest serving polymer", Rubber Developments, 41 (4), pp 102-109

Dizon, E.S., Hicks, A.E. and Chirico, V.E., (1974), "The effect of carbon black parameters on the fatigue life of filled rubber compounds", Journal of Rubber Chemistry and Technology, Vol.47, pp 231-249

Edwards, S.F. and Vilgis, Th., (1986), "The effect of entanglement in rubber elasticity", Polymer, Vol.27, pp 483-492

Erickson, E.R., Berntsen, R.A., Hill, E. L. and Paul Kusy, (1958), "The reaction of ozone with SBR Rubbers", ASTM Special Technical Publication No. 229, pp 11-29

Franta, I., (1989), "Elastomers and Rubber Compounding Materials", Franta, I., Ed., Elsevier Amsterdam-Oxford-New York-Tokyo, pp 325-331

Farley, F.J.M. and Rainey, R.C.T., (2006a), "Radical design options for wave-profiling wave energy converters", 21st International Workshop on Water Waves and Floating Bodies, Loughborough, UK, pp 1-4

Farley, F.J.M. and Rainey, R.C.T., (2006b), "Anaconda-The bulge wave sea energy converter", Maritime Energy Development Ltd., pp 1-12

Flory, Paul, J., (1947), "Thermodynamics of crystallization in high polymers. I. Crystallization induced by stretching", The Journal of Chemical Physics, Vol. 15, 6, pp 397-408

Flory, Paul, J., (1953), "Principles of Polymer Chemistry", Cornell University Press, Ithaca, New York, pp 1-672

Field, J.E., (1941), "An X-ray study of the proportion of crystalline and amorphous components in stretched rubber", Journal of Applied Physics, Vol.12, pp 23-34

Fuller, K.N.G., and Roberts A.D., (1999), "Longevity of natural rubber structural bearings", Rubber World, 221, 3, pp 36-47

Fujita, T., Ishida, K., Yoshizawa, T. Nishizawa, I. and Muramatu, Y., (1995), "Study for the prediction of the long-term durability of seismic isolators, PVP Vol. 319 ASME, pp 197-203

Garvey, B.S., (1965), "Rubber chemistry: A great adventure", Journal of Rubber Chemistry and Technology, Vol.38, Issue 3, pp 11-28

Gehman, S.D., (1967), "Heat transfer in processing and use of rubber", Journal of Rubber Chemistry and Technology, Vol. 40, pp 38-51

Gent, A.N., Lindley, P.B. and Thomas, A.G., (1964), "Cut growth and fatigue of rubbers. I. The relationship between cut growth and fatigue", Journal of Applied Polymer Science, Vol.8, pp 455-466

Gent, A.N. and Hindi, M., (1990), "Effect of oxygen on the tear strength of elastomer", Journal of Rubber Chemistry and Technology, Vol. 63, Issue 1, pp123-134

Gent, A.N. and Scott, K.W., (1992), "Engineering with rubber- how to design rubber components", Gent, A.N., Ed., Carl Hanser Verlag, Munich, Oxford University Press, Oxford, Chapter 4, pp 67-93

Girard and son, (1799), Prof. Grant E. Hearn's MSc. lecture notes on Wave Energy, University of Southampton

Greensmith, H.W. and Thomas, A.G., (1955), "Rupture of rubber. Part III. Determination of tear properties", Journal of Polymer Science, Vol.18, pp 189-200.

Greensmith, H.W., (1963), "Rupture of rubber. Part X. The change in stored energy on making a small cut in a test piece held in simple extension", Journal of Applied Polymer Science, 7, pp 993-1002

Gregory, M.J., (1979), "Stress/strain behaviour of filled rubbers at moderate strains", Plastic and rubber: Material and Applications, pp 184-188

Gough, J., Gregory, I.H. and Muhr, A.H., (1999), "Determination of the constitutive equations for vulcanised rubber", in "Finite Element Analysis of Elastomers", D. Boast and V.A Coveney, Eds., Prof. Eng. Publ. Ltd, London, pp 5-26

Gough, J., (2000), "Stress strain behaviour of rubber", Phd Thesis, Queen Mary University of London, pp 1-263

Gregory, I.H., Muhr, A.H. and Stephens, I.J., (1997), "Engineering applications of rubber in simple extension", Plastics, Rubber and Composites Processing and Applications, 26, 3, pp 118-122

Haigh, B.P., (1915), "Alternating stress tests of a sample of mild steel", The British Association Stress Committee. Report of British Association, 85, pp 163-170

Hamed, G.R., (1983), "Effect of crosslink density on the critical flaw size of a simple elastomer", Journal of Rubber Chemistry and Technology, Vol. 5, Issue 1, pp 244-251

Hamed, G.R., (1992), "Engineering with rubber, How to design rubber components", A. Gent, Ed., Carl Hanser Verlag, Munich, Chapter 2, pp 13-31

Harwood, J.A.C. Mullins, L. and Payne, A.R., (1965), "Stress softening in natural rubber vulcanizates Part II. Stress softening effect in pure gum and filler loaded rubbers", Journal of Applied Polymer Science, Vol.9, pp 3011-3021

Harwood, J.A.C. and Payne, A.R., (1966), "Stress softening in natural rubber vulcanizates. Part IV Unfilled vulcanizates", Journal of Applied Polymer Science, Vol.10, pp 1203-1211

Harwood, J.A.C., Mullins, L. and Payne, A.R., (1967a), "Stress softening in rubbers- A Review", Journal of the IRI, Vol. 1, No.1, pp 1-9

Harwood, J.A.C. and Payne, A.R., (1967b), "Stress softening in natural rubber vulcanizates. Part V. The anomalous tensile behaviour of natural rubber", Journal of Applied Polymer Science, Vol.11, pp 1825-1834

Harwood, J.A.C. and Schallamach, A., (1967), "Dynamic behaviour of natural rubber during large extension", Journal of Applied Polymer Science, Vol.11, pp 1835-1850

Hess, W.M., (1991), "Characterization of dispersion", Journal of Rubber Chemistry and Technology, Vol.64, pp 386-448

Huntink N.M., (2003), "Durability of rubber products", PhD Thesis, University of Twente, pp 1-207

http://www.direct.gov.uk/en/NI1/Newsroom/DG_179190

http://www.imo.org/blast/mainframe.asp?topic_id=233

http://e.wikipedia.org/wiki/Yoshio_Masuda

Jones, K.P., (1968), "The distribution of ozone at the earth's surface", Journal of the Institute Rubber Industries, pp 194-198

Kamaruddin, S., Le Gac, P-Y., Marco, Y. and Muhr, A.H., (2011), "Formation of crust on NR after ageing", Conference on Constitutive Models for Rubber VII, CRC Press Taylor & Francis Group, A Balkema Book, pp 197-201

Kamaruddin, S., Muhr, A.H., Le Gac, P-Y., Marco, Y. and Le Saux, V., (2013), "Modelling naturally aged NR mouldings", Conference on Constitutive Models for Rubber VIII, CRC Press Taylor & Francis Group, A Balkema Book, pp 37-42

Kato, M., Watanabe, Y., Yoneda, G., Tanimoto, E., Hirotani, T., Shirahama, K., Fukushima, Y., and Murazami, Y., (1996), "Investigation of aging effects for laminated rubber bearings of Pelham Bridge", Paper 1450, 11th World Conference Earthquake Engineering, Published Elsevier

Kempermann, Th., (1988), "Sulfur-free vulcanization systems for diene rubber", Journal of Rubber Chemistry and Technology, Vol.61, pp 422-447

Kingston, J.G.R. and Muhr, A.H., (2011), "Determination of effective flaw size for fatigue life prediction", Conference on Constitutive Models for Rubber VII, CRC Press Taylor & Francis Group, A Balkema Book, pp 337-342

Kingston, J.G.R. and Muhr, A.H., (2013), "Determination of effective flaw size for fatigue life prediction", to be submitted to the Journal of Polymer Rubber Chemistry

Knight, G.J. and Lim, H.S., (1975), "Factors influencing high temperature ageing of large natural rubber components", Proceeding of International Rubber Conference, Kuala Lumpur, pp 57-73

Kubelka, P., (1948), "New contributions to the optics of intensely light-scattering materials. Part I", Journal of the Optical Society of America, Vol. 38, Number 5, pp 448-457

Lake, G.J. and Lindley, P.B., (1964a), "Cut growth and fatigue of rubbers. II Experiments on a non-crystallizing rubber", Journal of Applied Polymer Science, Vol.8, pp 707-721

Lake, G.J. and Lindley, P.B., (1964b), "Ozone cracking, flex cracking and fatigue of rubber", Rubber Journal, pp 1-15

Lake, G.J. and Lindley, P.B., (1965), "The mechanical fatigue limit for rubber", Journal of Applied Polymer Science, Vol.9, pp 1233-1251

Lake, G.J. and Lindley, P.B., (1966), "Fatigue of rubber at low strains", Journal of Applied Polymer Science, Vol.10, pp 343-351

Lake, G.J. and Thomas, A.G., (1967a), "Physics of failure in rubber", Rubber and rubber-plastic from vintage reprint 20, Issue no.4, pp 211-217

Lake, G.J. and Thomas, A.G., (1967b), "Ozone attack on strained rubber", The Proceedings of the International Rubber Conference, pp 525-536

Lake, G.J. and Thomas, A.G., (1992), "Strength", Alan N. Gent, Ed., Engineering with rubber- How to design rubber components, Oxford University Press, Oxford, Chapter 5, pp 94-127

Lake, G.J., (1970), "Application of fracture mechanics to failure in rubber articles, with particular reference to tyre", Proceedings of International Conference on Yield Deformation and Fracture of Polymers, Cambridge, United Kingdom, pp 1-6

Lake, G.J., (1972), "Mechanical fatigue of rubber", Journal of Rubber Chemistry and Technology, Vol. 45, No.1, pp 309-328

Lake, G.J., (1983), "Aspects of fatigue and fracture of rubber", Progress of Rubber Technology, pp 89-143

Lake, G.J. and Pond, T.J., (1989), "Effects of aqueous environments on fatigue and elastic properties of rubber", Polymers in a Marine Environment, pp 141-147

Lake, G.J. and Mente, P.G., (1992), "Ozone cracking and protection of elastomers at high and low temperatures", Journal of Natural Rubber Research, 7, pp 1-13

Lake, G.J. and Thomas, A.G., (1992), "Engineering with rubber, how to design rubber components", A. Gent, Ed., Carl Hanser Verlag, Munich, Chapter 5, pp 95-127

Lake, G.J., (1995), "Fatigue and fracture of elastomers", Journal of Rubber Chemistry and Technology, Vol. 68, No.1, pp 435-460

Latos, E.J. and Sparks, A.K., (1969), "Water leaching of antioxidants", Rubber Journal, pp 21-28

Layer, R.W. and Lattimer, R.P., (1990), "Protection of rubber against ozone", Journal of Rubber Chemistry and Technology, Vol. 63, pp 426-450

Lewis, P.M., (1972), "Protecting natural rubber against ozone cracking", Natural Rubber Technology, 3, (1), No.1

Lindley, P.B., (1962), "Natural rubber in bridge bearings, TB7 Additional Information sheet A, Engineers' Edition of NRPRA Technical Bulletin 7

Lindley, P.B. and Thomas, A.G., (1962a), "Fundamental study of the fatigue of rubber", 4th Rubber Technology Conference, London, pp 1-14

Lindley, P.B., (1973), "Relation between hysteresis and the dynamic crack growth resistance of natural rubber", International Journal of Fracture, Vol.9, No.4, pp 449-462

Lindley, P.B., (1974), "Non-relaxing crack growth and fatigue in a non-crystallizing rubber", Rubber Chemistry and Technology, Vol.74, No.5, pp 1253-1264

Lindley, P.B. and Teo, S.C., (1977), "High temperature ageing of rubber blocks", Plastics and Rubber: Materials and Publications, pp 82-88

Lindley, P.B., Fuller, K.N.G. and Muhr, A.H., (1994), NR Technical Bulletin – Engineering design with natural rubber, pp 1-33

Loganathan, K.S., (2000), "Rubber Engineering-India Rubber India", McGraw-Hill, Chapter 2, pp56-113 and Chapter 6, pp 295-316

Lord Technical leaflet, (2010), HPC-5B and HPC-5C – Product information

Luchini, J.R., Peters, J.M. and Arthur, R.H., (1994), "Tire rolling loss computation with the finite element method", Tire Science and Technology, Vol.22, No.4, pp 206-222

Marlow, R.S., (2003), "A general first-invariant hyperelastic constitutive model", Constitutive Models for Rubber III, Busfield & Muhr (eds), pp 157-160

Mars, W.V., (2001), Multiaxial fatigue of rubber, Ph.D thesis, University of Toledo, pp 1-517

Mars, W.V. and Fatemi, A., (2002), "A literature survey on fatigue analysis approaches for rubber", International Journal of Fatigue, 24, pp 949-961

Mars, W.V. and Fatemi, A., (2003), "Fatigue crack nucleation and growth in filled natural rubber", Fatigue Fracture engineering Material Structure, 26, pp 779-789

Mars, W.V., (2004), "Factors that affect the fatigue life of rubber: a literature survey", Journal of Rubber Chemistry and Technology, Vol.77, pp 391-412

Mars, W.V. and Fatemi, A., (2006a), "Nucleation and growth of small fatigue cracks in filled natural rubber under multiaxial loading", Journal of Material Science, 41, pp 7324-7332

Mars, W.V. and Fatemi, A., (2006b), "Multiaxial stress effect on fatigue behaviour of filled natural rubber", International Journal of Fatigue, 28, pp 521-529

Medalia, A.I., (1987), "Effect of carbon black on ultimate properties of rubber vulcanizates", Journal of Rubber Chemistry and Technology, Vol.60, pp 45-61

Mitchell, J.C. and Meier, D.J. (1968), "Rapid stress-induced crystallization in natural rubber", Journal of Polymer Science, Part A-2, Vol. 6, pp 1689-1703

Moore, C.G., (1965), "Chemistry of vulcanization", Proceeding of the NRPRA Jubilee Conference, pp 167-194

Mooney, M. (1940), "A theory of large elastic deformation", Journal of Applied Physics, 11, pp 582-592

MRPRA, (1984), The Natural Rubber Formulary and Property Index, pp 1-345

Muhr, A.H., (2005), "Modeling the stress-strain behavior of rubber", Journal of Rubber Chemistry and Technology, Vol.78, pp 391-425

Muhr, A.H., (2013), "Use of Natural Rubber in wave energy conversion devices", to be submitted to the Journal Rubber Research

Muhr, A.H., (2006), "Fracture of rubber-steel laminated bearing", Chapter 15 in Elastomers and Components: Service Life Prediction", ed.V.A. Coveney, Woodhead Publishing in Materials, Cambridge

Muller, F. Horst, (1957), "The stress-strain behaviour of natural rubber", Journal of American Chemical Society, Vol.30, pp 1027-1044

Mullin, L., (1947), "Effect of stretching on the properties of rubber", Journal of Rubber Research, 16, pp 275-289

Nasdala, L., (2001), "Oxidative ageing of filled elastomers", Constitutive Models for Rubber II", ed Besdo, D., Schuster R.H. and Ihlemann, J., pp 205-211

Nasdala, R.G., Wei, Y. and Robert H., (2003), "Homogenisation techniques for the analysis of oxygen diffusion and reaction in fiber-reinforced elastomer", Constitutive Model for Rubber III, ed Busfield, J.J.C. and Muhr, A.H., pp 85-91

Natural Rubber Engineering Data Sheet, (1979), Published by the Malaysian Rubber Producers' Research Association, Tun Abdul Razak Laboratory

Oliver, W.C. and Pharr, G.M., (1992), "A new improved technique for determining hardness and elastic modulus using load and sensing indentation experiments", Journal of Materials Research, Vol.7, No. 6, pp 1564-1582

Omar A. Al-Hartomy, Falleh Al-Solamy, Ahmed Al-Ghanmdi, Nikolay Dishovsky, Milcho Ivanov, Mihail Mihaylov and Farid El-Tantawy, (2011), "Influence of carbon black structure and specific surface area on the mechanical and dielectric properties of filled rubber composite", International Journal of Polymer Science, Vol. 2011, pp 1-8

Ogden, R.W., (1972), "Elastic deformation of rubberlike solids", Mechanics of Solids, Pergamon, ed.H.G. Hopkins, M.J. Sewell, pp 1-10

Ostoja-Kuczynski E., Charrier, P., Verron, E., Gornet, L. and Marckmann, G., (2005), "Influence of mean stress and mean strain on fatigue life of carbon black filled natural rubber", Constitutive Models for Rubber IV, Austrell & Kari (eds), pp 15-21

Payne, A.R., (1965), "Strainwork dependence of filler-loaded vulcanizates", Journal of Applied Polymer Science, Vol.8, pp 2661-2686

Prufen und Messen, (2005), "New reference value for the description of filler dispersion with the Dispergrader 1000NT", KGK Kautschuk Gummi Kunstoffe, 58. Jahrgang, Nr. 7-8, pp 390-393

Rivlin, R.S., (1948), "Large elastic deformations of isotropic materials. IV. Further development of general theory", Philosophical Transactions of the Royal Society, Vol.241, A.835, pp 379-397

Rivlin, R.S. and Thomas, A.G., (1953), "Rupture of rubber. I. Characteristic energy for tearing", Journal of Polymer Science, Vol.10, No.3, pp 291-318

Rivlin, R.S., (1956), "Large elastic deformations", Rheology: Theory and Applications, Vol. 1, F.R Eirich ed., Academic Press, New York, pp 351-385

Rivlin, R.S. and Sauders, D.W., (1951), "Large elastic deformations of isotropic materials VII Experiments on deformation of rubber", Philosophical Transactions of the Royal Society, A243, pp 251-298

Roberts, D.E. and Mandelkern, L., (1955), "Thermodynamics of crystallization in high polymers: Natural rubber", Journal of Thermodynamics of Crystallization in Natural Rubber, 77, pp 781-786

Roth, J.A. and Sullivan, D.E., (1981), "Solubility of ozone in water", Journal of Industrial Engineering, Chemistry and Fundamental, Vol.20, pp 137-140

Steinke, L, Spreckels, J., Flamm, M. and Celina, M., (2011), "Model for heterogeneous aging of rubber products", Plastics Rubber and Composites, Vol.40, 4, pp 175-179

Thomas, A.G., (1955), "Rupture of rubber Part II. The strain concentration at an incision", Journal of Polymer Science, Vol.18, pp 177-188

Thomas, A.G., (1958), "Rupture of rubber Part V. Cut growth in natural rubber vulcanizates", Journal of Polymer Science, Vol.31, pp 467-480

Thomas, A.G., (1960), "Rupture of rubber Part VI. Further experiment on the tear criterion", Journal of Applied Polymer Science, 3, pp 168-174

Thomas, A.G., (1966), "Fracture of rubber", Physical Basis of Yield and Fracture: Conference Proceedings, pp 134-142

Thomas, A.G., (1974), "Crack growth and failure in rubbers", Reprinted from: Deformation and Fracture of High Polymers, Edited by H.Hennings Kausch, John A. Hassell and Robert I. Jaffee, Plenum Press, pp 467-469

Thomas, A.G., (1994), "The development of fracture mechanics for elastomers", Journal of Rubber Chemistry and Technology, Vol.67, pp 50-60; Goodyear Medal paper presented to the American Society Rubber Division Meeting, Chicago, April, 1994.

Timbrell, C., Wiehahn, M., Cook, G. and Muhr, A.H., (2003), "Simulation of crack propagation in rubber", Constitutive Model for Rubber III, Busfield & Muhr, Balkema, pp 11-20

Toki, S., Sics, I. Ran, S. Liu, L. and Hsiao, S.B., (2002), "New insight into structural development in natural rubber during uniaxial deformation by in situ synchrotron X-ray diffraction", Macromolecules, 35, pp 6578-6584

Treloar, L.R.G., (1949), "The physics of rubber elasticity", Oxford University Press, Amen House, London, pp 1-254

Treloar, L.R.G., (1975), "The physics of rubber elasticity", 3rd Edition, Clarendon Press Oxford, pp 1-310

Valentin, H. and Chaplin, J.R., (2011), "Dynamic mechanical analysis of rubber used in Anaconda", 9th European Wave and Tidal Energy Conference EWTEC, pp 1-10

van Amerongen, G. J., (1964), Diffusion in polymers", Journal of Rubber Chemistry and Technology, 37, pp 1065-1152

Vegvari, P.C., Hess, W.M. and Chirico, V.E., (1978), "Measurement of carbon black dispersion in rubber by surface analysis", Journal of Rubber Chemistry and Technology, Vol.51, pp817-839

William, F. Ames, (1969), Numerical methods for partial differential equations, Barnes & Noble, Inc., New York, 1969, pp 49-54

Wise, J., Gillen, K.T. and Clough, R.L., (1997), "Quantitative model for the time development of diffusion-limited oxidation profiles", Polymer, 38, pp 1929-1944

Wöhler, A., (1867), Wöhler's experiments on the strength of metals, Vol.2, pp 160

Yeoh, O.H., (1990), "Characterization of elastic properties of carbon-black-filled rubber vulcanizates", Journal of Rubber Chemistry and Technology, 63, pp 792-804

Yeoh, O.H. and Fleming, P.D., (1997), "A new attempt to reconcile the statistical and phenomenological theories of rubber elasticity", Journal of Polymer Science: Part B, Vol. 35, pp 1919-1931

Yeoh, O.H., (1997), "On Ogden strain-energy function", Journal of Rubber Chemistry and Technology, Vol.70, pp 175-182

Yeoh, O.H., (1998), "Strain energy release rates for some classical rubber test pieces by Finite Element Analysis", Paper presented at the 154th Meeting of the Rubber Division, American Chemical Society, September 29th – October 2nd, pp 1-18

Zuev, Yu.S. and Malofeevskaya,V.F., (1961), "Effect of moisture on the resistance of rubber to ozone cracking", Soviet Rubber Technology, 20, Vol.6, pp 23-26

APPENDIX A

Determination of Nominal Stress for the Edwards and Vilgis Model

This appendix first provides equations related to the nominal stress in tension and compression conditions.

The i$^{\text{th}}$ principal nominal stress is given by $f_i = \frac{\partial W}{\partial \lambda_i}$, so the true stress is given by

$$\sigma_i = \frac{f_i \lambda_i}{\lambda_1 \lambda_2 \lambda_3} \ . \tag{1}$$

Recalling that due to incompressibility of rubber $\lambda_1 \lambda_2 \lambda_3 = 1$, it follows that

$$\sigma_i = \lambda_i \frac{\partial W}{\partial \lambda_i} \ . \tag{2}$$

Here, no summation over the repeated index i is implied.

However, for an incompressible material, σ_i is known only to within an unknown stress σ. Thus for an incompressible material this implies

$$\sigma_i = \lambda_i \frac{\partial W}{\partial \lambda_i} + \sigma \tag{3}$$

hence,

$$\sigma_1 - \sigma_3 = \lambda_1 \frac{\partial W}{\partial \lambda_1} - \lambda_3 \frac{\partial W}{\partial \lambda_3} \ . \tag{4}$$

In the case of a sample being subjected to a simple tension then $\sigma_3 = 0$ and hence

$$\sigma_1 = \lambda_1 \frac{\partial W}{\partial \lambda_1} - \lambda_3 \frac{\partial W}{\partial \lambda_3} \tag{5}$$

or noting $\lambda_3 = \frac{1}{\sqrt{\lambda_1}}$ then

$$\sigma_1 = \lambda_1 \frac{\partial W}{\partial \lambda_1} - \frac{1}{\sqrt{\lambda_1}} \frac{\partial W}{\partial \lambda_3}. \tag{6}$$

For an incompressible material with $W = W(I_1, I_2)$, the equivalent corresponding alternative expression are:

$$\sigma_i = 2 \left[\lambda_i^2 \frac{\partial W}{\partial I_1} - \frac{1}{\lambda_i^2} \frac{\partial W}{\partial I_2} \right] + \sigma \tag{7}$$

and hence

$$\sigma_1 - \sigma_3 = 2 \left[\lambda_1^2 \frac{\partial W}{\partial I_1} - \frac{1}{\lambda_1^2} \frac{\partial W}{\partial I_2} \right] - 2 \left[\lambda_3^2 \frac{\partial W}{\partial I_1} - \frac{1}{\lambda_3^2} \frac{\partial W}{\partial I_2} \right] \ . \tag{8}$$

With $\lambda_1 = \lambda$ and $\lambda_3 = \frac{1}{\sqrt{\lambda}}$ then

$$\sigma_1 - \sigma_3 = 2\left[(\lambda^2 - \frac{1}{\lambda})\frac{\partial W}{\partial I_1} - (\frac{1}{\lambda^2} - \lambda)\frac{\partial W}{\partial I_2}\right] = 2(\lambda^2 - \frac{1}{\lambda})\left[\frac{\partial W}{\partial I_1} - \left(\frac{\frac{1}{\lambda^2} - \lambda}{\lambda^2 - \frac{1}{\lambda}}\right)\frac{\partial W}{\partial I_2}\right]. \tag{9}$$

In simple extension $\sigma_3 = 0$, and hence

$$\sigma_1 = 2\left(\lambda^2 - \frac{1}{\lambda}\right)\left[\frac{\partial W}{\partial I_1} + \frac{1}{\lambda}\frac{\partial W}{\partial I_2}\right] = 2\left(\lambda - \frac{1}{\lambda^2}\right)\left[\frac{\partial W}{\partial I_1} + \frac{1}{\lambda}\frac{\partial W}{\partial I_2}\right]. \tag{10}$$

Edwards & Vilgis (1986) give the strain energy function in the form:

$$\frac{W}{kT} = \frac{N_c}{2}\left\{\frac{\sum(1-\alpha^2)\lambda_i^2}{1-\alpha^2\sum\lambda_i^2} - \ln(1 - \alpha^2\sum\lambda_i^2)\right\} + \frac{N_s}{2}\left\{\sum\left[\frac{\lambda_i(1+\eta)(1-\alpha^2)}{(1+\eta\lambda_i^2)(1-\alpha^2\sum\lambda_i^2)} + \ln(1+\eta\lambda_i^2)\right] - \ln(1 - \alpha^2\sum\lambda_i^2)\right\} \tag{11}$$

where the Z in the denominator of the first fraction in the expression in the paper has been replaced by Σ, to correct an assumed a typo graphical error.

For our purpose, it is convenient to re-express W as a function of the invariants I_1 and I_2, as a step towards use of the Finger equation when implementing it.

Note that,

$$\sum \lambda_i^2 = I_1$$

$$\sum \ln(1 + \eta\lambda_i) = \ln\left(\prod(1 + \eta\lambda_i^2)\right)$$

where

$$\prod(1 + \eta\lambda_i^2) = 1 + \eta(\lambda_1^2 + \lambda_2^2 + \lambda_3^2) + \eta^2(\lambda_1^2\lambda_2^2 + \lambda_2^2\lambda_3^2 + \lambda_1^2\lambda_3^2) + \eta^3(\lambda_1^2\lambda_2^2\lambda_3^2)$$

$$= 1 + \eta I_1 + \eta^2 I_2 + \eta^3 \quad \text{if} \quad I_3 = 1$$

$$\sum \frac{\lambda_i^2}{(1 + \eta\lambda_i^2)} = \frac{\lambda_1^2(1 + \eta\lambda_2^2)(1 + \eta\lambda_3^2) + \lambda_2^2(1 + \eta\lambda_1^2)(1 + \eta\lambda_3^2) + \lambda_3^2(1 + \eta\lambda_1^2)(1 + \eta\lambda_2^2)}{\prod(1 + \eta\lambda_i^2)}$$

$$= \frac{I_1 + 2\eta I_2 + 3\eta^2}{1 + \eta I_1 + \eta^2 I_2 + \eta^3} \tag{12}$$

again assuming an isochoric deformation i.e $I_3 = 1$.

Writing $\frac{N_c kT}{2} = \frac{G_c}{2}$ and $\frac{N_s kT}{2} = \frac{G_s}{2}$, this leads to

$$W = \frac{G_c}{2}\left\{\frac{(1-\alpha^2)I_1}{1-\alpha^2 I_1} - \ln(1 - \alpha^2 I_1)\right\} + \frac{G_s}{2}\left\{\frac{(1+\eta)(1-\alpha^2)}{1-\alpha^2 I_1} \cdot \frac{I_1 + 2\eta I_2 + 3\eta^2}{1 + \eta I_1 + \eta^2 I_2 + \eta^3} + \ln(1 + \eta I_1 + \eta^2 I_2 + \eta^3) - \ln(1 - \alpha^2 I_1)\right\} \tag{13}$$

In more compact form:

$$W = \frac{G_c}{2}\left\{\frac{(1-\alpha^2)I_1}{A} - \ln(A)\right\} + \frac{G_s}{2}\left\{\frac{(1+\eta)(1-\alpha^2)}{A}\cdot\frac{C}{B} + \ln(B) - \ln(A)\right\} \qquad (14)$$

where,

$A = 1 - \alpha^2 I_1$

$\Rightarrow \frac{\partial A}{\partial I_1} = -\alpha^2, \quad \frac{\partial A}{\partial I_2} = 0$

$B = 1 + \eta I_1 + \eta^2 I_2 + \eta^3$

$\Rightarrow \frac{\partial B}{\partial I_1} = \eta, \quad \frac{\partial B}{\partial I_2} = \eta^2$

$C = I_1 + 2\eta I_2 + 3\eta^2$ $\qquad (15)$

$\Rightarrow \frac{\partial C}{\partial I_1} = 1, \quad \frac{\partial C}{\partial I_2} = 2\eta$

$\frac{\partial AB}{\partial I_1} = \frac{\partial A}{\partial I_1}\cdot B + A\cdot\frac{\partial B}{\partial I_1} = -\alpha^2 B + \eta A$

$\frac{\partial AB}{\partial I_2} = \frac{\partial A}{\partial I_2}\cdot B + A\cdot\frac{\partial B}{\partial I_2} = \eta^2 A$

Hence,

$$\frac{\partial W}{\partial I_1} = \frac{G_c}{2}\left\{\frac{1}{A} + \frac{\alpha^2(1-\alpha^2)}{A^2}\right\}$$
$$+ \frac{G_s}{2}\left\{\frac{(1-\eta)(1-\alpha^2)}{AB} - \frac{(1+\eta)(1-\alpha^2).C.(\eta A - \alpha^2 B)}{(AB)^2} + \frac{\eta}{B} + \frac{\alpha^2}{A}\right\}$$

$$\frac{\partial W}{\partial I_2} = \frac{G_s}{2}\left\{\frac{2\eta(1+\eta)(1+\alpha^2)}{AB} - \frac{\eta^2(1+\eta)(1-\alpha^2).AC}{(AB)^2} + \frac{\eta^2}{B}\right\}$$

$$(16)$$

1) $\ln(1-\alpha^2(I_1-3)) \rightarrow -\infty$ as $\alpha^2(I_1-3) \rightarrow 1$.

Let I_m be the value of I_1 such that $\alpha(I_1-3) = 1$

$\Rightarrow \alpha^2 = \frac{1}{I_m-3}$

2) as $(I_1-3) \rightarrow 0$, $\ln(1-\alpha^2(I_1-3)) \rightarrow \alpha(I_1-3)$.

$\Rightarrow \frac{(1-\alpha^2)(I_1-3)}{1-\alpha^2(I_1-3)} - \ln(1-\alpha^2(I_1-3))$

$$\rightarrow \frac{(1-\alpha^2)(I_1-3)-\alpha^2(I_1-3)(1-\alpha^2(I_1-3))}{1-\alpha^2(I_1-3)}$$

$$=\frac{(I_1-3)+\alpha^4(I_1-3)^2}{1-\alpha^2(I_1-3)}$$

$$=\frac{1-\alpha^4(I_1-3)}{1-\alpha^2(I_1-3)}\cdot(I_1-3)$$

$\sim (I_1\text{-}3)$ since both α^2 and $(I_1\text{-}3)$ are very small. In this way, the N_c term reduces to the neo-Hookean model, as does the Gent model. As I_i increases, the Edwards and Vilgis model will diverge a bit from the Gent model.

Note that as $I_1 \rightarrow I_m$, the upturn part of W is the same in both cases $\left(ln\left(1-\frac{I_1-3}{I_m-3}\right)\right)$ but for the Edwards and Vilgis model prefactor is smaller - just $\frac{1}{2}G$ instead of $\frac{1}{2}G(I_m-3)$.

APPENDIX B

The Integral Form of the Equation Describing
Crack Growth Rate versus Tearing Energy

The relationship between fatigue life N and cyclic crack growth rate dc/dn may be expressed as (see Equation 3.16):

$$N = \int_{c_i}^{\infty} \frac{dc}{dc/dn} = \int_{c_i}^{c_0} \frac{dc}{dc/dn} + \int_{c_0}^{c_t} \frac{dc}{dc/dn} + \int_{c_t}^{\infty} \frac{dc}{dc/dn} \qquad (1)$$

In the first integral $\frac{dc}{dn} = r$, a constant rate, and hence

$$\int_{c_i}^{c_0} \frac{dc}{dc/dn} = \int_{c_i}^{c_0} \frac{1}{r} dc = \frac{1}{r}(c_0 - c_i) \, . \qquad (2)$$

For the second integral:

$$\int_{c_0}^{c_t} \frac{dc}{dc/dn} = \int_{c_0}^{c_t} \frac{dc}{r_A \left\{ \frac{2kWc - T_0}{T_{ref}} \right\} + r} = \left[\frac{T_{ref}}{r_A 2kW} \ln \left\{ r_A \left(\frac{2kWc - T_0}{T_{ref}} \right) + r \right\} \right]_{c_0}^{c_t} = \frac{T_{ref}}{r_A 2kW} \ln \left[\frac{r_A \left(\frac{2kWc_t - T_0}{T_{ref}} \right) + r}{r_A \left(\frac{2kWc_0 - T_0}{T_{ref}} \right) + r} \right] \qquad (3)$$

which simplifies to

$$= \frac{T_{ref}}{r_A 2kW} \ln \left[\frac{2kWc_t - T_0 + \frac{r}{r_A} T_{ref}}{2kWc_0 - T_0 + \frac{r}{r_A} T_{ref}} \right] \qquad (4)$$

Finally for the third integral we have

$$\int_{c_t}^{\infty} \frac{dc}{dc/dn} = \int_{c_t}^{\infty} \frac{dc}{r_B \left(\frac{2kWc}{T_{ref}} \right)^{\beta} + r} \quad \text{and assuming } r \text{ is negligible, it follows that}$$

$$\int_{c_t}^{\infty} \frac{dc}{dc/dn} = \left[\left(\frac{T_{ref}}{2kW} \right)^{\beta} \frac{1}{r_B} \frac{c^{1-\beta}}{1-\beta} \right]_{c_t}^{\infty} = \left(\frac{T_{ref}}{2kW} \right)^{\beta} \frac{1}{r_B} \cdot \left[\frac{c_t^{1-\beta}}{1-\beta} \right] = \left(\frac{T_{ref}}{2kW} \right)^{\beta} \frac{1}{r_B (1-\beta) c_t^{\beta-1}} \qquad (5)$$

Hence summing the three distinct contributions

$$\int_{c_t}^{\infty} \frac{dc}{dc/dn} = \frac{1}{r}(c_0 - c_i) + \frac{T_{ref}}{r_A 2kW} \ln \left[\frac{2kWc_t - T_0 + \frac{r}{r_A} T_{ref}}{2kWc_0 - T_0 + \frac{r}{r_A} T_{ref}} \right] + \left(\frac{T_{ref}}{2kW} \right)^{\beta} \frac{1}{r_B (1-\beta) c_t^{\beta-1}}$$

$$(6)$$

APPENDIX C

Figures of Stress-Strain Curves in Relaxing and Non-Relaxing State Conditions for All Rubber Compounds and Visual Basic Dynamic Analysis Program

In Chapter 5 stress strain behaviour of filled and unfilled rubber was investigated. Sample stress strain hysteresis plots were provided in the chapter. A complete set of plots was generated for all the rubber formulation researched and those not covered in Chapter 5 are given here, namely R7, R8, R9, R10, R11, R12, R13, R14, R15, R16, R17, R18, R19, R20, R21, R22, R23, R24, R25 and R26.
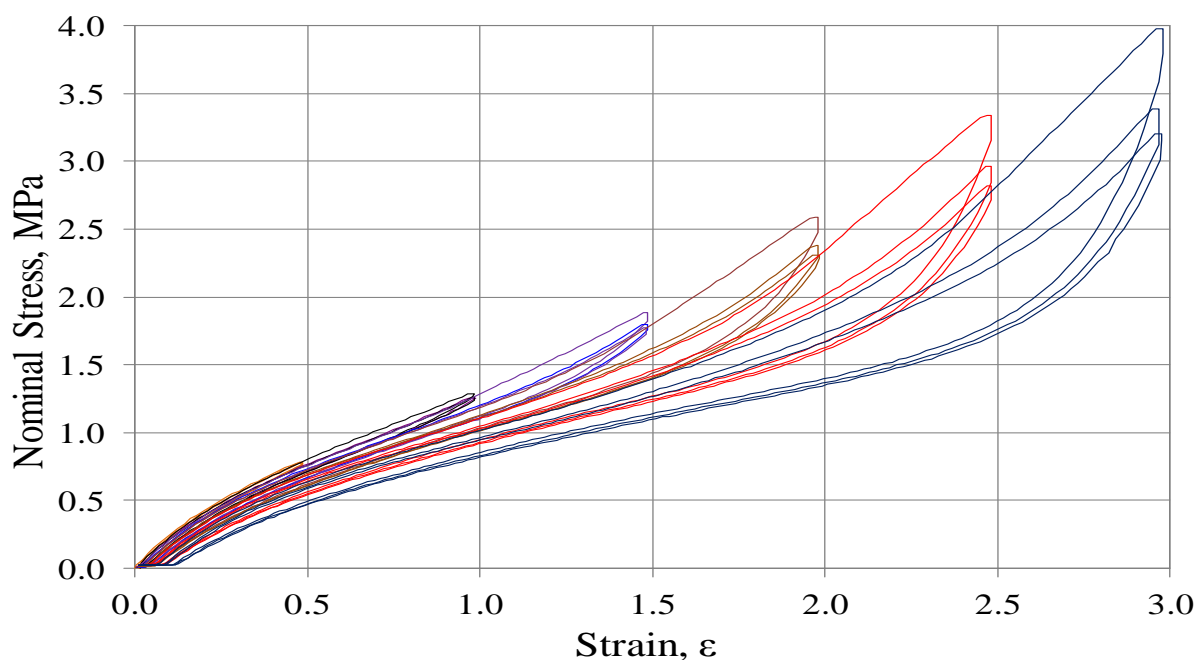
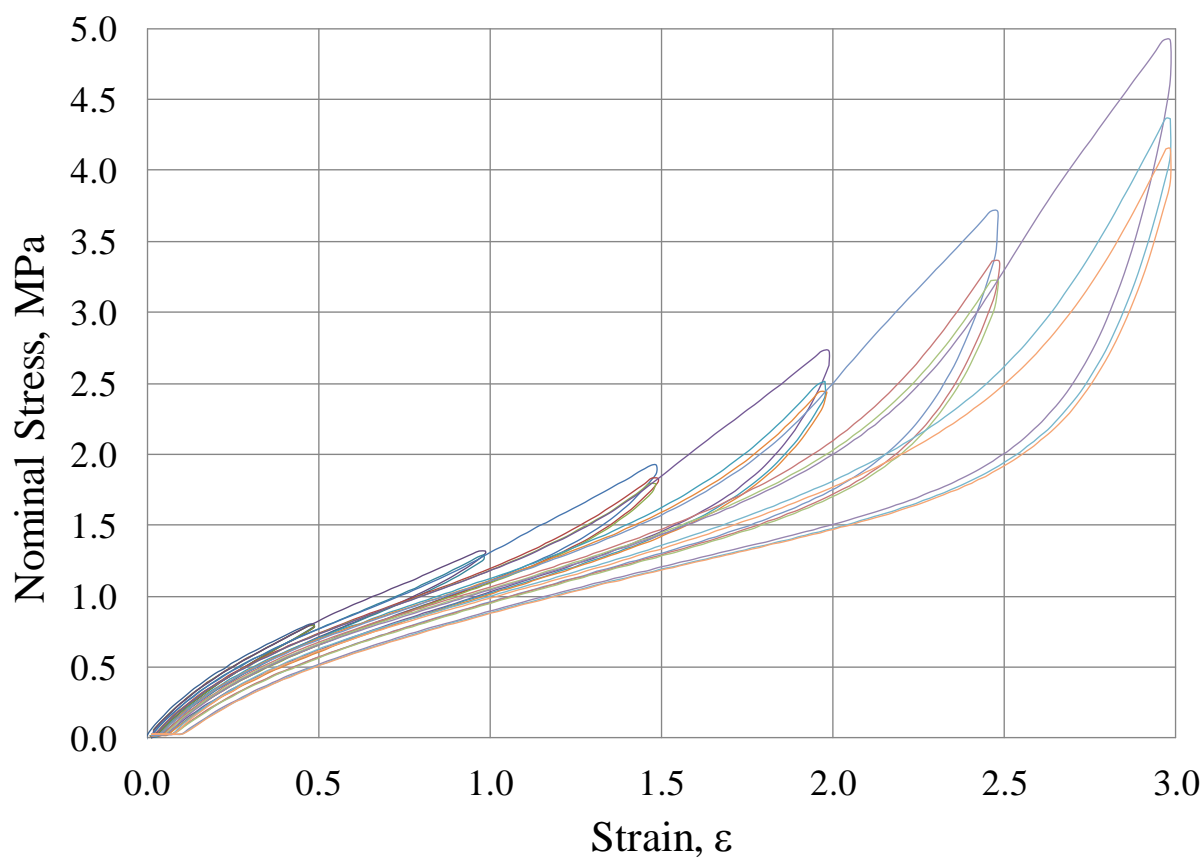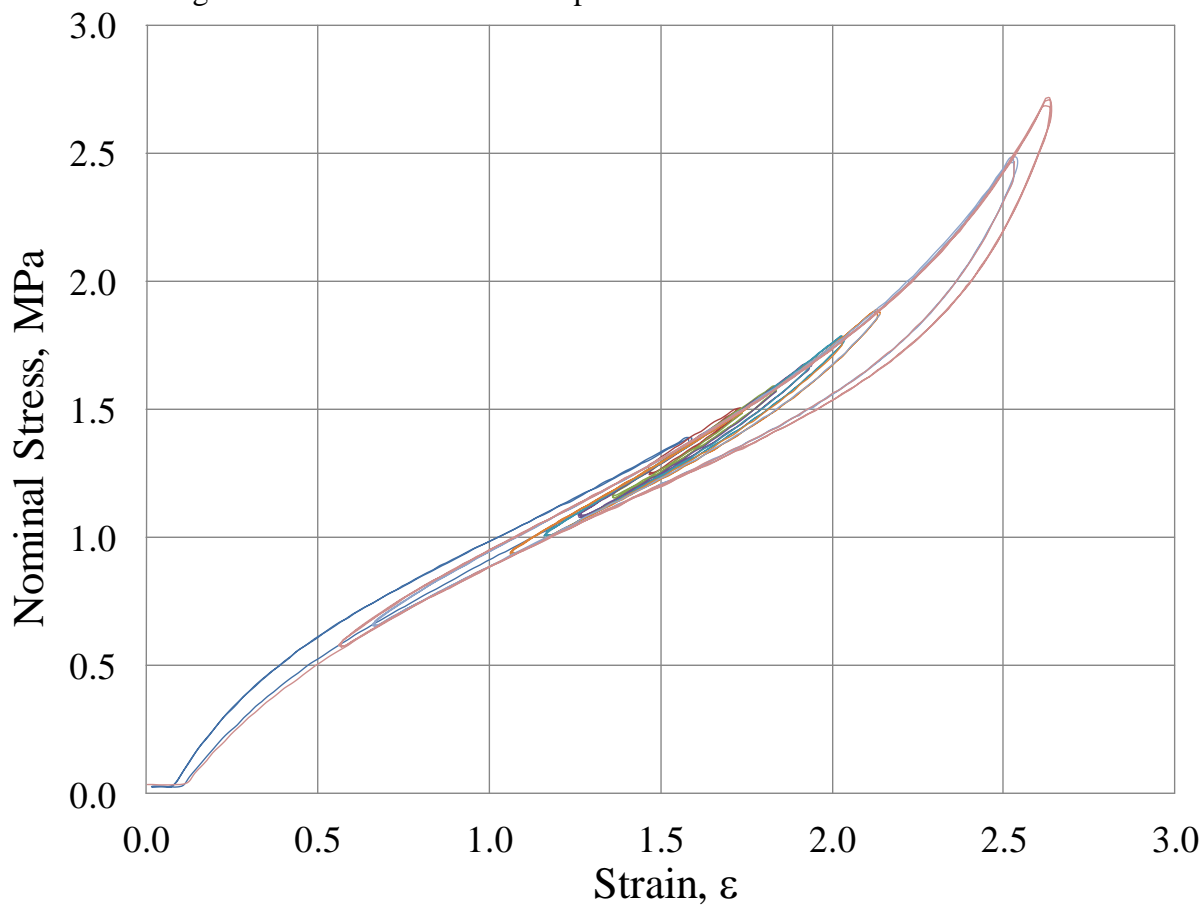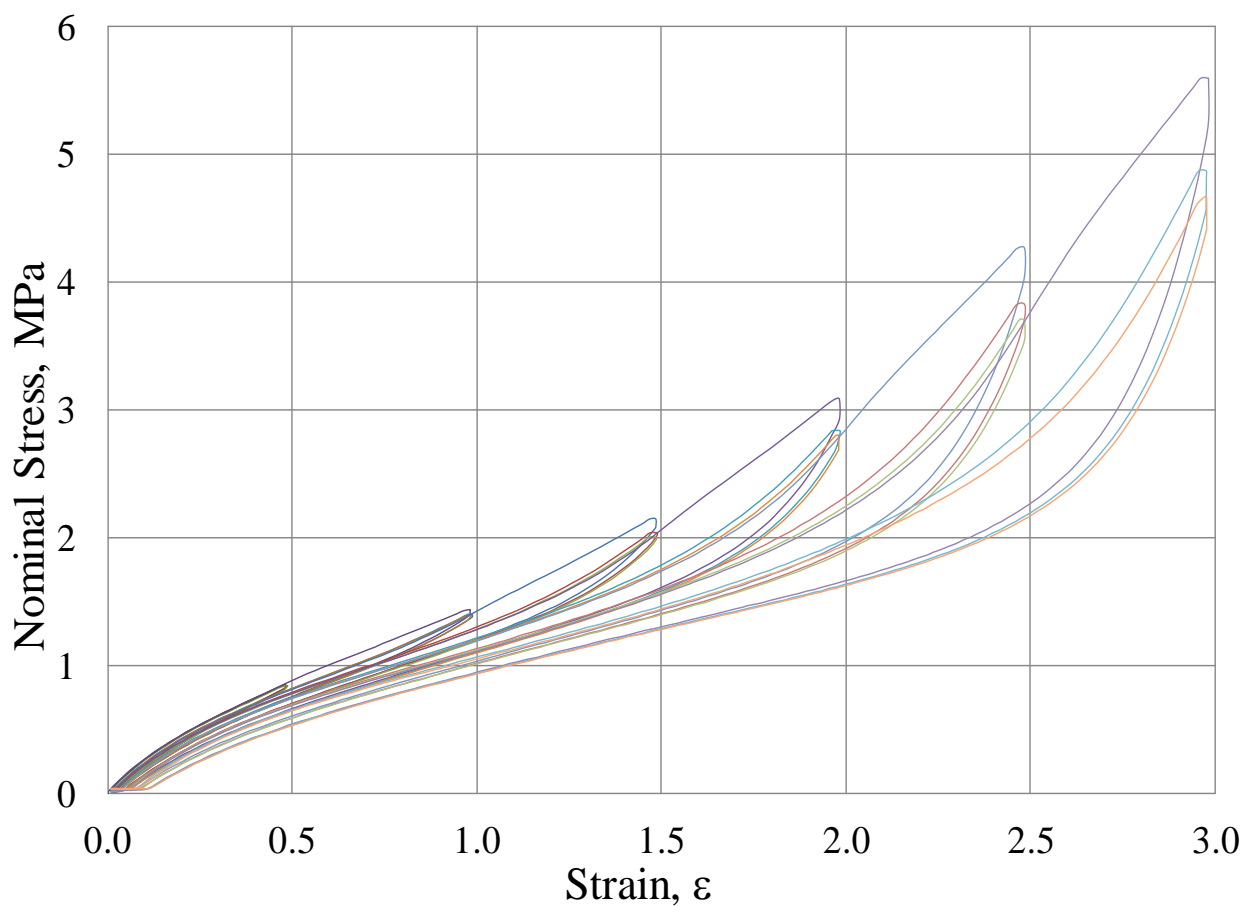Figure C1: Stress-strain in simple extension for R7 from zero strain.
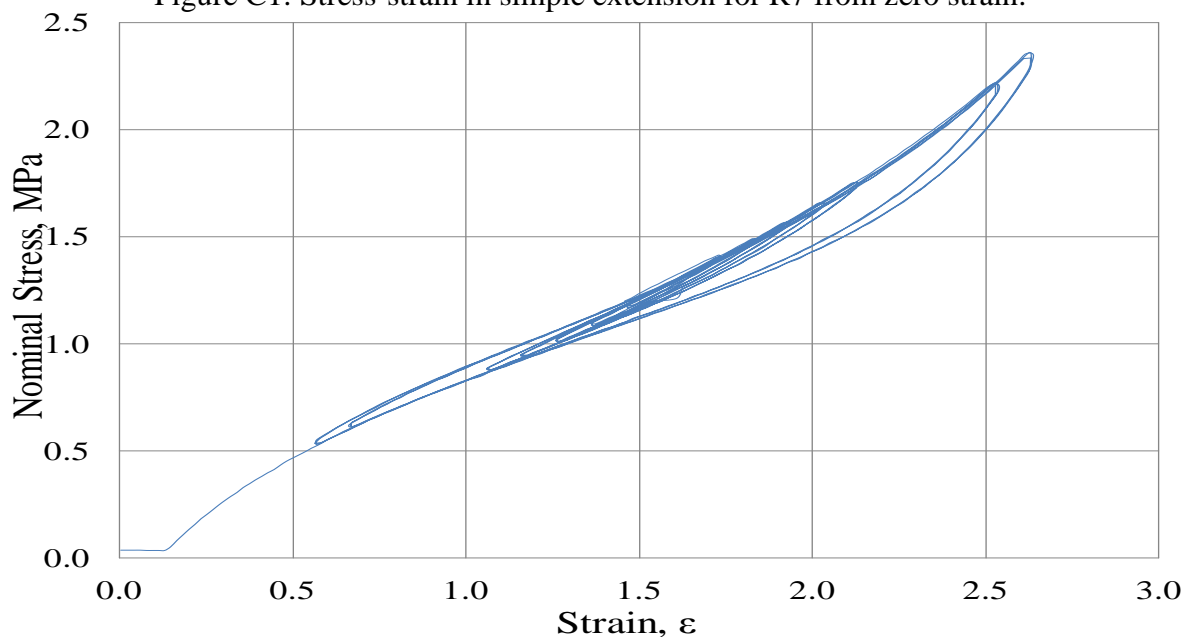
Figure C2: Typical non-relaxing stress-strain curves of R7 at strain amplitude of 15%, 25%, 35%, 45%, 55%, 95% and 105%.
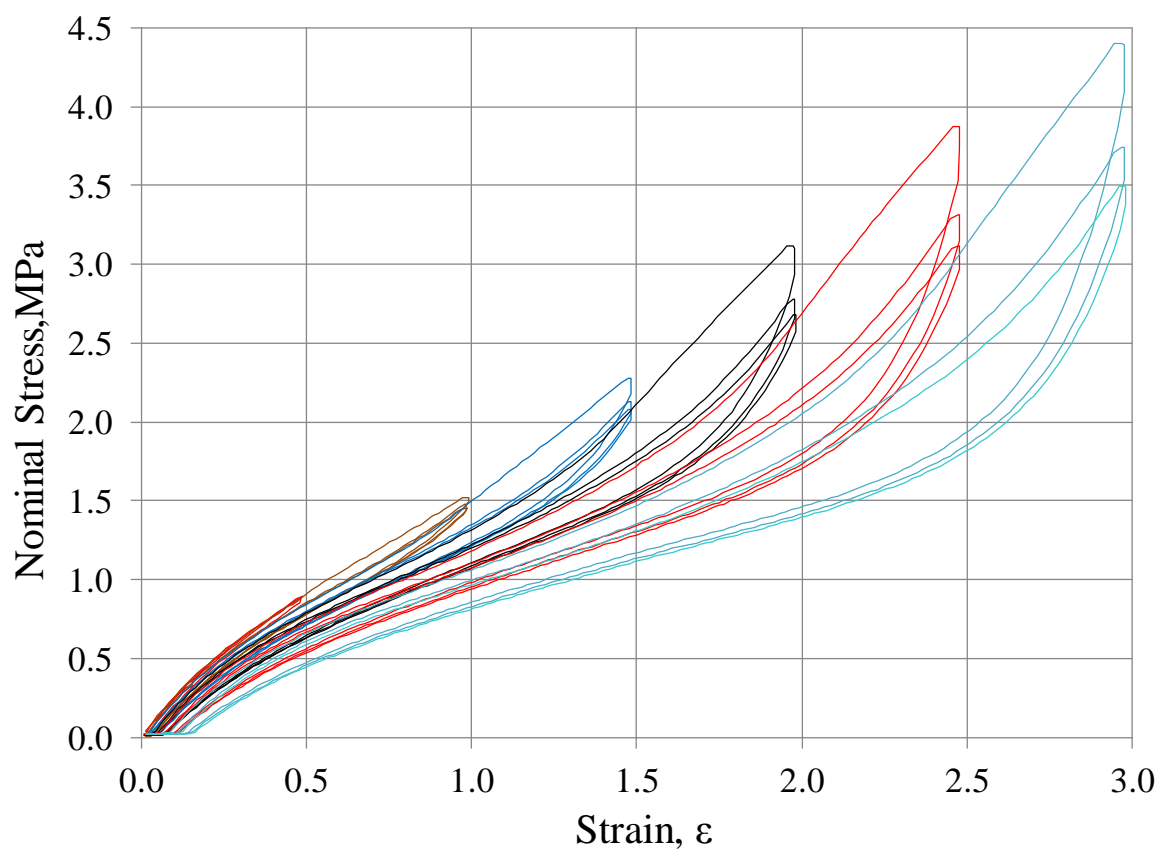
Figure C3: Stress-strain in simple extension for R8 from zero strain.
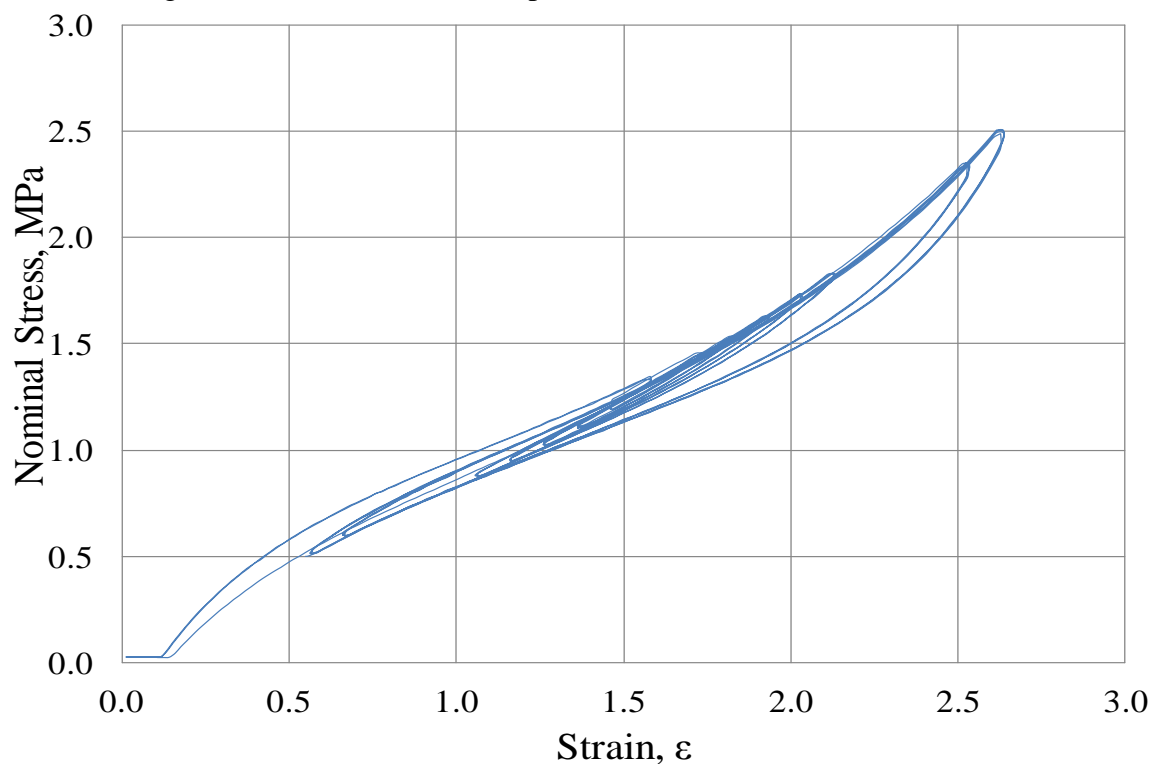
Figure C4: Typical non-relaxing stress-strain curves of R8 at strain amplitude of 15%, 25%, 35%, 45%, 55%, 95% and 105%.
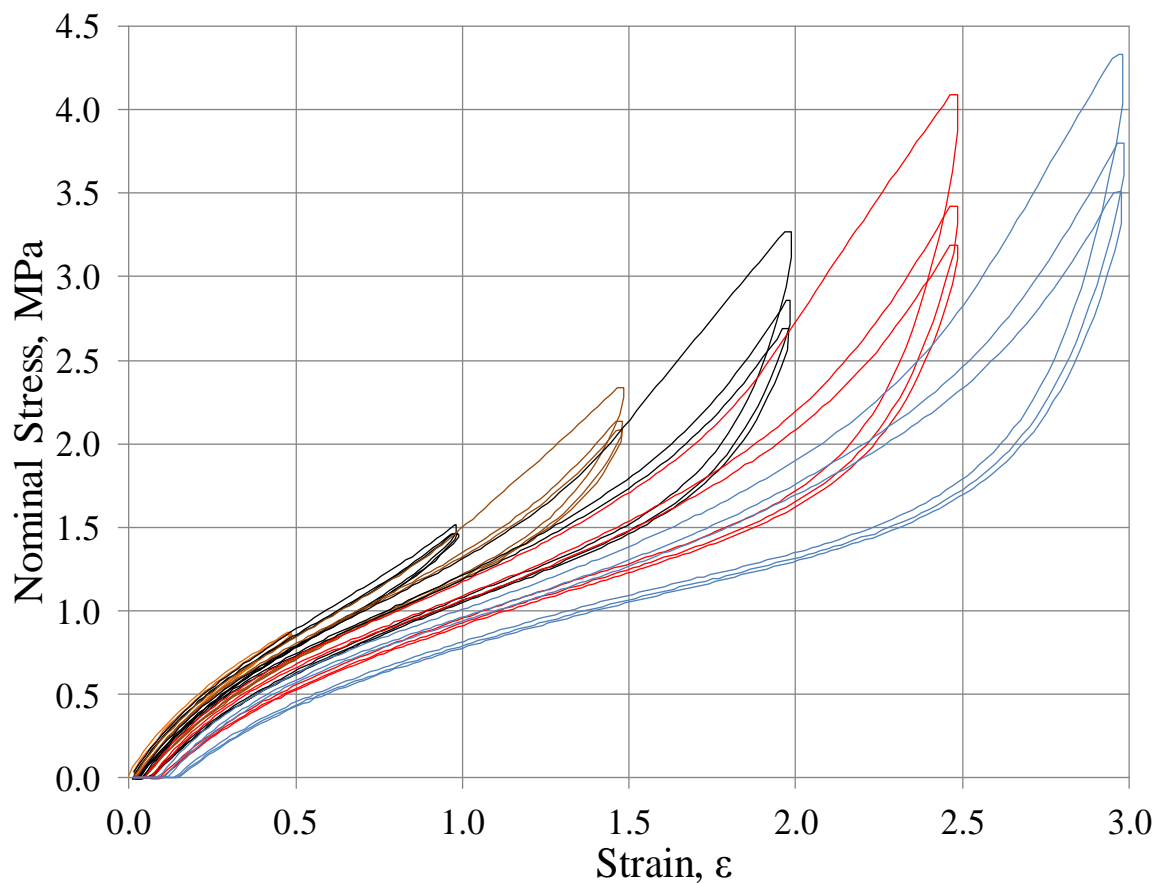
Figure C5: Stress-strain in simple extension for R9 from zero strain.
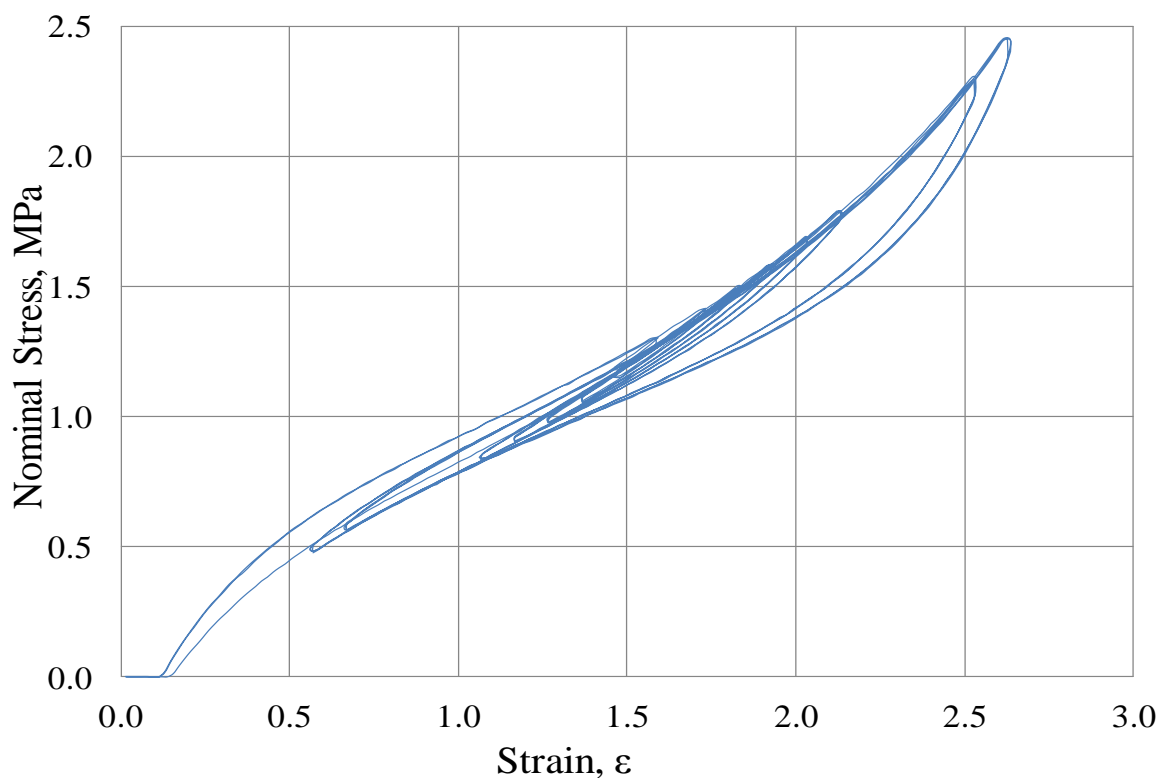
Figure C6: Typical non-relaxing stress-strain curves of R9 at strain amplitude of 15%, 25%, 35%, 45%, 55%, 95% and 105%.
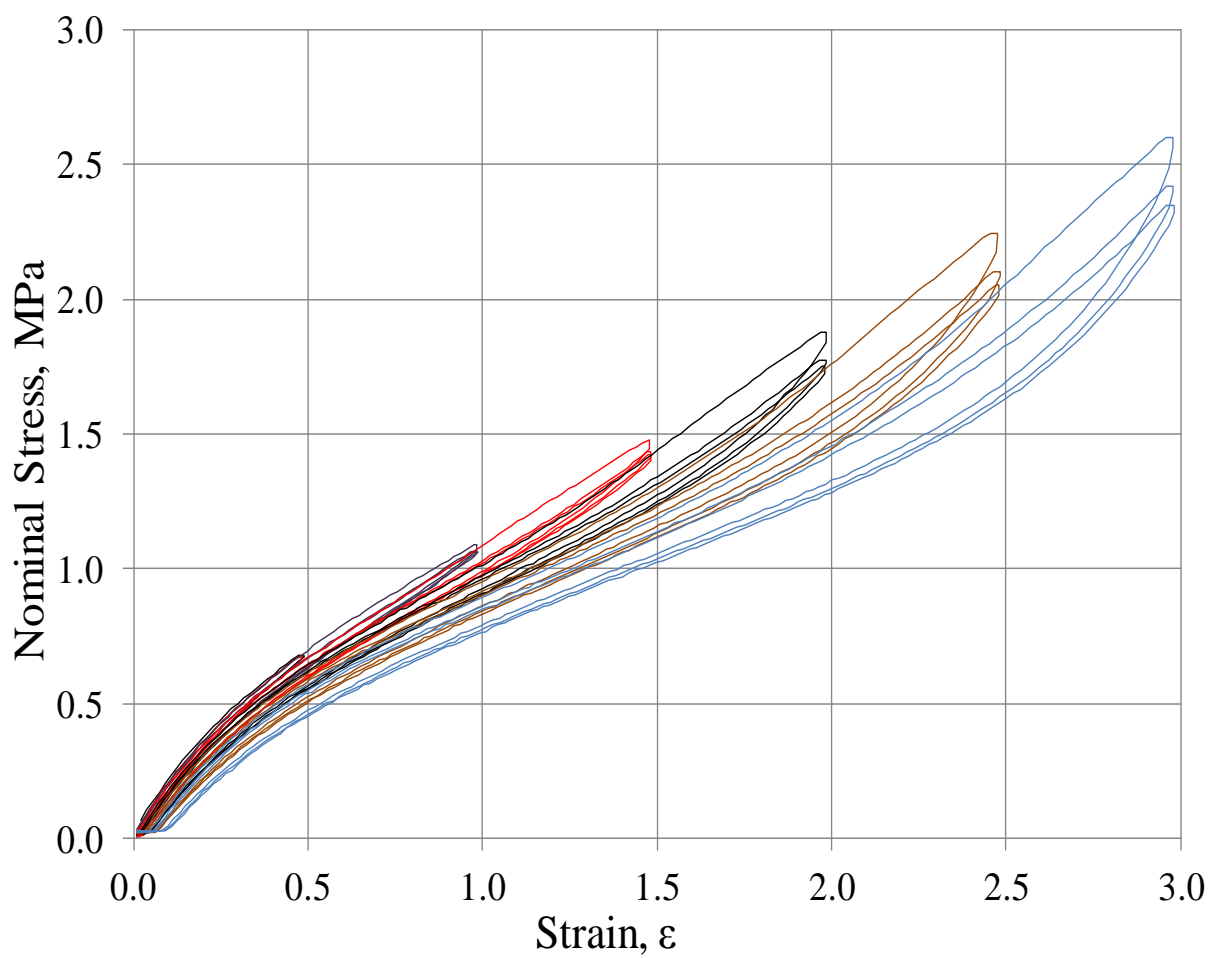
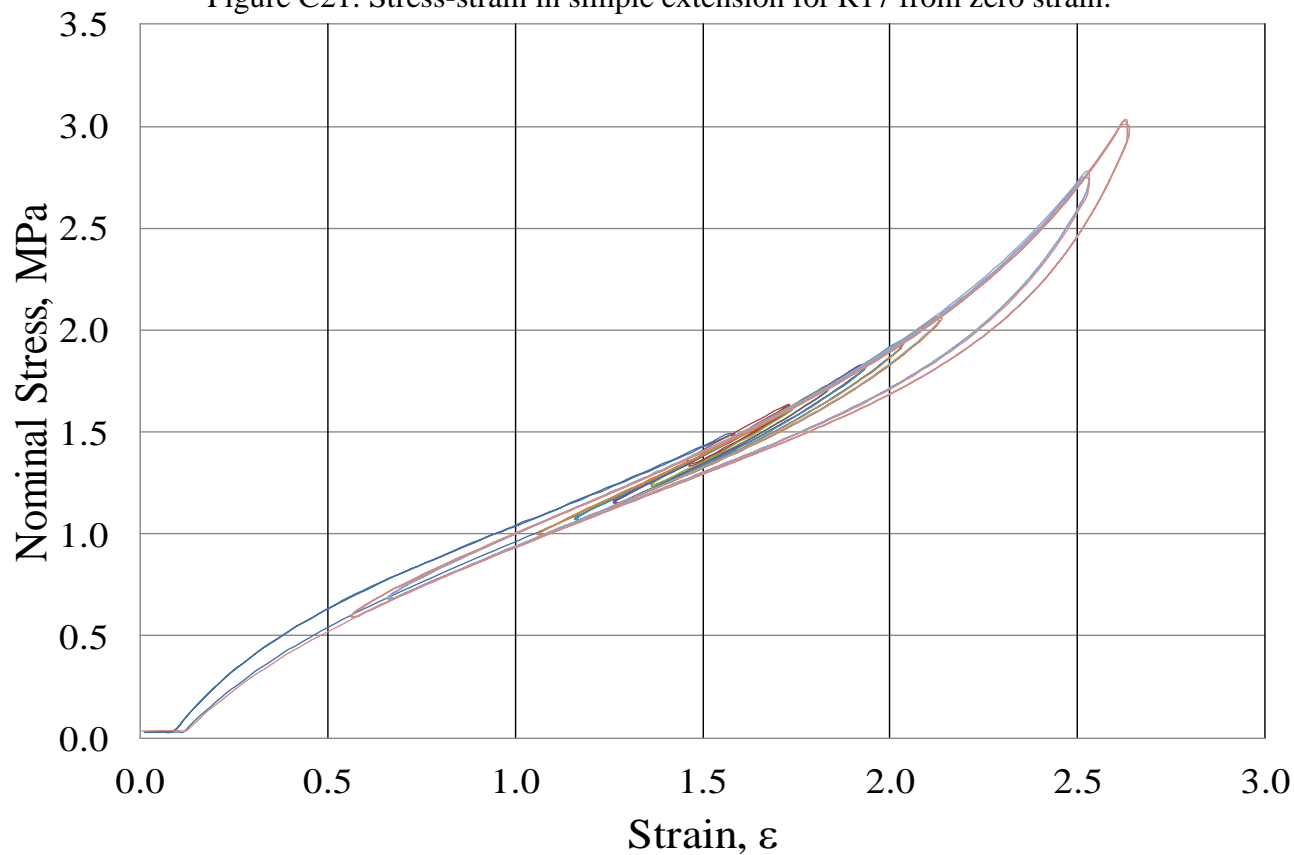Figure C7: Stress-strain in simple extension for R10 from zero strain.
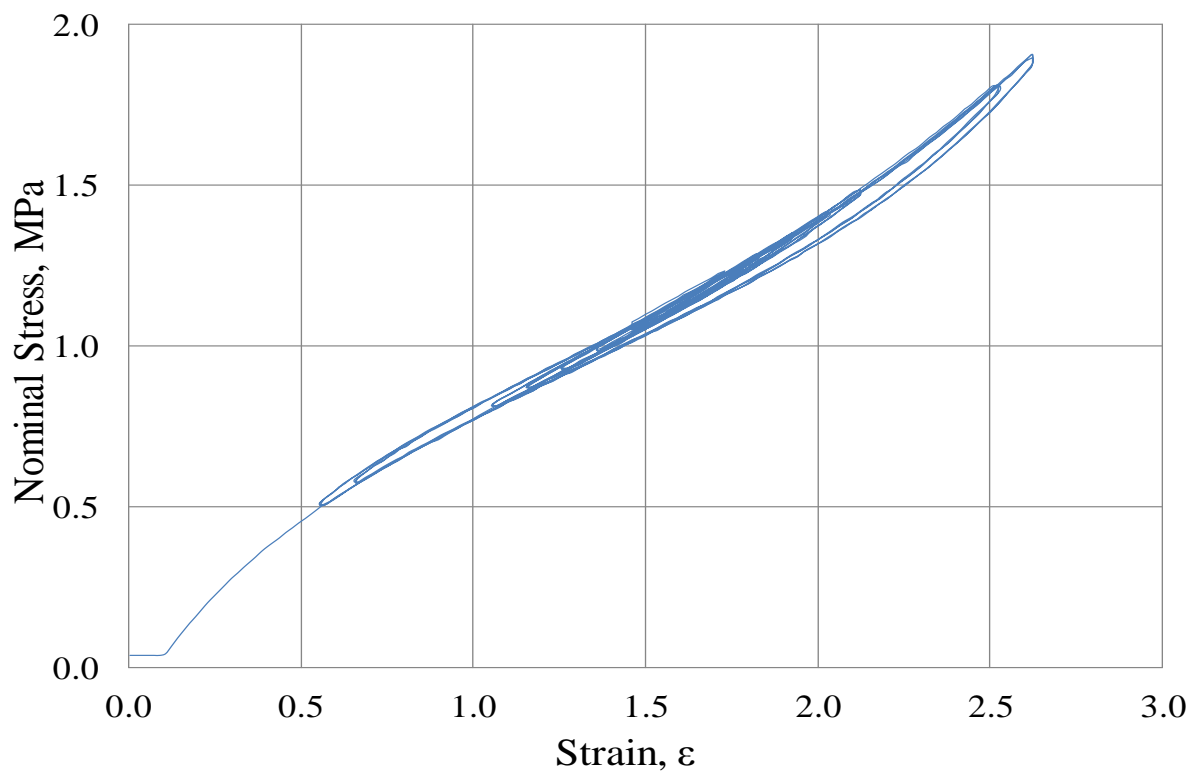
Figure C8: Typical non-relaxing stress-strain curves of R10 at strain amplitude of 15%, 25%, 35%, 45%, 55%, 95% and 105%.
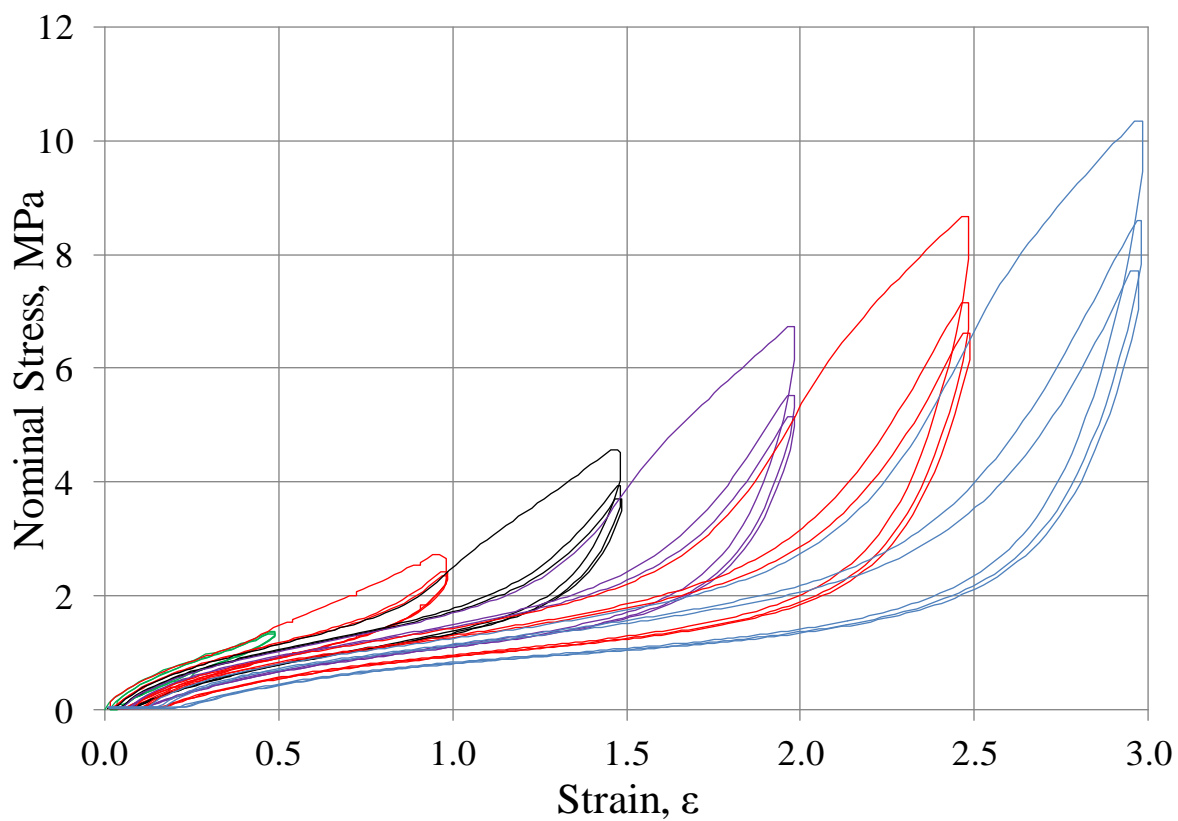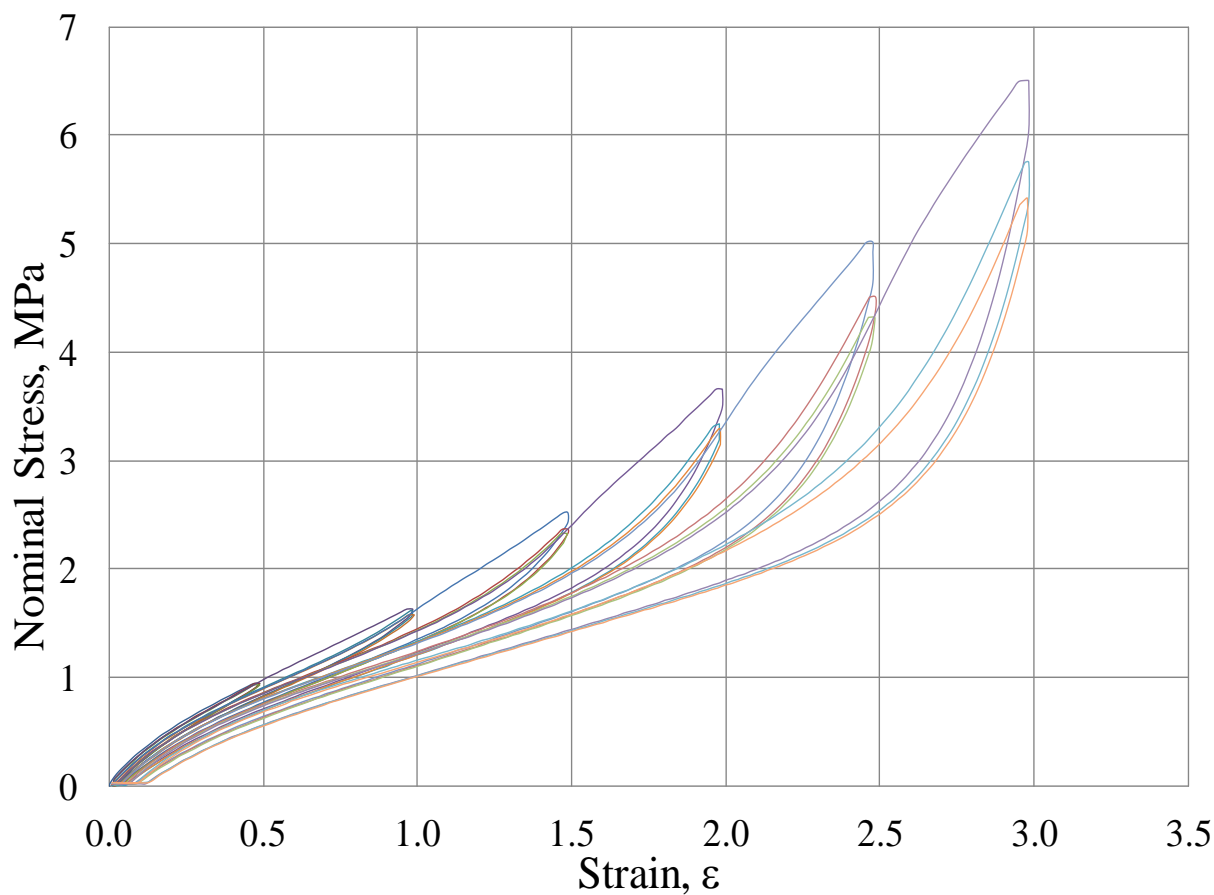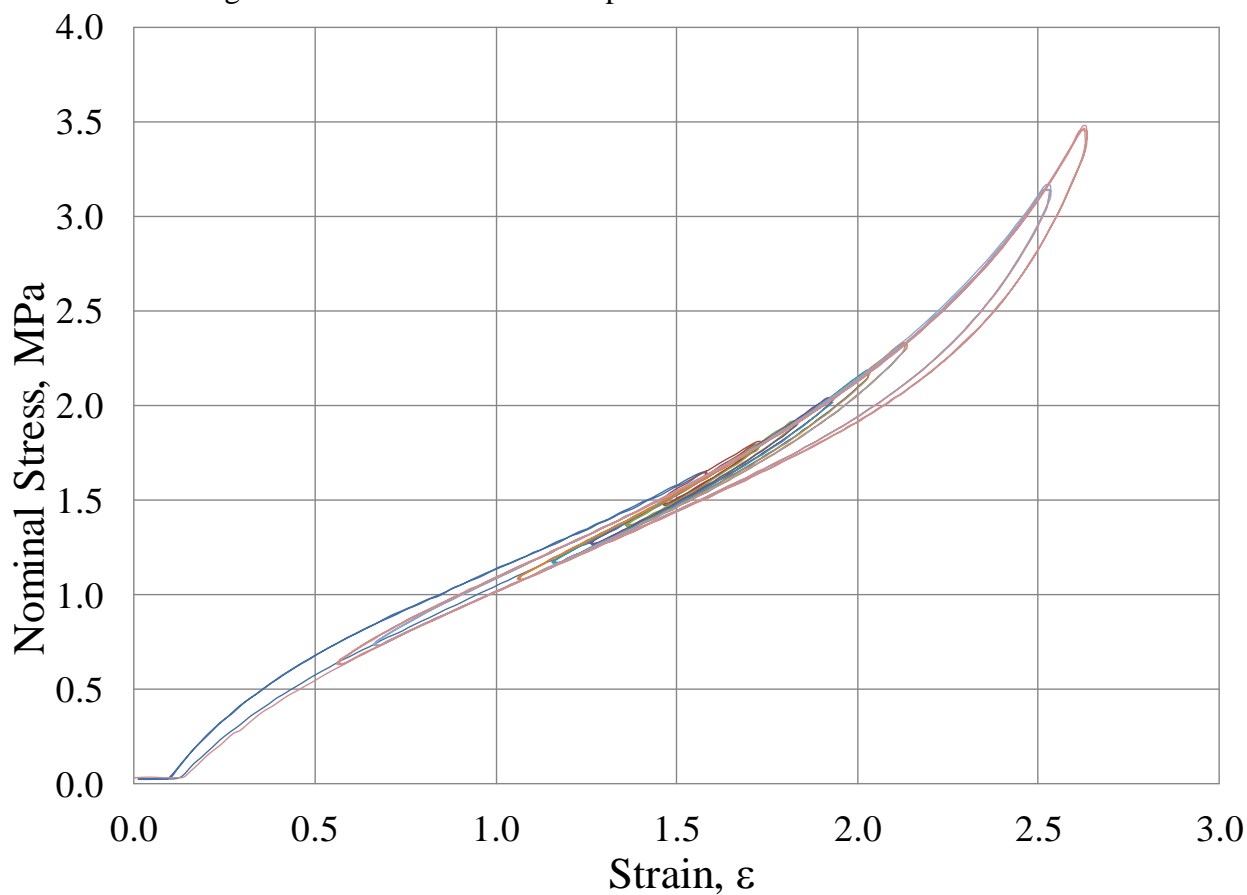
Figure C9: Stress-strain in simple extension for R11 from zero strain.
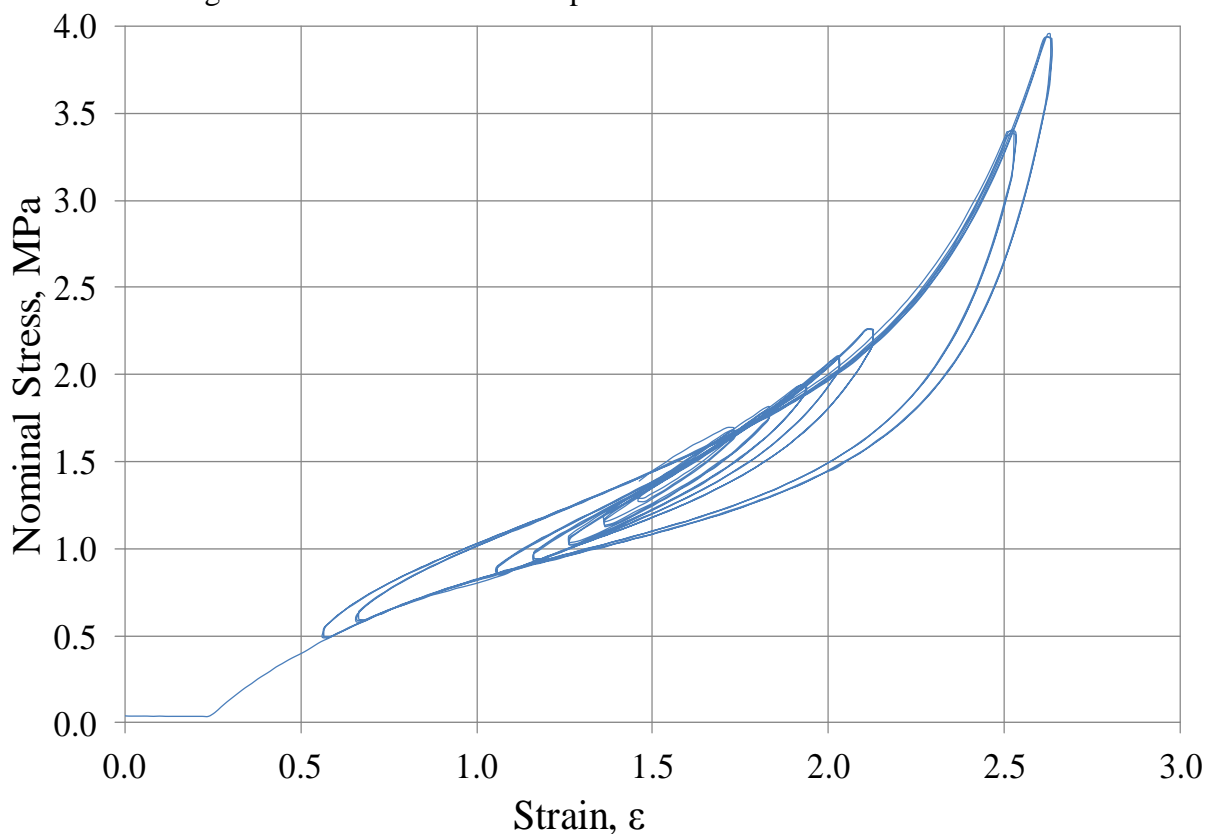
Figure C10: Typical non-relaxing stress-strain curves of R11 at strain amplitude of 15%, 25%, 35%, 45%, 55%, 95% and 105%.
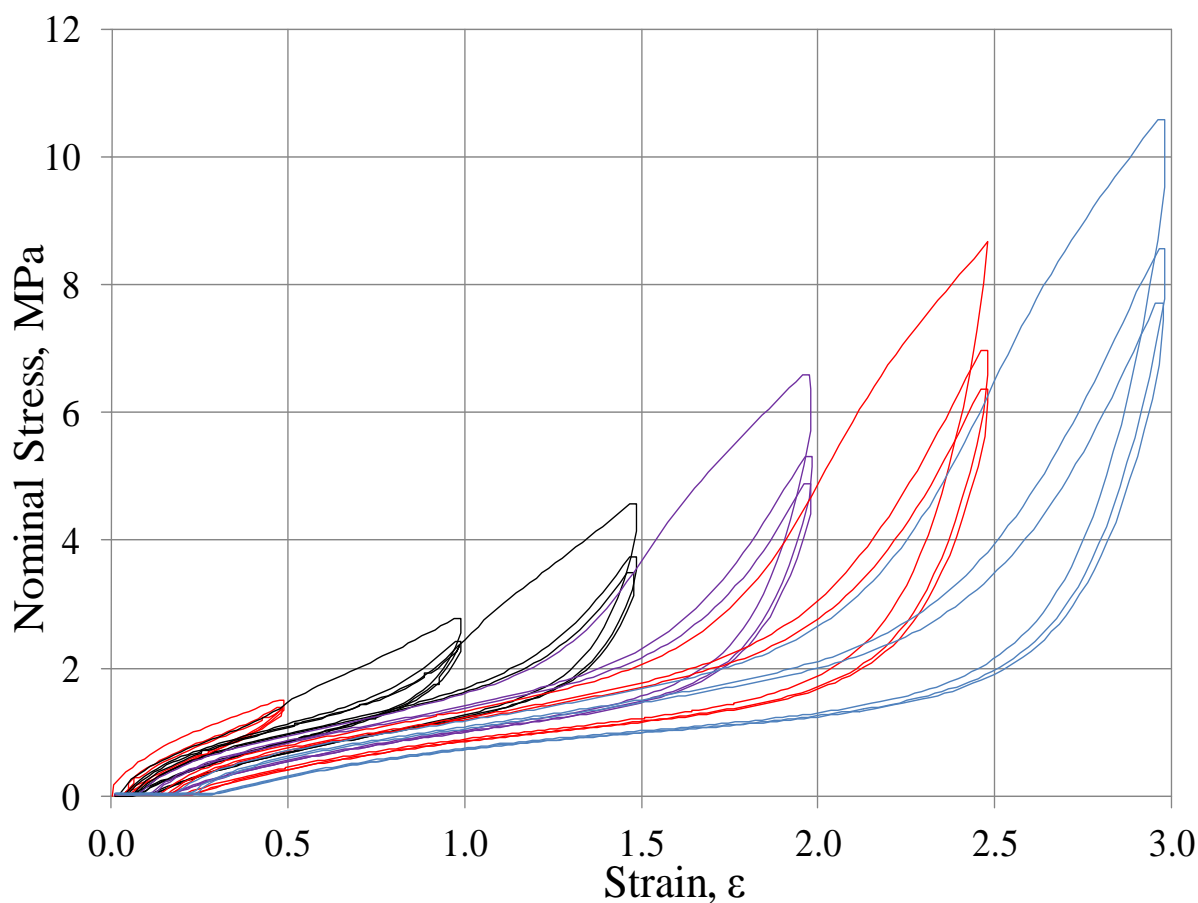
Figure C11: Stress-strain in simple extension for R12 from zero strain.
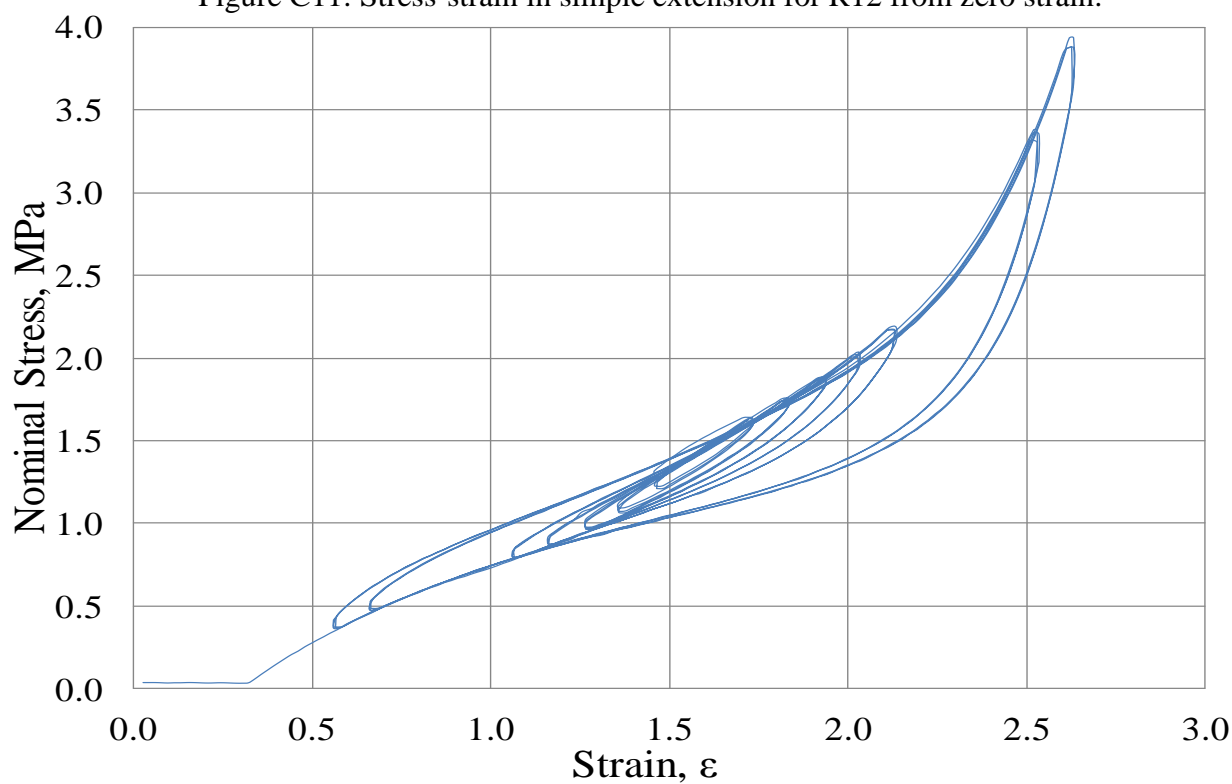
Figure C12: Typical non-relaxing stress-strain curves of R12 at strain amplitude of 15%, 25%, 35%, 45%, 55%, 95% and 105%.
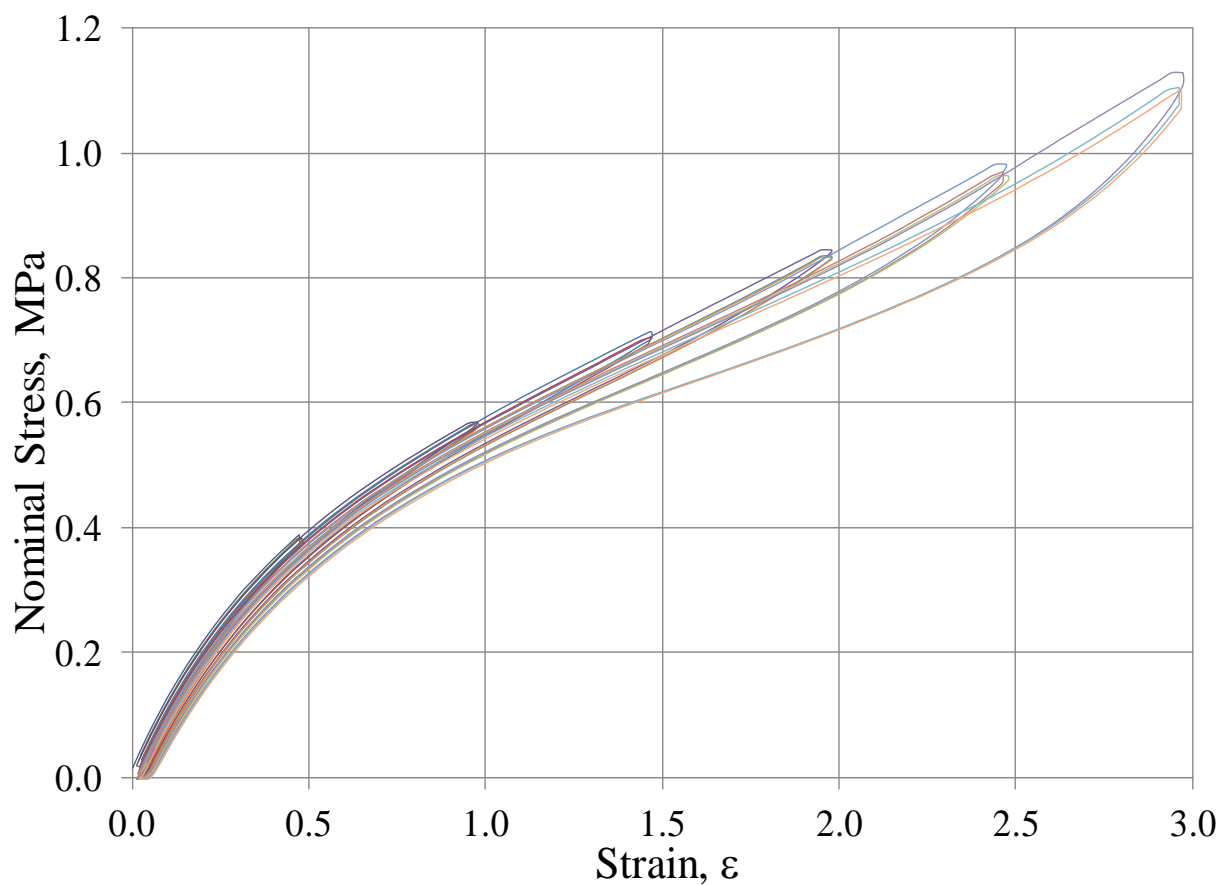
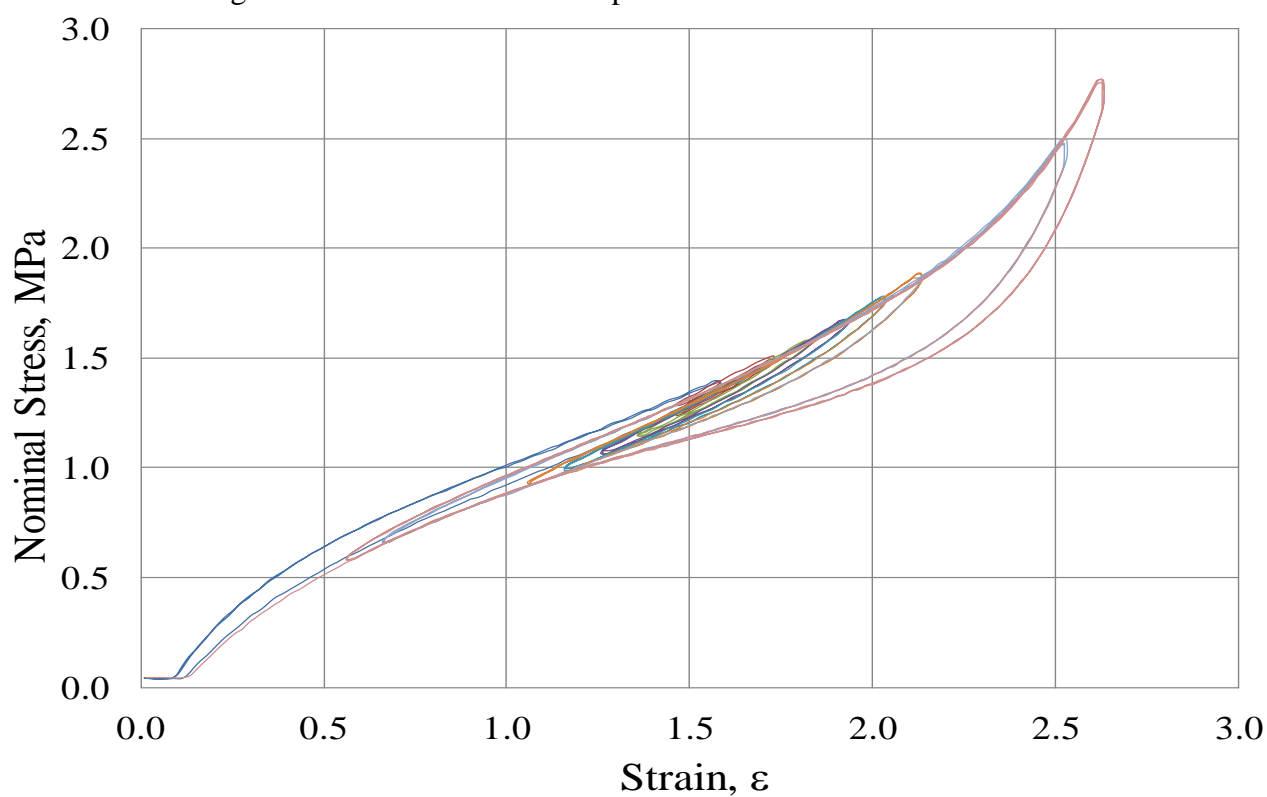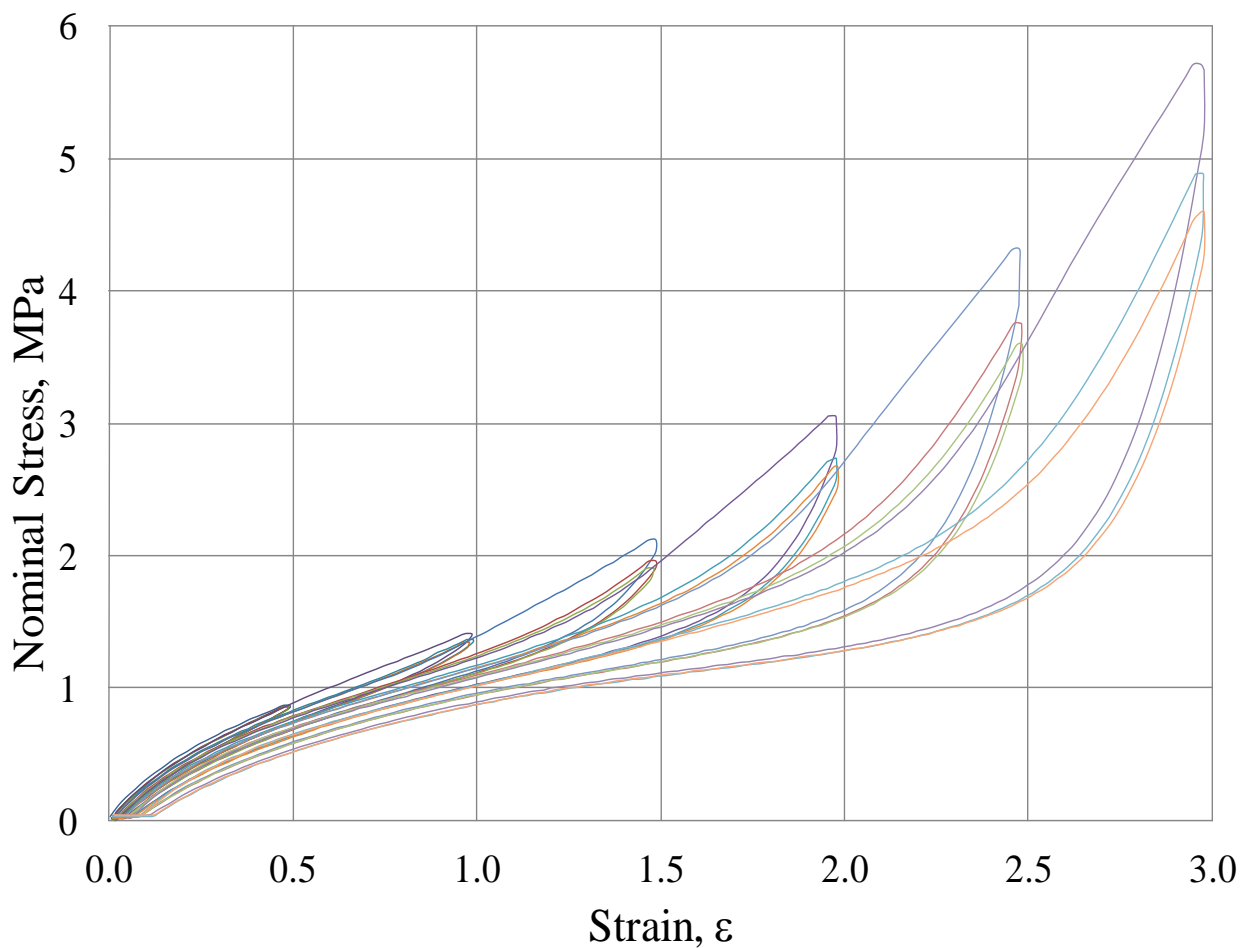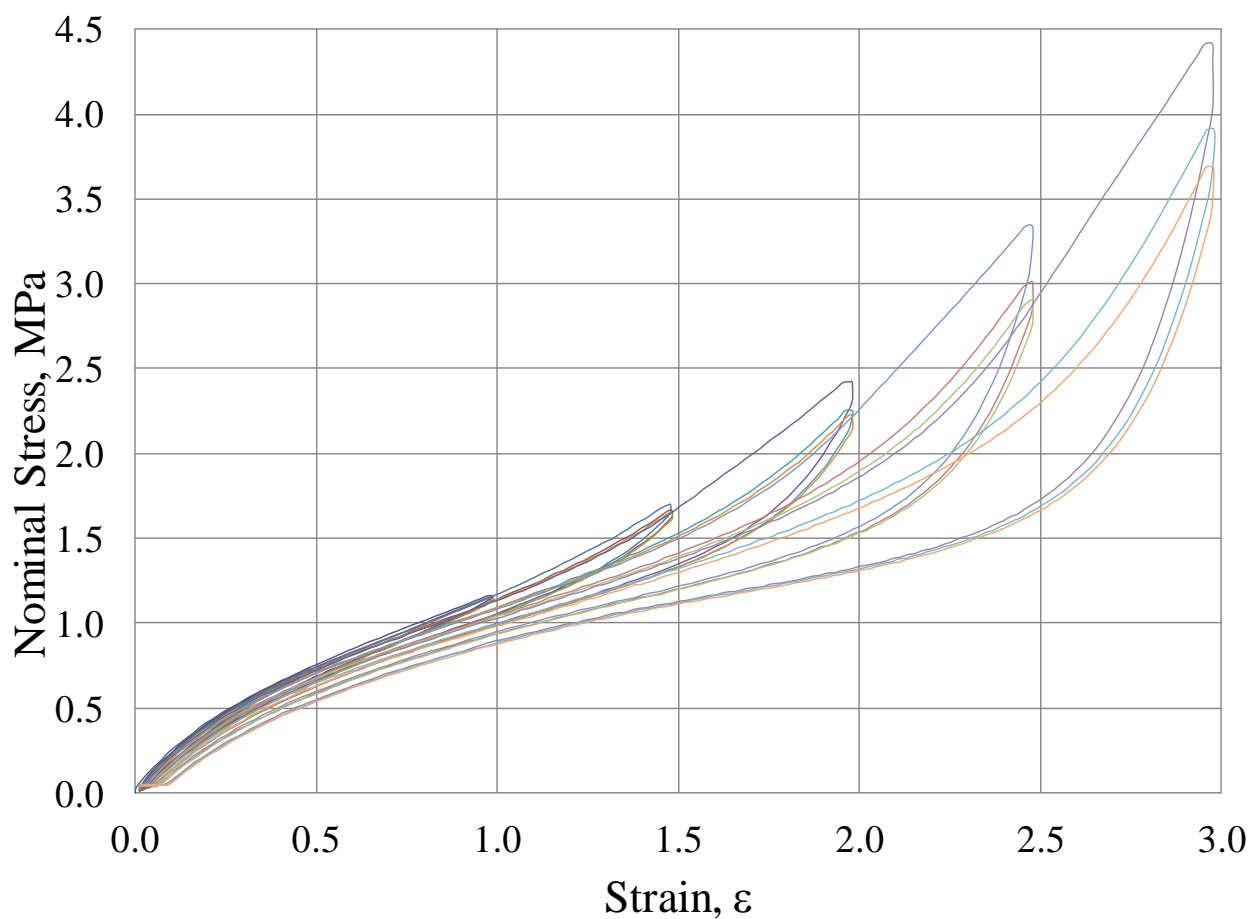Figure C13: Stress-strain in simple extension for R13 from zero strain.
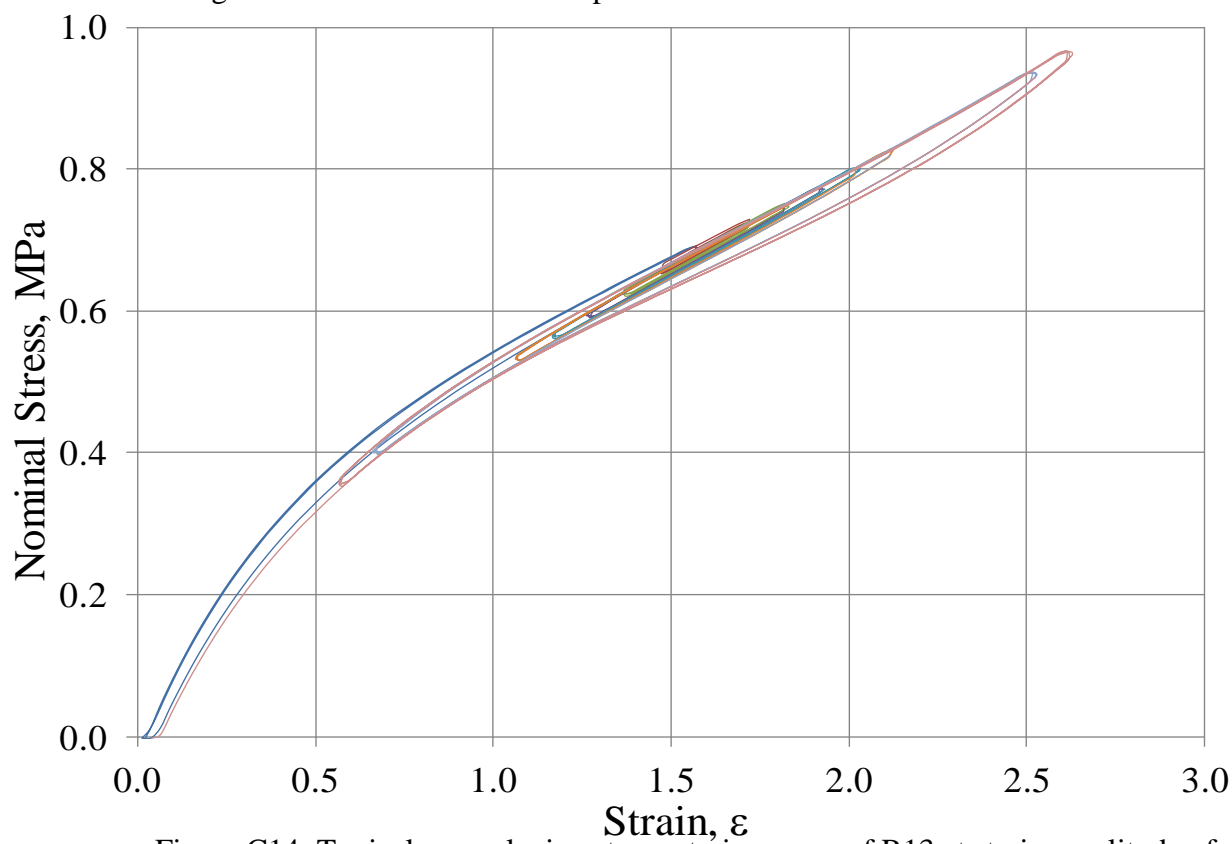
Figure C14: Typical non-relaxing stress-strain curves of R13 at strain amplitude of 15%, 25%, 35%, 45%, 55%, 95% and 105%.
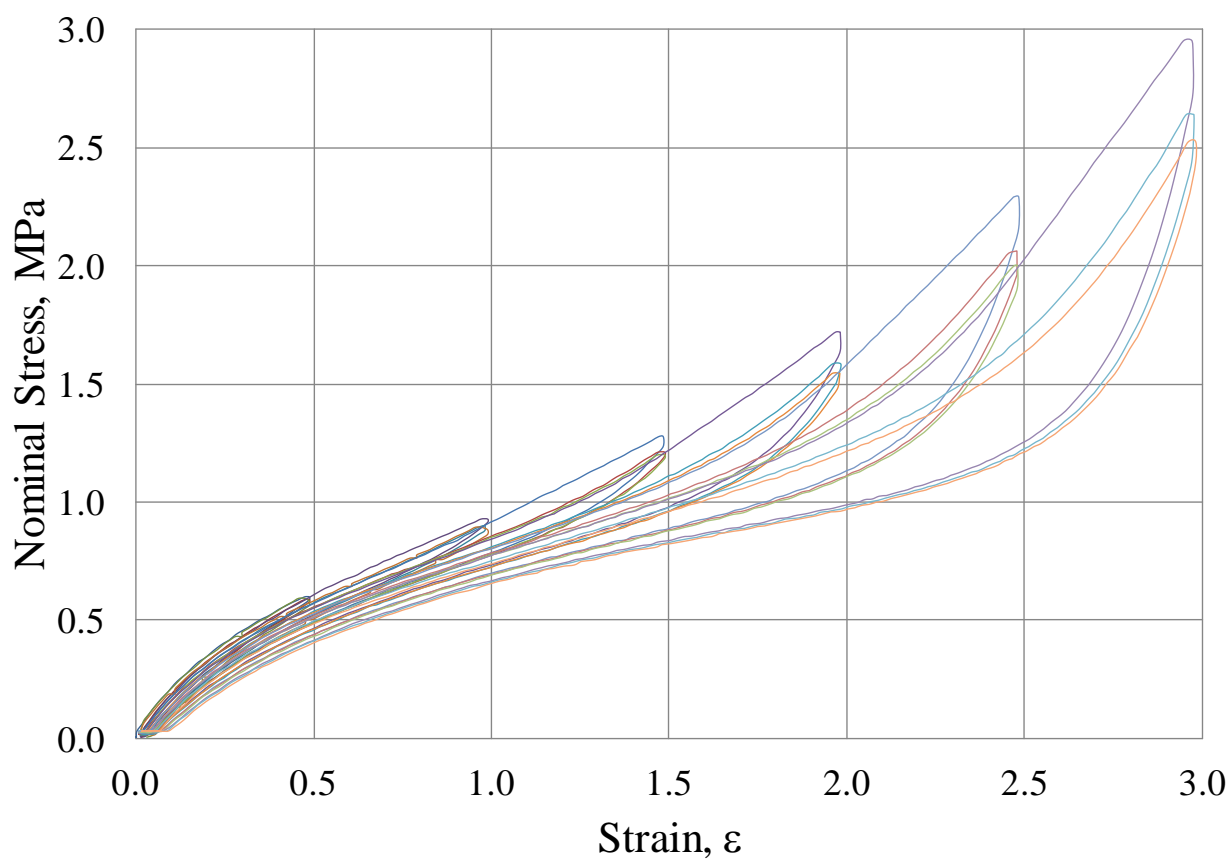
Figure C15: Stress-strain in simple extension for R14 from zero strain.
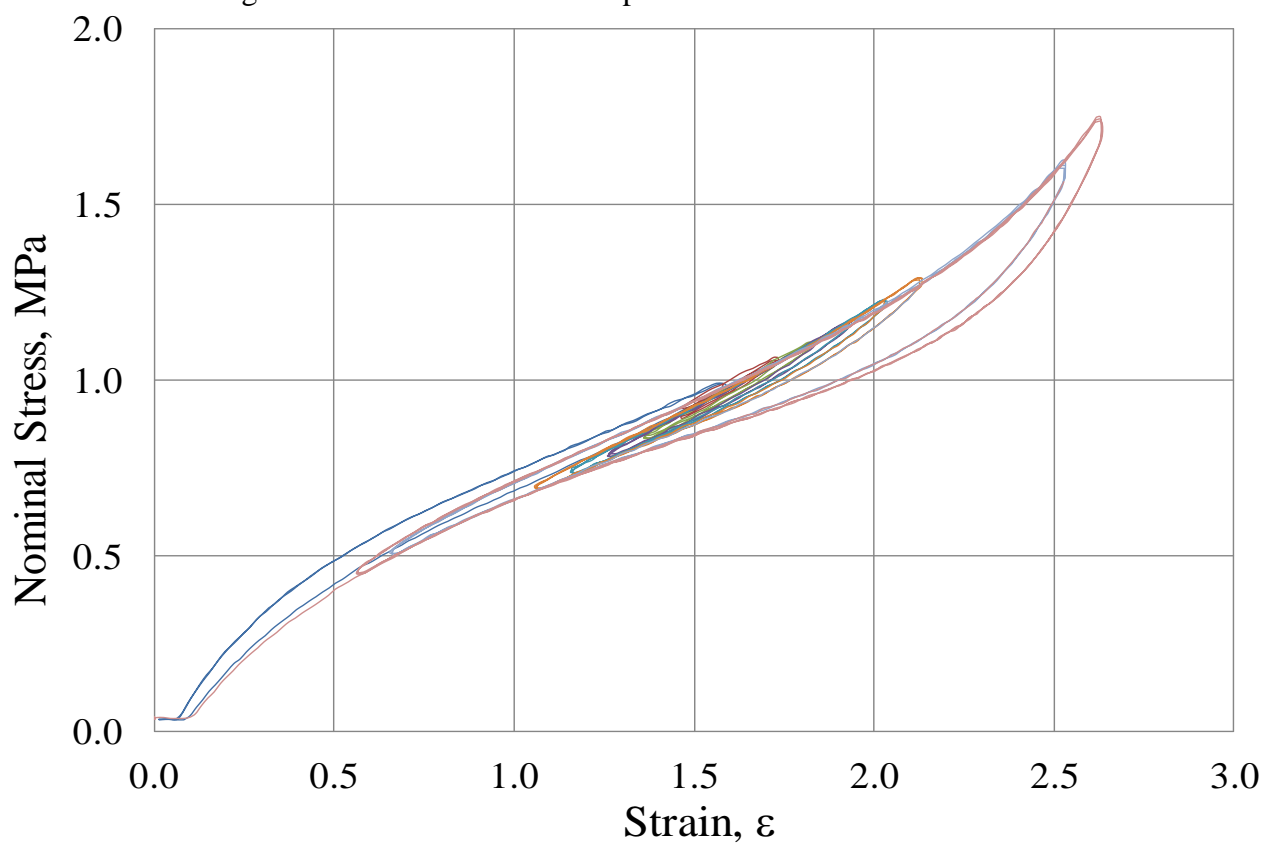
Figure C16: Typical non-relaxing stress-strain curves of R14 at strain amplitude of 15%, 25%, 35%, 45%, 55%, 95% and 105%.
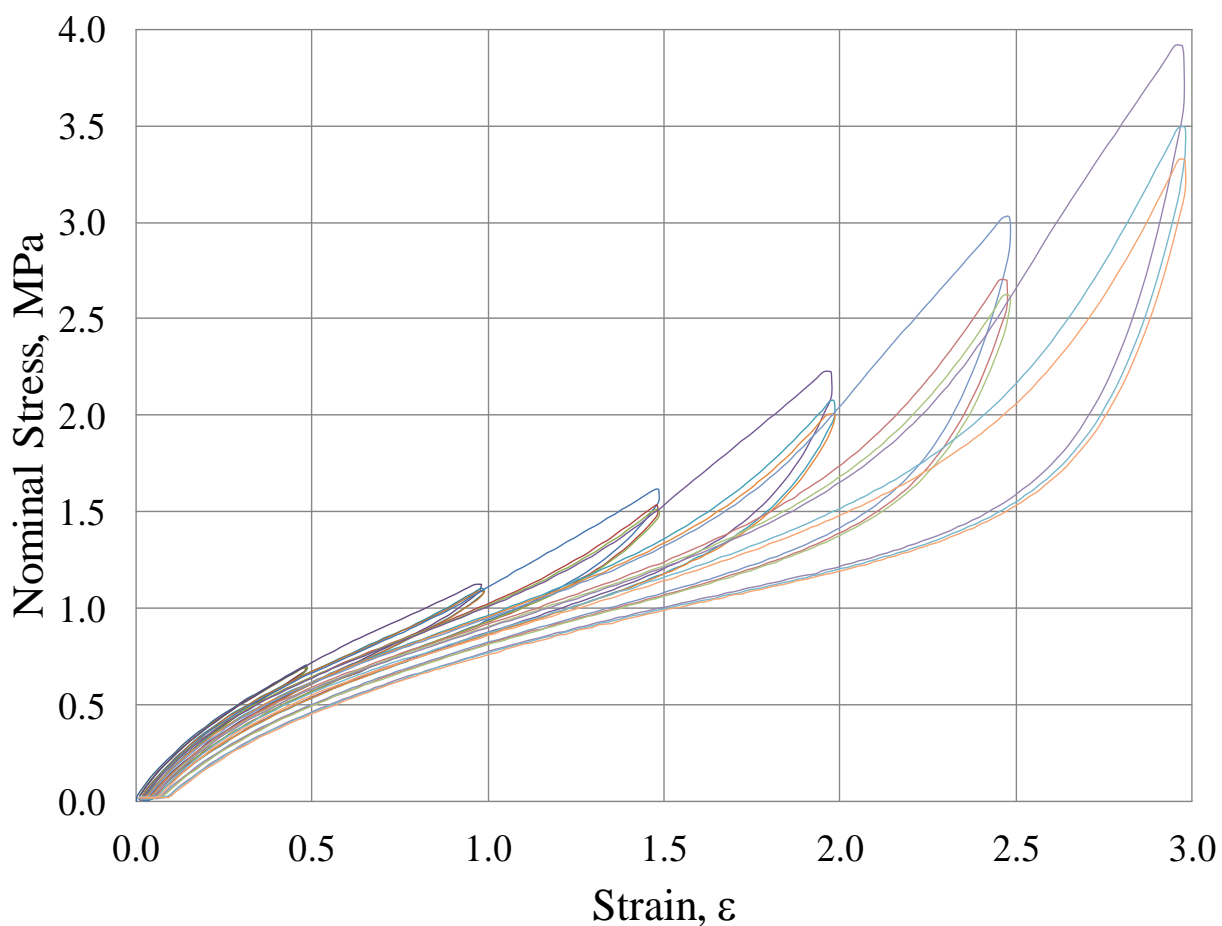
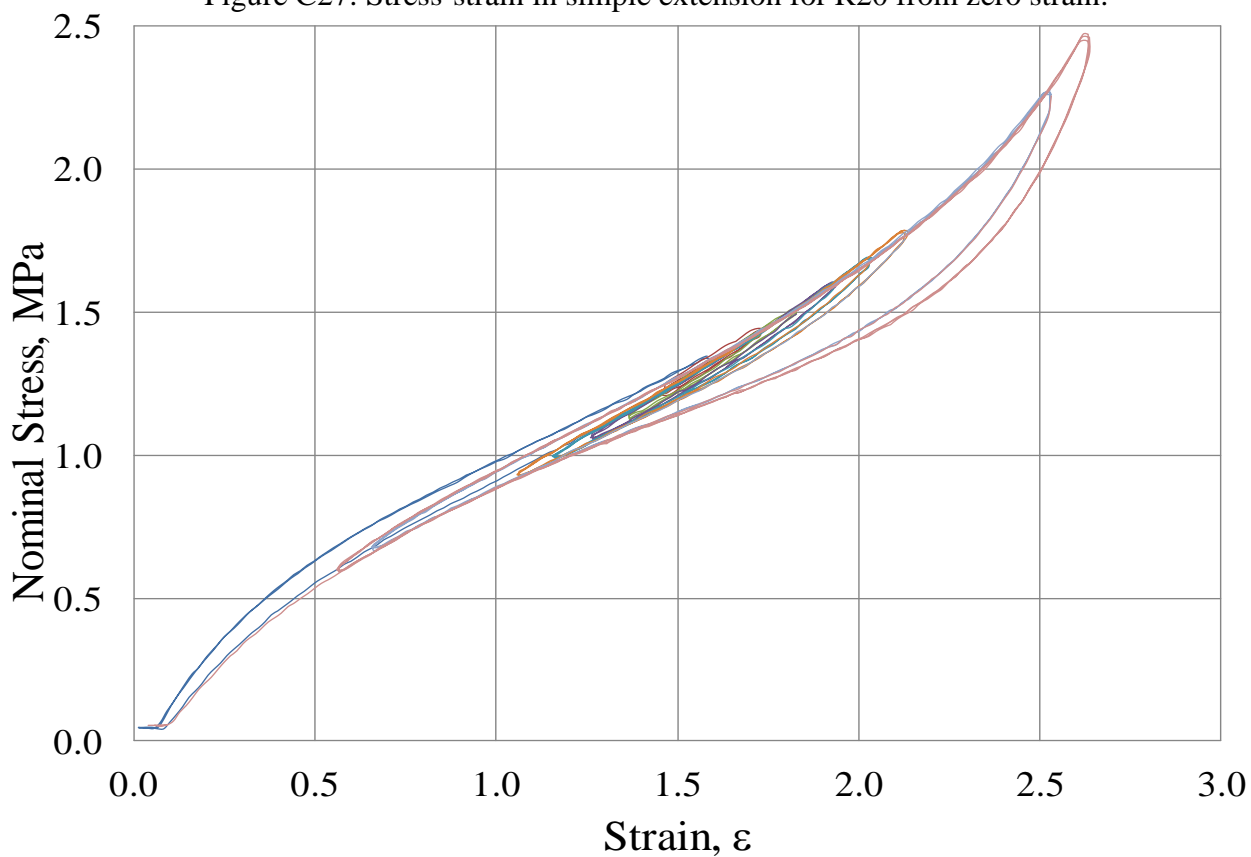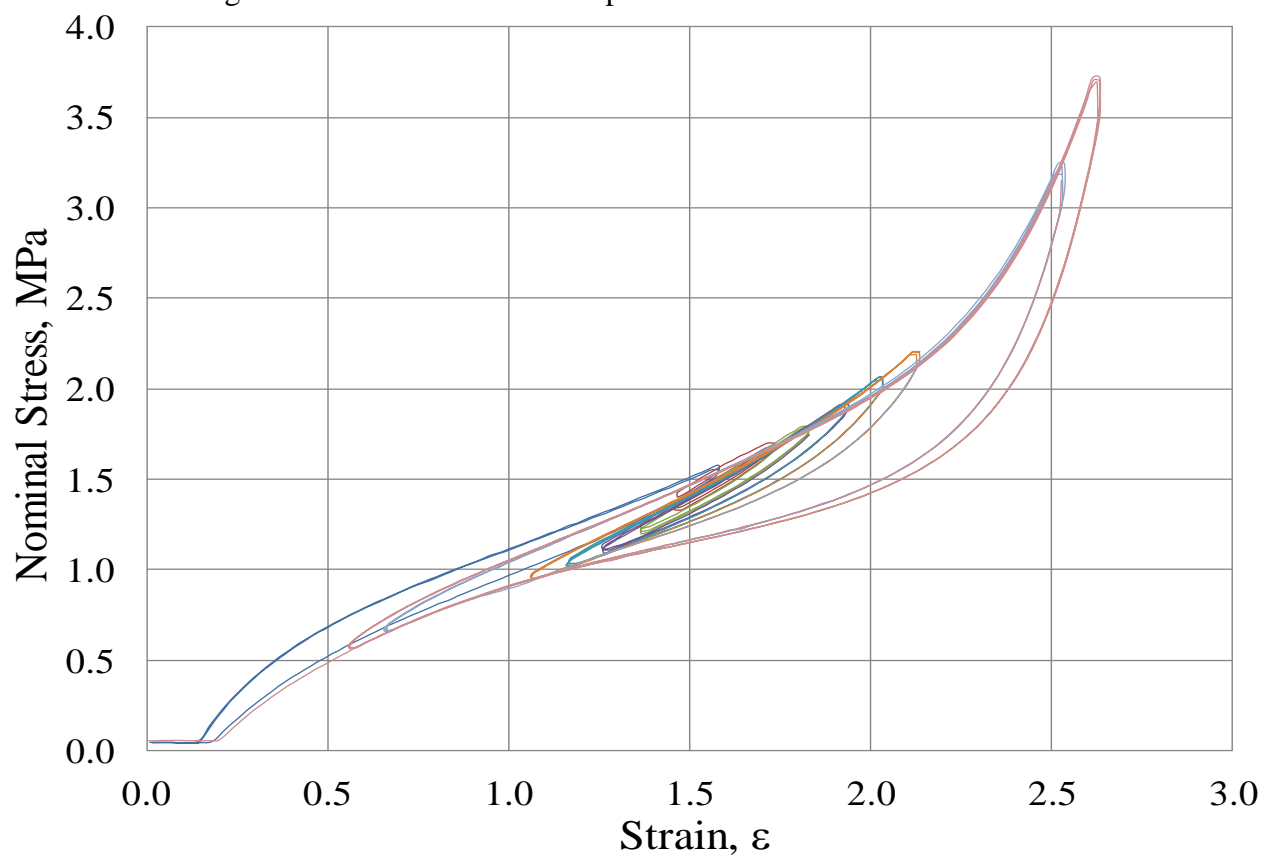Figure C17: Stress-strain in simple extension for R15 from zero strain.
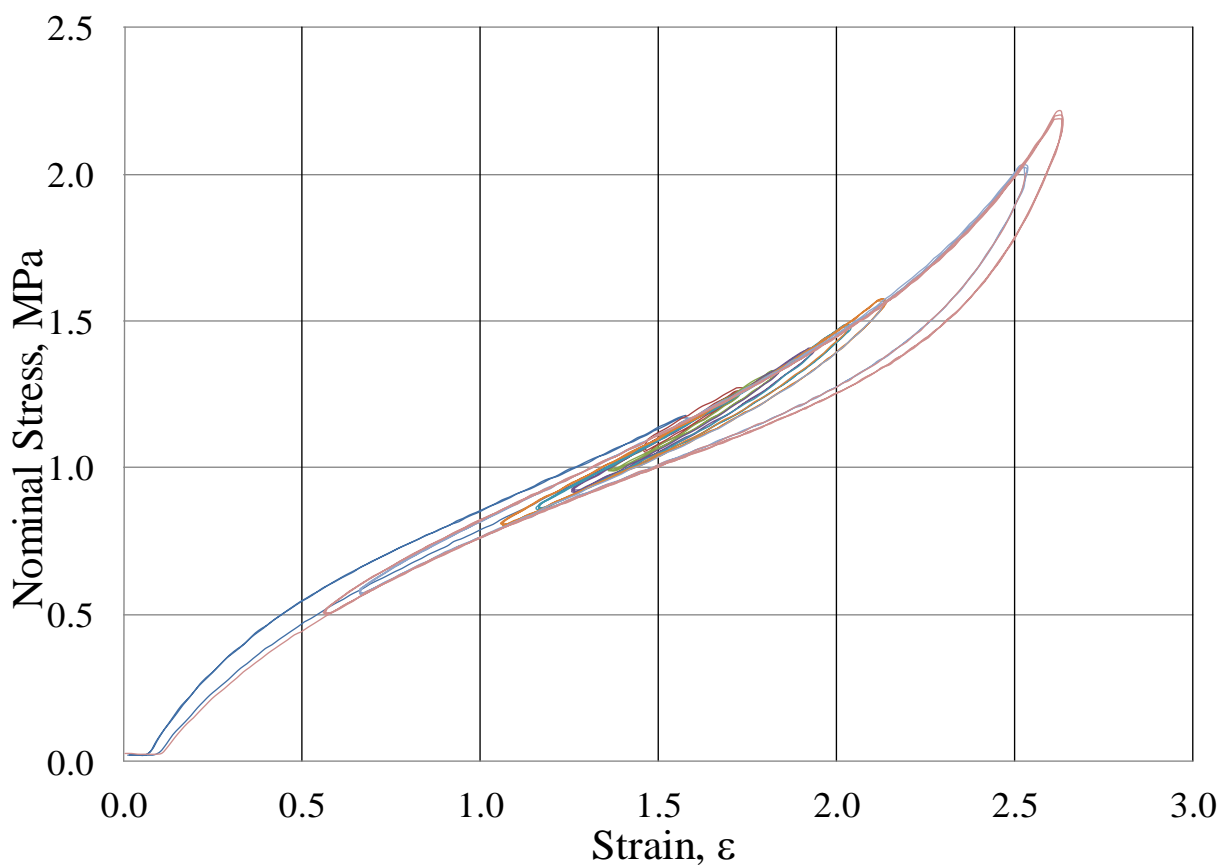
Figure C18: Typical non-relaxing stress-strain curves of R15 at strain amplitude of 15%, 25%, 35%, 45%, 55%, 95% and 105%.

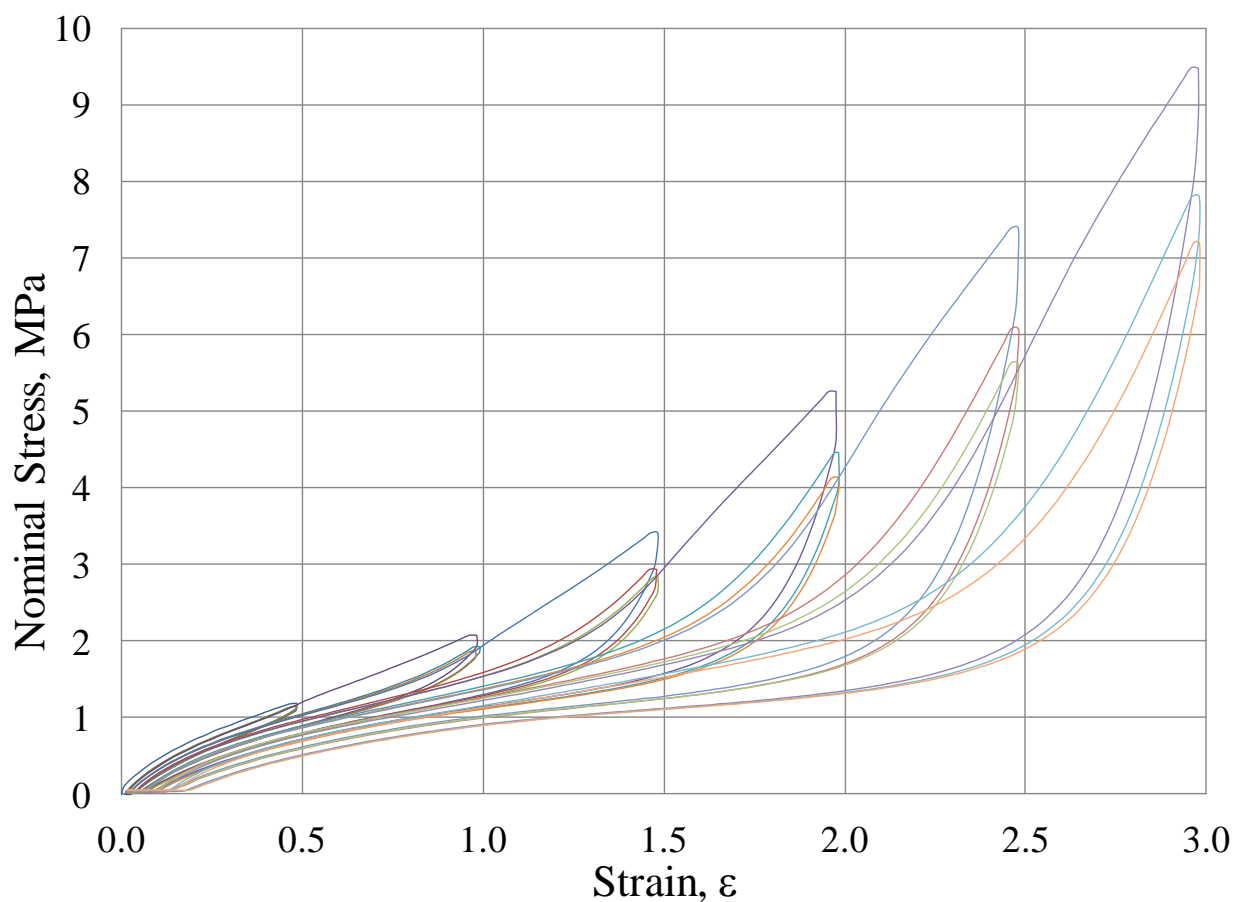Figure C19: Stress-strain in simple extension for R16 from zero strain.

Figure C20: Typical non-relaxing stress-strain curves of R16 at strain amplitude of 15%, 25%, 35%, 45%, 55%, 95% and 105%.
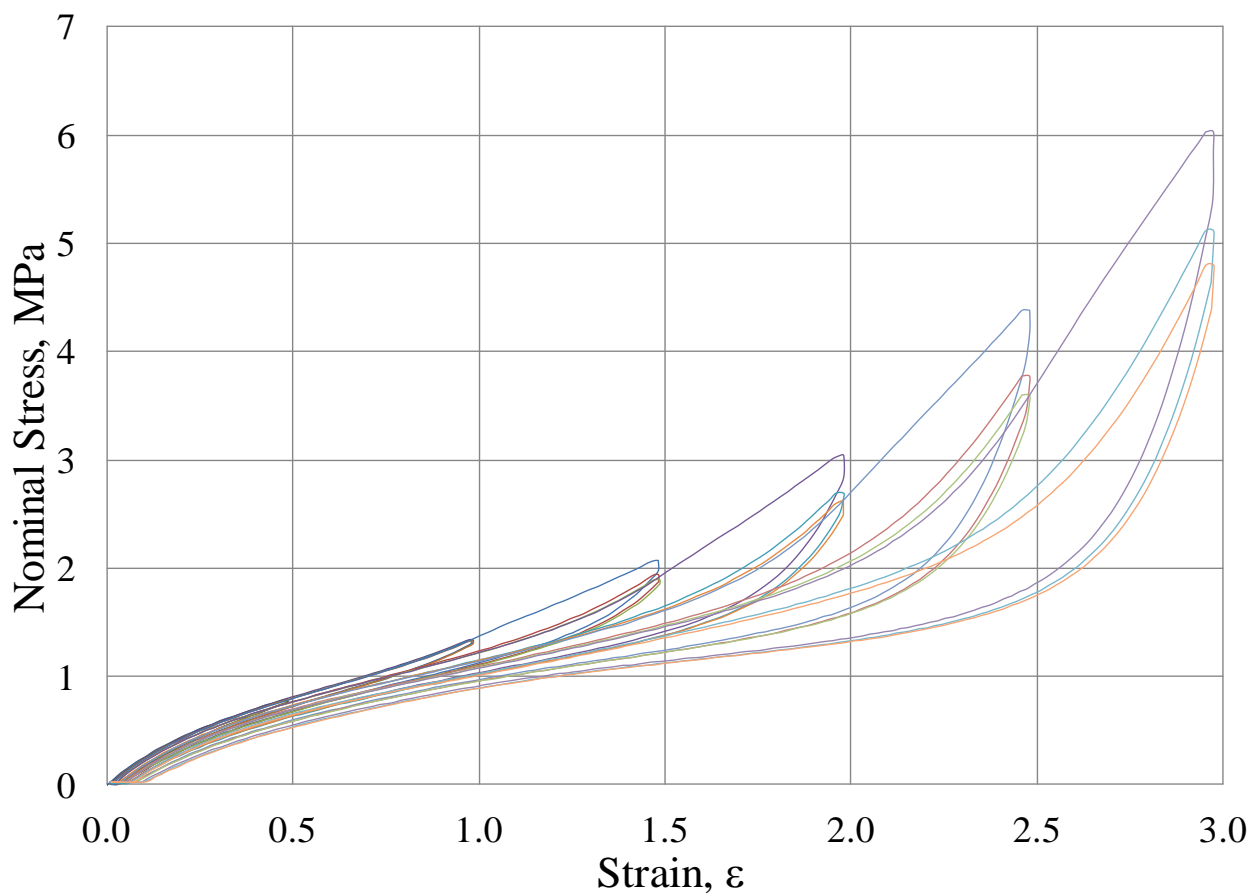
Figure C21: Stress-strain in simple extension for R17 from zero strain.

Figure C22: Typical non-relaxing stress-strain curves of R17 at strain amplitude of 15%, 25%, 35%, 45%, 55%, 95% and 105%.

Figure C23: Stress-strain in simple extension for R18 from zero strain.
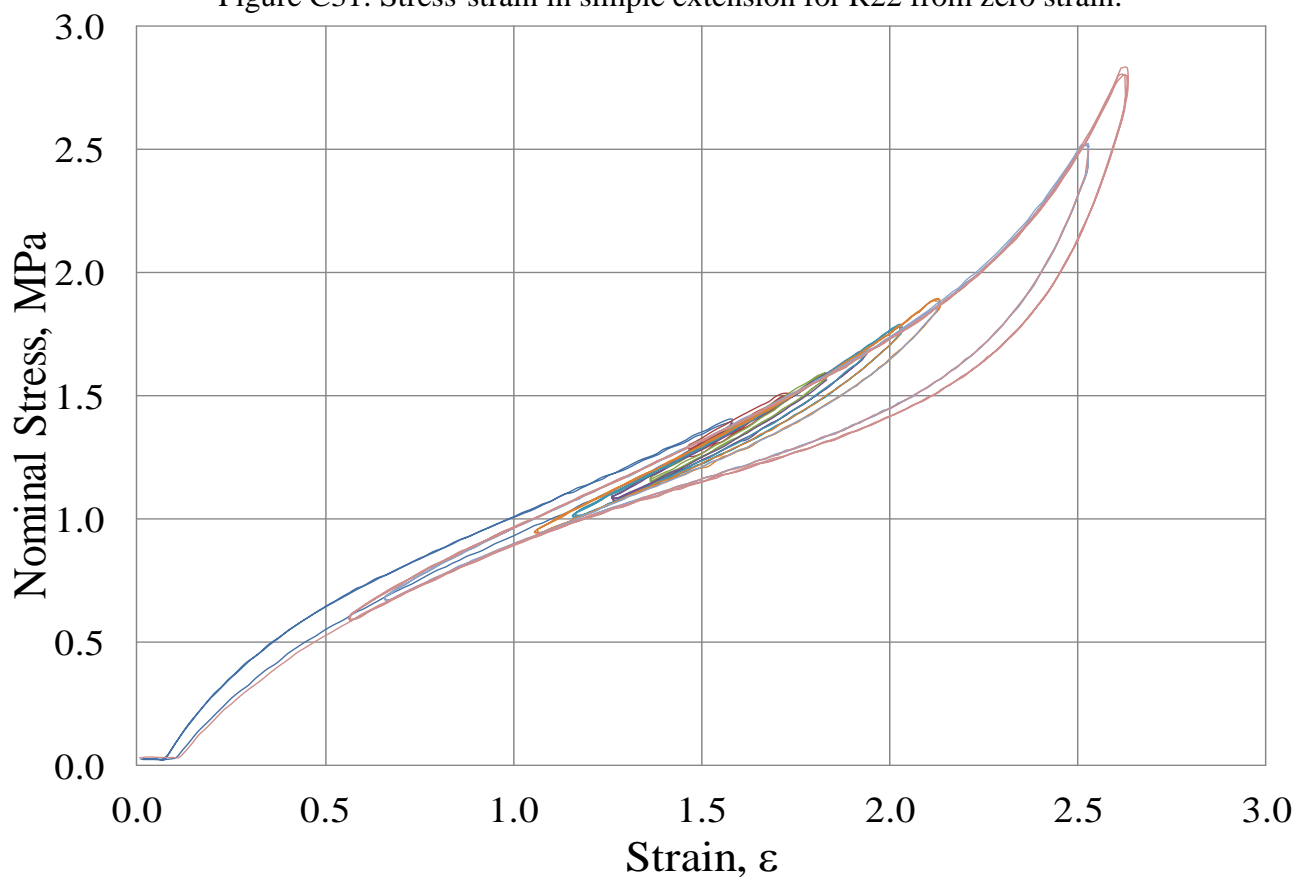

Figure C24: Typical non-relaxing stress-strain curves of R18 at strain amplitude of 15%, 25%, 35%, 45%, 55%, 95% and 105%.

Figure C25: Stress-strain in simple extension for R19 from zero strain.

Figure C26: Typical non-relaxing stress-strain curves of R19 at strain amplitude of 15%, 25%, 35%, 45%, 55%, 95% and 105%.

Figure C27: Stress-strain in simple extension for R20 from zero strain.

Figure C28: Typical non-relaxing stress-strain curves of R20 at strain amplitude of 15%, 25%, 35%, 45%, 55%, 95% and 105%.
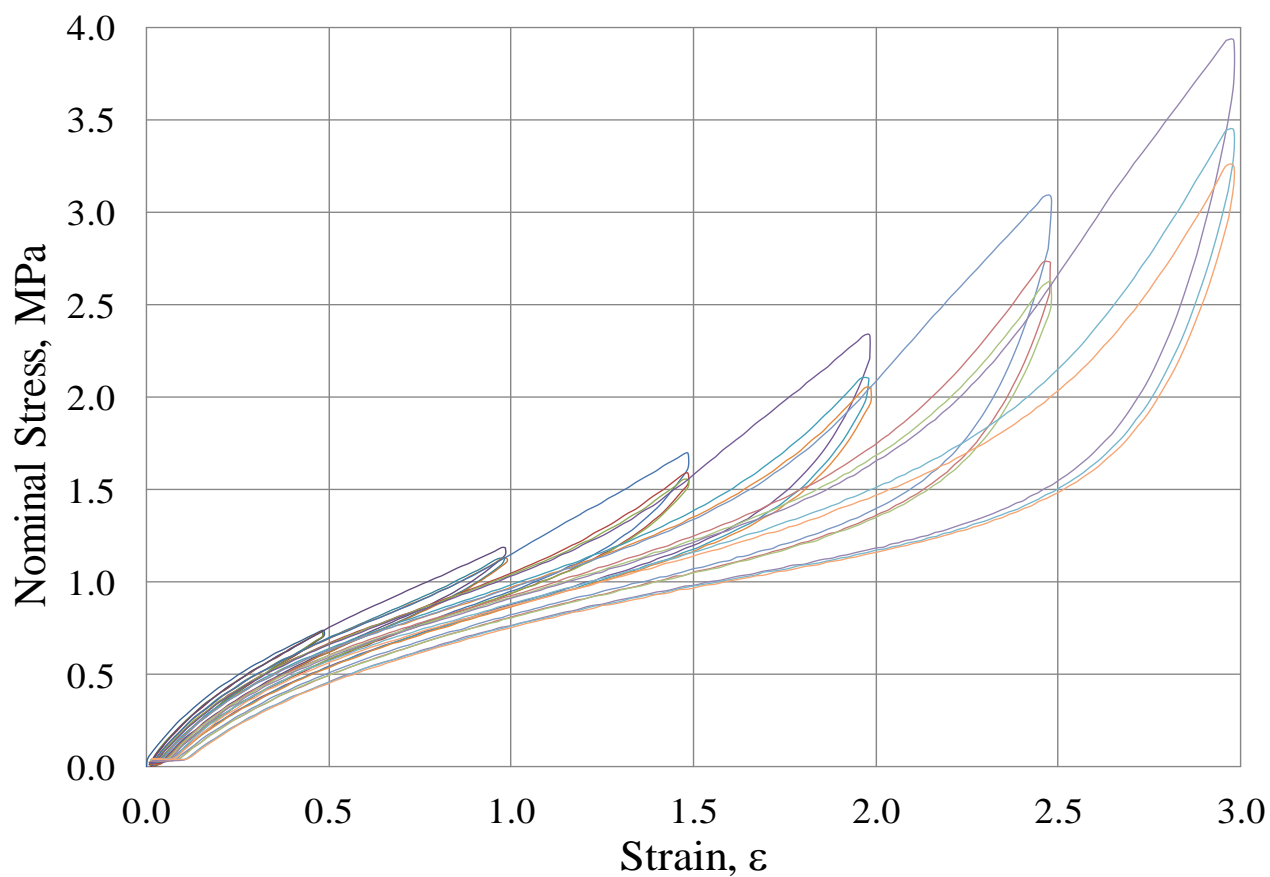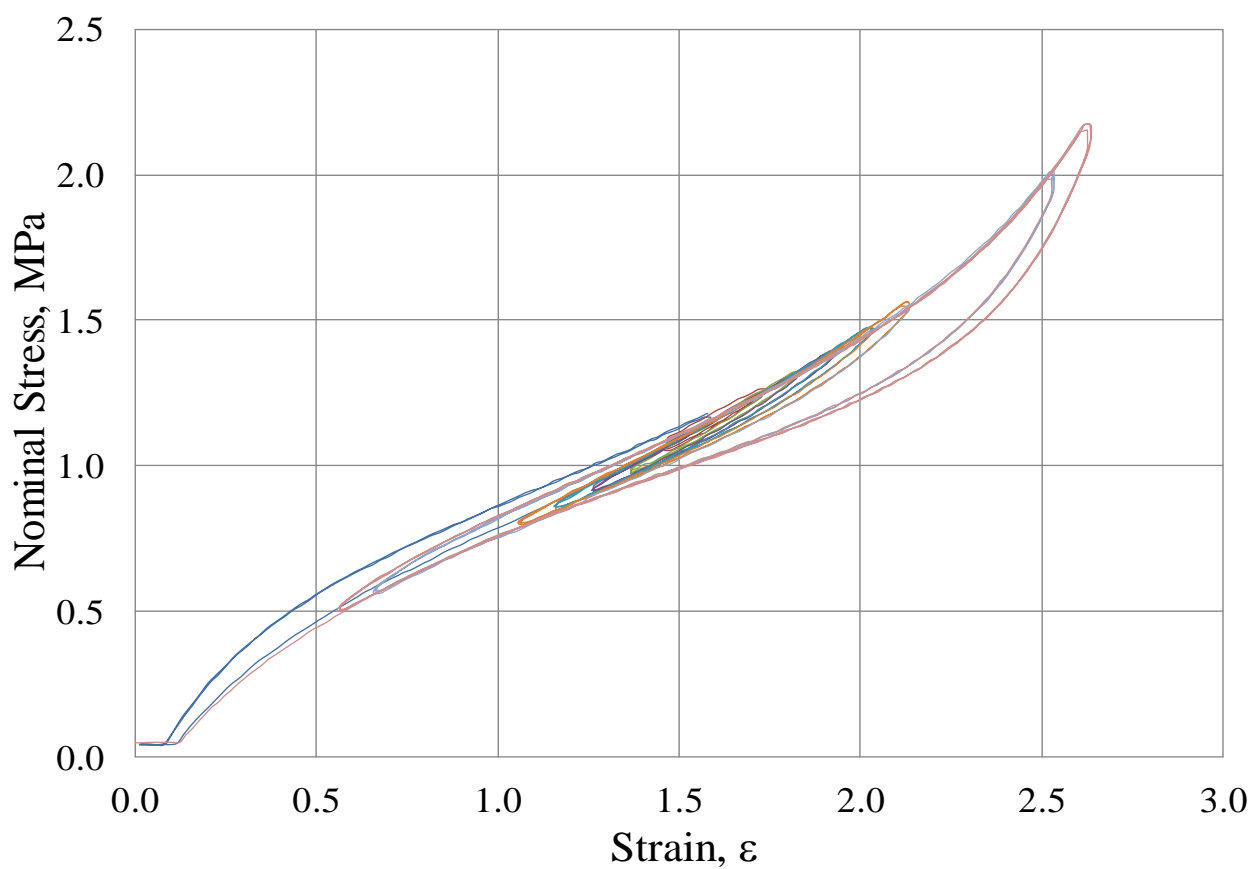
Figure C29: Stress-strain in simple extension for R21 from zero strain.

Figure C30: Typical non-relaxing stress-strain curves of R21 at strain amplitude of 15%, 25%, 35%, 45%, 55%, 95% and 105%.

Figure C31: Stress-strain in simple extension for R22 from zero strain.

Figure C32: Typical non-relaxing stress-strain curves of R22 at strain amplitude of 15%, 25%, 35%, 45%, 55%, 95% and 105%.
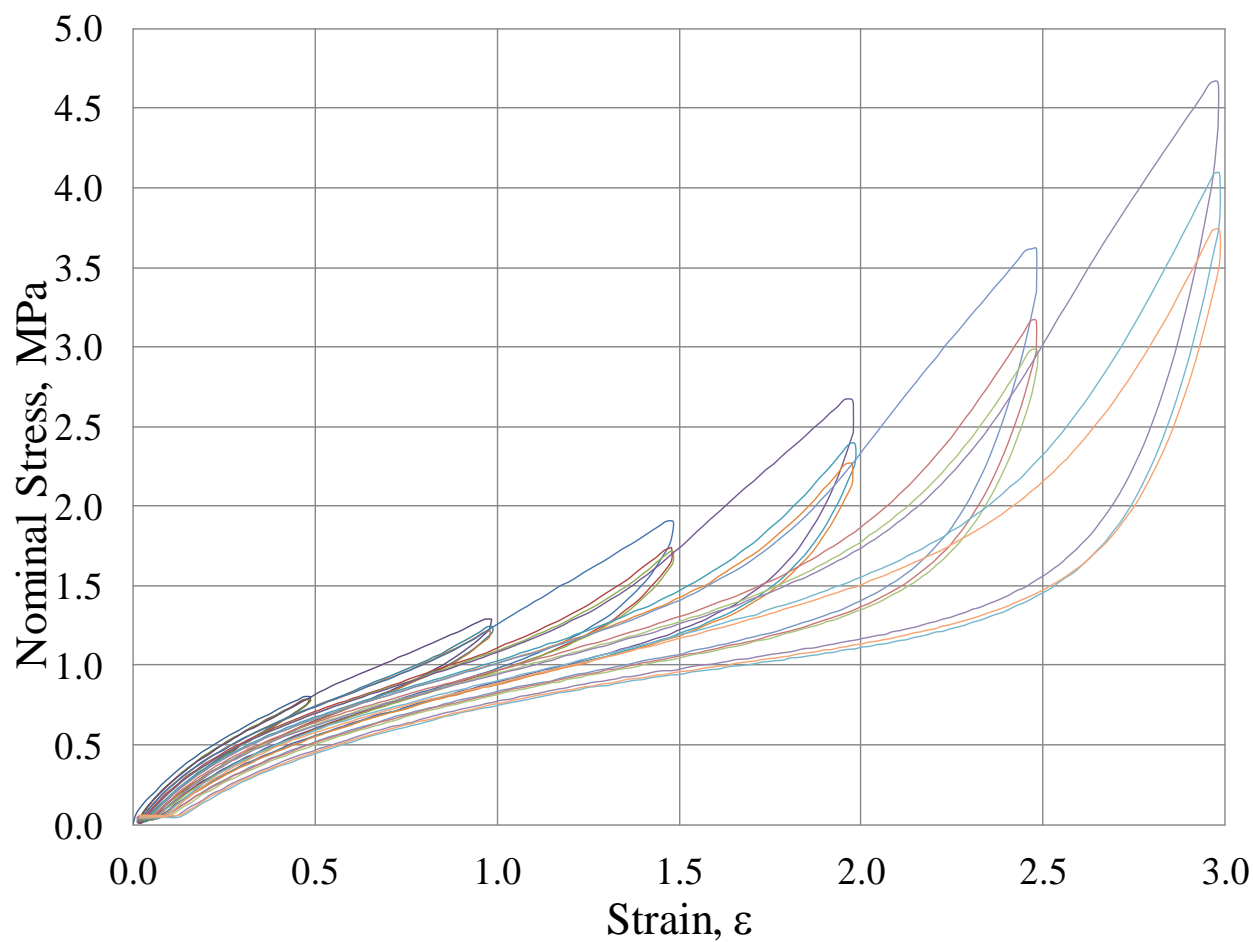
Figure C33: Stress-strain in simple extension for R23 from zero strain.

Figure C34: Typical non-relaxing stress-strain curves of R23 at strain amplitude of 15%, 25%, 35%, 45%, 55%, 95% and 105%.

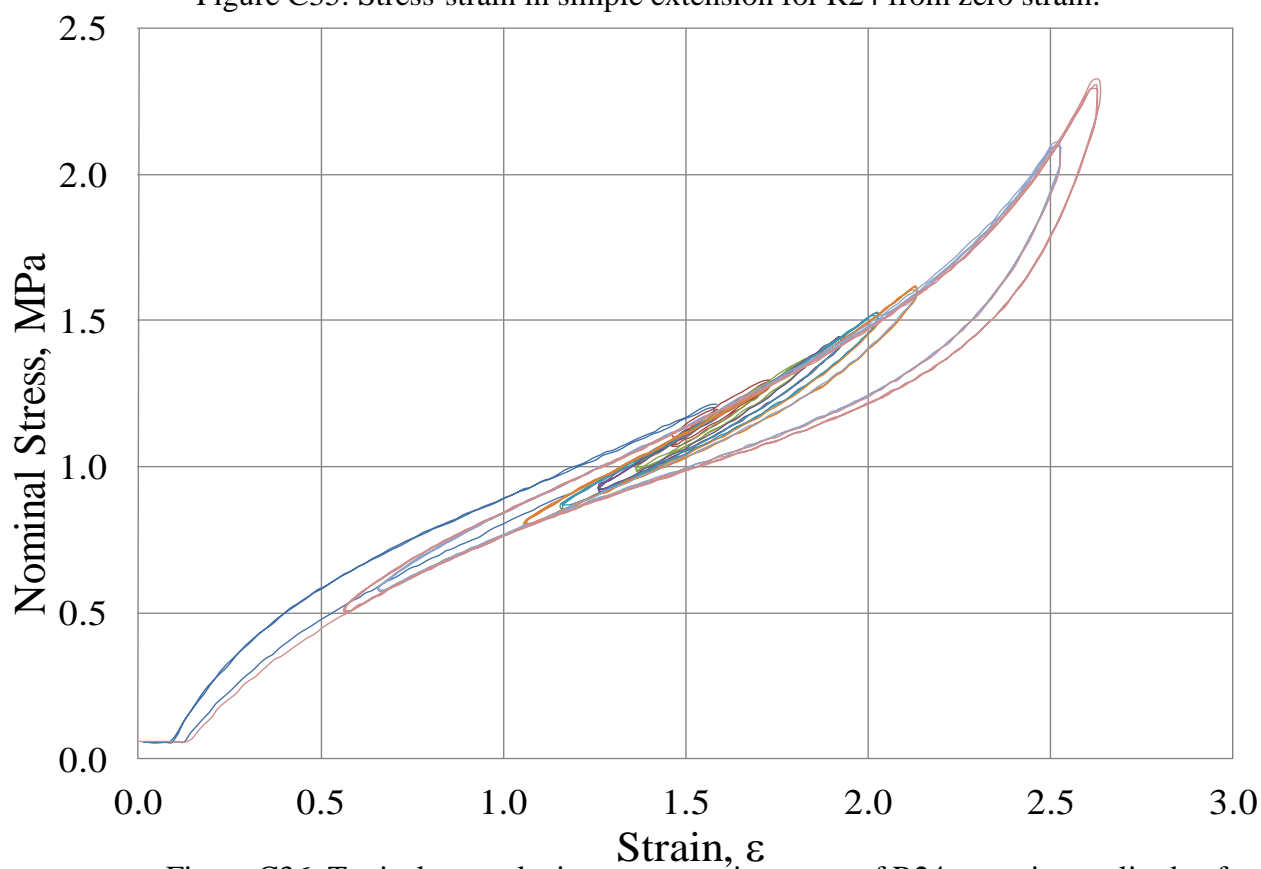Figure C35: Stress-strain in simple extension for R24 from zero strain.

Figure C36: Typical non-relaxing stress-strain curves of R24 at strain amplitude of 15%, 25%, 35%, 45%, 55%, 95% and 105%.
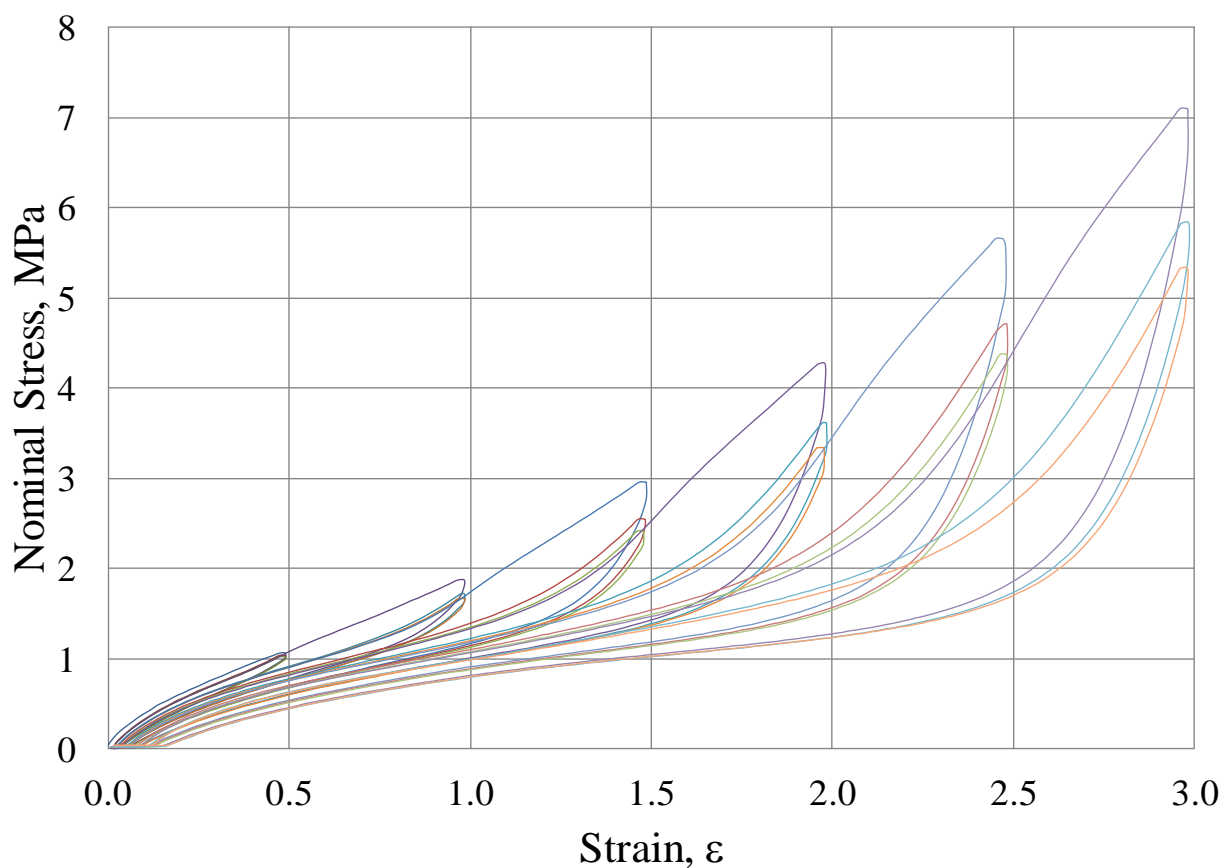
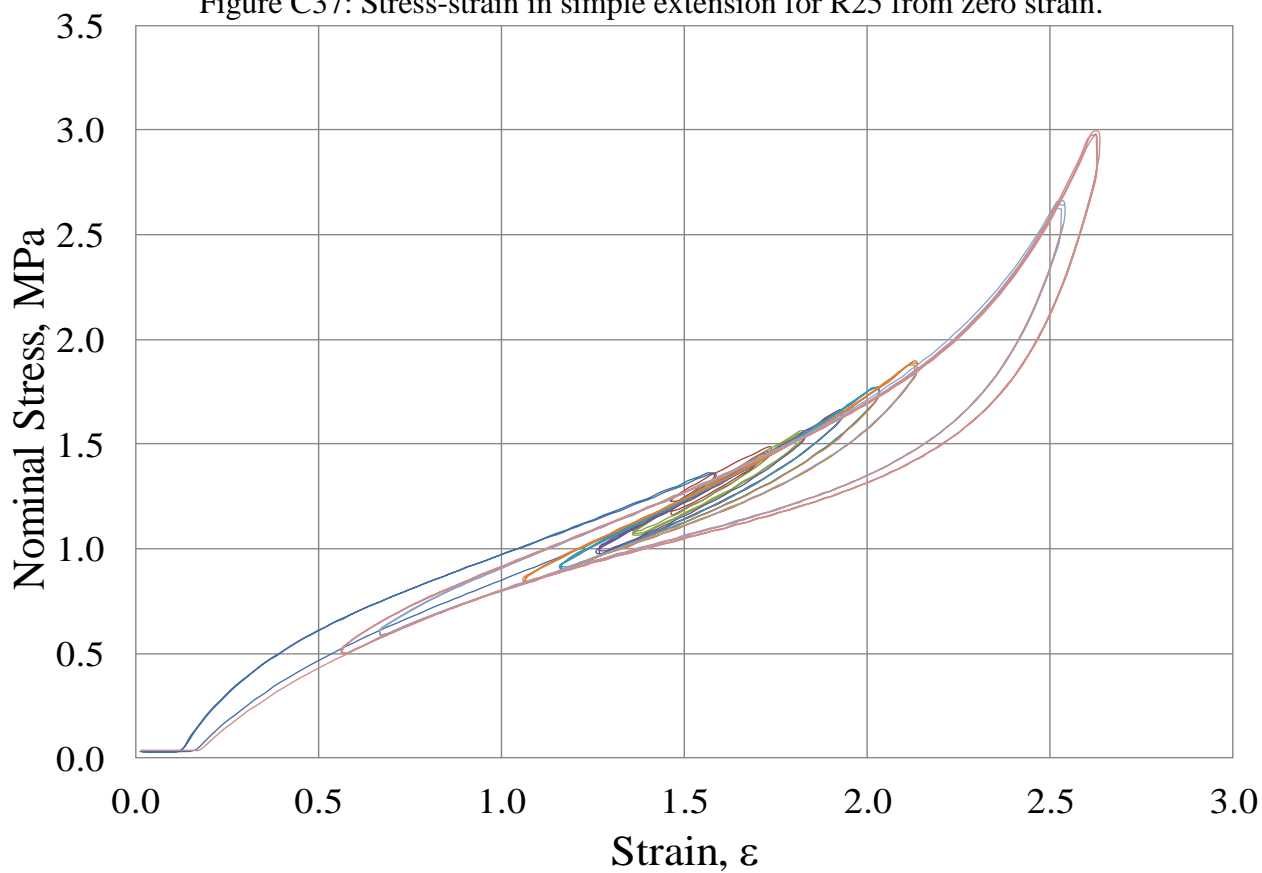Figure C37: Stress-strain in simple extension for R25 from zero strain.

Figure C38: Typical non-relaxing stress-strain curves of R25 at strain amplitude of 15%, 25%, 35%, 45%, 55%, 95% and 105%.
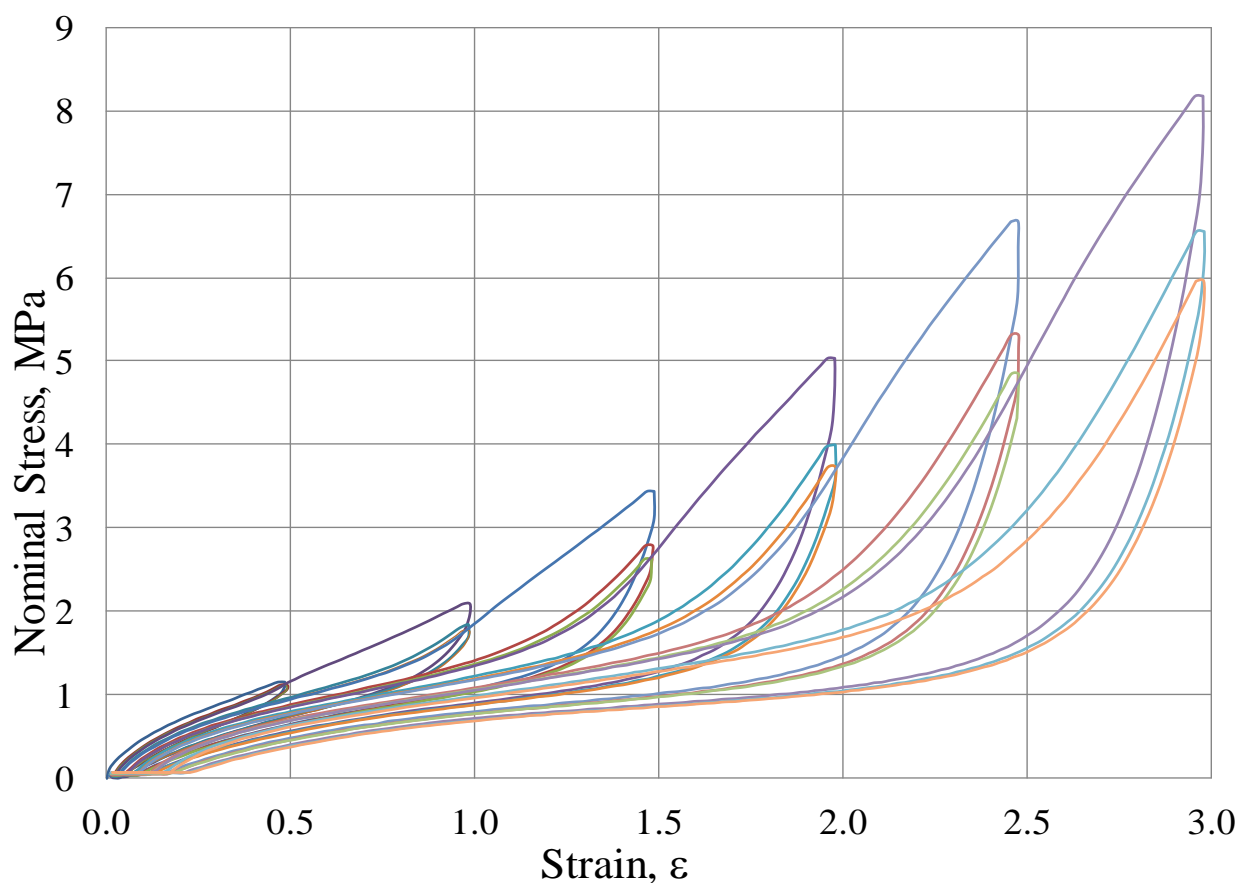
Figure C39: Stress-strain in simple extension for R26 from zero strain.
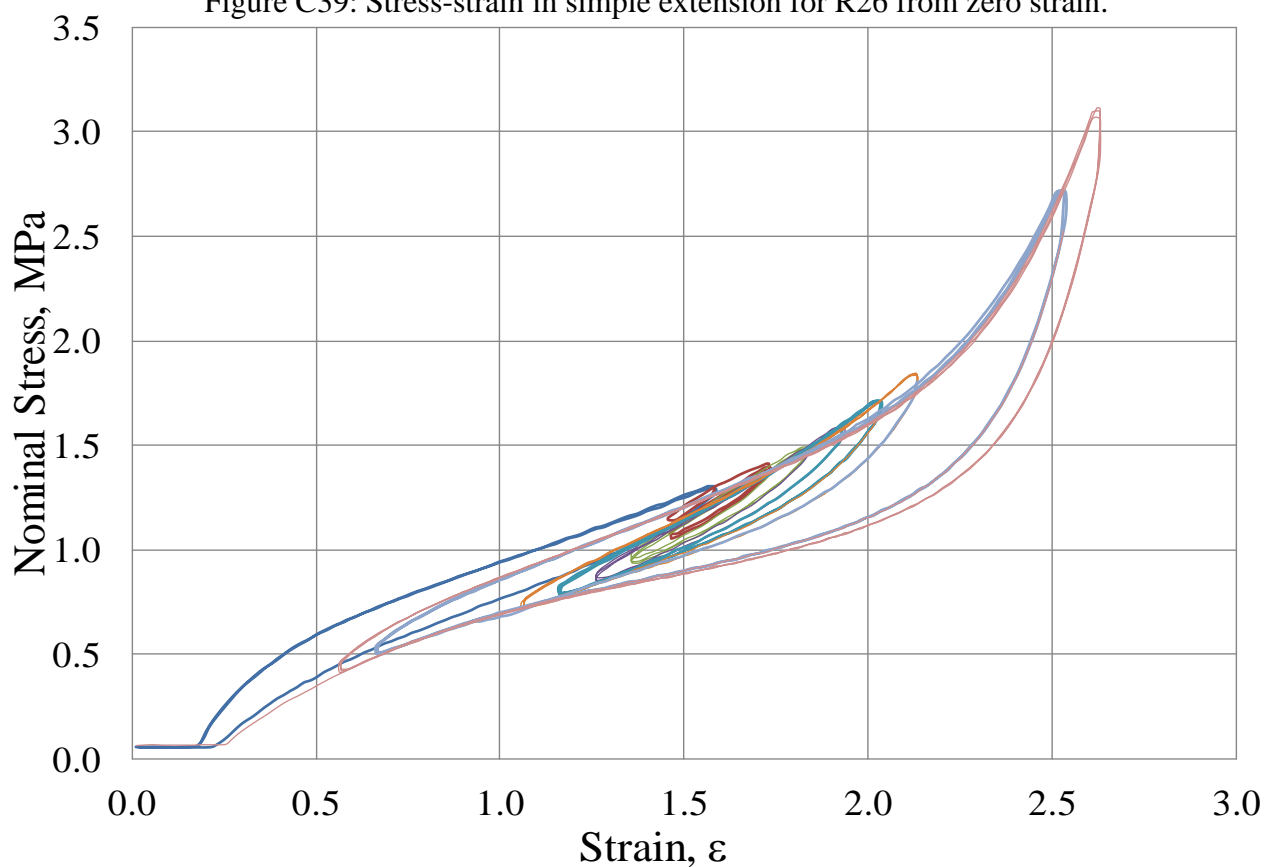

Figure C40: Typical non-relaxing stress-strain curves of R26 at strain amplitude of 15%, 25%, 35%, 45%, 55%, 95% and 105%.

The details of the Visual Basic program used to calculate the modulus and loss angle utilise data from the hysteresis loops subject to a non relaxing condition Figures C2, C4, ..., C40.

```vb
Sub stt()
UserForm1.Show False
End Sub
Public Function NameFromFullPath(FullPath As String) As String
'Input: Name/Full Path of a file  Returns: Name of file
Dim sPath As String, sList() As String, sAns As String, iArrayLen As Integer

If Len(FullPath) = 0 Then Exit Function
sList = Split(FullPath, "\")
iArrayLen = UBound(sList)
sAns = IIf(iArrayLen = 0, "", sList(iArrayLen))

NameFromFullPath = sAns
End Function

Function aver(l, t, rength) As Double

    aver = (Application.WorksheetFunction.Max(l) + Application.WorksheetFunction.Min(l)) / 2

End Function

Function summat(l, t, rength)
'works out the area via the trapezium rule array l of length rength
Dim i As Integer

For i = 0 To rength - 2
    summ = summ + (l(i + 1) + l(i)) * (t(i + 1) - t(i)) / 2
Next i
summ = summ + (l(0) + l(rength - 1)) * (t(0) - t(rength - 1)) / 2
summat = summ
End Function

Sub intoxl(fname As Variant)
'this sub should read data from text files into memory and do some dynamic analysis on it
'the input required is entered in UserForm1 and UserForm2
'the output is the results of the analysis and the data used in the analysis in a new workbook
'Sheet1 contains a summary of all the text files analysed
'The other sheets contain the data used from each text file with the analyses
Dim ReadLine As String, ColNdx As Integer, TempVal As Variant, Pos As Integer, NextPos As Integer, a As Integer, SaveColNdx As Integer, fmnw As String, RowNdx As Long, looptime As Double, noloop As Double, i As Integer, fcoswt() As Double, dummy() As Double, mult As Integer, harm As Integer
Dim x1(200000) As Double, X() As Double, F1(200000) As Double, F() As Double, t1(200000) As Double, t() As Double, justf() As Double, justx() As Double, E() As Double, sinwt() As Double, coswt() As Double, xsinwt() As Double, xcoswt() As Double, fsinwt() As Double, PhaseE As Variant, fn As String
Dim novo As Integer, cout As Integer, fidge As Double, rength As Integer, avf As Double, avx As Double, xreal As Double, ximag As Double, xphase As Double, freal As Double, fimag As Double,
```

```
fphase As Double, Disp As Double, Force As Double, Stiffness As Double, Phaseharm As Double,
Eloop As Double
Dim cycleno(200000)
'On Error GoTo ErrorHandler

Sep = ","
textattop = 1
novo = 0

Pi = Application.WorksheetFunction.Pi()

'set up new spreadsheet
Set newBook = Workbooks.Add
Application.ScreenUpdating = False
Sheets(1).Name = "Summary"
Cells(1, 1).Value = "Filename"
Cells(1, 2).Value = "Cycle number"
Cells(1, 3).Value = "Frequency (Hz)"
Cells(1, 4).Value = "Displacement (mm)"
Cells(1, 5).Value = "Load (N)"

Cells(1, 7).Value = "Stiffness (secant)"
Cells(1, 8).Value = "In-phase Stiffness (secant)"
Cells(1, 9).Value = "Out-of-phase Stiffness (secant)"
Cells(1, 10).Value = "Loss angle calculated from energy (secant)(degrees)"

If UserForm1!Modulus.Value = True Then
    Cells(1, 12).Value = "Strain (secant)"
    Cells(1, 13).Value = "Stress (secant)(MPa)"
    Cells(1, 14).Value = "In-phase Modulus (secant)(MPa)"
    Cells(1, 15).Value = "Out-of-phase Modulus (secant)(MPa)"
    Cells(1, 16).Value = "Modulus (secant)(MPa)"
    Cells(1, 17).Value = "Tan delta (secant)"
End If

For a = 1 To 16
    With Cells(1, a)
        .HorizontalAlignment = xlCenter
        .Font.Bold = True
    End With
Next a

'extract the data from the text file

For i = 1 To UBound(fname)

    fn = CStr(fname(i))

    Set fs = CreateObject("Scripting.FileSystemObject")
    Set oFSO = fs.OpenTextFile(fn, 1)

    SaveColNdx = 1
    RowNdx = 1

    While Not oFSO.AtEndOfStream
```

```
        ReadLine = oFSO.ReadLine

        If Right(ReadLine, 1) <> Sep Then
            ReadLine = ReadLine & Sep
        End If

        ColNdx = SaveColNdx
        Pos = 1
        NextPos = InStr(Pos, ReadLine, Sep)

        While NextPos >= 1
            TempVal = Mid(ReadLine, Pos, NextPos - Pos)

            If ColNdx = UserForm1!time.Value And RowNdx > textattop Then
                t1(RowNdx - textattop - 1) = CDbl(TempVal)
            ElseIf ColNdx = UserForm1!cycleno.Value And RowNdx > textattop Then
                cycleno(RowNdx - textattop) = CDbl(TempVal)
            ElseIf ColNdx = UserForm1!displace.Value And RowNdx > textattop Then
                x1(RowNdx - textattop - 1) = CDbl(TempVal)
            ElseIf ColNdx = UserForm1!load.Value And RowNdx > textattop Then
                F1(RowNdx - textattop - 1) = CDbl(TempVal)

            End If

            Pos = NextPos + 1
            ColNdx = ColNdx + 1
            NextPos = InStr(Pos, ReadLine, Sep)
        Wend
        RowNdx = RowNdx + 1
    Wend

    oFSO.Close
    Set oFSTR = Nothing

'work out the starting point
    rength1 = RowNdx - textattop - 1

numberhere = (cycleno(rength1) - 1)


For cyclecount1 = 1 To numberhere
    rength = 0
    For fish = 0 To rength1
        If cycleno(fish) = cyclecount1 Then rength = rength + 1
    Next fish

'calculate the values
    ReDim X(rength - 1), F(rength - 1), t(rength - 1), justf(rength - 1), justx(rength - 1), E(rength -
1), sinwt(rength - 1), coswt(rength - 1), xsinwt(rength - 1), xcoswt(rength - 1), fsinwt(rength - 1),
fcoswt(rength - 1)

    For a = 0 To rength - 1
        F(a) = F1(novo + a)
        X(a) = x1(novo + a)
        t(a) = t1(novo + a)
```

```
   Next a

   looptime1 = (t(samprate1 + 1) - t(1))

   avf = aver(F, t, rength)
   avx = aver(X, t, rength)

   For a = 0 To rength - 1
      justf(a) = F(a) - avf
      justx(a) = X(a) - avx
   Next a


       looptime = t(rength - 1) - t(0)
       samprate = rength
       noloop = 1
       Eloop = summat(justf, justx, rength) / noloop

'secant method
       Dispsec = Application.WorksheetFunction.Max(justx) / 2- Application.WorksheetFunction.
Min(justx) / 2
       Forcesec = Application.WorksheetFunction.Max(justf)  / 2 -
Application.WorksheetFunction.Min(justf)  / 2
       Stiffnesssec = Forcesec / Dispsec
       If (Eloop / (Pi * Stiffnesssec * Dispsec ^ 2)) < 1 And (Eloop / (Pi * Stiffnesssec * Dispsec ^
2)) > -1 Then
          PhaseEsec = (180 / Pi) * Application.WorksheetFunction.Asin(Eloop / (Pi * Stiffnesssec *
Dispsec ^ 2))
       Else
          PhaseEsec = "error"
       End If

'print the results


   Sheets(1).Cells(cyclecount1 + i + 1, 1).Value = NameFromFullPath(fn)
   Sheets(1).Cells(cyclecount1 + i + 1, 2).Value = cyclecount1
   Sheets(1).Cells(cyclecount1 + i + 1, 3).Value = 1 / looptime
   Sheets(1).Cells(cyclecount1 + i + 1, 4).Value = Dispsec
   Sheets(1).Cells(cyclecount1 + i + 1, 5).Value = Forcesec


   Sheets(1).Cells(cyclecount1 + i + 1, 7).Value = Stiffnesssec 'K*
   If PhaseEsec <> "error" Then
   Sheets(1).Cells(cyclecount1 + i + 1, 8).Value = Stiffnesssec * Cos(PhaseEsec * Pi / 180) 'K'
   Sheets(1).Cells(cyclecount1 + i + 1, 9).Value = Stiffnesssec * Sin(PhaseEsec * Pi / 180) 'K"
   End If
   Sheets(1).Cells(cyclecount1 + i + 1, 10).Value = PhaseEsec 'delta


   If UserForm1!Modulus.Value = True Then

   Sheets(1).Cells(cyclecount1 + i + 1, 12).Value = Dispsec / UserForm1!Length.Value
   Sheets(1).Cells(cyclecount1 + i + 1, 13).Value = Forcesec / UserForm1!Area.Value
```

```
    Sheets(1).Cells(cyclecount1 + i + 1, 14).Value = Stiffnesssec * UserForm1!Length /
UserForm1!Area.Value * Cos(PhaseEsec * Pi / 180) 'E'
    Sheets(1).Cells(cyclecount1 + i + 1, 15).Value = Stiffnesssec * UserForm1!Length /
UserForm1!Area.Value * Sin(PhaseEsec * Pi / 180) 'E''
    Sheets(1).Cells(cyclecount1 + i + 1, 16).Value = Stiffnesssec * UserForm1!Length /
UserForm1!Area.Value 'E*
    Sheets(1).Cells(cyclecount1 + i + 1, 17).Value = Tan(PhaseEsec * Pi / 180) 'tan delta
    End If


    For a = 1 To 23
       With Sheets(1).Cells(i + 1, a)
          .HorizontalAlignment = xlCenter
       End With
    Next a
novo = novo + rength
Next cyclecount1
Next i


'finish off
Application.ScreenUpdating = True
fnamenew = Application.GetSaveAsFilename(FileFilter:="Excel Files (*.xls), *.xls")

If fnamenew = False Then
   Exit Sub
End If

With newBook
   .SaveAs fileName:=fnamenew
End With

'ErrorHandler:
'Exit Sub

End Sub
```

APPENDIX D

Results of Agglomerates as a Function of Diameter of Particles Size in for All Rubber Compounds
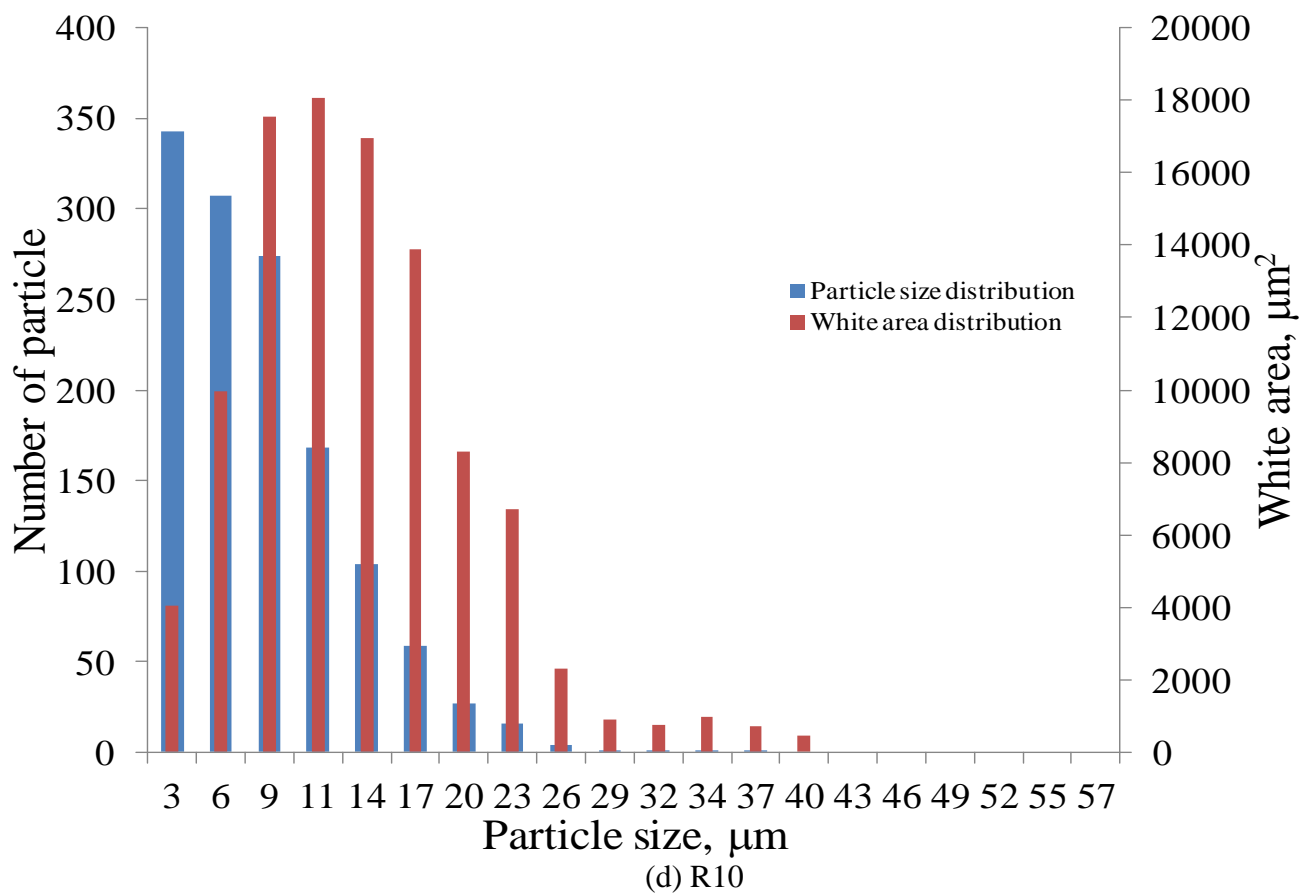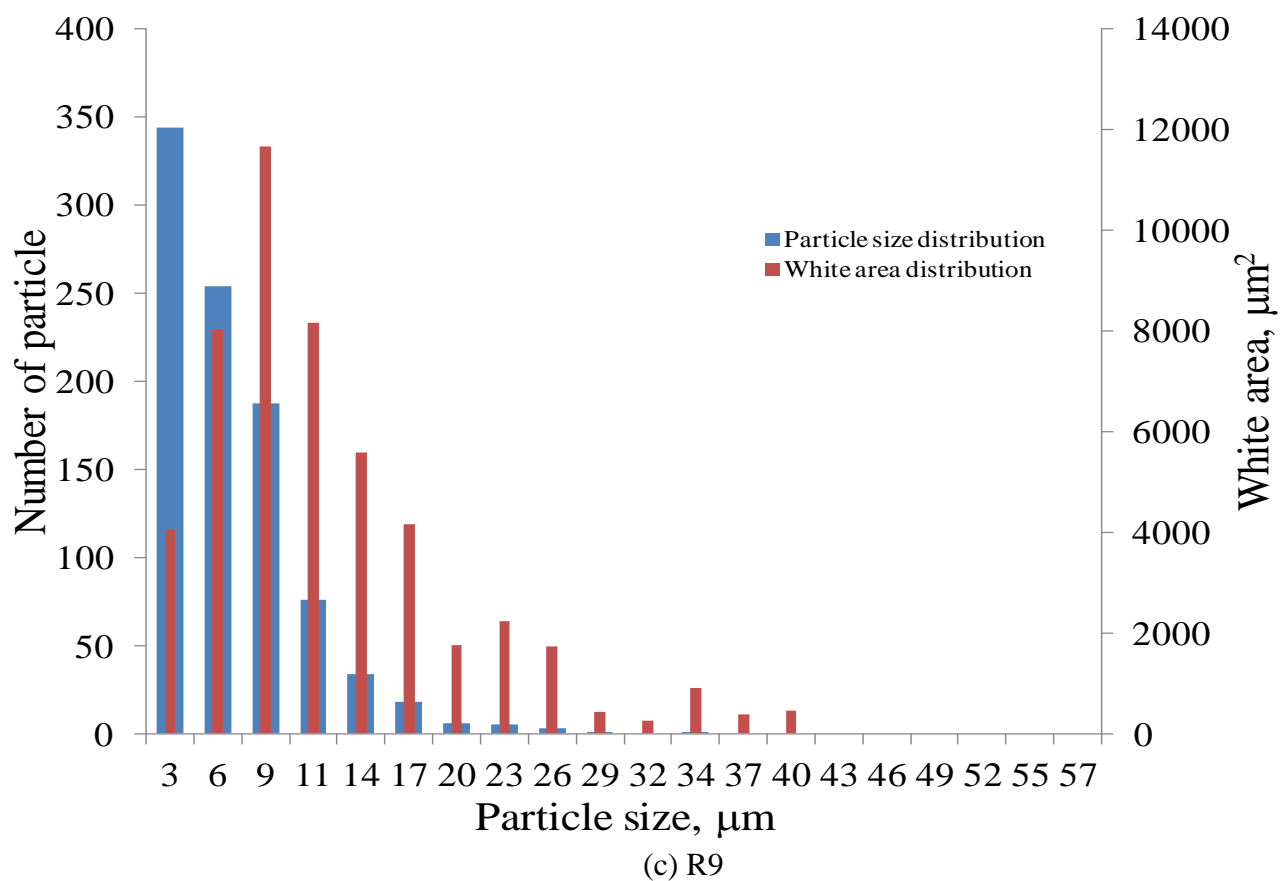
Chapter 6 addressed filler particle size/agglomerate distribution. Some results have been presented in Chapter 6. Here for comparison purpose results for all other rubbers investigated are provided as Figure D1(a) ~ (s).
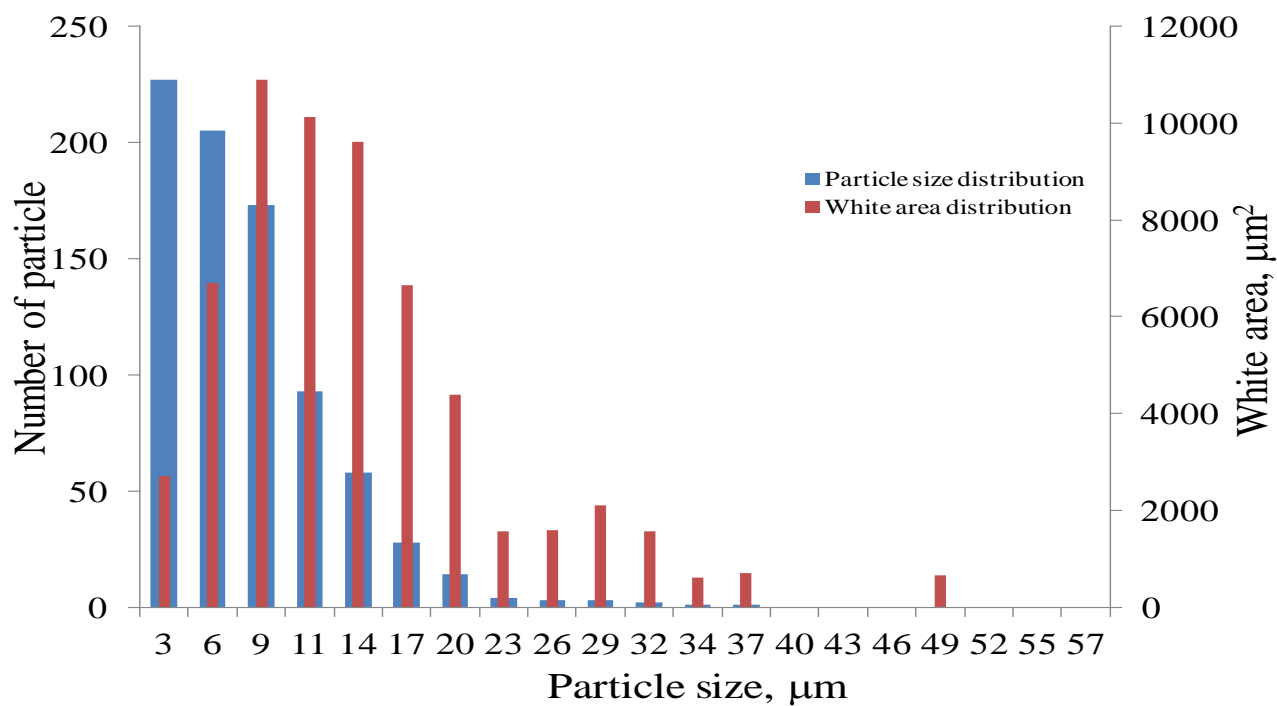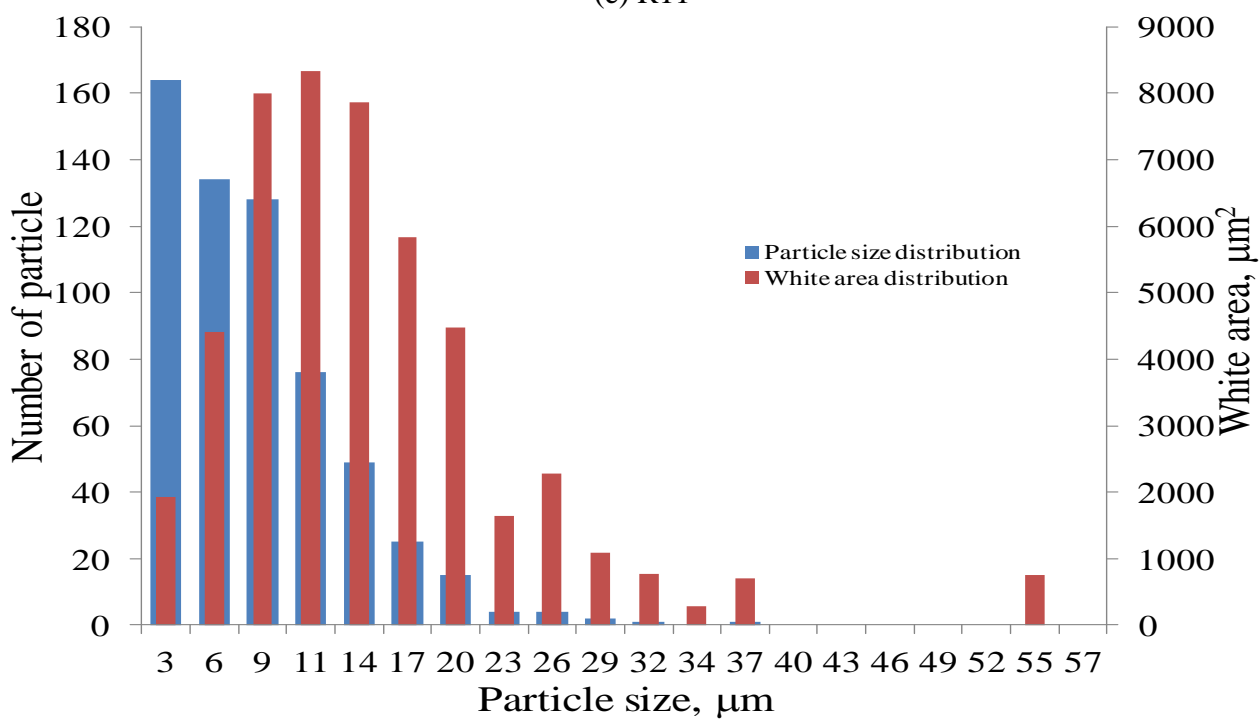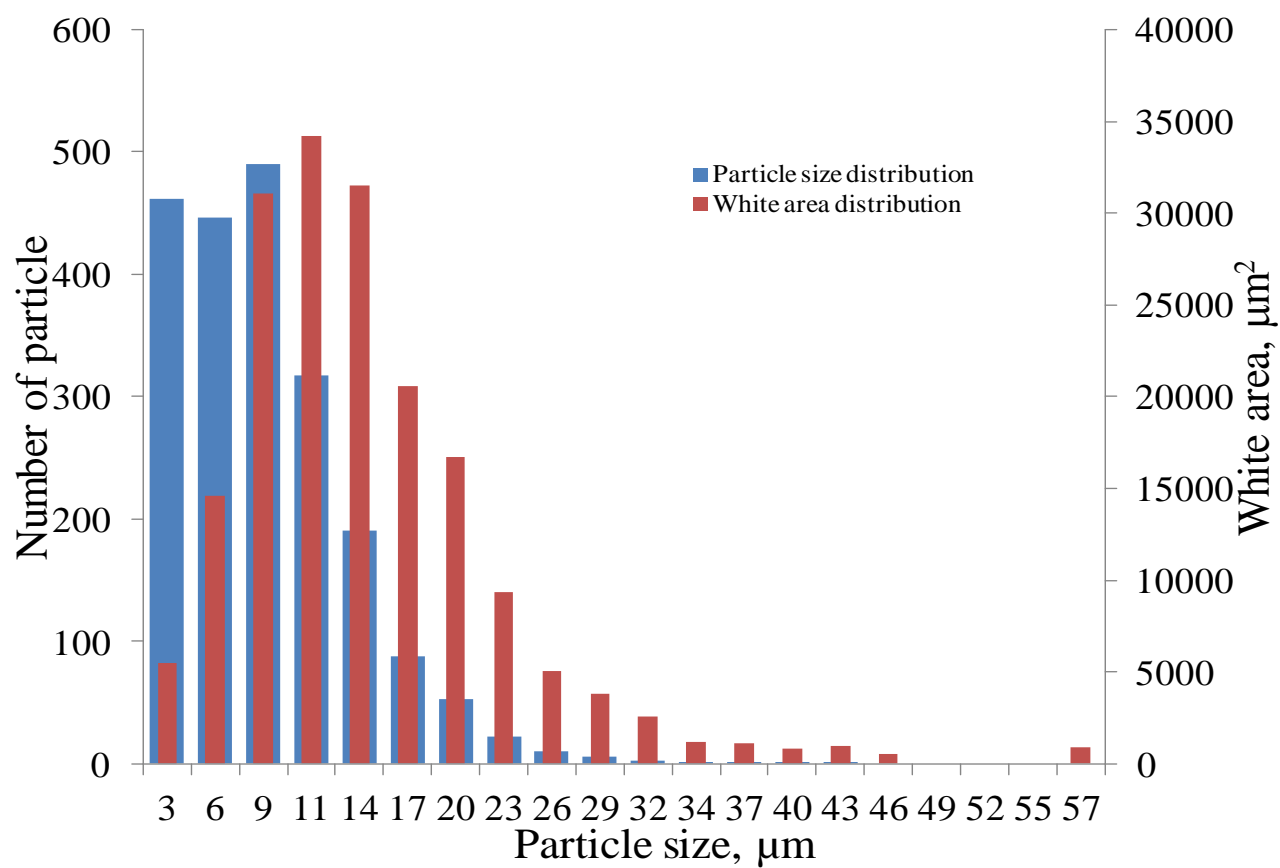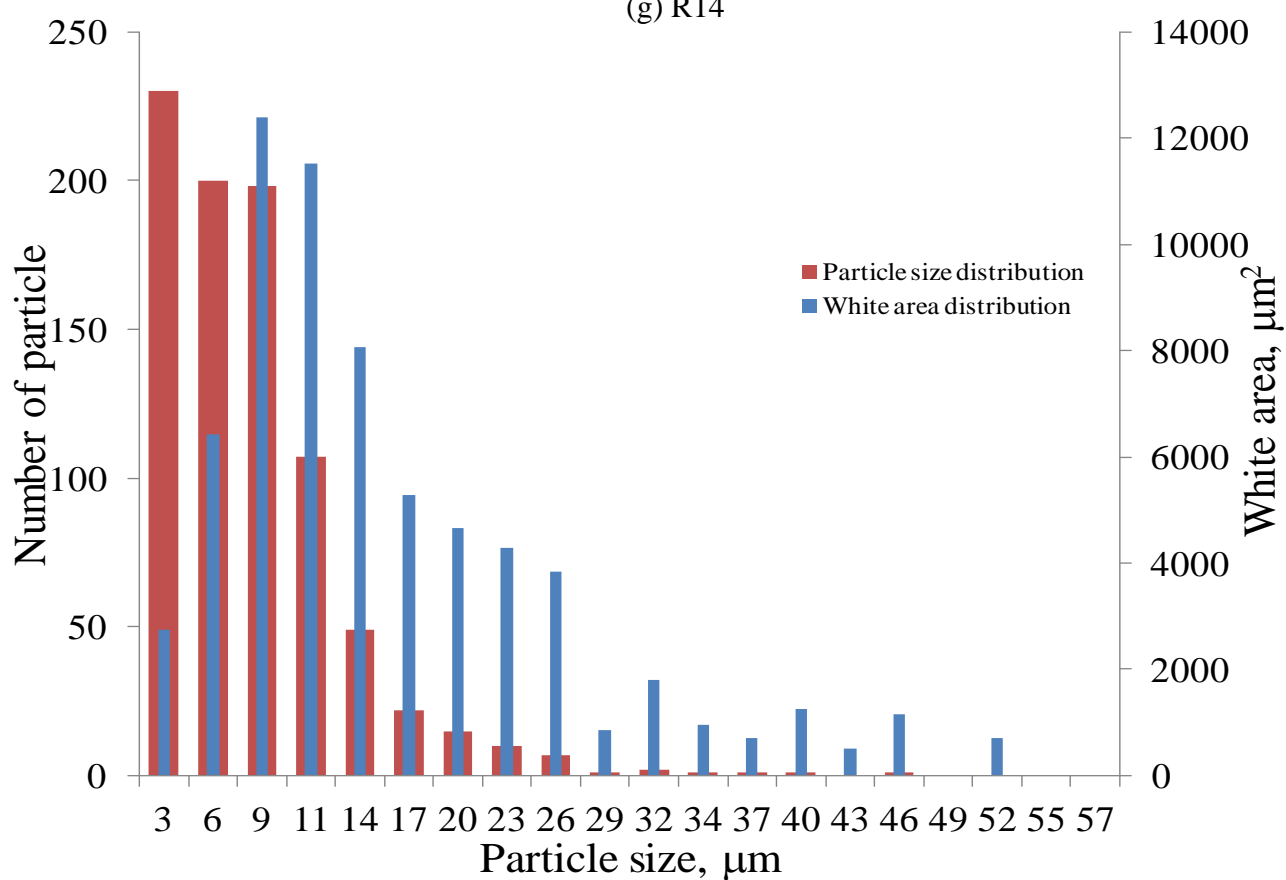

(a) R7

(b) R8

(c) R9

(d) R10
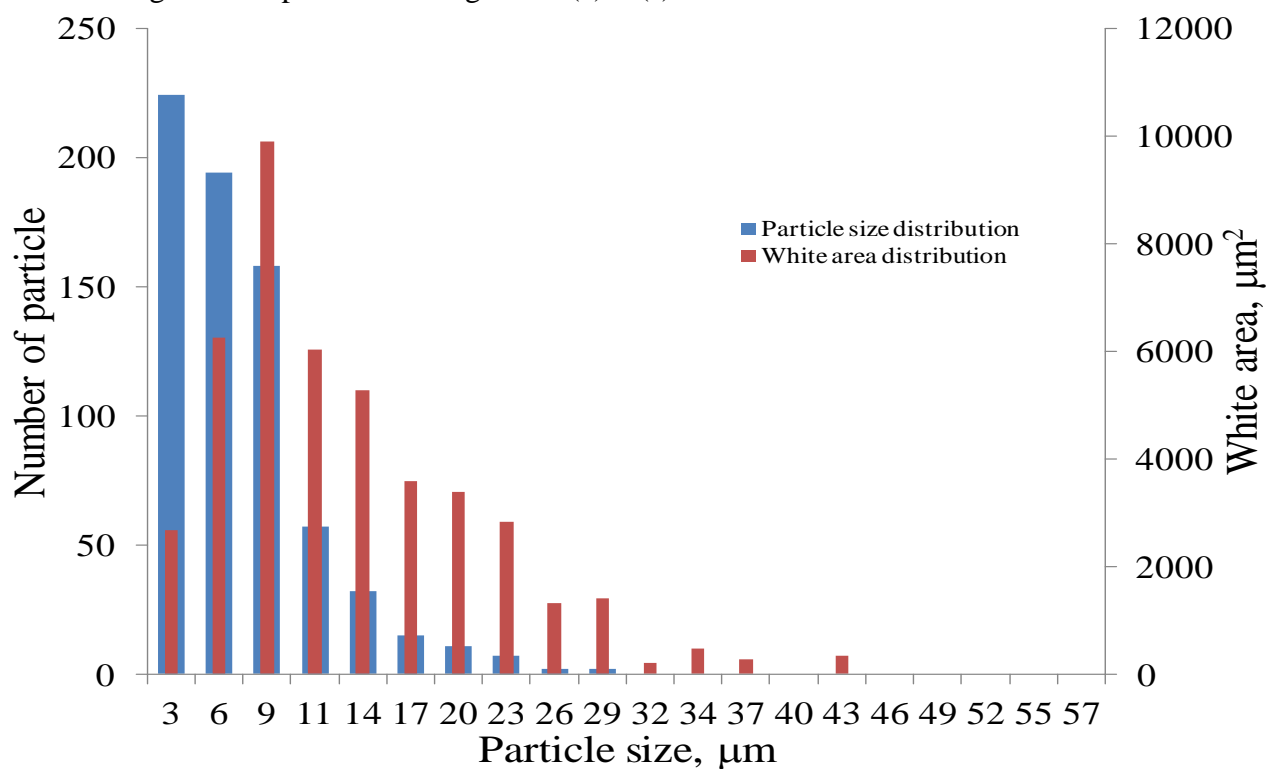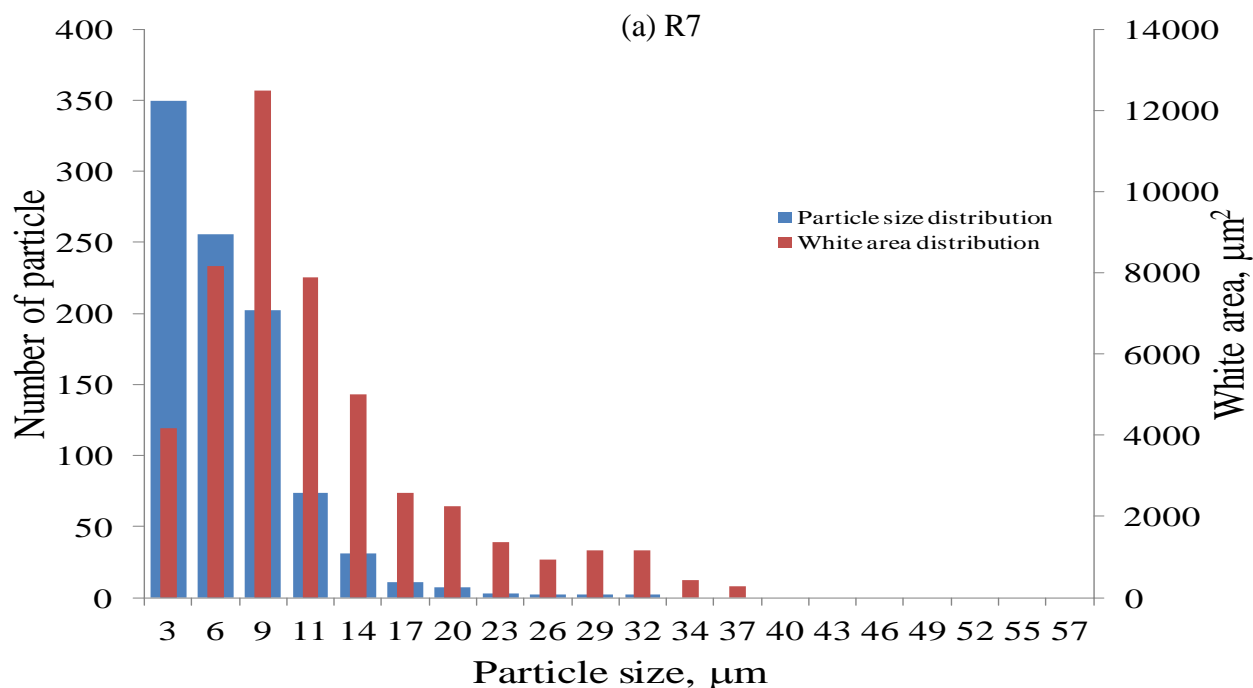
(e) R11

(f) R12

(g) R14

(h) R15

(i) R16

(j) R17

(k) R18

(l) R19

(m) R20

(n) R21

(o) R22

(p) R23

(q) R24

(r) R25

(s) R26
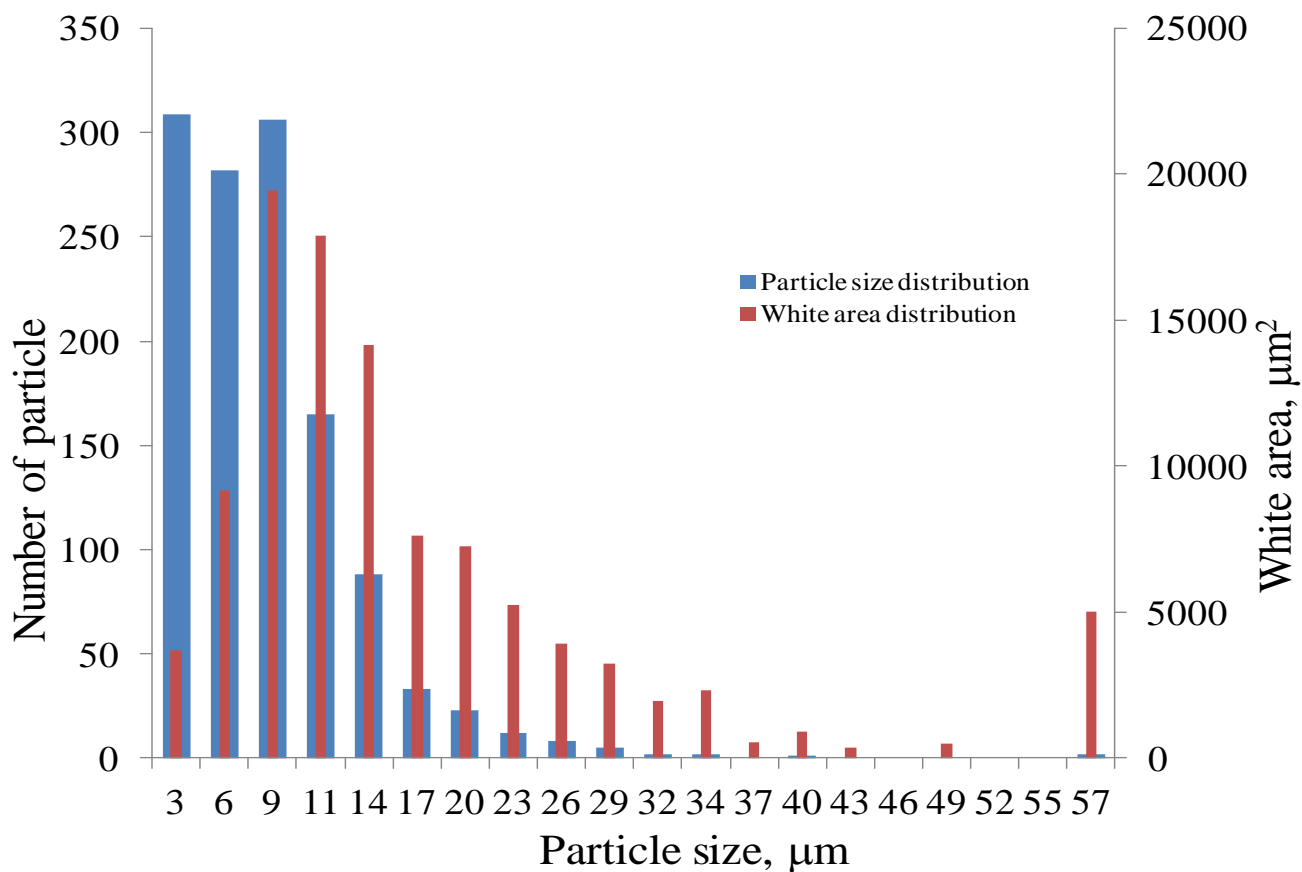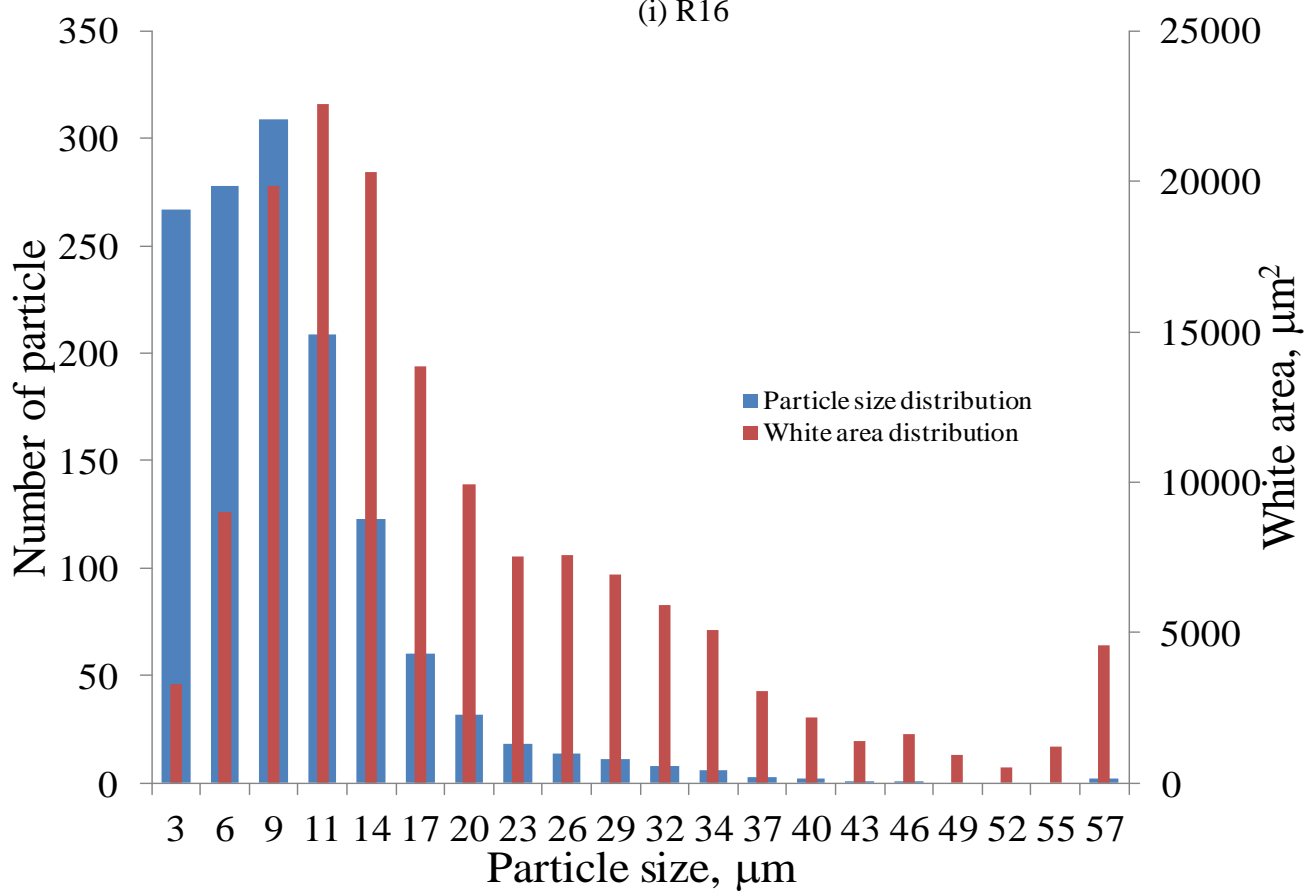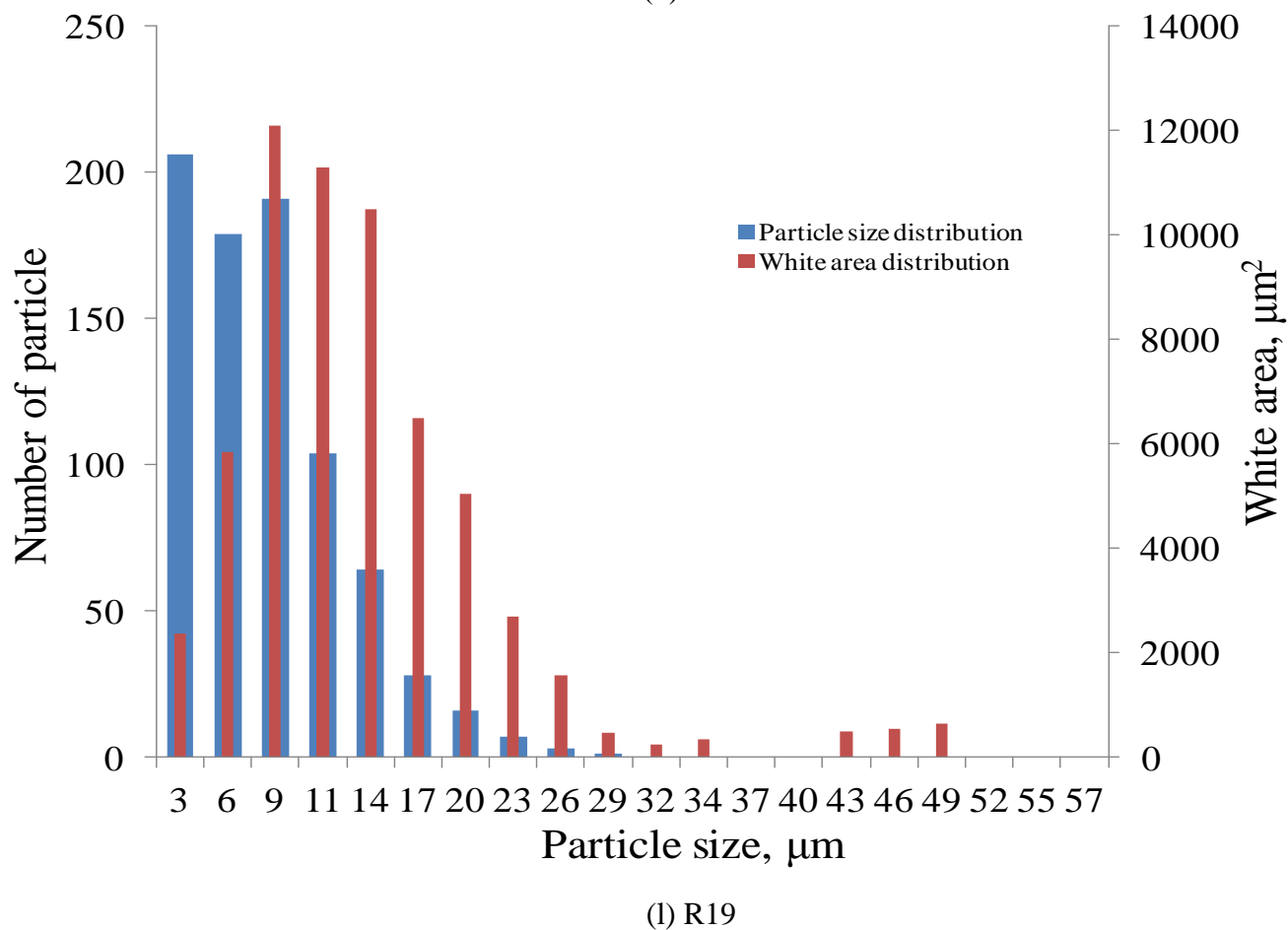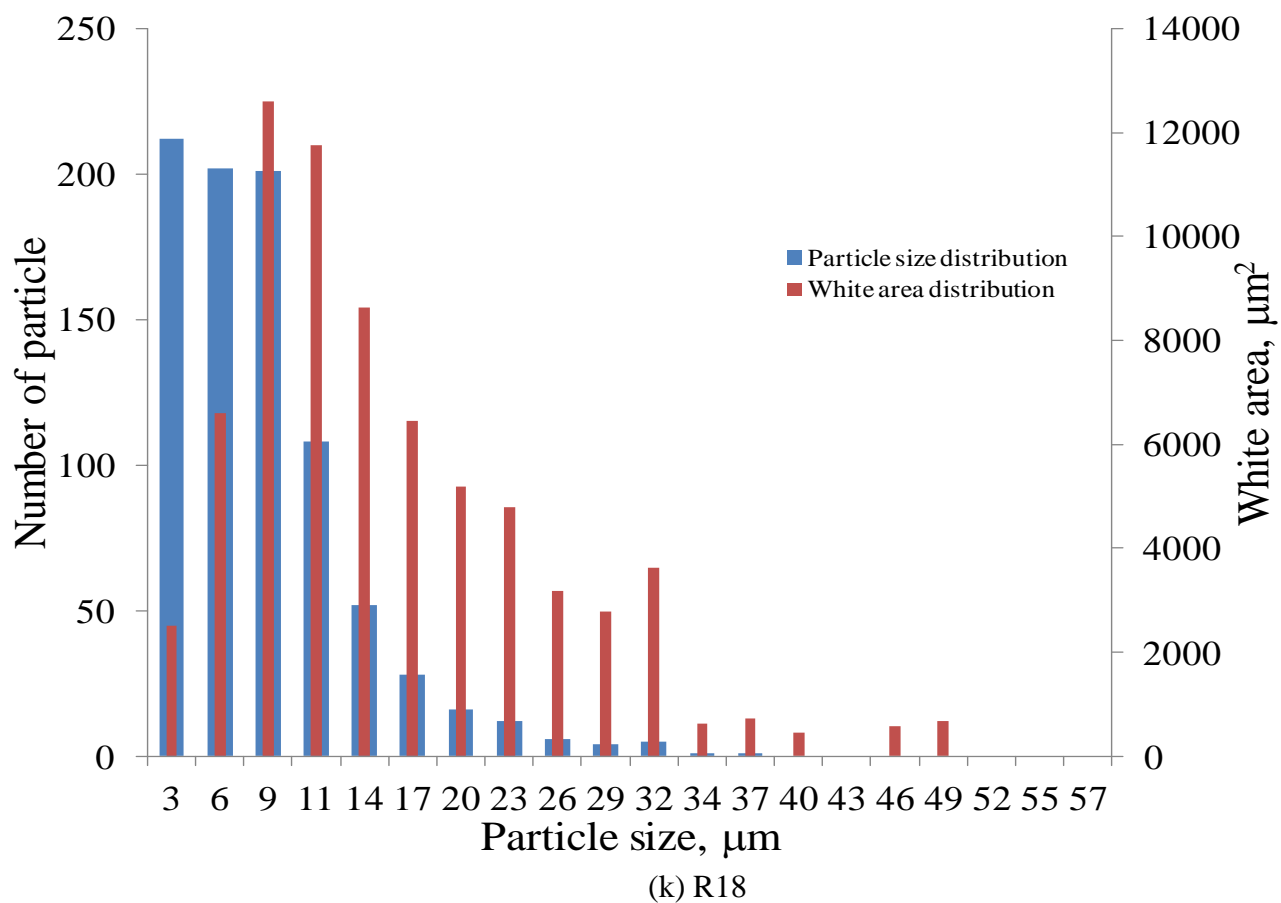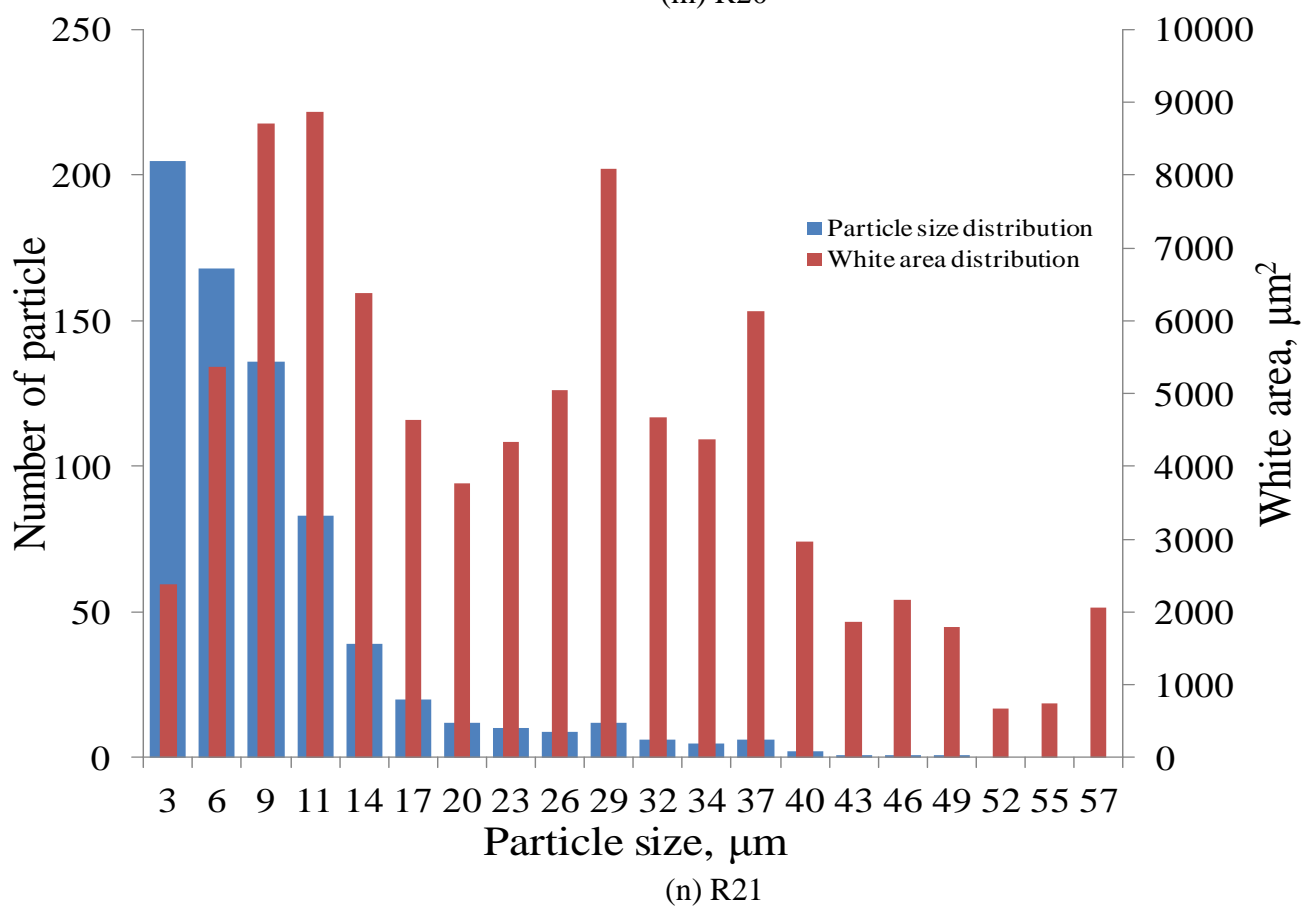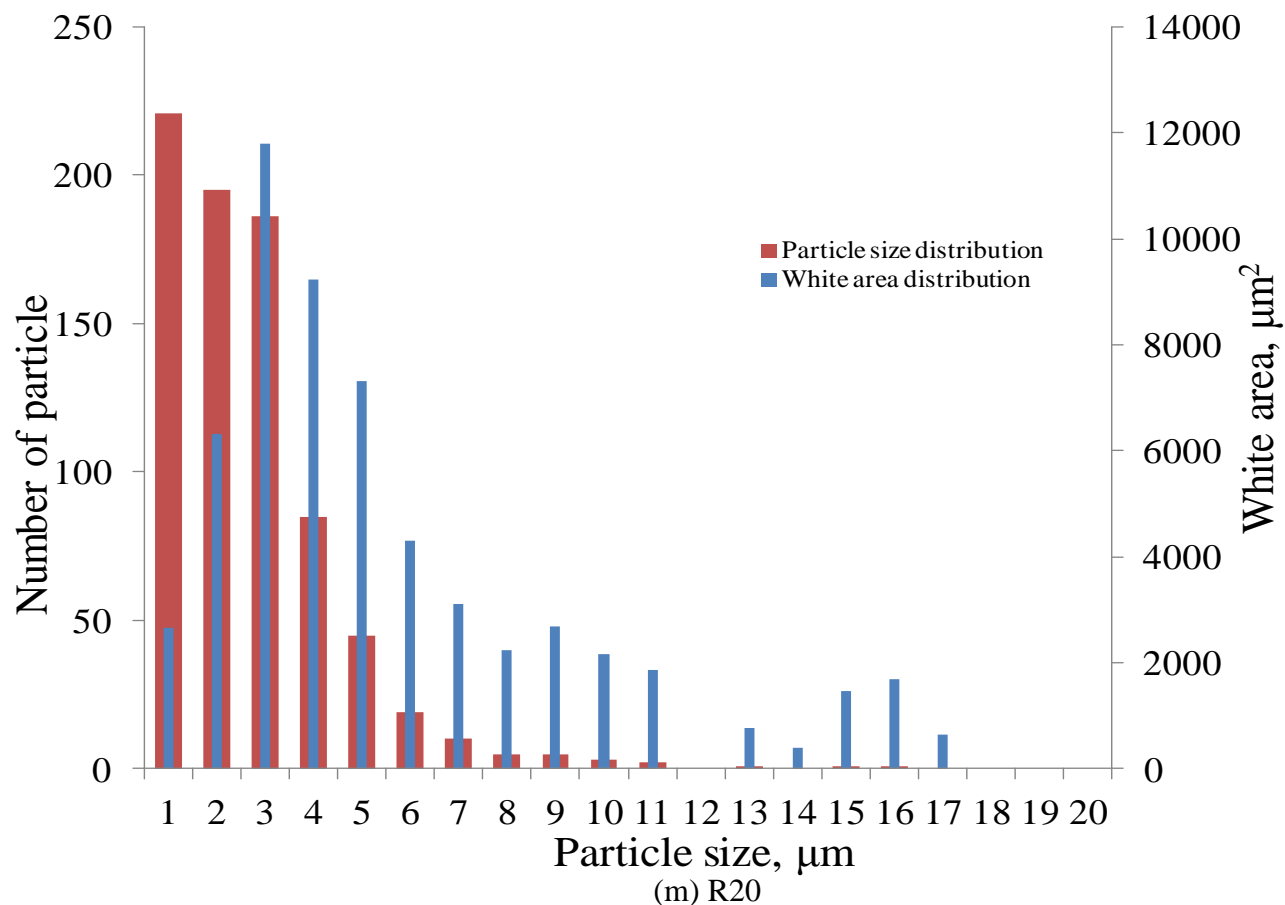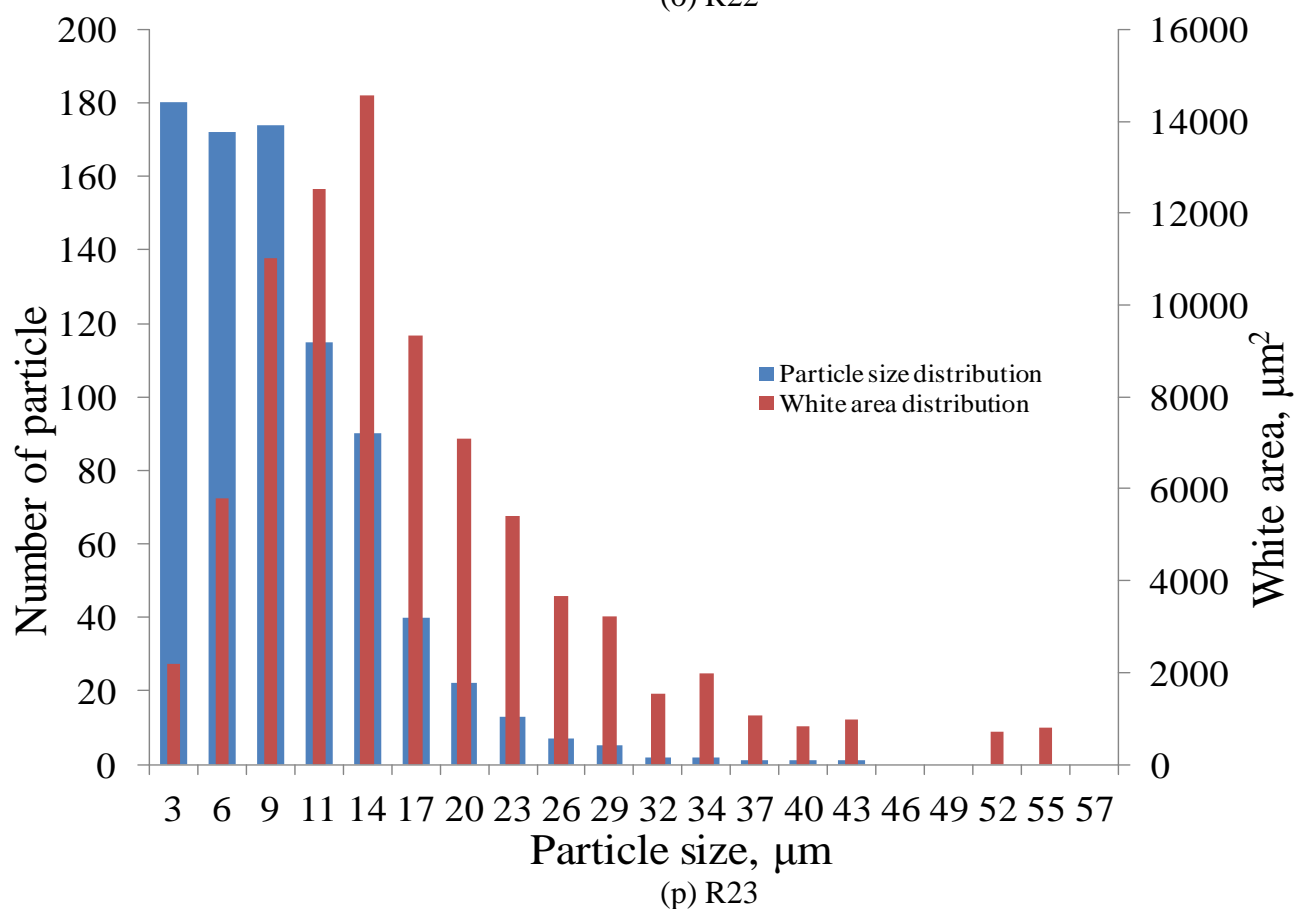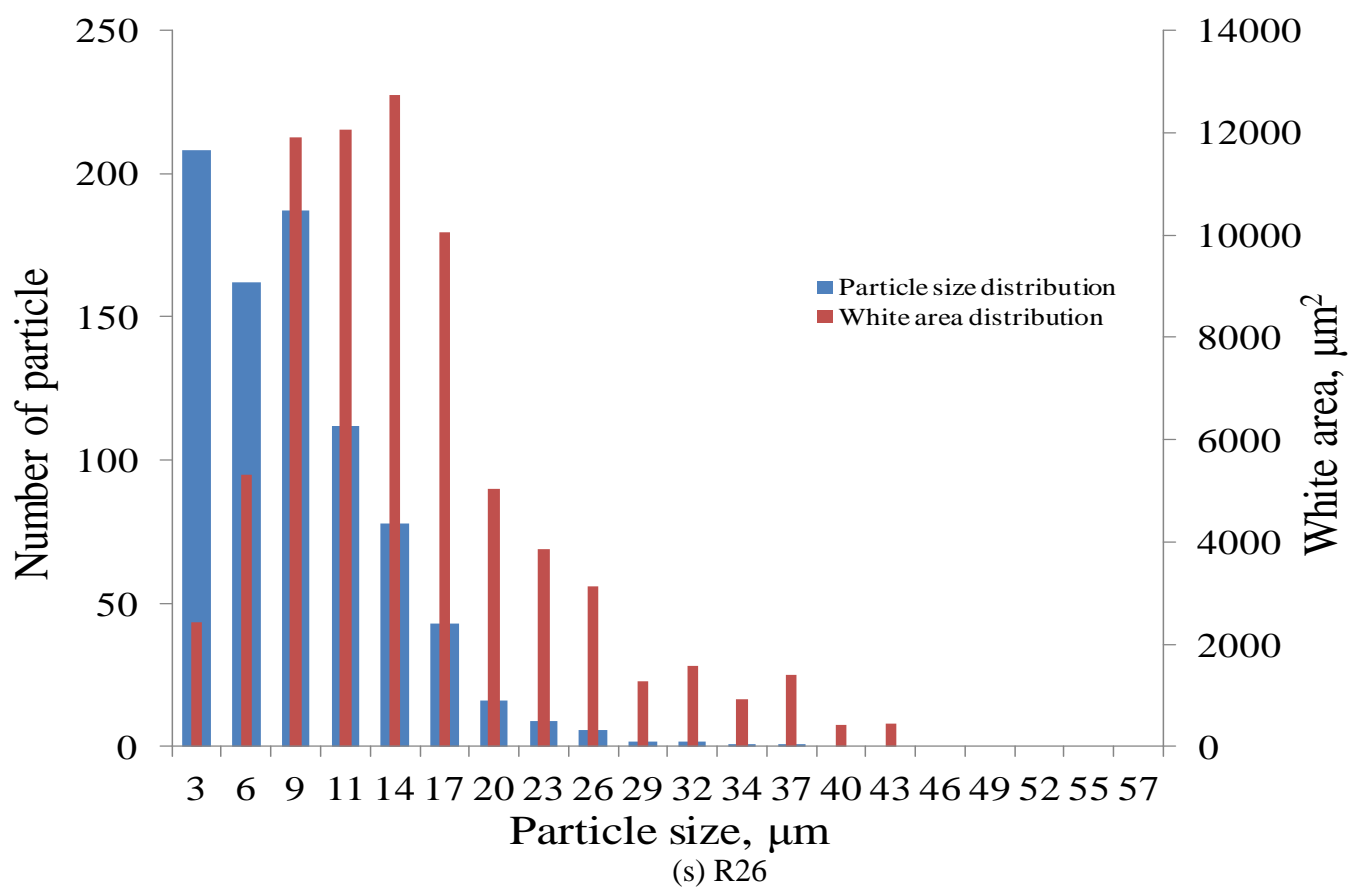
Figure D1: Results of agglomerates as a function of diameter of particle size in micron for EDS compounds. Area analysed $3.36 \times 10^6 \mu m^2$.

APPENDIX E

Explanation of the Reduced Modulus

The reduced modulus, E_r, is defined by the Oliver & Pharr (1982) in accordance with the equation:

$$\frac{1}{E_r} = \frac{(1-\nu^2)}{E} + \frac{(1-\nu_i^2)}{E_i} \,,$$

(1)

where E and ν are Young's modulus and Poisson's ratio for the specimen and E_i and ν_i are the corresponding parameter values for the indenter (the instrument used to asses material hardness).

A microhardness testing machine was used to obtain load-indentation, P, versus load displacement data. That is
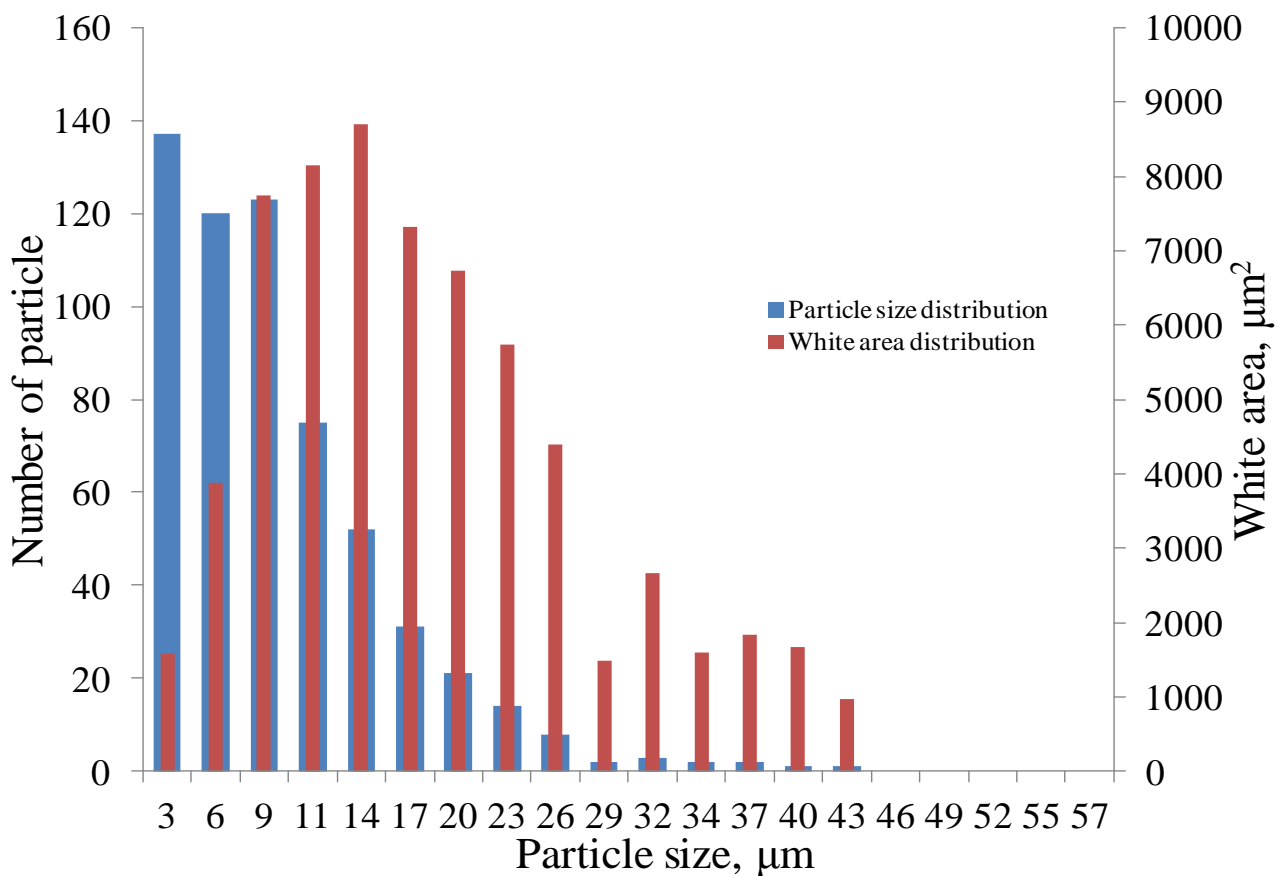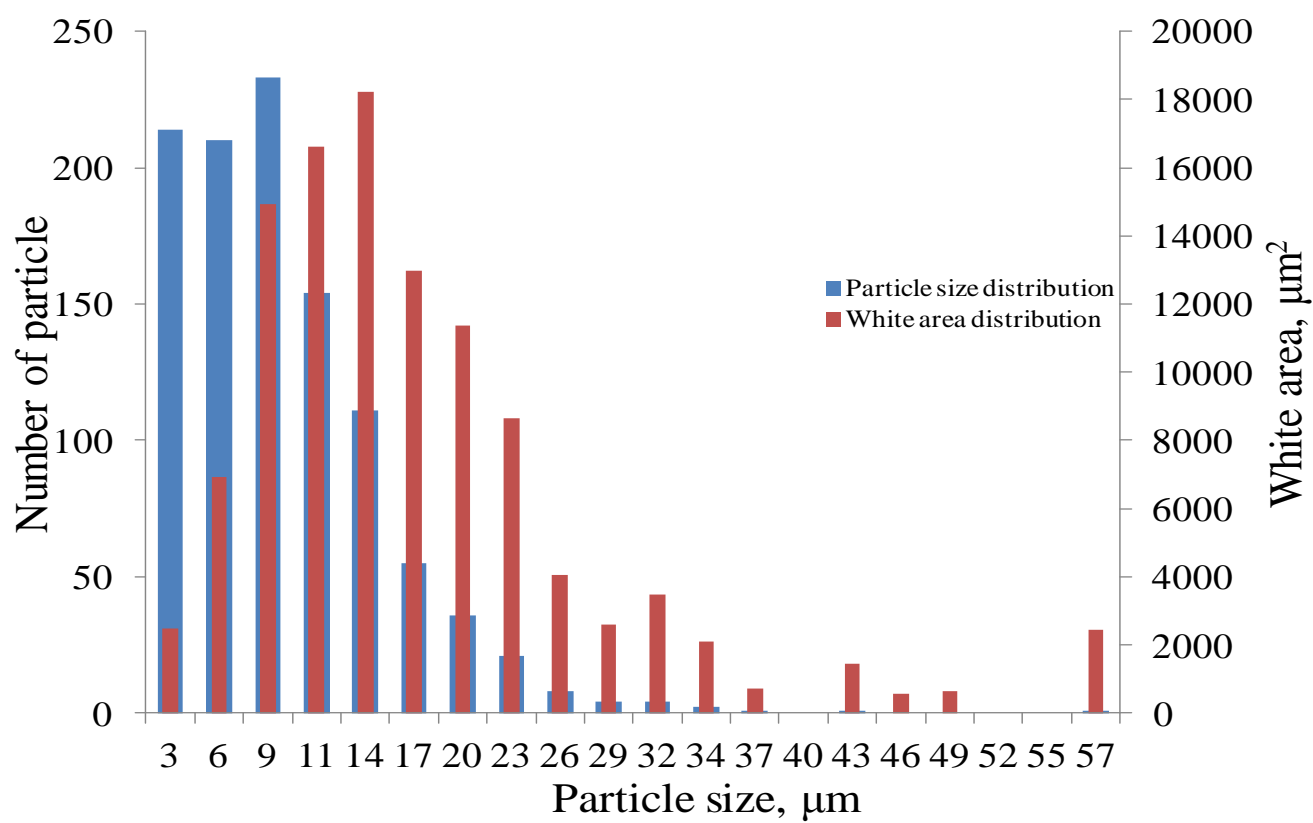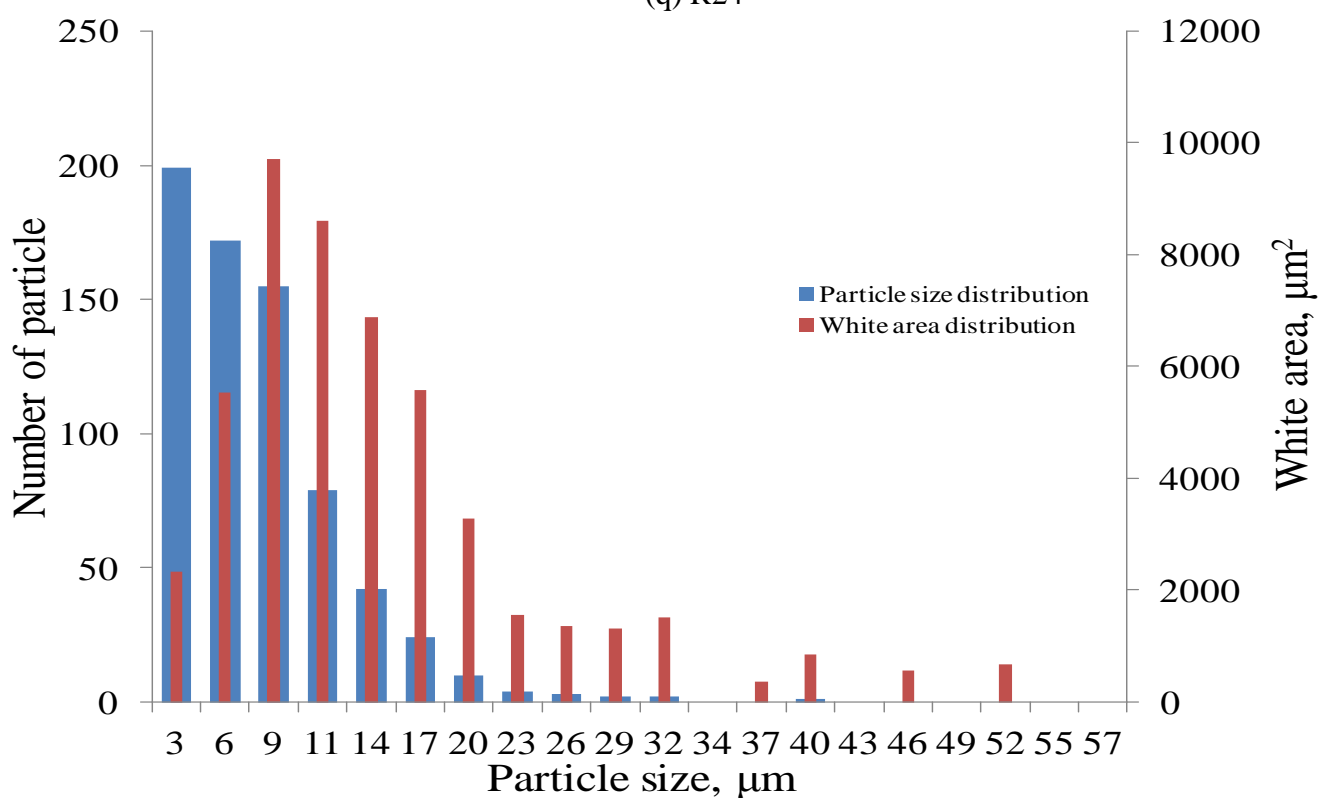
$$S = \frac{dP}{dh} = \frac{2}{\sqrt{\pi}} E_r \sqrt{A} \,,$$

(2)

with S corresponding to the experimentally measured stiffness of the upper portion of the unloading data recorded in Chapter 9, E_r is the reduced modulus and A is the projected area of the elastic contact. By measuring the initial unloading stiffness and assuming that the contact area is equal to the optically measured area of the hardness impression the modulus E_r is derived.

APPENDIX F

Explanation of Equation (9.1)

Kubelka (1948) and Munk (1931) developed equations for the absorption of light by particles embedded in a homogenous matrix, including effects of particle absorption and particle reflection. Although it is presumably possible to derive an equation for black particle (i.e. totally absorbent) as a limiting case from the Kubelka-Munk equations, the approach here is instead to derive the essence of such behaviour for first principle.

It is assumed that when the light passes through a representative thickness element of length L, as shown in Figure F1, the change in light intensity satisfies, $\Delta I = -f_A I$, where f_A is the opaque area fraction of black particles.

So over a sample thickness increment (>>L) Δx the drop in intensity ΔI is $\frac{\Delta x}{L} \cdot f_A I$ assuming the location of the opaque particles are not correlated for lengths greater than L. Thus

$$\Delta I = -\left(\frac{\Delta x}{L}\right) f_A I \tag{1}$$

or,

$$\frac{\Delta I}{\Delta x} = -\frac{f_A}{L} I \ . \tag{2}$$

From the Principle of Delesse, the volume fraction of black , φ, in the sample is the same as the fraction of cross sectional area occupied by black and hence $f_A = \varphi$. Thus

$$\frac{\Delta I}{\Delta x} = -\frac{\varphi}{L} I \ , \tag{3}$$

In the limit this yields

$$\frac{dI}{dx} = -\frac{\varphi}{L} I \tag{4}$$
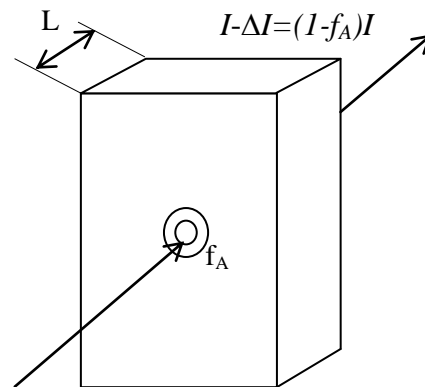
where, in summary, φ is the volume fraction of filler and L is a length scale over which the absorbing area in a section is not correlated with that of a subsequent section. It would be expected that L is of the order of the filler particle size.

APPENDIX G

Analytical Steady State Solution

The non-dimensional form of the diffusion Equation (9.10) (Cunliffe & Davis 1982) is

$$\frac{\partial \emptyset}{\partial T} = \frac{\partial^2 \emptyset}{\partial X^2} - \frac{\alpha \emptyset}{1 + \beta \emptyset}$$

where $\emptyset = \frac{c}{c_s}$, $T = \frac{Dt}{L^2}$, $X = \frac{x}{L}$, $\alpha = \frac{k_1 L^2}{D}$ and $\beta = k_2 c_2$ the subscript s denoting a value at the rubber surface.

The steady state case $\frac{\partial^2 \emptyset}{\partial X^2} - \frac{\alpha \phi}{1 + \beta \phi} = 0$ has an analytical solution if β=0 of the form

$$\emptyset = A e^{\sqrt{\alpha}X} + B e^{-\sqrt{\alpha}X} \tag{1}$$

as may readily be checked:

$$\frac{\partial \emptyset}{\partial X} = A\sqrt{\alpha}e^{\sqrt{\alpha}X} - B\sqrt{\alpha}e^{-\sqrt{\alpha}X} \quad \text{and} \tag{2}$$

$$\frac{\partial^2 \emptyset}{\partial X^2} = A\alpha e^{\sqrt{\alpha}X} - B\alpha e^{-\sqrt{\alpha}X} \tag{3}$$

$$\Rightarrow \frac{\partial^2 \emptyset}{\partial X^2} = \alpha \emptyset \tag{4}$$

To satisfy the boundary conditions $\frac{d\emptyset}{dX} = 0$ at $X = \frac{1}{2}$ and $\emptyset = 1$ at $X = 0$ we have:

$$0 = A e^{\frac{\sqrt{\alpha}}{2}} - B e^{\frac{-\sqrt{\alpha}}{2}} , \quad 1 = B + A .$$

Eliminating B from first equation using the second equation leads to

$$A = \frac{e^{\frac{-\sqrt{\alpha}}{2}}}{e^{\frac{\sqrt{\alpha}}{2}} - e^{\frac{-\sqrt{\alpha}}{2}}} = \frac{e^{\frac{-\sqrt{\alpha}}{2}}}{2\cosh\left(\frac{\sqrt{\alpha}}{2}\right)} \tag{5}$$

and hence

$$B = \frac{e^{\frac{\sqrt{\alpha}}{2}}}{2\cosh\left(\frac{\sqrt{\alpha}}{2}\right)} . \tag{6}$$

$$\emptyset = \left(\frac{e^{\frac{-\sqrt{\alpha}}{2}}}{2\cosh\left(\frac{\sqrt{\alpha}}{2}\right)} \right) e^{\sqrt{\alpha}X} + \left(\frac{e^{\frac{\sqrt{\alpha}}{2}}}{2\cosh\left(\frac{\sqrt{\alpha}}{2}\right)} \right) e^{-\sqrt{\alpha}X}$$

$$= \frac{e^{\sqrt{\alpha}\left(X - \frac{1}{2}\right)} + e^{-\sqrt{\alpha}\left(X + \frac{1}{2}\right)}}{2\cosh\left(\frac{\sqrt{\alpha}}{2}\right)} = \frac{\cosh\left(\sqrt{\alpha}\left(X - \frac{1}{2}\right)\right)}{\cosh\left(\frac{\sqrt{\alpha}}{2}\right)} \tag{7}$$

APPENDIX H

Layout of New Fatigue Testing Machine

This appendix, related to Chapter 7, provides annotated representation of the testing machine layout.

Position of roller eccentric used to adjust throw ②

Adjustable clamp ①
Used to locate top end of specimen in correct position with the required mean or maximum level strain

Carriage driven vertically as eccentric bearing on arm goes through each full circle

Fixed clamp
Used to fix bottom end of specimen block

Carriage$_{top}$

Cam fixed eccentrically on slides roller eccentric in this slot to drive vertical motion of the carriage.

Fixed clamp
Used to fix top end of specimen block

Carriage$_{bottom}$

Adjustable clamp
Used to locate bottom end of specimen in correct position with the required mean or maximum level strain
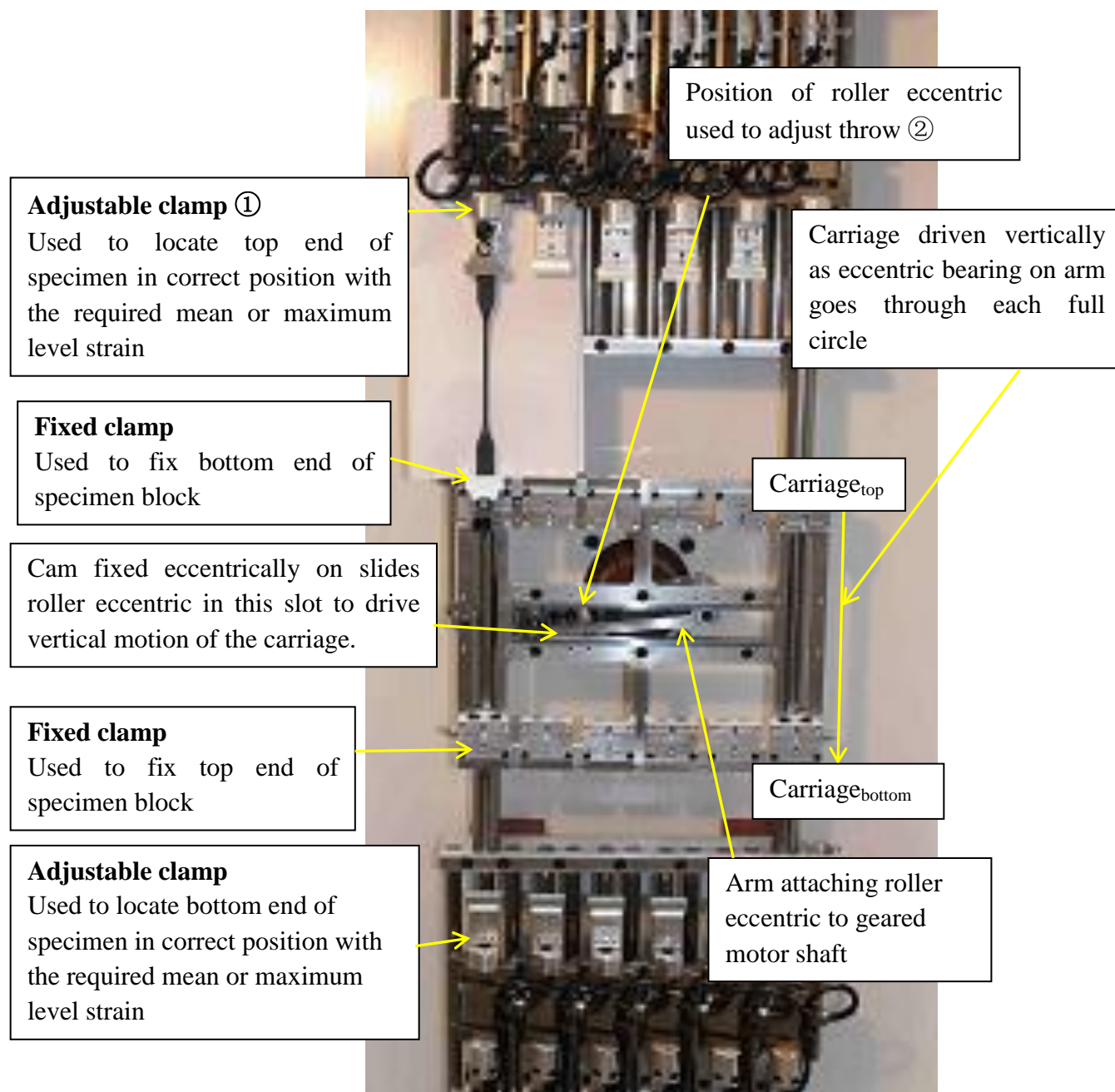
Arm attaching roller eccentric to geared motor shaft

Figure H1: New fatigue test machine layout.

Note:
Caption mean of adjustment to achieve.
① mean strain and ② strain range.

APPENDIX I

MATLAB Program – Diffusion Limited Oxidation

Chapter 9 looked at prediction of transient behaviour of oxygen concentration and absorption. The programme developed to undertaken related analysis is listed here. Explicit finite difference techniques impose a restriction on both the time and length interval used in solving the diffusion equation and so to remove this stability requirement the implicit Crank-Nicolson method (Crank & Nicolson 1947) is used.

```
%uniaxial DLO first order reaction using Crank-Nicolson
L=80;
% L is the total thickness of the slab in mm
NL=100;
%NL is no. of steps, so no. of grid points = NL+1
dx=L/NL;
D=7.7*10^-5;
%D is the diffusion coefficient in mm^2/s when M=0
N=4;
ZETA=10^-N*3.1536*10^7*(2*D)/dx^2;
%N is an integer chosen to ensure ZETA<1; 3.1536*10^7s =1year
dt=ZETA*(dx)^2/(2*D);
%dt (in seconds) is factored by ZETA to be eqivalent to 10^-N year and
%avoid oscillation (dt < (L/NL)^2/(2*D))
DELTAt=dt/(3.1536*10^7);
%DELTAt is the time incremenet expressed in years, and will be 10^-N year
NT=60000;
Cs=1;
% Cs is the surface concentration; assumed constant and same on both sides
k=-0.00000012;
% k is rate of first order reaction in s^-1; k falls to zero when M = Mmax
a=(dt*D)/(2*dx^2);
b=(k*dx^2)/D;
B=zeros(NL+1,NL+1);
A=zeros(NL+1,NL+1);
for j=1:NL+1
    if j==1||j==NL+1;
        A(j,j)=1;
        B(j,j)=1;
    else
        A(j,j-1)=-a;
        B(j,j-1)=a;
        A(j,j)=1+(2-b)*a;
        B(j,j)=1-(2-b)*a;
        A(j,j+1)=-a;
        B(j,j+1)=a;
    end
end
C=zeros(NL+1,NT+1);
```

```
for j=1:NT+1
   C(1,j)=Cs;
   C(NL+1,j)=Cs;
end
F=inv(A)*B;
C(:,2)=F*C(:,1);
M=zeros(NL+1,NT+1);
M(:,2)=-dt*k*C(:,1);
% M is amount reacted
%boundary conditions now set; next,  iterate with a,b,k updates

DN = zeros(NL+1,NT+1);
DN(:,1)=D;
kN=zeros(NL+1,NT+1);
kN(:,1)=k;
%DN, kN columns give spatial distribution of D, k=r/c after updates
%need rule for later columns of DN in terms of M, kN in terms of M,C
for i=2:NT+1
   DN(:,i) = D;
   k2=10;
   kN(:,i)=k./(1+k2*C(:,i));
   for j=1:NL+1
      if j==1||j==NL+1
      aN(j)=dt*D/(2*dx^2); %#ok<AGROW>
      else
         aN(j)=dt.*(DN(j+1,i)/4 + DN(j,i)-DN(j-1,i)/4)/(2*dx^2); %#ok<AGROW>
         zN(j)=dt.*(2*DN(j,i)-kN(j,i)*dx^2)/(2*dx^2); %#ok<AGROW>
      A(j,j-1)=-aN(j);
      B(j,j-1)=aN(j);
      A(j,j)=1+zN(j);
      B(j,j)=1-zN(j);
      A(j,j+1)=-aN(j);
      B(j,j+1)=+aN(j);
      end
   end
   F=inv(A)*B;
   C(:,i+1)=F*C(:,i);
   M(:,i+1)=-dt*kN(:,i).*(C(:,i)+C(:,i+1))/2 +M(:,i);
end

CR=zeros(NL+1,NT/100+1);
CR(:,1)=C(:,1);
MR=zeros(NL+1,NT/100+1);
MR(:,1)=M(:,1);

for s=1:NT/1000
   CR(:,s+1)=C(:,1000*s+1);
   MR(:,s+1)=M(:,1000*s+1);
end
% CR and MR provide an adequate subset of output for plotting
```

APPENDIX J

FEA Investigation of Stress Distribution in

Dumb-bell Test Pieces with Different Strains

In the experiments reported close to the "neck" or transition from the parallel region to the tab. In this appendix, numerical analyses using Finite Element Analysis (FEA) has been applied to determine the stress distribution in a dumb-bell test piece. Our objective is to identify the location and magnitude of any local maximum stress, and whether it might correlate with frequent sites of failure initiation.

Analysis Procedures

Dumb-bell test pieces types 1, 1A and 2 were modelled in 2D plane stress, using FEA-ABAQUS version 6.9 as a CAE preprocessor and solver to carry out several uniaxial tension simulations. Dimensions of each dumb-bell type are specified in BS ISO 6943:2007 and in BS ISO 37:2005. Figures J1, J2 and J3 show respectively one quarter of each dumb-bell test piece. Geometric symmetry is used to minimize the time of analysis.
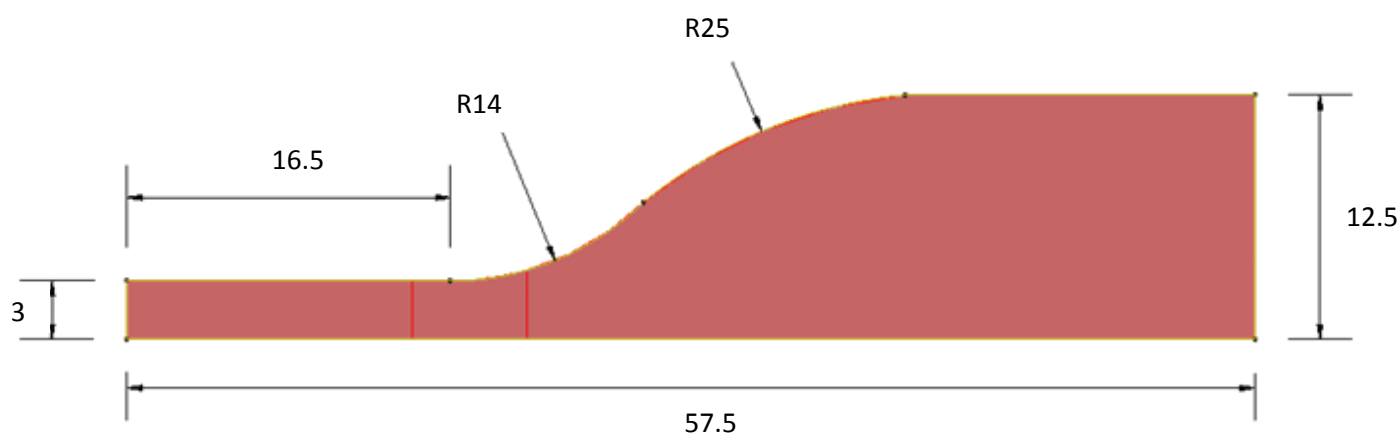

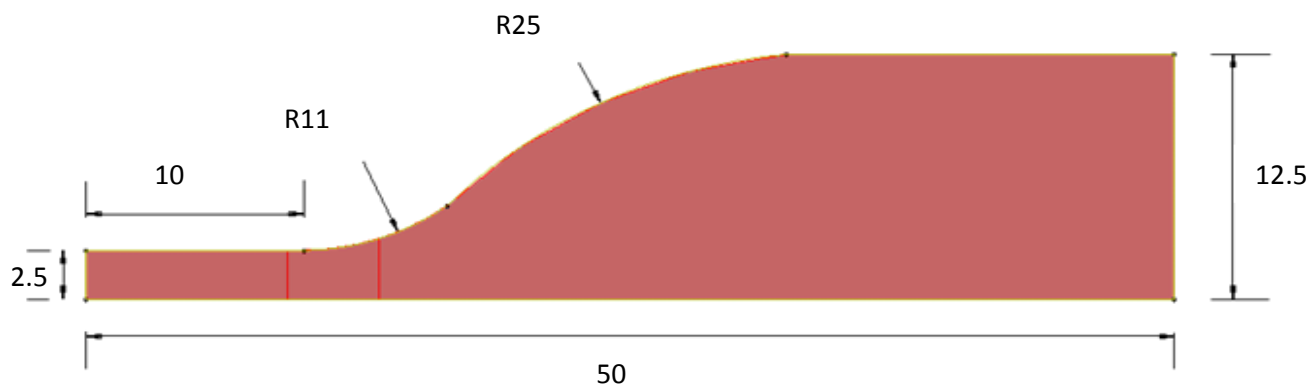Figure J1: Dimension (mm) of dumb-bell type 1 [BS ISO 6943:2007 & BS ISO 37:2005].

R25

R11

10

2.5

12.5

50

Figure J2: Dimension (mm) of dumb-bell type 1A [BS ISO 6943:2007 & BS ISO 37:2005].
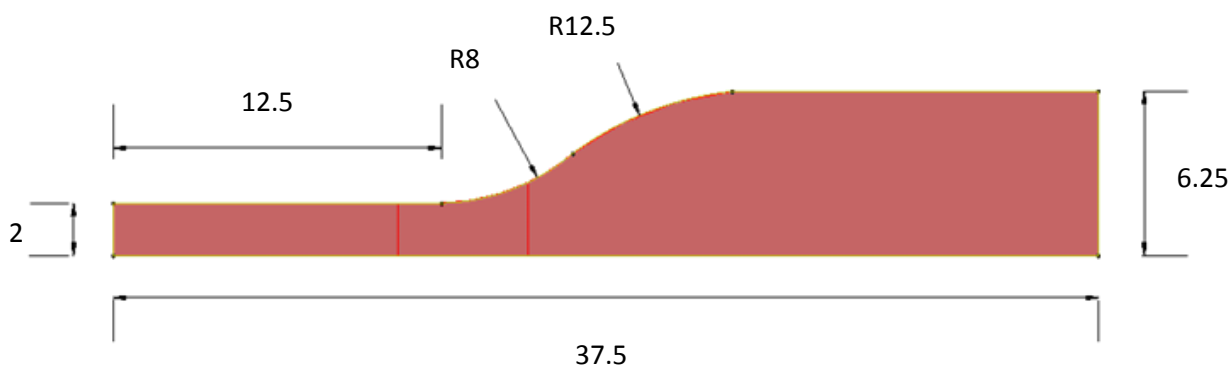
R12.5

R8

12.5

2

6.25

37.5

Figure J3: Dimension (mm) of dumb-bell type 2 [BS ISO 6943:2007 & BS ISO].

Plane stress was appropriate because the thickness is very small compared to the length and width. The material was modelled as a hyperelastic rubber with a neo-Hookean strain energy function. The shear modulus was 1MPa and the bulk modulus was 2000MPa. A number of simulations of a tension test were carried out at different maximum displacements (each corresponding to a specific value of strain). Constraints prevented any movement perpendicular to the planes of symmetry, shown as the red dashed lines in Figure J4. These boundary conditions were applied to the three described dumb-bells. All degrees of freedom of nodes along the test piece end (green line) were coupled with the corner node (N1). The black arrow indicates the direction of displacement. A path (Path line) was created by selecting nodes closed to the edge of the curvature side of each dumb-bell. These nodes were analyzed to evaluate the stress distributions at the curved side. The reaction force and displacement were collected at the coupled node (N1).
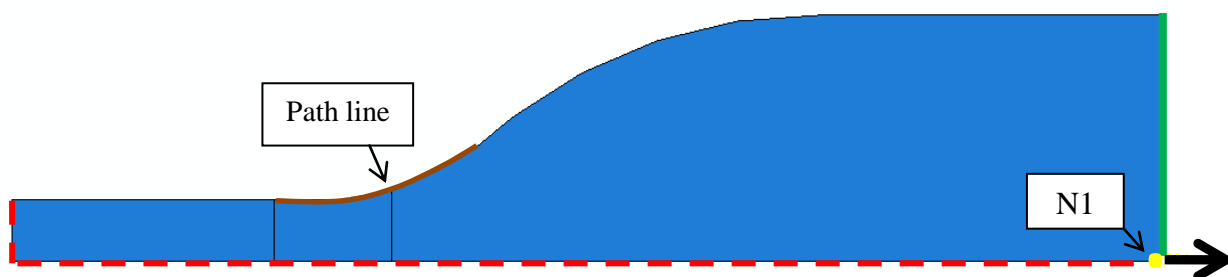
Figure J4: Example of boundary conditions for model of dumb-bell type 1. − − − lines of symmetry; black arrow, imposed displacement; node N1 – coupled to remaining nodes on tab end; force and displacement monitored.

Eight different displacements in uniaxial tension were simulated. The total force and displacement were calculated based on the symmetry of the model. Three partitions were made on the dumb-bell to properly mesh it. All Cauchy stresses and displacements at the narrow region of the dumb-bell test piece were obtained from ABAQUS software. Thereafter strains in the parallel section were calculated using Microsoft Excel software.

Two different densities of element were modelled for each dumb-bell type to investigate results consistency. Figure J5(a) to (f) show the different finite elements distributions and two paths of nodes were made using the ABAQUS software.
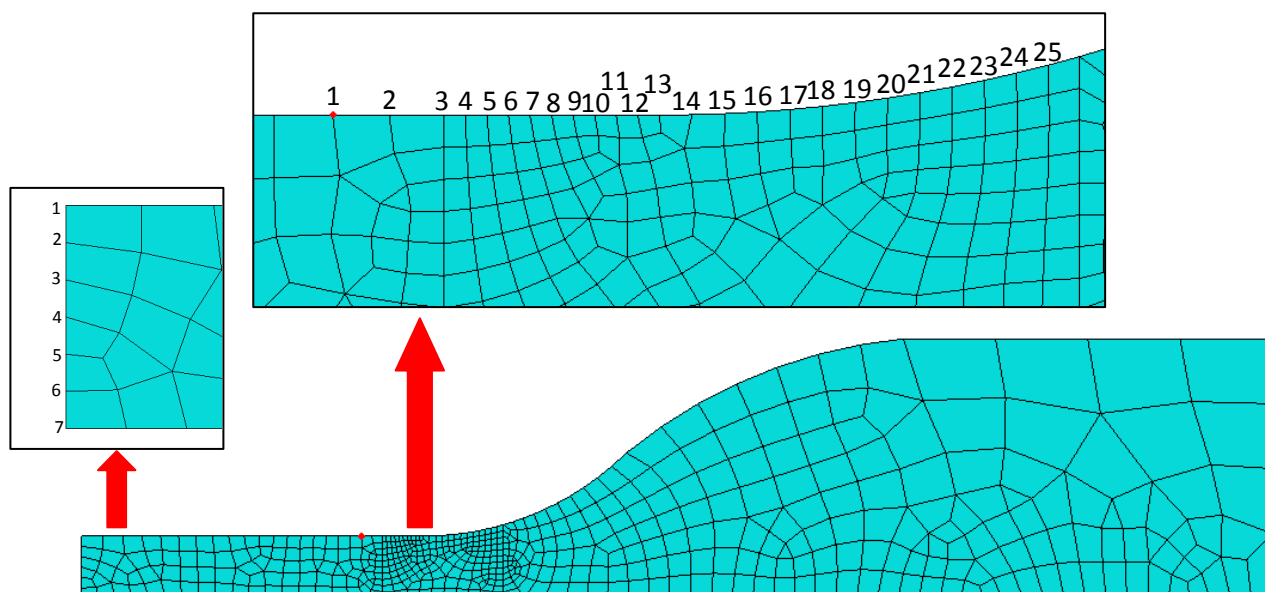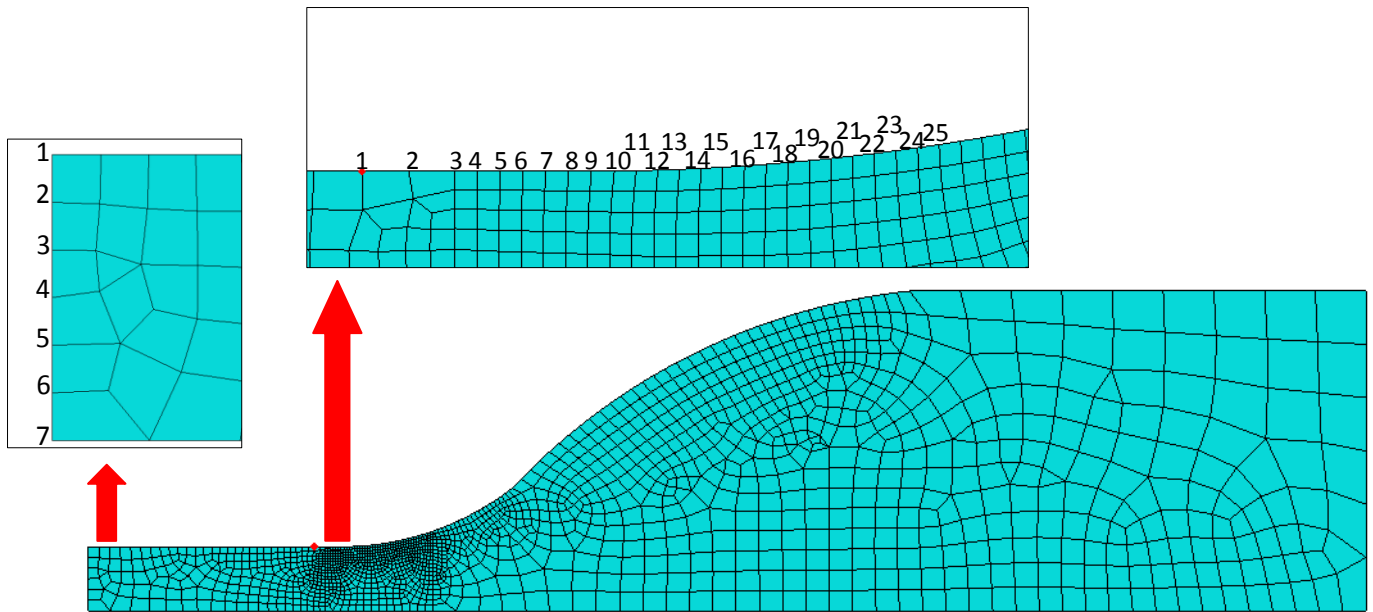

(a) Dumb-bell type 1 with 482 elements.
Path No.1-7 and Path No.1-25 are the selected nodes to determine true stresses.
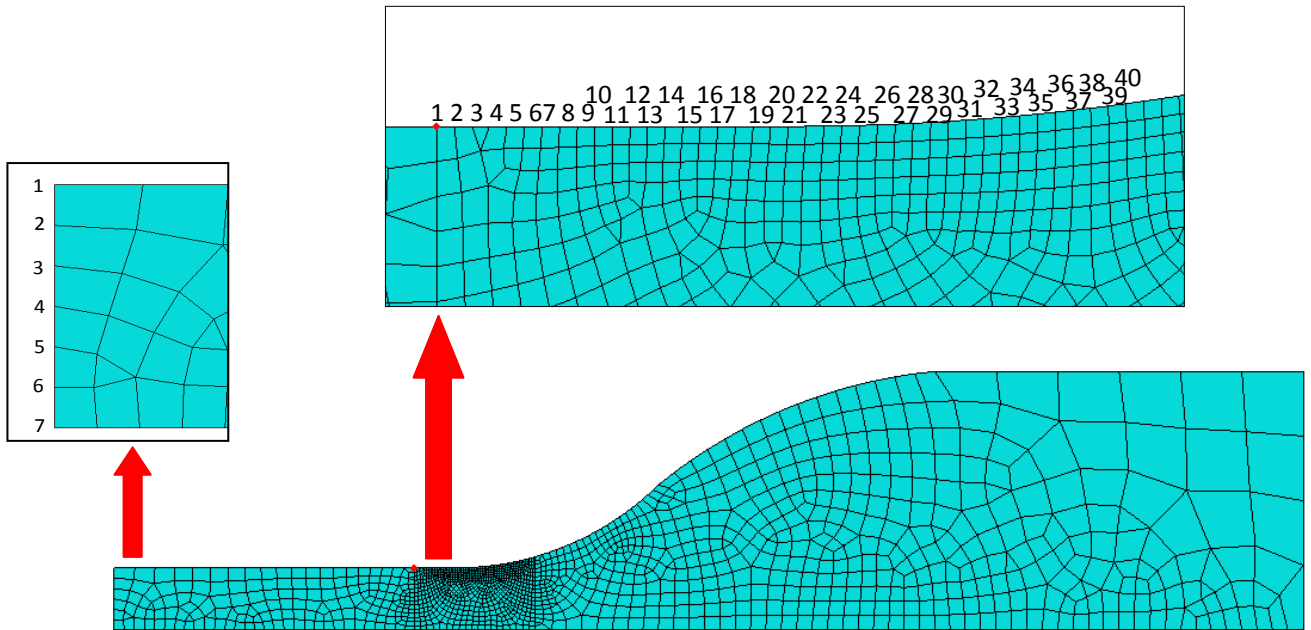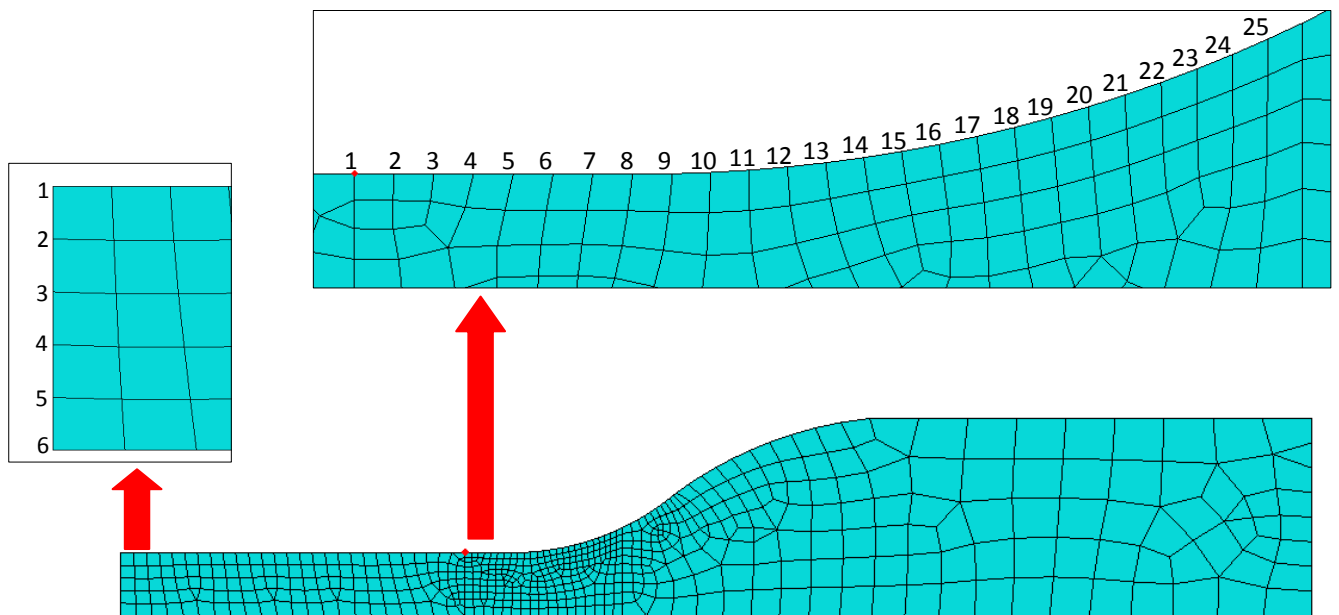
(b) Dumb-bell type 1 with 1400 elements.
Path No.1-7 and Path No.1-40 are the selected nodes to determine the stresses.
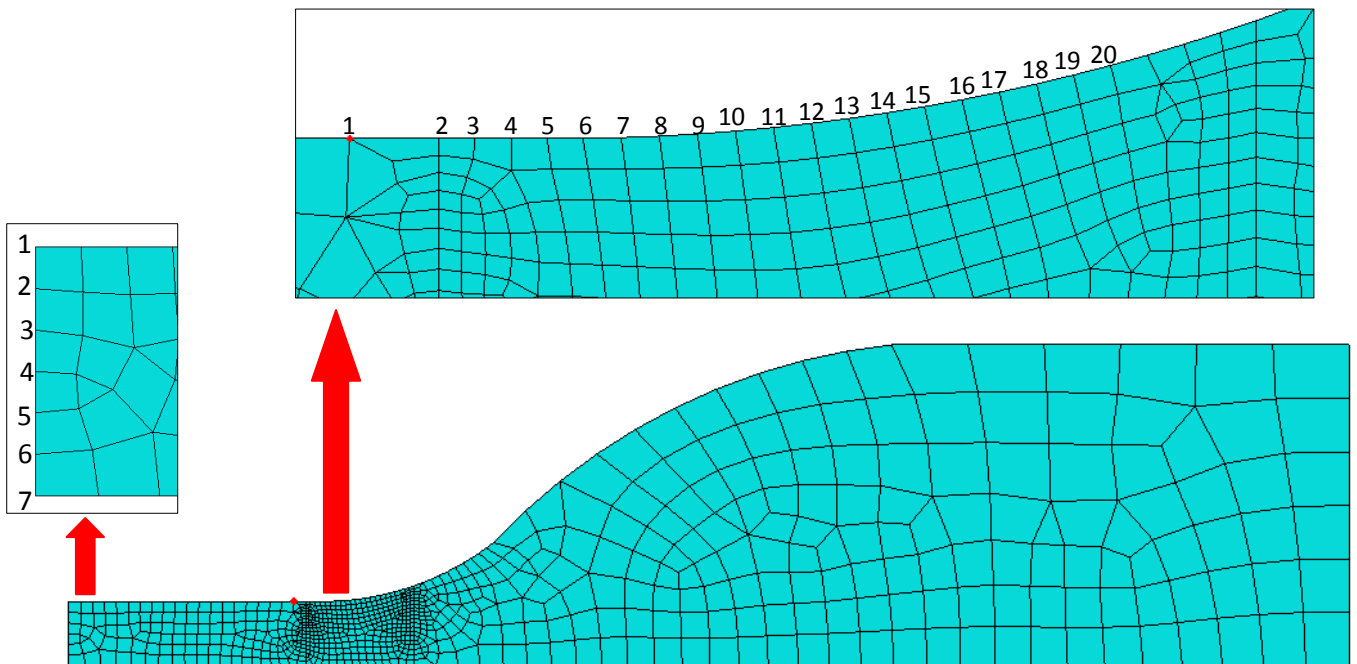
(c) Dumb-bell type 1A with 744 elements.
Path No.1-7 and Path No.1-20 are the selected nodes to determine the stresses.
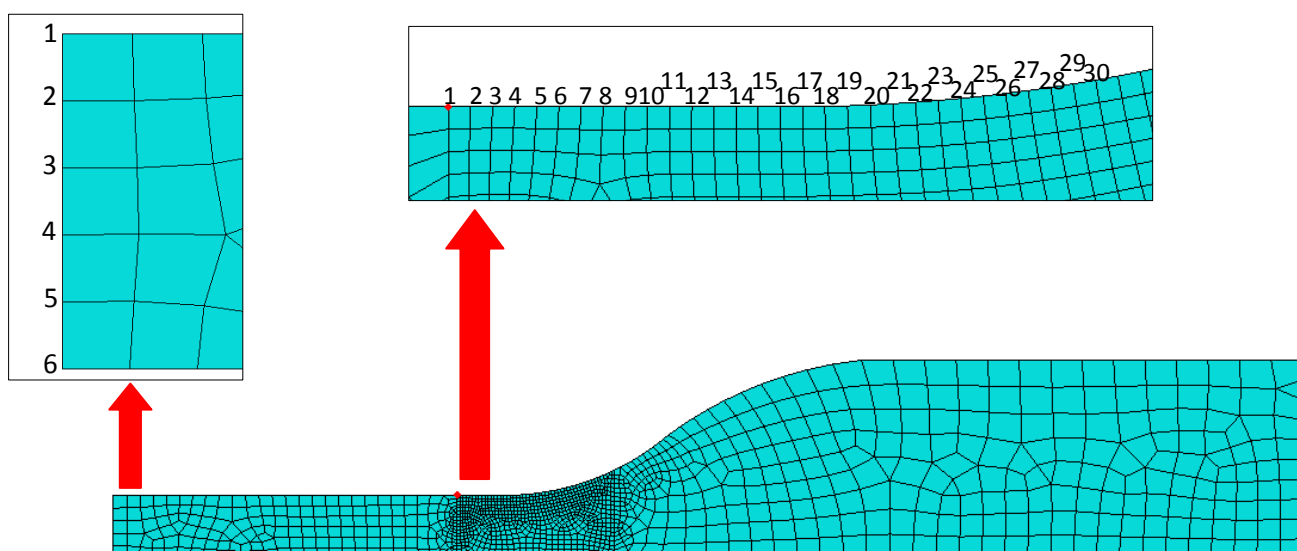
(d) Dumb-bell type 1A with 1555 elements.
Path No.1-7 and Path No.1-25 are the selected nodes to determine the stresses.

(e) Dumb-bell type 2 with 532 elements.
Path No.1-6 and Path No.1-25 are the selected nodes to determine the stresses.

(f) Dumb-bell type 2 with 1260 elements.
Path No.1-6 and Path No.1-30 are the selected nodes to determine the stresses.

Figure J5: Overall views of mesh for each model.

According to BS ISO 37:2005 Appendix C.4, there is a stress concentration associated with the transition from the narrow parallel-sided portion to the tab. The mesh was made fine in this region in an attempt to quantify the maximum local stress in the area of stress concentration. The ratio of highest local principal Cauchy stress to the value at the centre of the parallel-sided portion of the test piece was determined.

Analysis Results

Nominal stress was calculated by dividing the force obtained by the undeformed cross section area for the middle part of the dumb-bell for each of the dumb-bell types 1, 1A and 2. In contrast, the true stress was calculated by dividing the force by the strained cross section area. Figures J6, J7 and J8 provide the true and nominal stresses as a function of strain. All the values of force were obtained from the node point N1 indicated in Figure J4.

Figure J6: Value of nominal and true stresses in the parallel section as a function of strain in the parallel portion of dumb-bell type 1 for different density of element.
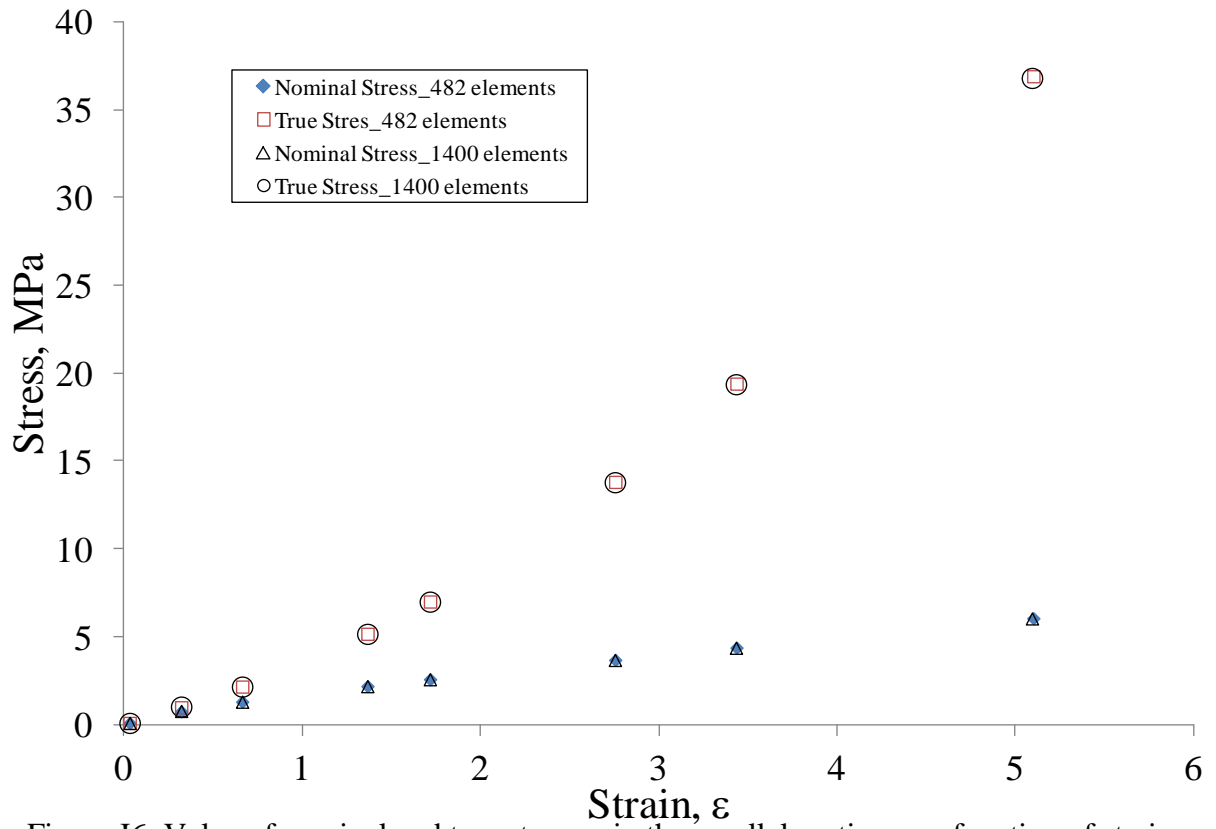

Figure J7: Values of nominal and true stresses in the parallel section as a function of strain in the parallel portion of dumb-bell type 1A for different density of element.
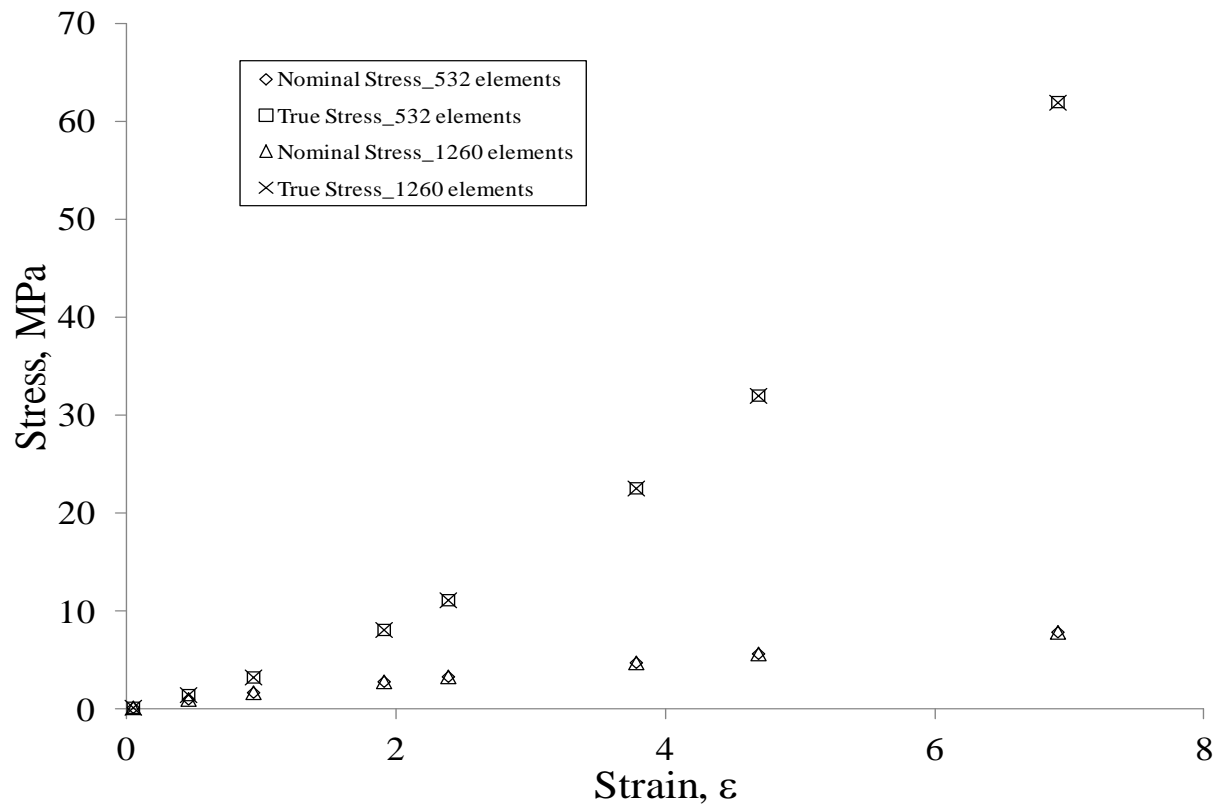
Figure J8: Values of nominal and true stresses in the parallel section as a function of strain in the parallel portion of dumb-bell type 2 for different density of element.
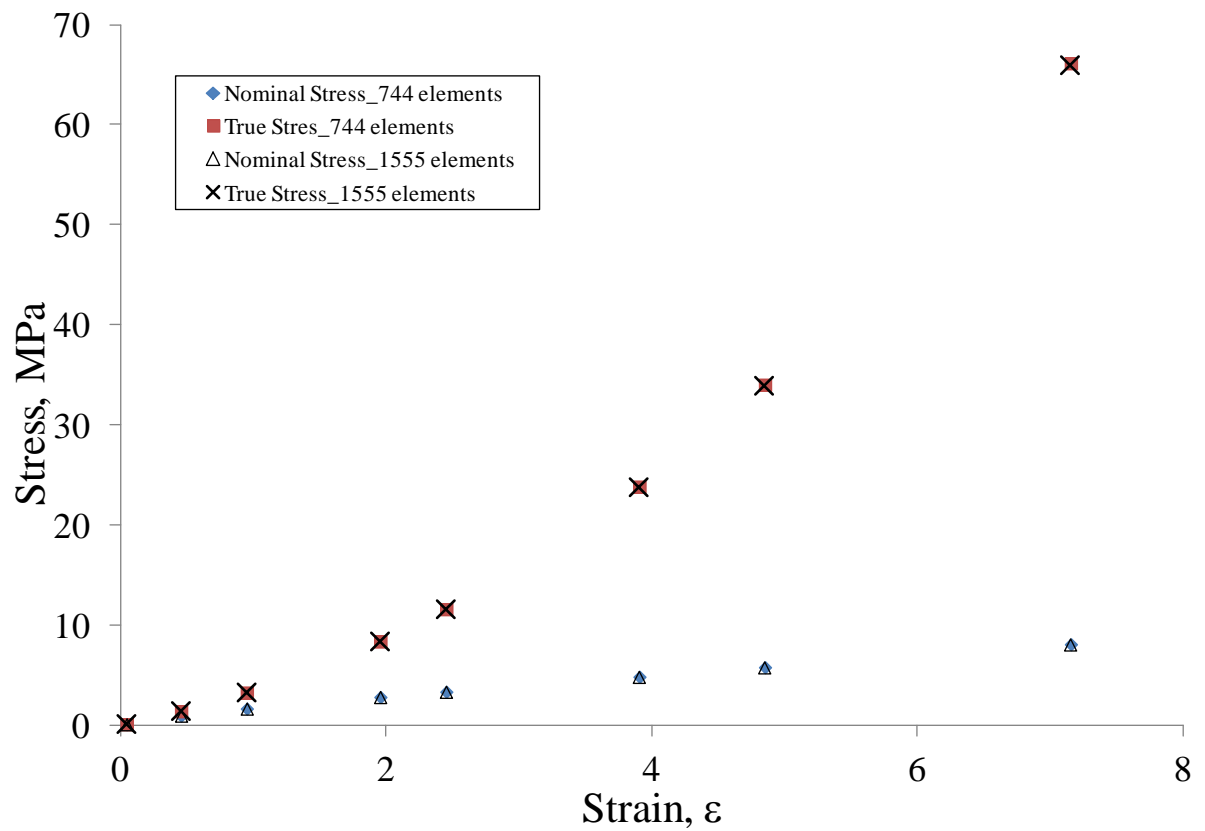
Different densities of element for dumb-bell types 1, 1A and 2 showed little difference of stress versus strain. Figure J9 provides plot contours of the undeformed shape of dumb-bell type 1 for different strains.

Figure J9: Maximum principal stress distribution for dumb-bell type 1 at the curved side for a range of strain on undeformed shape (given in label).

Different colours in a caption for each figure indicate different ranges of maximum principal stress. It was confirmed that the maximum principal stresses were higher near to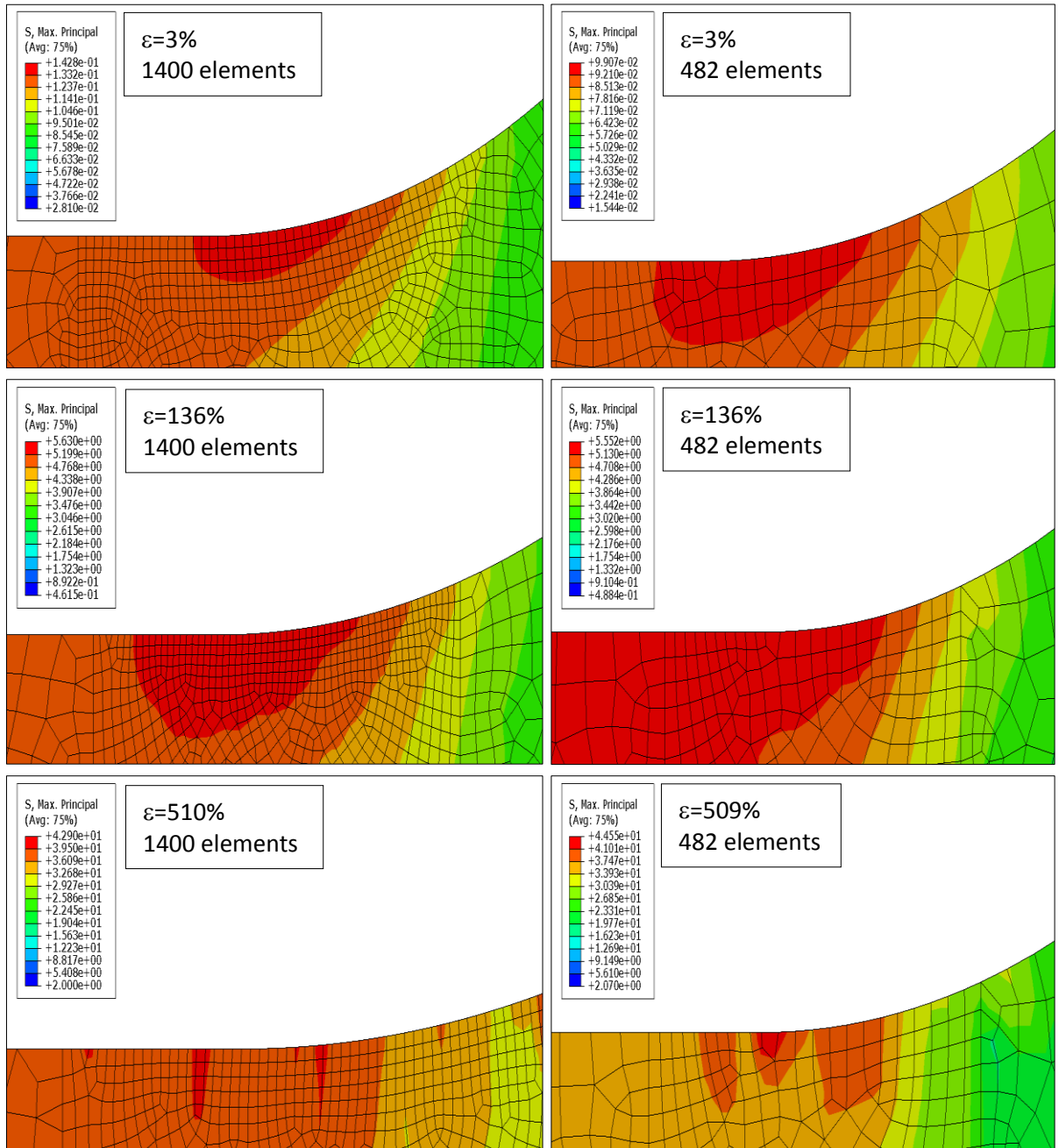 the curved side of the dumb-bell rather than for the narrow parallel-sided portion. Two or three areas were predicted to be subjected to high local stresses when the dumb-bell was stretched to a high strain; at low strains only one area near to the onset of curvature is apparent in Figure J9. These results suggest that failure would tend to initiate at the onset of the curved side of the dumb-bell. Predictions indicate that different element distributions do not affect the failure location. Tables J1 and J2 provide stress levels as a function of strain for two distinct density of element for dumb-bell type 1.

Table J1: Dumb-bell type 1 analysis results of true stress and the ratio for 482 elements.

Strain, %	True stress in the parallel section of dumb-bell, MPa	Max. true stress at the curved side, MPa	Ratio
3	0.09	0.10	1.09
32	0.98	1.06	1.08
66	2.16	2.31	1.07
136	5.16	5.55	1.08
172	6.99	7.56	1.08
276	13.77	15.13	1.10
344	19.34	21.51	1.11
510	36.64	44.55	1.22

Table J2: Dumb-bell type 1 analysis results of true stress and the ratio for 1400 elements.

Strain, %	True stress in the parallel section of dumb-bell, MPa	Max. true stress at the curved side, MPa	Ratio
3	0.09	0.10	1.10
32	0.98	1.07	1.09
66	2.16	2.35	1.09
136	5.15	5.63	1.09
172	6.98	7.64	1.09
275	13.75	15.17	1.10
343	19.30	21.40	1.11
509	36.58	40.80	1.12

The average ratio of maximum true stress and true stress in the middle part of the dumb-bell for 482 elements and 1400 elements was 1.10 in each case comparison of stresses in

Tables J1 and J2 shows good agreement, except for the highest strain, suggesting that further mesh refinement would not significantly influence the conclusions.

Figures J10 and J11 indicate the variation of true stress on the curved side of dumb-bell type 1 as a function of node position within the high stress region. True stress values were consistent at low strain but became inconsistent at high strain. More than one peak in stress can be observed when the strain increases beyond 275%. This is thought to indicate a problem with the discretisation, since it does not seem to be in accord with the smooth shape of the testpiece.
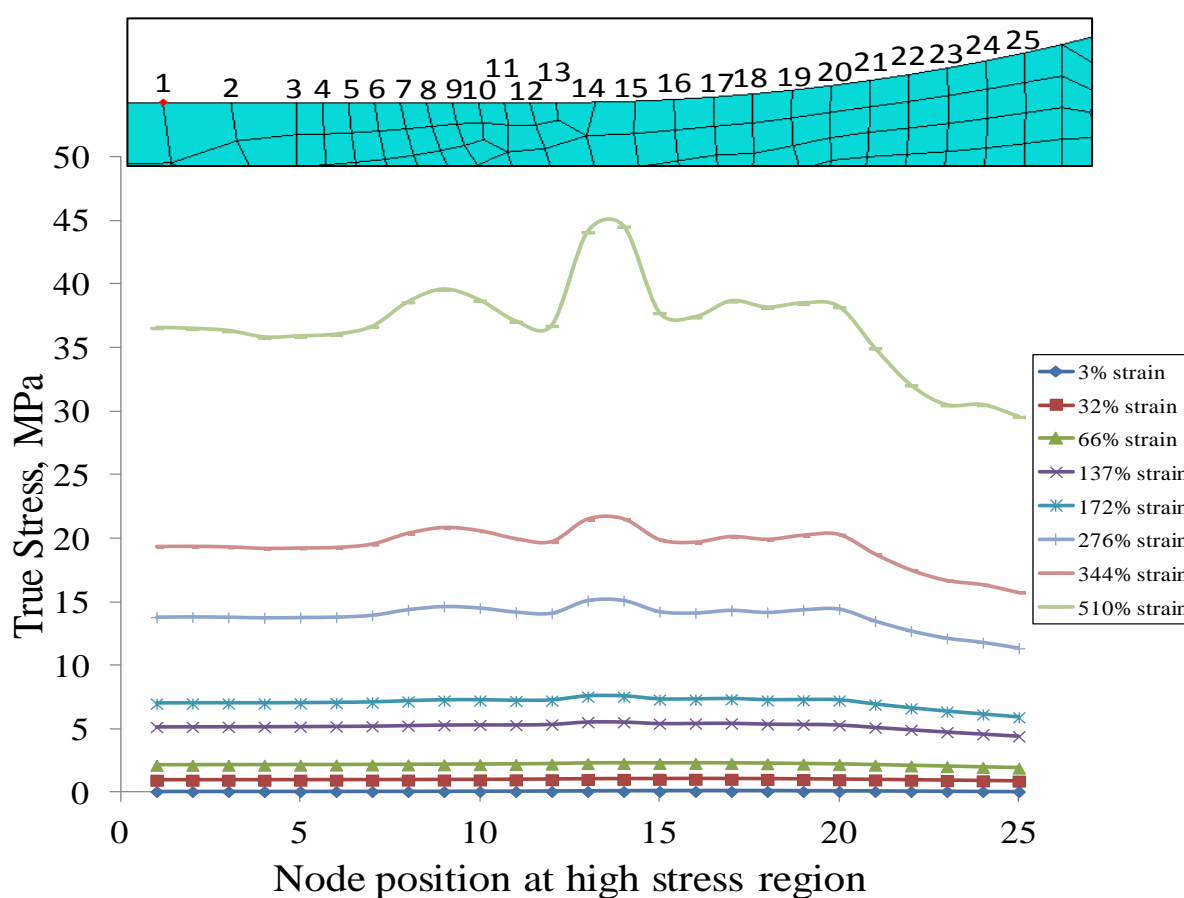

Figure J10: True stress as a function of node position for dumb-bell type 1
(482 elements).

In the finer mesh model the stresses fluctuated slightly at a strain of 343% and was obvious at a strain of 509%. In contrast, the stresses varied smoothly with a single local extremum over the strain range of 3~172%.
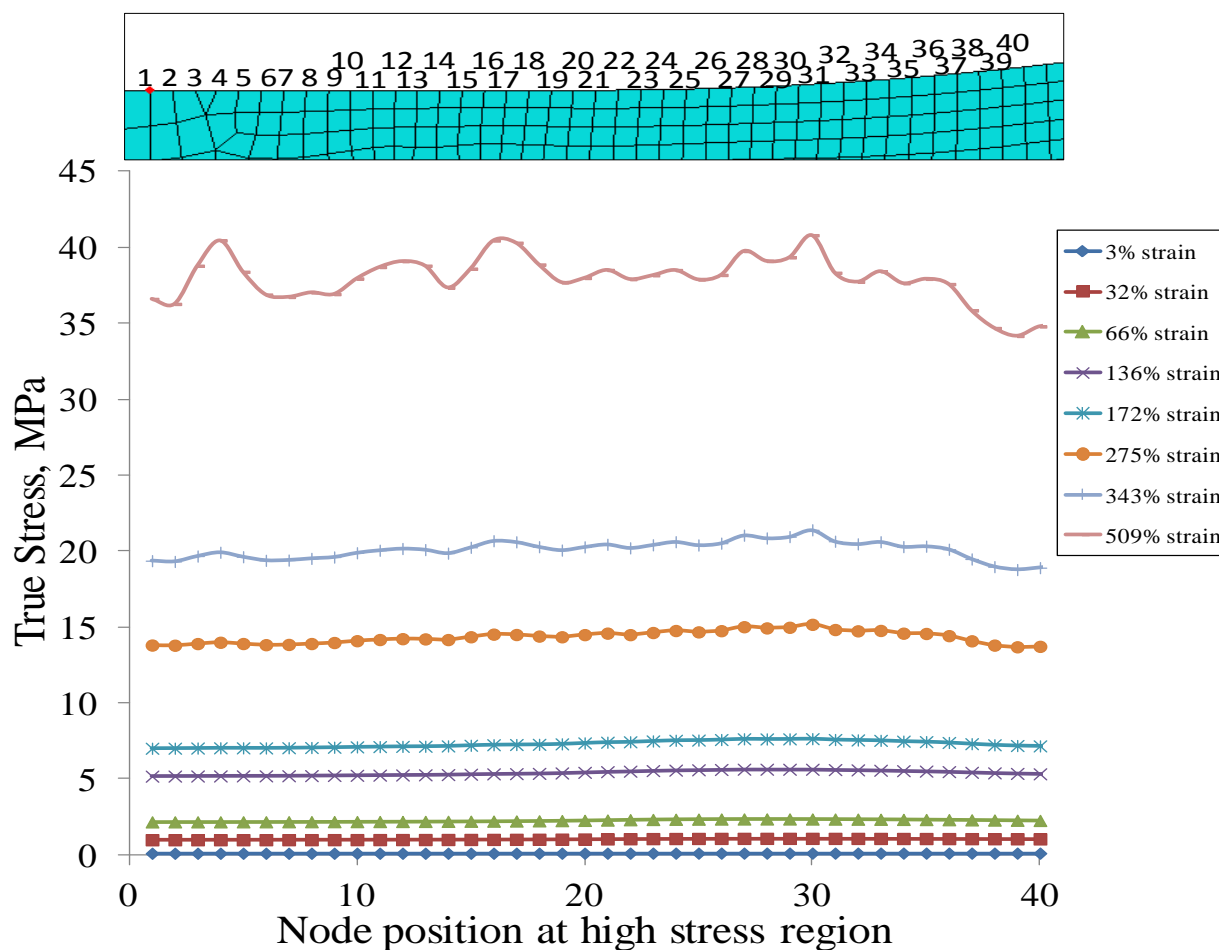

Figure J11: True stress as a function of node position for dumb-bell type 1 (1400 elements).

Figure J12 provides the ratio of stresses as a function of strain. The finer mesh yields a slightly higher ratio compared to the coarser mesh at low strain. At high strain the reverse holds.
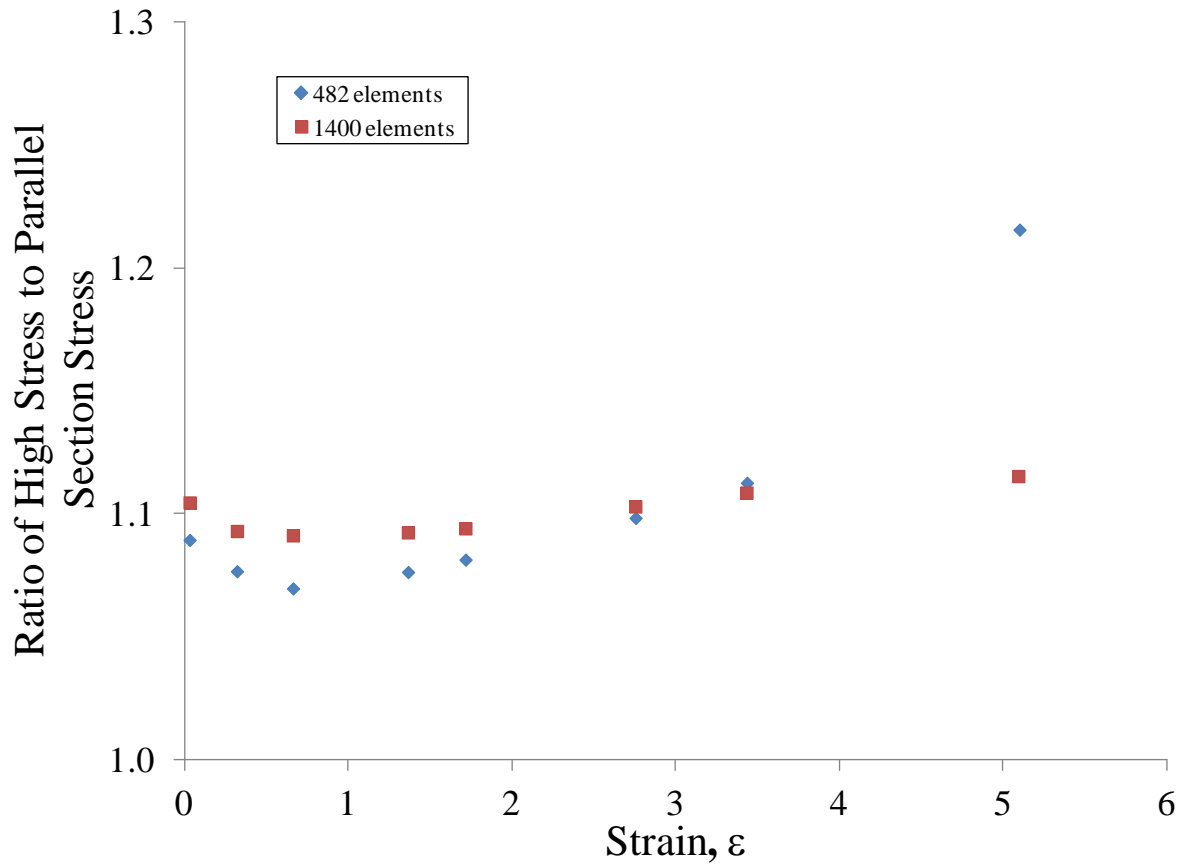

Figure J12: Graph of the ratio of true stresses as a function of strain for dumb-bell type 1.

Figure J13 shows the contour plots relate to undeformed Type 1A test piece.
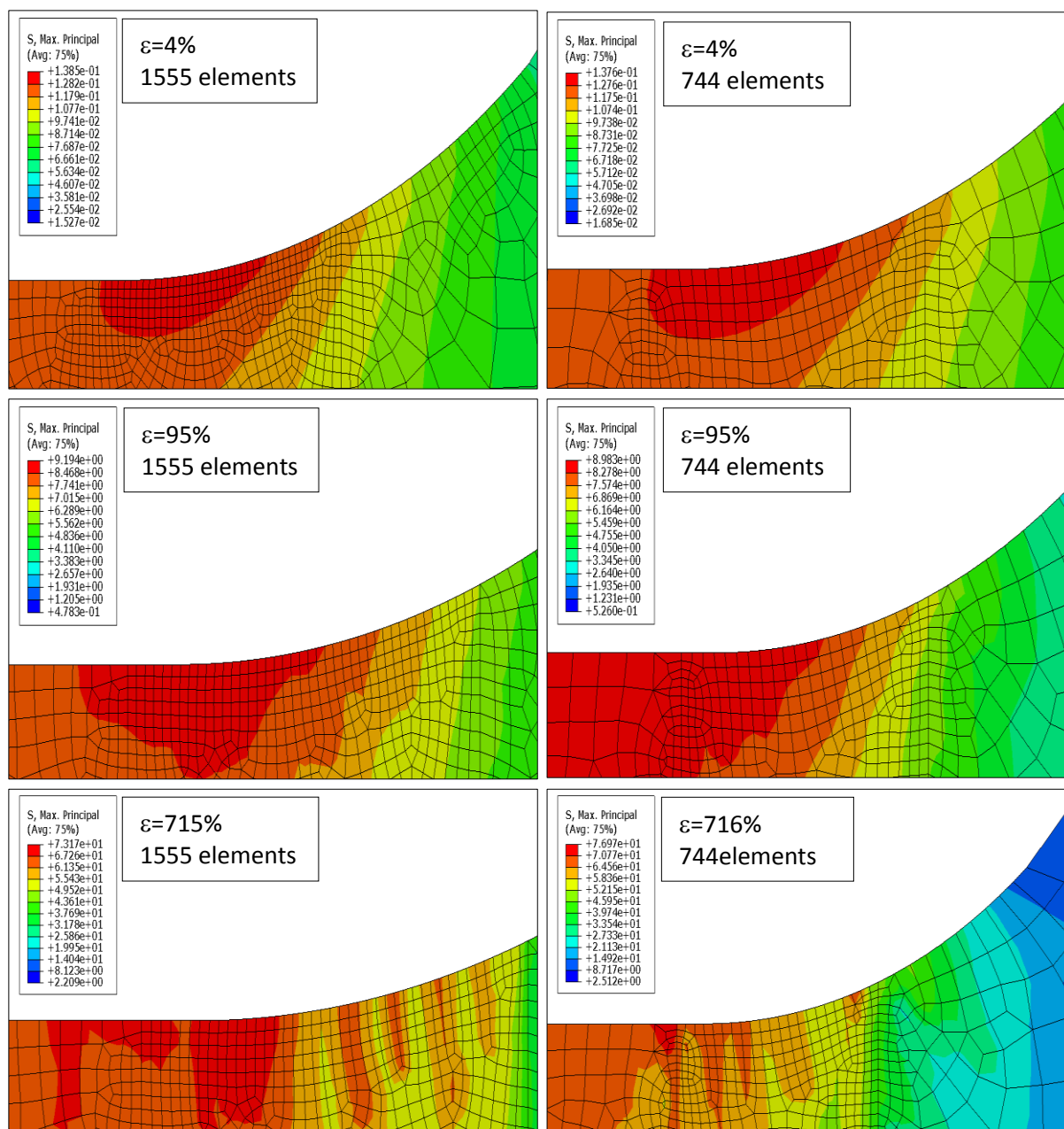
Figure J13: The plot contours of dumb-bell type 1A at the curved side for a range of strain on undeformed shape (given in label).

For dumb-bell type 1A more than two areas were predicted by FEA to be subject to high local stresses when the dumb-bell was stretched to a high strain. At low strains only one high stress area exists near to the onset of curvature (in Figure J13). The analysis results for dumb-bell type 1A indicate a failure would tend to initiate at the onset of the curved side of the dumb-bell. Tables J3 and J4 provide stress analyses for dumb-bell type 1A for two element distributions.

Table J3: Dumb-bell type 1A analysis results of true stress
and the ratio for 744 elements.

Strain, %	True Stress at the middle of dumb-bell, MPa	High True Stress at the curvature, MPa	Ratio
4	0.13	0.14	1.10
45	1.42	1.55	1.09
95	3.28	3.56	1.09
195	8.38	8.98	1.07
245	11.61	12.43	1.07
391	23.80	25.96	1.09
485	33.90	37.16	1.10
715	65.33	72.41	1.11

Table J4: Dumb-bell type 1A analysis results of true stress
and the ratio for 1555 elements.

Strain, %	True Stress at the middle of dumb-bell, MPa	High True Stress at the curvature, MPa	Ratio
4	0.12	0.14	1.11
45	1.42	1.56	1.09
95	3.28	3.59	1.10
195	8.37	9.18	1.10
245	11.58	12.74	1.10
390	23.71	26.15	1.10
485	33.78	37.60	1.11
715	65.31	72.94	1.12

The average ratio of maximum true stress and true stress in the middle part of dumb-bell for the 482 element and 1400 element distributions were both 1.10.

Figures J14 and J15 show the true stress along the curved side of the test piece as a function of node position within the high stress region. Values of true stress were consistent at low strain and became inconsistent at high strain. Some peak stress values are observed when the strain exceeds 245%. Figure J15 indicates that the true stresses are markedly fluctuated at a strain of 716% and decrease along the path of the curved side.
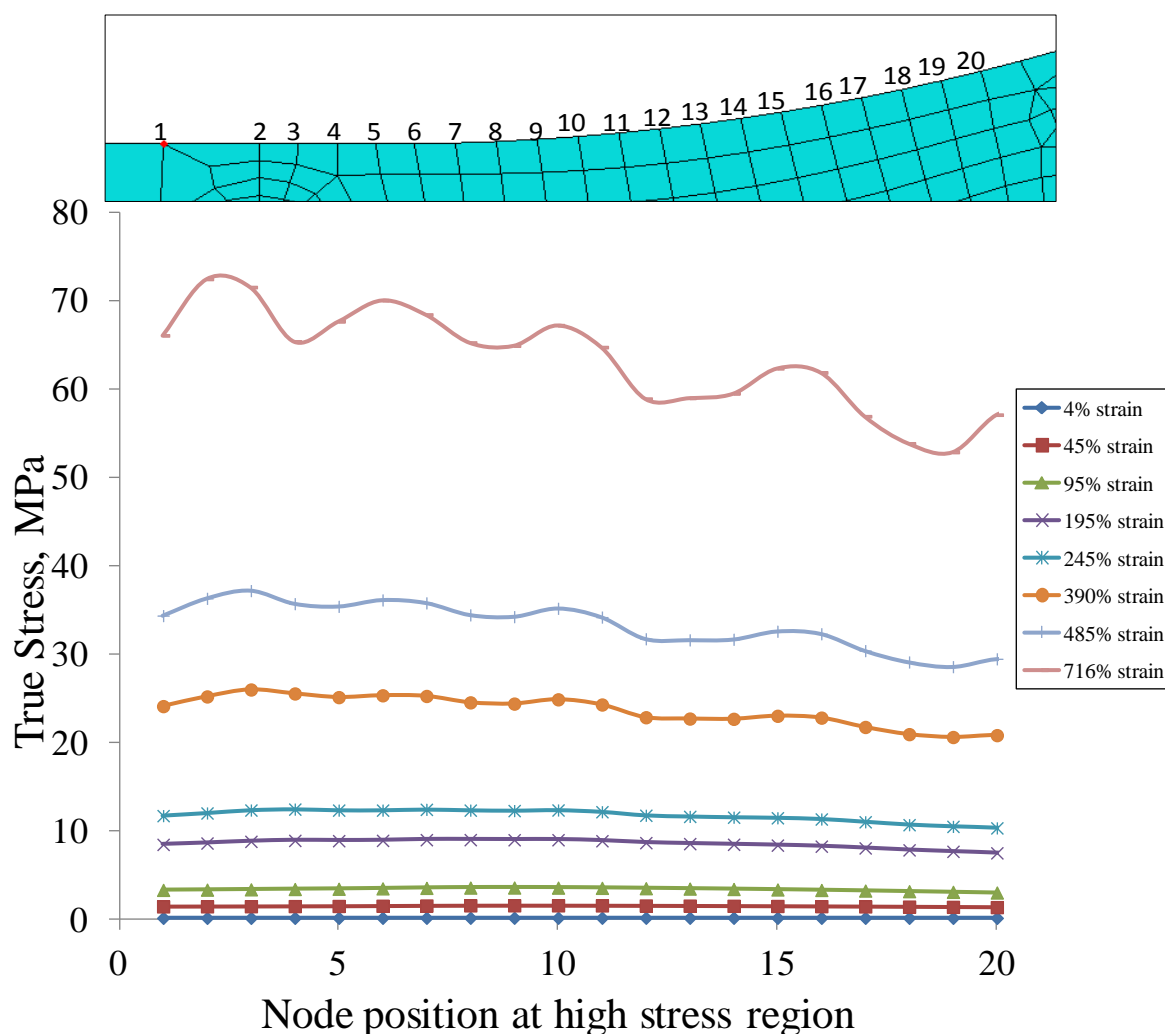

Figure J14: True stress as a function of node position for dumb-bell type 1A (744 elements).

The true stresses of the finer meshed curved side show a similar behaviour with the coarser mesh. However, it is apparent the stresses are fluctuated slightly at high strain and exhibit no significant differences within the strain range 4 to 245%.
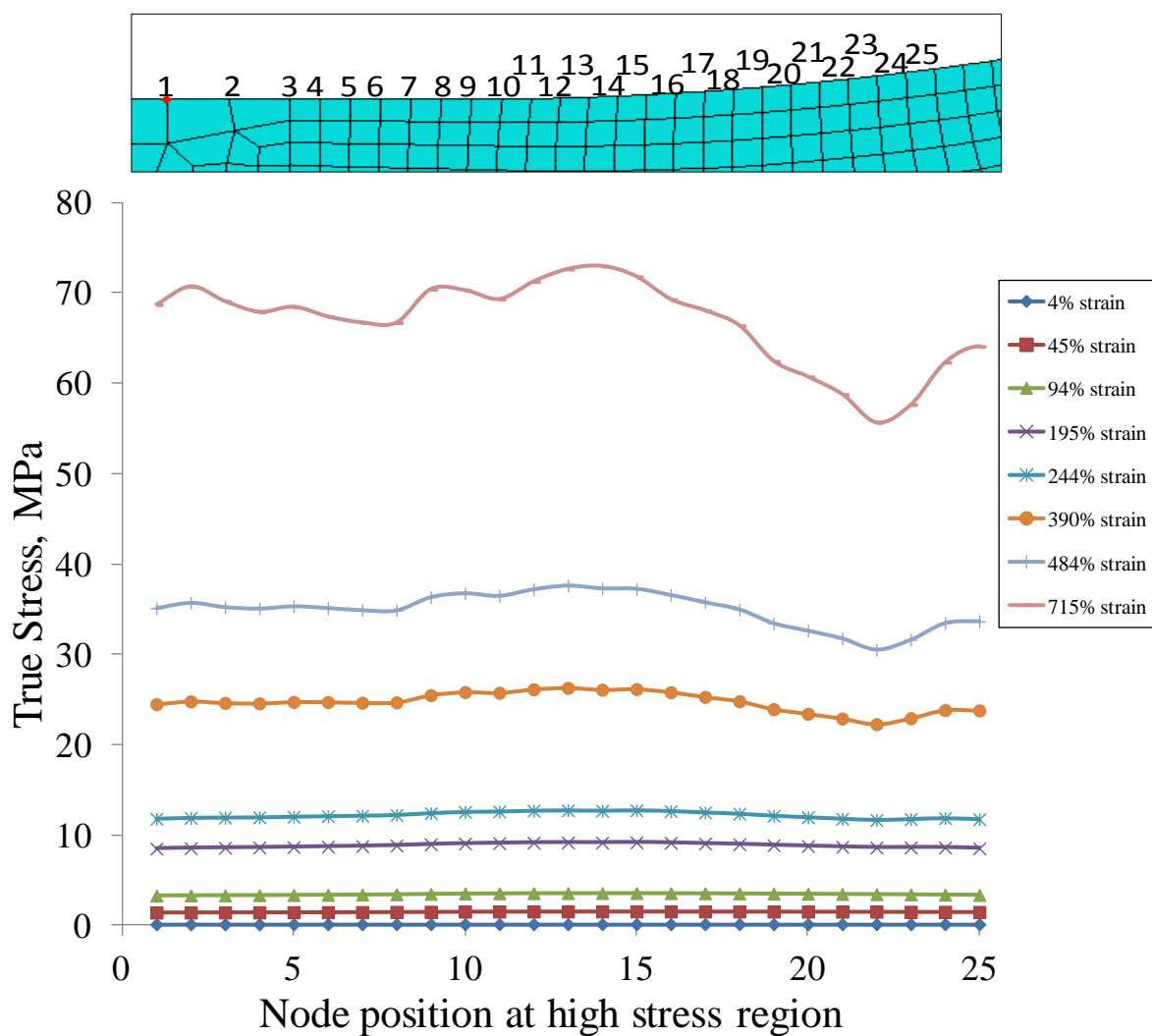

Figure J15: True stress as a function of node position for dumb-bell type 1A (1555 elements).

The average ratio of maximum true stress to that in the parallel sided section of dumb-bell representations of 744 elements and 1555 elements were both 1.10. This ratio of stresses is plotted as a function of strain in Figure J16. The finer mesh gives a slightly higher ratio compared to the coarser mesh at all strains. The finer the mesh for dumb-bell types 1 and 1A the more consistent the ratio of high stress to parallel section stress.
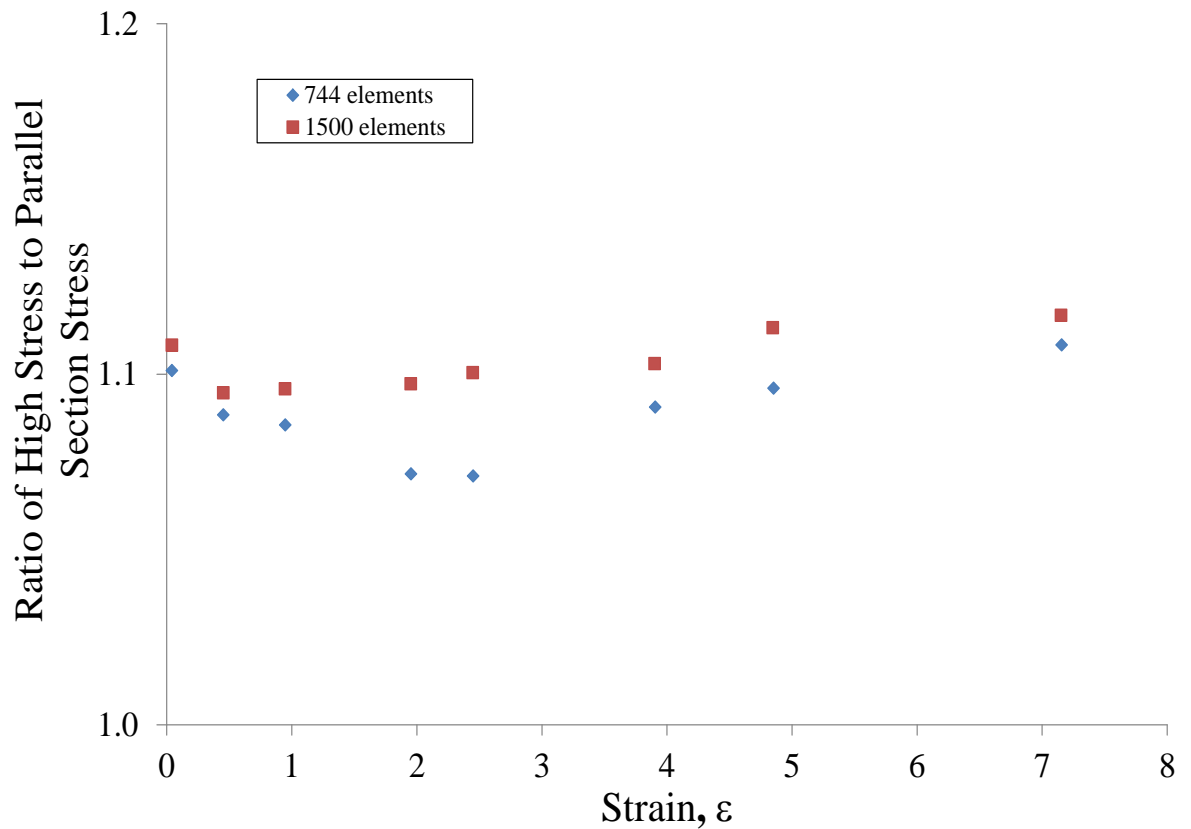

Figure J16: Graph of the ratio of true stresses as a function of strain for dumb-bell type 1A.

Figures J17 provides contour plots of the undeformed shape of Type 2.
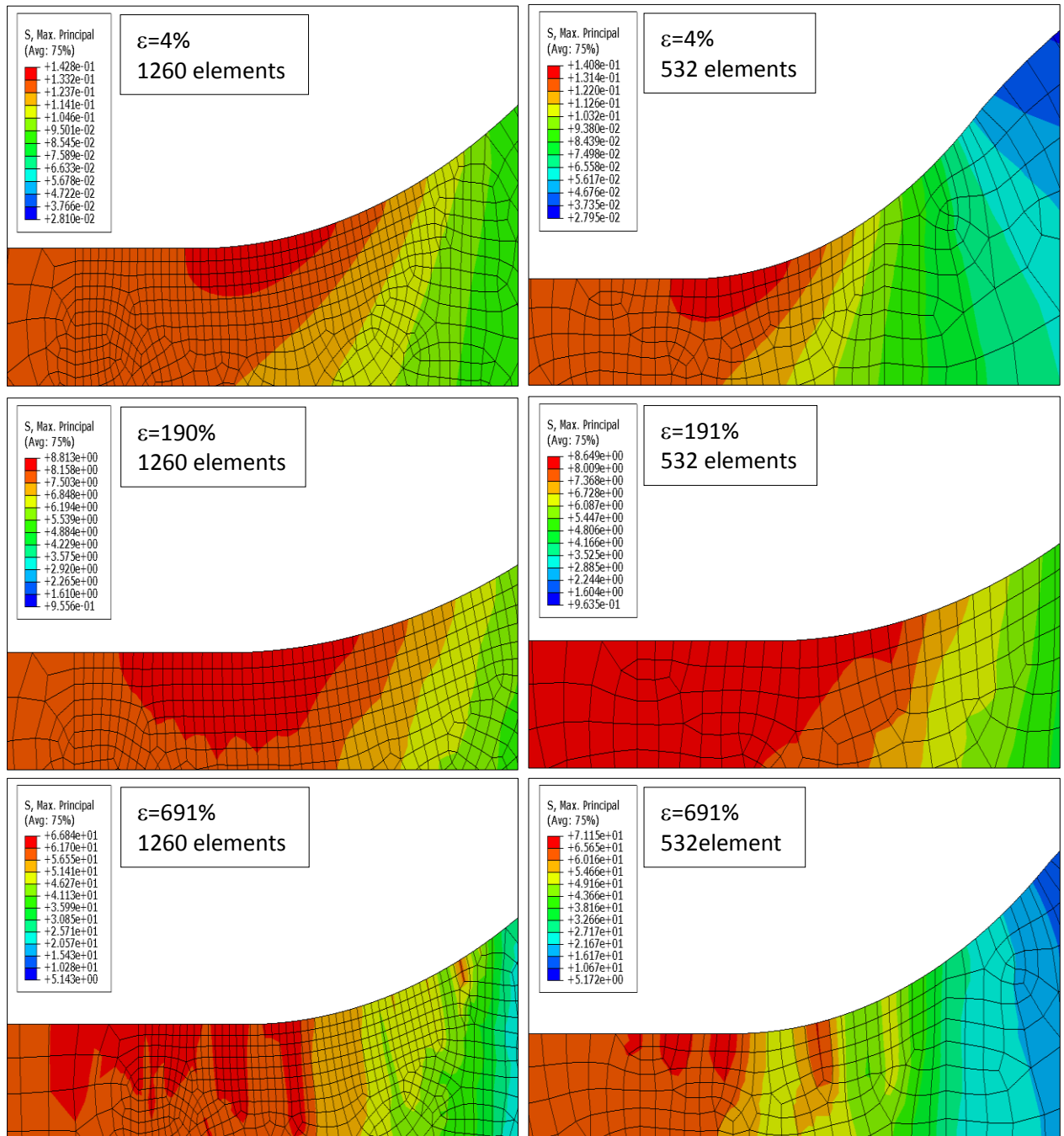
Figure J17: The simulation results of dumb-bell type 2 at the curved side for a range of strains in undeformed shape (given in label).

These contour plots indicate that the location of stress distributions in dumb-bell type 2 were similar to dumb-bell types 1 and 1A, although the dimensions of dumb-bell type 2 are smaller. There was a stress concentration near the start of the curvature. More than two areas of critical stresses were also observed at high strain in the plot contours of Figure J17.

The details of the true stresses within the stress concentration region and in the middle part of dumb-bell are presented in Tables J5 and J6.

Table J5: Dumb-bell type 2 analysis results of true stress and the ratio for 532 elements.

Strain, %	True stress in the parallel section of dumb-bell MPa	Max. true stress at the curved side, MPa	Ratio
4	0.13	0.14	1.10
45	1.42	1.54	1.08
94	3.22	3.46	1.07
191	8.05	8.65	1.07
238	11.08	11.97	1.08
378	22.43	24.57	1.10
469	31.80	35.63	1.12
691	61.07	71.10	1.16

Table J6: Dumb-bell type 2 analysis results of true stress and the ratio for 1260 elements.

Strain, %	True stress in the parallel section of dumb-bell, MPa	Max. true stress at the curved side , MPa	Ratio
4	0.13	0.14	1.12
45	1.42	1.57	1.11
94	3.21	3.55	1.10
191	8.04	8.81	1.10
238	11.06	12.07	1.09
378	22.39	24.20	1.08
469	31.75	34.16	1.08
691	61.18	66.84	1.09

The averages of the ratio for both type of elements was 1.10; this is similar to the behaviour of dumb-bells types 1 and 1A.

Figures J18 and J19 illustrate the true stress along the curved side of dumb-bell type 2 as a function of node position within high stress region. The same stress behaviour exhibited is similar to the other types of dumb-bells. Again true stress values are very smoothly with position at low strain and become inconsistent at high strain. Some peak stress values were considerably decreased when the strain increased beyond 300%. Figure J18 clearly indicates that the true stresses are markedly fluctuated at a strain of 691% and significantly decreased along the path of the curved side.
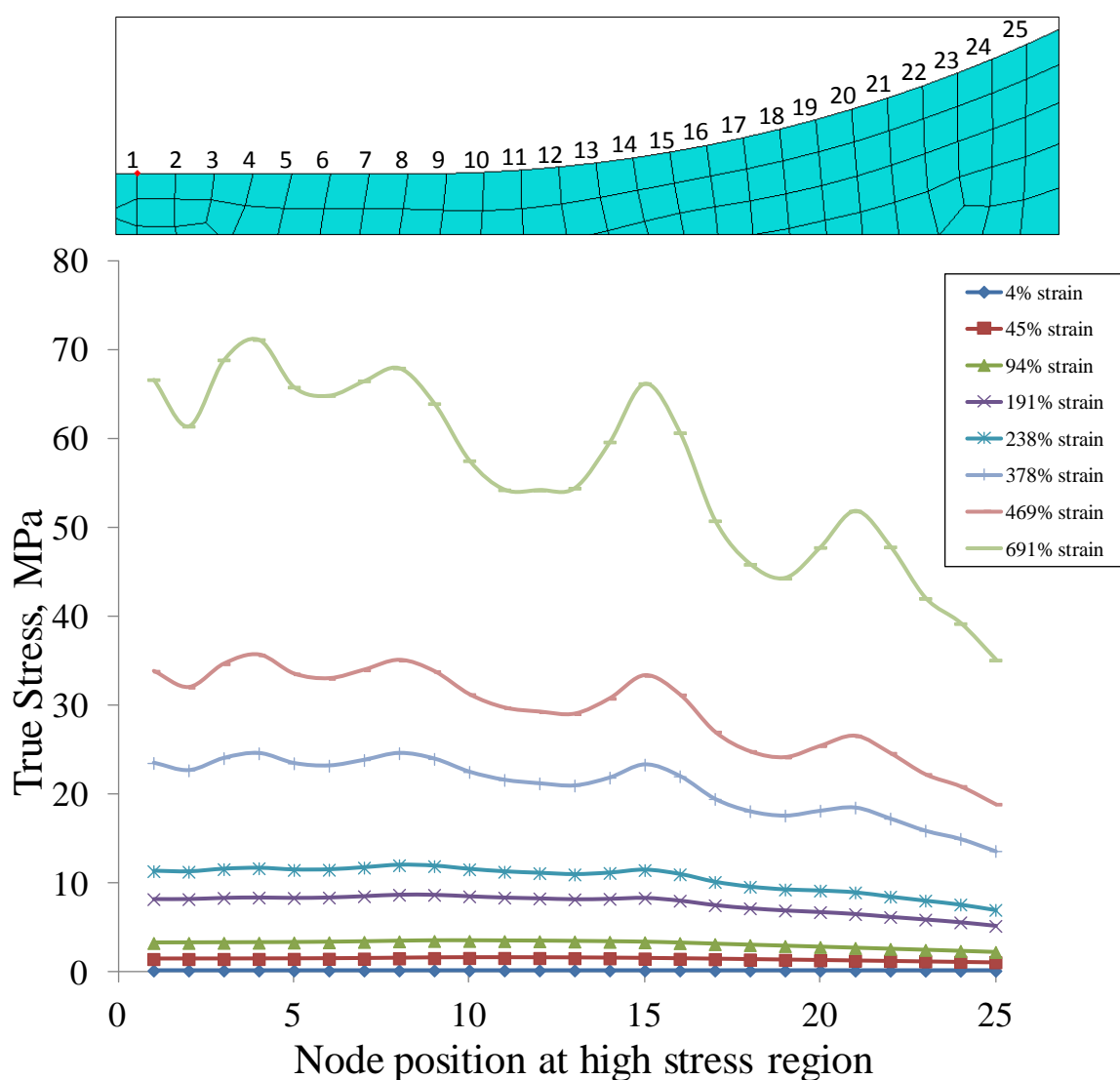

Figure J18: True stress as a function of node position for dumb-bell type 2 (532 elements).

Interestingly, the stress distribution of the dumb-bell type 2 finer mesh was only slightly decreased along the curved side path within the strain range of 375 to 690%.
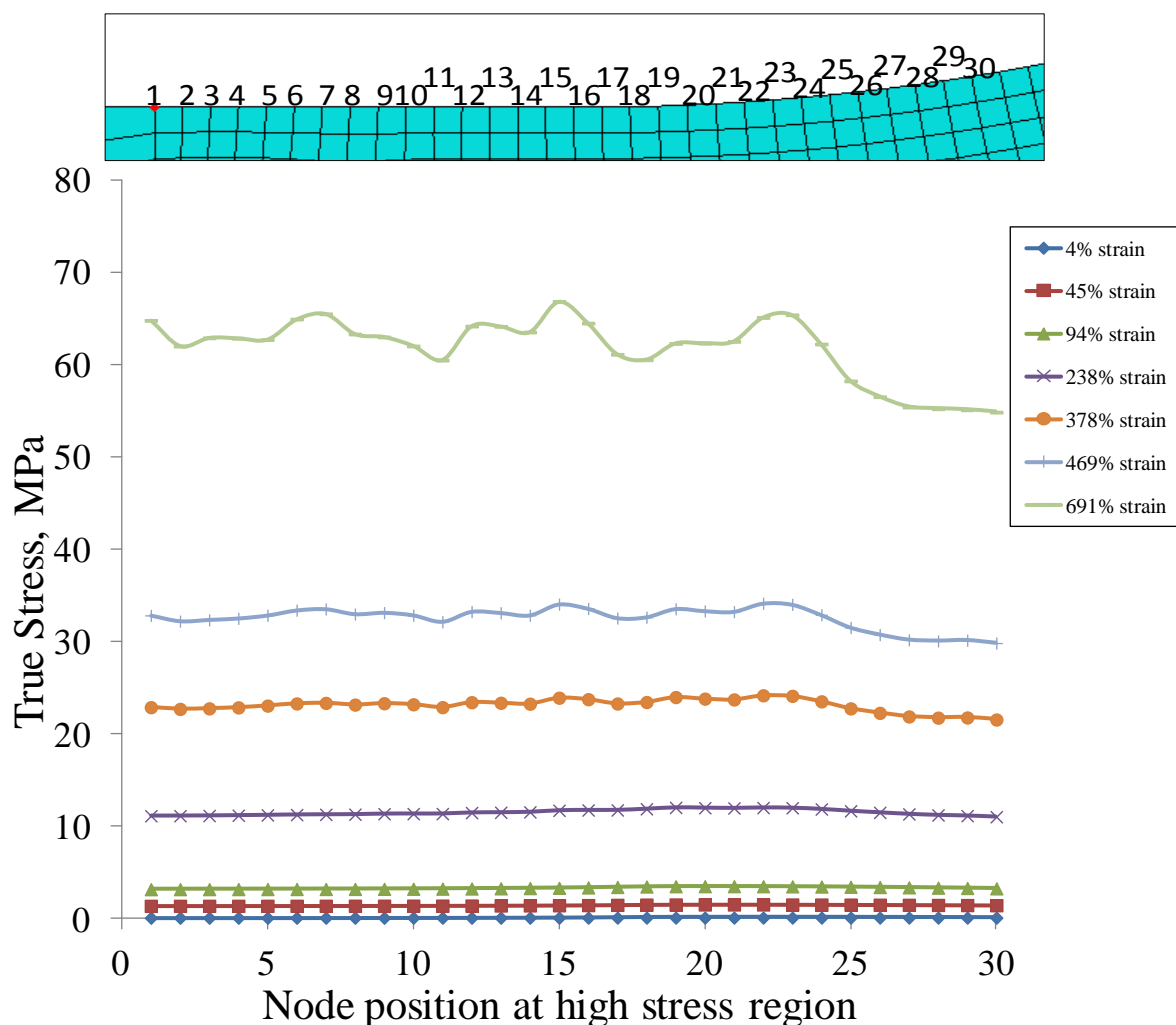

Figure J19: True stress as a function of node position for dumb-bell type 2 (1260 elements).

The fine mesh model tends to show a slightly higher ratio than the coarser mesh at low strain but at high strain the reverse is true. Figure J20 provides a comparison of both models. All stress concentrations at the onset of curvature of dumb-bell types 1, 1A and 2 were higher rather than in other regions, suggesting that the initiation of failure would tend to occur there.
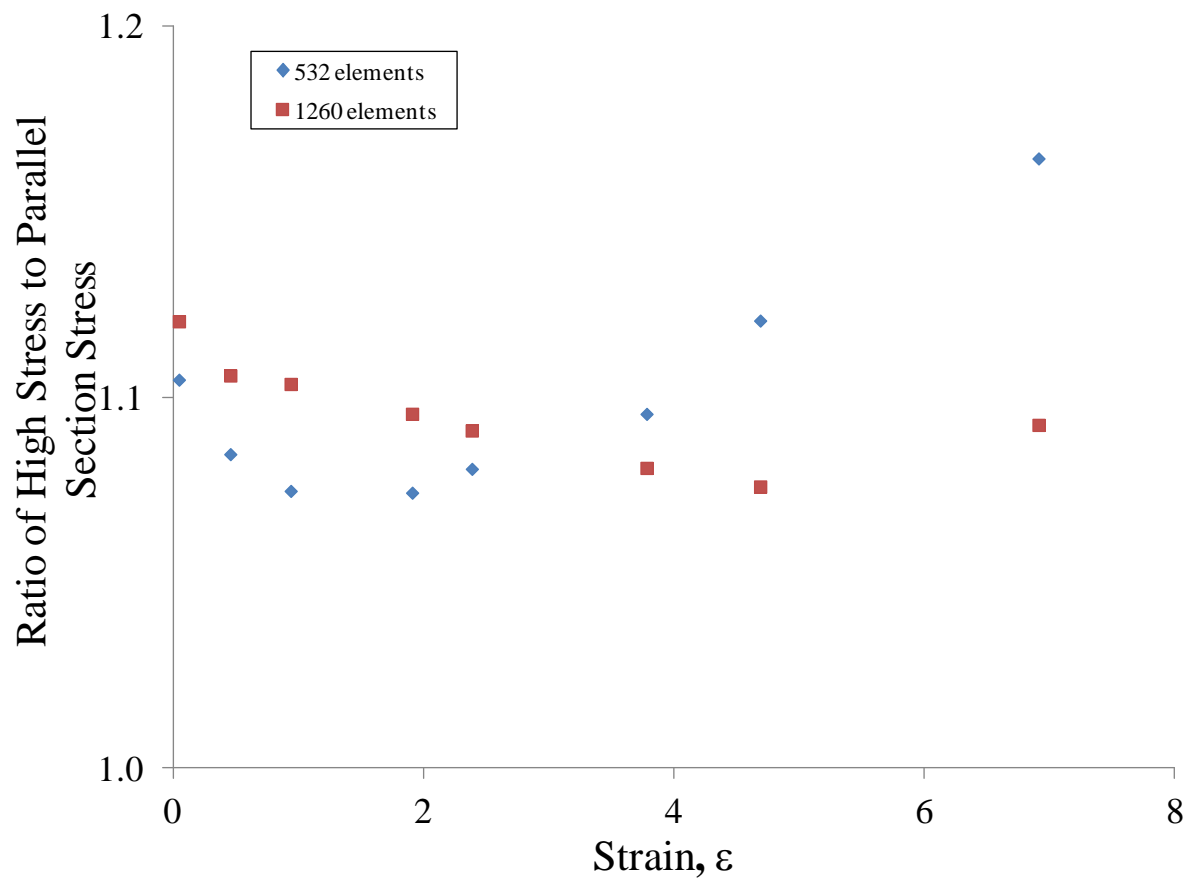

Figure J20: Graph of the ratio of true stresses as a function of strain for dumb-bell type 2.

British Standards [BS ISO 6943:2007 & BS 37:2005] specified the form of dumb-bell types 1, 1A and 2 normally used for fatigue and tensile strength tests. There seems to be no reason to select any one standard for conducting mechanical tests since the ratio of the maximum stress to the parallel section stress were observed here to be identical. Table J7 shows there is no correlation of dimension with the average of stress ratios.

Table J7: Comparison of dimension and stress ratio.

Dumb-bell	External radius/width of parallel-sided portion	Average of the stress ratio at the finer mesh
Type 1	2.3	1.10
Type 1A	2.2	1.10
Type 2	2	1.10

The testing machine stroke capability is important in terms of specifying which standard dumb-bell type is appropriate for a specific test. Most of the dumb-bells showed the peak value of the maximum principal stress to be near to the curved side at high strain. Figure J21 shows the FEA results of strain distributions from BS ISO 37:2005. These strain distributions in particular being different for each dumb-bell type, were not corroborated here. This may relate to the numerical difficulties in extracting plausible results at high strain, but no explanation for the discrepancy at low strain is evident.

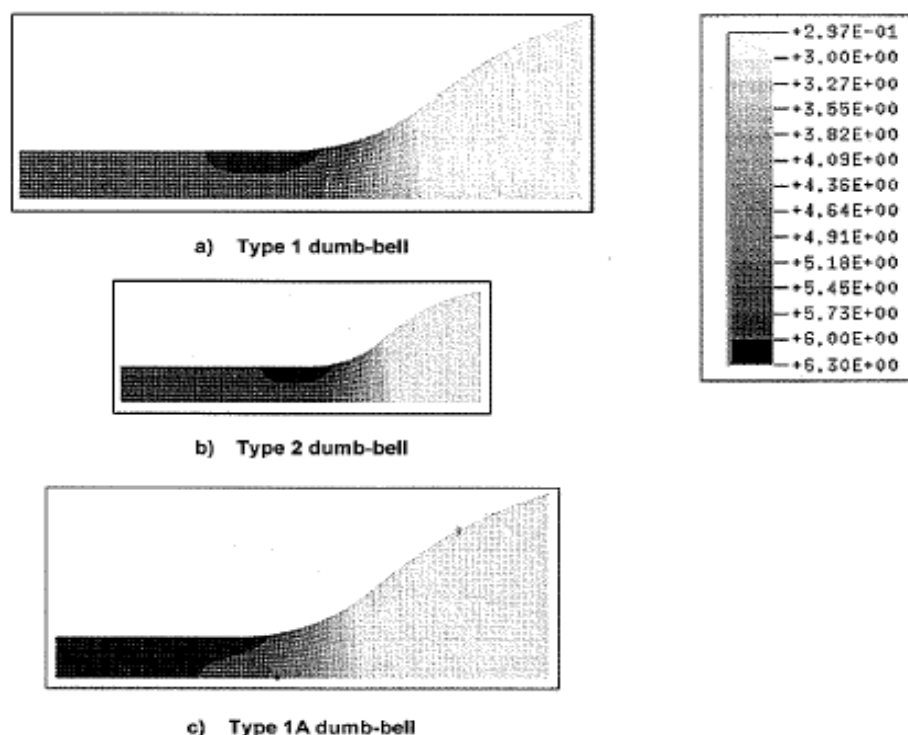Figure J21 shows the FEA results of strain distribution from BS ISO 37:2005.

a) Type 1 dumb-bell

b) Type 2 dumb-bell

c) Type 1A dumb-bell

Figure J21: Example of strain distribution obtained using "ABAQUS" – Figure C.3
[BS ISO 37:2005].

Based on the results generated and presented here, the maximum stress is not sensitive to dumb-bell mesh density.

Summary

Finite Element Analysis (FEA) has been used to predict the maximum local stress for a strained dumb-bell test piece at low and high strains. A stress concentration is present near the onset of curvature as the narrow part of the dumb-bell blends into the tab, with a stress around 7 to 10% higher for dumb-bell Type 2, 8 to 10% higher for Type 1 and 8 to 10% higher for Type 1A than the stresses in the parallel section, (depending on strain). At higher strain there are several local stress maxima but this seems most likely to be due to a problem of discretization.

It appears that the stress concentration is associated with the increase in width of the rubber. Although it seems likely that increasing the radius of curvature in this section assuming

always that the edge is asymptotic to the parallel-sided section would reduce the stress concentration, the results in Table J7 do not provide evidence for this.